UNCONTROLLED AEROBATIC TUMBLE MANOEUVRE MECHANICS

Stefano Fabrizio Piccolo

A dissertation submitted to the Faculty of Engineering and the Built Environment, University of the Witwatersrand, in fulfilment of the requirements for the degree of Master of Science in Engineering

Johannesburg, 2024

UNIVERSITY OF THE WITWATERSRAND, JOHANNESBURG

SCHOOL OF MECHANICAL, INDUSTRIAL AND AERONAUTICAL ENGINEERING

INDIVIDUAL DECLARATION WITH TASK SUBMITTED FOR ASSESSMENT

I, (name) **Stefano Fabrizio Piccolo**, (Student number) **533352**, am registered for Course No. **MECN8003A**, (course name) **MSc by Dissertation: Aerospace** in the year **2024**.

I herewith submit the following task, "**Uncontrolled Aerobatic Tumble Manoeuvre Mechanics.**" In fulfilment of the requirements of the above course.

I hereby declare the following:

- I am aware that plagiarism (the use of someone else's work without their permission and / or without acknowledging the original source) is wrong;
- I confirm that the work submitted herewith for assessment in the above course is my own unaided work except where we have explicitly indicated otherwise;
- This task has not been submitted before, either individually or jointly, for any course requirement, examination or degree at this or any other tertiary educational institution;
- I have followed the required conventions in referencing the thoughts and ideas of others;
- I understand that the University of the Witwatersrand may take disciplinary action against me if it can be shown that this task is not my own unaided work or that I have failed to acknowledge the sources of the ideas or words in my writing in this task.

Signature:  Date: **13-05-2024**

ABSTRACT

Despite advancements in aerobatic aircraft, the issues concerning aerobatic flight safety remain largely unresolved with incidents occurring at airshows, during training and during private flights, even with stable, predictable and reliable aircraft. The likelihood of aerobatic incidents has increased as aircraft are now capable of being flown in even more dangerous, low energy scenarios. Spins or tumble manoeuvres are typically the origin of loss-of-control accidents. Such scenarios occur generally in manoeuvres that result in low energy states. This dissertation aims to understand the mechanics behind a low energy aerobatic manoeuvre. The positive g tumble manoeuvre was selected as the manoeuvre to analyse, as it is one of the most difficult aerobatic manoeuvres to recover from. The Extra 330SC was selected as the model aircraft as it is one of the most popular aerobatic aircraft across all pilot skill levels. Additionally, the Extra Aircraft Corporation provided more information about the aircraft than any other aerobatic aircraft manufacturer.

Methods to develop mass, inertial and aerodynamic data were explored. The aerodynamic data was extended to high angles of attack. Aerodynamic models for the wing, fuselage, horizontal stabiliser and propeller were considered. Generated mass and inertial data were compared to reference data and demonstrated good correlation. Static aerodynamic data was compared to published experimental data (where possible). Good agreement was shown between the generated data and test data. Considerations for surfaces exposed to propeller slipstream and rotational dynamics were considered. No literature was available for direct comparison of these considerations.

A non-linear three degree of freedom model was developed to simulate the tumble manoeuvre. This was achieved by simplifying the equations of motion in the velocity axes. The velocity axes were appropriate in determining the flight path of the manoeuvre along with all affiliated parameters. The aircraft body axes were utilised in determining the rotational parameters during the tumble manoeuvre. Force components at high angles of attack were modelled in both the velocity and body axes. The current model does not include any lateral-directional forces or moments, assuming the manoeuvre is purely in the longitudinal plane.

A tumble manoeuvre is possible for a very specific aircraft configuration. An upgraded engine and propeller slipstream effects are essential in performing the tumble manoeuvre. It was shown the entire manoeuvre could be completed in a horizontal distance of ≈ 50 m and a vertical distance of ≈ 15 m for manoeuvre entry velocities of 25 m/s, 30 m/s, 35 m/s and 40 m/s. Each of the minimum radius tumble manoeuvres occurred at the most rearward centre of mass location. An entry velocity of 30 m/s provided the smallest possible radius tumble. The entry to the manoeuvre requires large decelerations and normal forces that were beyond the lift limits of the wing. Both these requirements were met by orientating the aircraft at large pitch angles and subsequently large angles of attack. The large angles of attack resulted in large decelerating forces and orientated various aircraft force components, other than

the wing, in the lift direction. Significant energy loses are seen through the manoeuvre resulting in large losses in airspeed and ultimately altitude. The risks associated with a tumble manoeuvre could be minimised by adjusting the normal forces and moments acting on the aircraft. By altering the propeller blade pitch angle, the normal forces and subsequently the moments from the propeller could be changed, altering the overall normal forces and moments acting on the aircraft. This resulted in a slightly larger overall manoeuvre but illustrated increased velocity values throughout the manoeuvre. A form of validation of the results was performed by comparing model results of tumble manoeuvres that were generated through a patchwork of images compiled from video footage of the manoeuvre. Good correlation was shown between the model data and video footage.

CONTENTS

LIST OF FIGURES

LIST OF TABLES

1. INTRODUCTION

1.1. Background

1.1.1. Aerobatic Flight and the Tumble Manoeuvre

Aerobatics is a category of flight in which an aircraft performs an intentional manoeuvre, involving aircraft attitudes, accelerations and altitudes, all of which are not required for normal flight [1], [2]. Aerobatic flight is one of the most spectacular aerial displays, which exemplifies the manoeuvring capabilities of an aircraft when controlled by an experienced pilot [3]. Aerobatic flying requires a wider set of piloting skills and may expose the aircraft to greater structural stresses than those seen in normal flight [4]. A myriad of aerobatic manoeuvres exist, some of the better known being rolls, loops, stall turns (hammerheads), spins, upward vertical flight, and whip stalls [2]. The roll (also known as the aileron roll) is one of the simpler aerobatic manoeuvres, illustrated in Figure 1. The manoeuvre involves a 360° rotation of the aircraft about the longitudinal axis of the aircraft (the axis extending from the nose to the tail of the aircraft down the centreline) and is achieved using the ailerons, while the elevator and rudder usually remain in the neutral position. This manoeuvre is generally performed in a smooth manner without any breaks or jerks. Variations of this manoeuvre include the snap roll, the slow roll and the barrel roll. These manoeuvres use elevator and rudder input in addition to aileron deflection.

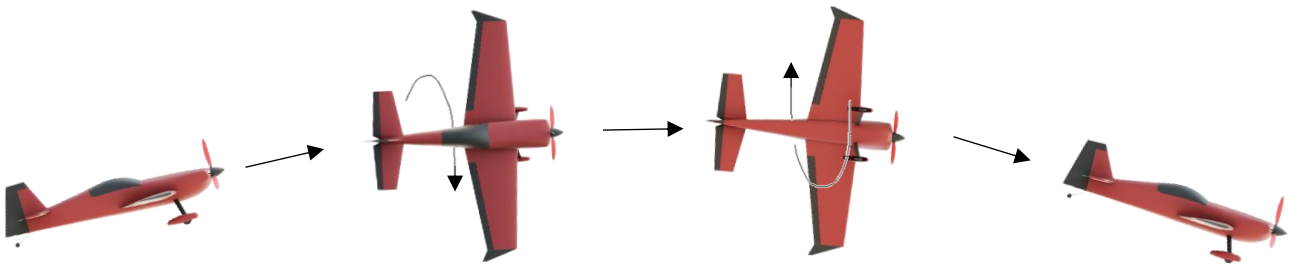

Figure 1: The aileron roll aerobatic manoeuvre

A loop manoeuvre involves creating a circular or elliptical shape in the sky. The most common types of loop manoeuvres consist of the inside loop and the outside loop. The inside loop is illustrated in Figure 2(a). The manoeuvre is entered by applying elevator, from a level flight attitude, such that the aircraft pitches up at approximately 3 g to 4 g. The elevator is applied until the aircraft is in a vertical orientation after which the elevator pressure is relaxed slowly so that the aircraft “floats” over the top of the loop. Beyond the top-most point, the back pressure from the elevator is slowly increased until the aircraft is once again in a level flight orientation. To perform the manoeuvre correctly there should be

no roll angle while the aircraft is following the flight path (traced out by the arrows in Figure 2(a)). This implies that some aileron input may be required. The rudder may also be required to maintain a constant heading. A perfect loop would involve entering and exiting the loop at the same point. The outside loop is identical to the inside loop; however, the aircraft is inverted with the top of the aircraft facing outwards throughout the loop. This is illustrated in Figure 2(b). Upon exiting the manoeuvre, the pilot will often transition into another manoeuvre or roll the aircraft back to the correct orientation.

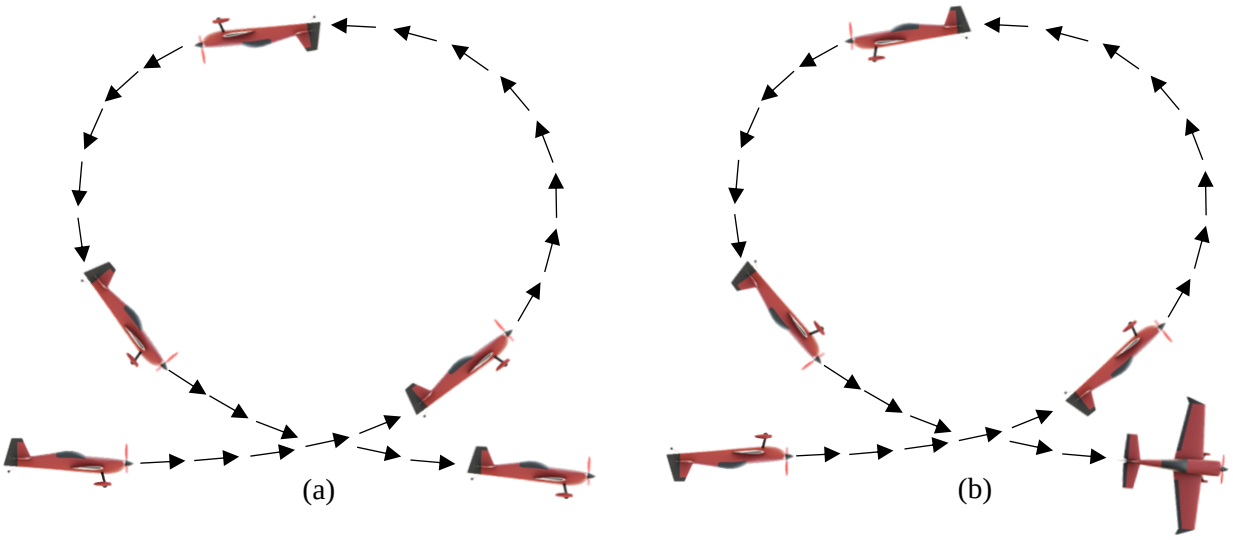

Figure 2: (a) The inside loop aerobatic manoeuvre (b) the outside loop aerobatic manoeuvre

The stall turn, also called the hammerhead, is another vertical manoeuvre like the loop manoeuvre and is illustrated in Figure 3. The stall turn allows the direction of the aircraft to be changed through 180° within a limited amount of airspace and without forfeiting much energy. The manoeuvre makes use of the rudder and is a relatively simple manoeuvre. The manoeuvre begins with a vertical climb. The pilot reduces power towards the apex of the manoeuvre. This is done to slow the aircraft down to a stop. Once this has occurred, full rudder is applied to rotate the aircraft by 180°, pointing the nose of the aircraft towards the ground. Unlike the loop manoeuvre the pilot need not pull as many g's while performing the manoeuvre.

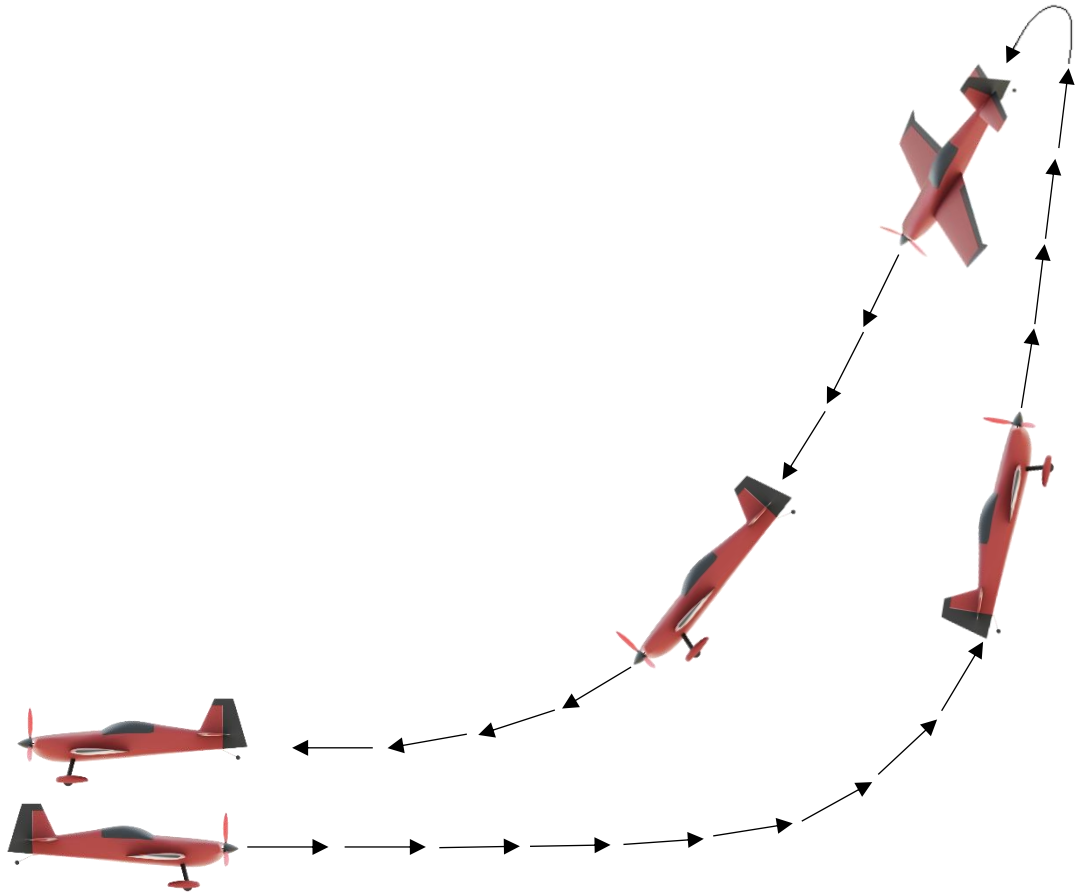

Figure 3: The stall turn aerobatic manoeuvre

Simple aerobatic manoeuvres such as rolls and loops can be performed together to form combined manoeuvres. An example of such a manoeuvre is the Cuban 8 which incorporates both rolls and loops. This is illustrated in Figure 4. The manoeuvre is initiated by flying straight and level. After a short time, full power and elevator is applied to pitch the aircraft up and enter a climb, in an identical manner to which the inside loop is initiated. The aircraft is allowed to go into a vertical climb and continues over onto its back at the top of the loop. Just after the aircraft has reached the top of the loop, ailerons are applied to smoothly roll through 180°, bringing the aircraft right side up. Power is then slightly reduced and elevator is used to maintain a 45° dive. After the brief dive the aircraft is levelled out at the same altitude at which the manoeuvre was entered. As soon as the aircraft is levelled out power is applied once again and a second loop is initiated. As with the first loop the aircraft is allowed to loop over onto its back before rolling through 180^0 and diving at 45° to the horizontal to resume straight level flight. An ideal manoeuvre would have the aircraft exiting the manoeuvre at the same height at which the aircraft entered the manoeuvre.

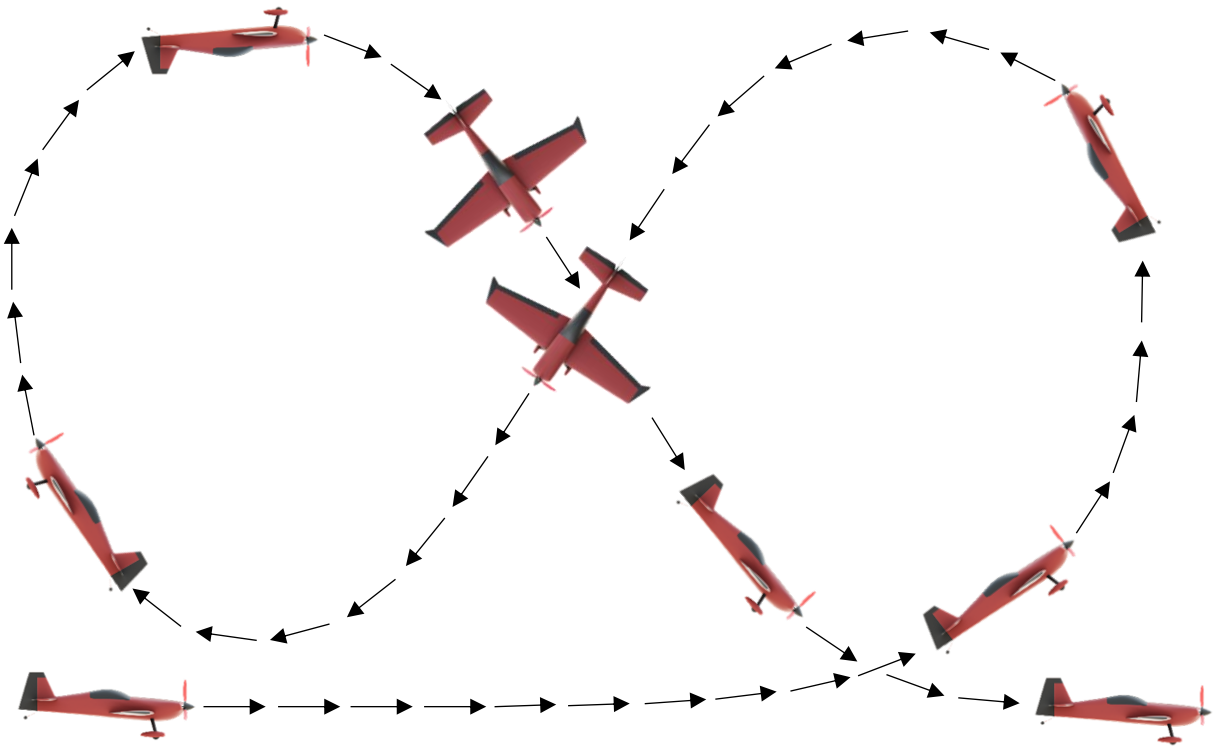

Figure 4: Cuban 8 aerobatic manoeuvre

Various manoeuvres are often combined and performed sequentially to form a complete aerobatic sequence. Aerial display sequences are performed both for entertainment and competition. An example of an aerobatic display sequence is illustrated in Figure 5.

In recent decades, advancements in aerodynamics and adaptive flight control have allowed aircraft to fly at higher angles of attack and at very low speeds, ushering in a new era of aerobatic flight. Aerobatic display aircraft have thus become even more manoeuvrable, expanding the operational domain of these aircraft, allowing even more dangerous manoeuvres to be performed. One such manoeuvre which has arisen, as a result of improved modern aircraft, is the aerobatic tumble manoeuvre. This manoeuvre will be the focus of this paper. The manoeuvre was selected due to the lack of information regarding the manoeuvre in the public domain. A Google Scholar search containing the search terms: “Aerobtaic tumble manoeuvre”, “Aerobatic tumbling manoeuvre”, “Aircraft backflip manoeuvre”, “Aircraft tumble” was performed. No published work was found for tumble manoeuvres of aerobatic aircraft.

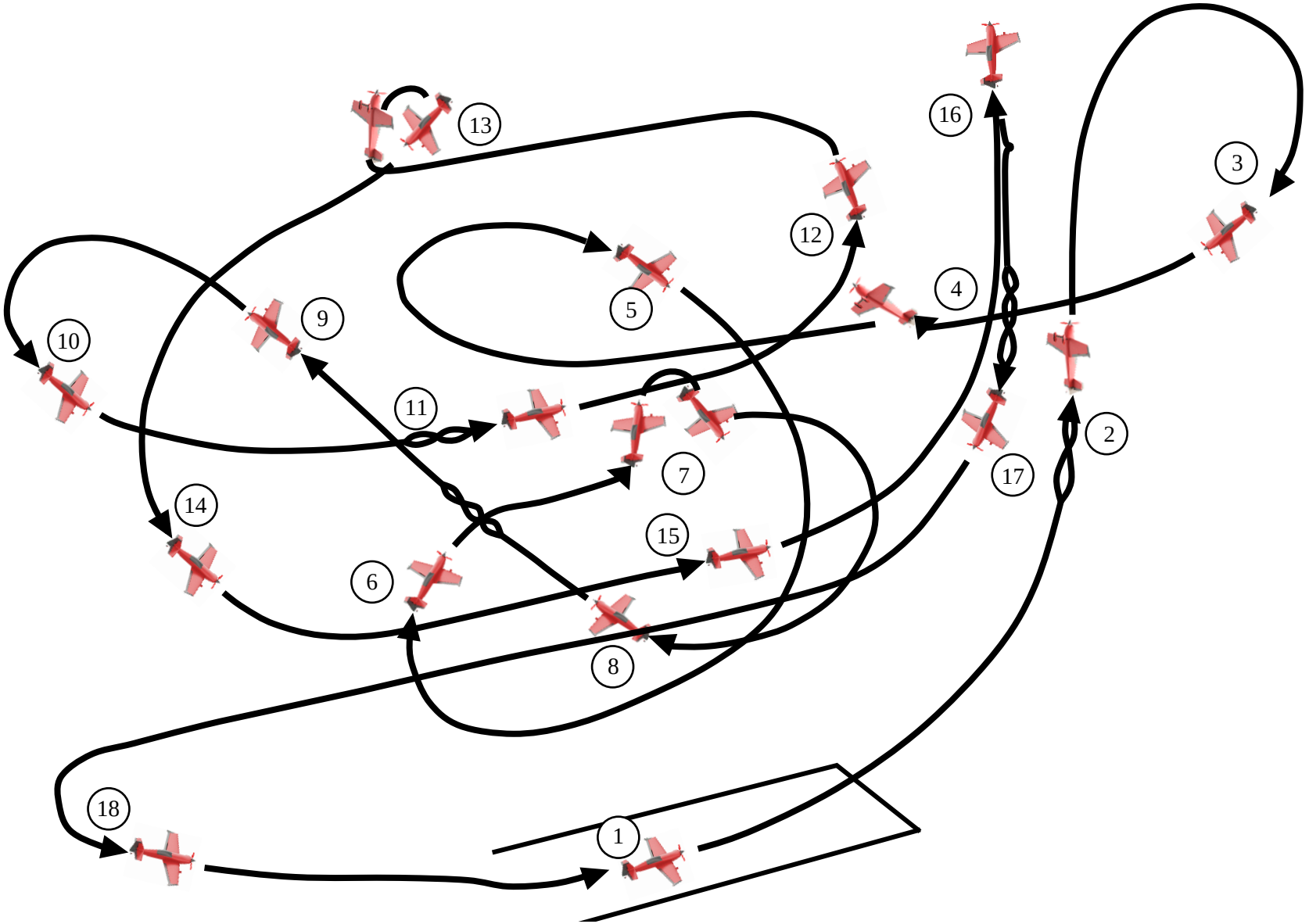

Figure 5: Example of an aerobatic display sequence

Energy Management

An important aspect in performing an aerobatic display is the management of aircraft energy. Energy management can be defined as the process of planning, monitoring, adjusting and controlling alititude and airspeed targets in relation to the state of energy of the aircraft. This is done in order to:

1. Attain and maintain desired non-horizontal flightpath-airspeed profiles [5]
2. Detect, correct and prevent unintentional altitude and airspeed deviations from the desired energy state [5]
3. Prevent irreversible deceleration and/or sink rate that results in a crash [5]

Emphasis of good energy management should be stressed to pilots in training, espcially those aiming to perform aerobatics. Mistakes in managing the energy state of the aircraft can be deadly. The mismanagement of mechanical energy (altitude and/or airspeed) is a contributing factor to the three most common types of fatal accidents in aviation: loss of control in flight (LOC-I), controlled flight into terrain (CFIT) and approach and landing accidents [5]. The total mechanical energy of an aircraft in flight is the sum of its potential energy (from altitude) and kinetic energy (from airspeed). A flying aircraft is an 'open' energy system, meanings that the aircraft can gain energy from some source (e.g. fuel) and lose energy to the environment (e.g. the surrounding air). Energy can be added to or removed from the total mechanical energy of the aircraft stored as altitude and airspeed [5]. Energy management is particularly important for manoeuvres such as the aerobatic tumble, as the aircraft brought to a very low (near zero) airspeed. This places the aircraft into a state of very low mechanical energy, requiring losses in altitude to recover airspeed and normal aircraft attitudes.

The Tumble Manoeuvre

The aerobatic tumble manoeuvre can most simply be understood as a minimum radius loop where the aircraft velocity reaches a near zero value. The tumble is an extreme aerobatic manoeuvre that involves a rotation of the aircraft about its lateral axis (the axis which extends from one wingtip to the other), with almost no forward speed. It is generally performed by single engine propeller driven aircraft. Some fourth and fifth generation fighter aircraft are likely also capable of performing this manoeuvre, however, the mechanics behind the manoeuvre will be different to those of a propeller driven, piston aircraft. The manoeuvre can be performed one of two ways, by rotating the tail of the aircraft under the nose (the positive g tumble) or by rotating the tail of the aircraft over the nose (the negative g tumble). The report will focus on the positive g tumble manoeuvre as it is the more difficult of the two types of tumble, both in entering and exiting the manoeuvre.

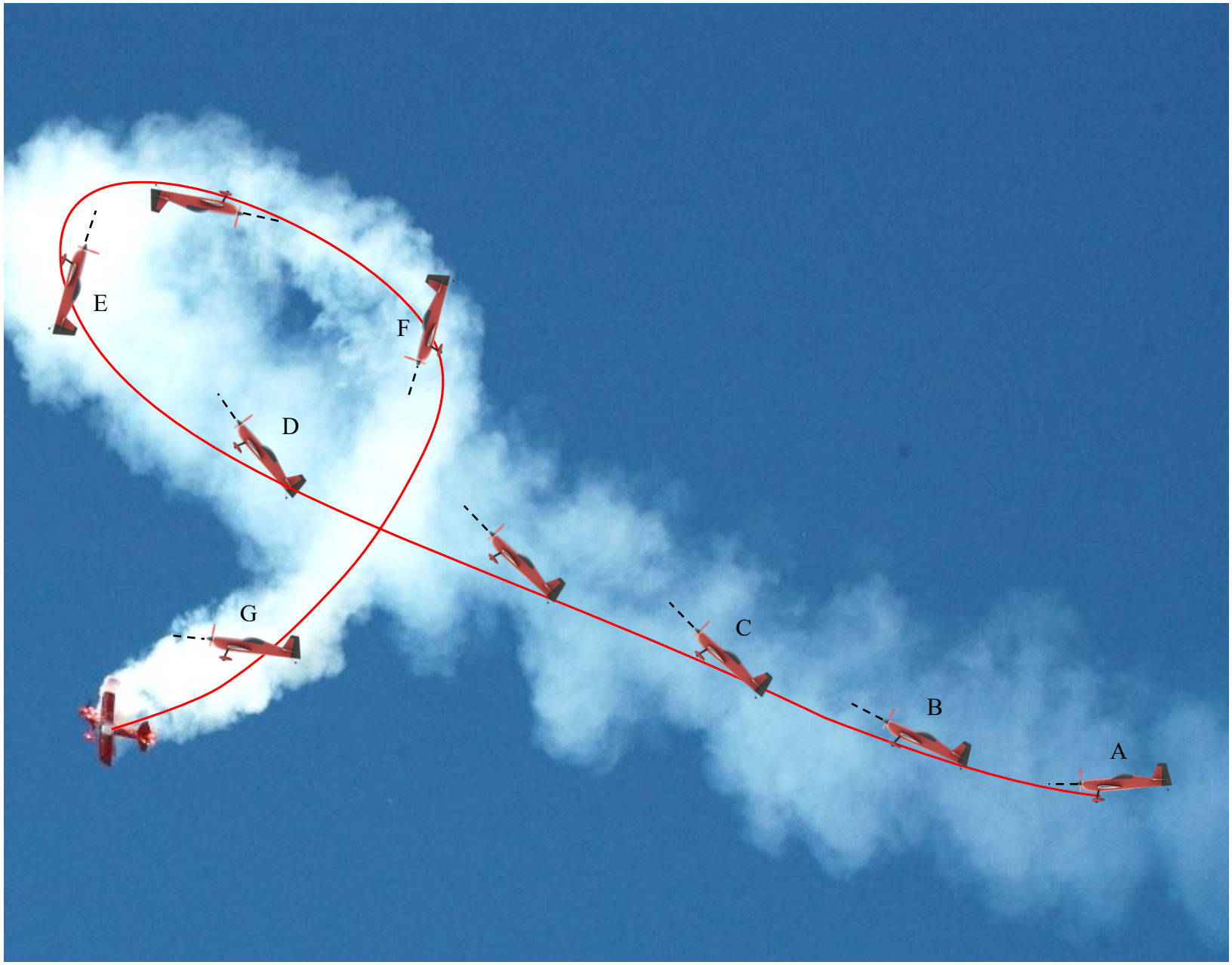

Figure 6: Sean D Tucker performing the positive g tumble manoeuvre ("Tucker Upper")

The Positive g Tumble Manoeuvre

Figure 6 provides a still image of an aircraft exiting a positive g tumble manoeuvre, with smoke emitted from the aircraft providing a visual trace of the aircraft flight path (also traced out by the red path line). Illustrations of the aircraft orientation throughout the manoeuvre have been overlaid to provide a complete graphic of the flight path with dotted black lines illustrating the orientation of the aircraft. The angle of attack of the aircraft is illustrated by the difference between the red path line and the dotted black lines. Just prior to entering the manoeuvre, the aircraft is typically oriented wings-level and flying at low airspeeds (30 m/s - 40 m/s), indicated by point A in Figure 6. To begin the manoeuvre the pilot applies full up elevator, pitching the nose of the aircraft rapidly upwards. This creates a destabilising moment on the airframe, illustrated by point B in Figure 6. Due to the large size of the elevator on aerobatic aircraft and increased velocity over the tail due to the propeller slipstream, the aircraft is pitched to an angle of attack well beyond stall ($> 45°$), seen at point C. The aircraft then remains briefly fixed at the new angle of attack and is unable to continue rotating, all while climbing and decelerating. This can be seen between points C and D. The aircraft remains "locked" at an angle of attack and is unable to rotate further due to opposing moments acting on the aircraft. The elevator forces and the propeller normal force create a destabilising, nose up moment, while all other aerodynamic and propulsive forces create opposing moments that act to stabilise the aircraft. The very large angle of attack results in the generation of a large drag force on the aircraft. This increased drag force acts to rapidly decelerate the aircraft and creates large stabilising aerodynamic moments. Once airspeed has reduced sufficiently, the destabilising moment from to the elevator becomes larger than the stabilising aerodynamic moments and the aircraft is able to continue pitching. This is seen at point E in Figure 6. The elevator remains effective, without any airspeed, due to the propeller slipstream that is blown over the empennage. With low airspeed the aircraft is able to continue rotating while moving very marginally forward (if viewed from the aircraft cockpit) and upward. The aircraft continues rotating to the point at which it is inverted. The aircraft then further rotates until the attitude of the aircraft is pointed toward the ground. This can be seen through points E to F. With the nose of the aircraft now pointing down and with a low kinetic energy level, the aircraft begins to lose altitude and rapidly gains airspeed. Should the pilot continue to hold full up elevator, the aircraft will continue to pitch during the exit of the manoeuvre, albeit at a reduced rate. This is illustrated from points F to G.

An important concept in the analysis of the tumble manoeuvre is the propeller slipstream. The propeller slipstream is the mechanism that allows a tumble manoeuvre to be completed. Even though the aircraft enters a completely stalled regime during a tumble manoeuvre and there is very little to no airspeed at various points throughout the manoeuvre, the propeller slipstream continues to blow air over the fuselage and empennage. This is inferred visually from the smoke emitted during the manoeuvre. The propeller slipstream allows the elevator to retain authority (though at a lower efficiency as compared to normal level flight), even though the aircraft has no airspeed. Figure 7 is a replication of Figure 6 with

the explanation of various points of the tumble manoeuvre overlaid so that the explanation of the manoeuvre can be more easily followed. It should be noted that the information provided from the still images in Figure 6 is inferred from video footage as no literature exists in the public domain describing the tumble manoeuvre and its characteristics.

While the tumble manoeuvre presented in Figure 6 is an example of a tumble, the manoeuvre, much like the traditional loop, can be performed differently. The radius can be altered to make the manoeuvre tighter, at the expense of airspeed or broader, with the aircraft carrying a greater airspeed through the manoeuvre. Tighter tumble manoeuvres will be termed minimal radius tumbles and broader manoeuvres will be termed minimised risk tumbles as the broader manoeuvres carry greater airspeed and thus possess a greater amount of mechanical energy.

The Negative g Tumble Manoeuvre

The negative g tumble manoeuvre is fundamentally identical to a positive g tumble, however, with a reversed direction of rotation. The negative g tumble is performed by rotating the nose of the aircraft downwards while the rear of the aircraft is rotated upwards, as illustrated in Figure 8. The manoevure is usually performed by flying upwards as steeply as possible to effectively reach a zero g state at the peak of the climb. At the apex of the manoeuvre, once the aircraft has reached near zero g, full down elevator is applied and the tail of the aircraft is rotated upwards while the nose is pushed over and downwards. The aircraft begins the rotation from a near zero g condition and the initial rotation rate is relatively high. Once the aircraft reaches a nose down attitude, however, it will begin to lose rotational velocity. This is due to the rise in aerodynamic drag acting on the aircraft as it rotates, creating a stabilising moment. The point at which the drag and stabilising moment are the greatest is when the aircraft is fully inverted, implying that the lowest rotational speed will be at this point. It is thus, more difficult for the aircraft to rotate the nose of the aircraft back upwards than it is to rotate it downwards. Full down elevator is held throughout the manoeuvre to continue rotating the aircraft. A single tumble can be performed or multiple tumbles, where one tumble leads into the next. As more tumbles are performed less recovery space (altitude and time) is afforded to the pilot.

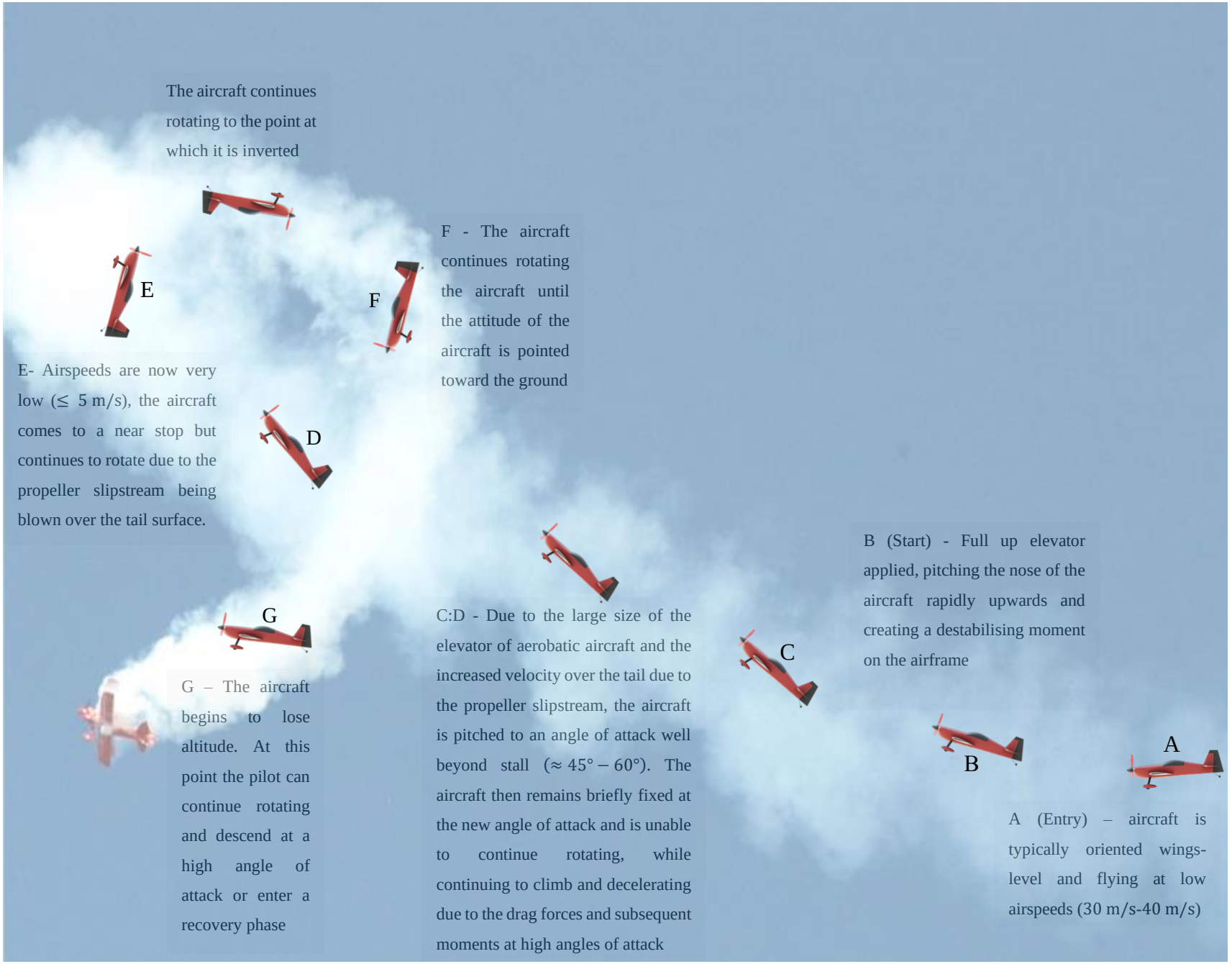

Figure 7: Positive g tumble illustration with overlaid explanation

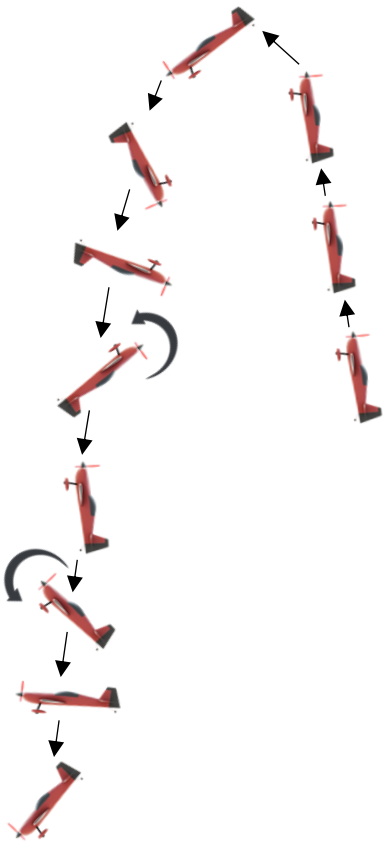

Figure 8: Negative *g* tumble manoeuvre

1.1.2. Aerobatic Aircraft

To better understand how tumble manoeuvres are performed and to model the manoeuvre as accurately as possible, the aircraft capable of performing tumble manoeuvres need also be examined. Some of the basic specifications of aerobatic aircraft are listed in Table 1. These specifications (along with many others) will be required for estimating aircraft parameters required in modeling a tumble manoeuvre.

Table 1: Aerobatic aircraft

Aircraft	Length [m]	Wingspan [m]	Wing Area [m^2]	[1]Acro Weight [kg]	Stall Speed Aerobatic [kts]	Maximum Horsepower	V_a Acro [kts]
Extra 330SC [6]	6.88	7.5	9.8	780	-	315	158
Pitts – S2A [7]	5.41	6.1	11.6	714	51	200	-
Sukhoi Su – 29 [8]	7.29	8.2	12.2	-	59	359	-
Edge 540 [9]	6.28	7.42	9.1	703	-	310	170
Extreme XA41 [10]	6.3	7.5	11.25	850	51	315	-
MX MX2 [11]	6.55	7.32	9.48	839	58	250-380	-

[1] The term acro refers to the specifications of an aircraft when it is set up to perform an aerobatic display. These configurations will be different to normal flying configurations.

Various specifications, such as those listed in Table 1, will be required to determine various aerodynamic and performance parameters. The necessary specifications required for various aerodynamic or performance parameters are outlined in the relevant sections.

A key feature on all aerobatic aircraft is the use of symmetrical profiles for the wing. Symmetrical profiles used on aerobatic aircraft give very similar handling characteristics for both normal and inverted flight, when mounted at a zero-incidence angle. This makes inverted flying far easier and safer for aerobatic pilots. The wings on aerobatic aircraft usually also have very little if any dihedral, such that the aircraft does not try to actively oppose the pilot when performing manoeuvres.

A somewhat limiting factor in the selection of aircraft to model a tumble manoeuvre is the information available in the public domain. The selected aircraft should have a sufficient amount of information available to allow for an acceptably accurate modelling, of all necessary parameters. From the aircraft listed in Table 1, the Extra Aircraft company provided more information about the entire aircraft than any other manufacturer. As such the Extra 330SC will be the aircraft primarily focused on in the modelling of a tumble manouevre. Additionally, the selection of the Extra 330SC can be justified by observing the aircraft present at the 2021 World Advanced Aerobatic Championship. Table 2 provides a list of the aircraft used by the 36 contestants. The Extra aircraft company has a very good showing, being used by 24 of the 36 pilots. Of the 24 Extra aircraft used 19 were the Extra 330SC. The aircraft was also flown by World Champions in various competitions in 2009, 2013, 2014, 2015, 2016, 2017 and 2019. The Extra 330SC is evidently a very capable and popular aerobatic aircraft and as such one could infer that it is flown by many pilots across the globe, making it a suitable choice in analysing aerobatic manoeuvres. A three view of the extra 330SC is illustrated in Figure 9 while technical data for the Extra 330SC is provided in Table 3. It should be noted that work contained within this dissertation can likely be extended to other aerobatic aircraft, provided they share similar specifications to the Extra 330SC. The required data would also need to be made available for the analysis.

Table 2: Aircraft type and number used in the 2021 World Advanced Aerobatic Championships [12]

Aircraft	Number
Extra 300 (L and S variants)	2 (L) 2(S)
Extra 330 (SC and LC variants)	19(SC) 1 (LC)
SBACH300 (XA-41)	4
XA-42	1
AVA432MXS	1
Sukhoi 31MX	2
Sukhoi 26M	1
CAP 232	1
GenR20	1
GenP20	1

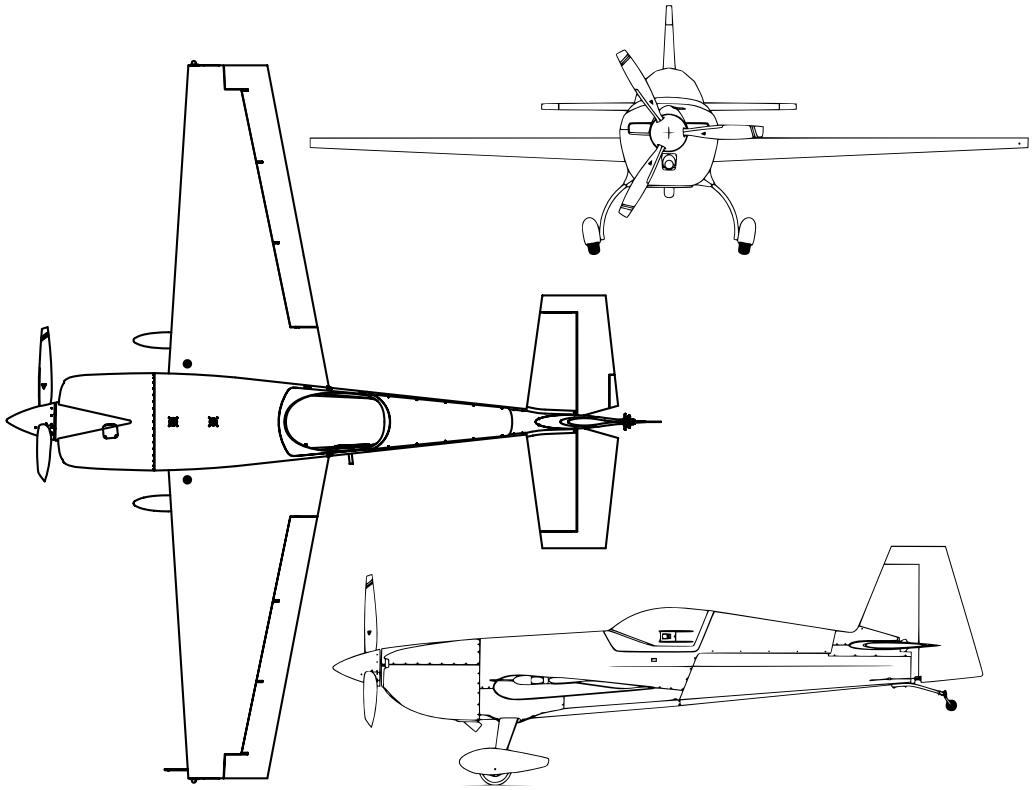

Figure 9: Extra 330SC 3-view [13]

Table 3: Extra 330SC technical data [13]

Main Data	
Length [m]	6.88
Height [m]	2.55
Wing Span [m]	7.50
Wheel Base [m]	4.87
Wheel Track [m]	1.80
Wing	
Wing Span [m]	7.50
Wing Area [m^2]	9.81
Airfoil	Root: MA 14.9 S
	Tip: MA 12 S
Chord [m]	Root: 1.786
	Tip: 0.830
MAC [m]	1.366
Aileron Area [m^2]	2 x 0.876
Aileron Deflection [deg]	Up/down 30, tolerance +/-2°
Horizontal Tail	
Span [m]	2.66
Area [m^2]	2.13
Airfoil	NACA 0009
Elevator	
Area [m^2]	1.04
Elevator Deflection [deg]	Up/down 25, tolerance +/- 1°
Trim-Tab Deflection [deg]	Up/down 32, tolerance +/- 2°
Vertical Tail	
Area [m^2]	1.55
Airfoil	Wortmann FX 71-L-150/30
Rudder	
Area [m^2]	0.75
Rudder Deflection [deg]	Left/right 30, tolerance +0°/-2°

1.1.3. Aerobatic Incidents

Airshows are public events where aircraft are put on exhibition, including aerial displays and static exhibits. It is a forum in which aviators can display their own abilities as well as the capabilities of their aircraft and is also an environment in which aircraft manufacturers can display and demonstrate the performance of their products. Airshows vary from very large scale shows with many aerial displays and ground exhibitions to small airshows with few aircraft and ground displays.

Aerobatic flight demonstrations invariably attract thousands of spectators, whether it be on a national or international scale. Regardless of the size of the airshow, a common issue, is always safety. Every year aircraft are damaged and lost. In some incidents pilots and even spectators are injured and killed. Figure 10 shows the number of incidents at airshows from 2006-2019.

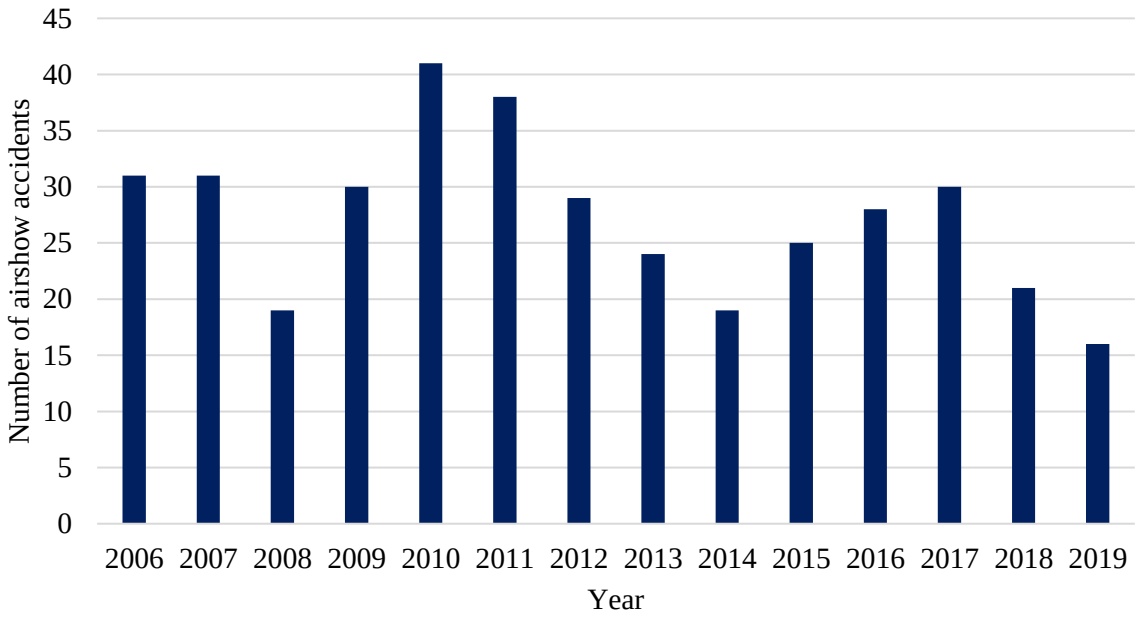

Figure 10: Global airshow accidents from 2006 to 2019 [14]

The number of annual incidents appears to follow a somewhat sinusoidal trend, consistently increasing and then decreasing over a period of 5-6 years. Illustrating a recurring pattern. Accidents appeared to decrease from 2006-2008 before increasing from 2008-2010, with 2010 providing the largest number of annual accidents in recent years. From 2010-2014 there was once again a decrease in the number of annual accidents. However, from 2014-2017 there was another increase in annual accidents. 2018 and 2019 provided fewer accidents that 2017, again showing a decrease in annual accidents. From historical data one might infer that a rise is expected to once again occur, not too long after 2019. However, due

to the COVID pandemic, airshows worldwide were limited in 2020 and 2021 and thus, a fair comparison cannot be made.

2019 proved to be a particularly safe year with the fewest number of annual accidents. The exact cause of this improved safety is not known; however, it is thought that a greater awareness of risk and risk management by pilots, air bosses and event organisers has given new impetus to 'risk aversion.' This has, in turn, induced greater oversight by regulators, new regulation and control mechanisms [14]. Another key aspect in improving the safety of airshows lies in understanding the mechanics behind the manoeuvres performed by pilots. A greater understanding of the physics involved can aid pilots in better managing their energy levels throughout their performances and allow for greater margins should any unexpected scenarios occur.

Airshow incidents are usually given far more public coverage due to the presence of spectators and media, however, incidents occurring outside of airshows should also be considered. While incidents occur across all aircraft types, incidents involving the Extra 300 series aircraft will be focused on, given that this aircraft has been selected as aircraft being analysed. Table 4 presents aircraft incidents involving the Extra 300 aircraft from 2006 onwards and includes incidents occurring at airshows, during training and private flights. While many cases have occurred involving the Extra 300 series of aircraft, the selected cases were limited to incidents that occurred as a result of pilot error while performing aerobatics. All incidents (while performing aerobatics) involving component failure or any factors outside of the control of the pilot were omitted. Cases prior to 2006 were not considered to keep with the timeline presented in Figure 10.

From Table 4 it is evident that a fair number of accidents have occurred as a result of pilot error in the Extra 300 series aircraft. The total number of incidents involving the Extra 300 series aircraft from 2006 is 70. This provides a ratio of $\frac{11}{70} = 15.71\ \%$ for pilot error to total number of cases. This may seem like a reasonably low value, however, when one considers that many incidents occurred on the ground and involved only minor damage, the number of cases involving pilot error seem far more worrying. Another noteworthy observation from the incidents presented in Table 4 is that many of the impact attitudes of the aircraft were near wings level, suggesting that the aircraft should have been able to recover before impacting the ground.

While the same number of incidents that have occurred in the Extra 300 series aircraft cannot be directly applied to other aerobatic aircraft, one could infer that a similar ratio of pilot error to total number of incidents could be applied to all popular aerobatic aircraft in the same time frame. The Extra 300 series aircraft is a very stable, reliable and predictable aircraft, more so than many other aerobatic aircraft, suggesting that the ratio of pilot error to total number of incidents for other, more difficult to fly, aerobatic aircraft could potentially be even higher.

Table 4: Extra 300 incidents

Date	Location	Nature	Flight Phase	Attitude on Impact	Reference
4-10-2006	Tucumcari, NM, USA	Airshow	Manoeuvring	Within 10° of wings level	[15]
14-14-2006	Culpeper, VA, USA	Airshow	Manoeuvring	Near wings level	[16]
11-03-2007	Lujan, province of Buenos Aires, Argentina	Airshow	Manoeuvring	Near wings level	[17]
19.04-2019	Santa Barbara, CA, USA	Private	Manoeuvring	Likely close to 45° nose down	[18]
31-12-2009	Grasmere, Gauteng South Africa	Private	Manoeuvring	Nose down	[19]
19.06-2010	Methley, West Yorkshire, UK	Airshow	Manoeuvring	Approximately 25° nose down	[20]
02-06-2013	Serpukhovsky district, Russia	Airshow	Manoeuvring	Near wings level	[21]
15-04-2013	SJIE, MT, Brazil	Private	Manoeuvring	Unknown	[22]
01-09-2015	Jerome, ID, USA	Private	Manoeuvring	Near wings level	[23]
17-04-2016	Near Cozumel Airport, Mexico	Airshow	Manoeuvring	Likely near wings level	[24]
21-10-2017	San Diego County, CA, USA	Training	Manoeuvring	Near vertical	[25]
17-12-2020	Aledo, TX, USA	Private	Manoeuvring	Unknown	[26]

Figure 11 shows the final moments of an Extra EA-300 before impacting the edge of the runway and bursting into flames near a first aid post and spectator stand in Belgium on the 26th of July 1997. The aircraft appeared to be pulling out of a nose-dive after a looping manoeuvre and was orientated in a near wings level position with the engine running at full power just before impact [27]. The orientation of the aircraft and engine setting would suggest that the aircraft was flying in a visually 'normal' state. This, however, is not the case. The height budgeted by the pilot was insufficient to recover from that altitude. While the aircraft was visually oriented in a near wings level position, the sink rate of the aircraft was incredibly high, meaning the vertical component of the velocity vector resulted in the aircraft being at a high angle of attack (likely larger than 20°) during the pull-up phase. The implications of this are low lift (less than is required during the pull up) and high drag. While the engine would have been running at full power, the high drag force, acting on the aircraft at this high angle of attack, would have meant that the aircraft was in a relatively low energy state. This means that the energy gain over the recovery phase was inadequate. The only way in which more energy could have been attained during

this recovery was by having more altitude. The altitude would have assisted in two ways, firstly the pilot would have been able to descend for a greater period of time, gaining a greater velocity (converting the potential energy to kinetic) and secondly, the pilot would have been able to perform the pull up more gradually, exerting less g's on the aircraft and keeping the angle of attack lower, thereby reducing the total drag force.

Figure 11: Belgian airshow crash July 1997 [27]

Two incidents, similar to the one presented in Figure 11, are presented in Figure 12 and Figure 13. While the final manoeuvres that lead to the incidents that occurred in both Figure 12 and Figure 13 were different, the end result and cause of all three incidents was identical. In each of the three cases the aircraft impacted the ground in a near wings-level orientation, with the engine running at full power and with a high sink rate. The nature of the ground impacts seen in these three cases illustrates that there was a loss in control of the aircraft. The three incidents occurred a number of years apart, illustrating that the same errors are being made even decades on. These kinds of incidents are also not limited to a particular type of aircraft as all three occurred in different aerobatic aircraft. Insufficient airspeeds and large angles of attack seen in these incidents are comparable with the airspeeds and angles one could expect while performing and recovering from a tumble manoeuvre. While the three presented incidents were not as a result of a tumble manoeuvre, the recoveries can all be compared to that of a tumble. The tumble manoeuvre being a worst-case scenario, as it should involve even lower airspeeds than the three presented incidents.

Figure 12: Argentinian airshow crash March 2007 (left) Exit of manoeuvre moments before crash (right) Moments before impact [28]

Figure 13: Austrian airshow crash September 2015 (left) Exit of manoeuvre moments before crash (right) Crash impact [29]

1.2. Motivation

Despite advancements in aerobatic aircraft, the issues concerning aerobatic flight safety remain largely unresolved with incidents occurring at airshows, during training and during private flights, even with stable, predictable and reliable aircraft. A large contributing factor to incidents is the limitations and shortcomings of the pilot. Insufficient knowledge of the aircraft and its capabilities coupled with poor decision making and physical limitations have all contributed to various aerobatic incidents over the years. Modern advancements in aerobatic aircraft have provided more capable and manoeuvrable aircraft, perhaps leading to the belief that these aircraft are safer to fly and should thus result in fewer aerobatic accidents. However, despite these advancements, the likelihood of aerobatic incidents has increased as aircraft are now capable of being flown in even more dangerous, low energy scenarios.

Spins or tumble manoeuvres are typically the origin of loss-of-control accidents at airshows. A rather concerning trend is that accidents resulting from an 'out of control' manoeuvre, in which a pilot may not have complete control of the aircraft and may have to abort, continues to go unabated each year [30]. Such scenarios occur generally in manoeuvres that result in low energy states, where the aircraft is at very low airspeeds and has very low rotational rates, be it in roll, pitch or yaw. Modelling extreme manoeuvres, such as the tumble manoeuvre, provides a numerical understanding of the altitude, airspeeds and load factors that result in low energy scenarios that are outside of normal operating envelope.

In many accidents that have occurred as a result of an 'out of control' manoeuvre, an interesting point to note is that the impact attitude of the aircraft was approximately horizontal with the engine running at full power. Incidents such as these may lead one to believe that the aircraft was in a normal flying state and that the pilot was in full control. In many (if not all) accidents, this is often not the case. What this does imply is that the height budgeted for a manoeuvre or sequence of manoeuvres was inadequate. It could be inferred that the recovery budget was incorrectly applied or that the energy losses while performing the manoeuvre were not repeatable or consistent, meaning that the manoeuvre would be slightly different each time it was performed. Being able to quantify the forces and dynamics of energy levels during manoeuvres, which have deviated from controlled flight, could reduce the loss of lives and help all those involved with aerobatic flight better understand the mechanism behind uncontrolled flight and how to recover from these situations. An understanding in transitioning from a low energy state to a state of energy which permits regular flight and the altitude losses associated with this transition of energy regions is not always understood by pilots performing aerobatic manoeuvres. A such, the transition of energy during recovery phases after a manoeuvre requires some quantification.

The positive g tumble manoeuvre was selected as the manoeuvre to analyse, as it is one of the most difficult aerobatic manoeuvres to recover from. The entry to the manoeuvre requires the pilot to exert many g's on the aircraft, leading to great losses in energy very early on in the manoeuvre and the exit

of the manoeuvre typically has the aircraft orientated nose down with little to no airspeed. This leaves the energy levels of the aircraft at the exit of the manoeuvre extremely low. The exit of a tumble can be viewed as a worst-case scenario for other manoeuvres, with the recovery portion performed in a similar manner, that is, trading altitude for airspeed.

1.3. Literature Review

1.3.1. Introduction

The literature review provides information regarding the modelling of aircraft motion and performance. The review starts by discussing the various reference frames that can be used to model aircraft forces and how these forces can be transferred from one reference frame to another. The equations of motion describing the forces and moments acting on the aircraft are covered next. A review of high angle attack aerodynamics is covered and includes some discussion on dynamic effects. A presentation of inertial and mass data for the Extra 330SC is provided. Finally, a review on aircraft energy is outlined.

1.3.2. Reference Axis System

In analysing the flight path of an aircraft care must be exercised in defining the framework of axes to which the motions of the aircraft can be referred. Several axis systems are used, since the forces acting on an aircraft arise from different sources. The equations of motion, derived from these axes, can be written in terms of the flight path in Earth-related axes (also known as the performance equations of motion) or as perturbation equations in aircraft related axes (stability equations of motion). All axis systems are right-handed, with their origins (O) at the centre of gravity (CG) of the aircraft such that only the angular relationships between the axis systems need be considered.

Figure 14 illustrates the most commonly used axis systems and provides definitions of some of the more important parameters in flight path performance and the relationships between them.

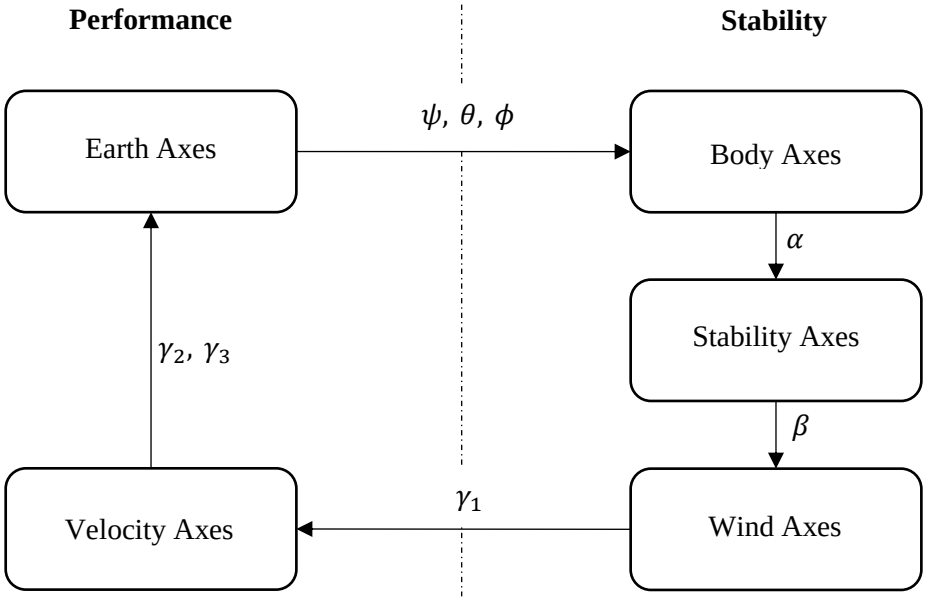

Figure 14: Reference axis systems [31]

1.3.2.1. Earth Axes

The local Earth axes is taken as the datum for aircraft motions and is defined by the horizontal plane at the geographical location of the aircraft. The positive directions of the Earth axis system are presented in Figure 15. The Earth axes are orientated OX_e Northerly and OY_e Easterly, in the horizontal plane, with OZ_e vertically downward. In some special circumstances, for instance, inertial navigation systems, the curvature of the Earth must be considered and consequently a rotation of the Earth axes with global position must considered [31]. Since the tumble manoeuvre takes place over a short distance (over the ground), a 'flat Earth' system will be assumed to exist.

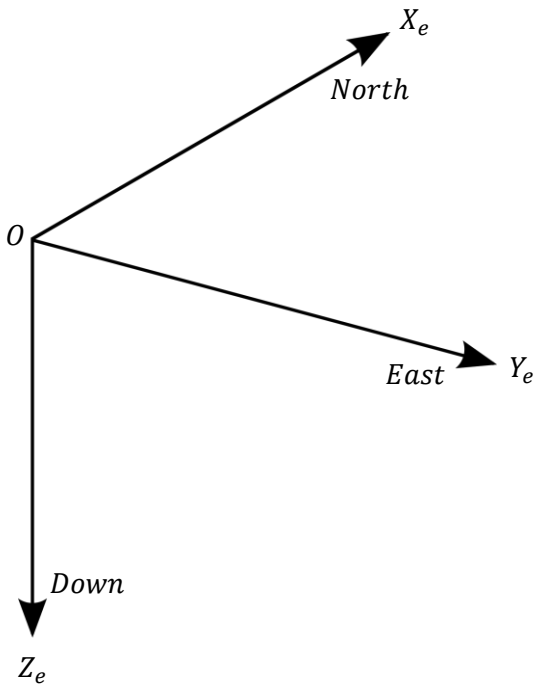

Figure 15: Earth axis system

1.3.2.2. Body Axes

Aircraft usually have a plane of symmetry that is taken as the basis for the body axis system. An illustration of the body axes and positive sign conventions is provided in Figure 16. The OX_b axis is taken to be forwards and parallel to a convenient aircraft datum, usually the aircraft fuselage datum line. The OY_b axis is normal to the plane of symmetry and positive starboard. The OZ_b axis is parallel to the plane of symmetry and points downwards. Aircraft instrumentation for the measurement of attitudes, rotational rates and accelerations is traditionally aligned to the body axis system [31]. Determination of

the forces acting in the body axes of an aircraft are important in understanding the limitations of the aircraft structure while performing various aerobatic manoeuvres.

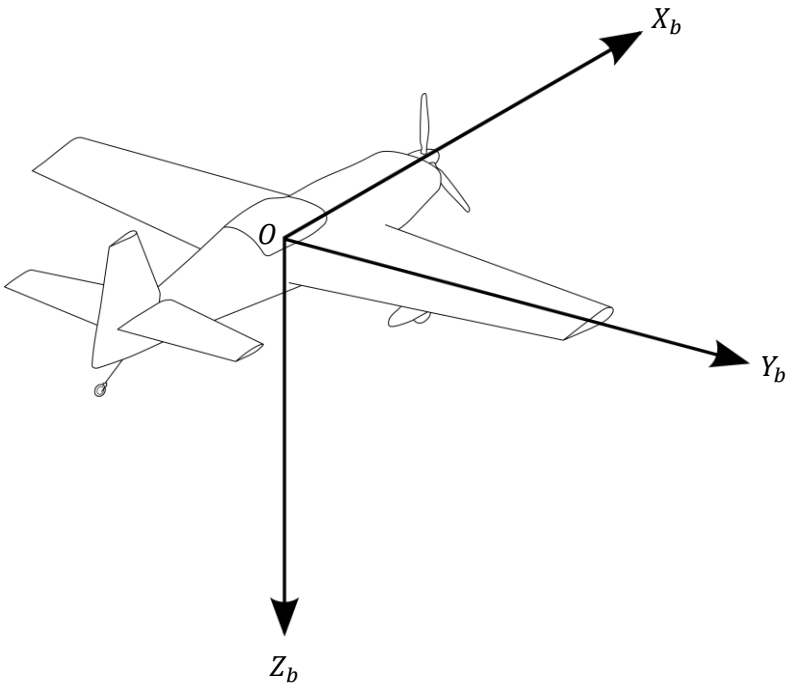

Figure 16: Body axis system

1.3.2.3. Body-to-Earth Axis Relationship

In flight an aircraft will change its orientation relative to the Earth. The body axes are related to the Earth axes by the aircraft attitude angles and are defined as follows [31]:

- The yaw attitude or azimuth (ψ). This provides the aircraft heading with respect to North. A positive rotation of ψ is from North to East. In most cases the aircraft heading does not affect the analysis of the aircraft. As such, it is assumed that the datum value of ψ is zero. ψ can then be taken to be the yaw attitude of the aircraft with respect to an arbitrary heading.
- The pitch attitude (θ) is the angle between the horizontal plane and the longitudinal body axis (OX_b) of the aircraft. θ is positive aircraft nose up.
- The bank attitude angle (ϕ) is the angle between the aircraft lateral body axis (OY_b) and the horizontal plane. ϕ is positive starboard wing down.

The transfer of force vectors between the Earth and body axes is performed by rotation through heading, pitch attitude and bank attitude, respectively [31]. These rotations are illustrated in Figure 17. The order in which the rotations are performed is important in the development of the equations of motion, described in §1.3.3.

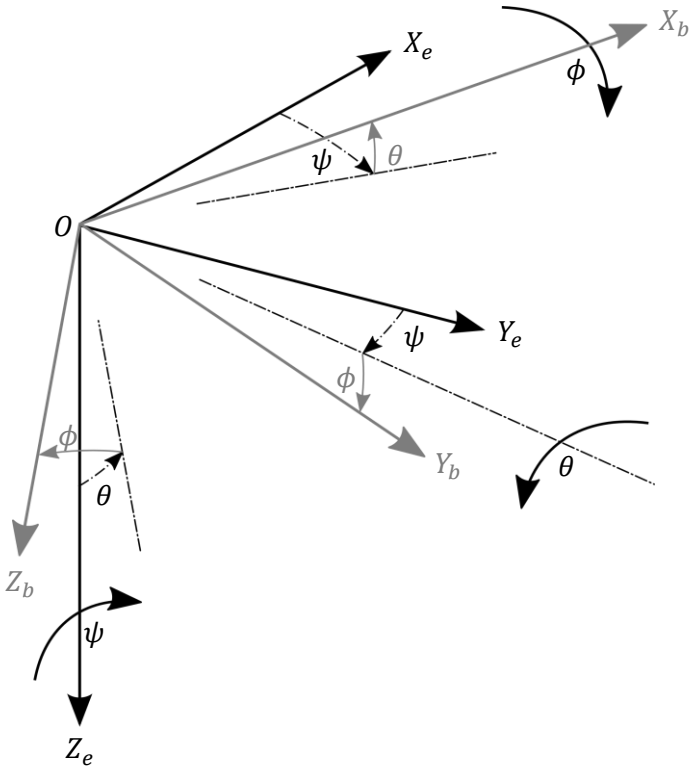

Figure 17: Earth to body axis transfer

1.3.2.4. Stability And Wind Axes

An aircraft obtains its lift from the angle of attack (α) of the wing in relation to the airflow. The body axis system of the aircraft is inclined to the flight path to provide the necessary angle of attack. Generally, the longitudinal body axis of an aircraft is not aligned with the zero-lift angle of attack of the wing and thus, the angle of attack may be measured from an arbitrary body axis datum. The stability analysis of an aircraft involves forces generated by a disturbance from the steady state (or trim condition) and as such, the reference axes for stability are relative to the undisturbed free-stream direction. Therefore, the body axis system is rotated through an angle of attack, about the OY_b axis. This is now the stability axis system, OX_s, OY_s and OZ_s.Normally, the angle of attack is taken as positive when the aircraft is nose-up with respect to the wind. This then means that the transfer from the body to stability axes involves a negative rotation about OY_b [31]

The stability axis system provides the basics for analysis of the forces resulting from a disturbance from flying in a symmetrical state. Cases do, however, exist in which the datum condition of flight is not symmetric. In asymmetric flight, the aircraft has an angle of sideslip (β) about the OZ_b axis, with β being positive to right of the aircraft when viewed from above. The flight axes now become the wind axes in which the principal direction, OX_w, is the direction of flight. The stability axes are a special case of the wind axes in which $\beta = 0$. The transfer from stability to wind axes is made by a positive rotation about OZ to starboard.

The transfer from body axes to stability and stability axes to wind axes is achieved by rotating through the angle of attack and the angle of sideslip respectively. This is illustrated in Figure 18, while Equations (1) and (2) describe these transfers [31].

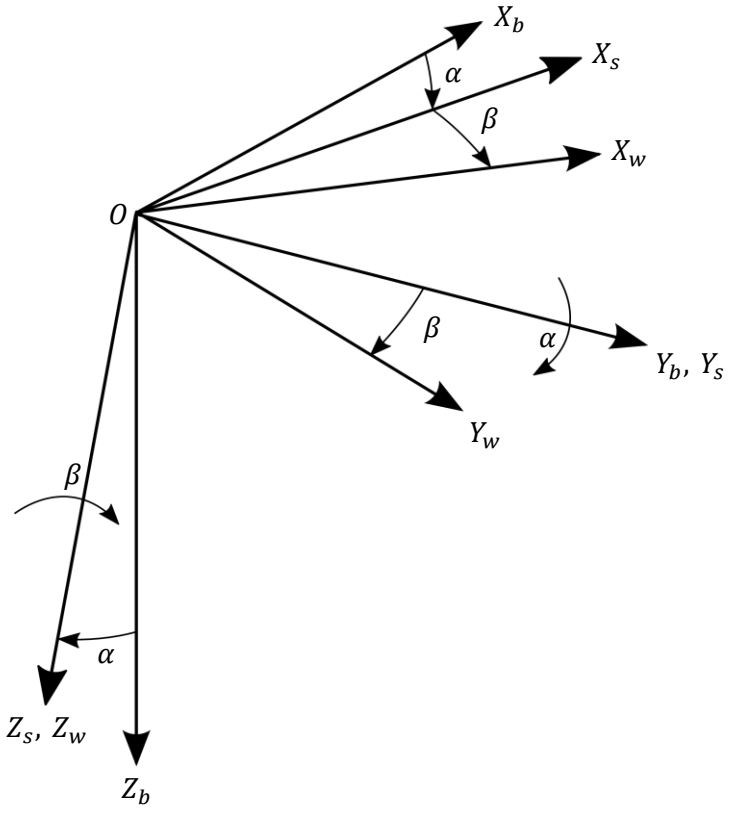

Figure 18: Body to stability and stability to wind axis transfer

$$[\boldsymbol{F}]_s = \begin{bmatrix} cos\,\alpha & 0 & sin\,\alpha \\ 0 & 1 & 0 \\ -sin\,\alpha & 0 & cos\,\alpha \end{bmatrix} [\boldsymbol{F}]_b \tag{1}$$

$$[\boldsymbol{F}]_w = \begin{bmatrix} cos\,\beta & sin\,\beta & 0 \\ -sin\,\beta & cos\,\beta & 0 \\ 0 & 0 & 1 \end{bmatrix} [\boldsymbol{F}]_s \tag{2}$$

1.3.2.5. Velocity Axes

The path of the aircraft relative to the Earth is described in the velocity axis system by defining the track (γ_3) relative to North in the horizontal plane and the flight path gradient (γ_2), the flight path angle relative to the horizontal plane. The reference direction OX_v is directed along the flight path and is co-incident with the wind axis OX_w. To define the flight path in terms of its gradient the OX_vZ_v plane must be vertical. Therefore, the velocity axes are produced by rotating the lateral wind axis, OY_w, back into the horizontal plane through the bank angle (γ_1) in the negative direction. The transfer of the force vector between the wind axes and the velocity axes is defined in Equation (3) and is illustrated in Figure 19 [31].

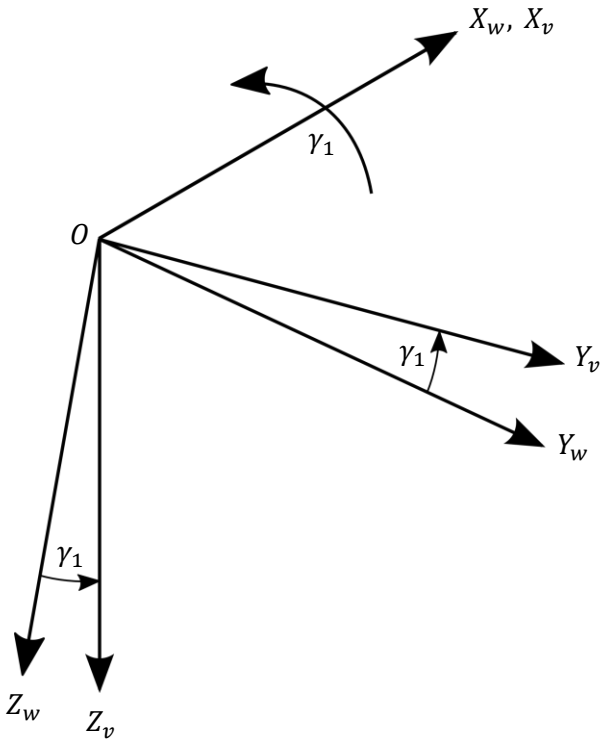

Figure 19: Wind to velocity axis transfer

$$[\boldsymbol{F}]_v = \begin{bmatrix} 1 & 0 & 0 \\ 0 & cos\,\gamma_1 & -sin\,\gamma_1 \\ 0 & sin\,\gamma_1 & cos\,\gamma_1 \end{bmatrix} [\boldsymbol{F}]_w \tag{3}$$

The velocity axes are related to the Earth axes by the track and the flight path gradient. Equation (4) describes the transfer of the force vector from the velocity axes to the Earth axes. Figure 20 illustrates the transfer of the force vector from the velocity axes to the Earth axes, both of which will be negative rotations in that direction [31].

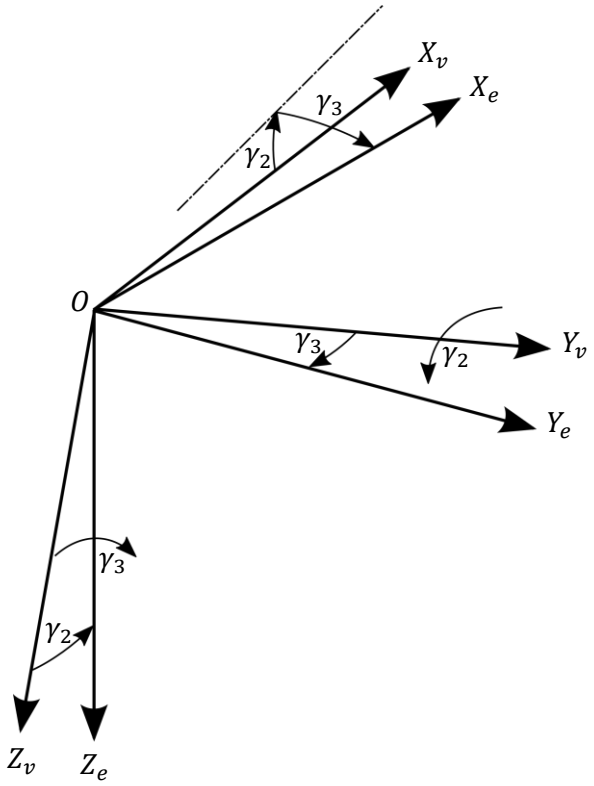

Figure 20: Velocity to Earth axis transfer

$$[\boldsymbol{F}]_e = \begin{bmatrix} cos\,\gamma_3 & -sin\,\gamma_3 & 0 \\ sin\,\gamma_3 & cos\,\gamma_3 & 0 \\ 0 & 0 & 1 \end{bmatrix} \begin{bmatrix} cos\,\gamma_2 & 0 & sin\,\gamma_2 \\ 0 & 1 & 0 \\ -sin\,\gamma_2 & 0 & cos\,\gamma_2 \end{bmatrix} [\boldsymbol{F}]_v \tag{4}$$

A summary of the axis transfers is described in Table 5.

Table 5: Axis transfers and angular relationships [31]

Axis Transfer	Earth to Body	Body to Stability	Stability to Wind	Wind to Velocity	Velocity to Earth
Pitch	θ	α	-	-	γ_2
Roll	ϕ	-	-	γ_1	-
Yaw	ψ	-	β	-	γ_3

1.3.2.6. Pitch Related Angles

The tumble manoeuvre is classified as a longitudinal manoeuvre (although in reality there may be some lateral-directional forces due to the nature of the manoeuvre) and as such the relationship between the various pitch angles should be understood.

Figure 21 illustrates the required pitch related angles. The pitch attitude (θ) is the angle between the horizontal plane in the earth axis and the aircraft longitudinal body axis. The pitch attitude is positive nose up. The flight path gradient (γ_2) is the angle of the velocity vector (principal velocity axis), relative to the horizontal. It is taken to be steady in a climb since it is calculated from the rate of climb (dH/dt) and true airspeed. It is not usually possible to observe the flight path gradient unless there is some form of physical reference near the aircraft. Such a reference could be the smoke emitted by aerobatic aircraft. Finally, the angle of attack (α) is the difference between the pitch attitude and the flight path gradient and is positive nose up. These relations are provided in Equation (5).

$$\theta = \alpha + \gamma_2 \tag{5}$$

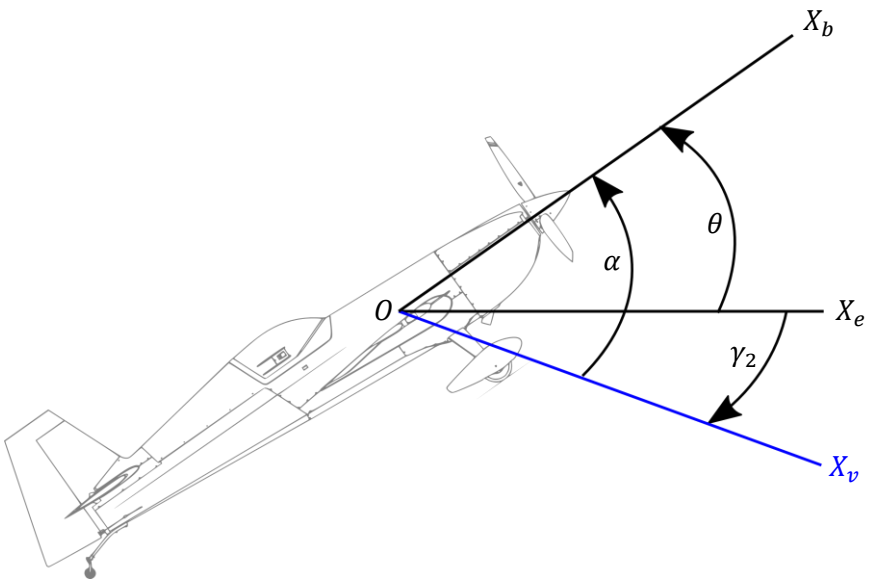

Figure 21: Angular relationships in pitch

1.3.3. Equations of Motion

Perhaps the most intrinsic method of describing the motion of an aircraft is by evaluating the equations of motion. The equations can be used to describe the motion in any orientation or state (provided that there is sufficient input data available to solve the equations). Aircraft dynamics are expressed as a set of ordinary differential equations (ODEs). For a flight vehicle, the equations of motion are generally written in a body-fixed axis system, with the centre of gravity/mass of the aircraft chosen as the origin [32]. The coordinate system and positive orientations are illustrated in Figure 22:

- The x axis points forward and lies in the plane of symmetry of the aircraft
- The y axis points out the right wing and is perpendicular to the plane of symmetry
- The z axis points down and is perpendicular to the x axis

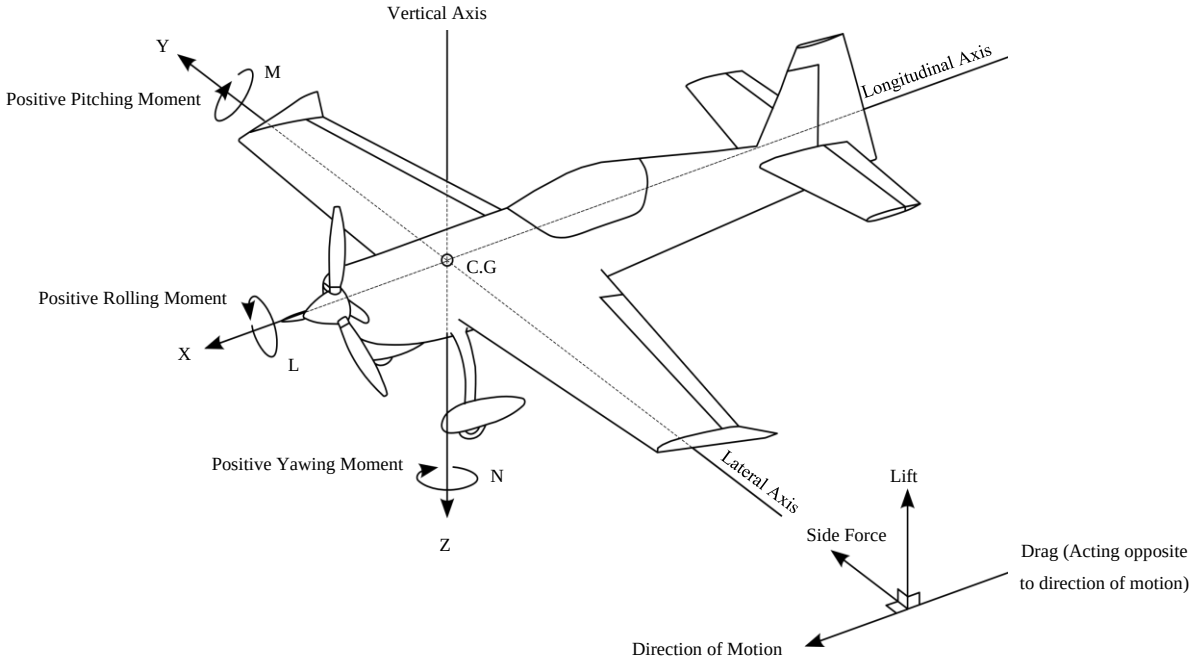

Figure 22: Aerodynamic forces and moments generated during flight with positive sign conventions

The equations of motion for an aircraft are well documented in literature. Any vehicle in flight has 6 degrees of freedom (DOF), 3 translational (force) equations and 3 rotational (moment) equations (one equation for each degree of freedom). These equations can be used to describe the flight characteristics at any instant in time [33]. The full non-linear equations of motion can be used to solve for linear and angular displacements, velocities and accelerations. These equations may also be used for nonlinear flight and are thus appropriate for use in the analysis of a tumble manoeuvre.

Force Equations:

The force equations are given by Equations (6), (7) and (8) for the x, y and z directions respectively [34].

$$X - mg_0 \sin\theta = m(\dot{u} - vr + wq) \tag{6}$$

$$Y + mg_0 \cos\theta \sin\phi = m(\dot{v} + ur - wp) \tag{7}$$

$$Z + mg_0 \cos\theta \cos\phi = m(\dot{w} - uq + vq) \tag{8}$$

Where:

- X, Y and Z are the forces acting the in x, y and z directions of the body axes, respectively [N]
- m is the mass of the aircraft [kg]
- g is gravitational acceleration [m/s^2]
- u, v and w are the linear velocities in the x, y and z direction of the body axes, respectively [m/s^2]
- p, q and r are the rotational velocities about the x, y and z directions of the body axes, respectively [rad/s]
- θ and ϕ are the pitch and roll angles of the aircraft, respectively [rad]

Moment Equations:

The rotational equations of motion are given by Equations (9), (10) and (11) [34].

$$L = I_x\dot{p} + (I_z - I_y)qr - I_{xz}(pq + \dot{r}) + qh'_z - rh'_y \tag{9}$$

$$M = I_y\dot{q} + (I_x - I_z)rp - I_{xz}(p^2 - r^2) + rh'_x - ph'_z \tag{10}$$

$$N = I_z\dot{r} + (I_y - I_x)pq - I_{xz}(qr - \dot{p}) + ph'_y - qh'_x \tag{11}$$

Where:

- L, M and N are the moments acting about the x, y and z directions of the body axes, respectively [Nm]
- I_x, I_y and I_z are the inertial values about the x, y and z directions of the body axes, respectively [kg.m^2]
- h'_x, h'_y and h'_z are the gyroscopic components of the engine about the x, y and z axes of the aircraft, respectively

In order to solve the force equations (Equations (6), (7) and (8)) and the moment equations (Equations (9), (10) and (11)), data relating to the aerodynamics of the aircraft is required. The aerodynamic data is required to determine the forces (X, Y and Z) and moments (L, M and N). For most conventional aircraft, aerodynamic data for angles of attack no greater than approximately $20°$ is required. For a tumble manoeuvre, however, aerodynamic data for angles of attack from $0°$ to $360°$ is required to adequately model the manoeuvre. Methods for determining the aerodynamic data required for various aircraft components, as well as the total aerodynamic data of the entire aircraft will be outlined in §2.

To determine the aircraft attitude and position with respect to the earth another three equations have been developed utilising the Euler angles. An additional set of equations is required as a rotation must be performed to rotate any parameters from the body axis system to the Earth axis system. The angles that describe the orientation of the aircraft relative to the earth are given by Equations (12), (13), and (14) [34].

$$\dot{\phi} = p + q \sin\phi \tan\theta + r \cos\phi \tan\theta \tag{12}$$

$$\dot{\theta} = q \cos\phi - r \sin\phi \tag{13}$$

$$\dot{\psi} = q \frac{\sin\phi}{\cos\theta} + r \frac{\cos\phi}{\cos\theta} \tag{14}$$

1.3.4. High Angle of Attack Aerodynamics

Angle of attack (α) is a term used in aerodynamics to represent the inclination of the wing chord line relative to the direction of the relative velocity vector of the aircraft. This is illustrated in Figure 23.

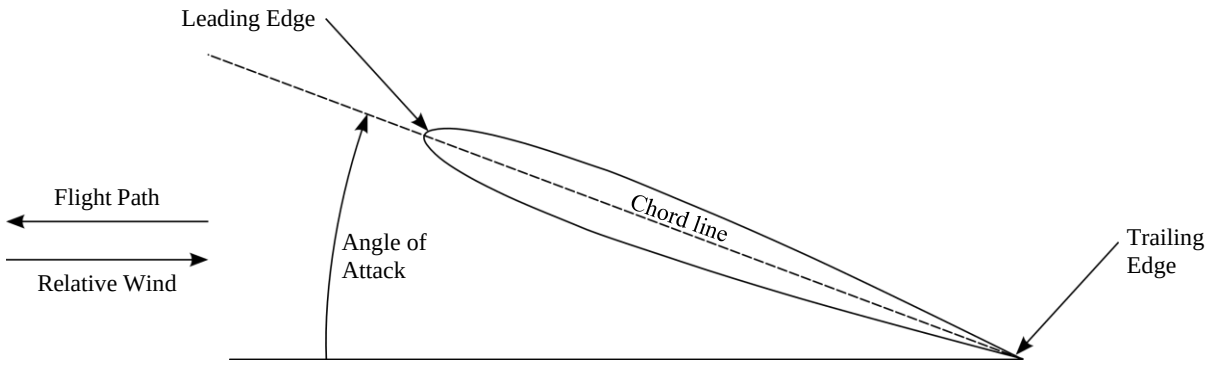

Figure 23: Angle of attack definition

Typically, the relationship between lift and angle of attack shows a linear relation at smaller angles, however, this is only up to a certain point, known as the maximum coefficient of lift $(C_{l_{max}})$. There is a small region between the linear section of the lift curve and $C_{l_{max}}$ that is non-linear. Beyond $C_{l_{max}}$ the lift curve slope has a negative gradient and is indicative of a stall occurrence, due to flow separation on the upper surface of the airfoil. With separated flow there may be changes in pitching and rolling moment characteristics as well as a notable increase in drag [35]. Depending on the severity of the stall effects, there may be limitation of the manoeuvring capabilities of the aircraft.

Airflow characteristics at various angles of attack are illustrated in Figure 24. It is evident that the flow is smooth and attached at lower angles of attack, however, as angle of attack is increased the flow starts to detach and finally separate, introducing a complex vortex. The consequence of the separation in the flow is a loss of lift and increase in drag.

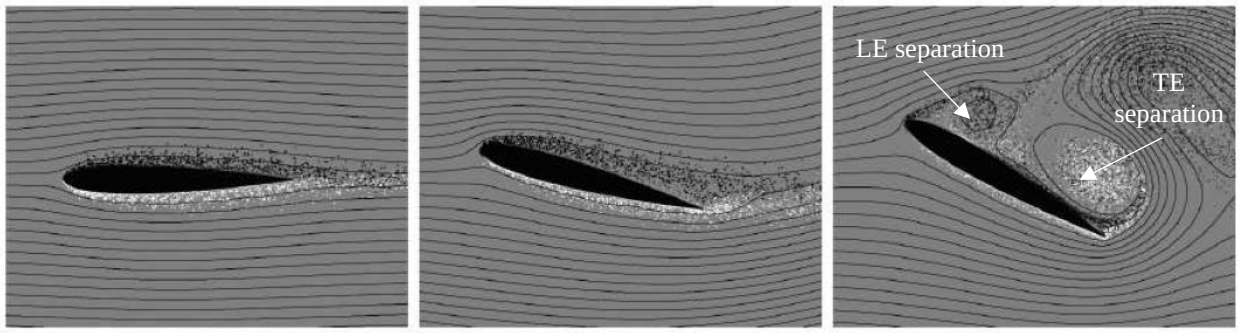

(a) (b) (c)

Figure 24: Flow characteristics at low angle of attack (a), moderate angle of attack (b) and high angle of attack (c) with separated flow, creating low pressure pockets behind the wing [36]

The variation of aerodynamic behavior as angle of attack increases is classified as either pre-stall, stall or post-stall domains. The domains reflect different stability tendencies. In the pre-stall domain, the behavior is linear, while in the stall and post-stall domains, the aerodynamics become nonlinear.

Aircraft at high angles of attack present a diverse set of nonlinear motions including stall, post-stall gyration, departure and different types of spins, all of which are considered as critical flight regimes. Different aircraft types tend to manifest different characteristics due to their design and shape, especially wing sections and tailplane position. Table 6 categorises the flight regime associated with angle of attack for different aircraft types and the possible flight attributes that they might encounter.

These attributes include [35]:

- Buffeting – caused by the turbulent airflow moving rearwards around the fuselage and tail.
- Wing Rock – involves lightly damped rolling oscillations. There are two types: a lateral unsteadiness with intermittent oscillations in roll of small amplitude and an angle of attack dependent limit cycle due to period changes of rolling moments with larger amplitude. This is typically associated with the involvement of separated flow and time dependent effects.
- Departure – defined as the initial state before the aircraft enters a spin, post-departure gyration or deep stall. It is considered as a large amplitude change (changes in roll, pitch or yaw $> 20°$) and continuously increases in a divergent manner.
- Deep Stall – occurs beyond the stall region when the aircraft is at a very high angles of attack. Recovery may be possible depending on the pitching moment coefficients, though it comprises an **out of control** flight condition.
- Post-stall Gyrations – a non-repeatable and irregular motion such as the falling leaf motion which occurs at high angles of attack and high sideslip angles.
- Spin – a complicated manoeuvre that involves simultaneous roll, pitch and dominant yaw rate at high angles of attack. The spin mode can be defined in three phases: incipient phases, developed phases and fully developed phases.

Based on video footage of tumble manoeuvres being performed it would appear that for a tumble manoeuvre the attribute that would be most relevant is deep stall. This assumption is based on the observations made between the angle of the aircraft and the smoke that is emitted during the manoeuvre.

Table 6: Typical flight regimes for General Aviation (GA), Jet Transport (JT) and Fighter (F) aircraft [37]

Aerodynamic Region	Flow Characteristics	Angle of Attack Range [deg]	Possible Flight Attributes
Low Angle of Attack	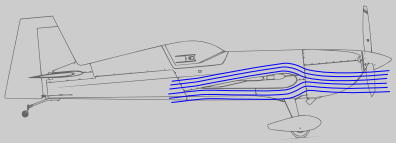	0-15 (GA, F) 0-10 (JT)	Conventional flight
Pre-Stall	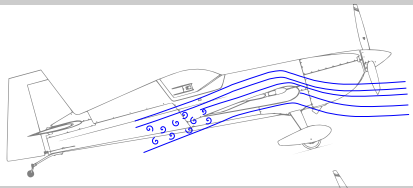	15-20 (GA) 10-15 (JT) 15-25 (F)	Unsteady effects (buffet, wing drop, wing rock)
Stall, Stall Break	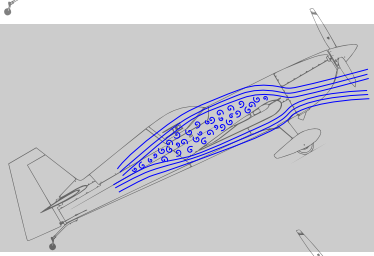	20-30 (GA) 15-25 (JT) 25-35 (F)	First lift peak, loss of lift, porpoising, loss of longitudinal and directional stability, adverse yaw
Post-Stall	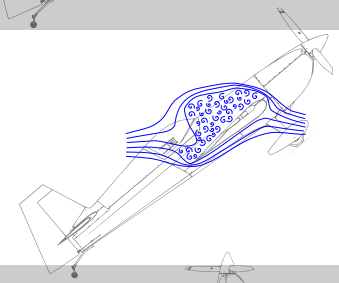	30-40 (GA) 25-40 (JT) 35-50 (F)	Departure, post-stall gyrations, incipient spin
Super-Stall	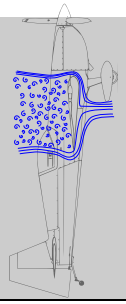	40-90 (GA, JT) 50-90 (F)	Second lift peak, deep stall, spin, supermanoeuvrability

1.3.4.1. NACA0012 Wind Tunnel Test Data

The coefficients of lift (C_l) and drag (C_d), as well as the quarter chord coefficient of pitching moment ($C_{m_{1/4}}$), for a NACA0012 airfoil section of infinite aspect ratio was investigated by Critzos [38]. The data for this thickness to chord (t/c) of 12% was selected as it is a fairly standard profile for aerobatic aircraft. The data was obtained for an airfoil in isolation to other aircraft components and spanned the length of the test section, giving it an infinite aspect ratio. The aerodynamic characteristics of the NACA0012 airfoil were obtained for angles of attack from 0° up to 360°. The coefficients of lift, drag and quarter chord pitching moment are presented in Figure 25.

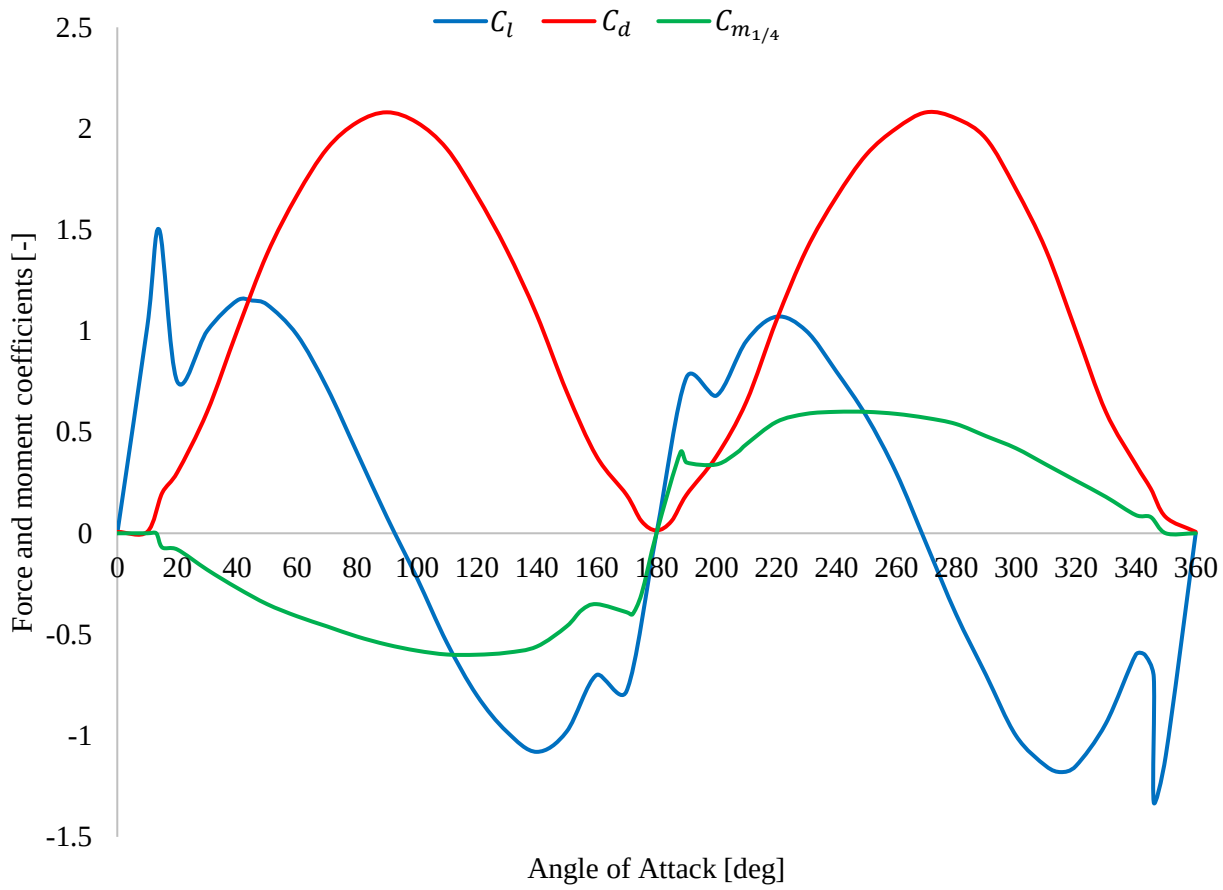

Figure 25: Coefficient of lift (C_l), drag (C_d) and quarter chord pitching moment $\left(C_{m_{1/4}}\right)$ of a NACA0012 airfoil profile [38]

Coefficient of Lift

The coefficient of lift has at a value of 0 at 0° angle of attack, which is expected for a symmetrical airfoil profile. The coefficient of lift increases linearly until 14° (stall angle of attack) where the section has a maximum coefficient of lift of 1.33. From 14° the coefficient of lift reduces to 56% of the maximum coefficient of lift $(C_{l_{max}})$ at 20°. The coefficient of lift then proceeds to increase once again to a second peak value of 1.15 at 45°. Beyond the second peak, the coefficient of lift continually decreases in a sinusoidal manner until 92° where the coefficient of lift is zero. The small amount of lift being generated at 90° may be attributed to the rounded leading edge of the profile. It is thus evident that even at a relatively large angle of attack an airfoil can continue to provide a reasonable amount of lift. The positive values of lift at large angles of attack, before 90°, might be enough to slow an aircraft descent, however, due to the drag increase (illustrated in the coefficient of drag distribution presented in Figure 25) the lift present may not be enough to prevent an uncontrolled descent. This is important when considered the recovery phase after an aerobatic manoeuvre is performed. Attempting to recover to quickly, may leave the aircraft at a high angle of attack where lift values are less than the required amount. From 90° to 180° angle of attack the coefficient of lift follows a similar trend to that from 0° to 90°, only mirrored and inverted, with the airfoil producing negative coefficients of lift. For a symmetrical airfoil profile, it would be expected that from 180° to 360° the coefficient of lift would be the mirrored and inverted image of the coefficient of lift curve from 0° to 180°, with the first and second peak values of the coefficient of lift occurring at 346° and 315° on the negative section of the curve respectively. This is illustrated in Figure 25. The two peaks occurring at 346° and 315° are the inverse of the values of coefficient of lift obtained at 14° and 45°, however, with different magnitudes. This difference in magnitudes might be due to the differences in geometry between the rounded leading edge and the sharp trailing edge of the airfoil. The coefficient of lift values are 0.77 and 1.07 at 346° and 315° respectively.

Coefficient of Drag

Referring to the coefficient of drag shown in Figure 25, the zero-lift coefficient of drag is given as 0.007 at an angle of attack of 0°. The coefficient of drag then follows a somewhat sinusoidal trend with a peak value of 2.08 at 90°, before decreasing to a value of 0.014 at 180°. The difference in value of the coefficient of drag at 0° and 180° is due to different leading edge and trailing edge radii. The leading edge of the airfoil is a smooth rounded section whereas the trailing edge is a sharp pointed section. An identical curve is observed from 180° to 360° as that seen from 0° to 180°, only mirrored, with a maximum value of 2.08 at 270°. The largest coefficient of drag is seen to be much larger than the largest coefficient of lift (156% larger than $C_{l_{max}}$). The coefficient of drag, notably, always has a positive value, unlike the coefficient of lift. This implies that the drag on the airfoil always acts in the same direction regardless of the orientation

of the aircraft. From an angle of attack of approximately 25° there is a substantial increase in drag. The implication of this is that substantially more thrust will be required to accelerate the aircraft or to maintain velocity in the forward direction beyond an angle of attack of approximately 25°. Where the coefficient of drag exceeds values of 1, it is most likely that an aircraft will not have enough thrust to overcome the drag and will subsequently decelerate and lose forward velocity, further implying that the lift being generated will decrease. The very large changes in the coefficient of drag once the stall angle has been exceeded are once again very important to aerobatic pilots. In a recovery phase, after exiting an aerobatic manoeuvre, care must be taken in preventing the aircraft from severely stalling due to the drag values. Acceleration is essential in recovering after an aerobatic manoeuvre and any hindrance to this could result in a crash.

Coefficient of Quarter Chord Pitching Moment

From the coefficient of quarter chord pitching moment plotted in Figure 25, it can be seen that the coefficient of quarter chord pitching moment has a value of 0 at 0°. This value remains until 14° (the stall angle of the airfoil profile). The zero value of coefficient of quarter chord pitching moment further illustrates that the airfoil profile is indeed symmetrical. For aerobatic aircraft this is quite favorable as there are no additional pitching moments during level flight conditions (i.e. on entry to most manoeuvres). The coefficient of quarter chord pitching moment then decreases from 0 to a maximum negative moment at approximately 115°, where the coefficient then increases back to 0 at 180°. Beyond 180° through to 360°, the coefficient of quarter chord pitching moment follows a similar trend to the trend presented from 0° to 180° angle of attack, only mirrored and inverted. The negative values from 14° to 180° indicate that the moment is restoring or nose down, with the airfoil trying to return to a neutral pre-stall angle of attack. The inverse is true beyond 180°. The two abrupt increases from zero quarter chord coefficient of pitching moment from 14° onward and from 346° onward are the points of separation. The two cusps around 180° are also due to separation. The two separation points around 180° are steeper and more sudden than at 14° and 346°, implying that around 180° a more rapid change in pitch will occur during any post-stall manoeuvre.

It should be noted that the data presented in Figure 25 was measured in the reference frame of the profile which is essentially the body axis system. Should the data be required in another axis system the coefficients will need to be rotated accordingly.

1.3.4.2. Lifting Surface Coefficients at High Angles of Attack with Control Surface Deflection

The aerodynamic coefficients for a lifting surface are altered when a control surface is deflected. The control surface could include aileron, rudder or elevator deflections. While there is very little data available in the public domain for high angle of attack aerodynamics of airfoils with control surface deflection, some aerodynamic coefficient data is presented by Selig [39]. This data is presented in Figure 26 for the coefficients of lift, drag and quarter chord coefficient of pitching moment. Positive deflections signify a downward rotation of the control surface while negative deflections are for upward rotations of the control surface. All curves presented are for a symmetrical profile with varying control surface deflections. While the plots provided in Figure 26 are for the deflection of an aileron this data could be applied to rudder and elevator deflections.

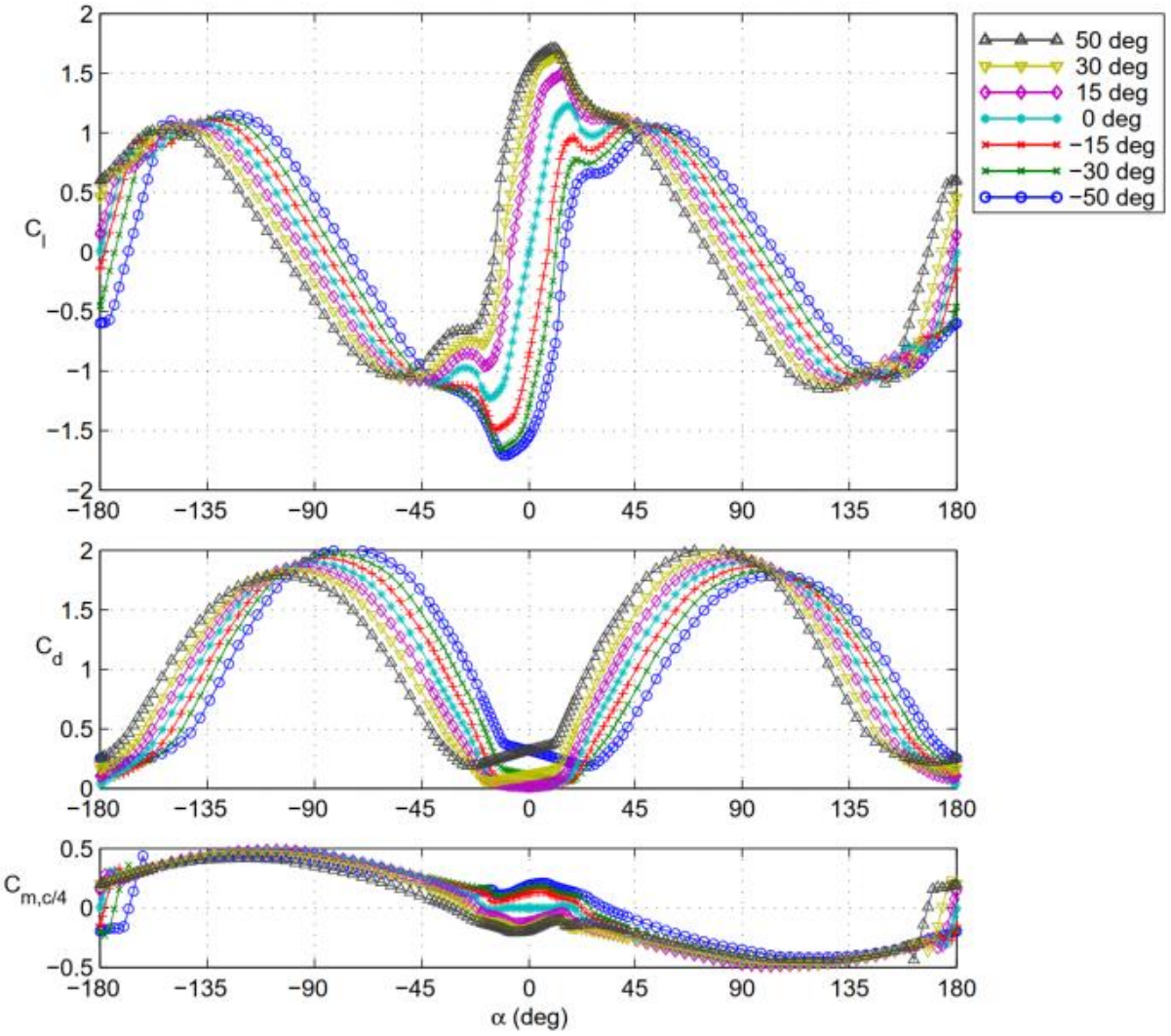

Figure 26: airfoil performance over the full ±180 angle of attack range for aileron deflection of ±0°, ±15°, ±30° and ±50° for a symmetrical profile [39]

The coefficient of lift is presented in the topmost plot of Figure 26. The effect of control surface deflections is to shift the coefficient of lift values up or down, left or right and to change the shape of the plot. A positive control surface deflection acts to shift the original lift curve upward and to the left. The pre-stall coefficient values are increased for both positive and negative angles of attack, across the entire pre-stall regime. The lift curve slope in the pre-stall regime remains largely unchanged, while the shape of stall in the negative pre-stall regime becomes more gentle the larger the control surface deflection. In the post-stall regime, the second peak is lower for positive angles of attack and increased for negative angles of attack. The lift curve slope in the post-stall regime for both positive and negative angles of attack is similar to that of the undeflected case. The zero-lift angles of attack and $C_{l_{max}}$ points in the post-stall regime also differ for different control surface deflection angles. Positive control surface deflections decrease the zero-lift angle of attack and angle at which the maximum coefficient of lift occurs, for positive angles of attack. For negative angles of attack this indicates that the zero-lift coefficient and the angle at which the minimum coefficient of lift occurs, will be at more negative angles of attack. For negative control surface deflections, the opposite occurs for both positive and negative angles of attack.

The shape of each curve and placement along the x axis are altered as a result of two fundamental changes when a control surface is deflected. By deflecting a control surface, the camber line and chord line are altered. This is illustrated in Figure 27 and Figure 28, respectively. The change in profile camber is illustrated in Figure 27, where it is evident that a downward deflection of the control surface increases the camber. The increased camber increases the coefficient of lift in the pre-stall regime but also acts to lower the stall angle. Both of these points are demonstrated in Figure 26 for all positive control surface deflections. A negative deflection of the control surface would create a profile with inverse camber, resulting in lower coefficient values, as is evident in Figure 26. Only marginal change to the positive stall angle of attack can be observed in Figure 26 for negative control surface deflections. Figure 28 illustrates the change in effective chord line. A positive control surface deflection is seen to increase the angle of the chord line relative to the horizontal. This increase in chord line angle increases the effective angle of attack of the entire profile, resulting in higher coefficient values at lower angles of attack (both in lift and drag). This is evident in Figure 26 in the pre-stall regime for both positive and negative angles of attack. With an alteration to the effective angle of attack of the profile, the zero-lift angle of attack and turn-around angle of attack can be expected to change. The change in angle is expected to be equal to the difference between the original chord line and the effective chord line resulting from control surface deflection. A negative control surface deflection will have the opposite effect, decreasing the effective angle of attack of the profile.

The coefficient of drag is presented in the middle plot in Figure 26. Similar to the coefficient of lift, the coefficient of drag sees both vertical shift, horizontal shifts as well as changes in curve shape with control surface deflections. In the pre-stall regime larger coefficient of drag values are seen when

compared to the original profile. This is expected as the lift induced drag increases for increasing control surface deflection, in the pre-stall regime. The angle at which the maximum value for the pre-stall coefficient of drag occurs corresponds to the angle at which maximum lift occurs, for both positive and negative control surface deflections. The angle of attack at which the maximum post-stall drag occurs corresponds to the angle of attack at which the coefficient of lift is zero in the post-stall regime. The peak values of the coefficient of drag in the post-stall regime are not identical for positive and negative angles of attack, meaning the curve is no longer symmetrical about the minimum drag angle. This asymmetry is due to the differences in the coefficient of lift values for positive and negative angles of attack, which is a result of the addition of camber with control surface deflection.

The coefficient of quarter chord pitching moment is shown in the bottom plot in Figure 26. Notable differences are observed in the pre-stall regime for both forward and reverse flow. The pitching moment values in the post-stall regime illustrate similar values for all cases. The large differences that exist in the pre-stall regime are likely due to the increase in lift and drag as a result of control surface deflections. These increased force magnitudes create a larger pitching moment effect about the quarter chord of the profile, as a result of shifts in the aerodynamic centre.

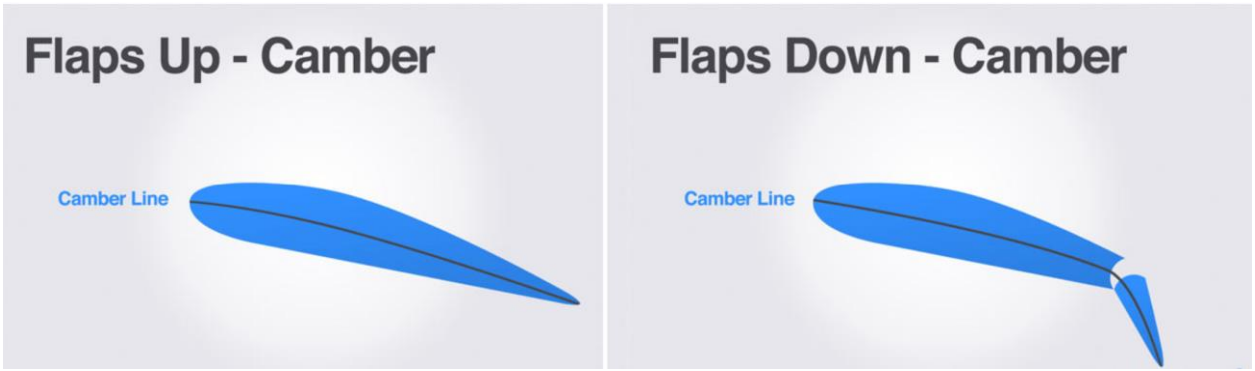

Figure 27: Change in camber for control surface deflection [40]

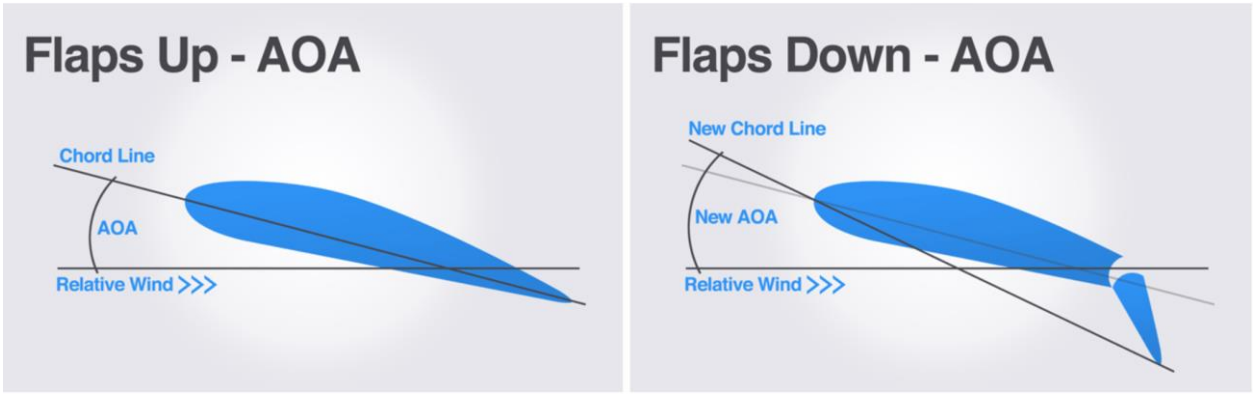

Figure 28: Change in effective chord line and angle of attack for control surface deflection [40]

1.3.4.3. NASA Fuselage Wind Tunnel Test Data

Airfoil profiles are used on all aircraft, with many of the same profiles being used across a great deal of aircraft. This makes it easy for an aircraft designer or analysts to obtain the necessary data to analyse a wing. Obtaining aerodynamic data for a fuselage is far more challenging as there is no standardised set of fuselage profiles available. This is particularly true when searching for high angle of attack data. Fuselage designs vary between manufacturers, even with the same class of aircraft. Fuselage designs are not standardized like airfoils. The best one can do is compare data to a similar fuselage shape and size.

While most aerobatic aircraft design companies do not openly share any aerodynamic data specifically pertaining to their fuselage, a study was conducted by Pamadi [41] in which aerodynamic data was presented for a fuselage of a general aviation aircraft not too dissimilar to that of an aerobatic aircraft. An illustration of the fuselage assessed by Pamadi [41] is provided in Figure 29. Pamadi compares data obtained from static wind-tunnel testing to data obtained from a semi-empirical method derived by Jorgensen [42]. The coefficients of lift, drag and pitching moment from Pamadis calculations and wind-tunnel test data are presented in Figure 30.

The calculated coefficient data presented by Pamadi [41] appears to predict higher values for each of the coefficients studied. Given that the calculations are performed using a semi-empirical method, the over-prediction of coefficients may be as a result of the semi-empirical factors required.

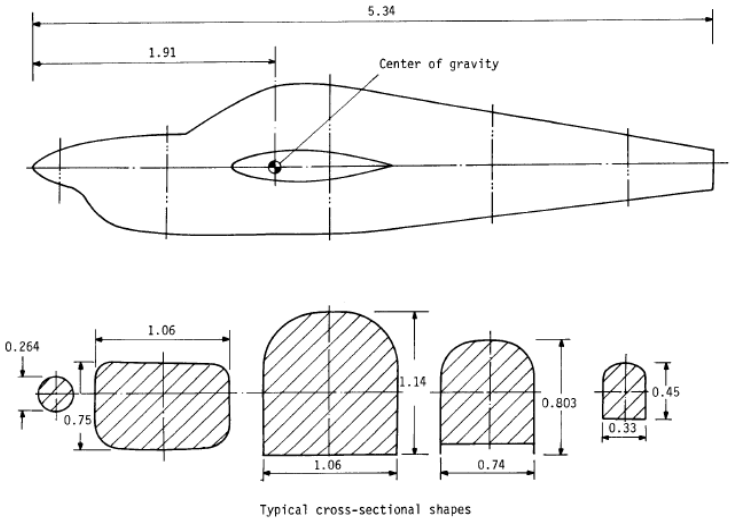

Figure 29: Geometry of the fuselage analysed by Pamadi [41]

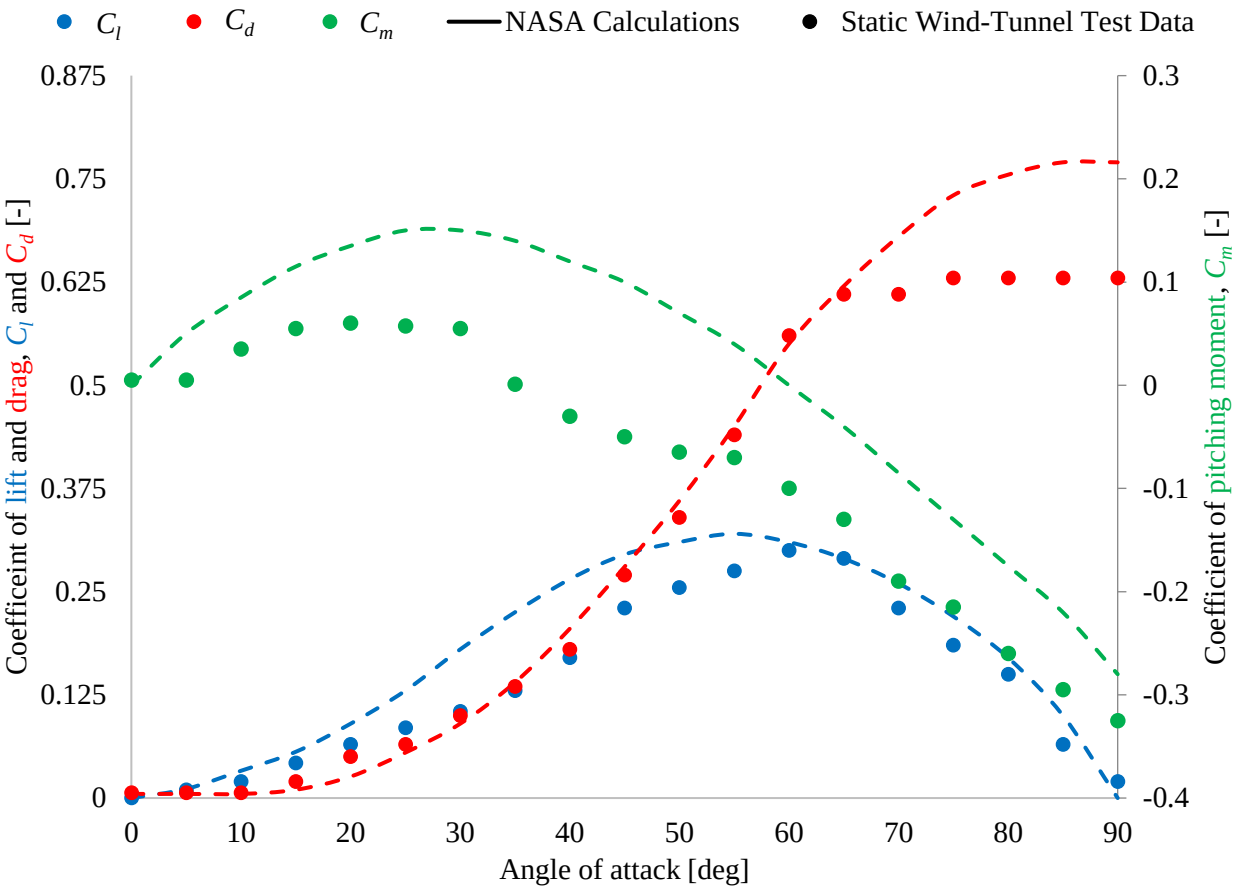

Figure 30: Coefficient of lift data for a general aviation aircraft fuselage presented by Pamadi [41]

Coefficient of Lift

The coefficient of lift is presented in Figure 30 for a general aviation fuselage. Results are presented for static wind-tunnel test data of the fuselage as well as for calculated values. Both sets of results follow a very similar trend, however, the calculated coefficient of lift data seems to overpredict when compared to the wind-tunnel test results and peaks approximately 5° sooner than the wind-tunnel test data. The shape of the curve (for both sets of data) appears almost sinusoidal, albeit skewed to the right, with the maximum value of 0.3 at 60° for the wind-tunnel test data. Unlike the coefficient of lift for airfoils there is no stall around 15° to 20°. The increasing lift value as angle of attack increases would suggest that the lift force generated by the fuselage has a far greater impact on the overall forces acting on the aircraft at higher angles of attack. It is also likely that the aerodynamic centre of the fuselage will shift as angle of attack increases, meaning that the moments acting on the aircraft will also be more influential at higher angles of attack. Depending on the location of the aerodynamic centre of the fuselage in relation to the centre of gravity, the increasing forces and potentially increasing moments may have a large influence on the ability to recover from high angles of attack after aerobatic manoeuvres are performed.

While not explicitly stated by Pamadi [41], it would appear that the coefficient of lift data has been normalised with respected to the largest fuselage cross-sectional area. Normalising this data with the wing reference area will result in far lower values than those presented by Pamadi [41]. These values can be obtained by multiplying the coefficient of lift data in Figure 30 by $\left(\frac{largest\ fuselage\ cross-sectional\ area}{wing\ reference\ area}\right)$. While the fuselage does act to provide a nose-down restoring moment, the values of the coefficient of lift are likely to be smaller than those created by lifting surfaces (the wing and horizontal stabiliser). As such, the fuselage is unlikely to be able to overcome any moments produced by the wing or horizontal stabiliser at lower angles of attack. Should the wing and horizontal stabiliser surfaces be in a deep stall scenario, then the difference in values are likely to be closer.

Coefficient of Drag

Coefficient of drag values are presented in Figure 30 for static wind-tunnel test data and calculated values. The data follows a similar trend to that of an airfoil profile, taking a somewhat sinusoidal shape. The calculated data matches very well with the test data up $\approx 65°$, after which the calculated data overpredicts the coefficient of drag. The coefficient of drag, for the wind-tunnel test data, remains reasonably low, at a value of ≈ 0.0065 at $0°$ and increases only marginally to an angle of $20°$. After $20°$ the coefficient of lift rapidly increases to a value of 0.62 at $65°$. From $65°$ to $90°$ the coefficient of drag remains approximately constant. Prior to stall the values of the coefficient of drag of the fuselage have a relatively minor influence on the forces and moments present on the aircraft. However, post-stall, the rapid increase in drag and shift of the aerodynamic centre of the fuselage create larger forces and potentially larger moments on the airframe. Depending on the location of the aerodynamic centre of the fuselage in relation to the centre of gravity, the moments may be extremely influential in the ability of an aircraft to recover from a high angle of attack scenario during or after an aerobatic manoeuvre. Once again, more representative values for the coefficient of drag can be obtained by multiplying the values presented in Figure 30 by $\left(\frac{largest\ fuselage\ cross-sectional\ area}{wing\ reference\ area}\right)$.

Coefficient of Pitching Moment

Coefficient of pitching moment data is provided in Figure 30 for wind-tunnel test data and calculated values. The basic stability trend is captured by the calculated data; that is, the static instability up until $30°$ and subsequent stability are predicted. Significant differences in magnitude are seen to exist between the calculated data and the wind-tunnel test data. The calculated data provides a positive moment until $60°$, while the wind-tunnel data provides positive values only up until $35°$. The calculated

data provide a very large over-estimation of the coefficient of pitching moment, more so than either the lift or drag. Pamadi [41] has defined a positive moment as nose-up or pitch up. Assessing the wind-tunnel test data, the coefficient of pitching moment of the fuselage has a nose-up tendency up until 35°, after which the fuselage acts to create a nose-down or restoring moment. The values of the coefficient of moment are smaller than either the coefficients of lift or drag. The maximum destabilising moment created by the fuselage occurs at around 20° at a value of 0.06. The coefficient of pitching moment rises from a value of 0.05 at 0° to the maximum and then decreases to 0 at 35°. Beyond 35° the coefficient of pitching moment decreases to a value of -0.325 at 90° in an almost linear fashion. The coefficient of pitching moment does not show values in the pre-stall region that would suggest a very large contribution to the overall pitching moment of the aircraft. Beyond stall, the ever increasing, destabilising, pitching moment with increasing angle of attack suggest that the fuselage could have a great influence on the ability of the aircraft to reach a stable flight orientation after high angles of attacks are attained.

A more representative set of values for the coefficient of pitching moemnt can be obtained by multiplying the values presented in Figure 30 by $\left(\frac{largest\ fuselage\ cross-sectional\ area * fuselage\ reference\ length}{wing\ reference\ area * wing\ reference\ length}\right)$. It should also be noted that the trend presented in Figure 30 may be different for a fuselage with a difference area distribution and centre of gravity location. While it is unlikely that the fuselage and centre of gravity of location of an aerobatic aircraft will be very different to the fuselage presented by Pamadi [37], the values and cross-over point on the x axis may be different.

1.3.4.4. Uniform Pitch Rate of an Axisymmetric Body

A series of tests were conducted by Smith [43] in which the effect of a uniform pitching motion on a slender axisymmetric body, undergoing a large excursion in angle of attack, was investigated. Force and moment measurements were obtained for the body over a range of free-stream Reynolds numbers from 5×10^4 to 1.4×10^5 while varying the angle of attack from 0° to 90° pitch rates between 0°/s and 281°/s. The data presented shows coefficients that are very high compared to any data previously presented. This difference is due to the reference area considered. The body presented by Smith [43] was normalised by the largest cross-sectional area. In this case the area is comparatively small. The important aspects of this section are the trends presented, rather than the numerical values.

The results for static coefficients of normal force at three values of free-stream Reynolds number are presented in Figure 31. The data presented in Figure 31 shows that a larger coefficient of normal force exists for $R_e = 5 \times 10^4$ than for either $R_e = 8 \times 10^4$ or 1.4×10^5. This suggests that a lower Reynolds number provides a greater coefficient of normal force. The reasoning behind these findings is due to

the boundary layer size over the body and the pressure recovery present near the rear of the body, for different Reynolds numbers.

Smith [43] states that the aerodynamic loads developed on an inclined body of revolution are strongly dependent upon the separation of the boundary layer fluid which feeds into regions of concentrated vorticity. Furthermore, the boundary layer thickness is inversely proportional to the square root of the Reynolds number [43]. Thus, increasing the Reynolds number decreases the boundary layer thickness at a given position. The tendency toward separation decreases with a thinner boundary layer. Therefore, the point of separation on a body moves further rearward with increasing Reynolds number, so long as the flow remains laminar [43]. As the point of separation moves further rearward, the form drag (the normal force) is decreased as a consequence of greater pressure recovery on the rear of the body.

The coefficient of normal force for the two larger Reynolds numbers are very similar, perhaps suggesting that the point of separation has moved a negligible amount further aft on the body for the increase in Reynolds number [43].

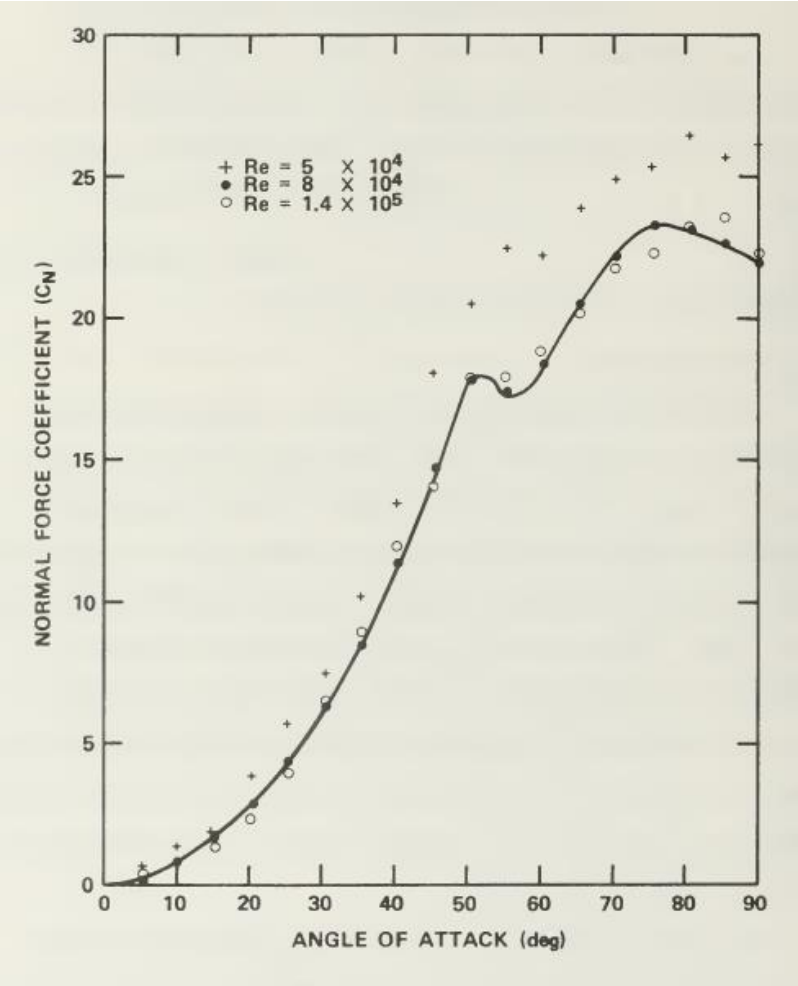

Figure 31: Static coefficient of normal force variation with angle of attack for various Reynolds numbers [43]

The coefficient of normal force presented in Figure 31 increases smoothly with increasing angle of attack from 0° to approximately 50°. From 50° to 60° there is an apparent stall and ensuing recovery. Beyond the stalled region there is a loss of normal force. Smith [43] attributed the existence of the inflection in the coefficient of normal force to flow unsteadiness during a transition from a flow dominated by the axial component to a flow in which the crossflow component dominates. For tractor configuration aerobatic aircraft, the influence of propeller slipstream may mitigate this transition as the slipstream will add to the axial component of the flow. Additionally, the smooth curves for the coefficients of lift and drag obtained by Pamadi [41] in §1.3.4.3 suggest that the inflection seen by slender cylinders may not be applicable to fuselages for general aviation aircraft configurations. The same basic trend is expected. The coefficient of normal force should increase to a turning point around 50°-70° (depending on the geometry), beyond which the coefficient of normal force would decrease.

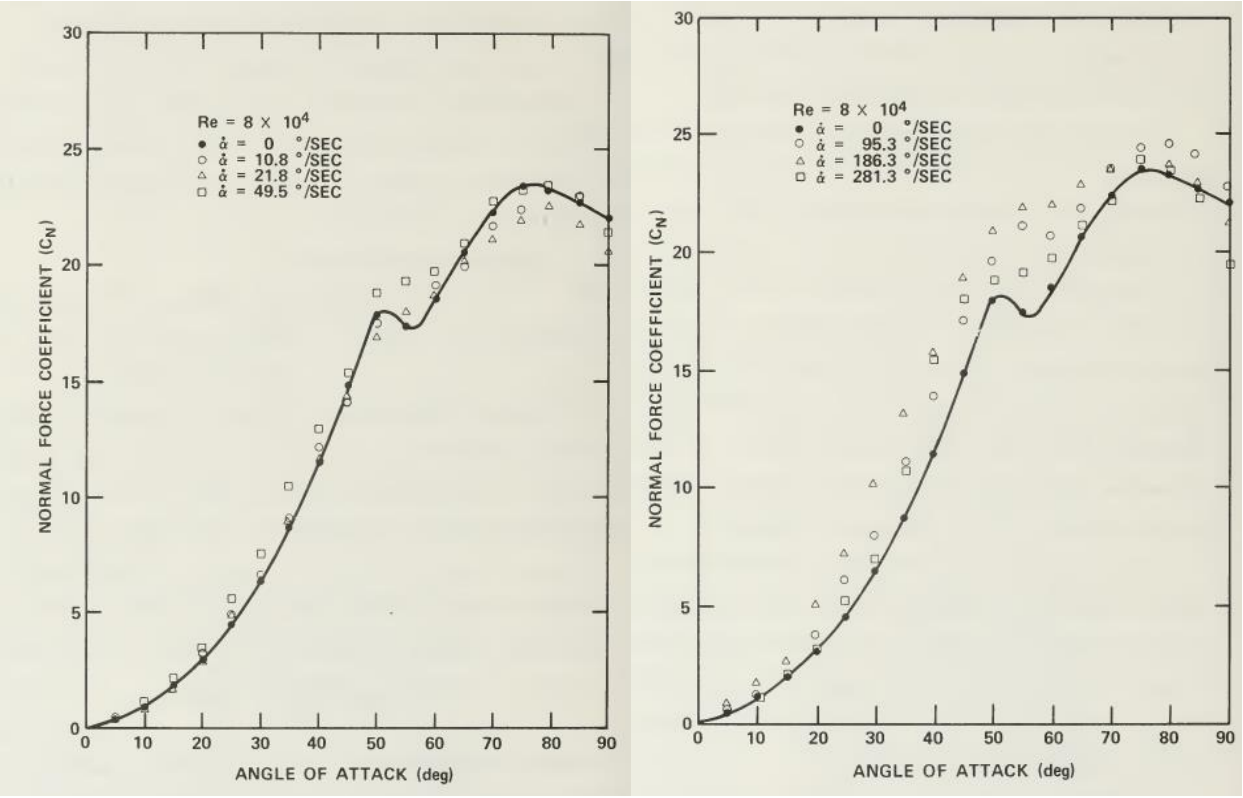

Figure 32: Coefficient of normal force variation with angle of attack for various pitch rates at $R_e = 8 \times 10\text{^}4$ [43]

The coefficient of normal force for various pitch rates at a Reynolds number of $R_e = 8 \times 10^4$ is presented in Figure 32. It is evident that for pitch rates of around 20°/s and lower the coefficient of normal force is not noticeably dissimilar to the static data, at least up until approximately 50°, beyond which the difference sufficiently indicates some pitch rate dependence. At higher angular velocities, specifically from 49.5°/s to 186.3°/s, an increasing coefficient magnitude, at any given angle of attack

above 20° and a shift of the angle at which the inflection occurs can be observed. At the largest angular velocity (281.3°/s) a trend reversal can be observed, however, given the incredibly high angular velocity this irregularity will not be discussed any further as such high pitch rates are not achievable by aerobatic aircraft. For angles up to 20° the coefficient of normal force is largely identical for angular velocities up until 96.3°/s.

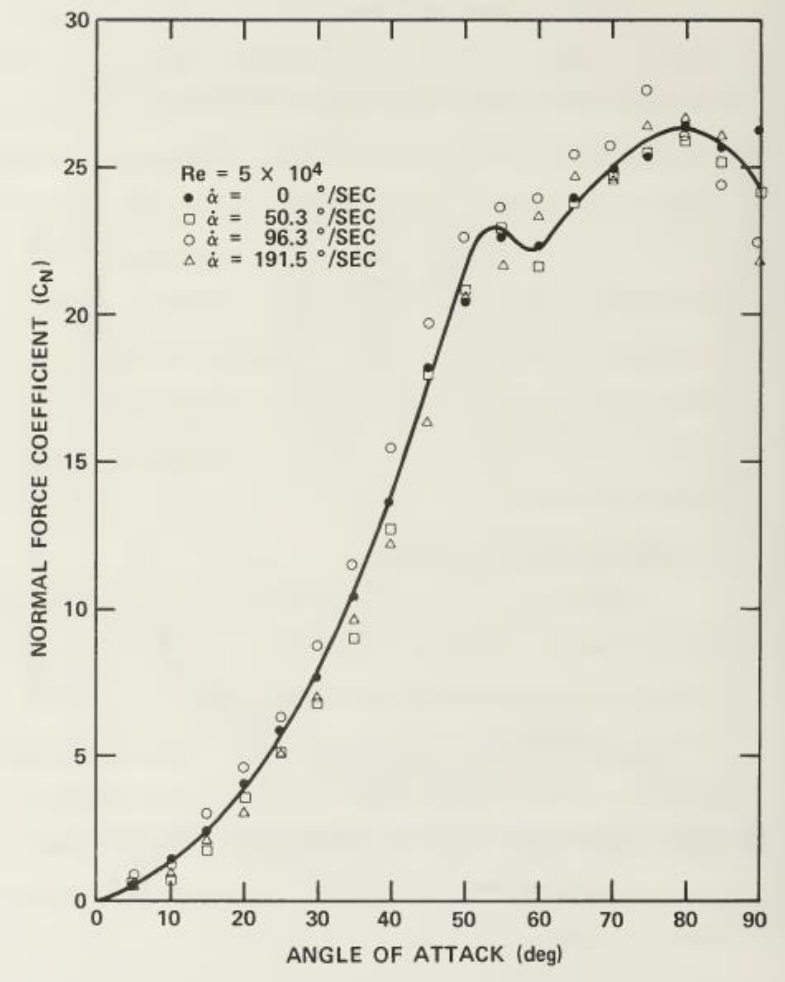

Figure 33: Coefficient of normal force variation with angle of attack for various pitch rates at $R_e = 5 \times 10\text{^}4$ [43]

The coefficient of normal force variation for various pitch rates at a Reynolds number of $R_e = 5 \times 10^4$ is presented in Figure 33. At this Reynolds number the pitch rate appears to have very little influence on the normal force. This result indicates that the variations in the coefficient of normal force due to pitch rate are related to the Reynolds number and that variations appear to be minimal at lower Reynolds numbers.

During a tumble manoeuvre the aircraft is brought to a near zero forward velocity, implying that the Reynolds numbers seen by the fuselage would be relatively low. These low Reynolds numbers, coupled with the propeller slipstreams contribution to the axial flow along the fuselage, would suggest that the dynamic effects due to pitch rate would likely not cause a large variation in the static coefficients seen on the fuselage of an aerobatic aircraft. During the entry phase to a tumble manoeuvre the aircraft may have a sufficiently high Reynolds number such that the effects of pitch rate may influence the coefficients of the fuselage. However, during this, higher speed, entry phase the angle of attack it expected to be around 20°-30°, an angle of attack range in which the pitch rate is expected to have little influence, as illustrated by Figure 32.

1.3.4.5. NASA Propeller Wind Tunnel Test Data

An investigation into the performance of three propellers was conducted by Yaggy [44] in the 1960s. The performance of the three propellers was measured for thrust axis angles of attack (α) from 0° to 85°, blade pitch angles at 75% blade radius (β) from 0° to 40° and included the measurement of in-plane forces and out of plane moments. The propellers differed widely in planform and were all selected to simulate the operating condition anticipated for VTOL/STOL aircraft in the take-off, landing and transition regime. Propeller 1 was of conventional design; propeller 2 was designed to produce large normal forces, with reduced shaft moments; and propeller 3 was designed with an articulated (flapping out-of-plane only) propeller designed to eliminated shaft moments. The physical characteristics of these propellers can be found in Yaggy [44]. While the operating regime of an aerobatic aircraft and a VTOL/STOL aircraft are largely dissimilar, the operating conditions and regime for the propellers of a VTOL/STOL aircraft are ideal for predicting forces and moments present on the propeller during a tumble manoeuvre, as the thrust axis angles of attack and advance ratios (the ratio of the free-stream fluid speed to the propeller tip speed) fall within the same region, that being very high angles of attack and very low advance ratios. Of the three propellers tested by Yaggy [44], the shape of propeller 1 most closely resembles that of the Extra 330SC propeller. It is also the propeller most suited to represent a conventional aircraft, given that it is stated to be of conventional design.

In assessing propeller coefficients of force and moment at high angles of attack the definition for advance ratio is required. The advance ratio (J) should be modeled to include the angle of attack effects on the free-stream component. This can be achieved by considering Equation (15), where V_∞ is the free-stream velocity, α is the angle of attack (assumed to be the same as the thrust axis angle of attack), n is the rotation speed in revolutions per second and D is the diameter of the propeller. The apostrophe next to the J term in Equation (15) indicates the modified advance ratio.

$$J' = \frac{V'}{nD} = \frac{V_\infty \cos \alpha}{nD} \tag{15}$$

The results of the investigation revealed that, for all three propellers, similar variations in the forces and moments were present. This was true for a range of thrust axis inclination angles and advance ratios. The thrust and power were nearly constant, with in-plane forces and out-of-plane moments increasing approximately linearly over a large range of thrust-axis angle of attack (for constant blade angles and effective advance ratios). Several other interesting conclusions were also drawn from the test data. Firstly, the slopes of the curves, for all force and moment components measured, increased with increasing angle of attack. Second, the slopes of components increased with disk loading (increasing β, the blade pitch angle) for all components except for the pitching moment, which increased to $\beta = 8°$ and then gradually decreased. Third, moderate changes in slope were observed up to values of thrust axis angle of attack of $45°$, after which changes occurred rapidly. These changes in slope occured more rapidly at higher angles of modified advance ratio, J'.

The data presented by Yaggy [44] was directed towards more heavily loaded, higher solidity propellers. Experimental data for more lightly loaded, lower solidity propeller data has been provided in McLemore [45]. Although Yaggy [44] and McLemore [45] tested very different propellers, the data provided by both papers shows almost identical trends across all measured coefficients for comparable modified advance ratios, J'. Yaggy [44] tested far lower modified advance ratios, going as low as $J' = 0.1$ and $J' = 0$ in some cases. The highest modified advance ratios tested by Yaggy [44] were $J' = 1.2$. McLemore [45] tested to much higher modified advance ratios, going as high as $J' = 6$, and going as low as $J' = 0.2$. An interesting finding from McLemore [45] (not presented by Yaggy [44]) is that the static thrust results indicate that the blade angle for the maximum figure of merit (ratio of the induced Power divided by power available) is slightly greater than $\beta = 8°$, for all tested angles of attack. The blade angle for maximum efficiency in forward flight at and near zero angle of attack is $\beta \approx 60°$. This result implies that lower blade pitch angles are required for slower flight, thus inferring that a lower blade pitch would likely be of great benefit during a tumble manoeuvre. Given the differences in size between an aerobatic aircraft propeller and a VTOL/STOL propeller it is likely that blade pitch angles slightly higher than $\beta = 8°$ would be required for an aerobatic aircraft performing a tumble manoeuvre.

Figure 34 presents the coefficients of thrust and power for propeller 1 of Yaggy [44] at a blade pitch angle of $\beta = 16°$. While Yaggy [44] presents data for many other blade pitch angles, the blade pitch angle was selected based on the findings of McLemore [45] for the ideal blade pitch angles required for very low modified advance ratios. Figure 34 illustrates relatively constant coefficients of thrust and power for a large range of angles of attack, at a variety of modified advance ratios. For each modified advance ratio, there is an angle of attack at which both the coefficients of thrust and power increase, with the inflection point occurring at higher angles for lower modified advance ratios. The implications

of the constant portions of the curve illustrate that a pilot cannot generate more thrust to aid in an unfavourable situation. While the force is predictable and constant, higher angles of attack do not provide the pilot with any benefits while performing aerobatics.

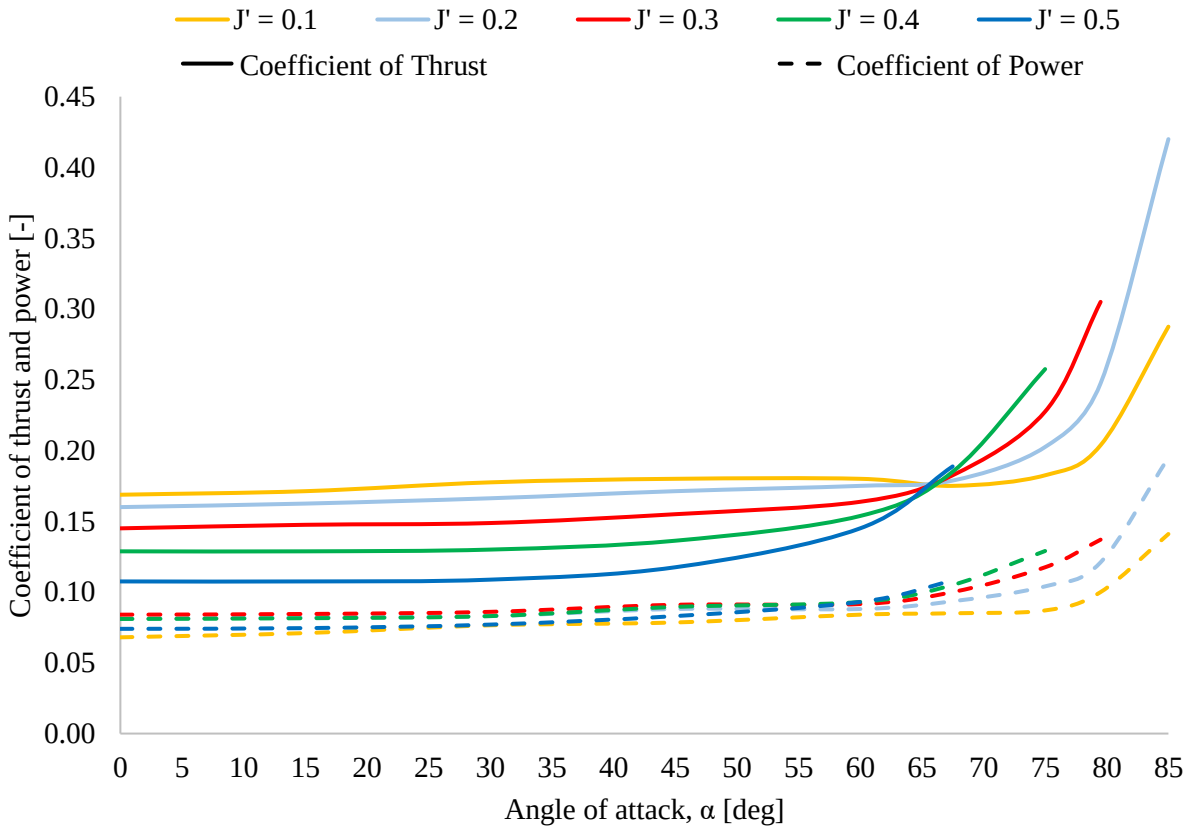

Figure 34: NACA TN D318 propeller 1 coefficient of thrust and power for $\beta = 16°$ [44]

The coefficient of normal force at various angles of attack, for a blade pitch angle of $\beta = 16°$ is plotted in Figure 35, for various modified advance ratios. The data presents results obtained by Yaggy [44] for propeller 1. The coefficient of normal force increases in a linear manner for all modified advance ratios until $\alpha \approx 45°$. The angle of attack at which the coefficient of normal force changes gradient and no longer follows a linear trend increases for decreasing modified advance ratio. This then means that the linear trend continues to much steeper angles of attack the slower the free-stream velocity component. As such, it is likely that during a tumble manoeuvre the propeller of an aerobatic aircraft is likely to experience linear changes in the coefficient of normal force throughout the manoeuvre. At lower modified advance ratios there is also a much smaller change in the coefficient of normal force since the angle of attack increases when compared to higher modified advance ratios. Higher modified advance ratios produce higher coefficients of normal force, particularly at higher angles of attack. The difference in coefficient of normal force between the various modified advance ratios increases with increasing angle of attack. The coefficient of normal force is largely identical and relatively small for all modified

advance ratios up until an angle of attack of $\alpha = 15°$. This point illustrates why the coefficient of normal force (from the propeller) is generally not considered for general aircraft performance calculations.

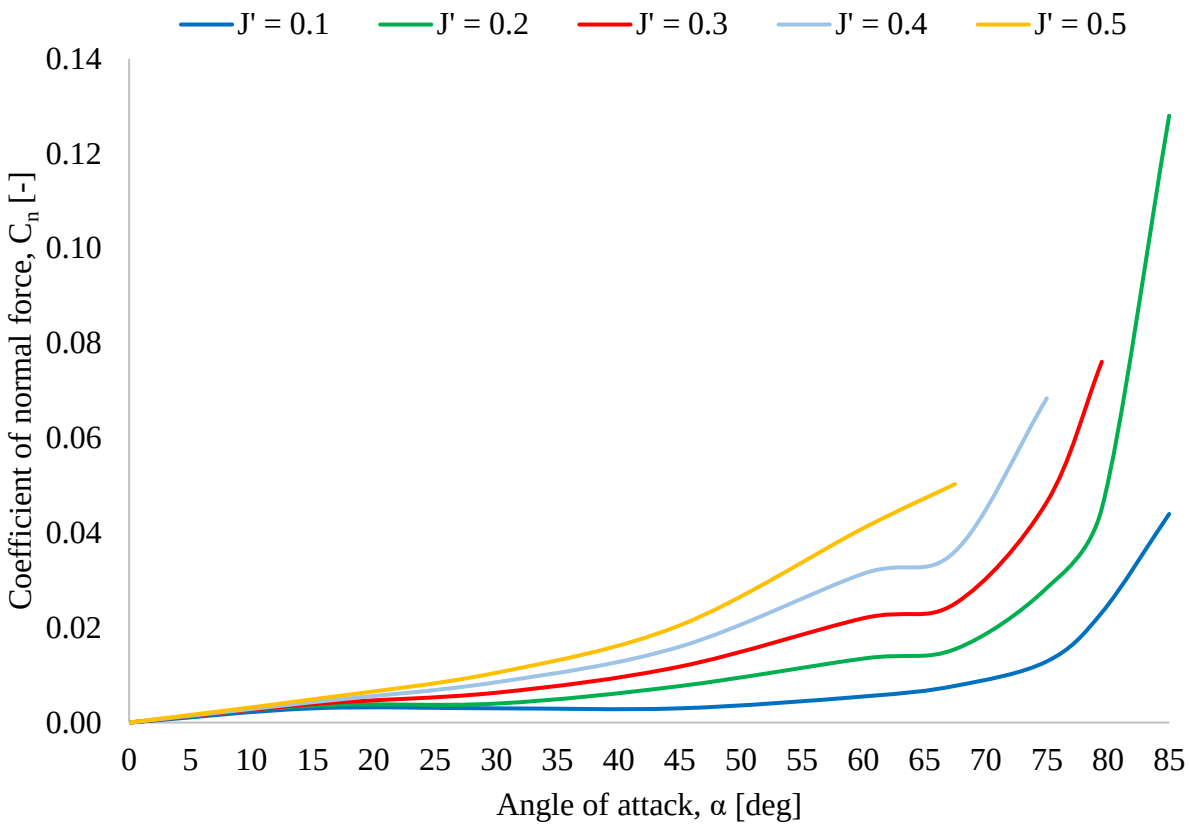

Figure 35: NACA TN D318 propeller 1 coefficient of normal force for β=16° [44]

Figure 36 shows the coefficient of pitching moment at various angles of attack, for a blade pitch angle of $\beta = 16°$ and for various modified advance ratios for data obtained by Yaggy [44] for propeller 1. Similarly, to the coefficient of normal force, the coefficient of pitching moment illustrates a linear trend to very high angles of attack, albeit with seemingly steeper gradients than the coefficient of normal force. While the gradient steepness may be higher for the coefficient of pitching moment, the coefficient values are lower than those of the coefficient of normal force, particularly at higher angles of attack. Similar trends are observed for the coefficient of pitching moment as compared to the coefficient of normal force. That is: the increasingly larger difference in coefficient values between different modified advance ratios for increasing angle of attack, the similarity in coefficient magnitude for various modified advance ratios angles of attack up until $\alpha \approx 15°$ and the changes in gradient at higher angles of attack.

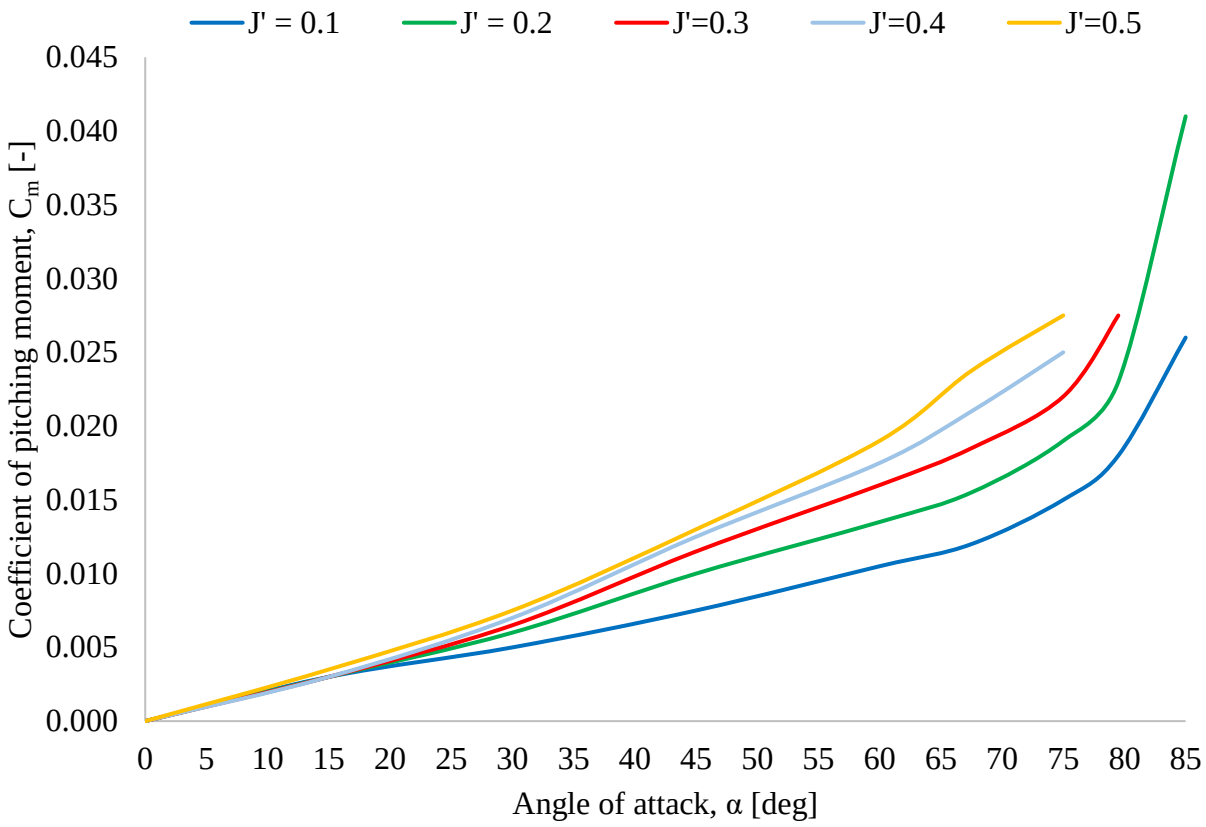

Figure 36: NACA TN D318 propeller 1 coefficient of pitching moment for β=16° [44]

1.3.5. Airfoil Dynamic Effects

When a wing or an airfoil approaches the stall angle at a significant rate such as might be encountered with a sudden pull-up of the aircraft, the stall angle of attack and the maximum coefficient of lift are increased as compared to the static (steady state) flow case [46]. When dynamic changes in angle of attack occur for the reverse case the lift does not revert to the value encountered at the lower angles seen for the forward case but instead falls below these values. This results in coefficients of lift that are below the values seen for the steady state case and causes a hysteresis loop. This is illustrated in Figure 37.

The increase in dynamic lift or 'overshoot' is caused by a delay of the adverse pressure gradient, which allows the airfoil to support a greater lift than during a steady state case. The oscillating airfoil derives lift from the frequency induced normal velocity and the effects of the change in the rate of angle of attack [46]. The effect of the frequency induced normal velocity is to essentially increase the section camber as α is increased and a corresponding decreased as α is reduced. Consequently, the rate of change of angle of attack, α, effectively increases and decreases the angle of attack when compared to the steady state case [46]. A certain amount of time is required for the boundary layer to build up. This

results in a delayed separation and the airfoil responds to the dynamic angle of attack change without stall. This also contributes to the lift overshoot [46].

The combination of pitch rate (q) and α effects influence the shape of the hysteresis loop and is a function of the reduced frequency, k. The reduced frequency is defined by Equation (16) and is essentially the measure of the rate of change of oscillation with respect to the free stream velocity [46].

$$k = c\omega/V \tag{16}$$

Where:

- ω is the oscillation frequency [rad/s]
- c is the mean aerodynamic chord [m]
- V is the free stream velocity [m/s]

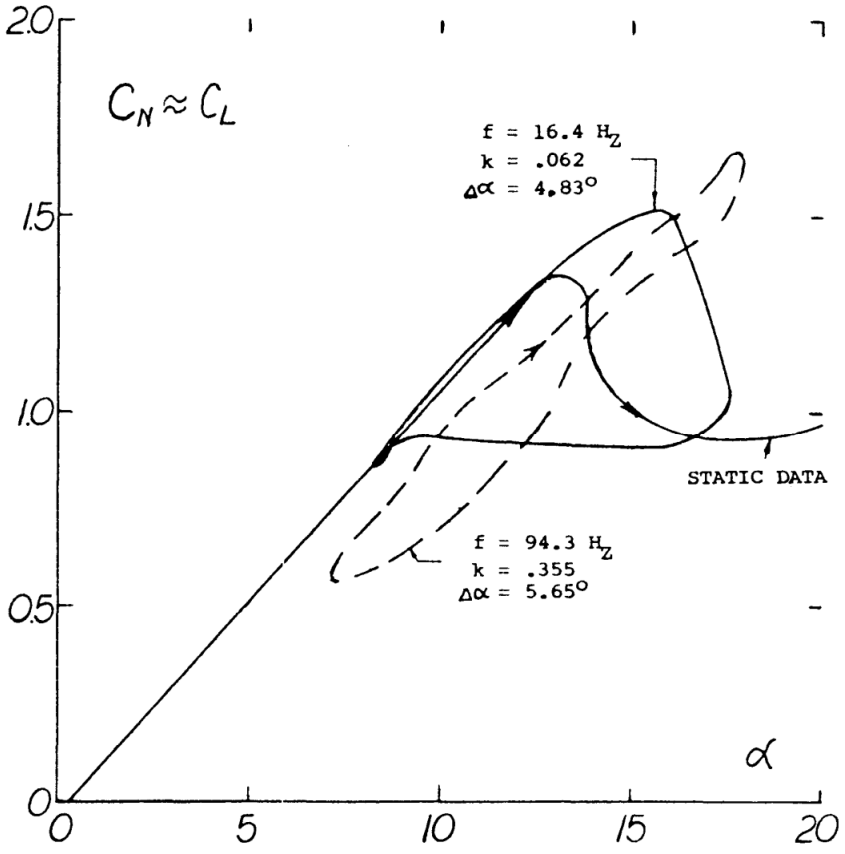

Figure 37: Frequency effect on hysteresis loop for oscillation airfoil [46]

The maximum coefficient of lift overshoot (ΔC_{LXd}) due to the dynamic condition at which it occurs ($\Delta\alpha_{Xd}$) is a function of the section shape, Reynolds number, type of stall and reduced frequency. Test data presented in Conner [47] illustrates that for a given level of reduced frequency, the maximum dynamic coefficient of lift overshoot reduces with increasing camber. Under static conditions C_{LX} changes with Reynolds number and Mach numbers while the lift overshoot is not affected. This is shown in Figure 38.

Wind tunnel test data from Anderson [48] illustrates that the maximum coefficient of lift values for the NACA 65-216 airfoil should be between 1.2 and 1.4 depending on the surface roughness and Reynolds number. Observing the maximum lift overshoot given in Figure 38 for the NACA 65-216 airfoil it would appear that the dynamic overshoot would be $\approx 10\%$ of the maximum value for the coefficient of lift for lower reduced frequency values. For higher reduced frequency values, the dynamic overshoot is $\approx 20\%$ of the maximum value for the coefficient of lift. Similar trends can be seen in references [49], [50] and [51] for various airfoil profiles and reduced frequencies. An additional finding seen in references [49], [50] and [51] is that the overshoot stall angle appears to range from $\alpha = 5° - 10°$.

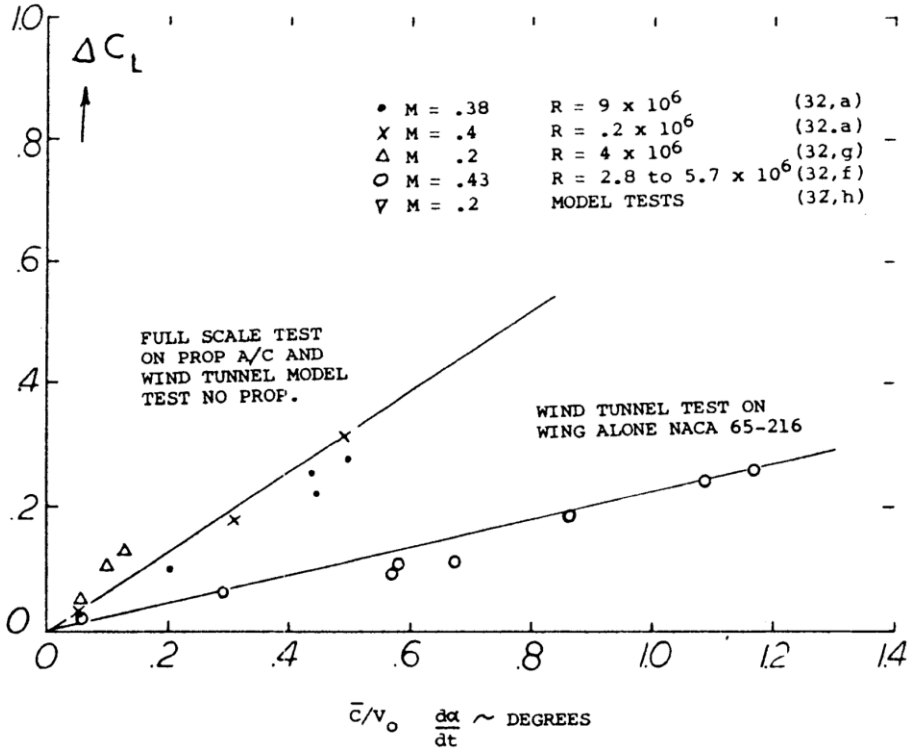

Figure 38: Lift increase due to dynamic change of angle of attack [46]

The basic shape of the dynamic lift curve through the stall region is dependent on the type of stall, in an identical manner to airfoils operating at steady state conditions. This is illustrated in Figure 39. Trailing edge stall will thus tend to yield a more rounded stall shape than leading edge stall. The type of motion and reduced frequency affect the stall and it appears that the stall becomes sharper as the reduced frequency increases.

Dynamic effects on airfoils create lift overshoot and hysteresis curves. The lift overshoot is a function of the pitch rate velocity and mean aerodynamic chord while the hysteresis curve depends on the airfoil shape reduced frequency and initial angle of attack range of the test section. The coefficient of drag will see an increase related to the increase in the coefficient of lift. The lift induced drag will increase with the lift overshoot.

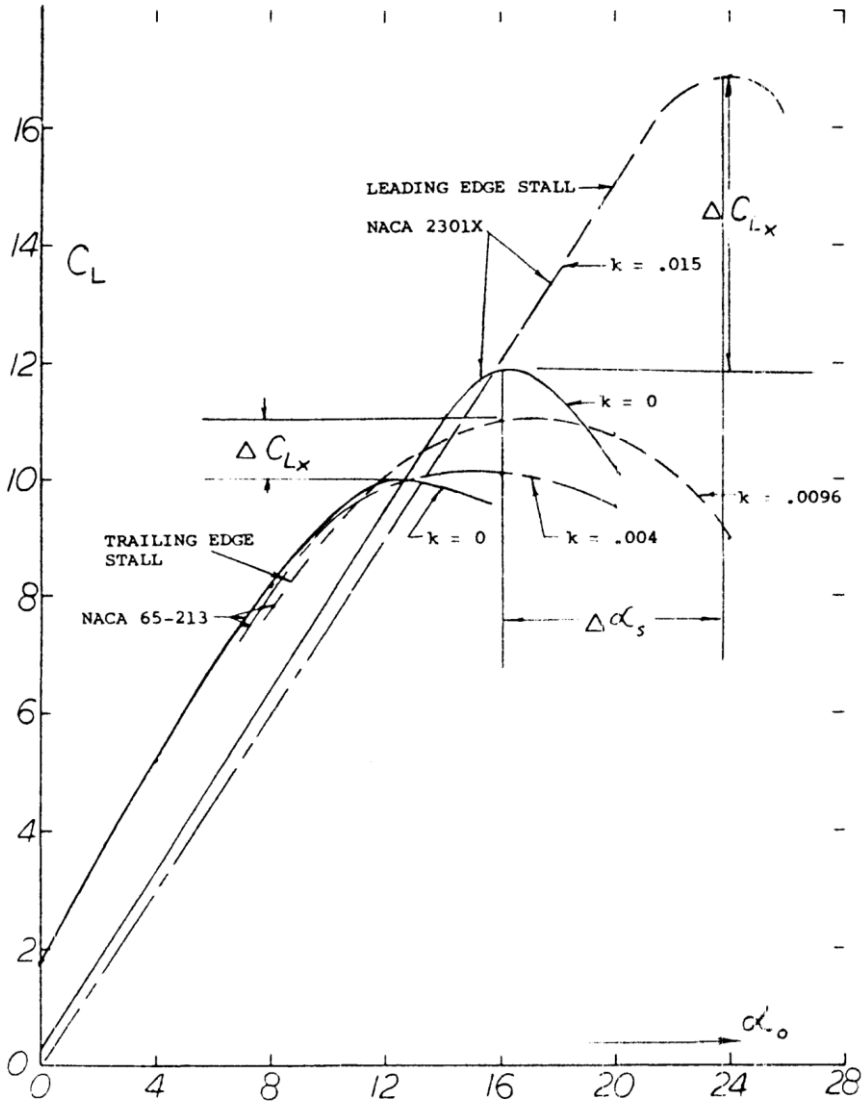

Figure 39: lift coefficient and angle of attack overshoot from static stall due to dynamic effects [46]

1.3.6. Inertial Data

The moment of inertia of a body is the resistance of a body to angular acceleration. The moments of inertia are the rotational equivalent of mass for linear motion [52]. An aircraft has three principle axes about which it rotates. These three axes (x, y and z) can be seen in Figure 22. Moments of inertia of aircraft are required so that the dynamic performance (or flying qualities) of the aircraft can be studied [53]. The moments of inertia are required for the analysis of a tumble manoeuvre as they will define how quickly and easily the aircraft will rotate.

For any conventional aircraft, the vehicle is symmetric about the XZ plane. As such the moments of inertia that are required are: I_{xx}, I_{yy}, I_{zz} and I_{xz}. The tumble maneovure is assumed to be a purely longitudinal manoeuvre and only the I_{yy} term is required.

Figure 40 presents a collection of pitch inertia values (I_{yy}) against the gross weight of the aircraft (GW) for a series of single engine, tractor configuration aircraft. The thirty-two unnamed NASA aircraft of fixed wing arrangement with high, mid and low wing configurations were investigated. Each of the aircraft had their respective inertial values obtained experimentally using the pendulum method. The aircraft listed in the report do not completely represent a modern aerobatic aircraft because the report was published in the 1940s. The results provide a baseline from which inertial estimates can be compared. Should the reader require further details of these aircraft they can be found in Gracey [54]. The Cessna aircraft data can be found in Roskam [55]. I_{xx}, I_{zz} and I_{xz} values were not presented as these inertial terms are not required for a tumble manoeuvre, as modelled in this report.

From Figure 40 it is clear that the pitch inertia of the aircraft increases with increasing gross weight. A somewhat linear trend is evident, with the exception of the heaviest aircraft. Given the maximum take-off weight for the Extra 330SC in the aerobatic configuration given in Table 1, the pitch moment of inertia is expected to be no more than $I_{yy} \approx 100$ kg.m^2.

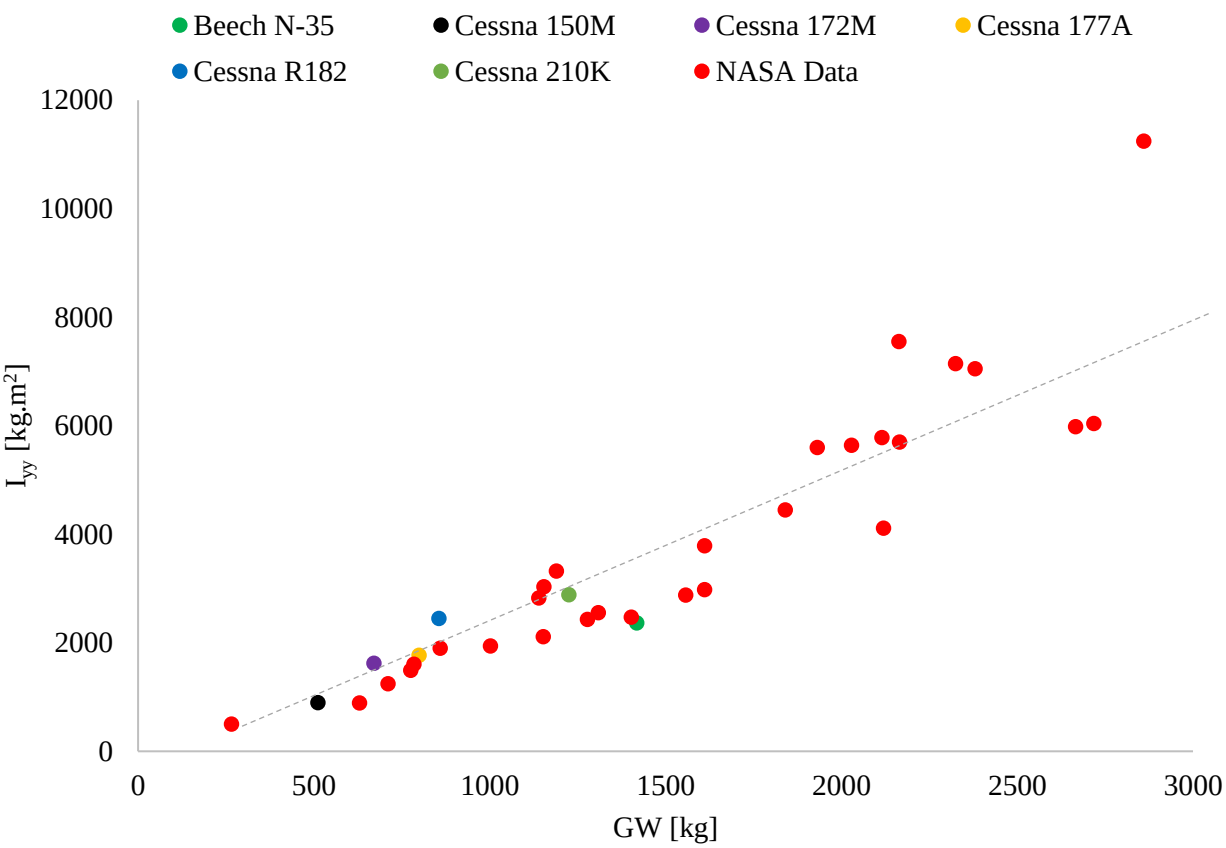

Figure 40: Collection of I_{yy} values for various single engine propeller driven aircraft

A preliminary method was generated by Lanham [53] in which the inertial values of an aircraft could be predicted, given a detailed mass distribution and overall geometry of the aircraft. Results from the use of this method compared to measured inertial values are provided in Table 7 for an assortment of aircraft types. It is apparent that the method generated by Lanham [53] is not completely accurate. The results generated with the use of this method are acceptably close to the actual inertial values in each of the required inertial directions, with the largest difference being 11.4% for I_x. Table 7 also illustrates that this method gives reasonable results for a different aircraft sizes, shapes and configurations. This method can therefore be applied to any aircraft. The limiting factor to this method is that a very detailed breakdown of various component masses and locations must be known to produce feasible results. The masses and locations of all aircraft components may not always be readily available.

Table 7: Summary of inertias of various aircraft [53]

Aircraft	Configuration	Moments of Inertia $\times 10^{+6}$ [lb-in^2]					
		Roll (I_x)		Pitch (I_y)		Yaw (I_z)	
		Actual	Calculated	Actual	Calculated	Actual	Calculated
Boeing F-15A	Operating Empty Weight	97.8	129.0	747.2	762.2	822.3	835.6
	Air Superiority Take-off Weight	166.5	190.8	824.0	829.2	946.0	951.8
Lockheed Martin C-5A	Operating Empty Weight	57909	54246	101486	98853	146944	140694
	Basic Flight Design Max Fuel	170867	158941	124744	116564	279748	266755
Boeing A-10	Empty Weight	168	203	413	356	580	543
	Ferry Mission Gross Weight	293	279	604	608	817	891
Boeing B-52G	Empty Weight	26011	23270	22551	19380	48562	42216
	Design Gross Weight	69163	64142	39520	37350	108683	92696
Average Error (%)		11.4		5.7		6.8	

1.3.7. Mass Modelling

Weight methodologies are classified into three main categories: (1) Empirical, (2) Analytical and (3) Semi-analytical [56]. Empirical methods are used to generate fast and accurate empty weight (EW), maximum take-off weight ($MTOW$) and weights for different aircraft configurations. Analytical methods are generally more accurate than empirical methods but may require far more detailed information. Semi-analytical methods tend to be more accurate and require far less information than analytical methods [56].

Generally, the $MTOW$, EW and weights of different aircraft configurations are supplied by aircraft manufacturers. For most performance predictions knowing these weights is sufficient. Aircraft inertial values are required for the analysis of manoeuvres involving angular rates. Most manufacturers do not supply any inertial data and as such, the aircraft analyst is left to predict these quantities. Predictions of aircraft inertia require component masses and their corresponding centroids from some reference axes. Some manufacturers provide detailed weights and locations of smaller components contained within the airframe. Aircraft manufacturers often do not specify the weight of structural and control components such as the wing, fuselage, control system etc. Weight estimation methods are required to predict the mass of these components as well as their centroids.

Several methods exist to estimate the weight of an aircraft and its components. The complexity and accuracy of these methods vary depending on the type and shape of aircraft in question [57]. The simplest weight estimation methods are generally intended for initial estimation only during the design phase and will only generate an approximate value [57]. The complex methods are expected to be more accurate. The methods require specific details about the geometry and other parameters [57].

It is more appropriate to use multiple weight estimation methods. Some of the more famous and accepted methods include methods from: Torenbeek [58], Raymer [59] and Roskam [55] as well as methods developed by aviation companies and operators such as the Cessna method and the United States Airforce (USAF) methods, both of which can be found in Roskam [55].

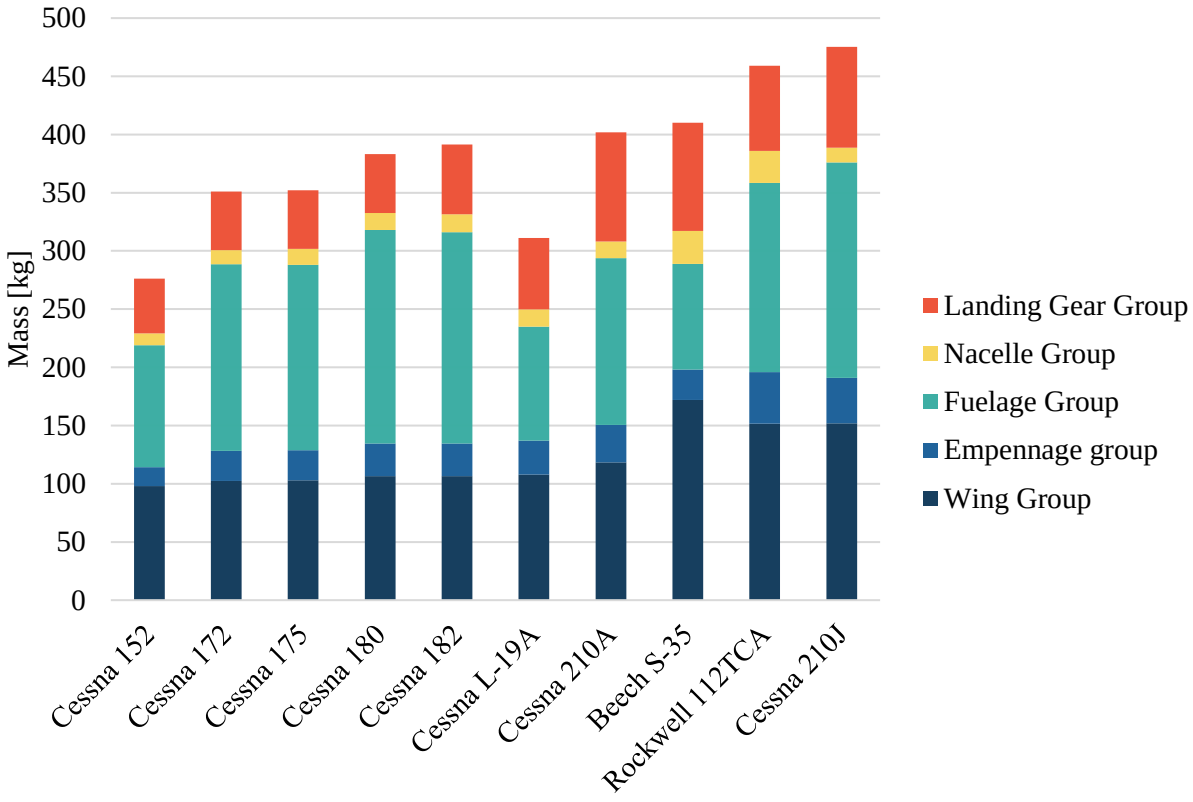

Figure 41: Structure component masses for various general aviation single engine propeller driven aircraft [55]

The masses of the main structural components for various general aviation, single engine propeller driven aircraft are presented in Figure 41. While the aircraft presented are by no means aerobatic competition aircraft, the aircraft are similar in size and configuration to aerobatic aircraft. The structural masses of these aircraft are likely to be similar to those of an aerobatic aircraft and should provide an indication of the expected masses of aerobatic aircraft. The aerobatic aircraft component masses may be slightly higher than those of the aircraft presented in Figure 41 as aerobatic aircraft are expected to experience higher load factors. From Figure 41 it is evident that the two heaviest groups of structure consist of the wing and the fuselage followed by the landing gear. The nacelle and empennage are groups that are lighter than the other structural groups. An average of the component masses for the

aircraft given in Figure 41 is presented in Table 8. These values can be used as a reference when estimating the structural component masses of an aerobatic aircraft.

Table 8: Average structural component masses for a general aviation, single engine, propeller driven aircraft

Mass Item	Average Mass [kg]
Wing Group	120
Empennage Group	30
Fuselage Group	145
Nacelle Group	16
Landing Gear Group	65

1.3.8. Aircraft Energy

The time-specific energy state of an aircraft is determined by the total amount and distribution of energy stored as altitude and airspeed. The frame of reference used by the pilot for managing the energy state during flight is aircraft-centric. It is a function of the indicated altitude and indicated airspeed and not height above ground or groundspeed. Changes in indicated altitude and airspeed are attained through forces resulting from the direct manipulation of the controls of the aircraft by the pilot. Gains in aircraft energy can be attained from the force of the engine thrust (T) and losses in aircraft energy from aerodynamic drag (D). The difference between the force in and out (T-D) is the net change. This net change determines whether the total mechanical energy increase, decreases or remains the same [5].

Since aircraft energy is gained from the engine thrust and lost through aerodynamic drag, energy flows continuously into and out of the aircraft while in flight. The rate of change of energy, usually measured as *Specific Excess Power* (SEP) and is a direct function of the difference between specific thrust and drag power. The Specific Excess Power is given as the thrust minus the drag multiplied by the aircraft velocity (airspeed) all divided by the aircraft weight. This is illustrated in Equation (17) [5].

$$SEP = \frac{(T - D)V}{W} \tag{17}$$

The thrust and drag forces multiplied by the velocity (FV and DV) are the thrust power and drag power respectiely. Dividing either of these two quantities by the mass of the aircraft results in the specific power. A fundamental relationship exists between changes in the total energy of the aircraft that results from the net energy flow and changes in the energy stored as altitude and airspeed. This energy relationship can be summarised through the aircraft energy balance equation seen in Figure 42.

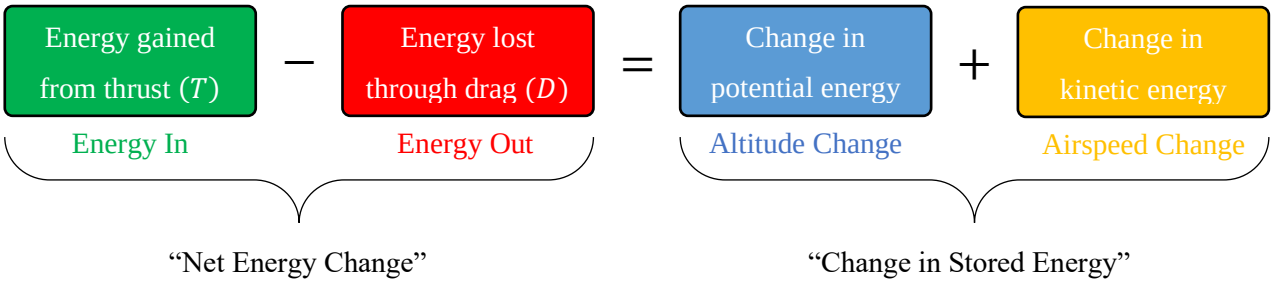

Figure 42: The energy balance equation [5]

The left hand side of the energy balance equation represents the net energy flow of the aircraft, while the right hand side reflects matching changes to the energy storage. A change in total energy resulting from the difference between thrust and drag on the left hand side of the equation always matches the change in total energy redistribution over altitude and airspeed on the right hand side. The rate of energy change varies during flight, becoming postive, negative or zero. Both sides of the energy balance equation are inexorably balanced regardless of whether the airplane is accelerating, decelerating, climbing, descending or maintaining constant altitude and airspeed [5].

The pilot controls the change in total energy on the left hand side of the energy balance equation, as well as the distribution of any changes in energy over altitude and airspeed on the right hand side. How the pilot coordinates the throttle and elevator to achieve desired altitudes and airspeeds as well as avoiding energy "crises" is at the core of energy management. This is particularly true for aerobatic performances which typically offer far less altitude with which the pilot can navigate.

A longitudinal manoeuvre is the result of an imbalance of thrust and drag, which results in either a linear acceleration or a steady rate of climb or in a combination of both acceleration and climb, in the direction of flight [31]. The accelerations that result from rates of pitch or turn are not directly involved, though may produce increases in the drag force. The increase in drag will have an indirect influence on the longitudinal force balance.

By expressing the gradient of a climb in terms of the true rate of climb and true airspeed, the longitudinal equation of motion for manoeuvring flight (as defined by Eshelby [31]), is given by Equation (18) [31].

$$[T - D]\frac{V}{W} = \frac{d}{dt}\left\{H + \frac{V^2}{2g}\right\} \tag{18}$$

Where:

- T is the thrust force [N]
- D is the overall drag of the aircraft [N]
- V is airspeed [m/s]
- W is the aircraft weight [N]
- H is the geopotential height [m]
- g is gravitational acceleration [m/s^2]

A number of energy exchanges can take place during flight in which altitude and airspeed are increased, decreased or remain unchanged. The energy exchanges that take place in level flight and a climb are presented in Table 9. These two scenarios depict energy transfers that would typically be seen in conventional flight. Two energy exchanges taking place during extreme flight scenarios are illustrated in Table 10.

Level Flight

In level flight altitude is neither gained not lost. Only airspeed is affected by a force imbalance. When the thrust exceeds the drag ($T - D > 0$) the total mechanical energy of the aircraft increases. This surplus in energy is stored as airspeed. When the drag exceeds the thrust ($T - D < 0$) the aircraft remains at the same altitude but loses airspeed. When energy gained equals that lost ($T - D = 0$) all thrust is spent on drag. The total amount of mechanical energy and its distribution over altitude and airspeed remains unchanged.

Climb

In climb both altitude and airspeed can be altered. If the thrust exceeds the drag ($T - D > 0$) the total increase in mechanical energy can be stored as either altitude or airspeed or a combination of the two. Surplus energy can be used to gain altitude while maintaining or increasing airspeed. If the total mechanical energy of the aircraft decreases ($T - D < 0$) stored energy must be consumed. This situation results in a descent and allows the aircraft to maintain constant airspeed while losing altitude. If the thrust force is set to match the drag force ($T - D = 0$) through a climb the total mechanical energy remains the same. The distribution of energy over altitude and airspeed has altered. Altitude has been gained at the expense of airspeed. To maintain this scenario the thrust force must be adjusted to match the drag force as airspeed decreases. During a climb or descent, a component of the aircraft mass acts in the direction of either the drag force or the thrust force. This is illustrated by the $W \sin\gamma$ component in Table 9.for a climb.

High Angle of Attack (Tumble Scenario)

For a high angle of attack manoeuvre taking place in the horizontal plane, only one scenario is feasible. Thrust is significantly outweighed by the drag force ($T - D \ll 0$). Such an extreme scenario is typically seen in the tumble manoeuvre. Energy from the propeller is used to generate a thrust force and propeller slipstream. The energy from the propeller slipstream is imparted to the horizontal stabiliser which in turn causes a pitch rate. The pitch rate results in large aircraft pitch angles and angles of attack changes. These large angles generate large drag forces. The mass forces may also become large and act in the drag direction should the flight path angle be sufficiently large. The large drag force results negative SEP values. Stored energy is consumed as the added energy from the thrust is now acting to rotate the aircraft and acts as the 'lift' force. Only a component of the thrust acts in the thrust direction. The rate what which stored energy is consumed is done so at a rapid rate. Initially airspeed is consumed without much change in altitude, creating a large deceleration. Once most of the airspeed has depleted, energy is taken from the altitude stores. This results in a loss of altitude to regain airspeed. A more powerful engine is able to generate more energy and will aid in slowing the consumption of energy from the mechanical stores. In this situation the lift force is insufficient to keep the aircraft flying. This means altitude cannot be gained and energy gains must be converted to airspeed. This implies that the pilot has little option but to lose altitude to gain airspeed. The minimum time to recover mechanical energy can be achieved by maximising the acceleration. This is achieved in a vertical dive where the mass vector acts in the same direction as the thrust.

Vertical Dive

In a vertical dive altitude is lost and airspeed gained. The orientation of the aircraft ($\theta = 270°$) means that the aircraft mass acts in the same direction as the thrust. The forces acting in the thrust direction greatly outweigh the drag ($T - D \gg 0$). This is particularly true at lower airspeeds. In the extreme case where the aircraft is at an airspeed of 0 m/s the aircraft has maximum acceleration when entering a vertical dive. At zero airspeed $SEP = 0$ but builds as the aircraft accelerates. Stored potential energy (altitude) is converted into kinetic energy (airspeed) during the dive. Additional energy is added by the thrust and mass of the aircraft as speed builds. At some point during the dive the trajectory of the aircraft must be altered and a pull up manoeuvre must be performed. This can be accomplished once a sufficient quantity of energy has been acquired (enough airspeed). The excess energy from the thrust force along with airspeed can be converted to altitude. Energy management is crucial in this scenario.

Table 9: Energy exchanges in conventional flight

Energy Exchange Example	Net Energy Change ($T - D$)	Change in Stored Energy		Resulting Aircraft Condition
		Altitude	Airspeed	
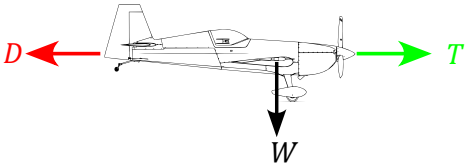 **Level Flight**	> 0	No change	Increase	Acceleration at constant altitude
	< 0	No change	Decrease	Deceleration at constant altitude
	$= 0$	No change	No change	Constant airspeed and altitude
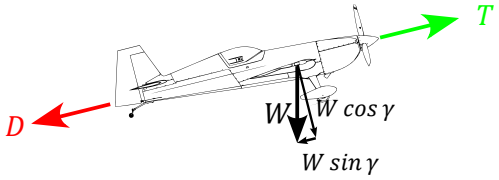 **Climb**	> 0	Increase	No change	Climb at constant speed
	< 0	Decrease	No change	Descent at constant speed
	$= 0$	Increase	Decrease	Decelerating climb

Table 10: Energy exchanges in extreme flight

Energy Exchange Example	Net Energy Change ($T - D$)	Change in Stored Energy		Resulting Aircraft Condition
		Altitude	Airspeed	
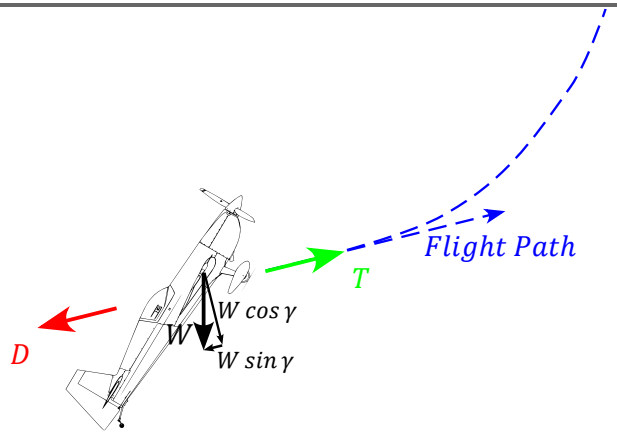 **High angle of attack manoeuvre (Horizontal)**	$\ll 0$	Constant/ Slight increase	Large decrease	Large deceleration with minimal altitude gains
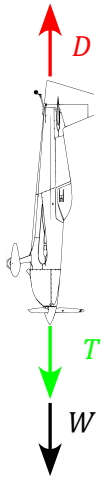 **Vertical Dive**	> 0	Decrease	Increase	Accelerating descent

SEP Chart

A SEP chart provides an energy envelope within which an aircraft is safe to fly. An example of a SEP chart is provided in Figure 43. The SEP chart may be used to determine how much additional energy an aircraft carries at various altitudes and airspeeds. It may be used to determine the energy requirements when performing a manoeuvre that involves alterations in altitude or airspeed.

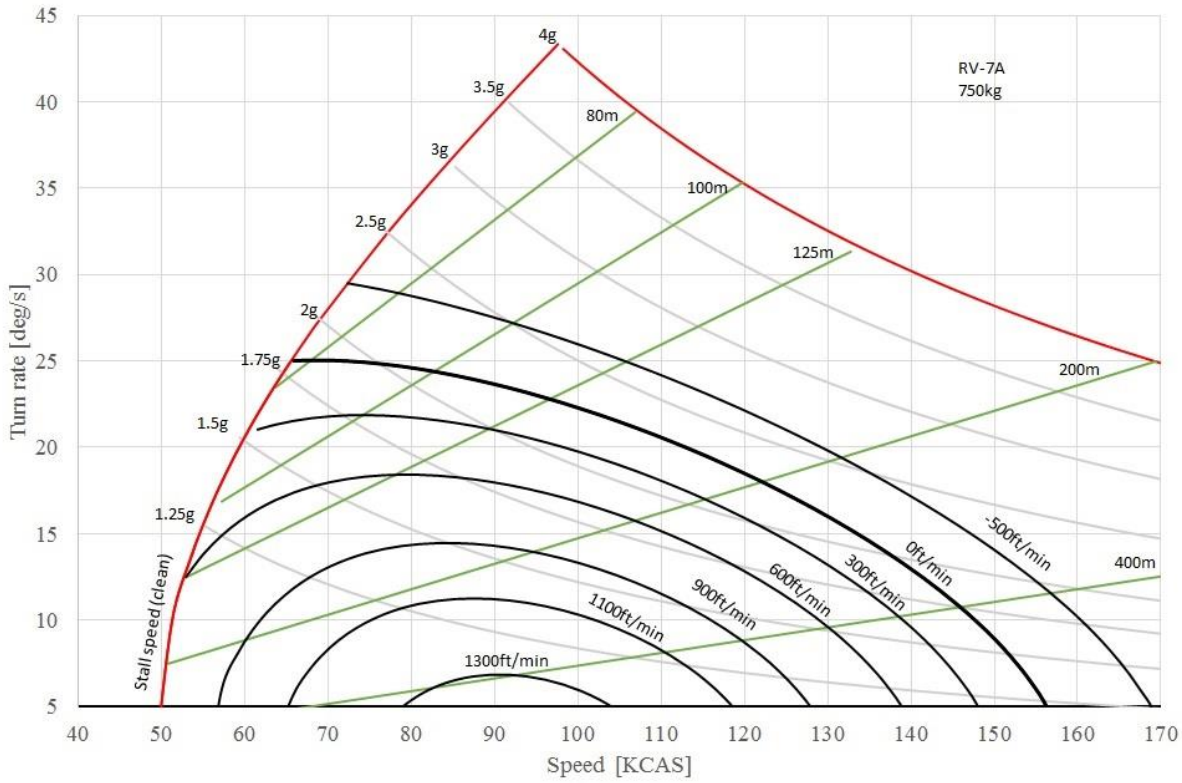

Figure 43: SEP chart example

1.4. Objectives

The research objectives are to:

1. Synthesise a model, incorporating all the post-stall and dynamic aerodynamic coefficients, to understand aircraft displacements, velocities and accelerations, before, during and after a tumble manoeuvre.
2. Determine safe operating entry and exit heights for pilots performing tumble manoeuvres so that an aircraft can recover from the manoeuvre.

1.5. Dissertation Outline

This dissertation consists of six chapters. Each chapter provides information that is used in subsequent chapters.

Chapter 2 presents various models for calculating the mass, inertial and aerodynamic input data.

Chapter 3 presents the input data generated for the Extra 330SC. using the models provided in chapter 2. A technical review of the data is outlined, comparing the generated data to any published results found in open literature. This was performed as a means of validation, where possible.

Chapter 4 outlines the methodology employed in the generation of the tumble model. Equations for forces and moments at high angles of attack are illustrated along with the resulting load factors in the velocity and body axes. A mathematical model is presented that outlines the steps and equations required to solve a complete tumble manoeuvre.

Chapter 5 presents the tumble model results and findings. Various performance parameters of the manoeuvre are provided. These include aircraft displacements (flight path), velocities, accelerations, forces and moments. Failed tumble manoeuvres attempts are presented and the shortcomings of the attempts are highlighted and briefly discussed. A minimised risk tumble manoeuvre is explained and the parameter adjustments required to complete this scenario are highlighted. A comparison of successful manoeuvres to video footage is outlined as a means of validation.

Chapter 6 concludes the findings presented in this dissertation and provides a list of recommendations for future work that may be useful in expanding the work developed within this dissertation.

2. MODELLING

2.1. Introduction

This section can essentially be thought of as somewhat of an extension of the literature review. This chapter provides detailed explanations and formulations of models that were used to generate the necessary input data required for modeling a tumble manoeuvre. The chapter begins by summarising a variety of mass estimation models for general aviation aircraft obtained from Roskam [55]. Next an inertial estimation model developed by Lanham [53] is outlined along with the necessary mass inputs. Aerodynamic models are then addressed starting with lifting surfaces (such as the wing and empennage surfaces). A semi-empirical method was created by Spera [60] that provides coefficient data for a lifting surface for infinite or finite aspect ratios. For fuselage aerodynamic data, a method established by Jorgensen [42] is presented with an explanation on the extension of the method to lower Mach numbers, as the Jorgensen [42] method is only validated from Mach number of 0.6 upwards. Finally, a method for predicting the aerodynamics of the propeller is explained. In the absence of an acceptably accurate formulation, coefficient data presented by Yaggy [44] in §1.3.4.4 was used for the propeller.

2.2. Mass Estimation Models

Aircraft component masses as well as the distribution of the masses are required to accurately determine inertial values and general aircraft performance. The overall masses of most aircraft are readily available; however, the masses of the individual aircraft components are generally not given. The masses of major component groups as well as some smaller individual components will need to be obtained or estimated.

Methods for mass estimations of major aircraft component groups were collected and published by Roskam [55]. The major component groups that were investigated are as follows:

1. Structural weight
2. Power plant weight
3. Fixed equipment weight

The mass estimation methods provided by Roskam [55] include the Cessna method, the USAF method and the Torenbeek method. The mass estimation equations for the three main component groups as well as subcomponents within each group for each of the three methods are provided in §2.2.1-2.2.3. Equations for each of the methods are provided in Table 11, Table 12 and Table 13.

2.2.1. Structural Mass

The structural mass group consists of subgroups which make up the entire aircraft structure. These groups are:

a. The wing mass, M_W
b. The empennage mass, M_{emp}
c. The fuselage mass, M_f
d. The nacelle mass, M_n
e. The landing gear mass, M_g

The total structural mass is the sum of all the subgroups: $M_{struct} = M_W + M_{emp} + M_f + M_n + M_g$.

a. Wing Mass

The Cessna, USAF and Torenbeek methods for estimating the wing mass are provided by Equations (20), (34) and (46) respectively.

Based on the recommended applicability of each method, the Cessna method would be the least appropriate, as it is for low performance aircraft (whereas aerobatic aircraft are high performance). For the Cessna method, the wing mass includes: the wingtips, any fairing, control surfaces, fuel tanks, wing-fuselage spar carry through and sweep angle. The USAF and Torenbeek methods only calculate the mass of the wing structure and as such, the Cessna method is expected to provide a larger mass estimate.

b. Empennage Mass

The empennage mass will be subdivided into two further categories: the horizontal tail mass M_h and the vertical tail mass M_v.

The Cessna method provides mass estimates for the horizontal tail and the vertical tail in Equations (21) and (22) respectively. The USAF methods provides horizontal tail and vertical tail mass estimates that are given by Equations (35) and (36), respectively. The Torenbeek methods provides a mass estimate for the entire empennage and is given by Equation (47). The Torenbeek method does not separate the horizontal and vertical tails into separate mass equations.

It is expected that the Cessna method will yield the least accurate results based on the recommended applicability of Equations (21) and (22). The Torenbeek method is not as useful as the Cessna and USAF methods because it does not provide the masses of the horizontal and vertical tail surfaces independently. It should also be noted that the sweep angle of the horizontal tail is not included in any of the methods. This may lead to an underestimation of the horizontal tail mass from all methods.

c. Fuselage Weight

The equations for estimating the fuselage masses are provided by Equations (23) and (24) for the Cessna method. These two equations are for a high-wing and low-wing configuration respectively. Equation (37) provides a mass estimate for the fuselage for the USAF method while Equation (48) provides the Torenbeek mass estimate for the fuselage.

The equation for the Cessna method (both high-wing and low-wing) is based on the number of passengers present in the aircraft. Since an aerobatic aircraft is usually occupied by a single person (the pilot), the Cessna method is expected to underestimate the mass of the fuselage. The Nicolai mass estimation [61], provided by Equation (19), was included as an additional method of analysis for the fuselage mass, given the expected shortcomings of the Cessna method. The Nicoli mass estimation is applicable to light aircraft.

$$M_f = 0.0737\left[2D_f V_D^{0.338} l_f^{0.857} (W_{TO} n_{ult})^{0.286}\right]^{1.1} \tag{19}$$

d. Nacelle Weight

The estimation of the nacelle mass is provided for a propeller driven aircraft. The structural mass associated with the external ducts and or cowls of the engine and the mass of the engine mounting trusses are all included in the formulae. The Cessna and Torenbeek methods for nacelle mass are provided by Equations (25) and (49) respectively. The USAF method accounts for the nacelle mass in the powerplant mass estimate.

The Torenbeek mass estimation, given by Equation (49), includes the entire engine section forward of the fuselage.

e. Landing Gear Mass

The Cessna methods provides mass estimations for the main gear and nose gear in Equations (26) and (27) respectively. The USAF method provides a mass estimation of the landing gear in Equation (39). Torenbeek does not provide a method for estimating the mass of the landing gear.

2.2.2. Powerplant Mass

The aircraft powerplant mass, M_{pwr}, will be assumed to consist of the following subgroups:

a. Engines, M_e: this is inclusive of the engine, exhaust, cooling, supercharger (if present) and lubrication system

b. Air induction system, M_{ai}: this includes the inlet ducts (other than nacelles), ramps, spikes and associated controls

c. Propeller, M_{prop}

d. Fuel system, M_{fs}

e. Propulsion system, M_{ps}: this includes engine controls, starting systems, propeller controls and provisions for engine installation.

The total powerplant weight will be a sum of all the subsystems, $M_{pwr} = M_e + M_{ai} + M_{prop} + M_{fs} + M_{ps}$.

It should be noted that Roskam [55] has strongly recommended that actual mass data, from engine manufacturers, be obtained for this group if it is readily available.

a. Engine Mass

Mass estimations for the engine are provided by Equations (28), (40) and (51) for the Cessna, USAF and Torenbeek methods respectively. For the Cessna method, all engine accessories are included, however, the engine oil is not.

b. Air Induction Mass

The Torenbeek method for the mass estimation of the air induction system is provided by Equation (52). The Cessna and USAF methods include the mass of the air induction system engine calculations.

c. Propeller Mass

The mass of the propeller is provided by Equation (53) for the Torenbeek method. The Cessna method does not provide a mass estimate for the propeller while the USAF method includes the propeller mass in the engine mass equation. It is recommended that propeller manufacturer data be used wherever possible. Propeller data for aircraft are generally readily available and as such, an investigation into methods other than the Torenbeek method will not be done. For the Extra 330SC data on the propeller weight as well as all system weights associated with the propeller are provided in the pilots operating handbook.

d. Fuel System Mass

Equations (31), (43) and (54) provide mass estimations for the fuel system for the Cessna, USAF and Torenbeek methods, respectively.

e. Propulsion System Mass

It is recommended that actual data be used.

2.2.3. Fixed Equipment Mass

The fixed equipment that is carried on aircraft varies significantly depending on the aircraft type and mission. For aerobatic aircraft a list of the fixed equipment masses and locations can be obtained from the pilots operating handbook (POH). Some information is not included. Two areas that will require a mass estimation have been identified:

a. Flight control system, M_{fc}

b. Electrical system, M_{els}

a. Flight Control System Mass

The Cessna, USAF and Torenbeek methods for the estimation of the flight control systems are provide by Equations (32), (44) and (55), respectively. The formulae given seem to be somewhat similar and are expected to yield similar results.

b. Electrical System Mass

Equations (33), (45) and (56) provide the mass estimations of the electrical system for the Cessna, USAF and Torenbeek methods respectively. The Cessna method estimates the mass of the electrical system as a function of the maximum takeoff mass. The USAF method predicts the electrical system mass as a function of the fuel system and instrumentation masses. The method given by Torenbeek gives the mass of the hydraulic and pneumatic system as well as the electrical system as a function of the aircraft empty weight. The three methods given take different approaches in estimating the mass of the electrical system and as such may yield very different results.

Table 11: Cessna method mass estimation equations

Group	Applicability	Component	Subcomponent	Equation	Equation No.	Notes
Structural	• Small, relatively low performance • $V_{max} < 200$ kts • Unpressurised fuselages	Wing	-	$W_W = 0.04674 W_{TO}^{0.397} S^{0.36} N_{ult}^{0.397} A^{1.712}$	(20)	Cantilevered Wings
		Empennage	Horizontal Tail	$W_h = \frac{3.184 W_{TO}^{0.887} S_n^{0.101} A_n^{0.138}}{57.5\ t_{r_n}^{0.223}}$	(21)	
			Vertical Tail	$W_v = \frac{1.68 W_{TO}^{0.567} S_v^{1.249} A_v^{0.482}}{15.6\ t_{r_v}^{0.747} \cos \Lambda_{\frac{1}{4}_v}^{0.882}}$	(22)	
		Fuselage	-	$W_f = \frac{0.04682\ W_{TO}^{0.692}\ N_{pax}^{0.374}\ l_{f-n}^{0.590}}{100}$	(23)	Low Wing aircraft
				$W_f = 14.86 W_{TO}^{0.144} \left(\frac{l_{f-n}}{P_{max}}\right)^{0.778} l_{f-n}^{0.383} N_{pax}^{0.455}$	(24)	High wing aircraft
		Nacelle		$W_n = K_n W_{TO}$	(25)	
		Landing Gear	Main Gear	$W_{g_m} = 0.013 W_{TO} + 0.146 W_L^{0.417} N_{ult.l}^{0.950} l_{s_m}^{0.183}$	(26)	
			Nose Gear	$W_{g_n} = 6.2 + 0.013 W_{TO} + 0.000143 W_L^{0.749} n_{ult.l} l_{s_n}^{0.788}$	(27)	
Powerplant		Engine	-	$W_e = K_p P_{TO}$	(28)	
		Air Induction		Included in W_p calculations	(29)	
		Propeller		N/A	(30)	
		Fuel System		$W_{fs} = 0.4 \frac{W_F}{K_{fsp}}$	(31)	Internal fuel systems (no tiptanks):
Fixed Equipment		Flight Control Systems		$W_{fc} = 0.0168 W_{TO}$	(32)	
	• Mechanical controls	Electrical System		$W_{els} = 0.0268 W_{TO}$	(33)	2 sets of flight controls

Table 12: USAF method mass estimation equations

Group	Applicability	Component	Subcomponent	Equation	Equation No.	Notes
Structural	• Light, utility aircraft • Speeds up until ≈ 300 kts	Wing	-	$W_W = 96.948\left[\left(\frac{W_{TO}N_{ult}}{10^5}\right)^{0.65}\left(\frac{A}{\cos\Lambda_{\frac{1}{4}}}\right)^{0.57}\left(\frac{S}{100}\right)^{0.61}\left(\frac{(1+\lambda)}{2\left(\frac{t}{c}\right)_m}\right)^{0.36}\left(1+\frac{V_H}{500}\right)^{0.5}\right]^{0.993}$	(34)	
		Empennage	Horizontal Tail	$W_h = 127\left[0.289\left(\frac{W_{TO}n_{ult}}{10^5}\right)^{0.87}\left(\frac{S_n}{100}\right)^{1.2}\left(\frac{l_h}{10}\right)^{0.483}\left(\frac{b_h}{t_{r_n}}\right)^{0.5}\right]^{0.458}$	(35)	
			Vertical Tail	$W_v = 98.5\left[0.289\left(\frac{W_{TO}n_{ult}}{10^5}\right)^{0.87}\left(\frac{S_v}{100}\right)^{1.2}\left(\frac{b_v}{t_{r_v}}\right)^{0.5}\right]^{0.458}$	(36)	
		Fuselage	-	$W_f = 200\left[\left(\frac{W_{TO}n_{ult}}{10^5}\right)^{0.286}\left(\frac{l_f}{10}\right)^{0.857}\left(\frac{W_f+h_f}{10}\right)\left(\frac{V_c}{100}\right)^{0.338}\right]^{1.1}$	(37)	
		Nacelle		Included in powerplant weight	(38)	
		Landing Gear		$W_g = 0.054 l_{sm}^{0.501}(W_L n_{ult.l})^{0.684}$	(39)	
Powerplant		Engine	-	$W_e + W_{ai} + W_{prop} + W_p = 2.575 W_{eng}^{0.922} N_e$	(40)	
		Air Induction		Included W_{eng} calculation	(41)	
		Propeller		Included W_{eng} calculation	(42)	
		Fuel System		$W_{fs} = 2.49\left[\left(\frac{W_F}{K_{fsp}}\right)^{0.6}\left(\frac{1}{1+int}\right)^{0.3} N_t^{0.2} N_e^{0.13}\right]^{1.21}$	(43)	
Fixed Equipment		Flight Control Systems		$W_{fc} = 1.066 W_{TO}^{0.626}$	(44)	
		Electrical System		$W_{els} = 426\left[\frac{(W_{fs}+W_{iae})}{1000}\right]^{0.51}$	(45)	Unpowered flight controls

Table 13: Torenbeek method mass estimation equations

Group	Applicability	Component	Subcomponent	Equation	Equation No.	Notes
Structural	• Light transport aircraft • $W_{TO} < 12500$ lbs • $V_D \leq 250$ kts	Wing	-	$W_W = 0.00125 W_{TO} \left(\frac{b}{\cos \Lambda_{\frac{1}{2}}}\right)^{0.75} \left(1 + \left\{\frac{6.3 \cos \Lambda_{\frac{1}{2}}}{b}\right\}^{0.5}\right) (n_{ult})^{0.55} \left(\frac{bS}{t_r W_{TO} \cos \Lambda_{\frac{1}{2}}}\right)^{0.3}$	(46)	
		Empennage		$W_{emp} = 0.04[n_{ult}(S_h + S_v)^2]^{0.75}$	(47)	Conventional tail configurations
		Fuselage	-	$W_f = 0.23 \left(S_{fus-wet}\right)^{1.2} \sqrt{\frac{V_{dive} l_f}{2 D_f}}$	(48)	
		Nacelle		$W_n = 2.5 P_{TO}^{0.5}$	(49)	Nacelle in fuselage nose
		Landing Gear		N/A	(50)	
Powerplant		Engine		$W_{pwr} = K_{pg}(W_e + 0.24 P_{TO})$	(51)	Single propeller driven, piston aircraft
		Air Induction		$W_{ai} + W_p = 1.03 N_e^{0.3} \left(\frac{P_{TO}}{N_e}\right)^{0.7}$	(52)	
		Propeller		$W_{prop} = K_{prop_2} + N_p^{0.218} \left[D_p P_{TO} N_{bl}^{0.5}\right]^{0.782}$	(53)	
		Fuel System		$W_{fs} = 2 \left(\frac{W_F}{5.87}\right)^{0.667}$	(54)	
Fixed Equipment		Flight Control Systems		$W_{fc} = 0.23 W_{TO}^{2/3}$	(55)	Unpowered, unduplicated flight controls
		Electrical System		$W_{hps} + W_{els} = 0.0078 W_E^{1.2}$	(56)	

2.3. Inertia Estimation Model

An inertial estimation method generated by Lanham [53] presents a somewhat rudimentary approach for calculating the inertial values of various aircraft components as well as the overall aircraft inertias. All equations and concepts developed within this section are obtained from Lanham [53].

The method is split into three main steps:

1. First the aircraft mass must be allocated to six separate groups:
    a. Wing group
    b. Horizontal tail group
    c. Vertical tail group
    d. Fuselage group
    e. Propulsion group
    f. Additional items

    The allocation of mass involves distributing the subsystems throughout the aircraft without identifying the actual location of each individual component [53]. It should also be noted that this approach is performed using an "historical" or "accepted design practice." Corrections may need to be made for design configurations with unusual concepts or mass distributions.

2. The moment of inertia of each group is then calculated about its own centroid and transferred to a set of remote axes.
3. The centre of gravity of the aircraft is determined and the inertias are then summed and translated back to the aircraft centre of gravity.

Some items which require further discussion are:

1. Fuel system – This item is distributed between the fuselage and wing group according to the fraction of fuel mass contained in each group.
2. Control Surfaces – This is summarised in Table 14.

Table 14: Surface control weight allocation [53]

Fraction of Total Surface Control Weight					
Configuration Code W,H,V*	**Wing**	**Horizontal Tail**	**Vertical Tail**	**Fuselage Cockpit**	**Fuselage Distribution**
0, 0, 0	0.532	0.128	0.124	0.038	0.178
0, 0, 1	0.457	0.110	0.247	0.033	0.153
0, 1, 0	0.464	0.239	0.108	0.034	0.155
0, 1, 1	0.406	0.209	0.220	0.029	0.136
1, 0, 0	0.608	0.108	0.103	0.032	0.149
1, 1, 0	0.541	0.205	0.092	0.029	0.133
1, 0, 1	0.534	0.094	0.213	0.028	0.131
1, 1, 1	0.482	0.182	0.192	0.026	0.118

*W = Wing	0 = fixed	1 = variable sweep
H = Horizontal Tail	0 = elevator type	1 = all moveable type
V = Vertical Tail	0 = rudder type	1 = all moveable type

3. Trapped Fuel – This is distributed between the wing group and the fuselage according to the fraction of fuel mass contained within each group.
4. Air induction system – If the engines are buried within the fuselage, the mass is added to the fuselage group. If the engines are podded, the mass is added to the engine group.
5. Wing Structure – Mass should be added to the wing group if there is a wing carry-through structure.

Group Inertias:

Before the centroidal inertias (I_0's) of each group can be calculated and then imposed on the remote set of axes, locations of components and geometric data must be known. All data must be referenced in accordance with the chosen set of axes illustrated in Figure 44. These axes are not set and can be varied. To simplify the calculation of the inertia the Z axis has been set at the nose of the aircraft.

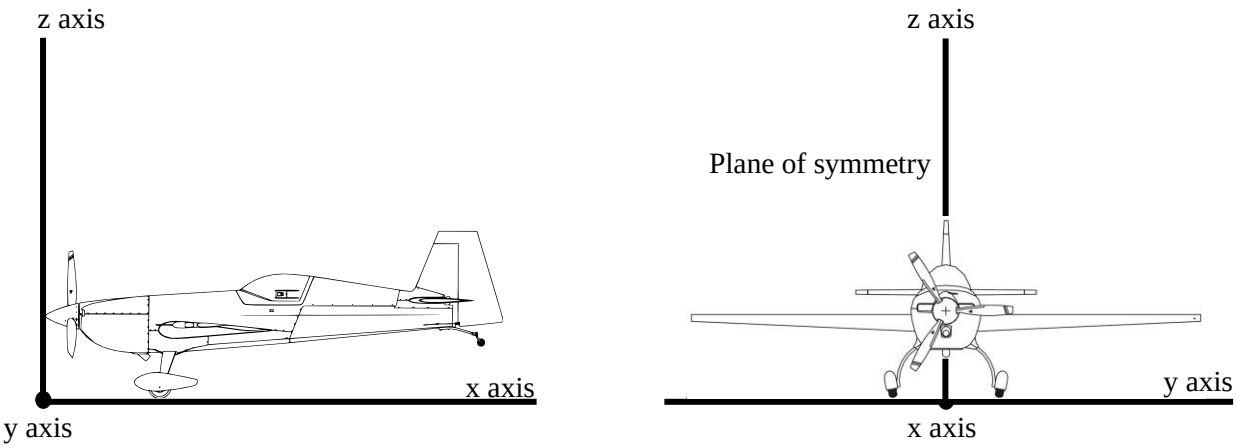

Figure 44: Reference axes for inertial calculations

2.3.1. Inertias of Surfaces

Surfaces include the wing, the horizontal stabiliser and the vertical stabiliser groups. To define the shape of the surface the normal planform (with only one side of the wing and horizontal tail due to symmetry) is used. The equations derived for the inertia of surfaces require the use of a trapezoidal panel with the actual thickness varying linearly from root to tip. Should the surface have an edge (a sudden step change in the leading or trailing edge line) or a change in thickness, the surface should then be discretised into inner and outer trapezoidal panels with the inertia calculated separately for each section. It will be assumed that the thickness is constant moving from leading edge to trailing edge and equal to the maximum for the section.

The moments of inertia for a surface are given by Equations (57), (58) and (59).

$$I_{1x} = \frac{M_s b^3}{V_S}\left\{\left[(t_r - t_t)\left(\frac{c}{4} + \frac{b\tan\Lambda_T}{5} - \frac{b\tan\Lambda_L}{5}\right)\right] + \left[t_r\left(\frac{c}{3} + \frac{b\tan\Lambda_T}{4} - \frac{b\tan\Lambda_L}{4}\right)\right]\right\}^2 \quad (57)$$

$$I_{1y} = \frac{M_s b}{V_S}\left\{\left[t_r\left(\frac{c^3}{3} + bc\tan\Lambda_T\left(\frac{c}{2} + \frac{b\tan\Lambda_T}{3}\right) + \frac{b^3}{12}(\tan^3\Lambda_T - \tan^3\Lambda_L)\right)\right] - \left[(t_r - t_t)\left(\frac{c^3}{6} + bc\tan\Lambda_T\left(\frac{c}{3} + \frac{b\tan\Lambda_T}{4}\right) + \frac{b^3}{15}(\tan^3\Lambda_T - \tan^3\Lambda_L)\right)\right]\right\} \quad (58)$$

$$I_{1z} = I_{1x} + I_{1y} \quad (59)$$

[2] It was found that an error existed in Equation (57), the terms in the first square bracket all had the incorrect sign in Lanham [53]. Equation (57) should read $I_{1x} = \left\{\left[(t_r - t_t)\left(-\frac{c}{4} - \frac{b\tan\Lambda_T}{5} + \frac{b\tan\Lambda_L}{5}\right)\right] + \left[t_r\left(\frac{c}{3} + \frac{b\tan\Lambda_T}{4} - \frac{b\tan\Lambda_L}{4}\right)\right]\right\}$

Where:

- M_s is the mass of the surface [lbs]
- b is the span of the surface [in]
- t_r is the thickness of the root chord [in]
- t_t is the thickness of the tip chord [in]
- c is the root chord of the surface [in]
- Λ_T is the sweep angle of the trailing edge of the surface [deg]
- Λ_L is the sweep angle of the leading edge of the surface [deg]
- V_s is the volume of the surface and can be obtained using Equation (60)

$$\mathrm{V}_s = \mathrm{b}\left\{t_r\left[c + \frac{b}{2}(\tan\Lambda_T - \tan\Lambda_L)\right] - (t_r - t_t)\left[\frac{c}{2} + \frac{b}{3}(\tan\Lambda_T - \tan\Lambda_L)\right]\right\} \tag{60}$$

A graphical representation of some of the surface inertia variables are illustrated in Figure 45. The axes presented in Figure 45 follow the convention outlined in Figure 44. Note that imperial units have been used in the definition of the surface group variables. The choice of imperial unit was made to keep with the units described in Lanham [53]. This allowed for a simpler comparison.

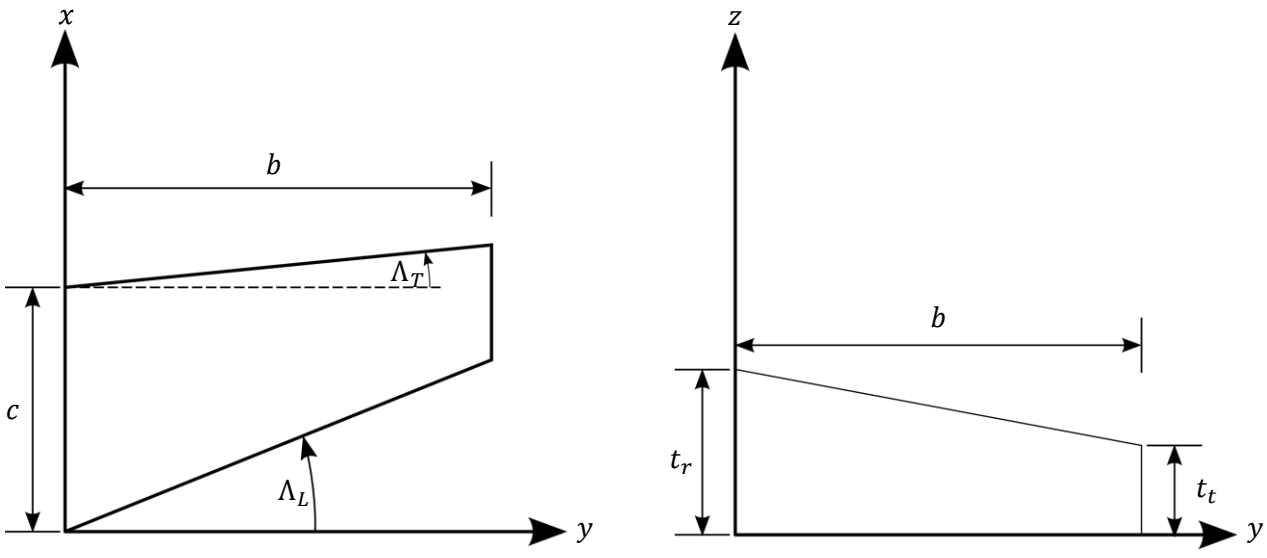

Figure 45: Surface inertia variable definitions

It was assumed, in the derivation of Equations (57), (58) and (59), that all surfaces lie in planes parallel to the XY plane of the remote axes. To account for any dihedral Equations (61) and (62**)** should be used.

$$True\ I_{1y} = \left(I_{1y}\cos\theta + I_{1z}\sin\theta\right) \tag{61}$$

$$True\ I_{1z} = \left(I_{1y}\sin\theta + I_{1z}\cos\theta\right) \tag{62}$$

Where:

- θ is the dihedral angle [deg]

I_{1x} is not affected by dihedral.

The required product of inertia (I_{xz}) is given by Equation (63)

$$\begin{aligned} I_{1xz} = {} & \frac{M_s}{V_s} t_r \sin\theta \left[\frac{c_r^2 b^2}{4} + \frac{c_r b^3}{3}\tan\Lambda_T + \frac{b^4}{8}\left(\tan^2\Lambda_T - \tan^2\Lambda_L\right)\right] \\ & - \frac{M_s}{V_s}\left(t_r - t_t\right)\sin\theta \left[\frac{c_r^2 b^2}{6} + \frac{c_r b^3}{4}\tan\Lambda_T + \frac{b^4}{10}\left(\tan^2\Lambda_T - \tan^2\Lambda_L\right)\right] \end{aligned} \tag{63}$$

Equations (57) to (63) can be used to calculate the required inertias for the entire wing, horizontal tail or vertical tail surfaces provided the total group is used.

If there is no wing carry-through structure, the exposed wing should be used and the symbols should be defined accordingly. Otherwise, a theoretical wing should be used that passes through the fuselage. All horizontal and vertical tail surfaces should be defined with the exposed parameters.

To correctly define the general symbols used in all equations concerning surfaces, Lanham [53] has suggested the use of Table 15 for each separate surface.

Table 15: Surface symbol definitions for inertial calculations [53]

	Defined Symbol			
General Symbol	**Wing (No change in thickness)**	**Inboard Surface**	**Outboard Surface**	**Horizontal and Vertical Surfaces**
$\boldsymbol{\Lambda_L}$	Λ_{L1}	Λ_{L1}	Λ_{L2}	Λ_{L1}
$\boldsymbol{\Lambda_T}$	Λ_{T1}	Λ_{T1}	Λ_{T2}	Λ_{T1}
$\boldsymbol{b}$	b_1	b_2	b_3	b_1
$\boldsymbol{c}$	c_r	c_r	c_2	c_1
$\boldsymbol{t_r}$	t_r	t_r	t_b	t_r
$\boldsymbol{t_t}$	t_t	t_b	t_t	t_t
$\boldsymbol{M}$	M_W	M_1	M_0	M_h, M_v
$\bar{\bar{\boldsymbol{x}}}$	$XS1$	$XS2$	$XS3$	$XS1$
$\bar{\bar{\boldsymbol{y}}}$	$YS1$ *	$YS2$ *	$YS3$	$YS1$ **
$\bar{\bar{\boldsymbol{z}}}$	$ZS3$ ***	$ZS4$ ***	$ZS5$ ***	$ZS3$ ***

* If $YS4 = 0$ and $\theta = 0$ set these terms = 0

** If $YS4 = 0$ and $\theta = 0$ set these terms = 0

*** Not required if $\theta = 0$

Before the surface I_0's can be obtained from the I_1 values, the centroids of the surfaces must be determined. All longitudinal surface centroids can be determined using a method developed by DATCOM, given that the parameters c, b and Λ_L are properly defined for each surface. These parameters are illustrated in Figure 45. The centroid in the X direction is given by Equation (64), the spanwise centroid or centroid in the Y direction is given by Equation (65) and the vertical centre of gravity can be calculated using Equations (66), (67) or (68). The numerical values next to the XS, YS and ZS parameters are defined in Table 15.

$$XS1, XS2, XS3 = \frac{\left(-C_a^2 + C_b^2 + C_c C_b + C_c^2\right)}{3(C_b + C_c - C_a)}\sqrt{K_0} \tag{64}$$

Where:

- C_a is the smallest of the following values: $c, b\tan\Lambda_L, b\tan\Lambda_L + c$
- C_b is the intermediate value from the same list of values and
- C_c is the largest value from the same list of values
- $K_0 = 0.703$ for a wing surface
- $K_0 = 0.771$ for a horizontal or vertical tail surface

$$YS1, YS2, YS3 = \frac{b^2}{V}\left[t_r\left(\frac{c}{2}+\frac{b}{3}(\tan\Lambda_T - \tan\Lambda_L)\right) - (t_r - t_t)\left(\frac{c}{3}+\frac{b}{4}(\tan\Lambda_T - \tan\Lambda_L)\right)\right] \quad (65)$$

All vertical centre of gravity distances are negligible for surfaces with $\theta = 0$ because of the small thickness of the surface when compared with the surface length and span. For surfaces with dihedral the vertical centre of gravity no longer lies in the XY plane and can be calculated with Equations (66), (67) or (68)

$$ZS1 = YS1\, sin\, \Theta \quad (66)$$

$$ZS2 = YS2\, sin\, \Theta \quad (67)$$

$$ZS3 = YS3\, sin\, \Theta \quad (68)$$

An illustration of the surface centroid can be seen in Figure 46. The thickness of the surface shown in the YZ axes has been greatly exaggerated for illustrative purposes. As such, the distance ZS will only be noticeable if the surface has any dihedral (i.e. the surfaces is rotated around the X axis).

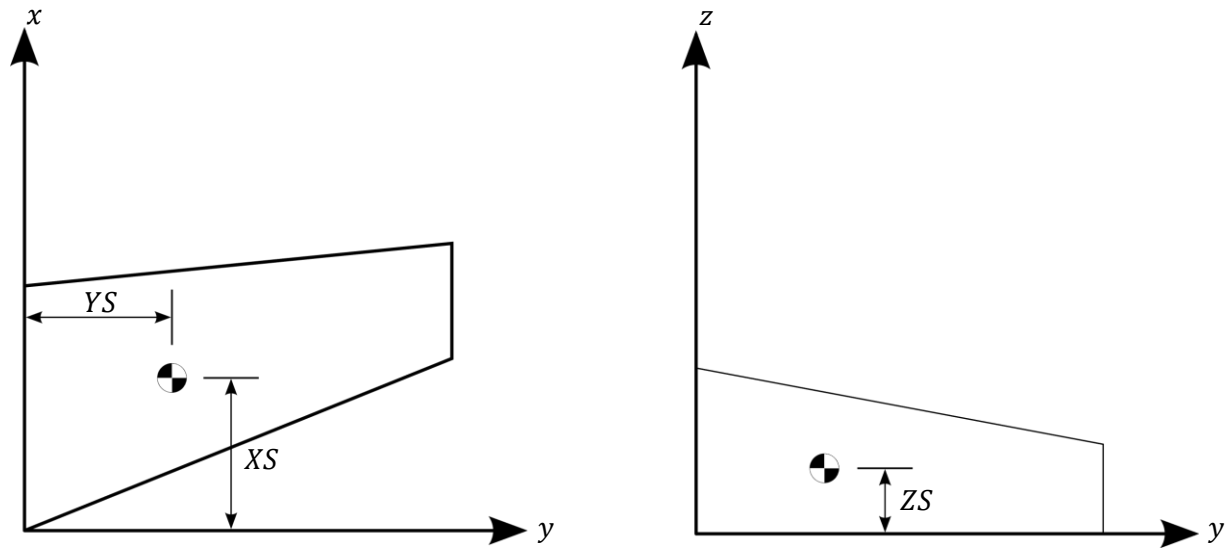

Figure 46: Surface centroid

With the centroids on the surface known, all I_1 inertias can be translated to the centroid and subsequently to the remote axes. For wings (with changes in thickness), horizontal and vertical tail surfaces, the inertial values (I) are calculated by Equations (69)-(72).

$$\mathrm{I_x} = \mathrm{I_{1x}} - M(YS1)^2 - M(ZS3)^2 + M(YS1 + YS4)^2 + M(ZS3 + ZS1)^2 \quad (69)$$

$$\mathrm{I_y} = \mathrm{I_{1y}} - \mathrm{M}(XS1)^2 - M(ZS3)^2 + M(XS1 + XS4)^2 + M(ZS3 + ZS1)^2 \quad (70)$$

$$\mathrm{I_z} = I_{1z} - M(XS1^2 + YS1^2) + M(XS1 + XS4)^2 + M(YS1 + YS4)^2 \quad (71)$$

$$\mathrm{I_{xz}} = I_{1xz} - M(XS1)(ZS3) + M(XS1 + XS4)(ZS3 + ZS1) \quad (72)$$

2.3.2. Inertias of the Fuselage

The fuselage mass is divided into four main areas:

- Structure
- Distributed contents
- Volume of mass
- Point masses

2.3.2.1. Structure

The structural mass of the fuselage should include any wing carry-through structure (if it has not already been added to the wing group) as well as air induction installation mass (if any engines are buried within the fuselage). This mass is assumed to be distributed between a conical nose shell, an open-ended right-cylindrical shell[3] and a tail conical shell, as illustrated in Figure 47. The conical shell is neglected if the engine installation is buried. The fuselage structure is distributed according to each geometric shape in proportion to the surface area of the shape $\left(\frac{mass}{area} = constant\right)$.

[3] An open-ended right-cylindical shell is a hollow cylindrical surface that is open on either end (uncapped). The ends of the shell are cut at right angles to the longitudinal axis of the cylinder.

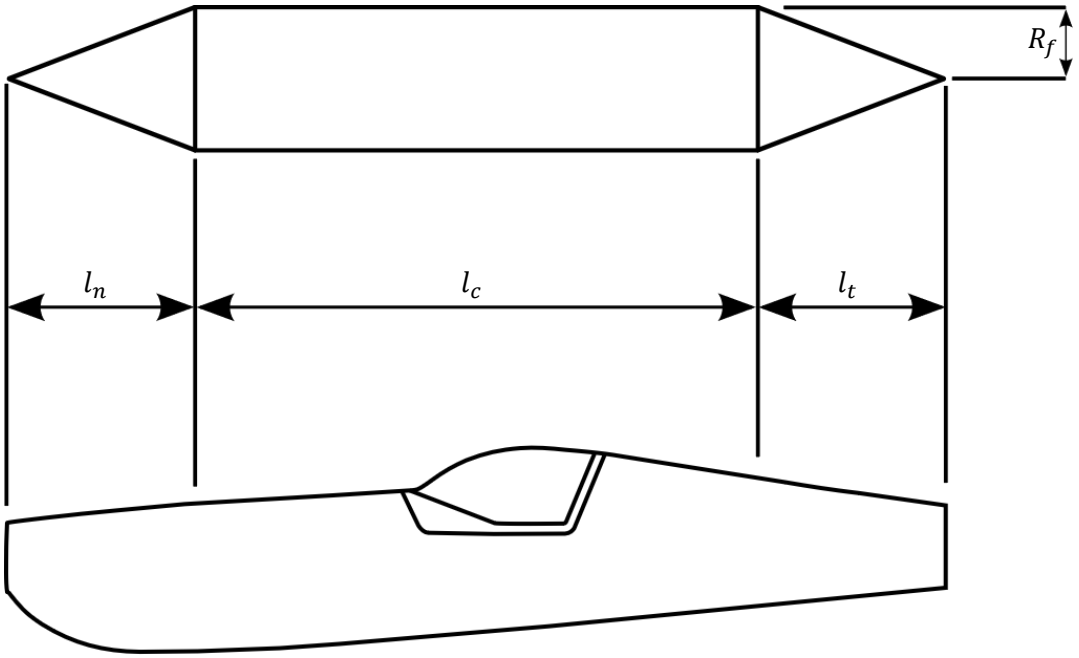

Figure 47: Fuselage structural definitions for inertial calculations [53]

The moments of inertia in the X,Y and Z directions for the fuselage structure are given by Equations (73), (74) and (75) respectively and the product of inertia is given by Equation (76).

$$\mathrm{I_x} = \frac{R_f^2}{2}(M_n + 2M_c + M_t) + M_s Z_b^2 \tag{73}$$

$$\mathrm{I_y} = \frac{R_f^2}{4}(M_n + 2M_c + M_t) + l_n^2\left(\frac{M_n}{2} + M_c + M_t\right) + l_c^2\left(\frac{M_c}{3} + M_t\right) + \frac{l_t^2 M_t}{6} + l_c l_n(M_c + 2M_t) + \frac{2}{3}l_t l_c M_t + \frac{2}{3}l_t l_n M_t + M_s Z_b^2 \tag{74}$$

$$\mathrm{I_z} = I_y - M_s Z_b^2 \tag{75}$$

$$\mathrm{I_{xz}} = M_n\left(\frac{3}{4}\, l_n Z_b\right) + M_c Z_b\left(l_n + \frac{l_c}{2}\right) + M_c Z_b\left(l_n + l_c + \frac{l_t}{4}\right) \tag{76}$$

Where:

- R_f is the radius of the open-ended right-cylindrical shell [in]
- Z_b is the perpendicular distance from the remote axes XY plane to the fuselage centreline [in]
- M_s is the total fuselage structural mass [lbs]
- l_n is the length of the conical nose shell [in]
- l_c is the length of the open-ended right-cylindrical shell [in]

- l_t is the length of the tail conical shell [in]
- M_n, M_c and M_t are the distributed masses of the conical nose shell, the open-ended right-cylindrical shell and the tail conical shell respectively [lbs]. They are given by Equations (77), (78) and (79), respectively
- S_n, S_c and S_t are the surface areas of the conical nose shell, the open-ended right-cylindrical shell and the tail conical shell respectively [in^3] and are given by Equations (80), (81) and (82), respectively

$$\mathrm{M_n} = \frac{S_n M_s}{S_n + S_c + S_t} \tag{77}$$

$$\mathrm{M_c} = \frac{S_c M_s}{S_n + S_c + S_t} \tag{78}$$

$$\mathrm{M_t} = \frac{S_t M_s}{S_n + S_c + S_t} \tag{79}$$

$$S_\mathrm{n} = \pi R\sqrt{R^2 + l_n^2} \tag{80}$$

$$\mathrm{S_c} = 2\pi R l_c \tag{81}$$

$$\mathrm{S_t} = \pi R\sqrt{R^2 + l_t^2} \tag{82}$$

2.3.2.2. Distributed Contents

This section consists of four main items:

a. Electrical system
b. Instruments and navigation
c. Hydraulics
d. Surface controls

These items are assumed to be randomly spread throughout the fuselage, from the cockpit to the leading edge of the horizontal tail in the shape of an open-ended right-cylindrical shell.

The moments of inertia about the remote axes of the distributed content are given by Equations (83)-(86).

$$I_x = M_{dc}R_{dc}^2 + M_{dc}Z_b^2 \tag{83}$$

$$I_y = \left(\frac{M_{dc}}{2}\right)\left(R_{dc}^2 + \frac{1}{6}\left[XS4 - CREW_{c.g}\right]^2\right) + M_{dc}\left[\frac{1}{2}\left(XS4 - CREW_{c.g}\right) + CREW_{c.g}\right]^2 + M_{dc}Z_b^2 \tag{84}$$

$$I_z = I_y - M_{dc}Z_b^2 \tag{85}$$

$$I_{xz} = \frac{M_{dc}}{2}\left[XS4 - CREW_{c.g}\right]Z_b \tag{86}$$

Where:

- M_{dc} consists of various masses including:
    - The mass of the surface controls allocated to the fuselage group.
    - The mass of the electrical systems allocated to the fuselage group.
    - the mass of the hydraulic systems allocated to the fuselage group.
    - 30% of the mass of instruments and navigation allocated to the fuselage group [lbs].

  If the masses and locations are any of these components are explicitly known, then they may be omitted from the distributed contents inertial calculations and may be calculated separately as point masses.
- R_{dc} is the radius of distributed contents assumed open-ended right-cylindrical shell [in]
- Z_b is the same definition as in §2.3.2
- XS4 is the perpendicular distance from the YZ plane of the remote axes to the leading edge of the surface root chord [in]
- $CREW_{c.g}$ is the perpendicular distance from the YZ plane of the remote axes to the crew centre of gravity [in]

2.3.2.3. Volumes of Mass

This section consists of items such as:

a. Fuel system within the fuselage
b. Avionics bay
c. Furnishings

Due to the variability of these items a decision must be made as to whether these items are used as volumes or point masses. Either a cylindrical shell or a solid rectangular shape can be used should volumes be chosen.

The inertial values for volumes of mass, about the remote axes, can be obtained with Equations (87)-(90) for a cylindrical shells and equations (91)-(94) for a rectangular solids.

Cylindrical Shell:

$$I_x = M_{vo}R_{vo_c}^2 + M_{vo}Z_{voc}^2 \tag{87}$$

$$I_y = \frac{M_{vo}}{2}\left[R_{vo_c}^2 + \frac{1}{6}l_{vo_c}^2\right] + M_{vo}[X_{vo}^2 + Z_{vo}^2] \tag{88}$$

$$I_z = \frac{M_{vo}}{2}\left[R_{vo_c}^2 + \frac{1}{6}l_{vo_c}^2\right] + M_{vo}X_{vo}^2 \tag{89}$$

$$I_{xz} = M_{vo}X_{vo}Z_{vo} \tag{90}$$

Where:

- M_{vo} is the mass of the volume [lbs]
- R_{vo_c} is the radius of the cylindrical shell [in^3]
- l_{vo_c} is the length of the cylindrical shell [in]
- Z_{vo} is the perpendicular distance from the XY plane of the remote axes to the centreline of the cylindrical shell [in]
- X_{vo} is the perpendicular distance from the YZ plane of the remote axes to the centre of the cylindrical shell [in]

Rectangular Solid:

$$I_x = \frac{M_{vo}}{12}\left[2R_{vo_r}^2 + 2R_{vo_r}^2\right] + M_{vo}Z_{vo}^2 \tag{91}$$

$$I_y = \frac{M_{vo}}{12}\left[l_{vo_r}^2 + 2R_{vo_r}^2\right] + M_{vo}[X_{vo}^2 + Z_{vo}^2] \tag{92}$$

$$I_z = \frac{M_{vo}}{12}\left[l_{vo_r}^2 + 2R_{vo_r}^2\right] + M_{vo}X_{vo}^2 \tag{93}$$

$$I_{xz} = M_{vo}X_{vo}Z_{vo} \tag{94}$$

Where:

- R_{vo_r} is the height/width of the rectangular solid [in]
- l_{vo_r} is the length of the rectangular solid [in]

2.3.2.4. Point Masses

For the calculation of inertias, point masses were considered separately. For the roll (I_x) inertia the total mass of the point masses was distributed between a solid cone and a solid right circular cylinder. All collective point masses located within the nose or tail cone of the airframe were put in the solid cone and all point masses in the centre section of the airframe are put in the right circular cylinder. I_y and I_z were lumped at some average location.

The inertial values for point masses, about the remote axes, within the fuselage are given by Equations (95)-(98).

$$I_x = \Sigma\left[M_{pm}(Y_{Pm}^2 + Z_{Pm}^2)\right] \; or \; I_x = \left[\frac{M_{pc}}{2}R_{Pm}^2 + \frac{3}{10}M_{pnc}R_{Pm}^2 + \left(M_{pc} + M_{pnc}\right)Z_b^2\right] \tag{95}$$

$$I_y = \Sigma\left[M_{pm}(X_{Pm}^2 + Z_{Pm}^2)\right] \tag{96}$$

$$I_z = \Sigma\left[M_{pm}(X_{Pm}^2 + Y_{Pm}^2)\right] \tag{97}$$

$$I_{xz} = \Sigma\left[M_{pm}X_{Pm}Z_{Pm}\right] \tag{98}$$

Where:

- M_{pm} is the mass of one point mass [lbs]
- M_{pc} is the total mass of the point masses in the fuselage centre section [lbs]
- M_{pnc} is the total mass of the point masses in the nose and tail cone sections [lbs]
- R_{pm} is the radius of the right circular cylinder [in]
- Z_b is the same definition as in §2.3.2
- X_{pm} is the perpendicular distance from the YZ plane of the remote axes to the point mass [in]
- Y_{pm} is the perpendicular distance from the XZ plane of the remote axes to the point mass [in]
- Z_{pm} is the perpendicular distance from the XY plane of the remote axes to the point mass [in]

2.3.3. Inertias of the Propulsive Unit

The total mass of this group is divided by the number of engines installed on the aircraft. This is the mass of each individual engine as well as its accessories.

If the I_0's of the engine(s) on the aircraft are not known, they can be estimated by making use of a solid cylinder.

The inertial values of the engine, about the remote axes, is given by Equations (99)-(102) for an approximate value of I_o. If the values of each I_o are known Equations (103)-(106) may be used

I_o approximated:

$$I_x = \frac{M_e R_e^2}{2} + M_e(YP^2 + ZP^2) \tag{99}$$

$$I_y = \frac{M_e}{12}(3R_e^2 + l_e^2) + M_e(XP^2 + ZP^2) \tag{100}$$

$$I_z = \frac{M_e}{12}(3R_e^2 + l_e^2) + M_e(XP^2 + YP^2) \tag{101}$$

$$I_{xz} = M_e \cdot XP \cdot ZP \tag{102}$$

I_o known:

$$I_x = I_{ox} + M_e(XY + ZP^2) \tag{103}$$

$$I_y = I_{oy} + M_e(XP^2 + ZP^2) \tag{104}$$

$$I_z = I_{oz} + M_e(XP^2 + YP^2) \tag{105}$$

$$I_{xz} = I_{oxz} + M_e \cdot XP \cdot ZP \tag{106}$$

Where:

- M_e is the total propulsive group mass divided by the number of engines [lbs]
- R_e is the average nacelle radius (for buried engines use the radius of the engine) [in]

- XP is the perpendicular distance from the YZ plane of the remote axes to the engine centre of gravity [in]
- YP is the perpendicular distance from the XZ plane of the remote axes to the engine centre of gravity [in]
- ZP is the perpendicular distance from the XY plane of the remote axes to the engine centre of gravity [in]
- I_{0x}, I_{0y}, I_{0z} and I_{0xz} are the known inertial values of the propulsive unit

2.3.4. Inertias of Internal Fuel

The fuel is split into two main groups:

- Wing fuel tanks
- Fuselage fuel tanks

Wing Fuel Tanks

The internal fuel present in the wings is defined in the same manner as the surfaces because of the wing fuel tank being a similar shape to the wing surface. It will be assumed that the wing tank is full and has a constant density.

The I_1 equations for surfaces (§2.3.1) can be used for the fuel tanks where ρ_f (the density of fuel) is substituted for $\left(\frac{M}{V}\right)$.

Thus, the inertial values of fuel tanks within the wing are given by Equations (107)-(110).

$$I_{4x} = 2b^3\rho\left[t_r\left(\frac{c}{3}+\frac{b}{4}[\tan\Lambda_T - \tan\Lambda_L]\right) + (t_r - t_t)\left(-\frac{c}{4}-\frac{b}{5}[\tan\Lambda_T - \tan\Lambda_L]\right)\right] \tag{107}$$

$$\begin{aligned} I_{4y} = 2b\rho\Bigg\{&\left[t_r\left(\frac{c^3}{3} + bc\tan\Lambda_T\left(\frac{c}{2}+\frac{b\tan\Lambda_T}{3}\right)+\frac{b^3}{12}(\tan^3\Lambda_T - \tan^3\Lambda_L)\right)\right] \\ &-\left[(t_r - t_t)\left(\frac{c^3}{6} + bc\tan\Lambda_T\left(\frac{c}{3}+\frac{b\tan\Lambda_T}{4}\right)+\frac{b^3}{15}(\tan^3\Lambda_T - \tan^3\Lambda_L)\right)\right]\Bigg\} \end{aligned} \tag{108}$$

$$I_{4z} = I_{4x} + I_{4y} \tag{109}$$

$$\begin{aligned} I_{4xz} = 2\rho\sin\theta\Bigg\{&\left[t_r\left(\frac{c^2b^2}{12}+\frac{cb^3}{12}\tan\Lambda_T+\frac{b^4}{40}(\tan^2\Lambda_T - \tan^2\Lambda_L)\right)\right] \\ &+\left[t_t\left(\frac{c^2b^2}{6}+\frac{cb^3}{4}\tan\Lambda_T+\frac{b^4}{10}(\tan^2\Lambda_T - \tan^2\Lambda_L)\right)\right]\Bigg\} \end{aligned} \tag{110}$$

The variables used in Equations (107)-(110) are defined as per §2.3.1, however, the variables are now sized for the surface fuel tank instead of the entire surface.

Equation (110) is only relevant if the aircraft has any dihedral. If there is dihedral then Equations (111) and (112) should be used in place of Equations (108) and (109) respectively.

$$\text{TRUE } I_{4y} = I_{4y}\cos\theta + I_{4z}\sin\theta \tag{111}$$

$$\text{TRUE } I_{4z} = I_{4y}\sin\theta + I_{4z}\cos\theta \tag{112}$$

I_{4x} is not affected by dihedral. Equations (107)-(112) can be used to calculate the total I_4 for the total wing fuel (both the right and left wing).

Once again, as was the case for surfaces (§2.3.1), the centroid of the fuel tank must be determined. The centroid is assumed to be approximately at the centre of volume of the tank. The centroids for the fuel tank are given by Equations (113)-(115).

$$XF1 = \frac{b}{V}\left\{\left[t_r\left(\frac{c^2}{2} + \frac{bc\,tan\,\Lambda_T}{2} + \frac{b^2}{6}(tan^2\,\Lambda_T - tan^2\,\Lambda_L)\right)\right] - \left[(t_r - t_t)\left(\frac{c^2}{4} + \frac{bc\,tan\,\Lambda_T}{3} + \frac{b^2}{8}(tan^2\,\Lambda_T - tan^2\,\Lambda_L)\right)\right]\right\} \tag{113}$$

$$YF1 = \frac{b^2}{V}\left\{\left[t_r\left(\frac{c}{2} + \frac{b}{3}(tan\,\Lambda_T - tan\,\Lambda_L)\right)\right] - \left[(t_r - t_t)\left(\frac{c}{3} + \frac{b}{4}(tan\,\Lambda_T - tan\,\Lambda_L)\right)\right]\right\} \tag{114}$$

$$ZF2 = YF1\,sin\,\theta \tag{115}$$

The variables used in Equations (113)-(115) are defined as per §2.3.1. The variables were sized for the surface fuel tank instead of the entire surface.

The I_4 inertial values of the fuel tank can now be translated to obtain I_o values. This is achieved using Equations (116)-(119).

$$I_x = I_{4x} YF1^2 - M_{fw}(ZF2)^2 + M_{fw}(YF1 + YF2)^2 + M_{fw}(ZF2 + ZF)^2 \quad (116)$$

$$I_y = I_{4y} - M_{fw} XF1^2 - M_{fw} ZF2^2 + M_{fw}(XF1 + XF2)^2 + M_{fw}(ZF2 + ZF)^2 \quad (117)$$

$$I_z = I_{4z} - M_{fw}(XF1^2 + YF1^2) + M_{fw}(XF1 + XF2)^2 + M_{fw}(YF1 + YF2)^2 \quad (118)$$

$$I_{xz} = I_{4xz} - MM_{fw}(XF1)(ZF2) + M_{fw}(XF1 + XF2)(ZF2 + ZF) \quad (119)$$

Where:

- M_{fw} is the mass of the fuel in both wing fuel tanks [lbs]
- $XF1$ is the distance from the wing fuel tank leading edge at the most inboard tank chord to the longitudinal tank centre of gravity [in]
- $XF2$ is the perpendicular distance from the YZ plane of the remote axes to the leading edge of the wing fuel tank at the most inboard chord
- $YF1$ is the distance from the wing fuel tank most inboard tank chord to the spanwise tank centre of gravity [in]
- $YF2$ is the perpendicular distance from the XZ plane of the remote axes to the leading edge of the wing fuel tank at the most inboard chord [in]
- ZF is the perpendicular distance from the XY plane of the remote axes to the wing fuel tank at the most inboard chord [in]
- $ZF2$ is the perpendicular distance from the XY plane of the win tank root chord to the vertical centre of gravity [in]. This variable is only required if the wing has either anhedral or dihedral ($YF1 \sin\theta$)

If there is more than one set of fuel tanks present in the wing, the procedure may be repeated for each subsequent set of fuel tanks.

Fuselage Fuel Tanks

The internal fuel within the fuselage is assumed to be in the shape of a solid right cylinder. For the inertial calculations it was assumed that the aircraft only undergoes short period rolling motions. The fuel would not experience any appreciable lateral motion. The inertia in roll of the fuel about its own axis is therefore assumed to be zero. The inertial values of the internal fuel within the fuselage about the remote axes are given by Equations (120)-(123).

$$I_{0x} = 0 \tag{120}$$

$$I_{oy} = \frac{M_{ff}}{12}\frac{\left(M_{ff} + l_f^2\right)}{\pi\rho l_f} + M_{ff}(X^2 + Z^2) \tag{121}$$

$$I_{oz} = \frac{M_{ff}}{12}\frac{\left(M_{ff} + l_f^2\right)}{\pi\rho l_f} + M_{ff}X^2 \tag{122}$$

$$I_{oxz} = M_{ff}XZ \tag{123}$$

Where:

- M_{ff} is the mass of fuel in the fuselage [lbs]
- l_f is the longitudinal length of the fuselage tank [in]
- X_{ff} is the perpendicular distance from the YZ plane of the remote axes to the fuselage tank centre of gravity [in]
- Z_{ff} is the perpendicular distance from the ZZ plane of the remote axes to the fuselage tank centre of gravity [in]

2.3.5. Inertias of Payload

The inertial values of the payload are estimated to be in the shape of a solid rectangular mass, or a series of masses as was the case for the volumes of mass in the fuselage. The inertial values of payload within the fuselage are given by Equations (124)-(127).

$$I_x = \frac{M_{pa}}{12}\left(d_{pa}^2 + d_{pa}^2\right) + M_{pa}Z_{pa}^2 \tag{124}$$

$$I_y = \frac{M_{pa}}{12}\left(l_{pa}^2 + d_{pa}^2\right) + M_{pa}\left(X_{pa}^2 + Z_{pa}^2\right) \tag{125}$$

$$I_z = \frac{M_{pa}}{12}\left(l_{pa}^2 + d_{pa}^2\right) + M_{pa}X_{pa}^2 \tag{126}$$

$$I_{xz} = M_{pa}X_{pa}Z_{pa} \tag{127}$$

Where:

- M_{pa} is the mass of the payload [lbs]
- d_{pa} is the width and height of the rectangular payload mass [in]
- l_{pa} is the length of the rectangular payload mass [in]

- X_{pa} is the perpendicular distance from the YZ plane of the remote axes to the centre of gravity of the rectangular payload mass [in]
- Y_{pa} is the perpendicular distance from the XZ plane of the remote axes to the centre of gravity of the rectangular payload mass [in]
- Z_{pa} is the perpendicular distance from the XY plane of the remote axes to the centre of gravity of the rectangular payload mass [in]

2.3.6. Total Aircraft Inertias

To obtain the total inertia of the entire aircraft about the remote axes, all groups are summed together to achieve a complete inertia in each inertial direction. To translate the inertial values about the remote axes back to the centre of gravity of the aircraft, the centre of gravity location must first be calculated. This can be done through the use of Equations (128)-(130).

$$\bar{X} = \frac{\Sigma MX}{\Sigma W} \tag{128}$$

$$\bar{Y} = 0 \tag{129}$$

$$\bar{Z} = \frac{\Sigma MZ}{\Sigma W} \tag{130}$$

Where X and Z are the distances to the item or group centroid. $\bar{Y}$ is assumed to be zero due to symmetry. ΣM should equal the total aircraft mass. The masses and distances to the remote axes should be known for all items and groups except for the fuselage structure longitudinal distances. These distances can be determined with Equations (131)-(133).

$$WX_{nose\ cone} = M_n\left(\frac{2}{3}l_n\right) \tag{131}$$

$$WX_{centre} = M_c\left(l_n + \frac{1}{2}l_c\right) \tag{132}$$

$$WX_{tail\ cone} = M_t\left(l_n + l_c + \frac{1}{3}l_t\right) \tag{133}$$

Finally, the translation of the total aircraft inertias from the remote axes to the aircraft centre of gravity can be done with the use of Equations (134)-(137).

$$I_{c.g_x} = I_x - M\bar{Z}^2 \tag{134}$$

$$I_{c.g_y} = I_y - M(\bar{Z}^2 + \bar{X}^2) \tag{135}$$

$$I_{c.g_z} = I_z - M\bar{Z}^2 \tag{136}$$

$$I_{c.g_{xz}} = I_{xz} - M\bar{X}\bar{Z} \tag{137}$$

2.4. Aerodynamics

2.4.1. Lifting Surfaces Models

Airfoils are used as lifting surfaces as they provide very high lift to drag ratios when compared to other shapes. A large quantity of data on the coefficient of lift, drag and quarter chord pitching moment has been complied by I. H. Abbott and A. E Von Doenhoff [62] for NACA (National Advisory Committee for Aeronautics) airfoils. This theory and data only applies to relatively small angles of attack (up to approximately 20°). For a tumble manoeuvre, post-stall aerodynamic data is required to capture the forces acting on the aircraft.

A method developed by Spera [60] was used to obtain pre-stall and post-stall aerodynamic data for airfoils of various camber profiles and for wings with various aspect ratios. The method was developed using an empirical approach where test data for a large variety of airfoils was used to model a set of algebraic equations. These equations were created using the best fit of the test data rather than aerodynamic theory. The reason being that aerodynamic theory and conventional aerodynamic models break down near and after stall [60]. Conventional aerodynamic theories do not extend beyond the linear, pre-stall region. Modelling post-stall, non-linear data is most simply done empirically, should the relevant resources be available. The method developed by Spera [60] was created such that the effects of thickness and aspect ratio were included as dependent variables. It should also be noted that the test data acquired was for static testing. Dynamic effects were not included.

The Spera [60] method for obtaining pre-stall and post-stall aerodynamic data is provided in §2.4.1.1 and §2.4.1.2 respectively. The method combines two models together, one capturing the pre-stall regime and the other the post-stall regime. This is illustrated in Figure 48, where the pre-stall and post-stall models are used to predict the aerodynamic coefficients of (a) lift and (b) drag for a NACA 4418 airfoil. The pre-stall and post-stall models overlap one another and it is at this point where the two models are joined together. Various key model positional points are also outlined in Figure 48. Further discussion on these points is outlined in §2.4.1.1 and §2.4.1.2.

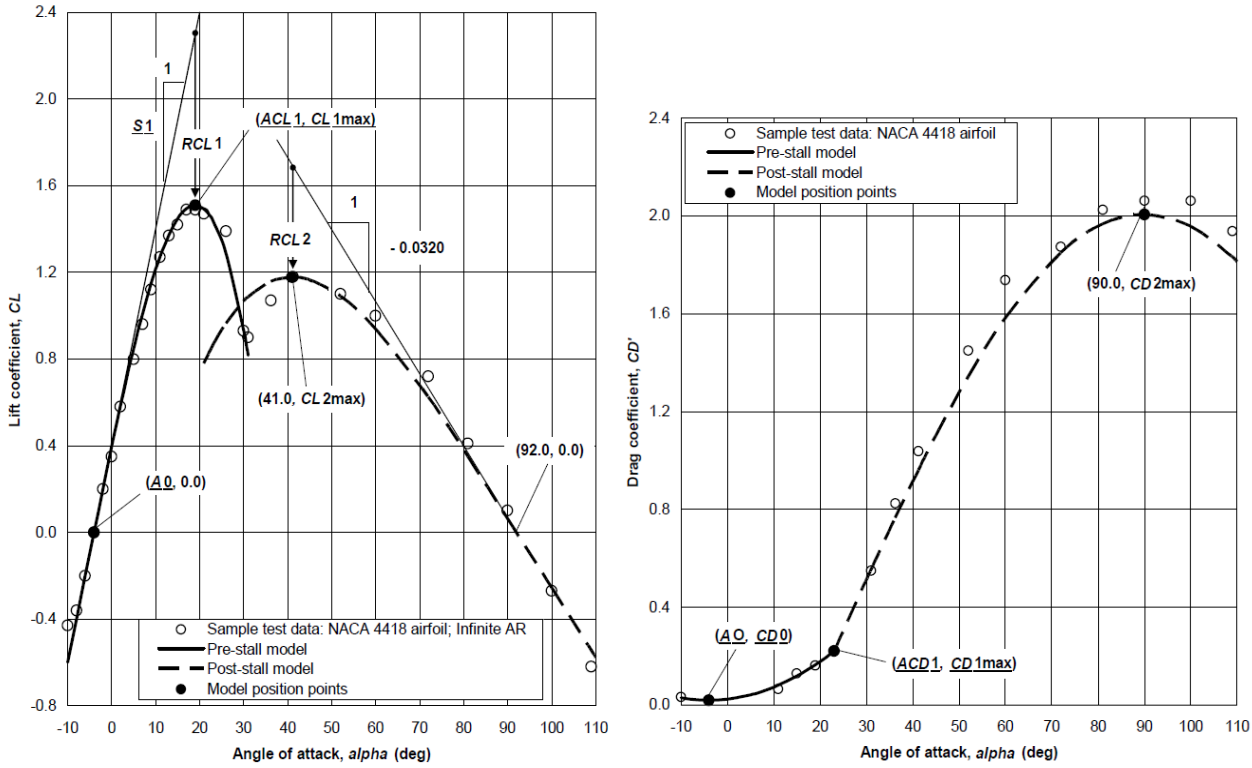

Figure 48: AERODAS model for (a) the coefficient of lift (b) the coefficient of drag

2.4.1.1. Pre-Stall Coefficients of Lift and Drag

Reference values of aerodynamic coefficients are usually given for infinite-span airfoils, meaning airfoils with no tip flow effects. Data for infinite-span airfoils must be modified before it can be applied to finite-span wings. This is done on the basis of the aspect ratio (AR). The aspect ratio of an airfoil is defined as the ratio of its span length to its representative chord width. For a fixed wing aircraft, wingspan is equal to the total aerodynamic length of two wings. In the case of a tapered fixed wing, the representative chord is the average chord, so that the aspect ratio of a fixed wing aircraft is equal to its total aerodynamic planform area (or reference area) divided by the square of its span.

Corrections for aspect ratio of finite wing sections must be determined before detailing the development of the equations for post-stall coefficients of lift and drag. Input data required from infinite aspect ratio airfoils is defined below and is illustrated in Figure 49. Parameters for infinite aspect ratio are designated by prime notation. The data presented in Figure 49 was generated using XFOIL software [63], which uses a high-order panel method and a fully-coupled viscous/inviscid interaction method. The use of this method explains the slight undulations seen in Figure 49.

- $A0$ – angle of attack for which the pre-stall lift is equal to zero for all aspect ratios [deg]
- $ACL1'$ – angle of attack at maximum pre-stall lift [deg]
- $CL1max'$ – maximum pre-stall coefficient of lift at $\alpha = ACL1'$ [-]
- $S1'$ – slope of linear segment of pre-stall lift curve [deg^{-1}]
- $CD0$ – minimum coefficient of drag at $\alpha = A0$ for all aspect ratios [-]
- $ACD1'$ – angle of attack at maximum pre-stall drag [deg]
- $CD1max'$ – maximum pre-stall coefficient of drag at $\alpha = ACD1'$ [-]

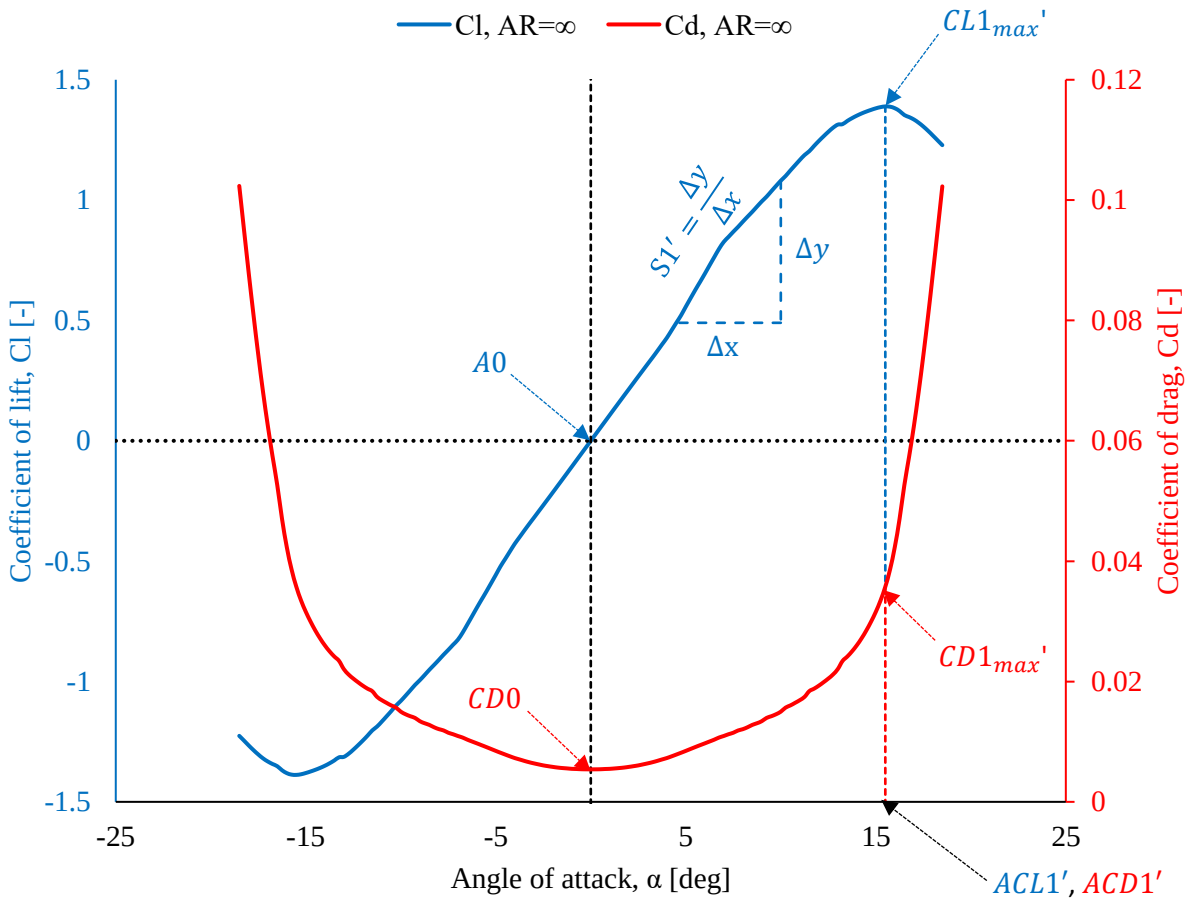

Figure 49: Pre-stall coefficient of lift (C_l) and drag (C_d) definitions for an infinite aspect ratio airfoil

The formulae to correct for aspect ratio, provided by Spera [60], are given by Equations (138) to (144):

$$\alpha = \alpha' + 18.2CL1' \cdot AR^{-0.9} \tag{138}$$

$$CD1 = CD1' + 0.28(CL1')^2 \cdot AR^{-0.9} \tag{139}$$

$$ACL1 = ACL1' + 18.2CL1_{max} \cdot AR^{-0.9} \tag{140}$$

$$S1 = \frac{S1'}{1 + 18.2S1' \cdot AR^{-0.9}} \tag{141}$$

$$ACD1 = ACD1' + 18.2CL1_{max} \cdot AR^{-0.9} \tag{142}$$

$$CD1_{max} = CD1'_{max} + 0.280{CD1'_{max}}^2 \cdot AR^{-0.9} \tag{143}$$

$$CL1_{max} = CL1'_{max}\left\{0.67 + 0.33e^{-\left(\frac{4}{AR}\right)^2}\right\} \tag{144}$$

Where:

- $CL1'$ - pre-stall coefficient of lift for infinite aspect ratio [-]
- α' - angle of attack for infinite aspect ratio for a coefficient of lift of $CL1'$ [deg]
- $CD1'$ - pre-stall coefficient of drag for infinite aspect ratio at a coefficient of lift of $CL1'$ [-]

The effects of aspect ratio on the coefficient of lift and coefficient of drag are illustrated by examples in Figure 50. These figures were produced by making use of Equations (138) to (144).

Pre-Stall Lift and Drag

With the corrections for aspect ratio accounted for, the equations for the pre-stall lift and drag coefficients can be developed. All equations pertaining to the coefficients of lift and drag can be found in Table 16 and Table 17 respectively. The coefficient of lift in the pre-stall regime can be determined using Equations (145) and (146). The coefficient of drag in the pre-stall regime is given by Equations (158) and (159).

Additional values are required to determine the coefficient of lift and drag in the pre-stall regime are:

- *RCL1* - the reduction from the extension of the linear segment of the lift curve to $CL1_{max}$ and is given by Equation (147)
- *N1* - the exponent defining the shape of the lift curve at $ACL1_{max}$ and is given by equation (148)

- M - an exponent that can be determined by curve fitting equation (158) to test data in a graph of the lift to drag ratio versus the angle of attack. A value of $M=2$ can be used as a good first approximation for most airfoils in the absence of specific data.

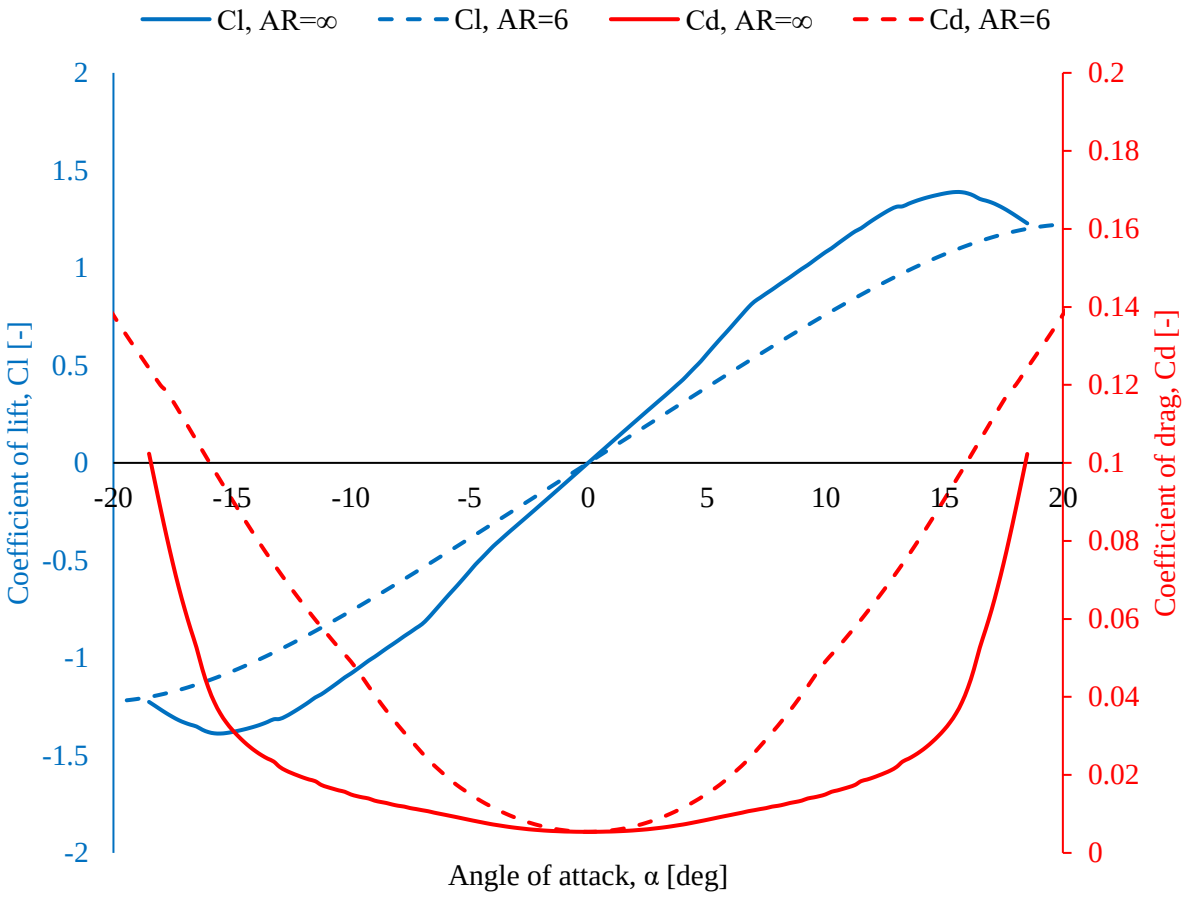

Figure 50: Effects of aspect ratio on the pre-stall coefficient of lift (C_l) and drag (C_d)

2.4.1.2. Post-Stall Coefficients of Lift and Drag

To determine the coefficients of lift and drag in the post-stall regime, the maximum post-stall coefficient of lift ($CL2max$) and coefficient of drag ($CD2max$) must first be defined. These two maximums are given by Equations (149) and (160) respectively. Terms $F1, G1$ are empirical functions based on the thickness-to-chord ratio (t/c) and are given by Equations (150) and (161) respectively. Terms $F2, G2$ are empirical functions based on aspect ratio (AR) and are given by Equations (151) and (162) respectively. The empirical functions were developed to give the best fit of the model calculations to two different types of test data, which included several sources. These sources are given on page 13 in Spera [60].

Post-Stall Lift

Using the coefficient of maximum lift given by Equation (149), the coefficient of lift in the post-stall regime can be defined using Equations (152), (153) and (154).

Additional values are required to determine the coefficient of lift in the post-stall regime are:

- *RCL2* - the reduction from the extension of the linear segment of the lift curve to $CL2_{max}$ and is given by equation (155).
- *N2* - the exponent defining the shape of the lift curve at $CL2_{max}$ and is given by equation (156).

Post-stall lift behavior at negative angles of attack is assumed (by Spera [60]) to be anti-symmetric about $\alpha = A0$, such that the post stall lift at negative angles of attack is defined by Equation (157).

Post-Stall Drag

The coefficient of drag in the post-stall regime can be defined using Equations (163) and (164), using the coefficient of maximum drag from Equation (160). At negative angles of attack, the post-stall coefficient of drag is assumed (by Spera [60]) to be symmetrical about $\alpha = A0$ and is given by Equation (165).

Table 16: Equations for calculating the coefficient of lift of a lifting body at all α angles [60]

Region	Equation	Region of Applicability	Equation No.	Notes
Pre-Stall	$CL1 = S1 \cdot (\alpha - A0) - RCL1\left[\frac{\alpha - A0}{ACL1 - A0}\right]^{N1}$	$\alpha \geq A0$	(145)	
	$CL1 = S1 \cdot (\alpha - A0) + RCL1\left[\frac{A0 - \alpha}{ACL1 - A0}\right]^{N1}$	$\alpha < A0$	(146)	
	$RCL1 = S1 \cdot (ACL1 - A0) - CL1_{max}$	–	(147)	
	$N1 = 1 + \frac{CL1_{max}}{RCL1}$	–	(148)	
Post-Stall	$CL2max = F1[t/c] \cdot F2[AR]$	$\alpha = 41°$	(149)	The α value at which $CL2max$ occurs may be changed depending on the airfoil
	$F1 = 1.190[1.0 - (t/c)^2]$	–	(150)	Empirical function based on thickness to chord ratio (t/c)
	$F2 = 0.65 + 0.35exp[-(9/AR)^{2.3}]$		(151)	Empirical function based on aspect ratioAR
	$CL2 = 0$	$0 < \alpha < ACL1$	(152)	
	$CL2 = -0.032 \cdot (\alpha - 92) - RCL2\left[\frac{92 - \alpha}{92 - ACL2}\right]^{N2}$	$ACL1 \leq \alpha \leq 92°$	(153)	
	$CL2 = -0.032 \cdot (\alpha - 92) + RCL2\left[\frac{\alpha - 92}{92 - ACL2}\right]^{N2}$	$\alpha > 92°$	(154)	
	$RCL2 = -0.032(ACL2 - 92) - CL2max$	–	(155)	
	$N2 = 1 + \frac{CL2max}{RCL2}$	–	(156)	
	$CL2[\alpha] = -CL2[-\alpha + 2A0]$	$\alpha < 0°$	(157)	

Table 17: Equations for calculating the coefficient of drag of a lifting body at all α angles [60]

Region	Equation	Use limits	Equation No.	Notes
Pre-Stall	$CD1 = CD0 + (CD1_{max} - CD0)\left(\frac{\alpha - A0}{ACD1 - A0}\right)^{M}$	$(2A0 - ACD1) \leq \alpha \leq ACD1$	(158)	*M* is an exponent that can be determined by curve fitting equation (158) to test data in a graph of the lift to drag ratio versus the angle of attack. A value of *M=2* can be used as a good first approximation for most airfoils in the absence of specific data.
	$CD1 = 0$	$\alpha \leq (2A0 - ACD1)$ or $\alpha > ACD1$	(159)	
Post-Stall	$CD2max = G1[t/c] \cdot G2[AR]$	$\alpha = 90°$	(160)	
	$G1 = 2.30exp\{-[0.65(t/c)]^{0.9}\}$	–	(161)	Empirical function based on thickness to chord ratio (t/c)
	$G2 = 0.52 + 0.48exp[-(6.5/AR)^{1.1}]$	–	(162)	Empirical function based on aspect ratioAR
	$CD2 = 0$	$(2A0 - ACD1) \leq \alpha \leq ACD1$	(163)	
	$CD2 = CD1max + (CD2max - CD1max)\, sin\left(\frac{\alpha - ACD1}{90 - ACD1} \cdot 90\right)$	$\alpha \geq ACD1$	(164)	
	$CD2[\alpha] = CD2[-\alpha + 2A0]$	$\alpha \leq (2A0 - ACD1)$	(165)	

2.4.1.3. Coefficient of Lift and Drag Corrections for Elevator Deflection

The method developed by Spera [60] assumes that no control surfaces are deflected on the wing. During a tumble manoeuvre elevator deflection is required to pitch the aircraft. Corrections to the coefficients of lift and drag for elevator deflections can be performed using Equations (166) and (167) respectively [64].

$$\Delta C_{L_{HS}} = a_2 \delta_e + a_3 \delta_{tab} \left(\frac{b_{tab}}{b_T} \right) \tag{166}$$

$$\Delta C_{D_{HS}} = 1.1 \left(\sin^2 \alpha \right) \frac{S_E}{S_{ref}} \tag{167}$$

Where:

- a_2 is the lift curve slope of the elevator [deg^{-1}]
- δ_e is the deflection angle of the elevator [deg]
- a_3 is the lift curve slope of the trim tab [deg^{-1}]
- δ_{tab} is the deflection angle of the tab [deg]
- b_{tab} is the span of the tab [m]
- b_T is the span of the horizontal tail [m]
- α is the angle of attack of the horizontal tail [deg]
- S_E is the area of the elevator [m^2]
- S_{ref} is the horizontal tail reference area [m^2]

In addition to the corrections made for elevator deflection, the coefficients of lift, drag and quarter chord coefficient of pitching moment can be corrected for the aspect ratio of the horizontal tail. This can be achieved with the use of Equations (168), (169) and (170) , obtained from Selig [39].

$$C_{l_{corrected}} = C_l [1 - w(1 - kC_d)] \tag{168}$$

$$C_{d_{corrected}} = C_d [1 - w(1 - kC_d)] \tag{169}$$

$$C_{m_{c/4}{}_{corrected}} = C_{m_{c/4}} [1 - w(1 - kC_d)] \tag{170}$$

Where:

- w is a cosine weighting function and is expressed by Equation (172)
- kC_d is a scaling factor and is provided by Equation (171)

$$kC_d = C_{d_{90}}/2.2 \tag{171}$$

$$w = \cos\left[\pi\left(\frac{\alpha - \alpha_{P_1}}{\alpha_{N_2} - \alpha_{p_1}}\right) - \frac{\pi}{2}\right] \tag{172}$$

The term $C_{d_{90}}$ in Equation (171) is a modification to the coefficient of drag at $\alpha = 90°$, accounting for aspect ratio and can be obtained through the use of Equation (173). α_{P_1} and α_{N_2} define the angle of attack range over which the correction applies, tapering to zero at the ends.

$$C_{d_{90}} = 2.2\{1 - 0.41[1 - \exp(-17/AR)]\} \tag{173}$$

While these corrections are based on the $90°$ coefficient of drag value they are applicable to the coefficient of lift as the relationship $C_L/C_d \approx 1/\tan\alpha$ holds true at all angles of attack (see Ref [65]). The moment in the post-stall regime is driven largely by the drag acting on the 50% chord location (the centre of pressure) and is also applicable to the coefficient of moment.

2.4.1.4. Coefficient of Quarter Chord Pitching Moment

The centre of pressure is the point on a body about which the aerodynamic moment is zero. The coefficients of lift and drag described are calculated at the aerodynamic centre of the airfoil, which is the chordwise position at which the coefficient of pitching moment for an airfoil does not vary with varying lift (in the pre-stall regime). For low thickness, symmetrical profiles the aerodynamic centre and centre of pressure are located at the same chordwise position. For thicker symmetrical sections and unsymmetrical airfoils, the aerodynamic centre and centre of pressure do not coincide. An additional moment will be required to obtain the total moment acting on the wing. The additional moment term will be determined at the quarter chord position on the chord of the airfoil.

Spera [60] does not provide a method for determining the coefficient of quarter chord pitching moment and as such another reference should be used. Lindenburg [66] provides a somewhat crude method of obtaining the coefficient of quarter chord pitching moment by assuming that the airfoil is approximately elliptical in shape. The coefficient of quarter chord pitching moment developed by Lindenburg [66] is given by Equation (174).

$$C_m = -\left(0.25 - 0.175\left(1 - \frac{\alpha}{90}\right)\right) C_n \tag{174}$$

C_n is the coefficient of normal force of the wing. The coefficient of normal force can be obtained using the coefficients of lift and drag, as shown by Equation (175)

$$C_n = C_l \cos\alpha + C_d \sin\alpha \tag{175}$$

The moment coefficient for reversed flow is calculated as if the lift and drag forces act at the 78% chord location, meaning that the coefficient of quarter chord pitching moment is anti-symmetric about $\alpha = A0$.

2.4.2. Fuselage

An engineering-type method was developed by Jorgensen [42] for computing the coefficients of normal-force, axial force and pitching moment for slender bodies of circular and noncircular cross-sectionsm, alone and with lifting surfaces. The method incorporates a semi-empirical term that represents a viscous crossflow value accounting for the potential-theory crossflow. For bodies of revolution the data generated by Jorgensen [42] was shown to agree with measured results for free-stream Mach numbers from 0.6 to 2.9. While these Mach numbers fall well outside the range of free-stream velocities seen during a tumble manoeuvre the method may be applied for any free-stream velocity in the range of $0 \leq M \leq 2.9$. The validation of this claim is justified by considering Selig [67] and Pamadi [41]. The method developed by Jorgensen [42] was used to develop data for the coefficients of normal force, axial force and pitching moment (and subsequently the coefficients of lift and drag), for general aviation aircraft.

The data generated by Selig [67] was compared to static test data generated by Bihrle [68] for a general aviation aircraft. Both the generated coefficients and test data coefficients can be used for general aviation aircraft at low speeds below those presented by Jorgensen [42]. The coefficients of normal and axial force were used by Selig [67] to calculate the coefficients of lift and drag. Comparisons of the data generated by Selig [67] and the static test results of Bihrle [68] are provided in Figure 51, Figure 52 and Figure 53 for the coefficients of lift, drag and pitching moment respectively.

It is evident in Figure 51 and Figure 52 that the calculated coefficients of lift and drag agree with the wind tunnel results at lower angles of attack ($\alpha \leq 20°$). The results deviate at higher angles of attack, when compared to the data predicted by Selig [67]. The coefficients of lift and drag are both underpredicted. The coefficient of pitching moment results for the fuselage provided by Selig [67] did not match the wind tunnels results. The notable differences in results may have been due to an ambiguous definition of the location of the coefficient of pitching moment given by Bihrle [68]. The location may not have been at the centre of gravity of the model that was assumed by Selig [67]. Measurements obtained by Pamadi [41] indicated that the shape of the coefficient pitching moment follows a very similar shape to that obtained by Selig [67] and the results published by Jorgensen [42].

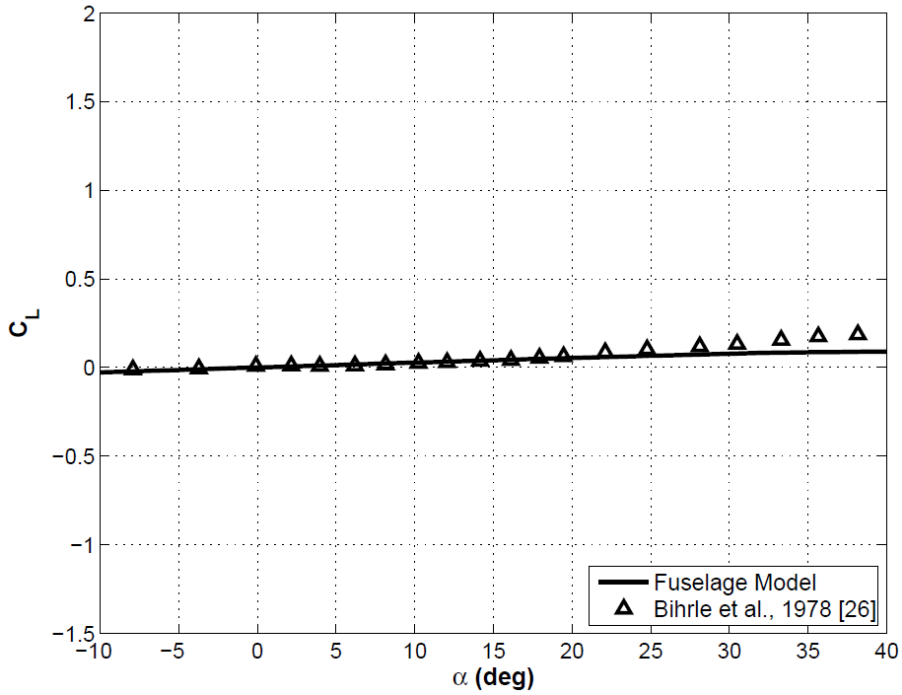

Figure 51: Fuselage coefficient of lift comparison between Selig [66] and Bihrle [67] at $R_e = 3.45 \times 10\text{^}6$, [67]

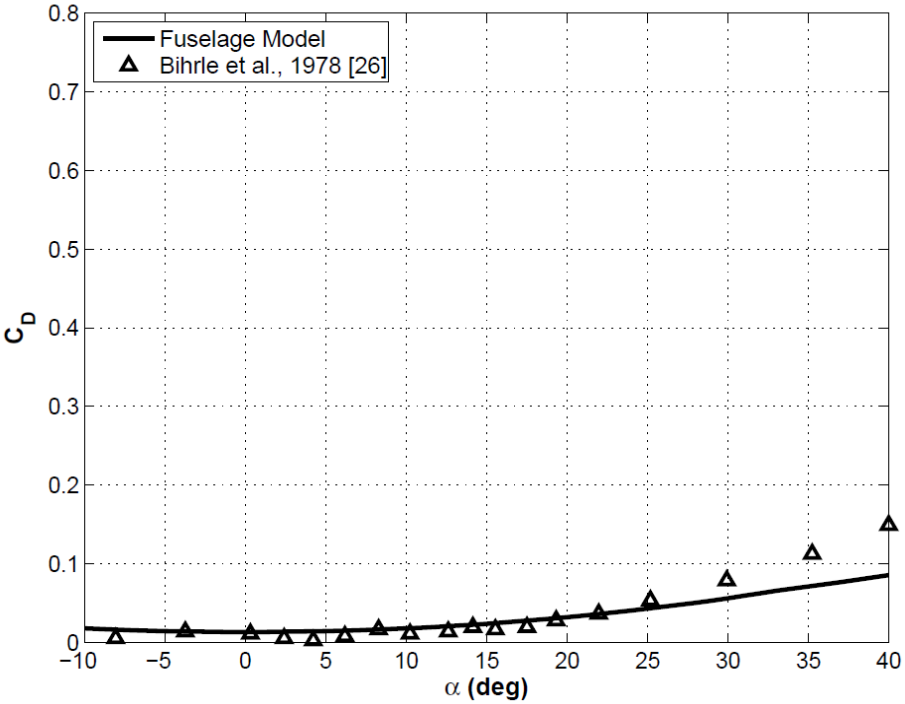

Figure 52: Fuselage coefficient of drag comparison between Selig [66] and Bihrle [67] at R_e=3.45×10^6, [67]

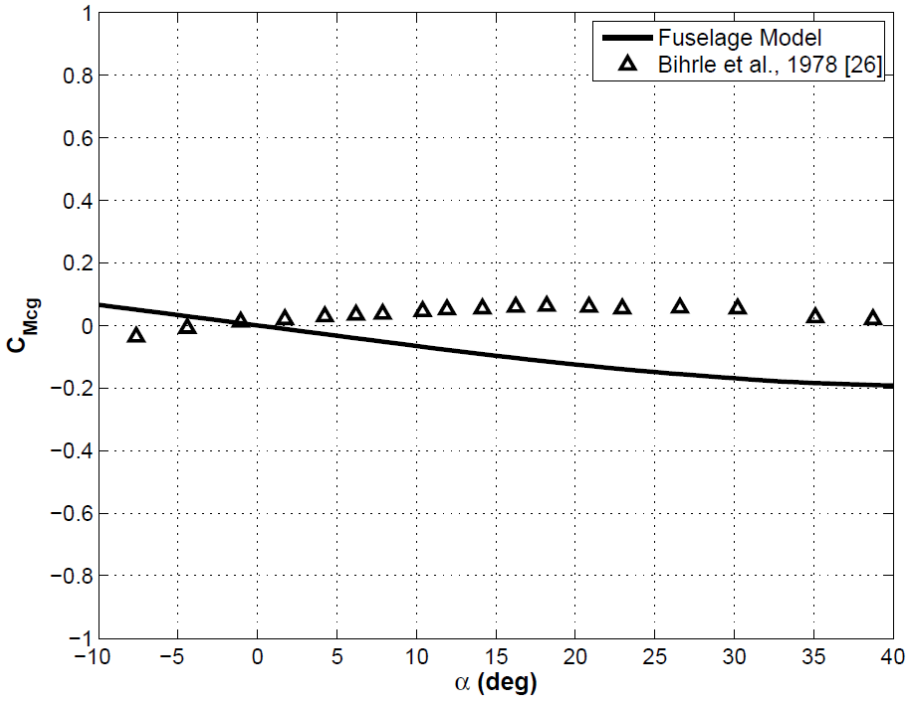

Figure 53: Fuselage coefficient of pitching moment comparison between Selig [65] and Bihrle [66] at R_e=3.45×10^6, [67]

Results comparing predicted data and wind tunnel results from Pamadi [41] are provided in Figure 54 for the coefficients of lift, drag and pitching moment. The predicted values for the coefficient of lift provided in Figure 54 illustrate good correlation with experimental data for low angles of attack ($\alpha \leq 20°$) and very high angles of attack ($\alpha \geq 70°$). For $20° < \alpha < 70°$ there appears to be an overprediction in the calculated coefficient of lift when compared to the measured data. The coefficient of drag, shown in Figure 54 shows good agreement with static test data up to high angles ($\alpha \leq 60°$). The calculated data overpredicts the coefficient of drag. The prediction of the coefficient of pitching moment given in Figure 54 captures the basic stability trend of the test data. Static instability is evident up until $\alpha \approx 30°$ and subsequent stability thereafter. Differences in magnitudes are noted. The coefficient of pitching moment is overpredicted. This is to be expected as the coefficients of lift and drag were overpredicted.

Despite the overpredictions of both Selig [67] and Pamadi [41], the data is within an acceptable range of agreement with test data. The Jorgensen method [42] provides acceptably accurate data for the estimation of fuselage aerodynamic coefficients, even at lower free-stream velocities. With the absence of any better prediction models and the inability to perform wind tunnel testing, the Jorgensen method [42] will be used to estimate the coefficients of the Extra 330 fuselage.

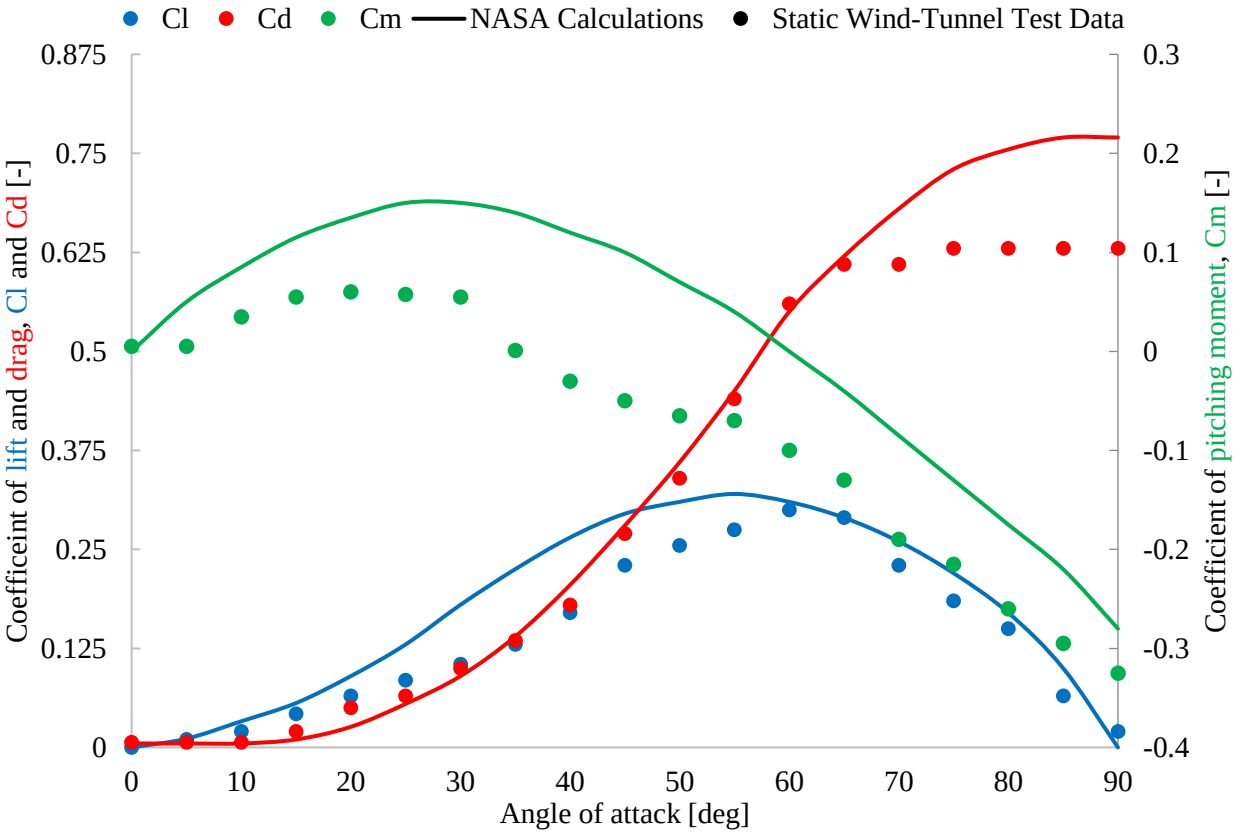

Figure 54: Fuselage coefficient of lift, drag and pitching moment comparisons between predicted and wind tunnel data for Pamadi [41] at $R_e = 0.288 \times 10\text{^}6$

The equations developed by Jorgensen built on work developed by Allen and Munk and incorporated a potential-flow solution for bodies of revolution combined with a viscous crossflow solution. These solutions could be used to derive the coefficient of normal force and pitching moment for bodies of revolution with largely constant cross-sectional area. Jorgensen [42] further generalised these equations by introducing an additional ratio term in both the potential and viscous crossflow components. The ratio relates the local coefficient of normal force per unit length (for the desired cross-sectional shape) to the similar coefficient of normal force for the equivalent circular shape having the same cross-sectional area.

For the general case of a slender body, with cross-sectional shape variation along the length, the coefficients of normal force, axial force and pitching moment can be obtained from Equations (176), (177) and (178) respectively.

$$C_N = \frac{sin2\alpha \cos(\alpha/2)}{A_r} \int_0^l \left(\frac{C_n}{C_{n_0}}\right)_{SB} \frac{dA}{dx} dx + \frac{2\eta C_{d_n} \sin^2 \alpha}{A_r} \int_0^l \left(\frac{C_n}{C_{n_0}}\right)_{Newt} r dx \qquad (176)$$

Where:

- α is the angle of attack [deg]
- A_r is the reference area [m^2] (in the formulation of these equations the reference area was typically taken as the largest fuselage cross-sectional area)
- C_{d_n} is the cross-flow drag coefficient [-]
- η is the drag proportionality factor (which accounts for 3 dimensional effects) [-]
- A is the fuselage area [m^2]
- $\left(\frac{C_n}{C_{n_0}}\right)_{SB}$ is the ratio of the local normal-force coefficient per unit length, C_n, for the desired cross-sectional shape to the similar coefficient C_{n_0} for the equivalent circular shape having the same cross-sectional area [-]. This value, for an elliptical cross-section, can be obtained using the slender body line provided in Figure 55. Where a and b are the semi-major and semi-minor lengths, respectively.
- $\left(\frac{C_n}{C_{n_0}}\right)_{Newt}$ is the ratio of C_n to C_{n_0} at each station x, and is assumed to be given by Newtonian impact theory [-]. This value, for an elliptical cross-section, can be obtained using the Newtonian impact theory line provided in Figure 55. Where a and b are the semi-major and semi-minor lengths, respectively.

$$C_A = \begin{cases} C_{A_{\alpha=0^\circ}} \cos^2 \alpha & 0^\circ \leq \alpha \leq 90^\circ \\ C_{A_{\alpha=1800^\circ}} \cos^2 \alpha & 90 < \alpha \leq 180^\circ \end{cases} \quad (177)$$

Where:

- $C_{A_{\alpha=0^\circ}}$ is the coefficient of axial force at $\alpha = 0^\circ$ [-]
- $C_{A_{\alpha=180^\circ}}$ is the coefficient of axial force at $\alpha = 180^\circ$ [-]

The $\cos^2 \alpha$ term is merely the ratio of the dynamic pressure in the axial direction to the dynamic pressure in the free-stream direction. Jorgensen [42] suggests that in general, it can be shown that for values of α well removed from $\alpha = 0^\circ$ and $\alpha = 180^\circ$ the precise prediction of the coefficient of axial force is not necessary in obtaining accurate values of both the coefficients of lift and drag. Equation (177) can be used as a rough engineering estimate for the coefficient of axial force.

$$C_M = \frac{sin2\alpha\cos(\alpha/2)}{A_r X}\int_0^l \left(\frac{C_n}{C_{n_0}}\right)_{SB}\frac{dA}{dx}(x_m - x)dx + \frac{2\eta C_{d_n}\sin^2\alpha}{A_r X}\int_0^l \left(\frac{C_n}{C_{n_0}}\right)_{Newt} r(x_m - x)dx \quad (178)$$

Where:

- X is the reference length [m]
- x_m is the axial distance from the nose to the pitching moment centre (the centre of gravity in this case) [m]

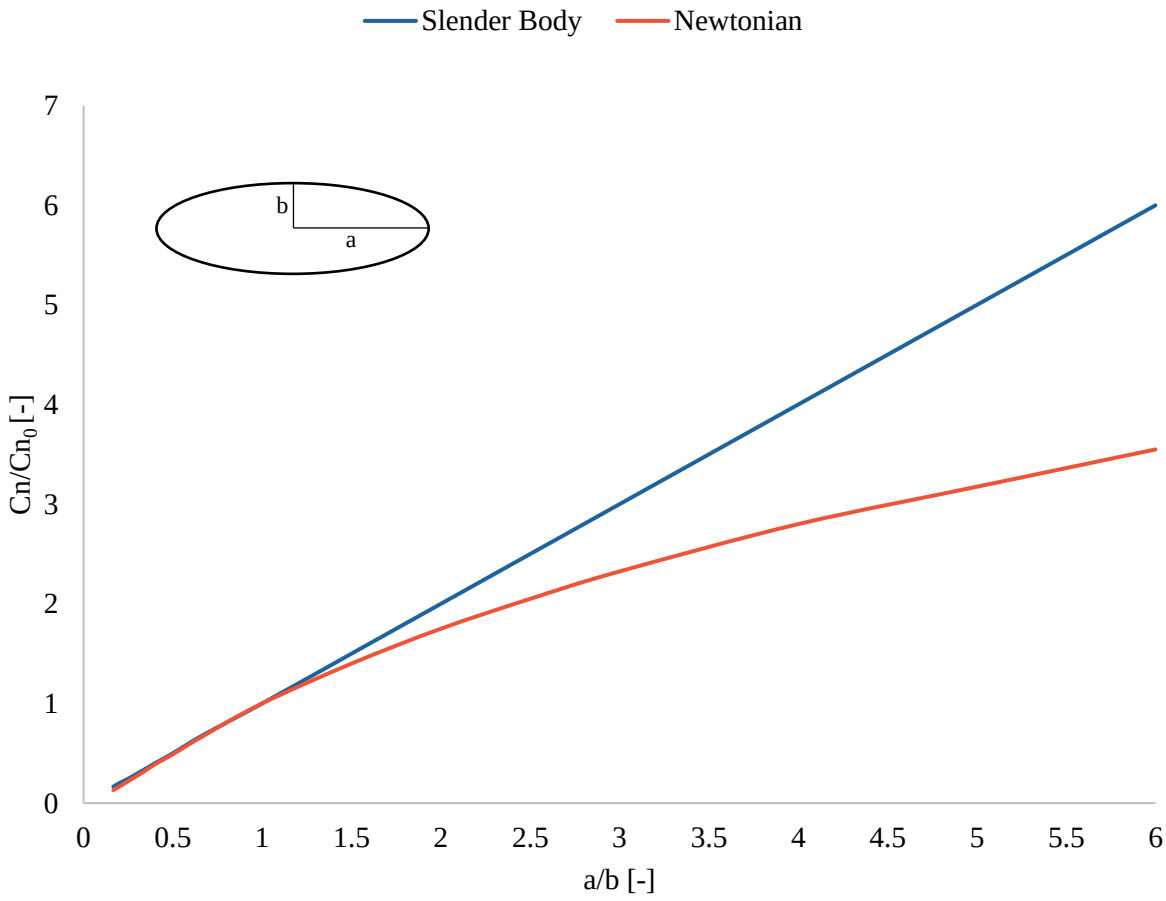

Figure 55: Cn/Cn_0 ratios for slender body and Newtonian-Impact theory for an elliptical cross-section [42]

The coefficients of lift and drag of the fuselage can be obtained using the coefficients of normal and axial force. The coefficient of lift is provided by Equation (179), while the coefficient of drag can be obtained using Equation (180).

$$C_L = C_N \cos\alpha - C_A \sin\alpha \tag{179}$$

$$C_D = C_N \sin\alpha + C_A \cos\alpha \tag{180}$$

The aerodynamic centre on the fuselage body can be obtained using Equation (181). Figure 56 illustrated the positive conventions for forces and moment arms in the derivation of Equation (181).

$$\frac{(l - x_{ac})}{d} = \frac{C_m}{C_n} + \frac{(l - x_m)}{d} \tag{181}$$

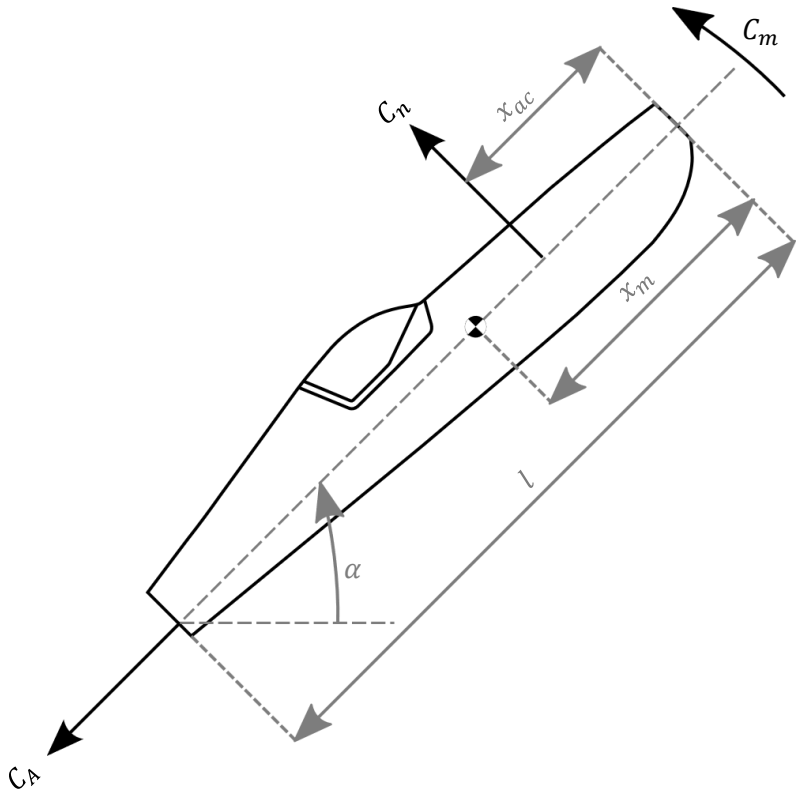

Figure 56: Fuselage positive force and moment convention used by Jorgensen [42]

2.4.3. Propeller

2.4.3.1. Propeller Thrust

Aerobatic aircraft are generally power by internal combustion engines which turn propellers to generate thrust. The propeller thrust can be obtained using Equation (182) and can be found in reference [69]. It should be noted that Equation (182) is applicable for finite airspeeds and cannot be used to accurately predict the static thrust.

$$T = \frac{\eta_P P_e}{V} \tag{182}$$

Where:

- η_p is the propeller efficiency [-]
- P_e is the power [horsepower]
- V is the airspeed [m/s]

Propeller diagrams can be used to determine the efficiency of a propeller. The coefficient of power (C_P) and advance ratio (J) are required to determine the propeller efficiency (η_P). The coefficient of power may be obtained using Equation (183) while the advance ratio can be calculated using Equation (184).

$$C_P = \frac{P_e}{\rho n^3 D^5} = \frac{P_e}{\rho\sigma n^3 D^5} \tag{183}$$

$$J = \frac{V}{nD} \tag{184}$$

Where:

- HP is the engine power [horsepower]
- $\rho\sigma$ is the density correction for altitude [kg/m^3]
- n is the propeller rotational speed [rps]
- D is the diameter of the propeller [m]
- V is the free stream velocity [m/s]

Equation (182) can be used to determine the propeller thrust for in flight conditions. To determine the static thrust of a propeller Equation (185), presented by Roskam [70] ,can be used.

$$T_{Static} = 33000\left(\frac{C_T}{C_P}\right)\left(\frac{SHP}{ND}\right) \tag{185}$$

Where:

- SHP is the shaft horsepower [horsepower]
- $\left(\frac{C_T}{C_P}\right)$ is a ratio of the propeller coefficient of thrust to the coefficient of power (the value of this ratio is obtained using static propeller charts) [-]
- N is the rotational velocity of the propeller [RPM]
- D is the propeller diameter [ft]

It is important to note that the propeller diameter must be used in units of ft, as the constant value (33000) in Equation (185) has been determined for the use of imperial units. The propeller charts required for determining the value of $\left(\frac{C_T}{C_P}\right)$ can be obtained in Appendix C of Roskam [70]. An example is illustrated in Figure 57. It should be noted that this is a generic chart and is not specific to the Extra

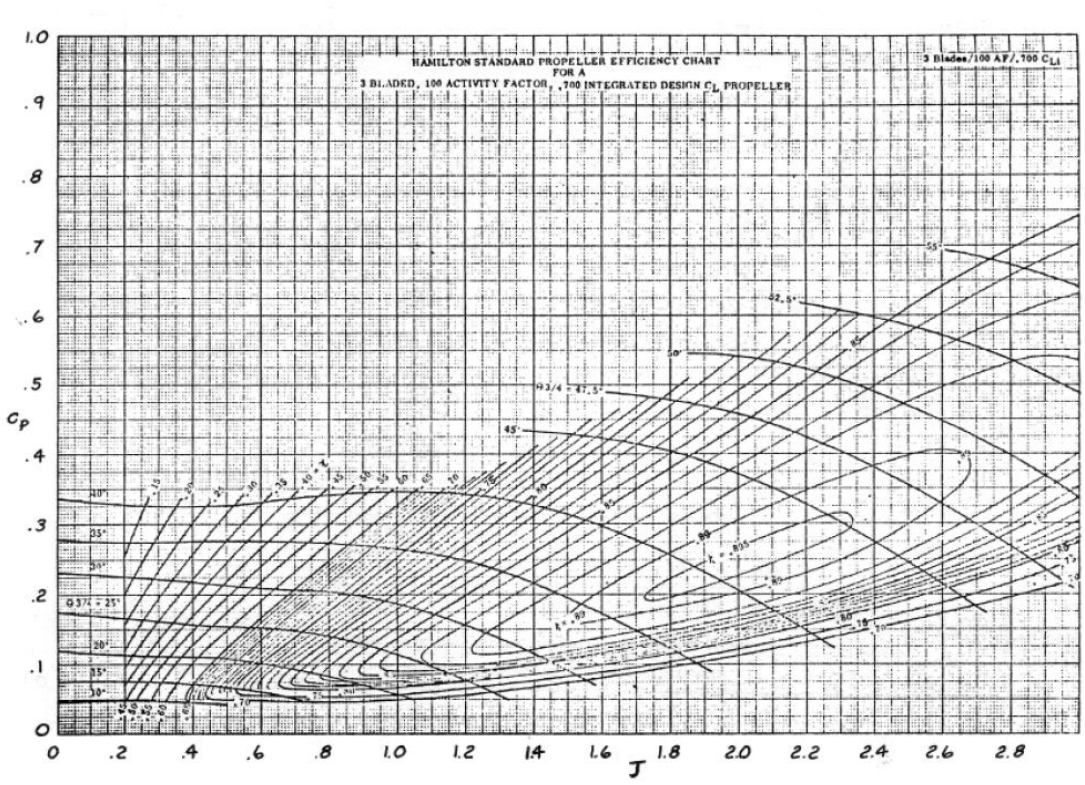

Figure 57: Hamilton standard propeller efficiency chart for a 3 bladed propeller with an activity factor of 100 and an integrated design C_L of 0.7

330SC. The chart is, however, still applicable in predicting the static thrust for the Extra 330SC. Propeller charts for the Extra 330SC aircraft are not available in the public domain.

2.4.3.2. Coefficient of Normal Force and Pitching Moment

There is an absence of accurate numerical model for predicting the coefficients for a propeller at high angles of attack and very low advance ratios. The coefficient data provided by Yaggy [44] will be used as the propeller input data for the Extra 330 propeller using modified advance ratios. The forces and moments of the Extra 330 propeller can be obtained by substituting the propeller diameter (D) and the operating revolutions per second (n) of the Extra 330 propeller into Equations (186) and (187) to obtain the normal force and pitching moment, respectively. The propeller thrust and power need not be obtained using the data from Yaggy [44] as it was shown in §1.3.4.4 that the thrust coefficient and power coefficient (at the given advance ratio) remain almost constant for changes in angle of attack (for the angles of attack expected during a tumble manoeuvre). The side force and torque will not be included as this dissertation is limited to longitudinal forces and moments only. The yawing moments are assumed negligible in the absence of any sideslip.

$$N = C_N \rho \sigma n^2 D^4 \tag{186}$$

$$M = C_M \rho \sigma n^2 D^5 \tag{187}$$

2.4.3.3. Propeller Slipstream

A formulation for the propeller slipstream is developed by Roskam [70]. In generating an expression for the propeller slipstream, a number of assumptions were made by Roskam. The flow through the propeller disk was assumed to be incompressible and irrotational. The physical propeller disk was replaced by a thin "actuator disk," that was assumed to consist of an infinite number of blades and to be uniformly loaded. The inflow and outflow were also assumed to be uniform. Figure 58 illustrates this idealised situation. Using these assumptions and the situation depicted in Figure 58 Roskam arrived at an expression for the induced velocity or propeller slipstream, shown by Equation (188).

$$v = -\frac{V}{2} + \sqrt{\left(\frac{V}{2}\right)^2 + \frac{T}{2A\rho}} \tag{188}$$

Where:

- V is the flight velocity [m/s]
- T is the thrust [N]
- A is the propeller disk area [m^2]
- ρ is the air density [kg/m^3]

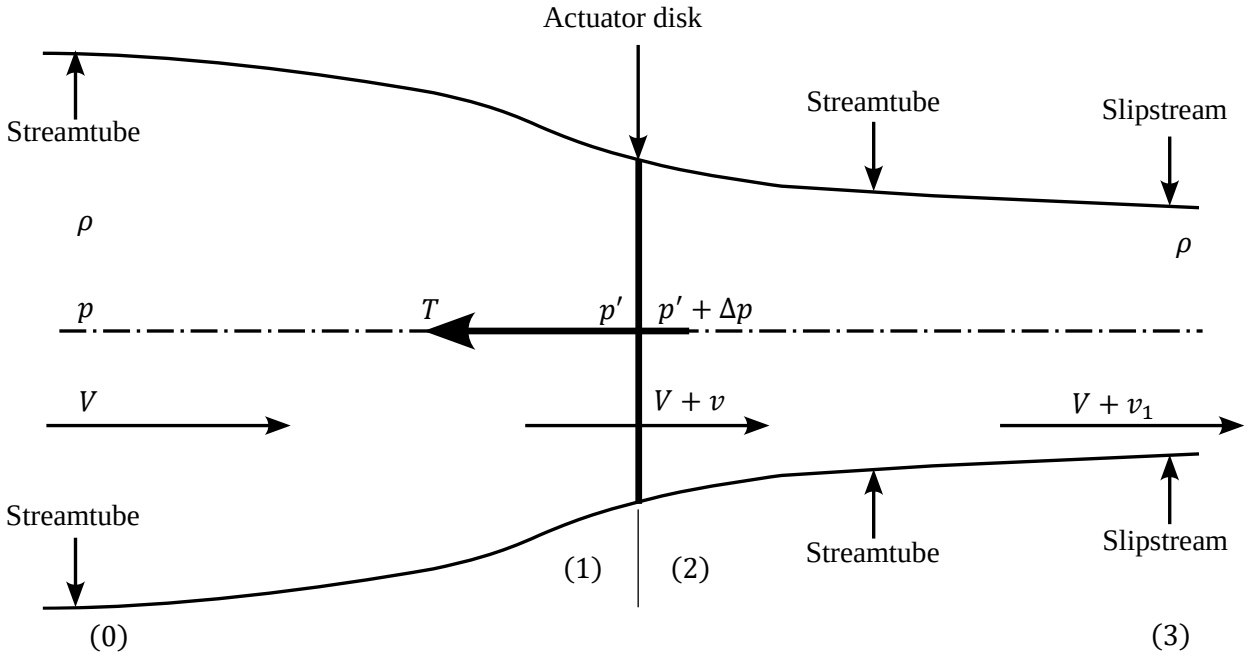

Figure 58: Streamtube through a thin propeller disk [70]

Equation (188) may be used to obtain the propeller slipstream velocity downstream of the propeller disc. It will be assumed that the horizontal tail is sufficiently close to the propeller for the slipstream velocity to not have decayed by a significant amount.

3. REVIEW OF TECHNICAL INPUT DATA

3.1. Introduction

The input data that was generated for modelling the tumble model is discussed in this section. A comparison to published data is also presented for each set of input data as a means of validation. Test data for the tumble manoeuvre is not available within the public domain.

Mass estimations for the Extra 330SC structure are presented. Inerital data was generated using the mass data. The overall mass and centre of gravity locations were compared to data presented in the Extra 330SC Pilot Operating Handbook (POH) [13] as a means of validating the mass estimates. The inertial data was compared to the values presented in Figure 40 in §1.3.6.

Aerodynamic coefficients of lift and drag together with quarter chord coefficients of pitching moment were generated for an infinite aspect ratio. This data was compared to NASA test data provided by Critzos [38]. Considerations for propeller slipstream were considered by dividing the wing into an inner wing section (exposed to the propeller slipstream) and an outer wing section (exposed to the free-stream). Corrections were made to the inner and outer wing sections for aspect ratio and propeller slipstream effects.

Fuselage aerodynamic coefficients of lift, drag and pitching moment were generated. The data was compared to data published by Pamadi [41].

Horizontal stabiliser coefficients of lift and drag along with the quarter chord coefficient of pitching moment were generated. Corrections for aspect ratio and elevator deflection were applied to the coefficients.

Propeller thrust and slipstream data was generated for the Extra 330SC engine and propeller specifications as provided by the POH [13]. The coefficient of normal force of the propeller was obtained by utilising data provided by Yaggy [44].

3.2. Mass and Inertia Data

3.2.1. Mass Data

Mass estimations were calculated using the methodologies outlined in §2.2. Where possible, data provided by Extra Aircraft Company for the Extra 330SC was used in place of estimated data, as this reduced the uncertainty. A great deal of mass data pertaining to the powerplant and the fixed equipment onboard the aircraft is provided by the Extra Aircraft Company in the POH [13]. The mass group for which little to no information was available was the structural group. As such, mass estimates of the relevant components contained within the structural group are provided in Table 18. For each component within the structural group, an average of the three methodologies was taken. Mass estimates that provided results that were thought to be an overestimation or an underestimation were omitted. The

result from the Nicolai mass estimation method for the fuselage is also presented in Table 18. While most variables require no further explanation, one item which warrants further discussion is the fuselage. The length of the fuselage required for mass estimates was specified as 4.55 m, which is some way off the 6.88 m aircraft length specified in Table 3. While the rear end of the aircraft is evidently allocated to the vertical stabiliser, an indiscernible loss in length of the fuselage section is at the very front of the aircraft. The fuselage structure does not end at the front of the aircraft as the body work may suggest but rather ≈ 1.76 m behind the frontmost point of the aircraft. This is due to the engine (and relevant systems) taking up the space at the front of the aircraft. This is clearly seen in Figure 59 and Figure 60. In Figure 59, with the front bodywork removed, it is evident that the fuselage structure does not extend further than the engine mounting point. This point is further emphasized in Figure 60 where the exposed fuselage structure (obtained from the Extra 330SC maintenance manual [71]) is illustrated. It is clear that the structure does not extend the complete length of the airframe, but rather terminates slightly forward of the wing main spar. As such, the fuselage structure will have an effective length of 4.55 m. The mass of the 'nacelle' section will be treated such that it acts at the very front of the fuselage sections and will be assumed to incorporate the mounting structure to the engine along with all affiliated parts. To account for fuselage body panels and additional components affiliated with the mounting of the engine, the frontmost section of the fuselage will be extended towards the front of the aircraft by an additional 0.23 m ($\approx 1/4$ the length of the section in front of the fuselage tubular structure). This will increase the effective fuselage structural length to 4.78 m in total.

Table 18: Structural group mass estimations

Component	**Subcomponent**	**Method Calculated Mass [kg]**					**Notes**
		Cessna	**USAF**	**Torenbeek**	**Other**	**Average**	
Wing	–	113.14	88.81	73.49	–	91.82	–
Empennage	Horizontal Tail	22.43	17.09	25.44	–	24.95	–
	Vertical Tail		7.37		–		–
Fuselage	–	–	66.88	82.96	74.59	74.81	Nicolai method presented as alternative
Nacelle	–	20.88	20.13	–	–	20.5	–
Landing Gear	Main Gear	–	26.68	–	–	26.68	–
	Nose/Tail Gear						–

Figure 59: Extra 330SC exposed engine (installed on airframe) [72]

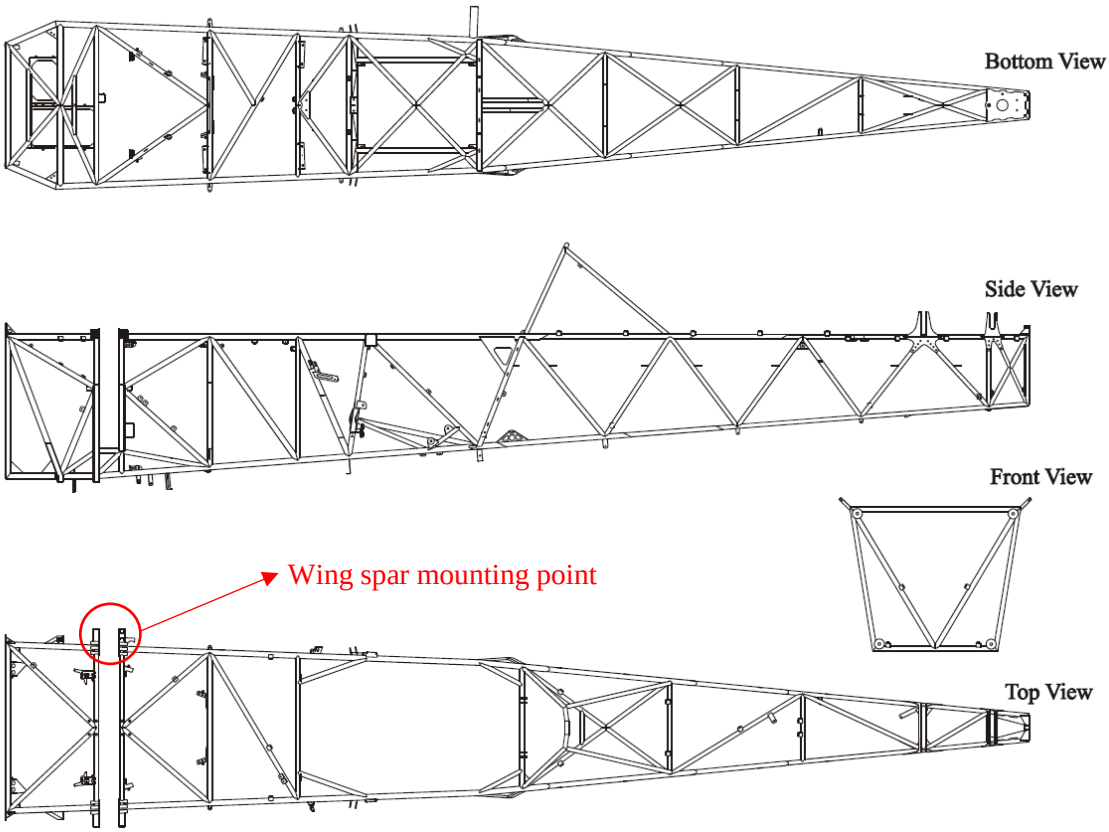

Figure 60: Extra 330SC steel tubular fuselage [71]

The mass estimations for the wing are markedly different from one another. The Cessna method estimates 15 kg more for the wing mass than the USAF method. The USAF estimates a wing mass of ≈ 15 kg more than the Torenbeek method. The methods all utilise different inputs to generate the mass estimates and it may not be completely unexpected that the various methods provide different results given that the wing was designed specifically for aerobatic flight. Aerobatic aircraft wings are generally shorter than most general aviation aircraft, experience far higher loads and experience higher loads far more frequently. Wing mass data presented in Figure 41 was normalised with respect to the wing reference area to obtain a better understand of the expected wing mass. The wing mass per unit of reference area (M_w/S_{ref}) for various general aviation aircraft is provided in Figure 61. The first seven aircraft listed in Figure 61 show a wing mass per unit of reference area of between 6.5 kg/m^2 and 7 kg/m^2, with the last three providing much higher values of between 9.5 kg/m^2 and 10.5 kg/m^2. It was expected that the Extra 330SC should have a wing mass per unit of reference area closer to the last three aircraft presented in Figure 61 as these aircraft have a wing loading similar to that of the Extra 330SC. The Extra 330SC was expected to have a wing mass per unit of reference area of between 9.5 kg/m^2 and 10.5 kg/m^2 and possibly higher due to the loads aerobatic aircraft wings are exposed to. The Torenbeek method provides an optimistic M_w/S_{ref} of 7.49 kg/m^2. The Cessna and Torenbeek methods provide values of $M_w/S_{ref} = 11.53$ kg/m^2 and $M_w/S_{ref} = 9.05$ kg/m^2 respectively. Taking an average of the mass estimates provides a mass of 91.82 kg and $M_w/S_{ref} = 9.36$ kg/m^2. This value compares well with published data. A wing mass of 91.82 kg was used.

The mass estimates for the empennage and nacelle were approximately identical for the various methods. The fuselage mass estimates illustrate a similar issue to that of the wing mass estimates. An average of the fuselage masses was used, with a similar argument to that of the wing driving this decision.

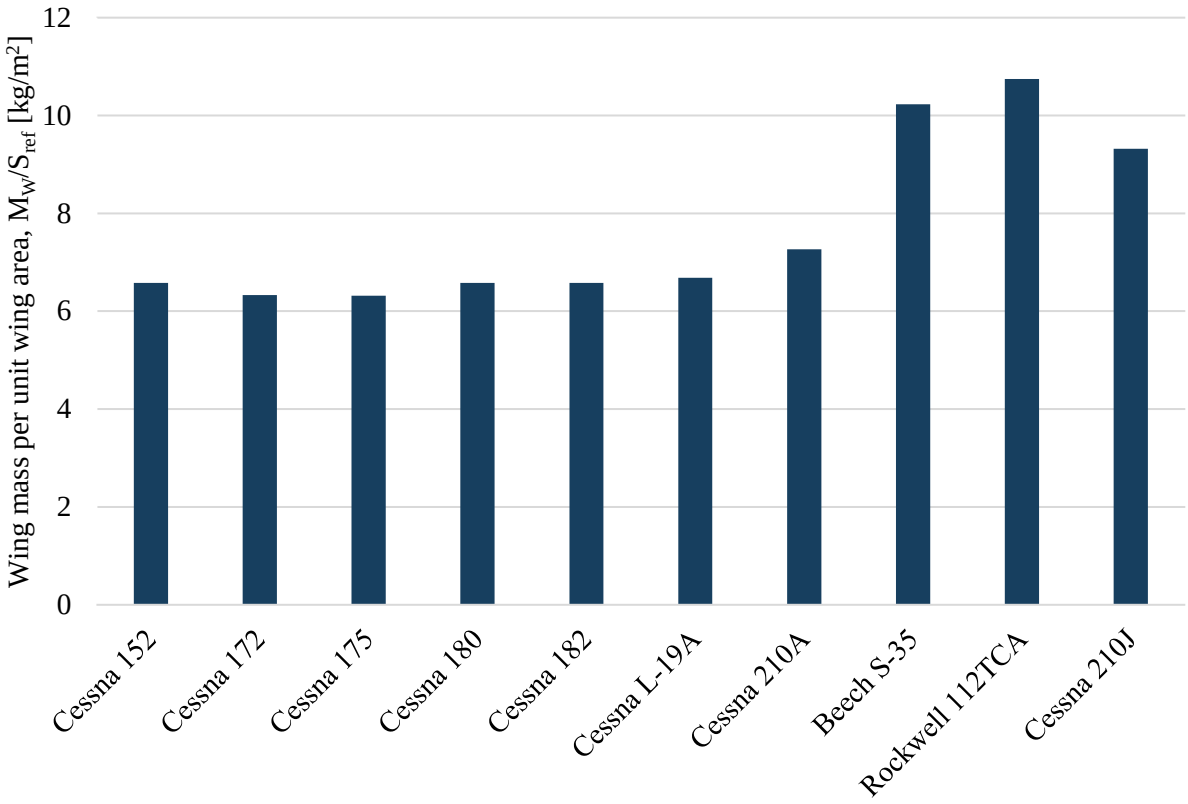

Figure 61: Mass per unit of wing area of various general aviation single engine propeller driven aircraft

The published empty mass of the Extra 330SC is 590 kg [13]. A summation of the estimated structural mass components with all available mass data (including all avionics, engine and affiliated components, sensors, etc) provided a mass of 554.5 kg. Given that the published mass data is completely known, the only discrepancy possible was the structural component mass estimations. It was found that an increase of 15% of the mass of the wing, fuselage and empennage groups provided a very close approximation of the empty mass at 588.3 kg. The landing gear mass was not increased as the landing loads were not expected to be any higher than conventional general aviation aircraft. The increases in structural mass for the various components can be seen in Table 19. The results see the wing mass increase to $M_{wing} = 105.59$ kg and increasing $M_w/S_{ref} = 10.76$ kg/m^2, which is on the higher end of the published data.

A comparison of the Extra 330SC structural masses is presented in Figure 62, together with the structural component masses from Figure 41. It is evident that the structure of Extra 330SC is lighter than the other general aviation aircraft presented. This is to be expected as the Extra 330SC has a short wingspan and length, with a shorter landing gear. Two very noticeably lighter areas are the fuselage and landing gear. The gear is expected to be far light given that the Extra 3330SC is a tail dragger and has a very small rear gear set when compared to the other aircraft presented. The main gear is also significantly different in design to the other aircraft presented. It comprises of a fibreglass spring as

Table 19: Structural component mass estimate corrections

Component	Original Mass Estimate [kg]	Additional Mass (+15% Original Mass) [kg]	New Component Mass [kg]
Wing	91.82	13.77	105.59
Horizontal Tail	17.09	1.11	8.48
Vertical Tail	7.37	4.58	21.67
Fuselage and Nacelle	95.31	14.3	109.61
Σ	211.59	33.76	245.35

compared to a full suspension design for all other aircraft provided. The lighter gear may also be due to the experience levels required to fly aerobatic type aircraft. Generally aerobatic aircraft are flown by more skilled and experienced pilots that are capable of precision flying. This means that lighter and shorter gear may be used as landings are expected to be accurate. The fuselage mass deficit of the Extra 330SC when compared to the other listed aircraft is also not completely unexpected as the Extra 330SC seats a single occupant, whereas the other aircraft provided seat between 2 and 4 occupants. Being an aerobatic aircraft, the Extra 330SC is also not expected to carry any additional mass such as baggage, whereas the other aircraft are. Some listed aircraft have a high-wing configuration, meaning that the fuselage structure will need to be stronger and heavier in the case of a roll over, further increasing the fuselage mass.

A more informative comparation of the various mass components can be done by finding the ratio of each component mass to the overall structural mass. This is illustrated in Figure 63. The ratios of the wing and empennage mass to the overall structural mass seems to be fairly consistent across all aircraft illustrated in Figure 63 (including the Extra 330SC). The exception is the Beech S-35 where it is likely that part of the fuselage group was included in the wing structure of the Beech S-35 since wing carry-through given that the fuselage group of the Beech S-35 is far less than any other aircraft provided. The fuselage of the Extra 330SC seems to show a smaller ratio of the overall mass than any other aircraft shown (excluding the Beech S-35 for the previously stated reasons). Once again this is to be expected given the passenger number and cargo requirements of the fuselage. The nacelle group ratio shows the Extra 330SC with a far greater portion than the other aircraft provided. This can be justified as aerobatic aircraft have far more powerful engines than most general aviation aircraft and thus require stronger and heavier mounting structure.

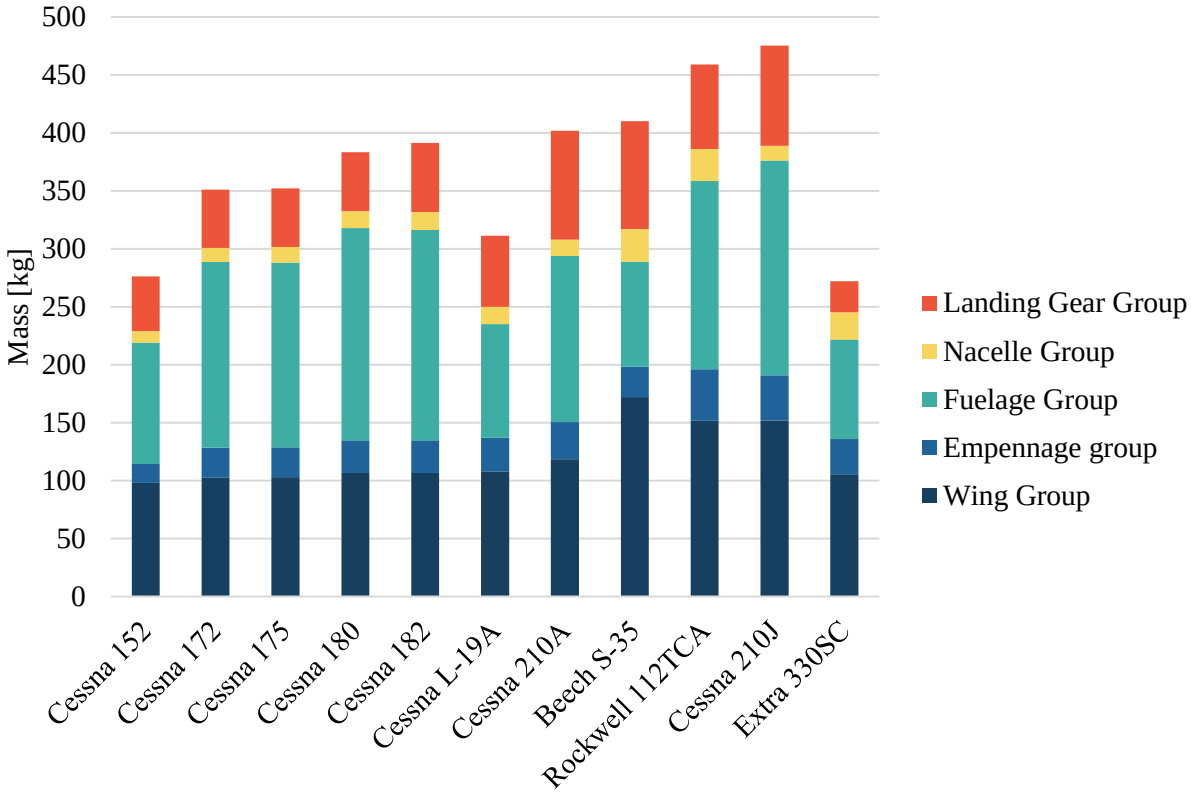

Figure 62: Comparison of structural component masses for various general aviation single engine propeller driven aircraft and the Extra 330SC

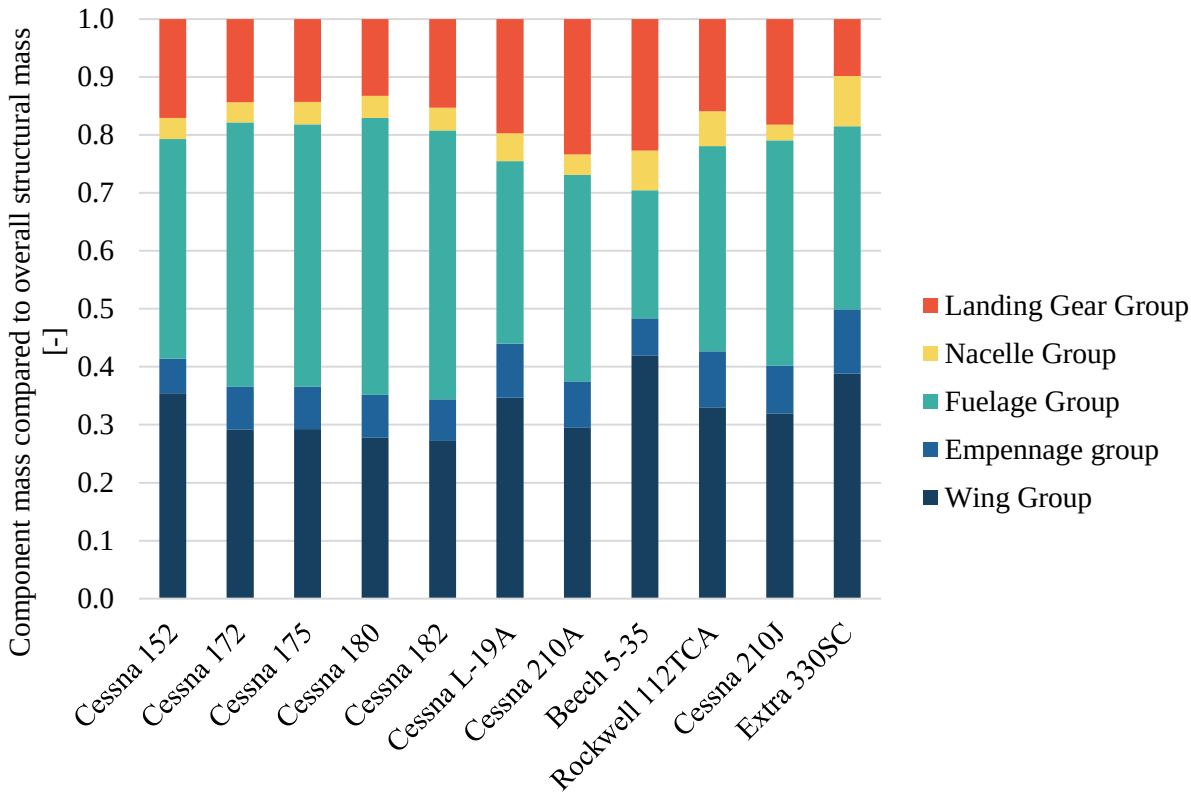

Figure 63: Comparison of structural component mass ratios for various general aviation single engine propeller driven aircraft and the Extra330SC

Further justification of the mass estimates of the Extra 330SC is provided in Figure 64, where the mass per unit length is provided and the mass per unit of wingspan (width) is provided. The Extra 330SC is seen to have a mass per unit length close to the lower end of the values illustrated for the given generation aviation aircraft. The mass per unit length falls within the range of values. This illustrates that the structural mass per unit of length of the aircraft is within reason. The mass per unit length of the Rockwell 112TCA and Cessna 210J are likely higher than the other aircraft provided due to both aircraft having a much larger and heavier engine than the other aircraft listed. The mass per unit wingspan shows the Extra 330SC tending towards the higher values presented for the given general aviation aircraft. The value obtained for the aerobatic Extra 330SC is well within the range of values and is likely correctly placed towards the upper end of the values presented. Despite the various differences, the Extra 330SC is not overly dissimilar to the general aviation aircraft provided and thus, the mass estimates for the structure of the Extra 330SC are acceptable.

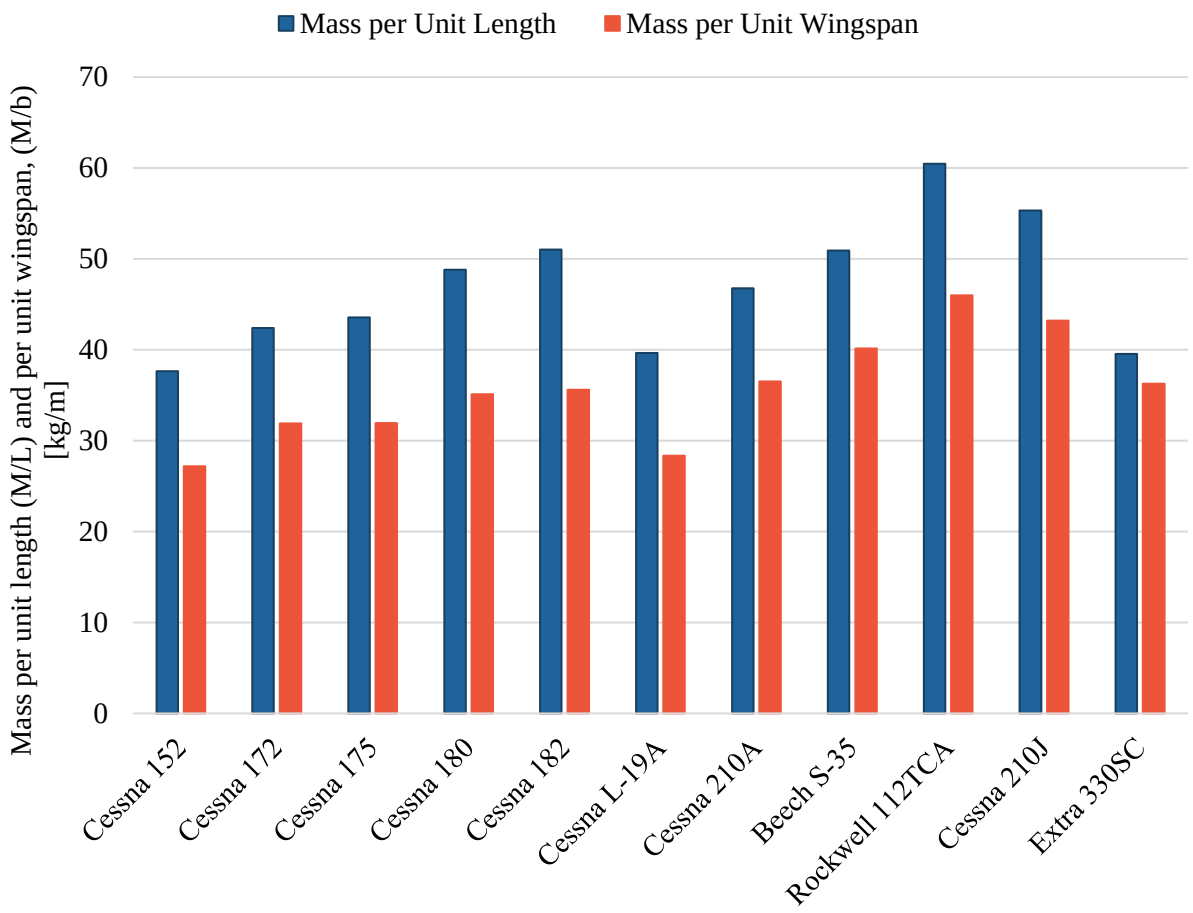

Figure 64: Comparison of mass per unit length and per unit span of various general aviation single engine propeller driven aircraft and the Extra 330SC

With the unknown mass components estimated, a complete list of the masses of the Extra 330SC was completed and can be seen in Table 20. The summation of all the components contained within Table 20 provides the maximum take-off mass of the aircraft. The shortfall of 1.72 kg of structural mass estimates was carried over to the maximum take-off mass, providing a mass of 868.28 kg. It should be noted that the landing gear mass of 11.84 kg presented in Table 20 is the mass estimated from Table 18 less the masses of the main wheels, the main tyres, the front brake assembly and the front brake cylinder. Thus, the term "landing gear" in Table 20 essentially refers to the fibreglass spring.

Table 20: Complete list of Extra 330SC component masses

Item	Mass [kg]	Actual (A) or Estimation (E)	% Total Weight	Group
Wing	105.59	E	12.16	Wing
Horizontal Tail	21.67	E	2.50	Empennage
Vertical Tail	8.48	E	0.98	
Fuselage	86.03	E	9.91	Fuselage + Nacelle
Nacelle	23.58	E	2.72	
Engine (AEIO-580-B1A)	191.80	A	22.09	Engine and Systems
Inverted oil pickup; VAC-2/6	0.31	A	0.04	
Governor	1.10	A	0.13	
Alternator SD-8 (14V, 8 Amps)	1.32	A	0.15	
Single Oil Cooler Rear, 8000353	1.65	A	0.19	
Fuel Injector	3.90	A	0.45	
Starter	4.63	A	0.53	
Engine Oil	1.20	A	0.14	
Engine Electrics	0.50	E	0.06	
Acro Tank	6.50	A	0.75	Fuel
Front Centre Tank	38.90	A	4.48	
Rear Centre Tank	29.50	A	3.40	
Smoke Tank	19.60	A	2.26	
Wing Tanks	86.40	A	9.95	
Propeller, MTV-9-B-C/C 198-25 (3 Blade)	30.50	A	3.51	Point Masses
Spinner, P-810-2	0.80	A	0.09	
Exhaust System "6 in 1" (incl. Silencer)	8.48	A	0.98	
Battery	10.52	A	1.21	
Oil Temp. Probe	0.08	A	0.01	
Oil Press. Sender	0.12	A	0.01	
Fuel Qty Probe Front Centre Tank	0.184	A	0.02	
Fuel Qty Probe Rear Centre Tank	0.184	A	0.02	
Fuel Qty Probe Wing Tank	0.12	A	0.01	
Altimeter 2	0.61	A	0.07	
Main Wheel Tyre L	2.447	A	0.28	

Item	Mass [kg]	Actual (A) or Estimation (E)	% Total Weight	Group
Main Wheel Tyre R	2.447	A	0.28	Point Masses
Wheel Fairing L	1.50	A	0.17	
Wheel Fairing R	1.50	A	0.17	
Bottom Fuselage Cover (Belly Fairing)	5.20	A	0.60	
Instrument Panel	0.40	A	0.05	
Single Pump Smoke System	4.591	A	0.53	
Safety Belt Assembly (Seat Belts w. single ratchet, shoulder harness and crotch strap)	3.30	A	0.38	
Throttle Control	0.42	A	0.05	
Single Oil Cooler Rear	1.65	A	0.19	
Additional Oil Cooler System	2.00	A	0.23	
Landing Gear	11.84	E	1.36	
Electric Actuator Pedal Adjust.	3.25	A	0.37	
Magneto L/H	2.30	A	0.26	
Magneto R/H	2.00	A	0.23	
Shock Mounts L1	0.425	A	0.05	
Shock Mounts L2	0.425	A	0.05	
Shock Mounts R1	0.425	A	0.05	
Shock Mounts R2	0.425	A	0.05	
Main Wheel L	4.00	A	0.46	
Main Wheel R	4.00	A	0.46	
Brake Assy	1.40	A	0.16	
Brake Cyl., front	0.55	A	0.06	
Tail Wheel 5"	5.50	A	0.63	
Seat Rear Standard	2.70	A	0.31	
Canopy	10.00	A	1.15	
Pilot + Parachute	99.00	A	11.40	
Surface Controls	3.00	E	0.35	Other
Electrical	1.00	E	0.12	
Avionics	6.334	A	0.72	
TOTAL MASS [kg]	**868.28**			

The single largest contributor to the total mass is the engine, contributing 22.09% of the total mass, followed by the wing (12.16%) and then the pilot and parachute (11.40%-assuming a pilot and parachute mass of 99 kg). A visual representation of the contributions of each group can be seen in Figure 65. While the landing gear and affiliated components have been grouped in the point masses (as per the POH [13]) in Table 20, the main landing gear and its components have been separated out of the point masses to better understand the mass contribution of the landing gear system and structural system. The largest contributing group to the aircraft mass is the engine and systems group with a contribution of around 24%. The entire

structural group, consisting of the wing, fuselage, empennage and landing gear contributes just under one third of the mass at 31%.

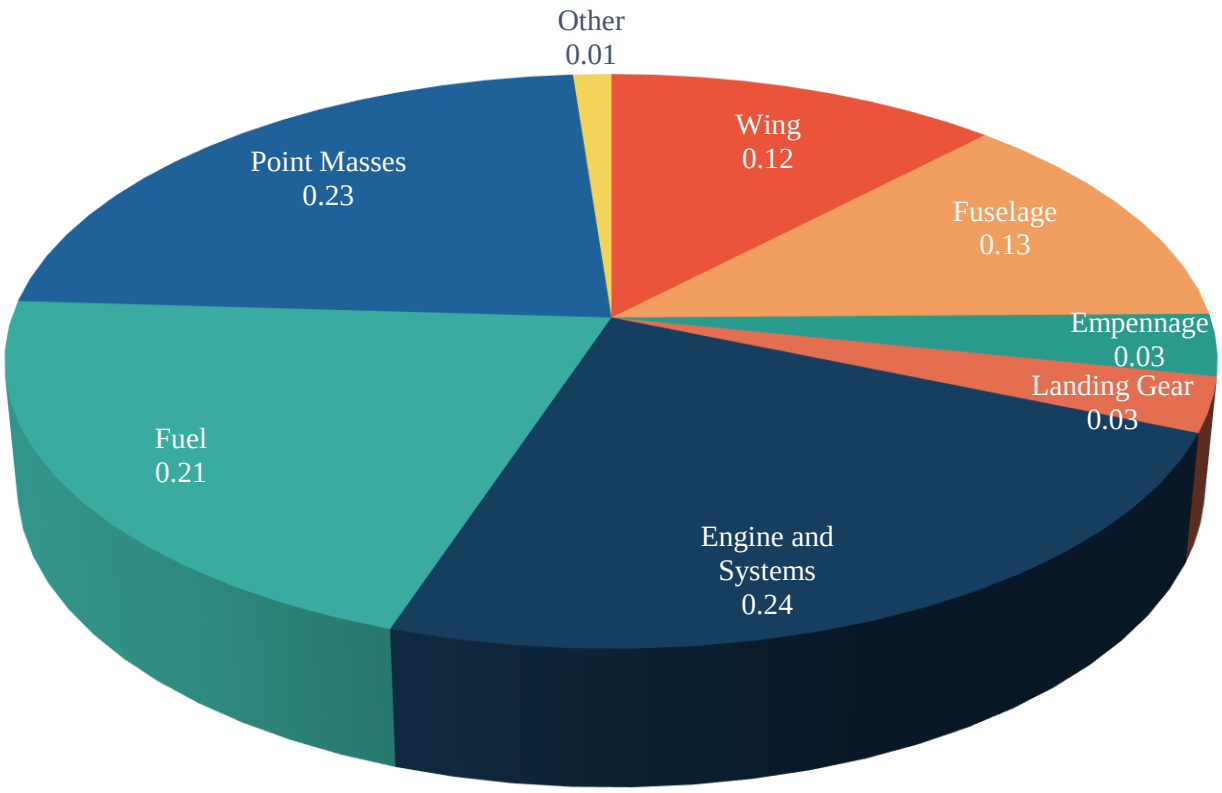

Figure 65: Extra 330SC component mass portions for maximum take-off mass

The mass centroid locations in the X and Z direction for each component were determined using the mass components. These mass centroid of the various components can be found in Table 21. The surface controls and electrical components within the fuselage were combined in a distributed fuselage mass group. The avionics component was placed in a fuselage volumes group. The fuselage structure and nacelle were combined in a single component termed “fuselage.” The components making up the engine and systems group were placed into a single group termed “propulsion.” These changes were done to simplify the inertial calculations in §3.2.2. The values of the X and Z distances are measured relative to the front most part of the aircraft (the nose of the propeller spinner) and follow the conventions outlined in Figure 44.

All component masses provided within the POH [13] were accompanied by a distance (in the X direction), given relative to the firewall of the aircraft. These distances were then determined relative to the apex point

of the aircraft spinner. While the POH [13] did provide distances in the X direction, no values were provided for the Z direction. As such, each of the Z values presented in Table 21 were estimated and the “actual or estimated” column is only for values in the X direction. Centroids that were estimated were all obtained using the methods outlined in §2.3.

Table 21: Extra 330SC mass component centroids

Item	Mass [kg]	X[m]	Z[m]	Actual (A) or Estimation (E)
Wing	105.59	2.323	1.088	E
Fuselage	109.61	2.814	1.100	E
Horizontal Tail	21.67	5.983	1.501	E
Vertical Tail	8.48	6.280	1.900	E
Fuselage Distributed Masses (Surface Controls and Electrical)	4.00	2.810	1.100	E
Fuselage Volumes (Avionics)	6.23	2.920	1.200	E
Propulsion	206.41	0.75	1.130	A
Acro Tank	6.50	1.802	0.870	A
Front Centre Tank	38.90	1.782	1.000	A
Rear Centre Tank	29.50	2.230	1.000	A
Smoke Tank	19.60	2.210	0.870	A
Wing Tanks	86.40	1.846	1.088	A
Propeller, MTV-9-B-C/C 198-25 (3 Blade)	30.50	0.395	1.219	A
Spinner, P-810-2	0.80	0.345	1.219	A
Exhaust System "6 in 1" (incl. Silencer)	8.48	1.155	0.827	A
Battery	10.52	1.720	1.130	A
Oil Temp. Probe	0.08	1.435	1.000	A
Oil Press. Sender	0.12	1.585	1.219	A
Fuel Qty Probe Front Centre Tank	0.18	1.765	1.088	A
Fuel Qty Probe Rear Centre Tank	0.18	2.245	1.088	A
Fuel Qty Probe Wing Tank	0.12	1.825	1.088	A
Altimeter 2	0.61	2.825	1.400	A
Main Wheel Tyre L	2.45	1.655	0.174	A
Main Wheel Tyre R	2.45	1.655	0.174	A
Wheel Fairing L	1.50	1.705	0.240	A
Wheel Fairing R	1.50	1.705	0.240	A
Bottom Fuselage Cover (Belly Fairing)	5.20	2.107	0.910	A
Instrument Panel	0.40	2.845	1.400	A
Single Pump Smoke System	4.59	2.15	0.783	A
Safety Belt Assembly (Seat Belts w. single ratchet, shoulder harness and crotch strap)	3.30	3.495	1.088	A
Throttle Control	0.42	1.595	1.310	A
Single Oil Cooler Rear	1.65	1.325	1.040	A

Item	Mass [kg]	X[m]	Z[m]	Actual (A) or Estimation (E)
Additional Oil Cooler System	2.00	0.745	1.040	A
Landing Gear	11.84	1.845	0.522	A
Electric Actuator Pedal Adjust.	3.25	3.150	0.000	A
Magneto L/H	2.30	1.395	1.090	A
Magneto R/H	2.00	1.395	1.090	A
Shock Mounts L1	0.43	1.255	0.805	A
Shock Mounts L2	0.43	1.255	0.805	A
Shock Mounts R1	0.43	1.255	0.805	A
Shock Mounts R2	0.43	1.255	0.805	A
Main Wheel L	4.00	1.719	0.174	A
Main Wheel R	4.00	1.719	0.174	A
Brake Assy	1.40	1.719	0.174	A
Brake Cyl., front	0.55	1.719	0.174	A
Tail Wheel 5"	5.50	6.505	0.957	A
Seat Rear Standard	2.70	3.635	1.044	A
Canopy	10.00	3.375	1.610	A
Pilot + Parachute	99.00	3.445	1.000	A

Using the values provided in Table 21, centre of gravity locations were obtained for different mass configurations. The various mass configurations that were considered, were chosen such that they aligned with the sample centre of gravity locations provided in the Extra 330SC POH [13]. Centre of gravity locations for various mass configurations were obtained and compared with the values provided in the POH [13], as seen in Figure 66. This comparison of mass and corresponding centre of gravity locations served as a form of verification for the mass component estimates and corresponding mass centroid estimations.

The estimated mass and centre of gravity locations were overlayed on the mass and centre of gravity locations provided by the Extra 330SC POH [13]. This is shown in Figure 66. The calculated forward centre of gravity locations are indicated by the blue dots while the aft centre of gravity calculations are shown by the orange dots. The changes in mass and centre of gravity location were obtained by adding various mass components and using the centre of gravity locations, both provided in Table 22. Using the empty mass of the aircraft, the pilot and then fuel masses for the different fuel tanks were added. Corresponding moment arms were used to calculate the centre of gravity for each additional mass component. All points on Figure 66 were compared with those given in the Extra 330SC POH [13], with the exception of step 6. This step was omitted as the additional mass provided in Table 22 did not correspond with the mass increase presented in Figure 66. The estimated results show a good correlation with the data provided by the Extra aircraft company. These results may not necessarily mean that the component masses and mass distributions are entirely correct. The correlation should suggest that the overall mass distribution of the aircraft is likely

near those of the actual aircraft. The results show a mass that is slightly less than the values provided by the Extra 330SC POH [13]. This mass deficit is equal to the missing 1.72 kg of structural mass.

Using the comparisons and conclusions drawn from mass and centre of gravity estimates provided throughout this section, the mass estimates and corresponding centroid locations are acceptably defined. A layout of the centroid locations of the structural group components and engine is provided in Figure 67 along with the empty mass centre of gravity. Excluding the empty mass symbol, the size of each "bubble" present on Figure 67 indicates the mass of each component relative to the other listed components. The larger the bubble the larger the mass of the component compared to the other components. It is evident that the wing and engine bring the mass of the aircraft forward and counteract the rearward mass shifts of the fuselage, vertical stabiliser and horizontal stabiliser.

While most component masses are fixed, some masses such as the pilot (and parachute), the fuel tanks and the smoke tanks may be altered. Various combinations such as pilot (and parachute) mass and pilot seat locations as well as fuel mass can be obtained, along with various centre of gravity locations to provide a mass against the centre of gravity envelope. This envelope is illustrated in Figure 68. The values of 1.7 m and 1.9 m in brackets of the legend indicate the pilot seat location. The extremities of the mass and centre of gravity combinations have been used to create the boundaries of the envelope. The cases that form the boundary of the envelope will also serve as the test matrix to compare tumble manoeuvres for various mass and centre of gravity locations. Inertial values for the mass and centre of gravity combinations will also be included.

Table 22: Extra 330 loading weights and moment arms for centre of gravity calculations [13]

Position on Figure 66	Pilot & Parachute		Fuel in Acro Tank ($9l$)		Fuel in Rear C. Tank ($41l$)		Fuel in front C. Tank ($54l$)		Oil in Smoke Tank ($23l$)		Fuel In Wing Tank ($120l$)	
	Mass [kg]	Moment Arm [cm]	Mass [kg]	Moment Arm [cm]	Mass [kg]	Moment Arm [cm]	Mass [kg]	Moment Arm [cm]	Mass [kg]	Moment Arm [cm]	Mass [kg]	Moment Arm [cm]
1	69	170/190	-	25.8	-		-	-	-	-	-	-
2	69	170/190	6.5	25.8	-		-	-	-	-	-	-
3	69	170/190	6.5	25.8	29.5	68.5	-	-	-	-	-	-
4	69	170/190	6.5	25.8	29.5	68.5	38.9	23.7	-	-	-	-
5	69	170/190	6.5	25.8	29.5	68.5	38.9	23.7	19.6	66.5	-	-
6	69	170/190	6.5	25.8	29.5	68.5	38.9	23.7	19.6	66.5	86.4	33
7	99	170/190	-	-	-	-	-	-	-	-	-	-
8	99	170/190	6.5	25.8	-	-	-	-	-	-	-	-
9	99	170/190	6.5	25.8	29.5	68.5	-	-	-	-	-	-
10	99	170/190	6.5	25.8	29.5	68.5	38.9	23.7	-	-	-	-
11	99	170/190	6.5	25.8	29.5	68.5	38.9	23.7	19.6	66.5	-	-
12	99	170/190	6.5	25.8	29.5	68.5	38.9	23.7	19.6	66.5	86.4	33

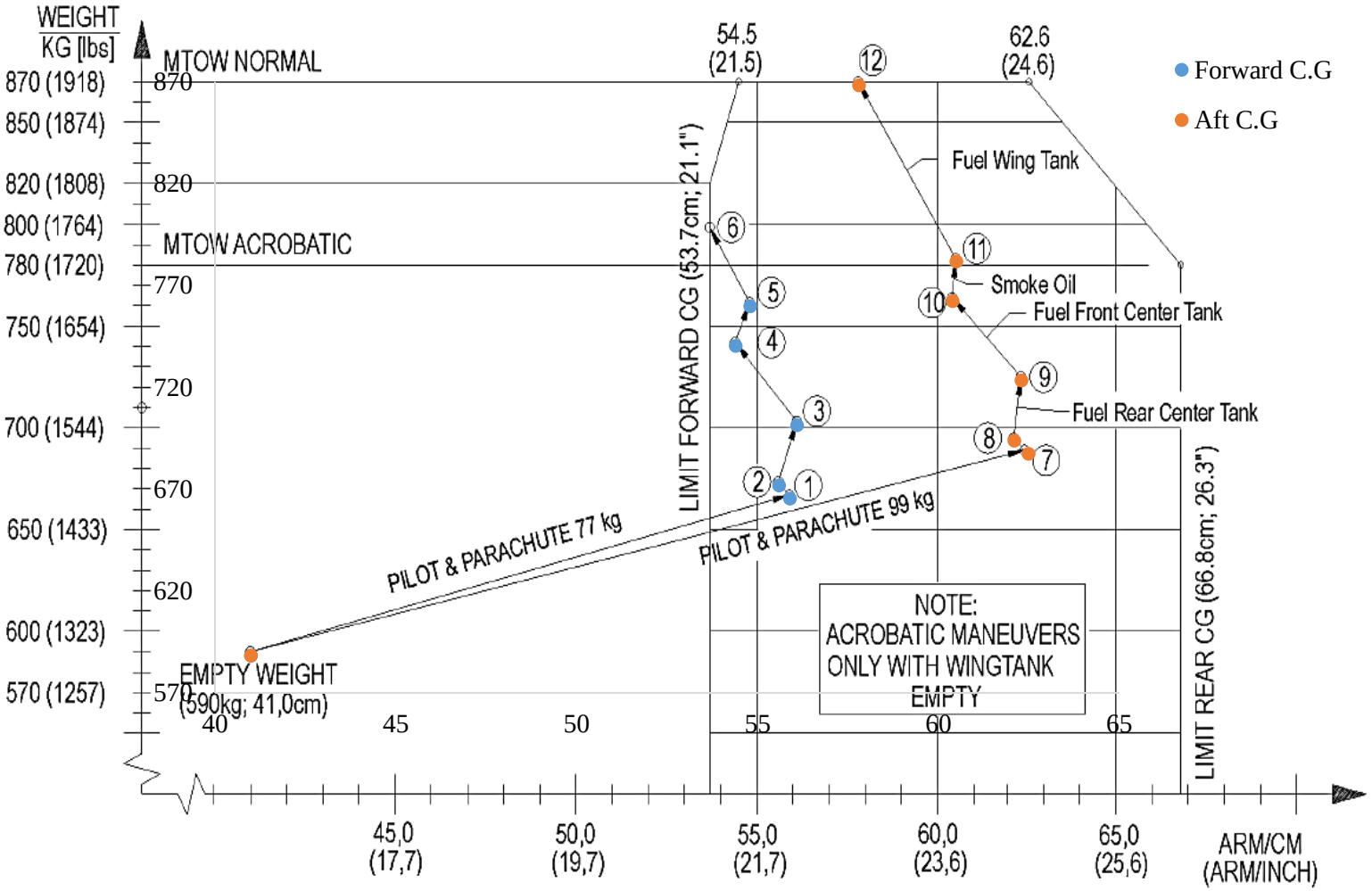

Figure 66: Extra 330 mass and corresponding centre of gravity location calculation chart [13]

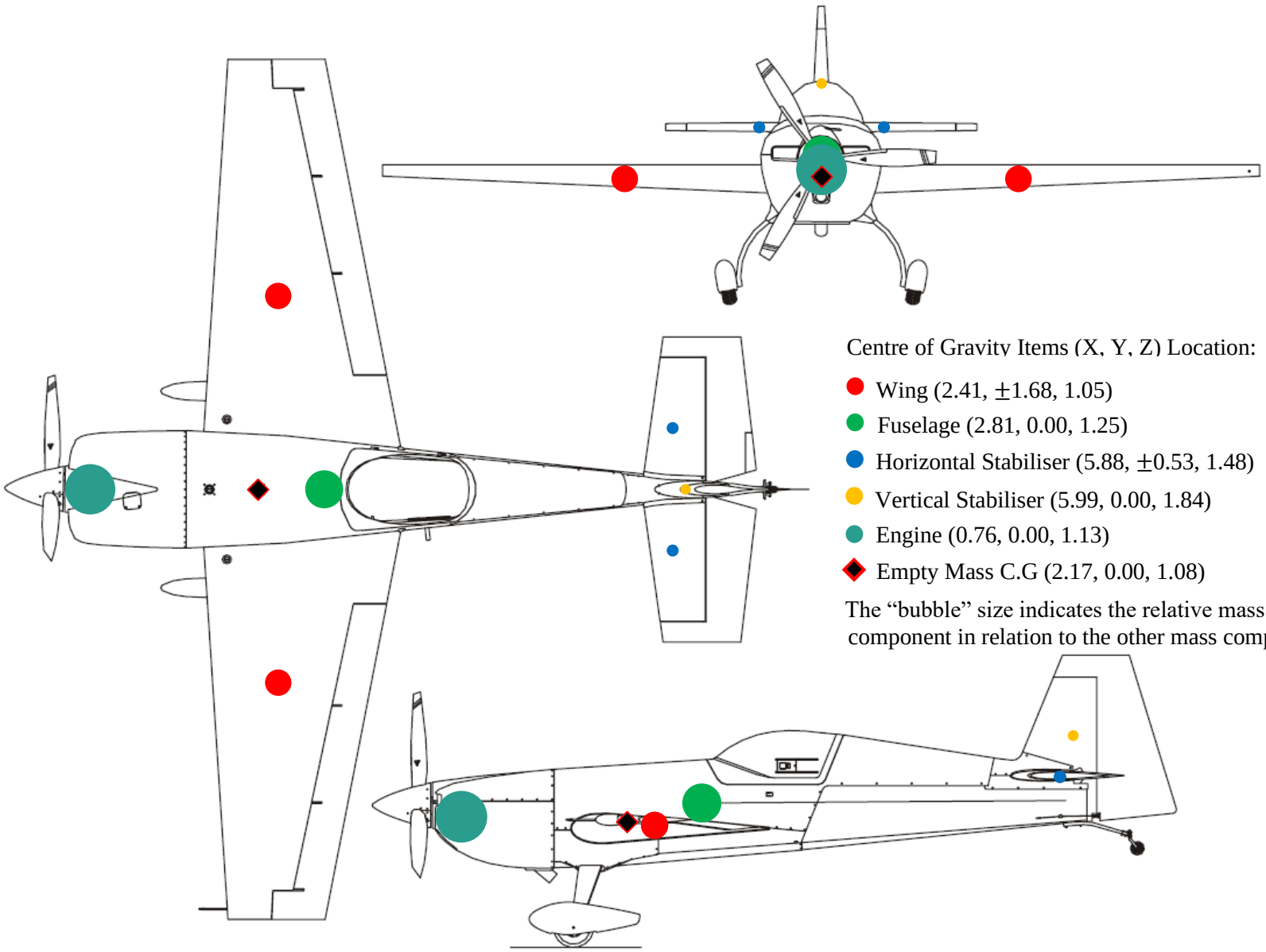

Figure 67: Extra 330SC main component centre of gravity locations and empty mass centre of gravity location

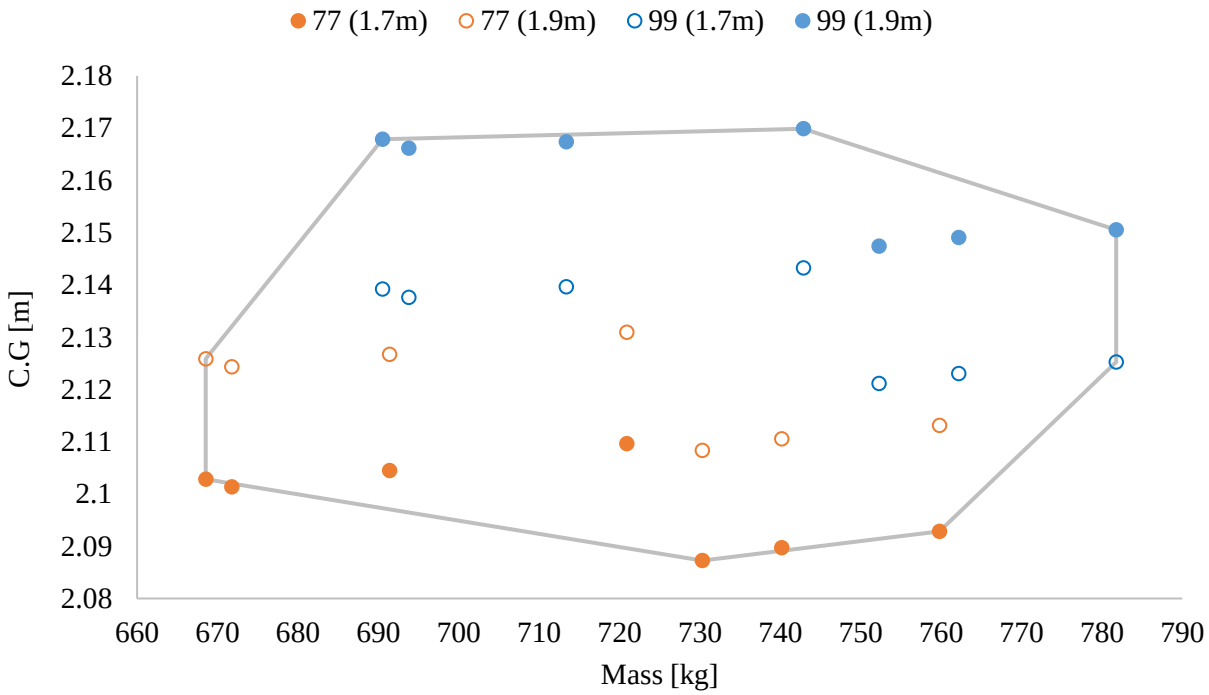

Figure 68: Mass vs centre of gravity envelope

3.2.2. Inertial Data

Using the mass and centroid data generated for the Extra 330SC in §3.2.1, inertial values were obtained utilising the equations provided in §2.3. In addition to data obtained from the Extra 330SC POH [13] various input variables required for each inertial group were obtained through measurement off the 3-view as well as various component images provided in the Extra 330SC maintenance manual [71].

The input variables for the inertial calculations of the lifting surfaces are presented in Table 23. The span, (b), root thickness, (t_r) and root chord, (c_r) of the various lifting surfaces were measured from the point at which the lifting surface attaches to the fuselage. The vertical stabiliser was modelled by setting the dihedral angle to $\theta = 90°$. It should also be noted that the values provided for the wing and horizontal stabiliser were calculated for a single wing and horizontal stabiliser surface.

Table 23: Lifting surface inertial estimation input variables

Item	Wing	Horizontal Stabiliser	Vertical Stabiliser
$\boldsymbol{\Lambda_L}$ [deg]	4.00	8.00	22.50
$\boldsymbol{\Lambda_T}$ [deg]	-10.00	-6.50	-16.50
$\boldsymbol{b}$ [m]	3.32	1.22	1.22
$\boldsymbol{c}$ [m]	1.66	0.96	1.39
$\boldsymbol{t_r}$ [m]	0.27	0.09	0.22
$\boldsymbol{t_t}$ [m]	0.10	0.06	0.09
$\boldsymbol{XS4}$ [m]	1.70	5.45	5.35
$\boldsymbol{ZS1}$ [m]	1.00	1.48	1.40
$\boldsymbol{YS4}$ [m]	0.44	0.00	0.00
$\boldsymbol{\theta}$ [deg]	2.50	0.00	90.00
$\boldsymbol{V}$ [m^3]	0.79	0.07	0.19
$\boldsymbol{M}$ [kg]	105.59	17.09	7.37

The variables required for inertial modelling of the fuselage are presented in Table 24. The input variables presented are for the structural group, the distributed contents group and the avionics group. The structural group and distributed contents group have been combined as these two groups share a number of variables. The point mass group has not been included as all necessary information for the point mass inertial calculations has already been defined in Table 21.

Once again, the fuselage variables require some explanation, as some variables have not been measured exactly as they appear in the 3-view. The length of what is defined as the "nose" section of the fuselage in §2.3.2.1 has been set to a value of 0 m. The reasoning behind this decision stems from the argument made in §3.2.1, where the front section of the aircraft is occupied by engine and affiliated systems only and not by fuselage structure. The inertial estimates of the fuselage were made using an open-ended right cylindrical shell and a tail conical shell. The length of the fuselage structural group totals 4.78 m with the structure being split into two sections. The first section (the open-ended right cylindrical shell) has a length of 3.82 m and the second section (the tail section conical shell) has a length of 0.96 m. The radius of open-ended right shell and base of the conical shell were set to 0.52 m. These values were determined by overlaying the open ended right cylindrical shell and the conical shell on the structural illustrations. The shapes were sized to match the area of the structure with the shapes. An approximation was required as the open-ended right cylindrical shell does not taper, unlike the fuselage. The conical shell also does not follow the profile of the side view of the rear end of the structure. To accommodate these issues, the shapes were overlayed such that the area lost to taper was accounted for by having a smaller shape radius at sections where the fuselage structure did not taper. This is illustrated in Figure 69. Note that the open-ended right cylindrical shell extends slightly beyond the front of the structure, as discussed in §3.2.1.

Table 24: Fuselage inertial estimation input variables

	Fuselage	
	Item	**Value**
Structure and Distributed Contents	l_n [m]	0
	l_c [m]	3.82
	l_t [m]	0.96
	R [m]	0.52
	z_b [m]	1.26
	W_s [kg]	74.81
	$CREW_{c \cdot g}$ [m]	3.45
	$XS4$ [m]	2.51
	$XS4_{HT}$ [m]	5.45
Avionics	W_{vo} [kg]	6.23
	R_v [m]	0.61
	l_v [m]	0.15
	X [m]	2.92
	Z [m]	1.20

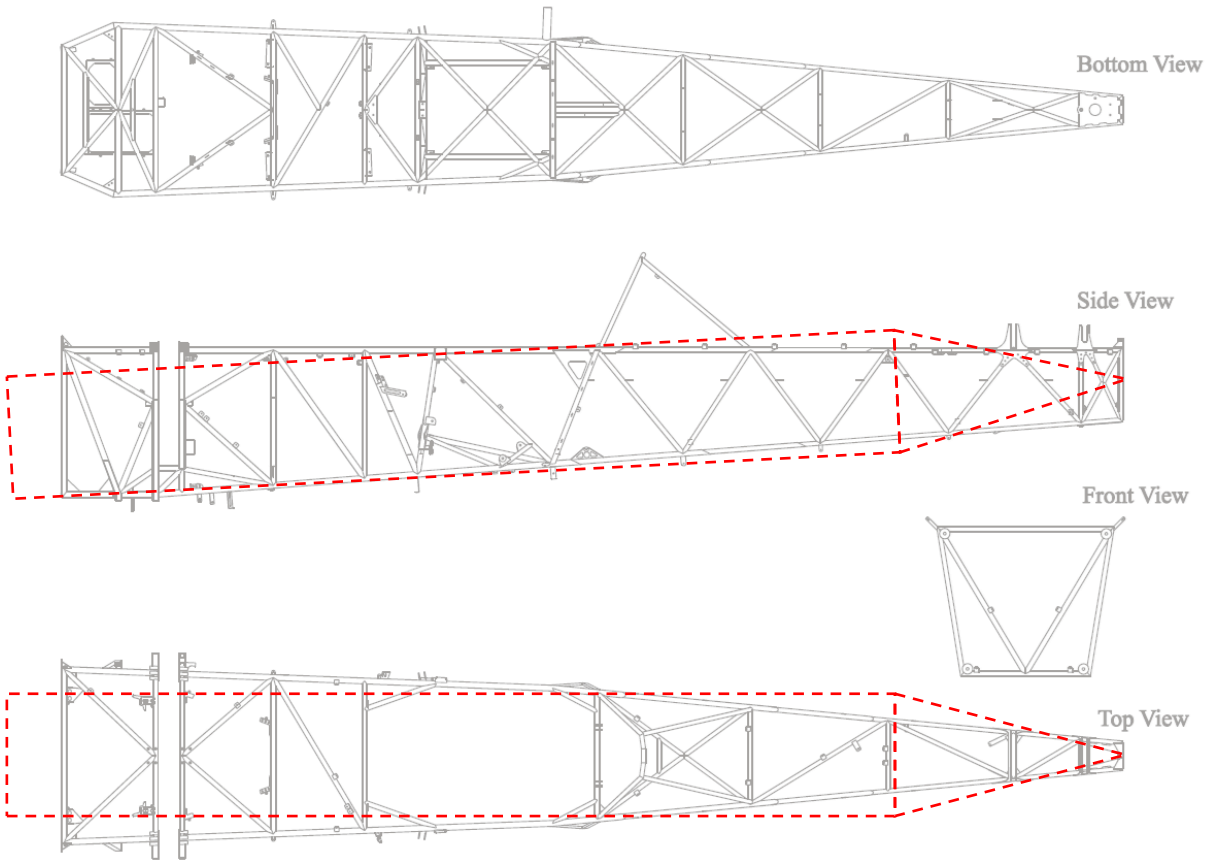

Figure 69: Fuselage inertia estimation shape approximations

The propulsive group input variables for inertial calculations are provided in Table 25. The propulsive group was modelled as a solid cylinder. A single engine is presented on the Extra 330SC and is situated in the nose of the aircraft. The length and radius of the cylinder were approximated using data provided by the engine manufacture (Lycoming).

Table 25: Propulsion group inertial estimation input variables

Propulsion	
Item	**Value**
$\boldsymbol{R_e}$ [m]	0.41
$\boldsymbol{l_e}$ [m]	1.00
$\boldsymbol{XP1}$ [m]	0.75
$\boldsymbol{XP2}$ [m]	0.00
$\boldsymbol{YP1}$ [m]	0.00
$\boldsymbol{YP2}$ [m]	0.00
$\boldsymbol{ZP1}$ [m]	1.09
$\boldsymbol{ZP2}$ [m]	0.00
No. of Engines [-]	1
$\boldsymbol{W_e}$ (Per Engine) [kg]	206.41

The input variables for estimation of the inertial values of the fuel contained within the fuselage are presented in Table 26. The fuel in each tank was assumed to be in the shape of a rectangular prism. The volumetric shape of the fuselage fuel tank was determined by inspecting the drawings provided in the Maintenance Manual of the Extra 330SC [71]. An image of each fuel tank contained within the fuselage is illustrated in Figure 70. It was assumed that there were no components contained within the tanks and as such, the fuel was assumed to take the shape of its container. The mass and density of the fuel for the engine fuel and smoke fuel was provided by the Extra aircraft corporation in the POH [13]. These values were used to estimate the dimensions of the various fuel tanks.

Table 26: Fuselage fuel inertial estimation input variables

Item	**Value**			
	Acro Tank	**Front Center Tank**	**Rear Center Tank**	**Smoke Tank**
$\boldsymbol{W_{ff}}$ [kg]	6.50	38.90	29.50	19.60
$\boldsymbol{L_f}$ [m]	0.31	0.30	0.22	0.23
$\boldsymbol{\rho}$ [kg/m^3]	722.22	722.22	722.22	850.00
$\boldsymbol{X}$ [m]	1.80	1.78	2.23	2.21
$\boldsymbol{Z}$ [m]	0.87	1.00	1.00	0.87
$\boldsymbol{w}$ [m]	0.17	0.60	0.60	0.45
$\boldsymbol{h}$ [m]	0.17	0.30	0.30	0.23
$\boldsymbol{l}$ [m]	0.31	0.30	0.22	0.23

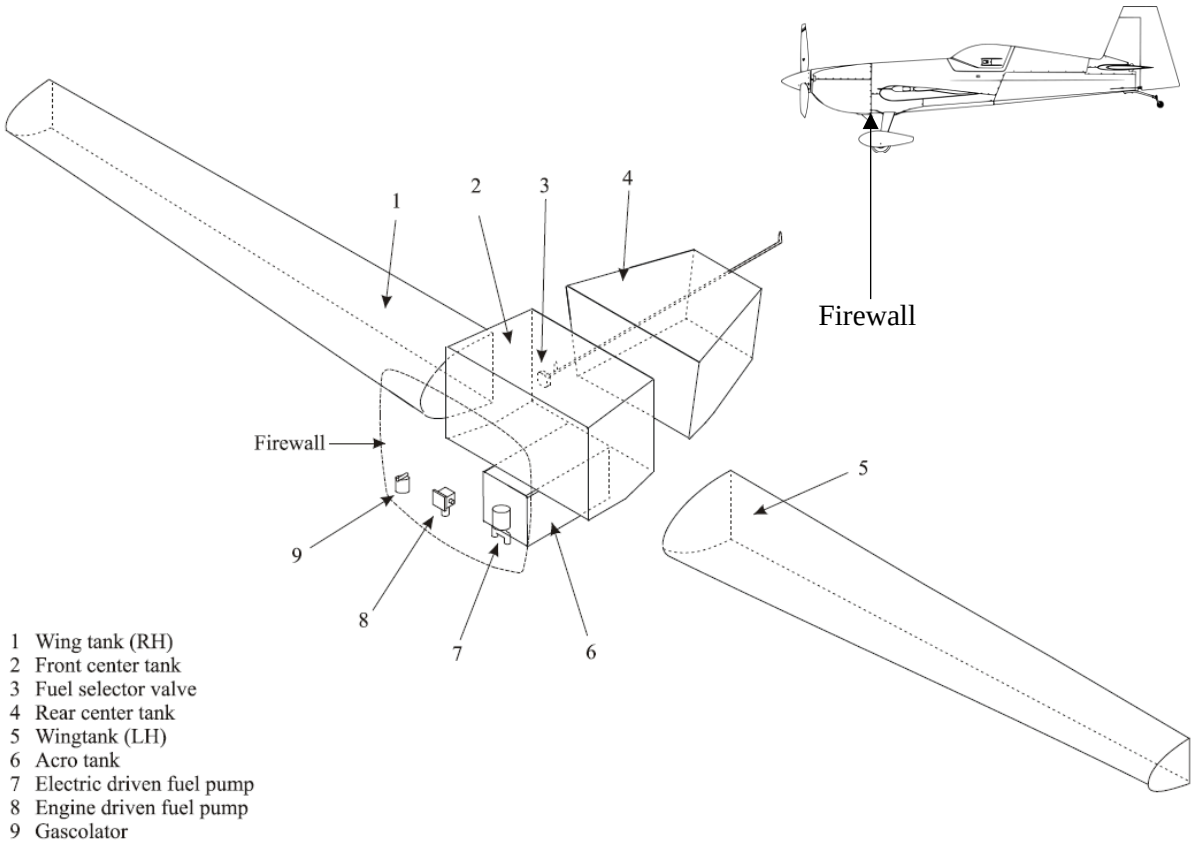

Figure 70: Extra 330SC fuselage and wing fuel tanks

Input variables for the inertial estimations of fuel contained within the Extra 330SC wings are presented in Table 27. The wing fuel tanks take the same shape as the leading edge of the wing. This can be seen in Figure 70. The variables for the wing fuel are similar to those of the wing. The span (b), and the chord (c), of the tanks are shortened as the wing fuel tanks only stretch ≈ 43 % of the length of each wing and ≈ 23 % of the wing chord. The wing fuel tanks do not extend over the entire span of the wing and terminate inboard of the wing tip.

Table 27: Wing fuel inertial estimation input variables

Wing Tanks	
Item	**Value**
$\boldsymbol{\Lambda_L}$ [deg]	4.00
$\boldsymbol{\Lambda_T}$ [deg]	0.00
$\boldsymbol{b}$ [m]	1.50
$\boldsymbol{c}$ [m]	0.41
$\boldsymbol{t_r}$ [m]	0.27
$\boldsymbol{t_t}$ [m]	0.17
$\boldsymbol{XF2}$ [m]	1.70
$\boldsymbol{ZF1}$ [m]	1.00
$\boldsymbol{YF2}$ [m]	0.50
$\boldsymbol{\theta}$ [deg]	2.50
$\boldsymbol{X}$ [m]	1.87
$\boldsymbol{Z}$ [m]	1.38
$\boldsymbol{\rho}$ [kg/m^3]	722.22
$\boldsymbol{V}$ [m^3]	4.18
$\boldsymbol{W_{wf}}$ [kg]	95.24

Using the data provided in Table 23-Table 27, the inertia of each main group was determined. The inertial estimations for the main component groups of the Extra 330SC at maximum take-off mass are provided in Table 28. The pilot and parachute mass were set to 99 kg. The inertial values of the lifting surface group and the propulsion group would remain unchanged throughout flight and through configuration changes. The fuselage structural, distributed contents and avionics groups would also remain unchanged. The point mass group would change depending on the mass and position of the pilot. The fuel group inertial values would change throughout flight with fuel burn and depend on the configuration chosen. For instance, if the aerobatic configuration is chosen, the aircraft would fly without any fuel in the wing tanks.

Figure 71 illustrates the inertial contributions of each component group for (a) empty mass, (b) an aerobatic configuration (in which the front, rear, aerobatic and smoke tanks would be filled to capacity) and (c) the maximum take-off mass in SI units (kg.m^2). The pitch and yaw inertias (I_y and I_z) are evidently higher than the roll inertia (I_x). This is plausible given that the Extra 330SC can achieve roll rates of up to 420 °/s [73]. The pitch and yaw rates observed from video footage (no published values for pitch and yaw rates were available), are noticeably slower. This is likely due (in part) to higher inertial values in the pitch and yaw directions. The addition of a 99 kg pilot and parachute at the most rearward seating position increases the fuselage contribution to the pitch and yaw inertias by a considerable amount. This is not unexpected as the pilot is located a fair distance aft of the centre of gravity of the aircraft. A lighter pilot should allow for greater pitch and yaw rates, but perhaps not by a significant amount.

It has been assumed that the tumble manoeuvre is purely in the longitudinal plane and as such, the only significant inertial value is the pitch inertia (I_y). Given the importance of this inertial value in particular, the pitch inertia has been plotted together in Figure 71 for three configurations about the remote axes. It is interesting to note is that the fuel in the wings does not impact the pitch inertia of the aircraft significantly. This can be seen by comparing the pitch inertia of the aerobatic configuration and maximum take-off mass configuration. This result seems feasible as the wing fuel is located very close to the centre of gravity of the aircraft and as such should not influence the pitch characteristics significantly.

Table 28: Inertial estimation of the Extra 330SC in the maximum take-off mass configuration

Inertia Component [lbs.in^2]	**Lifting Surface**			**Fuselage**				**Propulsion**	**Fuel Tanks**				
	Wing	**Horizontal Stabiliser**	**Vertical Stabiliser**	**Structure**	**Distributed Contents**	**Avionics**	**Point Masses**	**Engine and Systems**	**Acro**	**Front Tank**	**Rear Tank**	**Wing Tanks**	**Smoke Tank**
I_{1_x}	8.45E+05	2.36E+04	7.45E+03	5.66E+05	3.13E+04	3.20E+04	8.12E+05	8.97E+05	1.692E+04	1.38E+05	1.05E+05	3.59E+05	1.69E+04
I_{1_y}	2.68E+05	1.72E+04	1.57E+04	2.03E+06	1.49E+05	2.13E+05	7.06E+06	1.32E+06	8.916E+04	5.60E+05	6.04E+05	3.69E+04	3.79E+05
I_{1_z}	1.11E+06	4.07E+04	2.32E+04	1.63E+06	1.27E+05	1.82E+05	6.32E+06	4.85E+05	7.235E+04	4.24E+05	5.03E+05	3.95E+05	3.28E+05
True I_x	8.45E+05	2.36E+04	7.45E+03	N/A				N/A	N/A			3.59E+05	N/A
True I_y	3.16E+05	1.72E+04	2.32E+04									5.41E+04	
True I_z	1.12E+06	4.07E+04	1.57E+04									3.97E+05	
I_x	1.71E+06	1.51E+05	8.79E+04	5.66E+05	3.13E+04	3.20E+04	8.12E+05	8.97E+05	1.69E+04	1.38E+05	1.05E+05	6.49E+05	1.69E+04
I_y	2.53E+06	2.15E+06	9.98E+05	2.02E+06	1.49E+05	2.13E+05	7.06E+06	1.32E+06	8.92E+04	5.60E+05	6.04E+05	7.54E+05	3.79E+05
I_z	3.40E+06	2.05E+06	9.10E+05	1.63E+06	1.27E+05	1.82E+05	6.32E+06	4.85E+05	7.24E+04	4.24E+05	5.03E+05	1.07E+06	3.28E+05
Group I_x	1.95E+06			1.56E+06				8.97E+05	9.25E+05 – With wing tanks / 2.76E+05 – Without wing tanks				
Group I_y	5.68E+06			1.03E+07				1.32E+06	2.38E+06 – With wing tanks / 1.63E+06 – Without wing tanks				
Group I_z	6.36E+06			8.94E+06				4.85E+05	2.40E+06 – With wing tanks / 1.33E+06 – Without wing tanks				
Total I_x	5.33E+06												
Total I_y	1.97E+07												
Total I_z	1.82E+07												

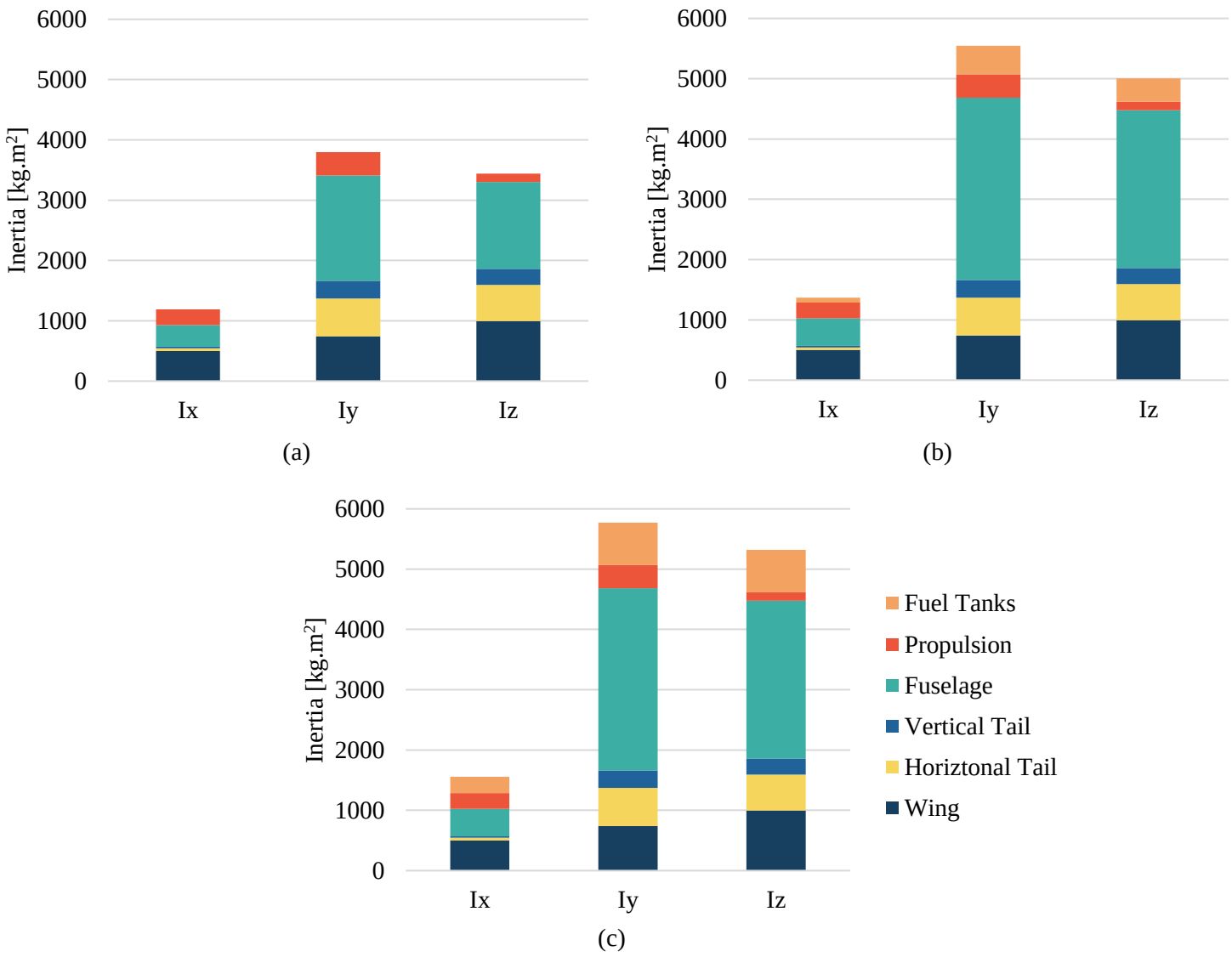

Figure 71: Extra330SC inertial component contributions for (a) empty mass (b) aerobatic mass and (c) maximum takeoff mass about the remote axes

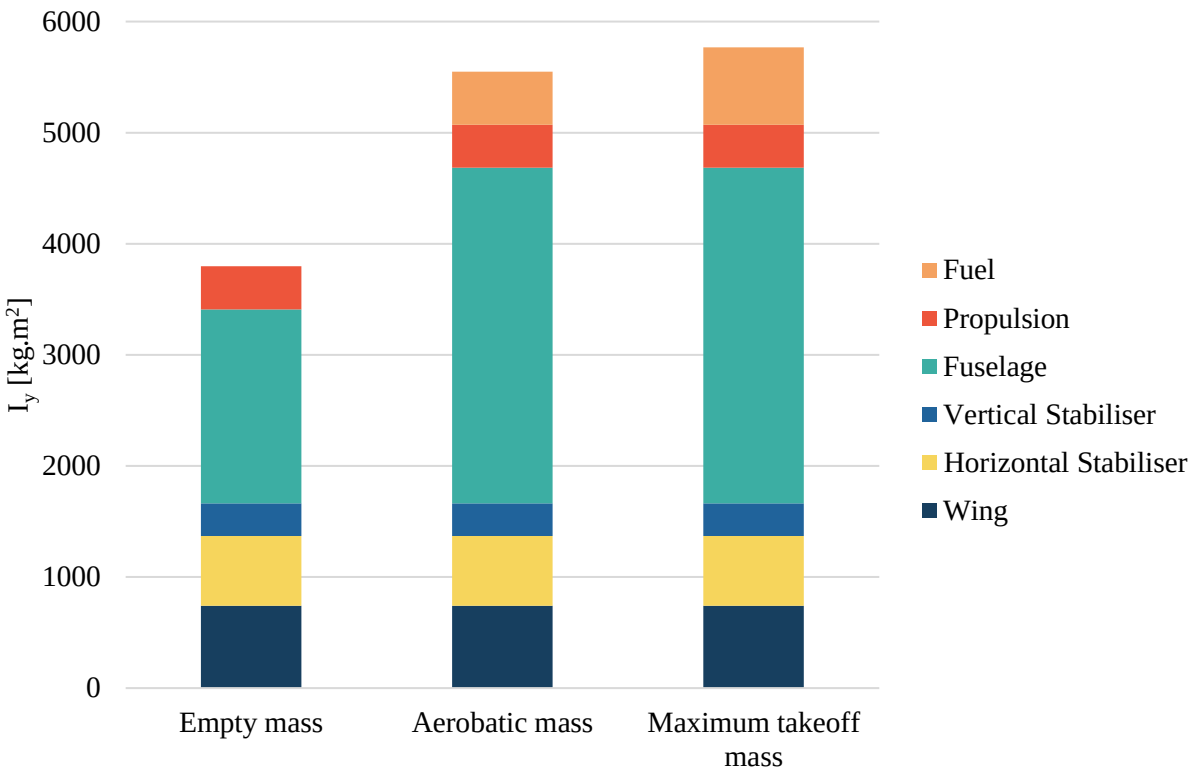

Figure 72: Extra 330SC pitch inertia (I_y) estimations for various aircraft configurations about the remote axes

To validate the numbers presented in Table 28, the overall pitch inertia (I_y)values of the Extra 330SC were compared to the values presented in Figure 40 from §1.3.6. This comparison is presented in Figure 73. The estimated inertial value for the aircraft empty mass appears to correspond quite well with data presented for other aircraft in the same mass range. The aerobatic and maximum take-off configuration pitch inertia estimations are a fair amount lower than published data for aircraft of a similar mass. This result does not appear to be incorrect as aerobatic aircraft are designed to be very manoeuvrable and as such are expected to have lower inertial values. Aerobatic aircraft such as the Extra 330SC are also far more modern than the aircraft listed in Figure 73 and as such, should have composite material incorporated into the design. This then implies that the aircraft may have lighter components throughout the airframe, leading to lower inertial values. The Extra 330SC is also a shorter aircraft than those provided in Figure 73. This should result in the longitudinal mass distribution being distributed nearer to the C.G than the other aircraft listed.

While the empty mass has provided some insight in validation, experimental test values used within the modelling of a tumble manoeuvre would consist of pitch inertias that fall within the values between the aerobatic and maximum take-off mass configurations. While there is a difference in mass between these

two configurations, there is not a significantly large difference in the inertial values. This would suggest that the pitch inertia of the aircraft does not change significantly during an aerobatic display sequence. This is a favorable outcome for an aerobatic aircraft as the control characteristics of the airframe remain consistent throughout an aerobatic display sequence. The same logic should apply to fuel being used up during a display, considering the proximity of the fuel tanks to the centre of gravity of the aircraft.

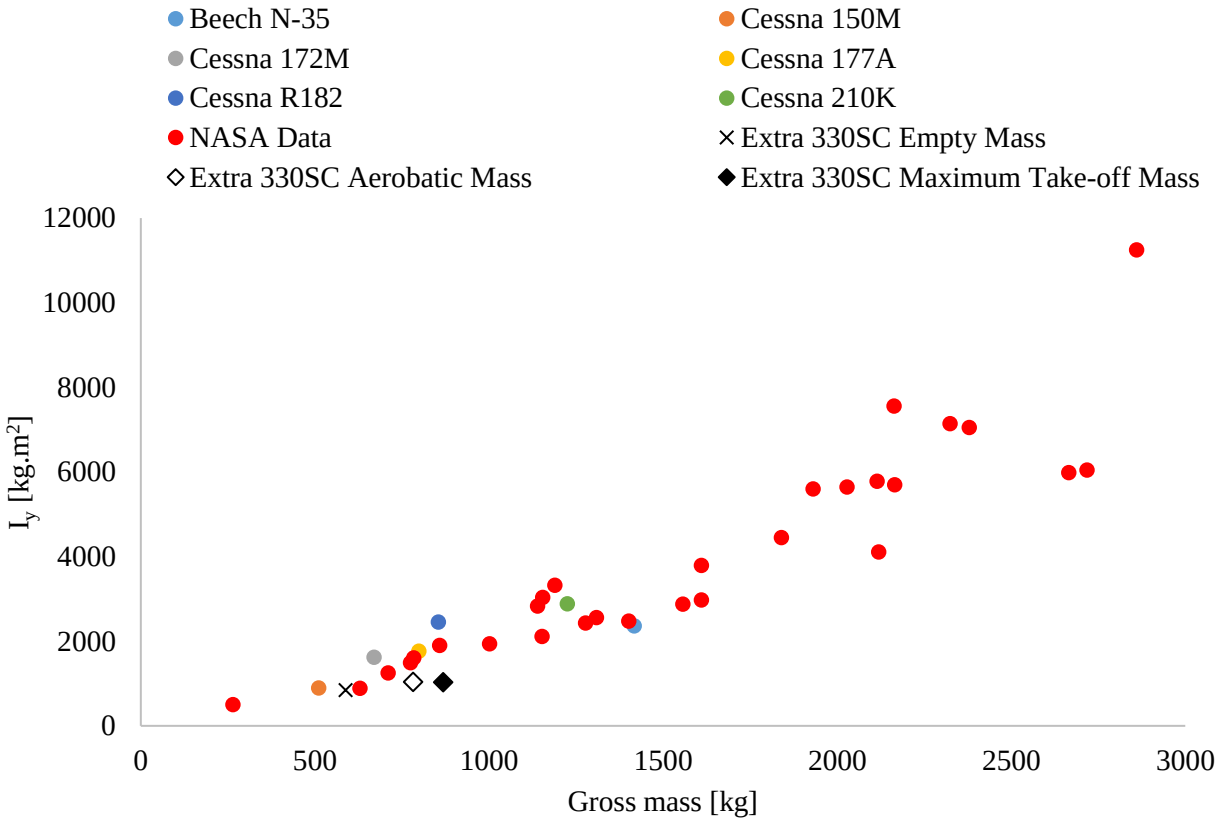

Figure 73: Comparison of I_y values for various single engine propeller driven aircraft and the Extra 330SC about the centre of gravity

3.2.3. Test Matrix

Using the envelope created in Figure 68 the mass values were used to obtain corresponding inertia and centre of gravity values. These values are presented in Table 29 and will serve as the test matrix data. A tumble manoeuvre will be assessed for each of the cases presented in Table 29 at various manoeuvre entry velocities.

Table 29: Test matrix for various aircraft configurations

Case Number	Mass [kg]	I_y [kg·m^2]	$C.G_x$ [m]
1	690.53	981.99	2.168
2	742.88	975.26	2.170
3	781.78	1040.5	2.151
4	781.78	990.25	2.125
5	759.78	961.76	2.093
6	730.28	979.41	2.087
7	668.53	929.83	2.103
8	668.53	961.30	2.126

3.3. Aerodynamic Data

Using the methods outlined in §2.4 aerodynamic data was generated for the wing, horizontal stabiliser, fuselage and propeller.

3.3.1. Lifting Surface Infinite Aspect Ratio Coefficients

The AERODAS model [60] and Lindenburg model [66] allow for the generation of aerodynamic data for any aspect ratio. Literature on high angle of attack aerodynamics does not exist within the public domain for a finite ratio wing the size and planform of those seen on aerobatic aircraft. Aerodynamic coefficient data from wind tunnel testing exists for symmetrical profiles of infinite aspect ratio with thickness-to-chord ratios of between 12% and 15%. The coefficients obtained from the Spera method [60] and the Lindenburg method [66] were compared to wind tunnel test data. This comparison provided the validation of the generated aerodynamic coefficients prior to any additional corrections that were made for aspect ratio, blown air effects or dynamics.

The Extra 330SC wing makes use a of MA 14.9 S profile at the root and a MA 12 S profile at the tip. While the aerodynamic data for these profiles was not readily available, the airfoil properties are expected to be similar to the NACA0015 and NACA0012. Both sets of profiles are symmetrical and have the same thickness-to-chord ratios. While it was not clear as to the position along the chord at which the maximum thickness-to-chord occurs, it was assumed that the two sets of profiles were similar enough to be comparable. The coefficients of lift and drag in the pre-stall regime are similar enough for the NACA0015

and NACA0012 that the values of a single profile can be used. The comparison of the coefficients of lift and drag between the two profiles is presented in Figure 74.

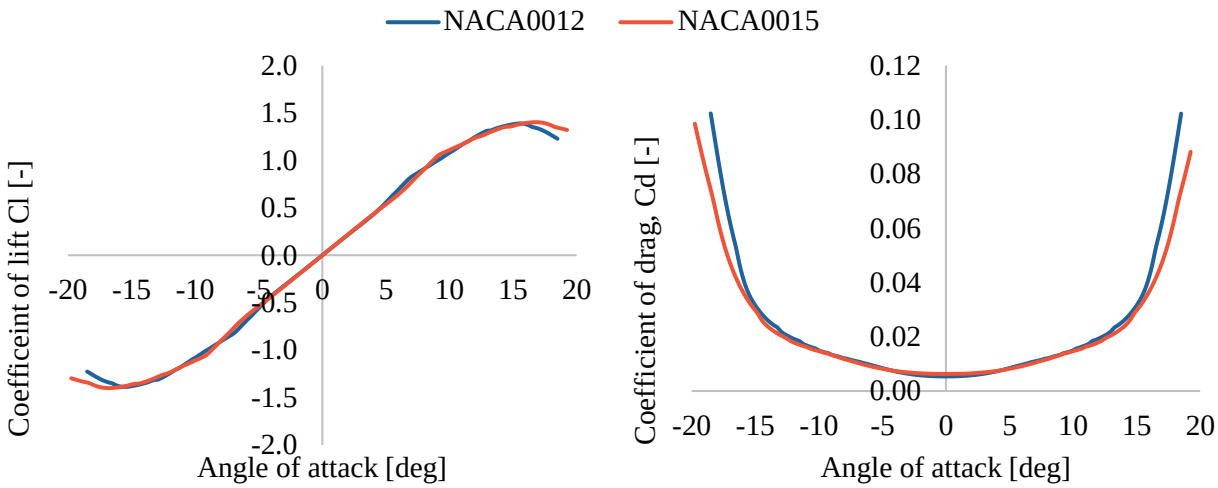

Figure 74: Comparison of the coefficients of lift and drag for the NACA0012 and NACA0015 airfoil profiles [74]

With the selection of the NACA0012 profile for the Extra 330SC, aerodynamic coefficients were generated for an infinite aspect ratio and compared to wind tunnel test data produced by NASA for the same profile. The test data can be seen in §1.3.4.1. A plot of the coefficient of lift for both the generated data and wind tunnel test data can be seen in Figure 75. The data shows good correlation across the entire angle of attack range, capturing the changes in gradient and axis intercepts while showing little deviation from the test data. A slight mismatch in the data occurs when $330° < \alpha < 345°$. The test data appears to have lower (less negative) values than the predicted data. The predicted data was mirrored and negative about the $0°/360°$ angle of attack. This assumption seemed logical given that the airfoil is symmetrical. The lift values when the airfoil is pitched downwards were expected to be identical in magnitude to the lift values when the airfoil is pitched upwards. This notion does appear to hold true for the values obtained from the wind tunnel test data when the trailing edge is the front-most section. The lift values appear to be mirrored and negative about the $180°$ angle of attack line. It is unclear as to why this discrepancy exists when the airfoil profile is pitched downwards. It is thought that stall effects may have influenced the results as the inconsistencies occur near the stall point.

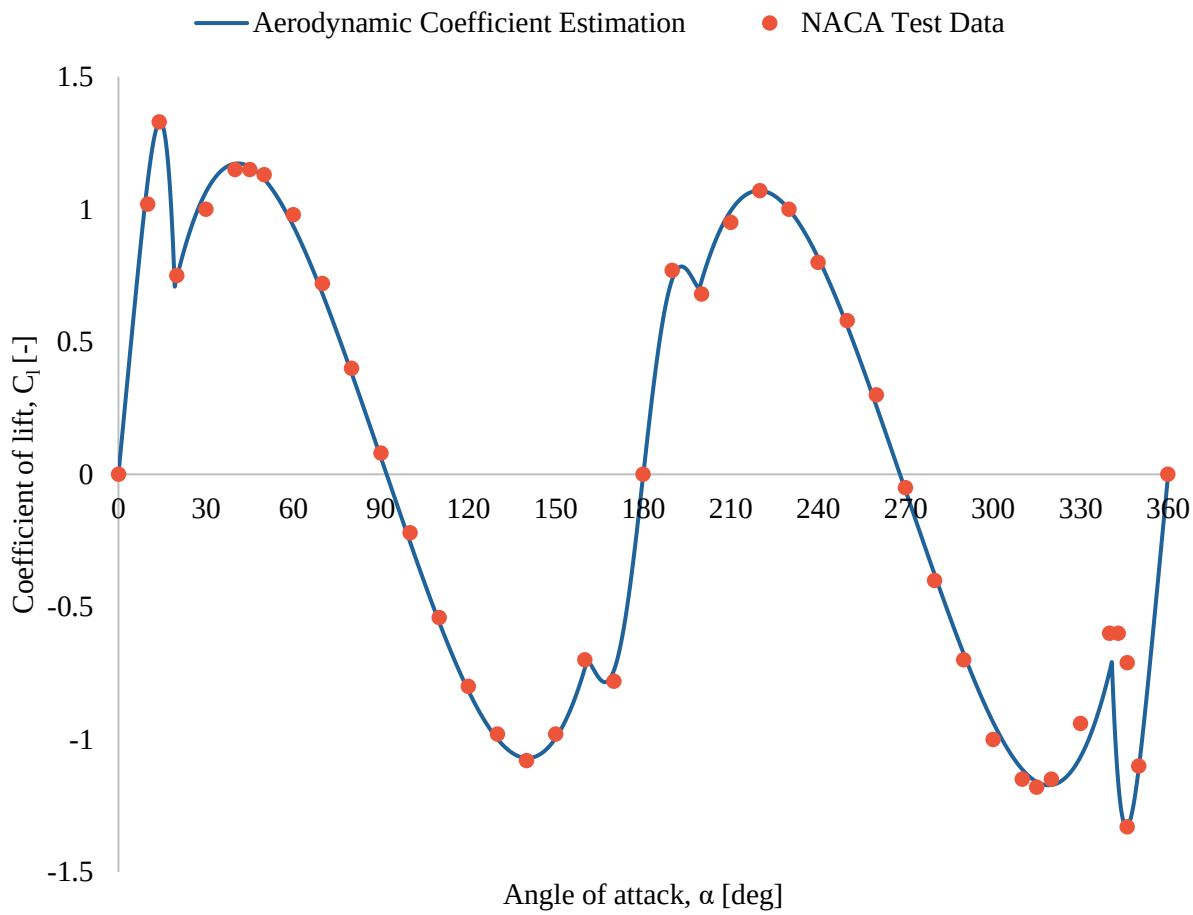

Figure 75: Comparison of the coefficient of lift for estimated results (produced using the AERODAS model [60]) and wind tunnel test data for a NACA0012 from $0° - 360°$ angle of attack

The coefficient of drag for the generated data and wind tunnel test data is presented in Figure 76. The two sets of data show very good correlation throughout the angle of attack range with only minor differences being noted. The changes in gradient that occur between the different regions are adequately captured by the data generated using the AERODAS model. The peak values and angle of attack at which these peaks occur are accurately captured by the generated data. The peak values for both the coefficients of lift and drag are pre-set and warrant some additional discussion.

The angle at which the maximum coefficients of lift and drag occur in the post-stall regime and the angle at which zero lift occurred in the post-stall regime were given by Spera [60] without much explanation. However, given that the values obtained in the modelling developed by Spera [60] were based on empirical data, it was assumed that the angles of the maximum post-stall coefficients and the angle of zero lift in the post-stall regime were obtained from this same empirical data. Spera [60] provides the reader with mean

deviation of the model developed from test data, as well as mean deviations for other existing models from the same test data. The data for a large number of airfoils of different aspect ratios and thickness-to-chord ratios was provided. The results of the model developed by Spera [60] provided accuracy which is equivalent or better than comparable models, particularly for finite length airfoil data. The mean deviations also illustrate that the model developed by Spera [60] predicts maximum post-stall coefficients with acceptable accuracy for a wide range of airfoils and airfoil conditions. Based on this information, the angle given for the maximum coefficients of lift and drag and the angle of zero lift in the post-stall regime were deemed acceptable.

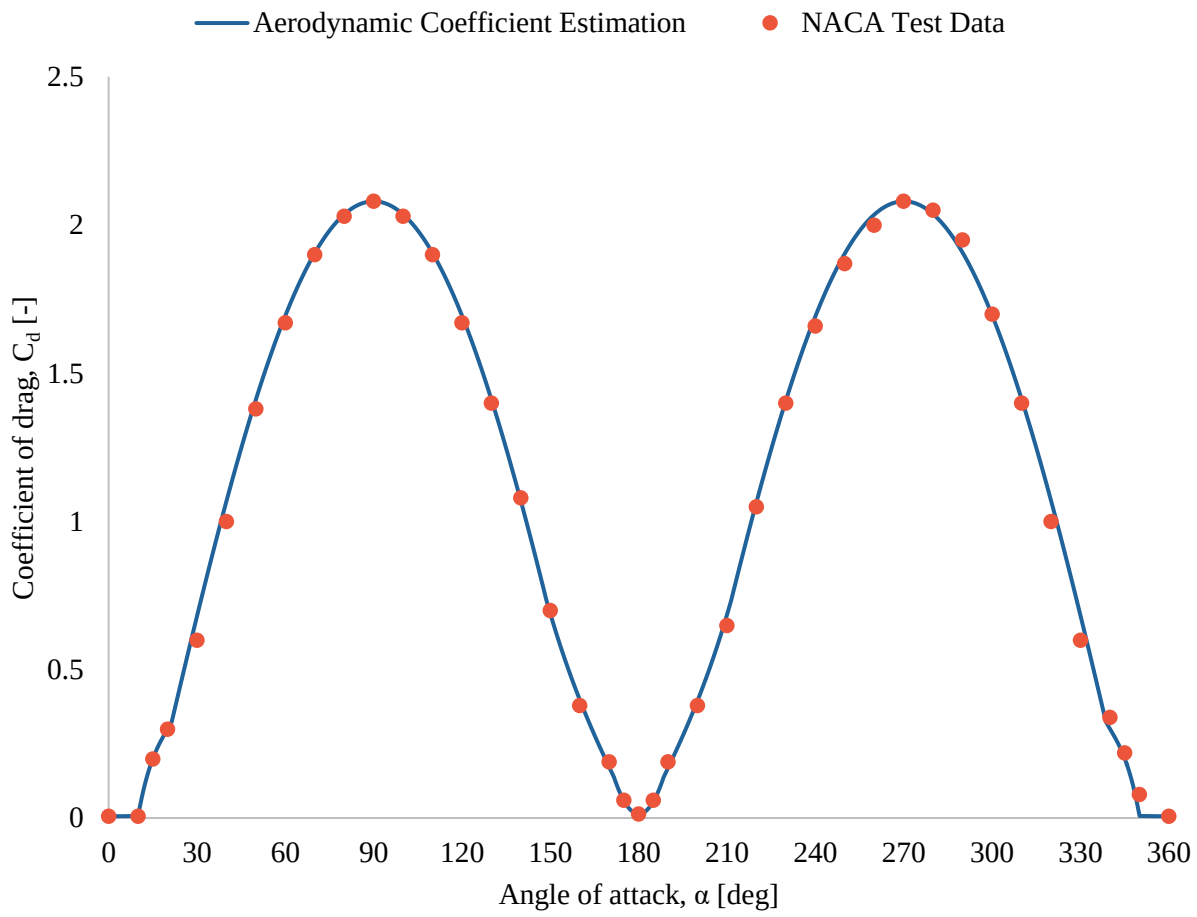

Figure 76: Comparison of the coefficient of drag for estimated results (produced using the AERODAS model [60]) and wind tunnel test data for a NACA0012 from $0° - 360°$ angle of attack

The coefficient of quarter chord pitching moment for the generated data and wind tunnel test data are presented in Figure 77 for the NACA0012 airfoil. The two sets of results do not show good correlation in the pre-stall and transition regions for both forward (leading edge into the wind) and backward (trailing edge into the wind) orientations of the airfoil. While the post-stall regime does provide a better correlation of the data, the results do not match as well as the coefficients of lift and drag. The method developed by Lindenburg [54] is far less developed than the Spera method [60] as elliptical data is used rather than empirical airfoil data. It is more of an approximation. In the absence of any other methods the Lindenburg method was used.

During a tumble manoeuvre the angle of attack is not expected to reach $\alpha = 150°$. This is illustrated in Figure 7 in §1.1.1. At no point during the tumble manoeuvre does the aircraft reach a pitch angle of greater than 90°. Thus, the deficiencies of the model in predictions for $155° \leq \alpha \leq 210°$ should not hamper the overall modeling of the manoeuvre. The inaccurate modelling of the coefficient from $0° \leq \alpha \leq 20°$ should be corrected. This can be achieved by using test data in place of generated data in this angle range.

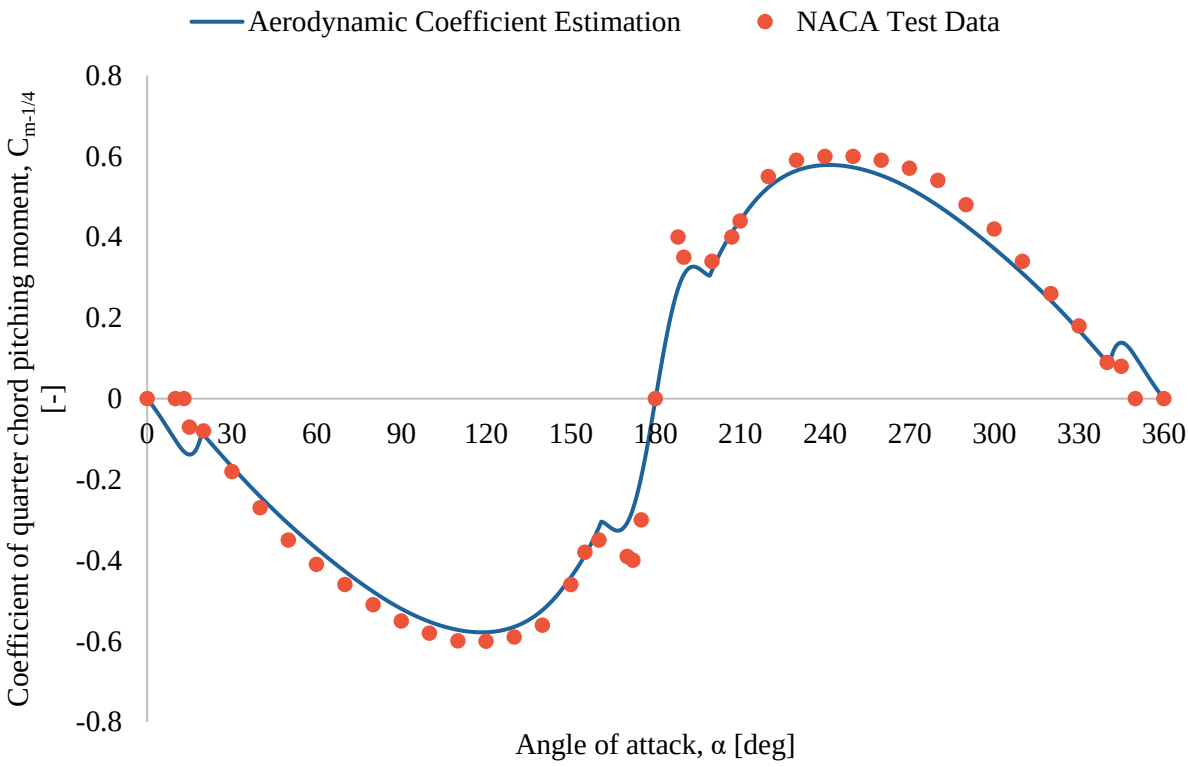

Figure 77: Comparison of the coefficient of quarter chord pitching moment for estimated results (produced using the Lindenburg model [65])and wind tunnel test data for a NACA0012 from $0° - 360°$ angle of attack

3.3.2. Inner Wing Aerodynamic Coefficients

While the wing is one complete surface it is exposed to two separate flows, both with differences in angle and velocity. The inner wing surface is exposed to the propeller slipstream and at times a combination of the propeller slipstream as well as the free-stream velocity. The outer wing section is exposed to the free-stream velocity only. The rotational rates experienced during a tumble result in an additional velocity component. This rotational velocity component is expected to be small compared to the free-stream and propeller slipstream velocities. While the rotational rate may be high the moment arm is small enough that the rotational velocity component is small. The close proximity of the aerodynamic centre of the wing to the centre of gravity results in a small moment arm. This does not imply that dynamic effects can be ignored.

In splitting the wing into inner and outer sections, the wing area, wingspan and aspect ratio may no longer be used. Each wing section will therefore have specific wing area, effective span and aspect ratio. The inner wing section was extended to the edges of the propeller slipstream 'tube.' It was assumed that the propeller slipstream did not contract. The 'tube' diameter would be the same diameter as the propeller. In reality, this may not be the case. The short distance from the propeller to the wing of the aircraft means that the contraction effects over this distance would be negligible. The span of the inner wing section will thus be twice that of the propeller radius, giving an inner wingspan of $b_I = 2$ m. The reference area and aspect ratio were calculated as $S_{ref_I} = 3.32$ m^2 and $AR_I = 1.2$, respectively. The remaining wingspan was allocated to the outer wing section. A comparison of various specifications for the inner and outer wing sections is provided in Table 30. These values were used as the input values in generating the various aerodynamic coefficients for both the inner and outer wing sections.

Table 30: Inner and outer wing specifications

Specification	Inner Wing Section Value	Outer Wing Section Value	Units
Airfoil	$NACA0012$	$NACA0012$	-
$\boldsymbol{A0}$	0	0	deg
$\boldsymbol{ACL1'}$	$[14.3, 10]$	$[14.3, 10]$	deg
$\boldsymbol{CL1max'}$	$[1.33, 0.77]$	$[1.33, 0.77]$	-
$\boldsymbol{S1'}$	$[0.115, 0.11]$	$[0.115, 0.11]$	$1/°$
$\boldsymbol{CD0}$	$[0.006, 0.014]$	$[0.006, 0.014]$	-
$\boldsymbol{ACD1'}$	$[14, 10]$	$[14, 10]$	deg
$\boldsymbol{CD1max'}$	$[0.008, 0.019]$	$[0.008, 0.019]$	-
$\boldsymbol{b}$	2	5.5	m
$\boldsymbol{AR}$	1.2	4.66	-
$\boldsymbol{S\_ref}$	3.32	6.49	m^2
$\boldsymbol{C_{L_{\alpha_{wing}}}}$	0.102	0.102	$1/°$

The effects of aspect ratio on the static aerodynamic coefficients were introduced using the methods provided by Spera [60] and Lindenburg [66]. Including the effects due to rotational dynamics was a greater challenge, particularly at low airspeeds. Published data and methods used to predict dynamic coefficients usually do not consider the effects of a finite wing and only considers oscillations. An additional shortfall in the literature is the lack of data for the coefficients of drag and pitching moment. Determining the complete effects of dynamics on the aerodynamic coefficients of the wing was beyond the scope of this dissertation. While a fully validated dynamic model was not produced, the effects due to dynamics were crudely included by increasing the maximum coefficient of lift and drag and delaying the stall point of the coefficient of lift. Hysteresis in the lift curve was not considered as the aircraft only pitches upwards during a tumble. Based on the discussions presented in §1.3.5, the static aerodynamic coefficient of lift values will be multiplied by 1.2. The stall angle for the coefficient of lift was increased by $5°$. The static coefficient of drag values (corrected for aspect ratio) were multiplied by 1.3. A value of 1.3 was used instead of 1.2 to factor in interference effects from the wing-fuselage joint. This value was an assumption and was based on an evaluation of the model results. The coefficient of pitching moment was calculated based on the coefficient of normal force which was corrected for dynamic effects based on the coefficient of lift and drag. The coefficient of pitching moment illustrates the changes that have been included in the coefficients of lift and drag by increasing the pitching moment values across all angles of attack.

The coefficients of lift, drag and quarter chord pitching moment are presented in Figure 78, Figure 79 and Figure 80 respectively. For each coefficient, three cases are presented: the coefficients for an infinite aspect ratio (obtained from wind tunnel test data), the coefficients for a finite wing without any consideration for dynamic effects and coefficients for a finite wing with consideration for dynamic effects. While the angles of attack experienced during a tumble manoeuvre are expected to be within the bounds of $-20° \leq \alpha \leq 90°$, the aerodynamic coefficients corrected for aspect ratio and with dynamic considerations have been provided across the entire angle of attack range ($-180° \leq \alpha \leq 180°$) for completeness.

No additional smoothing was implemented for the data in Figure 78. This was because the curve presented for the coefficient of lift (corrected for aspect ratio and with dynamic considerations) is already smooth and cannot be smoothed much further.

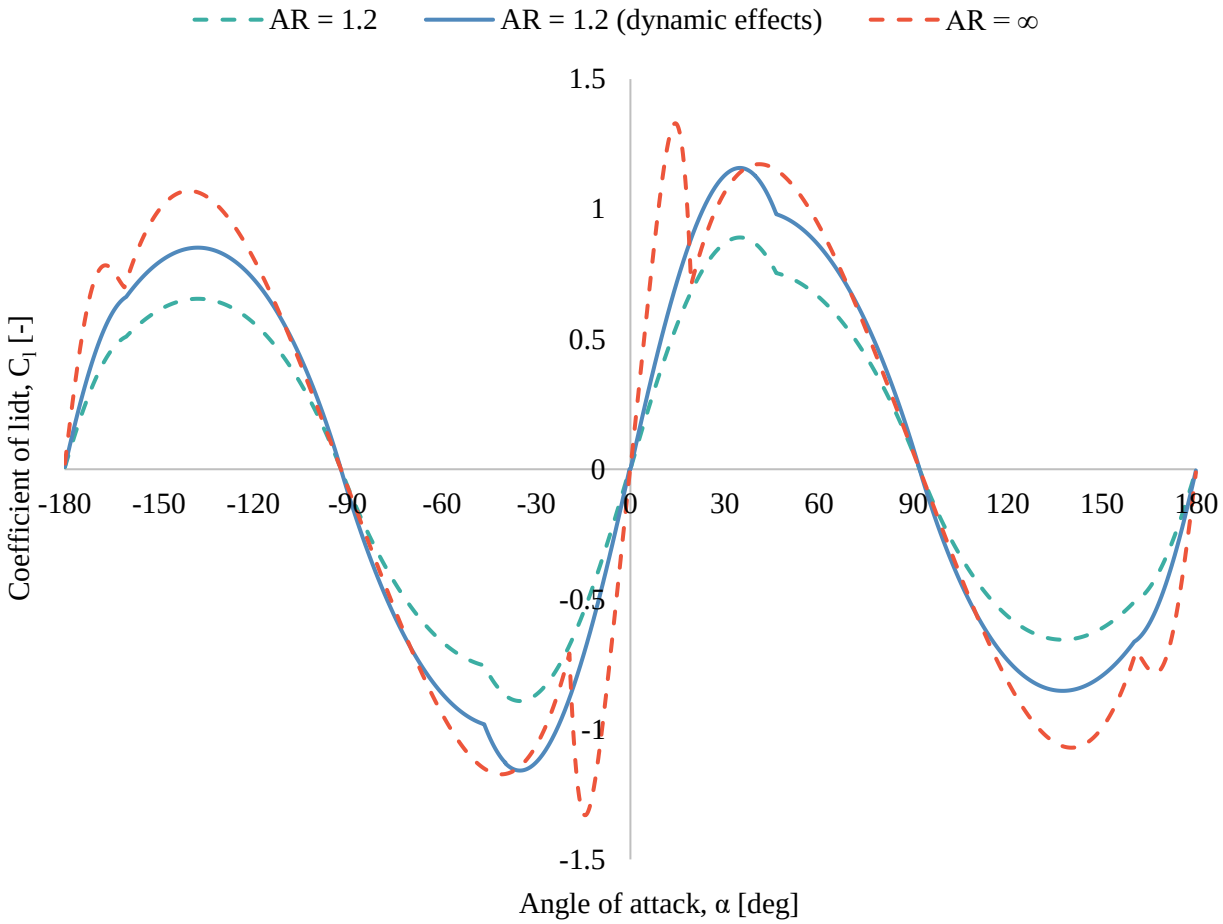

Figure 78: Coefficient of lift for an infinite aspect ratio wing, an aspect ratio of 1.2 with and without dynamic effects

It is evident in Figure 78 that the influence of the very low aspect ratio removes the first stall point of the wing and lowers the lift values at all angles of attack up until ≈ 85°. The wing then effectively has only a single stall point at around 30°. The slope of the lift curve slope is shallower for the low aspect ratio wing in the pre-stall regime. The consideration given to dynamic effects increases the coefficient of lift values such that the new curve is similar to the infinite aspect ratio curve in the post-stall regime. This finding was purely coincidental.

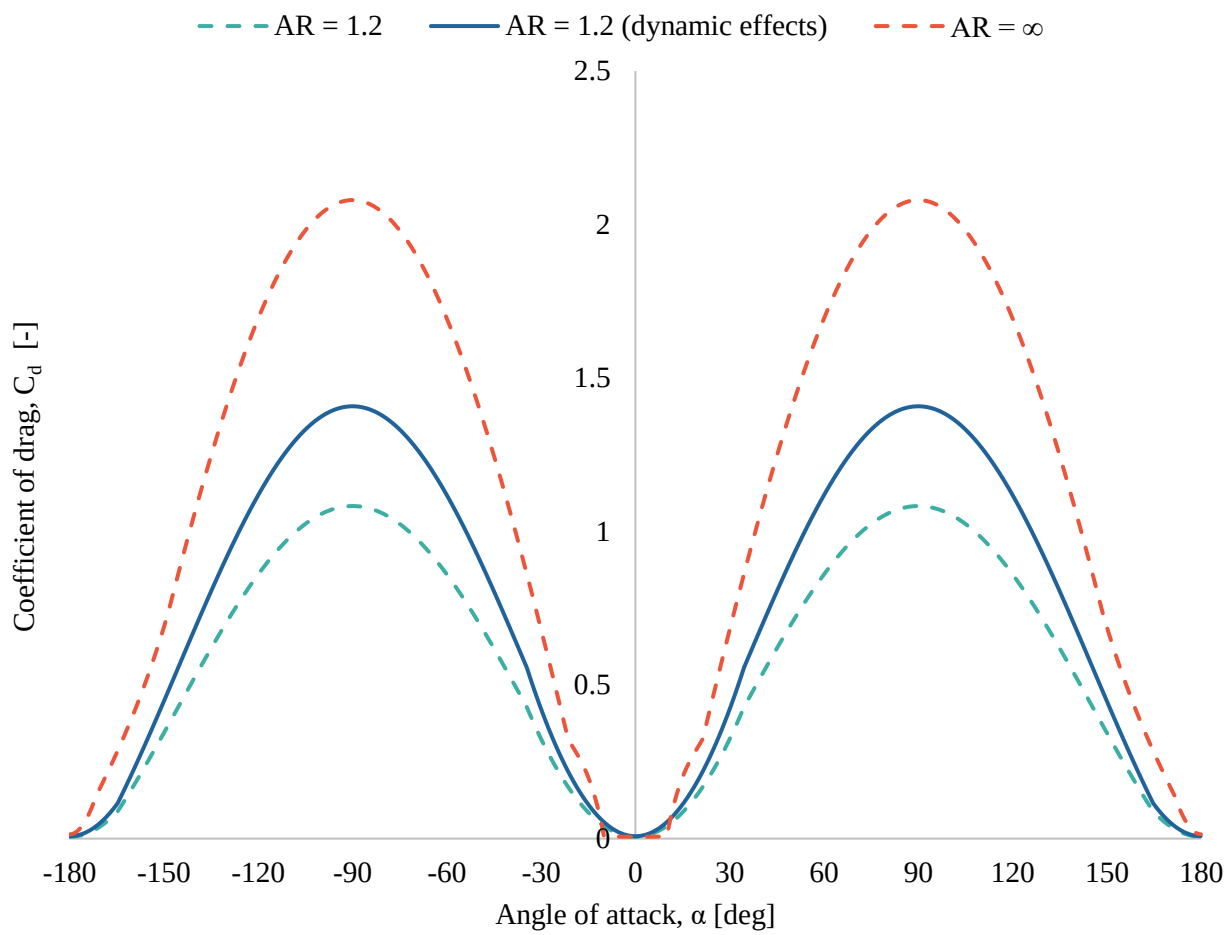

Figure 79: Coefficient of drag for an infinite aspect ratio wing, an aspect ratio of 1.2 with and without dynamic effects

The coefficient of drag is presented in Figure 79. A reduction in the magnitude of the coefficient of drag is shown for the low aspect ratio wing without dynamic considerations. Subsequently this reduction is seen for the curve where dynamic effects were considered, albeit to a lesser extent. The most notable difference in the shape of the curve corrected for aspect ratio from that of infinite aspect ratio is in the pre-stall regime. The curve that is corrected for aspect ratio appears to produce higher values of drag throughout the pre-stall regime. This might be attributed to the 'stubbiness' of the wing, where 3D effects may result over a much larger section of the wing given the small aspect ratio. The curve for a finite wing also does not show the same sudden change in slope when transitioning from the pre-stall to the post-stall regime. This is probably due to the gentle stall of the lift coefficient for the finite wing.

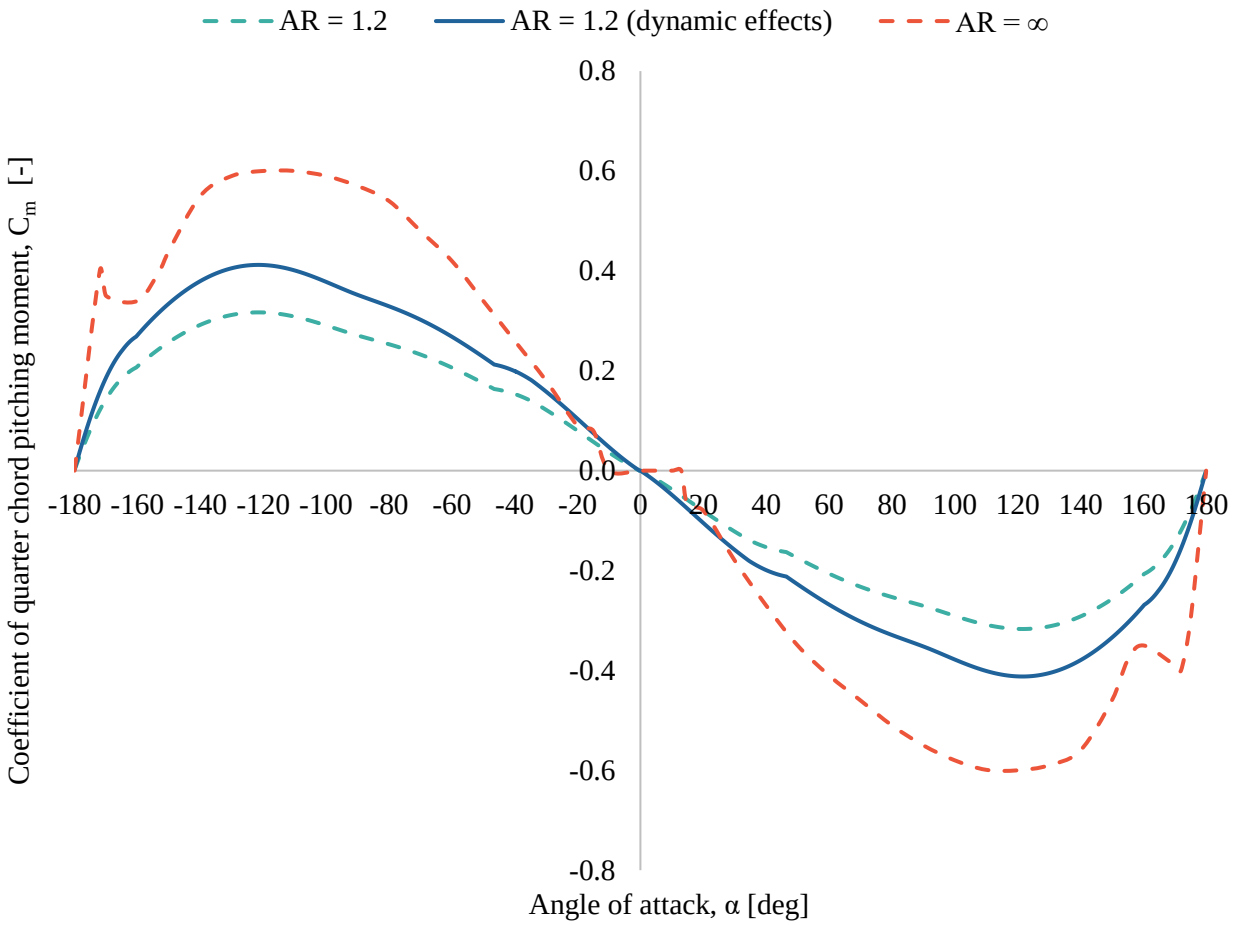

Figure 80: Coefficient of quarter chord pitching moment for an infinite aspect ratio wing, an aspect ratio of 1.2 with and without dynamic effects

The coefficient of quarter chord pitching moment is presented in Figure 80. As discussed in §3.3, the method provided in Lindenburg [66] is an approximation and does not capture the finer details of the pitching moment curve. This is evident for the coefficient values presented in the pre-stall regime where the coefficient of quarter chord pitching moment is far greater than it should be. The curve that is corrected for aspect ratio and considers dynamic effects crosses the infinite aspect ratio curve at $\alpha \approx 15°$. The curve that is correct for aspect ratio and that considers dynamic effects used the data provided for an infinite aspect ratio for all angles less than $15°$. Coefficient values for angles greater than $15°$ used the data as presented in Figure 80.

3.3.3. Outer Wing Aerodynamic Coefficients

The outer wing section is outside of the influence of the propeller slipstream. The specifications of the outer wing section are shown in Table 30. The considerations made for dynamic effects for the inner wing section were also applied to the outer wing sections. That is, the coefficient of lift, once corrected for aspect ratio, was multiplied by 1.2 and the stall angle shifted by 5°. The coefficient of drag was multiplied by a value of 1.2 instead of the 1.3 multiplier used for the inner wing section as the outer wing section is not expected to see any interference from the fuselage. No corrections were made to smooth out the data as the outer wing sections are not influenced by the propeller slipstream.

The coefficients of lift, drag and quarter chord pitching moment are provided in Figure 81, Figure 82 and Figure 83 respectively. Once again curves are provided for an infinite aspect ratio profile, a wing corrected for aspect ratio and a wing correct for aspect ratio and including considerations for dynamic effects.

The predicted coefficient of lift for the outer wing sections is provided in Figure 81. The correction for aspect ratio reduces the peak value of lift both in the pre-stall and post-stall regimes. At this aspect ratio a lift recovery is not seen in the post-stall regime but rather a further reduction in lift is postponed. The consideration for dynamic effects increase the initial peak to a value close to that of the infinite aspect ratio profile albeit at a higher stall angle. The values present on the curve for the outer wing sections are higher than those present for the inner wing section due to the higher aspect ratio. As the outer wing sections are not influenced by the propeller slipstream no additional smoothing was done to the curve.

The coefficient of drag for the outer wing section is provided in Figure 82. The curves illustrate the same characteristics discussed for the inner wing section. The magnitude of the coefficient is different due to the different aspect ratio. The transition from the pre-stall to the post-stall regime is sharper for the outer wing section than it is for the inner wing section. This difference can be attributed to the difference in the first stall present in the coefficient of lift figures. The stall for the outer wing section is far steeper than that of the inner wing section, resulting in a larger change in the lift-induced drag.

The coefficient of quarter chord pitching moment follows a similar trend to that of the inner wing section. This is shown in Figure 83. The most notable difference is in the region where the flow transitions from the pre-stall to the post-stall regime. The change at this point is far smoother for the inner wing section than it is for the outer wing section. This difference is due to the type of stall seen in the coefficient of lift for each wing section.

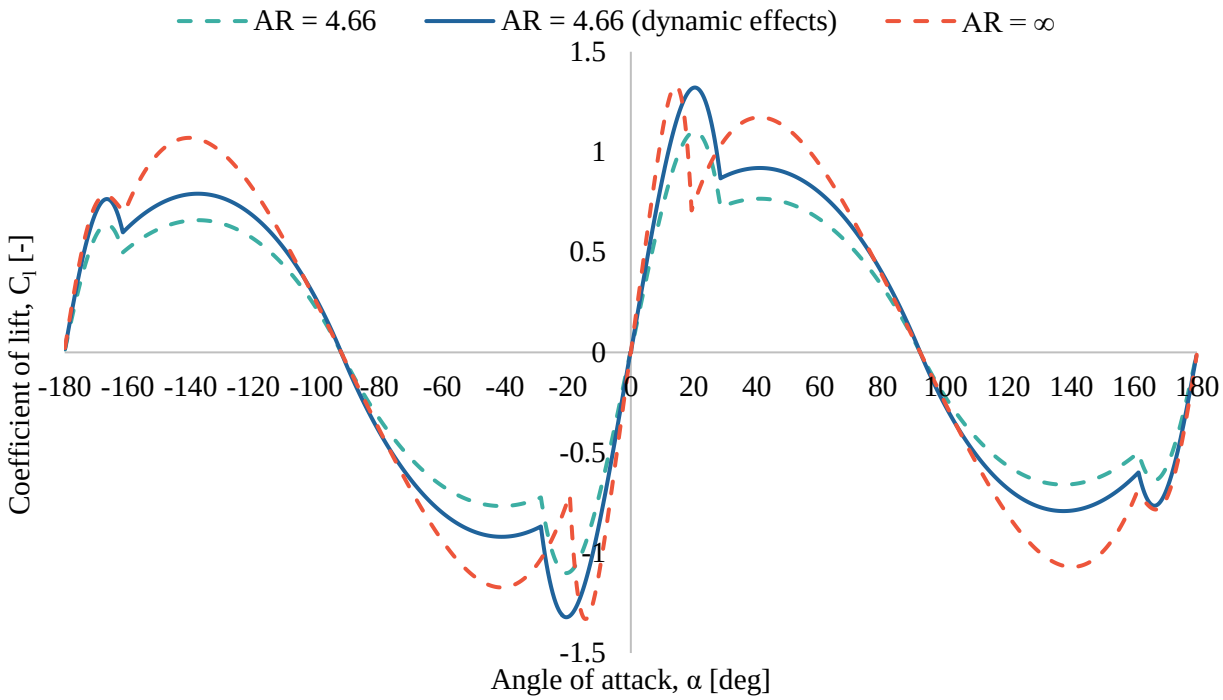

Figure 81: Coefficient of lift for an infinite aspect ratio wing, an aspect ratio of 4.66 with and without dynamic effects

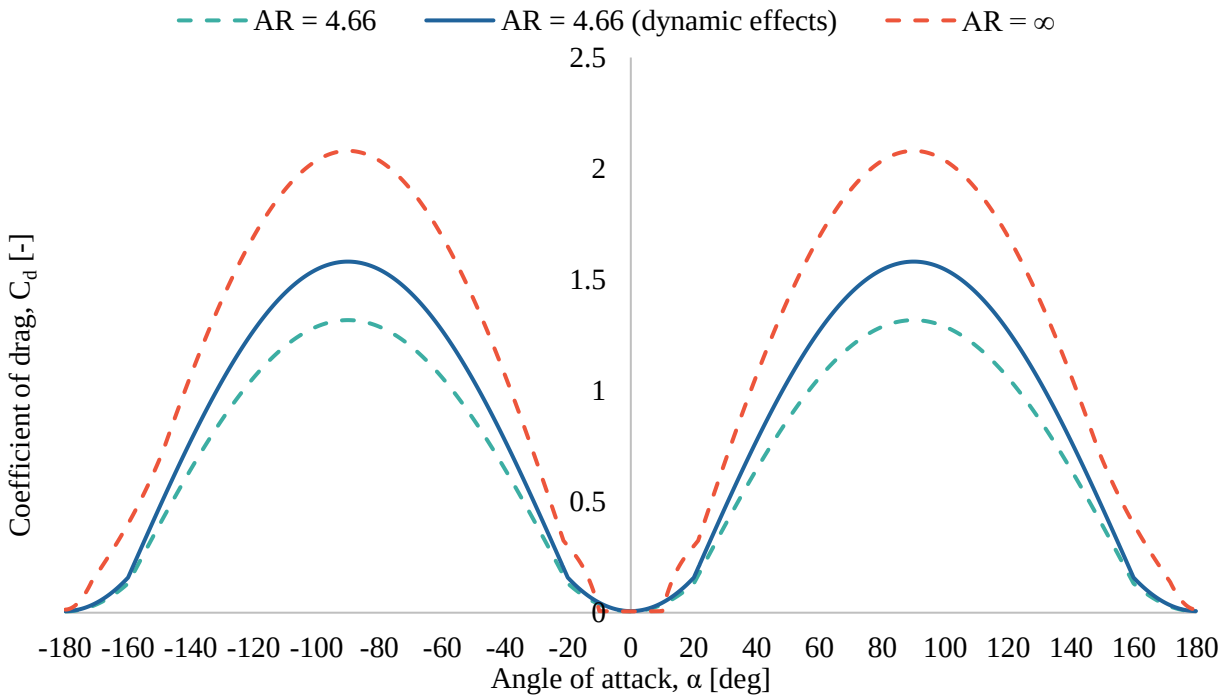

Figure 82: Coefficient of drag for an infinite aspect ratio wing, an aspect ratio of 4.66 with and without dynamic effects

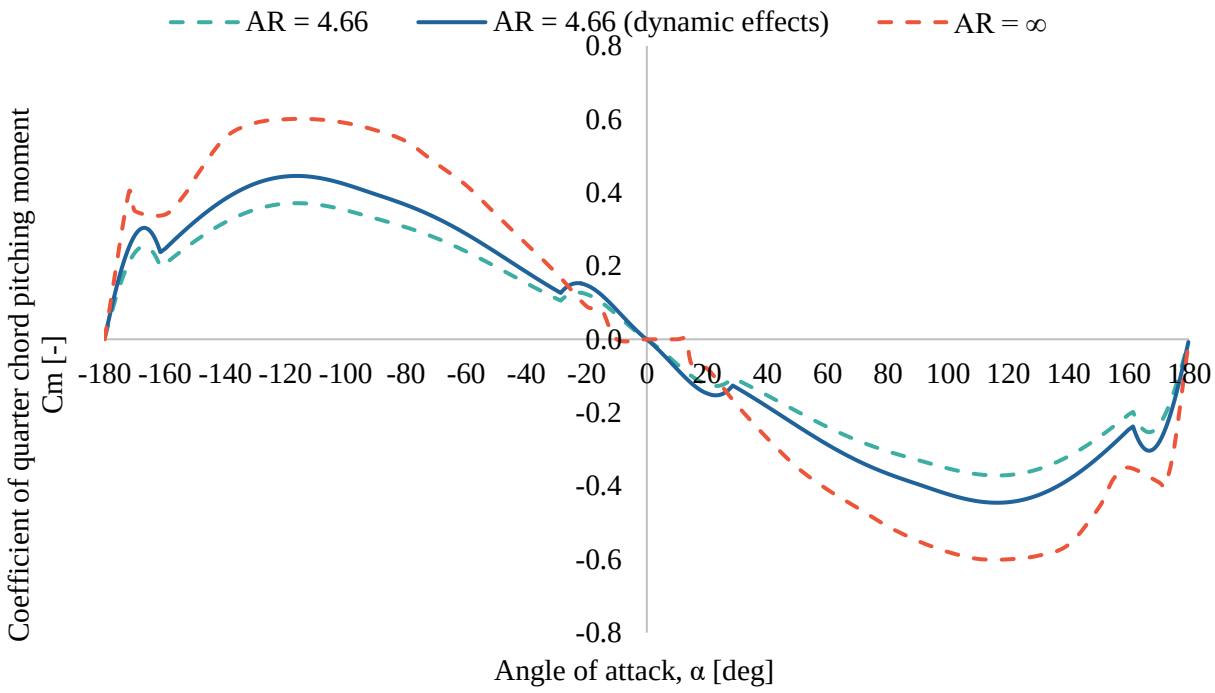

Figure 83: Coefficient of quarter chord pitching moment for an infinite aspect ratio wing, an aspect ratio of 4.66 with and without dynamic effects

3.3.4. Fuselage Aerodynamic Coefficients

The aerodynamic coefficients for the fuselage were generated using fuselage geometry obtained from an aircraft 3-view. While cross-sectional areas are not available for the Extra 330SC, the fuselage-cross sectional geometry were approximated using the 3-view provided in the POH [13]. The fuselage cross-sections were approximated as elliptical sections. The semi-major and semi-minor lengths that make up each ellipse were measured at various stations as half of the width of the fuselage top and side views. These measurements are illustrated in Figure 84. The measurement (a) represents the half widths measured off the top view, while the measurement (b), represents the half heights measured off the side view. The lengthwise distributions of the variables (a) and (b) are provided in Figure 85.

The distribution of (a) and (b) were used to obtain the cross-sectional area distribution of the fuselage. The resulting distribution of the fuselage area was then used to find a distribution of the radius of equivalent circular sections along the fuselage. Both distributions have been plotted in Figure 86. It is evident that a very large portion of the fuselage area is located at the front of the Extra 330SC. This is because the engine is located at the front of the fuselage. This forward bias in fuselage area results in the aerodynamic centre

of the fuselage being located further forward, near the centre of mass of the aircraft. This minimises pitching moment effects of the fuselage.

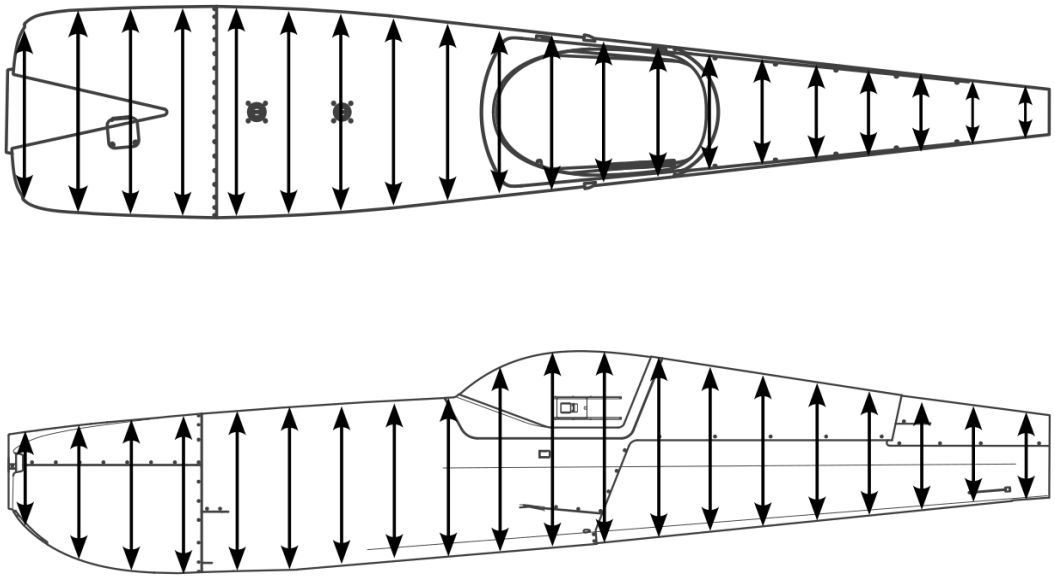

Figure 84: Fuselage width and height measurements at various lengthwise stations

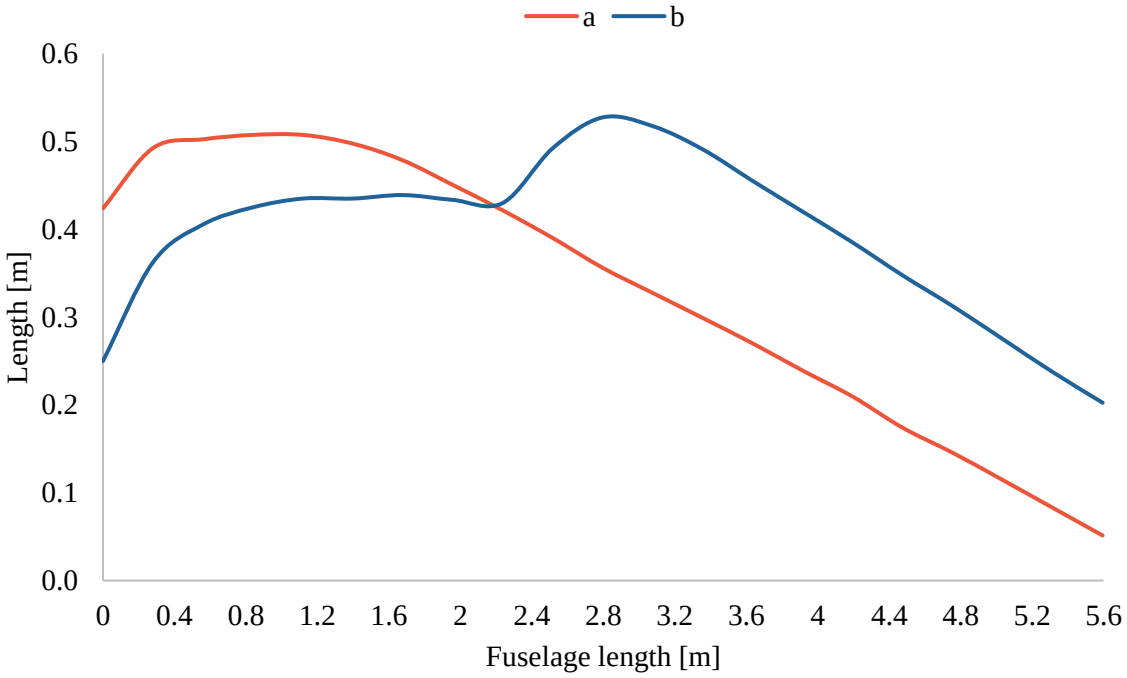

Figure 85: Lengthwise distributions of variables a, b along the fuselage

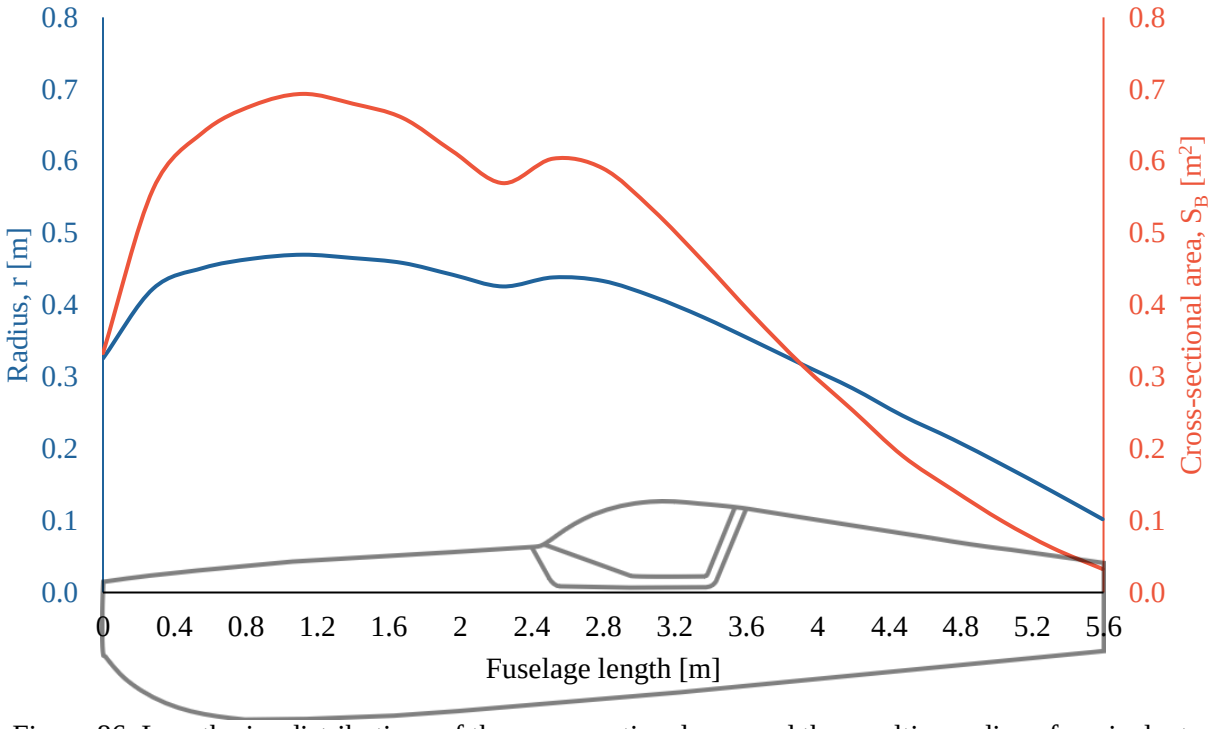

Figure 86: Lengthwise distributions of the cross-sectional area and the resulting radius of equivalent circular sections

The distribution of the width-to-height ratio (a/b) of the Extra 330SC fuselage is provided in Figure 87. The distribution in Figure 87 was used to obtain the distribution of the ratio of the local normal-force coefficient per unit length (C_n) for an elliptical cross-sectional shape to the similar coefficient (C_{n_0}) for the equivalent circular shape having the same cross-sectional area. This applies to both slender body theory as well as Newtonian impact theory. Figure 87 indicates that the fuselage is wider than taller in the front sections and then gradually transitions to having a larger height than width, at the cockpit and continues to the rear of the fuselage. The distributions for the slender body coefficient of normal force ratio $(c_n/c_{n_0})_{SB}$ and Newtonian coefficient of normal force ratio $(c_n/c_{n_0})_{Newt}$ ratio are provided in Figure 88.

The distributions for the slender body coefficient of normal force ratio and the Newtonian coefficient of normal force ratio are a function of the ratio width-to-height ratio. The width-to-height ratio does not have any large bias in either width or height at the front of the fuselage for the Extra 330SS. The differences in the values of the slender body coefficient of normal force ratio and the Newtonian coefficient of normal force ratio are small. Moving rearward from the start of the fuselage cockpit, the height begins to outweigh the width of the fuselage, implying that the width-to-height ratio becomes less than unity. For values of width-to-height ratio less than 1, the differences in slender body coefficient of normal force ratio and Newtonian coefficient of normal force ratio are minimal. Given the larger height over width from the start

of the cockpit, the values of slender body coefficient of normal force ratio and Newtonian coefficient of normal force ratio for the Extra 330SC fuselage are very similar in magnitude. This is illustrated in Figure 88 rearward of $L_{fuselage} \approx 2.2$ m.

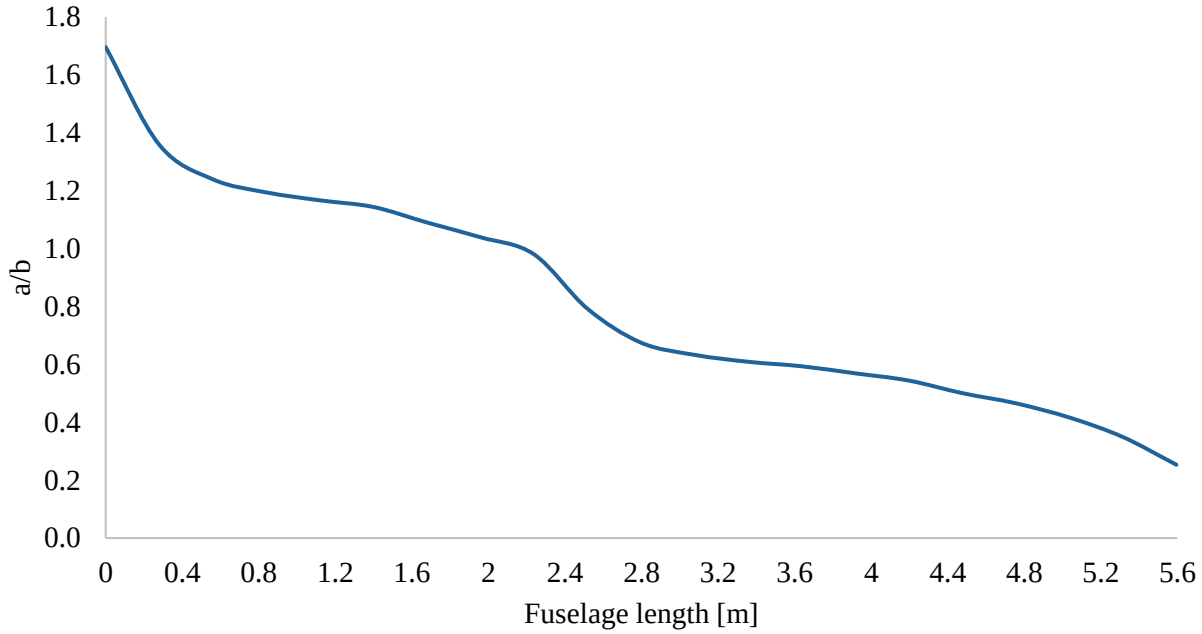

Figure 87: Lengthwise distribution of the fuselage width-to-height ratio (a/b) for the Extra 330SC

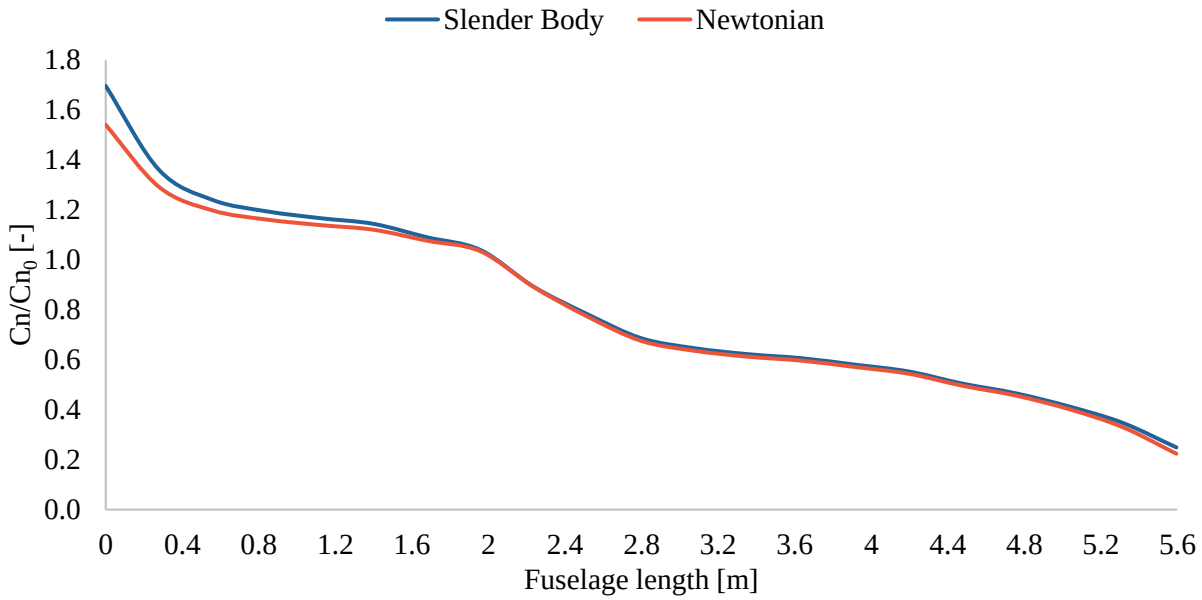

Figure 88: Distribution of the slender body and Newtonian coefficient of normal force ratio for the Extra 330SC

The cross-flow coefficient of drag (C_{d_n}), required as input to Equations (176) and (178) from §2.4.2, was obtained using Figure 89. The low-speed nature of the tumble manoeuvre ($M_{tumble} << 0.2$) would indicate that a coefficient of $C_{d_n} = 1.2$ would be applicable to cylinders of all sizes. While the chart does not extend to a Mach number of near zero, the data towards zero can be extrapolated and the conclusion that $C_{d_n} = 1.2$ is correct.

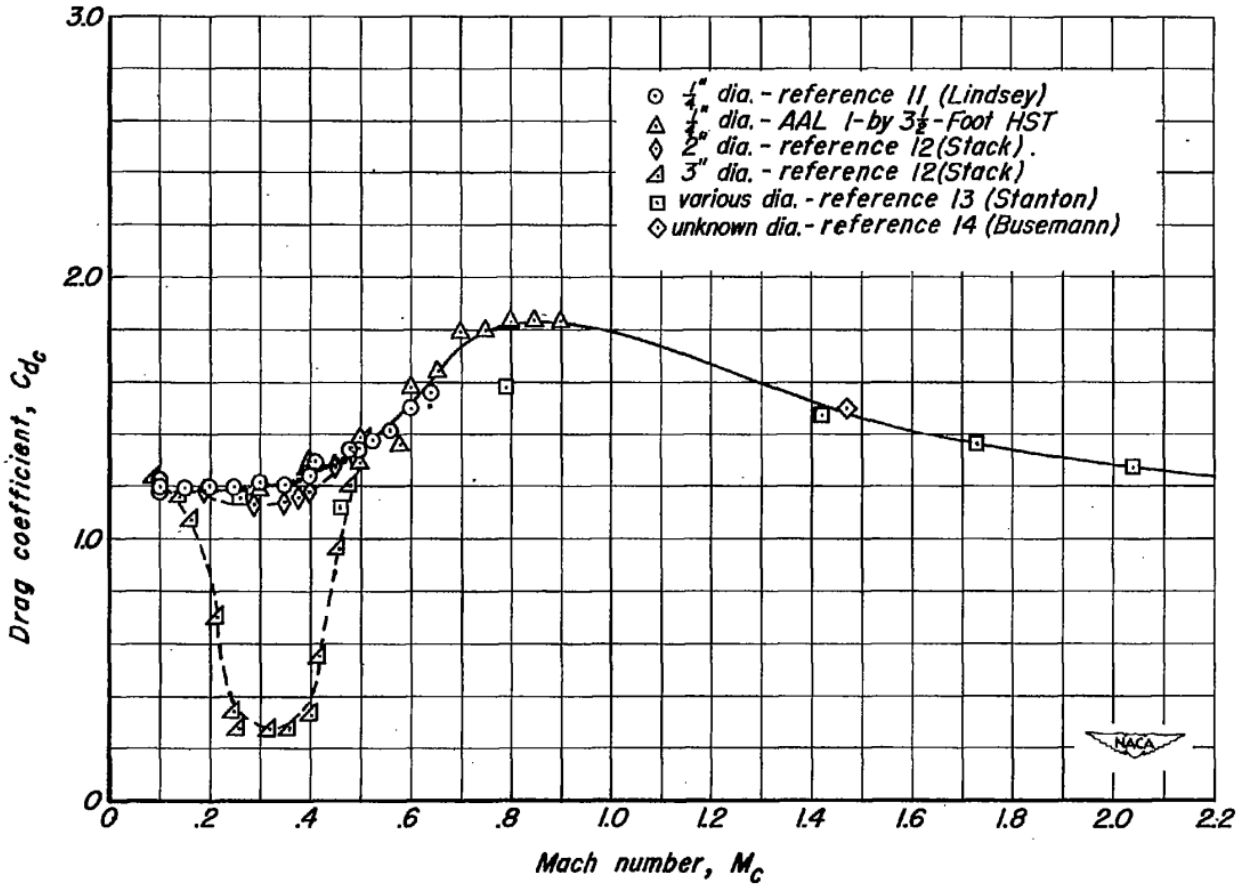

Figure 89: Drag coefficients of circular cylinders of various sizes as a function of Mach number [75]

The drag proportionality factor (η) required for Equations (176) and (178), was obtained through the use of Figure 90. The length-to-diameter ratio of the cylinder in question was required to obtain a value for the drag proportionality factor. The data presented in Figure 90 was generated for a constant cross-sectional area. The fuselage of the Extra 330SC is constantly varying and an average diameter was taken from the distribution of the radius of an equivalent circular cylinder (Figure 86). The average diameter was calculated to be $D_{ave} = 0.707$ m. The length of the Extra 330SC fuselage was taken as $L_{fuse} = 5.595$ m, giving a

length to diameter ratio of $L_{fuse}/D_{ave} = 7.92$. Using this length-to-diameter ratio, a value of $\eta \approx 0.655$ was obtained.

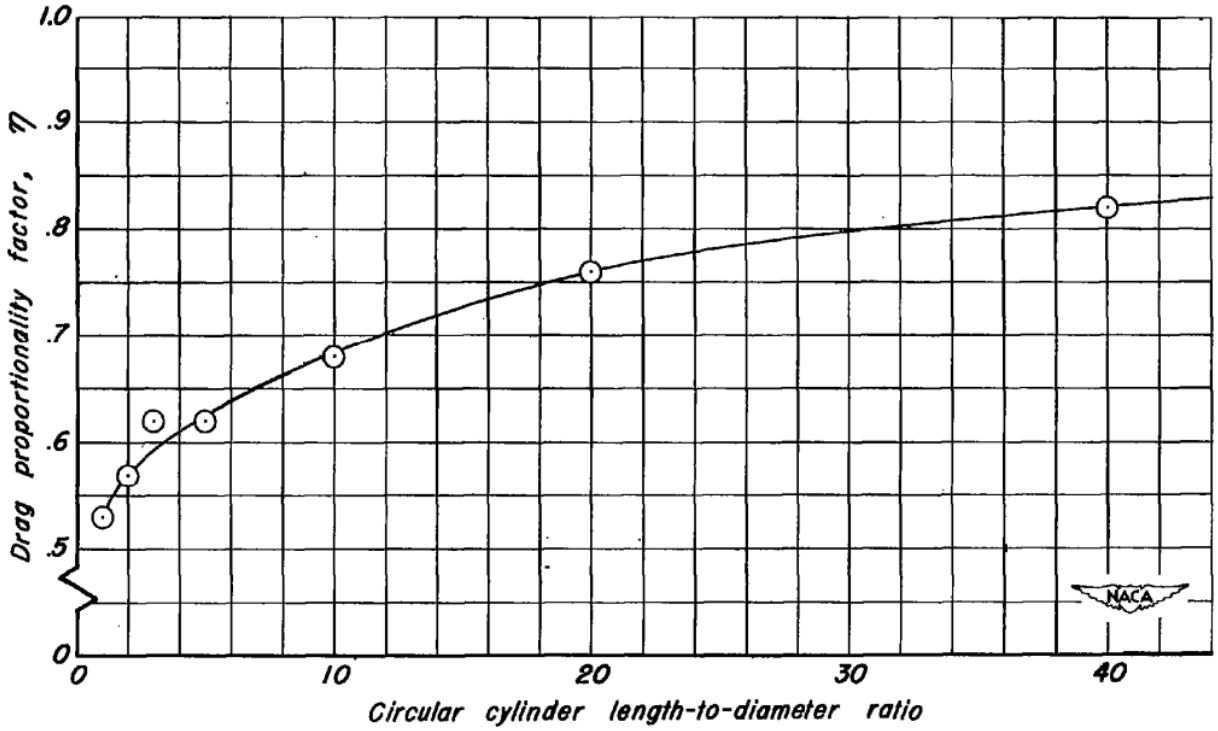

Figure 90: Ratio of the drag coefficient of a circular cylinder of finite length to that of a cylinder of infinite length, η, as a function of the length-to-diameter ratio ($R_c = 88\,000$) [75]

An attempt was made to recreate the fuselage data provided by Pamadi [41] to ensure that the method provided by Jorgensen [42] was correctly applied. While not all input data was clearly given, sufficient data was provided in the report to reproduce the curves for coefficients of lift, drag and pitching moment. A drag proportionality factor of 0.85 provided good correlation in results. This can be seen in Figure 91 and Figure 92, where the coefficients of lift and drag have been reproduced for the fuselage data. The slight mismatch in the curves is thought to be as a result of an area distribution that was not completely representative of the one used by Pamadi [41]. An area distribution was approximated based on limited data. While an area distribution is provided in Figure 21 of Pamadi [41], the values presented appear to be incorrect, which results in an incorrect distribution for the derivative of area with respect to length. It may be that the area distribution that is provided was that of the scale test model instead of the full-scale aircraft. The report also states that an 'idealised' rear fuselage was used in place of the actual geometry. The results from the coefficients of lift and drag were acceptably close to conclude that the model presented by Jorgensen [42]

was being applied correctly. The coefficient of pitching moment was also reproduced. Using the geometry and variables derived for the coefficients of lift and drag yielded a curve that had an identical shape to that provided by Pamadi [41]. The magnitude of the two curves was marginally different. The difference arose as a result of the location of the centre of gravity. Using the centre of gravity location provided by Pamadi [41] ($x_{c.g} = 1.91$ m) resulted in a curve that had a greater magnitude, than the curve provided. This difference occurred from $\alpha \approx 30°$ onward. Using a centre of gravity location of $x_{c.g} = 1.4$ m provided very good correlation between the two sets of results. The location about which the pitching moment was taken is not explicitly stated by Pamadi [41] and a location may have been selected to match that of the wind tunnel test data. It was assumed that the curve was obtained about a location that is approximately 1.4 m from the nose of the aircraft. As with the coefficients of lift and drag, the slight differences in the coefficient of pitching moment are likely due to an area distribution that is not identical to that of Pamadi [41].

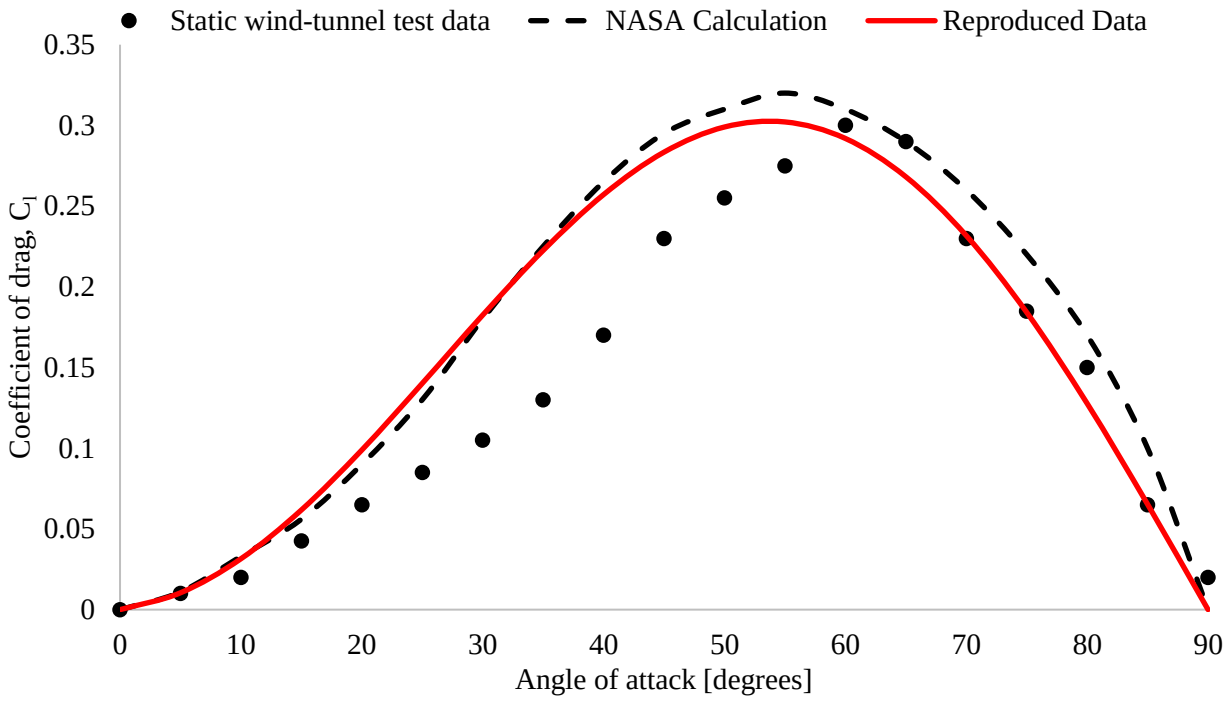

Figure 91: Fuselage coefficient of lift, reproduced for data provided in Pamadi [41]

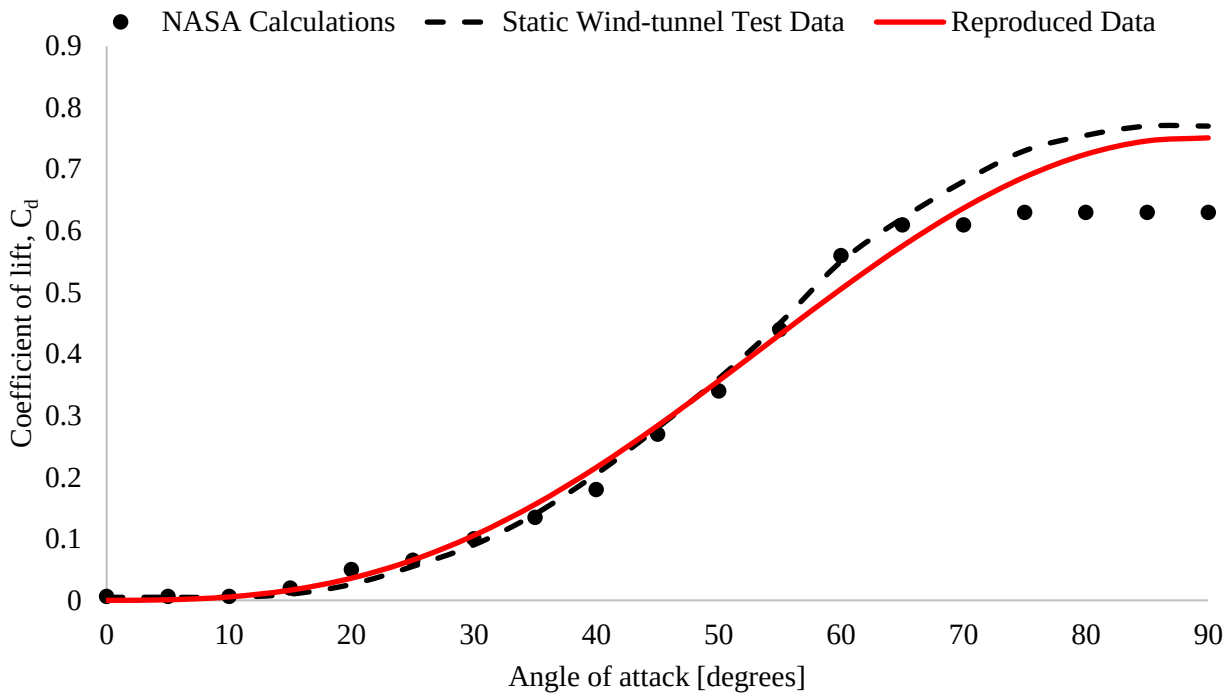

Figure 92: Fuselage coefficient of drag, reproduced for data provided in Pamadi [41]

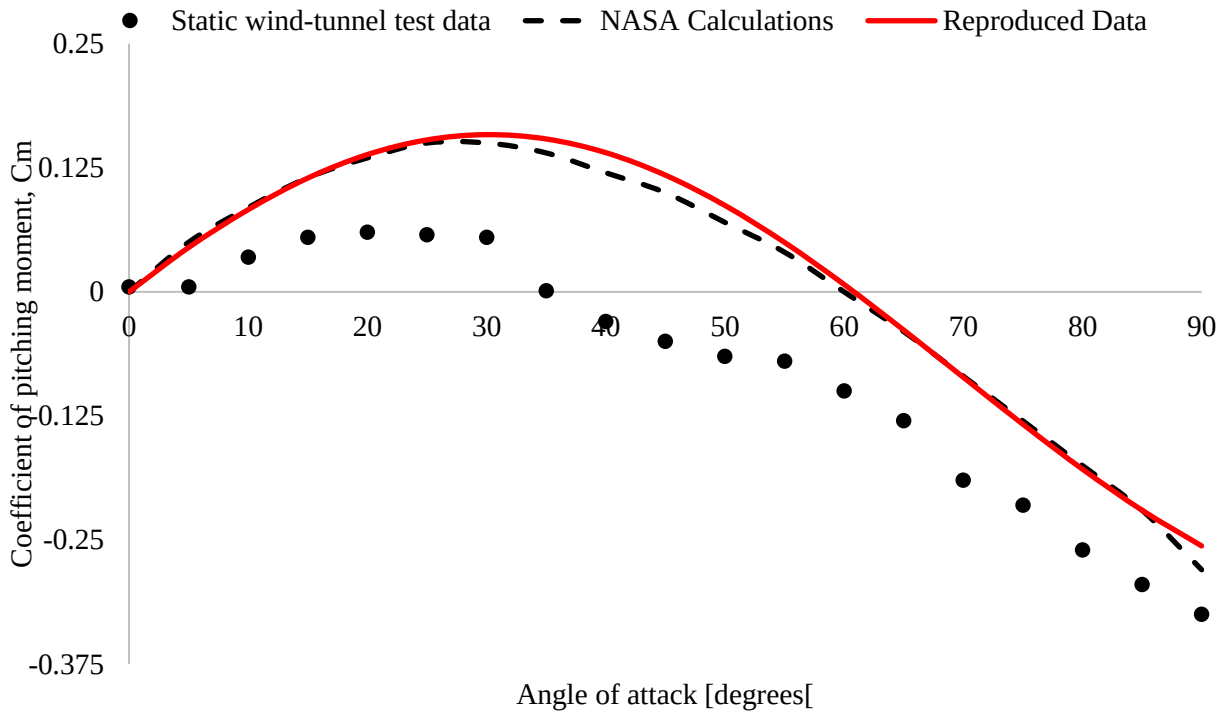

Figure 93: Fuselage coefficient of pitching moment, reproduced for data provided in Pamadi [37]

It is possible that the changes in area along the fuselage result in a cylinder that has a greater length-to-diameter ratio than that predicted by simply taking the average diameter of the body. Jorgensen [42] strongly recommends obtaining the values of the drag proportionality factor and cross-flow coefficient of drag through experimentation. Such data is not available for the Extra 330SC geometry at the time of writing and as such the values of the drag proportionality factor and cross-flow coefficient of drag that are discussed in this section were used.

A summary of the input data for the estimation of the aerodynamic coefficients of the fuselage of the Extra 300SC is presented in Table 31. The relevant figure for each input variable is provided.

Table 31: Summary of fuselage aerodynamic coefficient input data

Input Variable	Value/Figure	Units
L_{fuse}, X	5.595	m
A_r	0.694	m^2
η	0.85	-
C_{d_n}	1.2	-
x_m	1.567	m
dA/dx		-
r	Figure 86	m
$\left(\frac{C_n}{C_{n_0}}\right)_{SB}$	Figure 88	-
$\left(\frac{C_n}{C_{n_0}}\right)_{Newt}$	Figure 88	-

The predicted coefficient of lift for the Extra 330SC fuselage is plotted in Figure 94 along with the coefficient of lift presented by Pamadi [41]. The NASA GA aircraft fuselage coefficient of lift is presented for calculated values using the method developed by Jorgensen [42] and for static wind tunnel test data. While each data set follows a similar trend the magnitudes show very large disparities. The calculated NASA data and the estimated Extra 330SC coefficients follow a similar shape both peaking at $\alpha \approx 55°$. The wind tunnel test data peaks at $\alpha \approx 60°$ following a similar trend. Pamadi [41] states that a constant value of slender body coefficient of normal force ratio $= 1.19$ was used. A constant value of Newtonian coefficient of normal force ratio $= 2$ appears to have been used but is not explicitly stated. A potential contributing factor to the difference in magnitudes could be due to the assumed shapes of each of the fuselages. The NASA GA fuselage is more 'square' in cross-sectional shape when compared to the more elliptically shaped Extra 330SC. The elliptical cross-section has a lower cross-flow coefficient of drag value. While Pamadi [41] did not clearly indicate the value of the cross-flow coefficient of drag it would

appear that a value higher than 1.2 was used. Increasing the assumed value of the cross-flow coefficient of drag for the Extra 330SC fuselage to a value of 2 provides a much closer match of the data. An additional contributing factor to the difference in values could also be due to the area distributions between the two fuselages. The fuselage area of the Extra 300SC is less than that of the NASA GA fuselage along the entire length. This resulted in a lower coefficient of lift.

Notable differences are seen in Figure 94 between the two sets of calculated values. The estimated Extra 330SC values and the wind tunnel test data illustrate a good correlation in magnitude up to an angle of attack of $\approx 35°$. The coefficient of lift of the fuselage for all data sets is relatively small when compared to those of the wing. These values are not expected to influence the overall results significantly. This does not imply that the forces can be omitted from calculations. Particularly because the fuselage is constantly being blown by propeller slipstream effects throughout a tumble manoeuvre. The presence of propeller slipstream implies that the angles of attack seen over the fuselage should be relatively low $(\alpha_{fuse} \leq 30°)$, unless a strong headwind exists. The noted differences in results are likely due to different cross-flow coefficients of drag and areas. The coefficient of lift data estimated for the aircraft was deemed acceptable due to the relatively good correlation between static test data and estimated Extra 330SC fuselage data along with the expected low angles of attack.

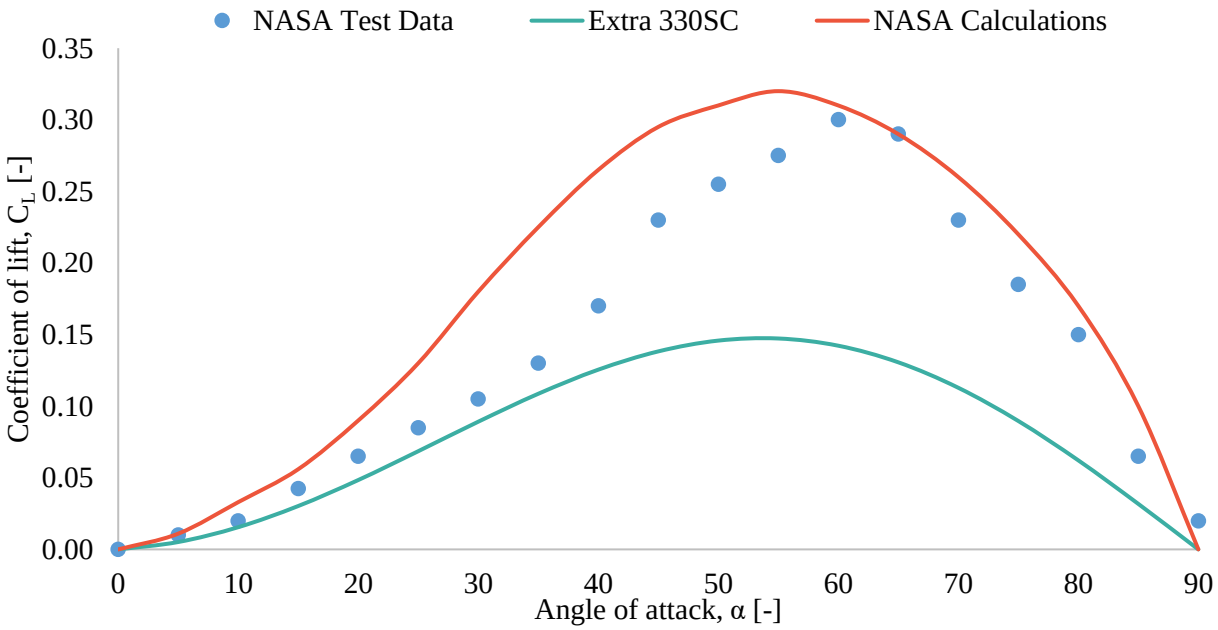

Figure 94: Comparison of the coefficient of lift for the Extra 330SC fuselage and a NASA GA aircraft fuselage presented in Pamadi [41]

The coefficient of drag for varying angles of attack for the Extra 300SC fuselage is plotted Figure 95. The coefficient of drag values for a NASA GA aircraft provided in Pamadi [41] are also plotted. Calculated and wind tunnel test data were provided for the NASA GA aircraft. As with the coefficient of lift large discrepancies exist between the data for each fuselage. The same arguments made for the differences in the coefficient of lift may be applied to the coefficient of drag. Similar curves exist between the Extra 330SC fuselage data and the calculated NASA data. The differences in magnitude are due to a lower cross-flow coefficient of drag and a lower overall fuselage area for the Extra 330SC. A notable difference does exist between calculated and test data. The calculated NASA data follows the static test data more closely at lower angles of attack than the Extra 330SC. This is likely due to the differences in the cross-flow coefficient of drag value and fuselage geometry. Despite these differences, the values calculated for the Extra 330SC were used as is for the same reasons as those provided for the coefficient of lift.

The magnitude of the coefficient of drag of the Extra 330SC fuselage is not dissimilar to those of the coefficient of lift for angles of attack up until $\approx 50°$. A key difference exists for angles of attack $> 50°$ where the coefficient of lift decreases while the coefficient of drag continues to increase. This illustrates a shift in direction of the fuselage forces at higher angles of attack. The coefficient of drag of the Extra 330SC fuselage, much like the coefficient of lift, has magnitudes lower than that of the wing and are not expected to alter the results by a significant amount. Their inclusion is still necessary.

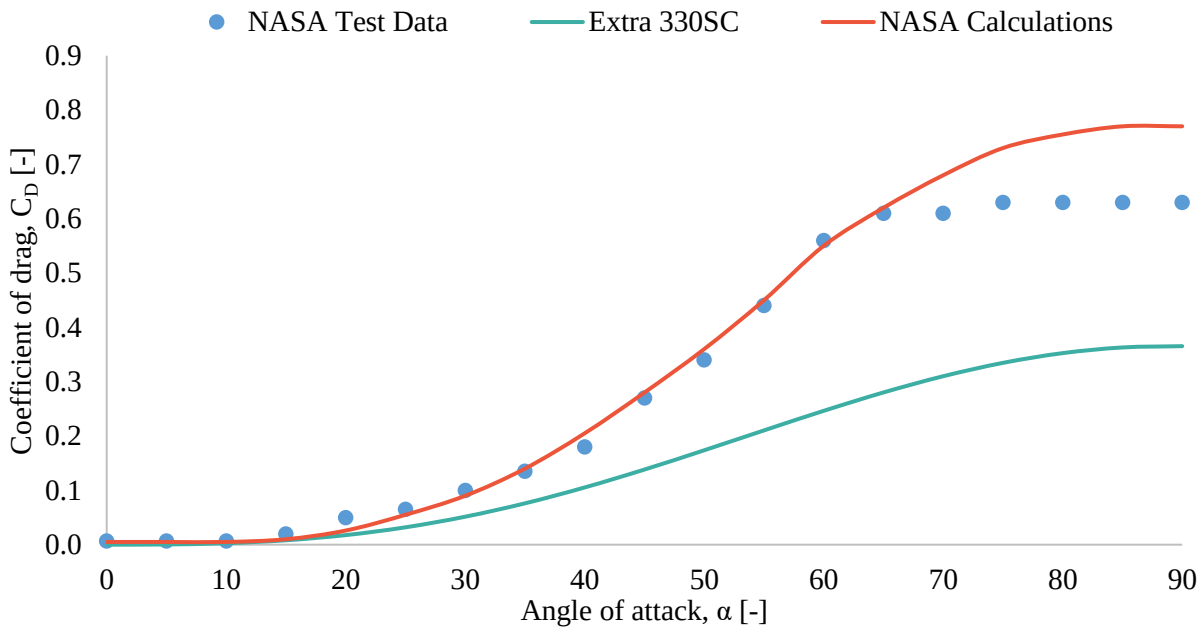

Figure 95: Comparison of the coefficient of drag for the Extra 330SC fuselage and a NASA GA aircraft fuselage presented in Pamadi [41]

The coefficient of pitching moment for both Extra 330SC fuselage and the NASA GA fuselage presented by Pamadi [41], are given in Figure 96. The coefficient of pitching moment for the NASA GA fuselage is presented for static wind tunnel test data and calculated data. The only correlation in data can be seen between the wind tunnel test data and the estimated Extra 330SC data up to an angle of attack of $\approx 30°$. This correlation is likely purely coincidental. The coefficient of pitching moment is a function of the distribution of the fuselage area and the location of the centre of gravity of the aircraft. The area distribution determines where the aerodynamic centre of the fuselage forces is located. This location relative to the centre of gravity provides a pitching moment.

The fuselage of the Extra 330SC illustrates a forward cross-sectional area bias. This bias results in a difference in shape of the pitching moment curve when compared to the NASA GA fuselage. The large portion of area at the front of the Extra 330SC fuselage suggests that the aerodynamic centre of the fuselage would be located near the front section of the fuselage. This results in a fuselage force that is forward of the centre of gravity of the aircraft. The forward force creates destabilising, nose-up moments across a large angle of attack range. The different shape seen in the coefficient of pitching moment for the NASA GA aircraft is due to a different area distribution and centre of gravity location with respect to the aerodynamic centre of the fuselage.

The magnitude of the coefficient of pitching moment is small, with the Extra 330SC fuselage providing a nose-up moment until an angle of attack of $\approx 82°$. The small values seen in Figure 96 are due to the close proximity of the aerodynamic centre of the fuselage and the centre of gravity. This feature may have been intended by the aircraft manufacture to limit the effects of the fuselage in pitch throughout a wide range of angles of attack. The position of the aerodynamic centre as a function of the normalised Extra 330SC fuselage length is provided in Figure 97. It is clear that the aerodynamic centre of the Extra 330SC fuselage is located near the front of the aircraft. The large areas seen on the front and side view of the fuselage suggest a forward bias in aerodynamic centre. While the area distribution of the side of the aircraft seems to be split almost evenly about the half length of the fuselage, the top view provides a significant bias in area towards the front of the fuselage.

Without any directly comparable test data available for the Extra 330SC the coefficient of pitching moment curve provided in Figure 96 will be used in analysing a tumble manoeuvre. It should also be noted that the coefficient of pitching moment was presented for a single centre of gravity location. Since the centre of gravity is changed for different aircraft configurations, the coefficient of pitching moment was recalculated for each aircraft configuration. It is likely that the aerodynamic coefficients of the fuselage will have a minor influence on the results and the disparities noted should not alter the results significantly.

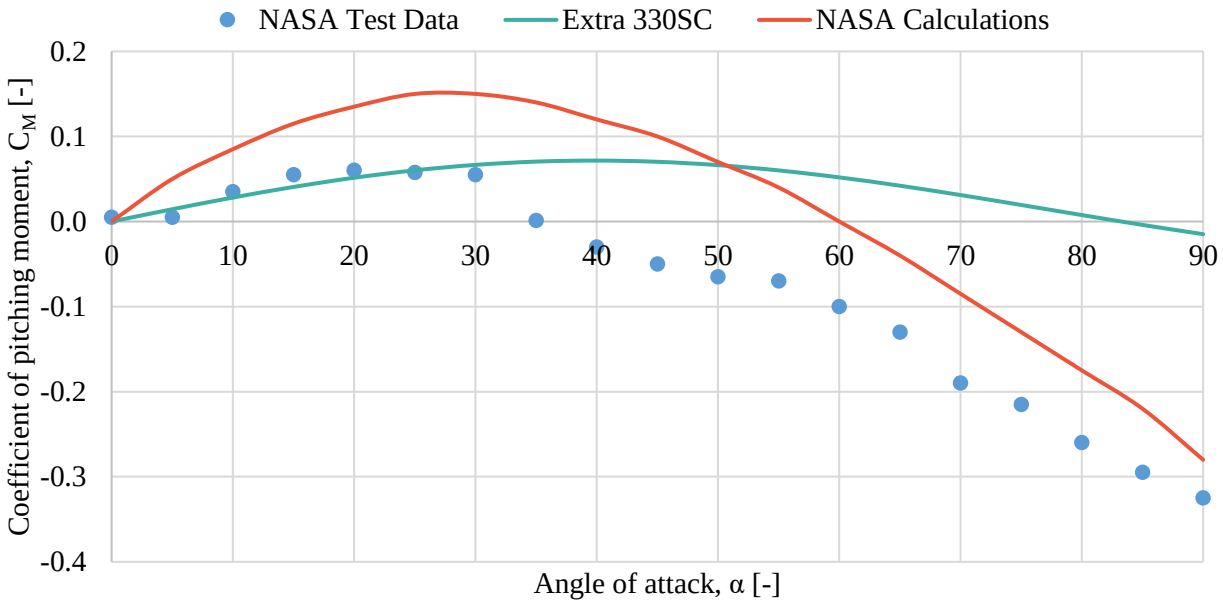

Figure 96: Comparison of the coefficient of pitching moment for the Extra 330SC fuselage and a NASA GA aircraft fuselage

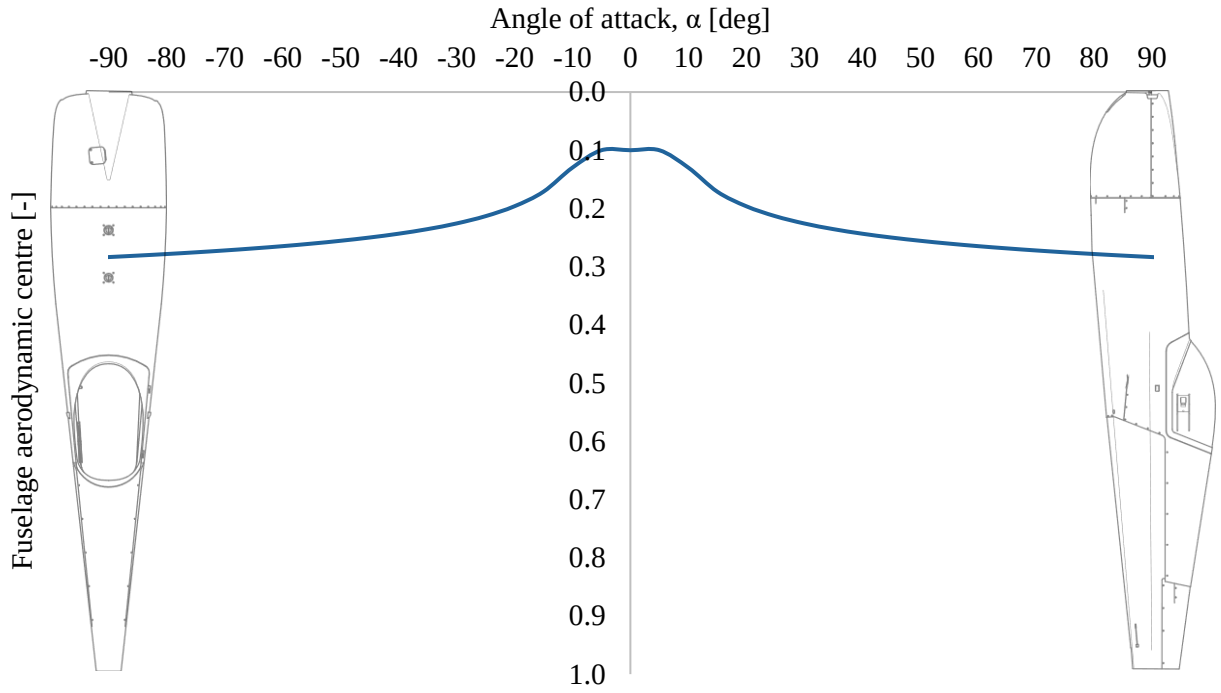

Figure 97: Extra 330SC fuselage aerodynamic centre as a function of normalised fuselage length

3.3.5. Horizontal Stabiliser Aerodynamic Coefficients

The coefficients of lift and drag for the horizontal stabiliser were calculated using the method outlined in §2.4.1 and are presented in Figure 98 for an infinite aspect ratio. Test data for the coefficient of lift of a NACA0009 (infinite aspect ratio) is presented in Figure 98 alongside the calculated values. The values presented in Table 32 were used as the input values in generating the coefficients of lift and drag for the Extra 330SC horizontal stabiliser. From the test data, the estimated coefficient of lift shows acceptable correlation with some minor overpredictions near the first and second stall points. An interesting feature of the NACA0009 is that the second coefficient of lift peak is higher than the first. This suggests that the shape of the profile is tending towards that of a flat plate, while still retaining the traits of an airfoil profile. The coefficient of drag follows a similar trend to those seen in §3.3.1, with a high peak value of 2.08.

Table 32: Summary of horizontal stabliser aerodynamic coefficient input data

Input Variable	Value/Figure	Units
Airfoil	$NACA0009$	-
$\boldsymbol{A0}$	0	deg
$\boldsymbol{ACL1'}$	[12, 12]	deg
$\boldsymbol{CL1max'}$	[0.8, 0.8]	-
$\boldsymbol{S1'}$	[0.1, 0.1]	1/°
$\boldsymbol{CD0}$	[0.0055, 0.005]	-
$\boldsymbol{ACD1'}$	13	deg
$\boldsymbol{CD1max'}$	[0.009, 0.019]	-
$\boldsymbol{b_{HS}}$	2.66	m^2
$\boldsymbol{AR_{HS}}$	3.32	-
$\boldsymbol{S_{HS}}$	2.13	m^2
$\boldsymbol{S_e}$	1.04	m^2
$\boldsymbol{C_{L_{\alpha_{wing}}}}$	0.102	1/°
$\boldsymbol{a_1}$	$0.6C_{L_{\alpha_{wing}}}$	-
$\boldsymbol{a_2}$	$0.6a_1$	-
$\boldsymbol{\alpha_{0_{HS}}}$	0	deg
$\boldsymbol{\delta_e}$	-25	deg

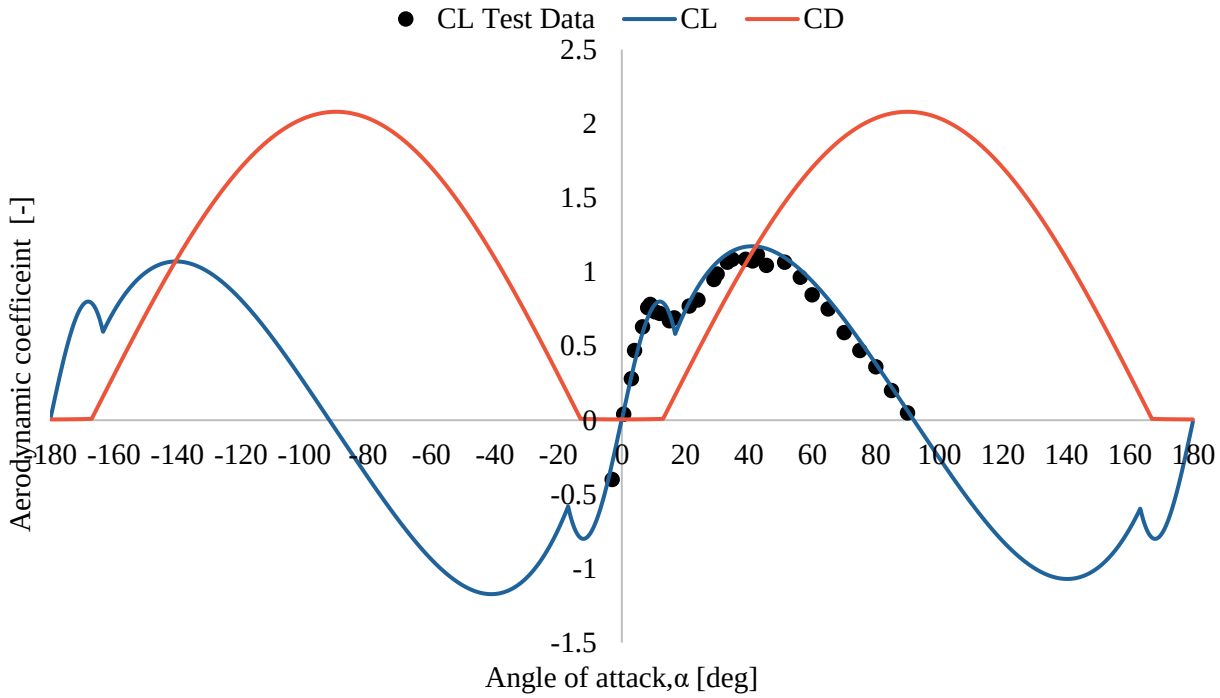

Figure 98: Estimated coefficient of lift and drag data for a NACA0009 (test data [76] is provided for the coefficient of lift)

Corrections to the coefficient of lift and drag data to include the influence of an elevator deflection (δ_e) of $-25°$ and aspect ratio of the horizontal stabiliser (AR_{HS}) of 3.32 was performed. The effect of the deflected elevator on the coefficient of lift acts to shift the entire curve upwards or downwards. For an upward elevator deflection ($-\delta_e$) the entire coefficient of lift curve is shifted downwards. The shift in value at each angle of attack was determined with the aid of Equation (166) from §2.4.1.3. Using this equation, a coefficient of lift delta could be obtained at each angle of attack. A value of $\Delta C_L = 0.6 * 0.6 * 0.102 * -25 = -0.918$ was applied to each data point of the $C_L - \alpha$ plot, shifting the entire curve down. An elevator deflection of $-25°$ shifts the effective chord line of the lift and drag curves of the horizontal stabiliser by approximately 11°. The elevator deflection angle for the geometry of the Extra 330SC is presented in Figure 99. The elevator geometry and angles were obtained from the Extra 330SC POH [13]. The influence of the elevator deflection and aspect ratio on the coefficient of lift and drag are presented in Figure 100, together with the original uncorrected, infinite aspect ratio coefficients of lift and drag.

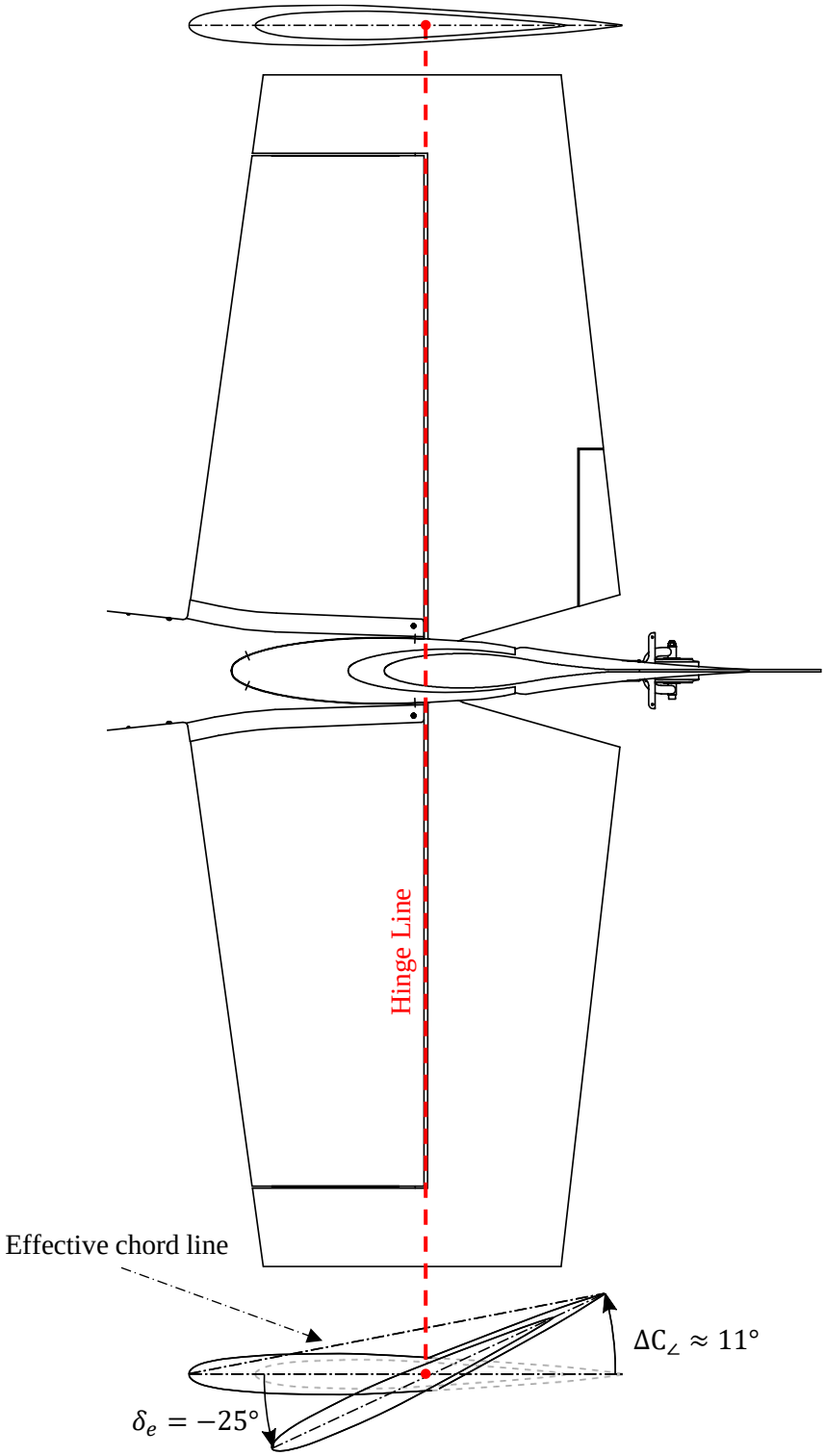

Figure 99: Extra 330SC elevator deflection angles

In Figure 100 the coefficient of lift for corrected horizontal tail aspect ratio and elevator deflection is seen to be maximum (negative) at zero degrees angle of attack. This is perhaps why the elevator deflection of the Extra 330SC is limited to $\pm 25°$. As angle of attack increases the coefficient of lift increases but remains negative up until an of an angle of attack of $\approx 20°$. This indicates that the elevator is effective up to angle of attack of $\approx 20°$. The stall angle of the horizontal stabiliser with elevator deflection is observed to be $\approx 23°$. The coefficient of lift decreases after the stall angle and becomes negative at an angle of attack of $25.6°$. At an angle of attack of $27.8°$ a sharp cusp is seen. The coefficient of lift is seen to increases in value beyond this cusp. The coefficient of lift becomes positive in value at an angle of attack of $31°$. This dip and recovery is unlikely to occur and the coefficient of lift is more likely to follow a smoother path. This is illustrated by the dotted blue line connecting the first and second peaks of the coefficient of lift. The deflection of the elevator is seen to result in positive lift values from $20° < \alpha < 80°$. In this region the elevator will not be capable of providing the necessary force and subsequent moment for completing a tumble manoeuvre. The direction of the force in this region will create a counteracting moment. This suggests that horizontal stabiliser angles of attack of $\leq 20°$ are required to supply part of the destabilising, nose-up moment to tumble an aircraft. This can be achieved by directing propeller slipstream over the tail. Propeller slipstream velocity directed at low angles of attack ($\leq 5°$) over the horizontal stabiliser will reduce the overall angle of attack of the horizontal tail. The propeller slipstream will be particularly effective at slower airspeeds. The $3D$ aspect ratio corrections do not influence the shape of the coefficient of lift curve in the pre-stall regime. The magnitude and slope of the coefficient of lift in the post-stall regime are reduced.

The coefficient of drag of the horizontal stabiliser with elevator deflection and aspect ratio corrections in Figure 100 is notably higher in the pre-stall region. This is due to the large increase in the coefficient of lift in that region caused by elevator deflection. The finite aspect ratio post-stall coefficient of drag follows a similar trend to that of the infinite aspect ratio. The correction for aspect ratio results in a smaller peak value. This is due to the reductions in the coefficient of lift magnitude in the post-stall regime for a finite aspect ratio. The shift between the finite and infinite aspect ratio drag curves is due the change in chord line due to elevator deflection.

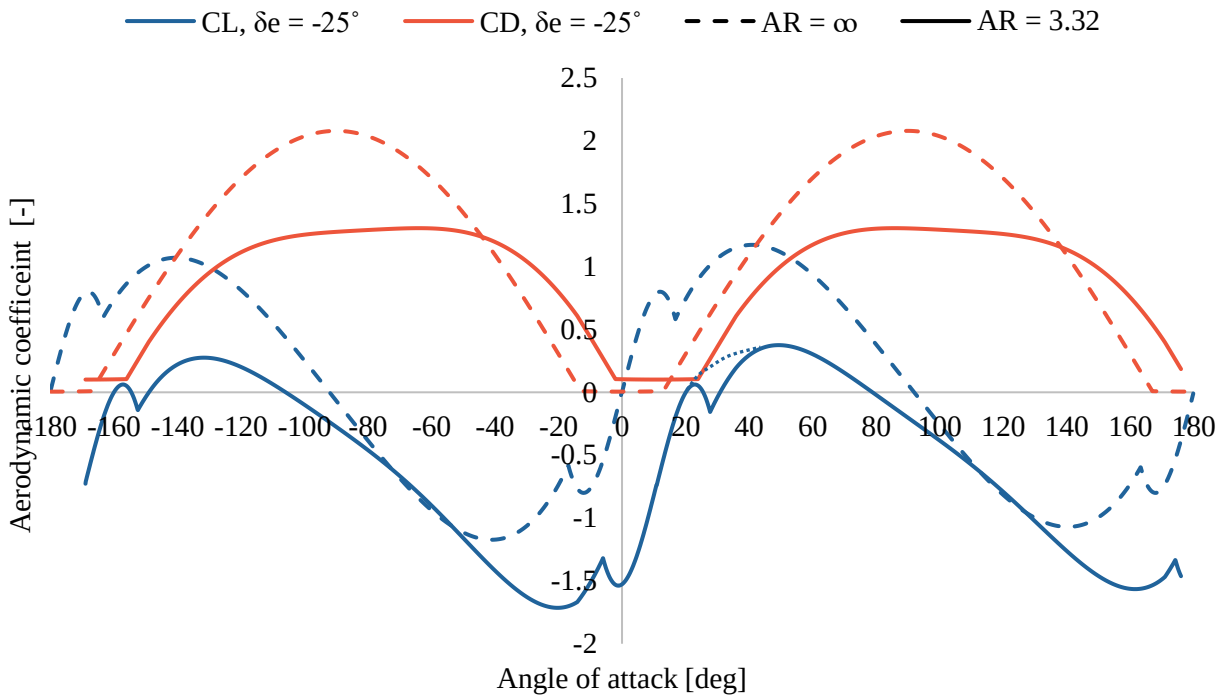

Figure 100: Horizontal stabiliser coefficient of lift and drag, for infinite aspect ratio with no elevator deflection and corrected for an aspect ratio of $AR_{HT} = 3.32$ and an elevator deflection of $\delta_e = -25°$

The quarter chord pitching moment coefficient for the horizontal stabiliser is presented in Figure 101. Data is presented for both an infinite aspect ratio stabiliser with no elevator deflection and for a stabiliser with an aspect ratio of 3.32 with an elevator deflection of $-25°$. The values of the quarter chord coefficient of pitching moment are lower than the coefficients of lift and drag. The overall trend follows a somewhat flat sinusoidal shape. Minor changes in slope can be seen at the stall angles. The curve of the quarter chord coefficient of pitching moment corrected aspect ratio and elevator deflection follows a very similar trend to that of the uncorrected data, with the most notable difference being the $11°$ shift in the data due to elevator deflection. The shift does results in a quarter chord coefficient of pitching moment that acts to create a stabilising moment up until an elevator angle of attack of $\alpha \approx 13°$.

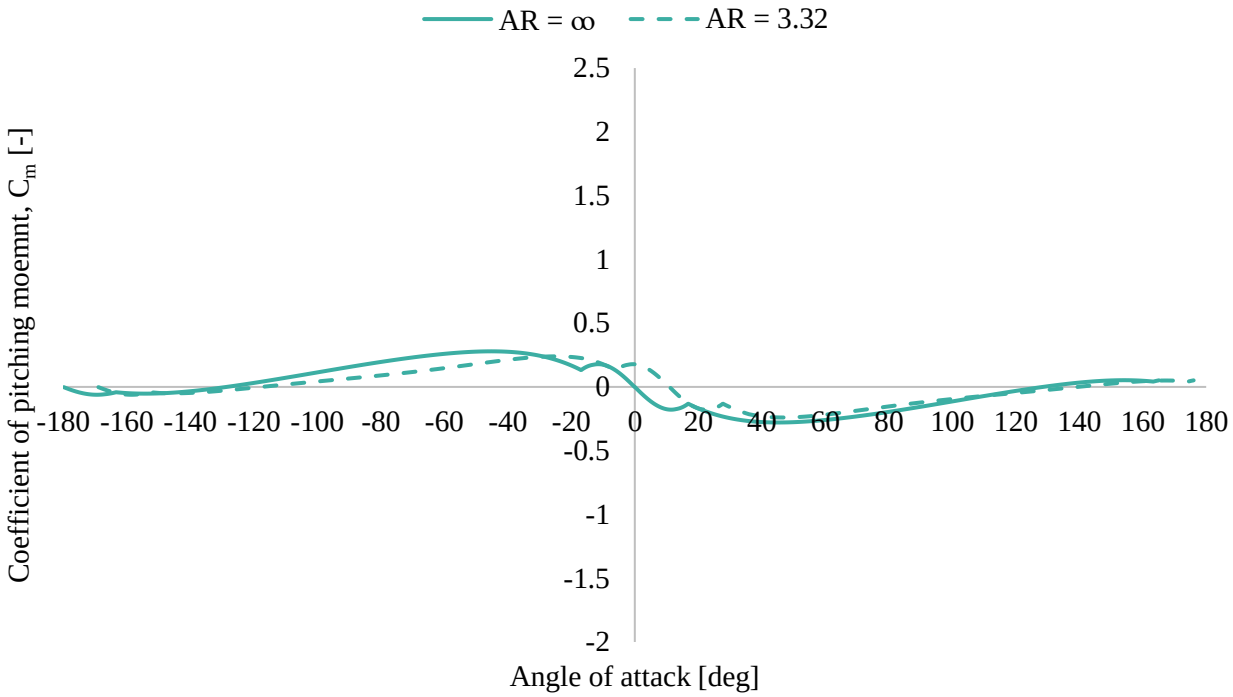

Figure 101: Horizontal stabiliser coefficient pitching moment, for infinite aspect ratio with no elevator deflection and corrected for an aspect ratio of $AR = 3.32$ and an elevator deflection of $\delta_e = -25°$

3.3.6. Propeller Aerodynamic Data

The propeller thrust and slipstream distributions were determined using the values provided in Table 33. The activity factor (AF) of the Extra 330SC propeller was not provided by either the aircraft manufacturer or the propeller manufacturer. The NASA propeller outlined in §1.3.4.5 had an activity factor of 150. The propeller on the Extra 330SC is similar in shape to the NASA propeller though is slightly slimmer along the blade length. This suggests that the propeller on the Extra 330SC has a slightly lower activity factor than 150. It was estimated that the propeller of the Extra 330SC would have an activity factor of ≈ 120. The design coefficient of lift (C_{l_d}) was assumed to be ≈ 0.7 to match that of the propeller provided in §2.4.3. Given the similar shape and aspect ratios of the two propellers it is very likely that the design coefficient of lift would be similar.

The coefficient of power of the Extra 330SC propeller was calculated using Equation (183). It was assumed that the propeller was operating near sea level conditions. The coefficient of power of the Extra 330SC propeller was calculated as $C_p = 0.062$. Using this value, $C_T/C_p = 2.5$ was obtained from Chart C2 of Roskam [70]. The static thrust (T_{static}) was determined through the use of Equation (185). The resulting static thrust was determined to be 630 kg.

Table 33: Summary of propeller aerodynamic input data

Input Variable	Value/Figure	Units
Propeller	MTV-9-B-C/C198-25	-
$\boldsymbol{B}$	3	-
$\boldsymbol{RPM}$	2700 -Max Continuous	RPM
Engine Horsepower	315 (400)	HP
$\boldsymbol{\eta_e}$	95	%
$\boldsymbol{D}$	2	m
$\boldsymbol{S_{Prop}}$	3.14	m^2
$\boldsymbol{C_T/C_p}$	2.5	-

The thrust curve efficiencies were determined using charts C16 and C20 from Roskam [70]. These two charts are provided for an $AF = 100$ and $AF = 140$ respectively. Since an activity factor of 120 was estimated for the Extra 330SC propeller, an interpolation of values was performed between these two charts. The propeller thrust from 0 m/s to 50 m/s for the standard Extra 330SC engine (1x Thrust) is presented in Figure 102 by the dotted blue line. The only aircraft to have successfully performed the tumble manoeuvre are all equipped with engines that had 30 % more power (400 HP). They are also presumed to utilise custom propellers. Information regarding these custom engines and propellers has not been made publicly available. With the increase in power, an increase in thrust was also be expected. Calculating a new, increased thrust distribution for an Extra 330SC would be difficult without any engine or propeller specifications. To account for the increase in engine power the original thrust curve for the Extra 330SC was scaled by a constant value. The factor by which the thrust values were scaled was based on the aircraft mass. The Prop Hang or hover manoeuvre involves holding an aircraft in a stationary vertical position without it torque rolling. This manoeuvre requires that the thrust-to-weight ratio be equal to or very close to unity. The Prop Hang is performed in displays by these modified 400 HP aircraft. It was assumed that this thrust was equal to the maximum take-off mass of the aircraft (820 kg). This provides a thrust scale factor of 1.3. The thrust distribution of the Extra 330SC was scaled by this factor. The increased thrust distribution (1.3x Thrust) is illustrated in Figure 102 by the solid blue line.

The propeller slipstream velocity delta (ΔV_{ss}) was calculated using Equation (188). The distribution of the original propeller slipstream delta for the Extra 330SC (1x V_{SS}) is presented by the dotted orange line in Figure 102. Using the same argument made for the propeller thrust, the propeller slipstream was also scaled by a value of 1.3. This resulted in an increased propeller slipstream delta distribution (1.3x V_{ss}) which is presented in Figure 102 by the solid orange line. It should be noted that the propeller slipstream delta

velocities provided in Figure 102 are the values by which the free-stream velocity is increased. To obtain the total velocity of the propeller slipstream, the slipstream delta should be added to the free-stream velocity.

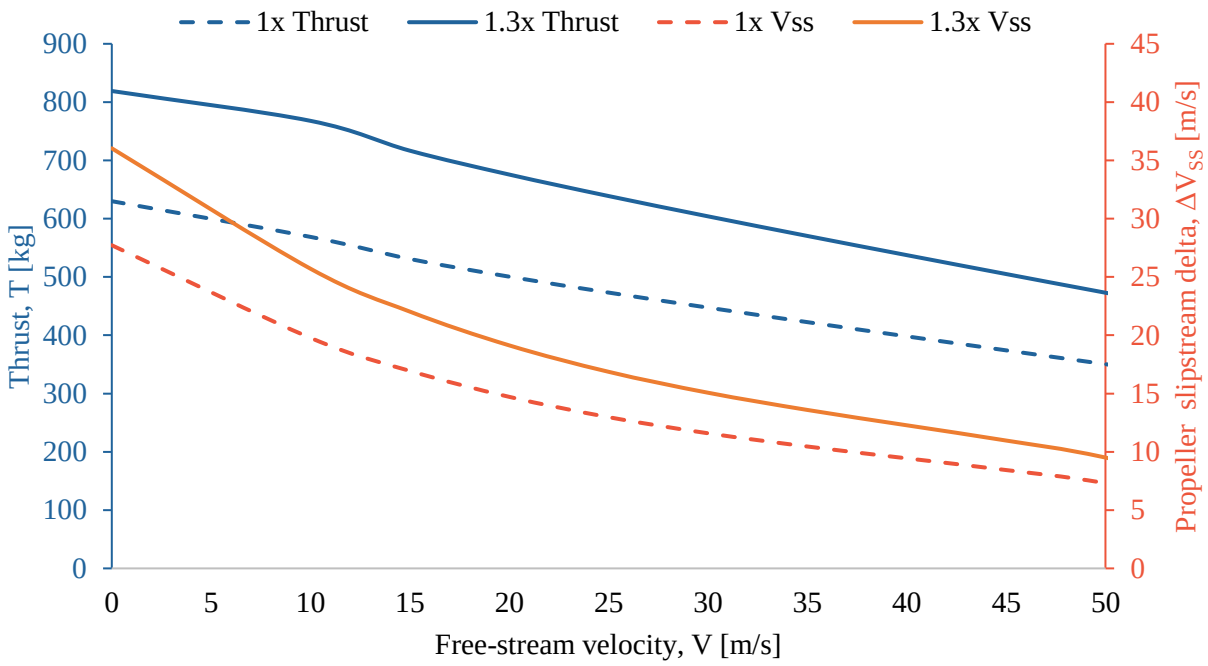

Figure 102: Extra 330SC propeller thrust and slipstream distributions (for as calculated and for 1.3x calculated)

The coefficient of normal force produced by the propeller in §2.4.3.2 is re-presented in Figure 103 for various modified advance ratios (J'). The distributions for the coefficient of normal force are used in the absence of an acceptably accurate method and insufficient propeller data. The coefficients of normal force presented in Figure 103 were measured for a propeller that was larger than that of the Extra 330SC. The input power could also be increased to meet the required torque and thus drag requirements. Care must be taken when using the coefficient of normal force data for the Extra 330SC. Coefficients may only be used if the torque requirements do not exceed the capabilities of the engine of the Extra 330SC.

The coefficient of normal force illustrates similar values for all modified advance ratios up until an angle of attack of $\approx 15°$. These values are quite small in magnitude. Beyond an angle of attack of $15°$ the distributions for each of the modified advance ratios begin to diverge. Larger modified advance ratios produce larger normal forces. A change to a steeper gradient is seen for all advance ratios at an angle of attack of $\approx 70°$. Values of pitching moment due to the propeller were found to be negligibly small and were omitted from any calculations. As such no data will be presented.

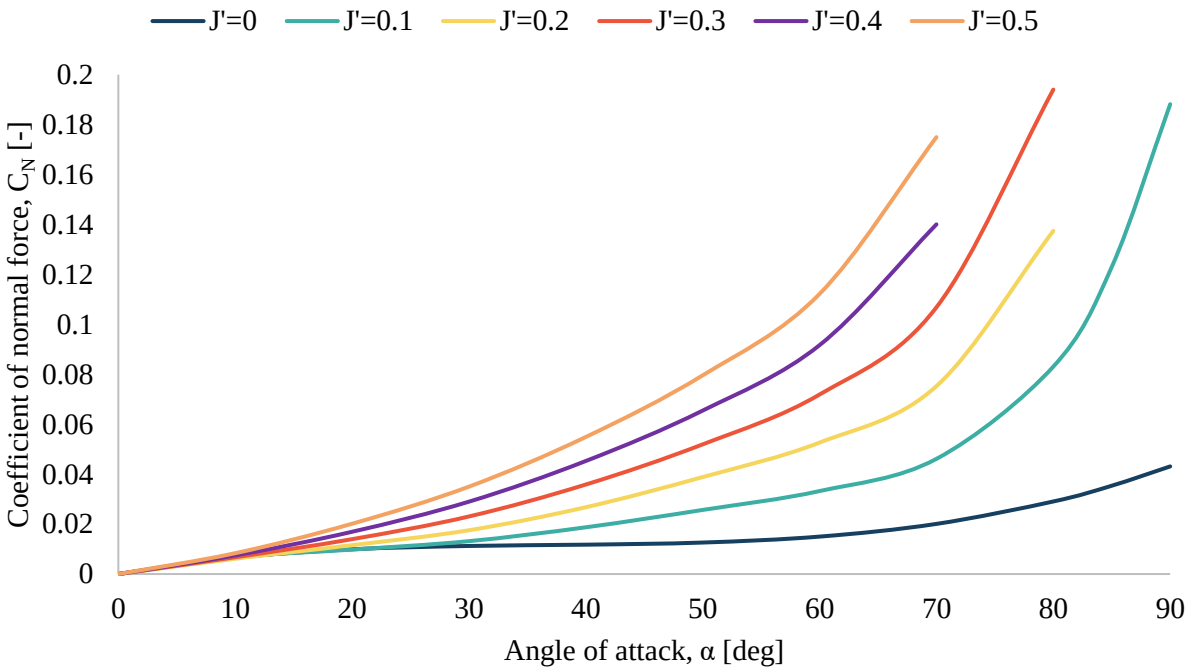

Figure 103: NACA TN D318 propeller 1 coefficient of normal force for β=16° [44]

4. METHODOLOGY

4.1. Introduction

The development of a model for the performance characteristics of a manoeuvre requires an establishment of the forces acting on the aircraft. These forces arise from gravitational, aerodynamics and propulsive sources. These external forces acting on the aircraft under Newton's law cause the aircraft to accelerate and change its state of motion. The general equation of motion for force can thus be expressed by Equation (189),

$$[F_a] + [F_p] + [F_g] = [F_I] \tag{189}$$

where $[F_a]$, $[F_p]$ and $[F_g]$ are the aerodynamic, propulsive (powerplant) and gravitational force vectors respectively. $[F_I]$ is the resultant inertial force vector. The trajectory (flight path) of the aircraft is related to the Earth by its velocity vector. It is necessary to derive the general force equation of motion, of the aircraft, in terms of the velocity axis system as defined in §1.3.2. The inertial, gravitational, aerodynamic and propulsive forces were developed and are presented in §4.2.

4.2. Force Equations of Motion Modelling in the Velocity Axes

4.2.1. Inertial Forces

The inertial forces given in Equation (6) were developed in the body axis. The selected modelling approach is developed in the velocity axes. As such, the inertial forces are rederived in the velocity axes.

The external forces acting on the aircraft produce the accelerations that alter its flight path. They can be written in the velocity axes, provided in Equation (190).

$$[F_I]_v = \begin{bmatrix} F_x \\ F_y \\ F_z \end{bmatrix} = \frac{d(mV)_v}{dt} = m\left(\dot{V} + \omega \times V\right)_v + \dot{m}(V)_v \tag{190}$$

Where (ω) is the angular velocity vector of the aircraft and is defined by the rate of pitch $(\dot{\gamma}_2)$ and the rate of turn $(\dot{\gamma}_3)$. These rates can be resolved into the velocity axis system. This leads to the development of Equation (191)

$$(\omega)_v = \begin{bmatrix} 0 \\ \dot{\gamma}_2 \\ 0 \end{bmatrix} + \begin{bmatrix} \cos\gamma_2 & 0 & -\sin\gamma_2 \\ 0 & 1 & 0 \\ \sin\gamma_2 & 0 & \cos\gamma_2 \end{bmatrix} \begin{bmatrix} 0 \\ 0 \\ \dot{\gamma}_3 \end{bmatrix} = \begin{bmatrix} -\dot{\gamma}_3 \\ \dot{\gamma}_2 \\ \dot{\gamma}_3 \cos\gamma_2 \end{bmatrix}_v \tag{191}$$

Substituting Equation (191) into Equation (190) leads to Equation (192), which is the expression for the angular velocity of the aircraft in the velocity axes.

$$[F_I]_v = m \begin{bmatrix} \dot{V} \\ 0 \\ 0 \end{bmatrix}_v + m \begin{bmatrix} -\dot{\gamma}_3 \sin\gamma_2 \\ \dot{\gamma}_2 \\ \dot{\gamma}_3 \cos\gamma_2 \end{bmatrix} \times \begin{bmatrix} V \\ 0 \\ 0 \end{bmatrix} + \dot{m} \begin{bmatrix} V \\ 0 \\ 0 \end{bmatrix}_v \tag{192}$$

Finally simplifying Equation (192) leads to Equation (193).

$$\begin{bmatrix} F_x \\ F_y \\ F_z \end{bmatrix}_v = m \begin{bmatrix} \dot{V} \\ V\dot{\gamma}_3 \cos\gamma_2 \\ -V\dot{\gamma}_2 \end{bmatrix} + \dot{m} \begin{bmatrix} V \\ 0 \\ 0 \end{bmatrix}_v \tag{193}$$

In modelling the tumble manoeuvre, mass change is small enough to be considered negligible. This results in a rate of change of mass ($\dot{m}$) equal to 0.

The forces in the X, Y and Z directions of the velocity axis will comprise of the aerodynamic, propulsive and gravitational forces, illustrated by Equation (194).

$$\begin{bmatrix} X \\ Y \\ Z \end{bmatrix} = [F_a]_v + \left[F_p\right]_v + \left[F_g\right]_v \tag{194}$$

4.2.2. Gravitational Forces

The gravitational forces provided in Equation (6) are given in the body axis. The gravitational forces are required in the velocity axes. This was achieved by rotating gravitational force from the body axes to the Earth axes followed by a rotation from the Earth axes to the velocity axes. Performing the necessary rotations leads to the gravitational forces in the velocity axes provided in Equation (195).

$$\left[F_g\right]_v = \begin{bmatrix} -mg\sin\gamma_2 \\ 0 \\ mg\cos\gamma_2 \end{bmatrix}_v \tag{195}$$

4.2.3. Aerodynamic Forces

The general aerodynamic forces act in the wind axis system and can be expressed by Equation (196). It should be noted that the forces provided in Equation (196) are representative of the overall force axis in each direction within the coordinate system and may comprise of several different components from different parts of the aircraft.

$$[F_a]_w = \begin{bmatrix} F_{ax} \\ F_{ay} \\ F_{az} \end{bmatrix}_w = \begin{bmatrix} -D \\ Y \\ -L \end{bmatrix}_w \tag{196}$$

Transforming the aerodynamic forces in the wind axis to the velocity axes through the bank angle (γ_1) results in Equation (197).

$$[F_a]_v = \begin{bmatrix} -D \\ Y\cos\gamma_1 + L\sin\gamma_1 \\ Y\sin\gamma_1 - L\cos\gamma_1 \end{bmatrix}_v \tag{197}$$

4.2.4. Propulsive Forces

The thrust force on an aircraft may be considered to have both vertical (τ_1) and horizontal (τ_2) deflection angles with respect to the body axis of the aircraft. Since the aerobatic aircraft being considered is a single engine aircraft horizontal thrust deflections will not be considered. The simplified propulsive gross thrust vector in the velocity axes is given by Equation (198).

$$\left[F_p\right]_v = \begin{bmatrix} T\cos(\alpha+\tau_1)\cos\beta \\ T\{-\cos(\alpha+\tau_1)\sin\beta\cos\gamma_1 + \sin(\alpha+\tau_1)\sin\gamma_1\} \\ T\{-\cos(\alpha+\tau_1)\sin\beta\sin\gamma_1 + \sin(\alpha+\tau_1)\cos\gamma_1\} \end{bmatrix} \tag{198}$$

4.2.5. Force Equations of Motion in the Velocity Axes

Substituting Equations (193), (195), (196), (197) and (198) into Equation (189) provides the general performance equations of motion, provided by Equation (199).

$$\begin{bmatrix} -D + \{T\cos(\alpha+\tau_1)\cos\beta\} - mg\sin\gamma_2 = m\dot{V} \\ Y\cos\gamma_1 + L\sin\gamma_1 + T\{-\cos(\alpha+\tau_1)\sin\beta\cos\gamma_1 + \sin(\alpha+\tau_1)\sin\gamma_1\} = mV\dot{\gamma}_3\cos\gamma_2 \\ Y\sin\gamma_1 - L\cos\gamma_1 + T\{-\cos(\alpha+\tau_1)\sin\beta\sin\gamma_1 + \sin(\alpha+\tau_1)\cos\gamma_1\} + W\cos\gamma_2 = -mV\dot{\gamma}_2 \end{bmatrix}_v \quad (199)$$

The tumble manoeuvre is a minimum radius loop and as such may utilise the same simplifying assumptions as a pull-up manoeuvre or loop. The tumble can be considered a manoeuvre that is coordinated in the vertical or pitching plane with no rate of turn or sideslip. The simplifying assumptions that will be used in the modelling of the tumble manoeuvre are provided in Table 34.

Table 34: Simplifying assumptions for the force equations of motion

Simplification No.	Simplification	Description
1	$\gamma_1 = 0$	No bank angle
2	$\dot{\gamma}_3 = 0$	No rate of turn
3	$\beta = 0$	No sideslip

Using these simplifying assumptions, the force equations of motion can be simplified to Equation (200), acting in the velocity axes.

$$\begin{bmatrix} T\cos(\alpha+\tau_1) - D - mg\sin\gamma_2 = m\dot{V} \\ Y = 0 \\ -L - T\sin(\alpha+\tau_1) + mg\cos\gamma_2 = -m\dot{\gamma}_2 \end{bmatrix}_v \quad (200)$$

With the force equations of motion having been derived in the velocity axes (Equation (200)), the force equations in the three axes directions can be rearranged to determine various parameters of a longitudinal manoeuvre.

Using the force equation in the X direction of the velocity axes, the terms can be rearranged to provide the linear acceleration in the velocity frame. This is shown by Equation (201). The linear accelerations in the velocity axes are thus a function of the sum of the forces in the X direction of the velocity axis and the mass of the aircraft.

$$\dot{V} = \frac{T\cos(\alpha + \tau_1) - D - mg\sin\gamma_2}{m} \tag{201}$$

Using the definition for the instantaneous rate of pitch, $\dot{\gamma}_2 = \frac{V}{R}$, and the force in the Z direction of the velocity axes, an expression for the radius of a longitudinal looping manoeuvre can be obtained. This is given by Equation (202).

$$R = \frac{mV^2}{L + T\sin(\alpha + \tau_1) - mg\cos\gamma_2} \tag{202}$$

Equation (202) can be developed further by including the load factor. The load factor on an aircraft is the sum of the forces in the normal direction (of the particular set of axes in question) divided by the weight of the aircraft. Taking an "mg" term out of the denominator of Equation (202) leads to the expression $mg\left(\frac{L+T\sin(\alpha+\tau_1)}{mg} - \cos\gamma_2\right)$. The term $\left(\frac{L+T\sin(\alpha+\tau_1)}{mg}\right)$ is the sum of the forces in the Z direction (normal or vertical direction) of the velocity axes and is the load factor in the velocity axes. Using this definition, Equation (202), can be rewritten as Equation (203), which defines the radius of a longitudinal looping manoeuvre in terms of the velocity, gravitational acceleration, the load factor and the flight path angle.

$$R = \frac{V^2}{g(n - \cos\gamma_2)} \tag{203}$$

Equation (203) can be used to determine the radius for a longitudinal looping manoeuvre from a very large loop to a tumble manoeuvre (minimum radius loop). In the case of a minimum radius loop additional forces will develop in the normal direction due to the high angle of attack nature of the manoeuvre. Along with high angle of attack normal forces, high angle longitudinal forces must also be accounted for and will influence the acceleration given by Equation (201). These high angle of attack forces are discussed further

in §4.4, while the contribution of the additional forces to the load factor (in both the velocity and body axes) is addressed in §4.5.

4.3. Moments in the Body Reference Axes

Unlike the force equations of motion, the moment components of the equations of motion remain in the body axes. The reason behind this decision is so that the pitching moment component of the rotational equations of motion can be used to determine the pitch angle of the aircraft. The pitch angle was used with Equation (5) and the flight path angle of the aircraft to determine the angle of attack of the aircraft. The analysis of the moments in the body reference frame will yield aircraft rates and angles relative to the horizontal, which can then be used to determine the angular displacements along the manoeuvre (the pitch angle in this case).

The full rotational equations of motion in the body axis are given by Equation (7). Given that the tumble manoeuvre has been assumed to take place purely in the longitudinal plane, some simplifying assumptions can be made. These assumptions omit any angular accelerations and velocities in the lateral-direction plane. These simplifications are provided in Table 35.

Table 35: Simplifying assumptions for the moment equations of motion

Simplification No.	Simplification	Description
1	$\dot{p} = 0$	Zero angular acceleration in roll
2	$\dot{r} = 0$	Zero angular acceleration in yaw
3	$p = 0$	Zero angular velocity in roll
4	$r = 0$	Zero angular velocity in yaw
5	$h'_x = h'_y = h'_z = 0$	No engine gyroscopic moments

With the simplifying assumptions provided in Table 35, the moment components of the equations of motion (in the body frame) reduce to Equation (204).

$$\begin{bmatrix} L = 0 \\ M = I_y \dot{q} \\ N = 0 \end{bmatrix} \tag{204}$$

Applying the simplifying assumptions presented in Table 35, along with zero angular displacements in both roll and yaw ($i.e. \phi = \psi = 0$), the kinematic relationships provided in Equation (12) can also be simplified and reduce to Equation (205)

$$\begin{bmatrix} \dot{\phi} = 0 \\ \dot{\theta} = q \\ \dot{\psi} = 0 \end{bmatrix} \tag{205}$$

Taking the derivative of the second term in Equation (205), results in the expression $\ddot{\theta} = \dot{q}$, which can then be substituted into Equation (204), and leads to the development of Equation (206).

$$\begin{bmatrix} L = 0 \\ M = I_y \ddot{\theta} \\ N = 0 \end{bmatrix} \tag{206}$$

Equation (206) can be used to obtain the acceleration in pitch by calculating the total moments acting on the aircraft (in the body axes) and then dividing by the pitch inertia (I_y) of the aircraft. The acceleration in pitch can then be used to determine the pitch velocity and angular displacement in pitch at each point during a tumble manoeuvre (discussed further in §4.6).

The moments acting on the aircraft are related to the forces developed. As discussed in §4.2 the forces fall into the high angle of attack regime during a tumble manoeuvre. Along with these high angle of attack forces, the moment arm from the centre of gravity of the aircraft to the line of action of the force, needs to be determined to obtain the moments acting on the aircraft. While moment arms are fixed for low angle of attack aerodynamics of lifting surfaces, the moment arms for high angle of attack aerodynamics are variable, shifting as the angle of attack is increased. Models to capture the variability of these moment arms are discussed in §4.4, along with the high angle of attack forces for propulsive unit, fuselage, wing and tail.

4.4. High Angle of Attack Aerodynamics

It is evident from video footage of tumble manoeuvres, that the aircraft pitches to large angles of attack, as seen in Figure 104. Pitching to these large angles aids in decelerating the aircraft and generates additional forces in the lift direction, from all surfaces of the aircraft (not solely the wing), allowing the pilot to rotate the aircraft around in the smallest possible space.

§4.4.1 - 4.4.4 outline the forces in both the velocity and body axes for the propeller, wing, fuselage and tail.

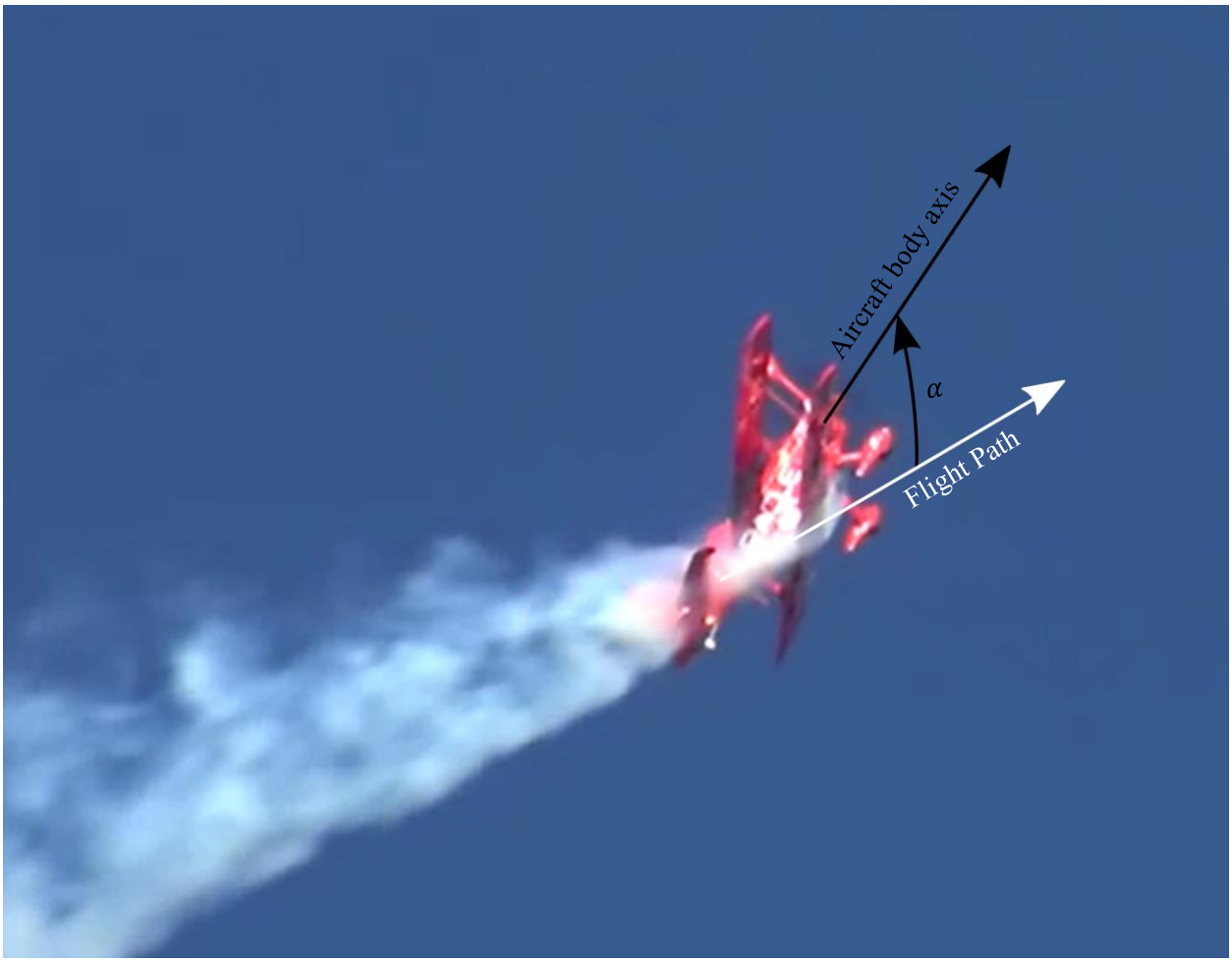

Figure 104: Illustration of high alpha flight during a tumble manoeuvre

4.4.1. Propeller

The propeller plays a vital role in performing a tumble manoeuvre. Normal forces generated by the propeller aid in rotating the aircraft in the desired direction. The slipstream velocity provides tail authority at low free-stream velocities and high angles of attack. Without the secondary propeller effects, a tumble manoeuvre would not be possible in an aerobatic aircraft. At lower angles of attack the propeller produces a thrust force in the longitudinal direction and a negligible normal force in the vertical direction. The forces generated by the propeller in the velocity axis and body axis at high angles of attack are provided in Figure 105.

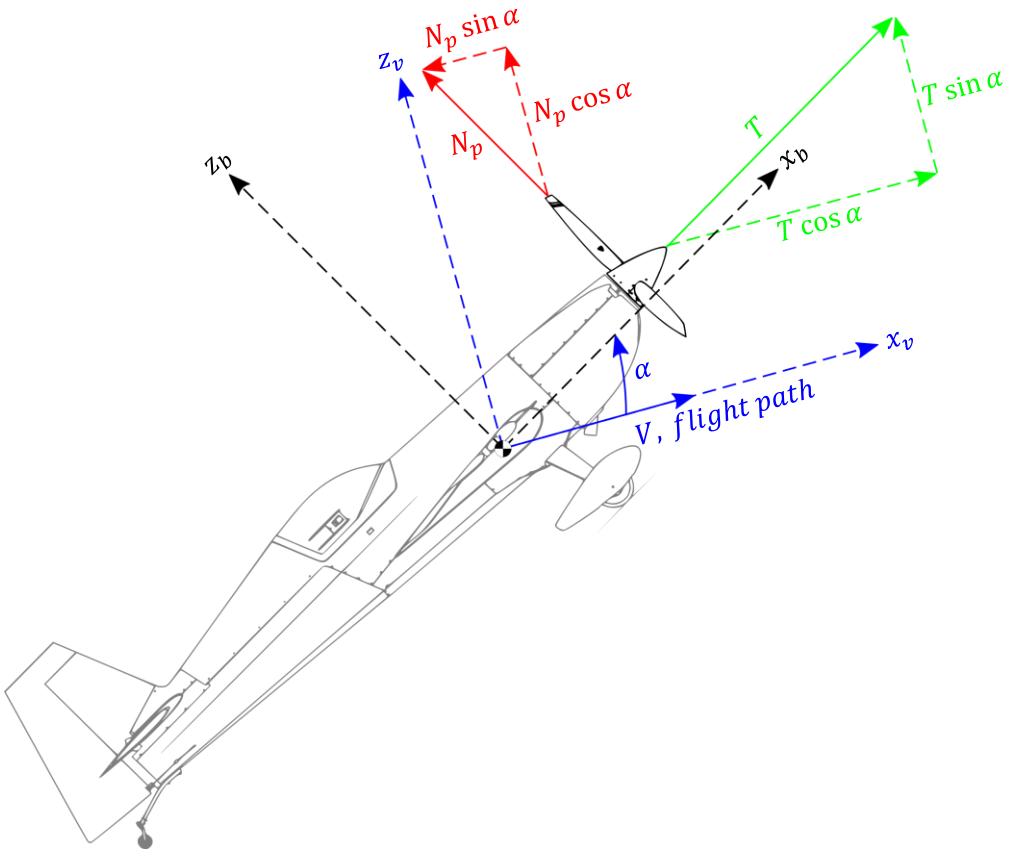

Figure 105: Propeller forces at high angles of attack in the body and velocity axes

The X and Z forces in the velocity axis are provided in Equations (207) and (208) respectively, while the forces in the X and Z direction of the body axis are provided in Equations (209) and (210) respectively.

$$X_v = T \cos \alpha - N_p \sin \alpha \tag{207}$$

$$Z_v = T \sin \alpha + N_p \cos \alpha \tag{208}$$

$$X_b = T \tag{209}$$

$$Z_b = N_p \tag{210}$$

Where:

- T is the propeller thrust [N]
- N_P is the propeller normal force [N]
- α is the angle of attack [deg]

4.4.2. Wing

The forces acting on the wing at high angles of attack are presented in Figure 106 in the velocity axis (a) and the body axis (b). The wing is split into an inner and outer section. The inner wing section is blown by the propeller slipstream while the outer wing section is unaffected by the propeller slipstream. The inner wing section will thus be affected by two velocity components at higher angles of attack ($>\approx 20°$), the free-stream velocity and the propeller slipstream, while at lower angles of attack the propeller slipstream will be the only velocity component affecting the inner wing section. As such the inner wing section will be at a lower angle of attack than the angle of attack of the outer wing section. The inner wing velocity vectors angle relative to the longitudinal direction of the body axis is indicated in Figure 106 as α_I.

The X and Z forces in the velocity axis are provided in Equation (211) and (212) respectively. Equations (213) and (214) provide the X and Z forces in the body axis, respectively. What is evident in Equations (211)- (214), is that there are lift forces acting in what would traditional be the pure drag direction and drag forces acting in what would traditionally be the lift direction, creating additional forces in both directions.

$$X_v = -D_O - L_I \sin \Delta\alpha_W - D_I \cos \Delta\alpha_W \tag{211}$$

$$Z_v = L_O + L_I \cos \Delta\alpha_W - D_I \sin \Delta\alpha_W \tag{212}$$

$$X_b = L_I \sin \alpha_I - D_I \cos \alpha_I + L_O \sin \alpha - D_O \cos \alpha \tag{213}$$

$$Z_b = L_I \cos \alpha_I + D_I \sin \alpha_I + L_O \cos \alpha + D_O \sin \alpha \tag{214}$$

Where:

- L_I, L_O are inner and outer wing lift [N]
- D_O, D_I are the inner and outer wing drag [N]
- $\Delta\alpha_W$ is the angle between the free-stream velocity vector and the vector of the overall inner wing velocity [deg]

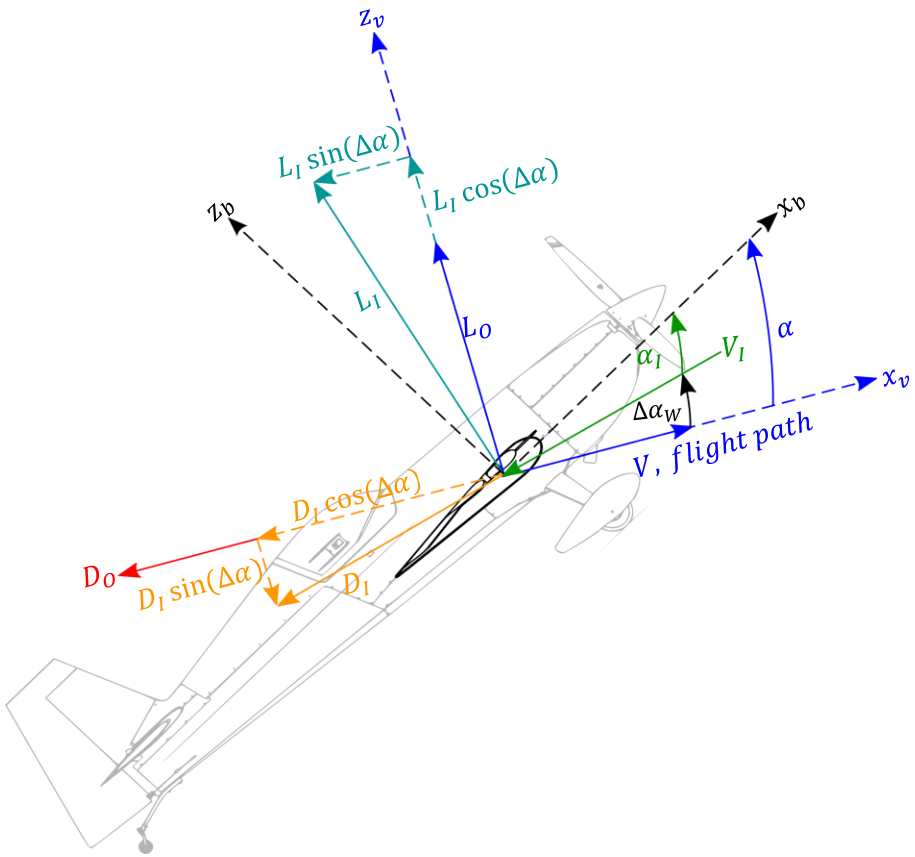

(a)

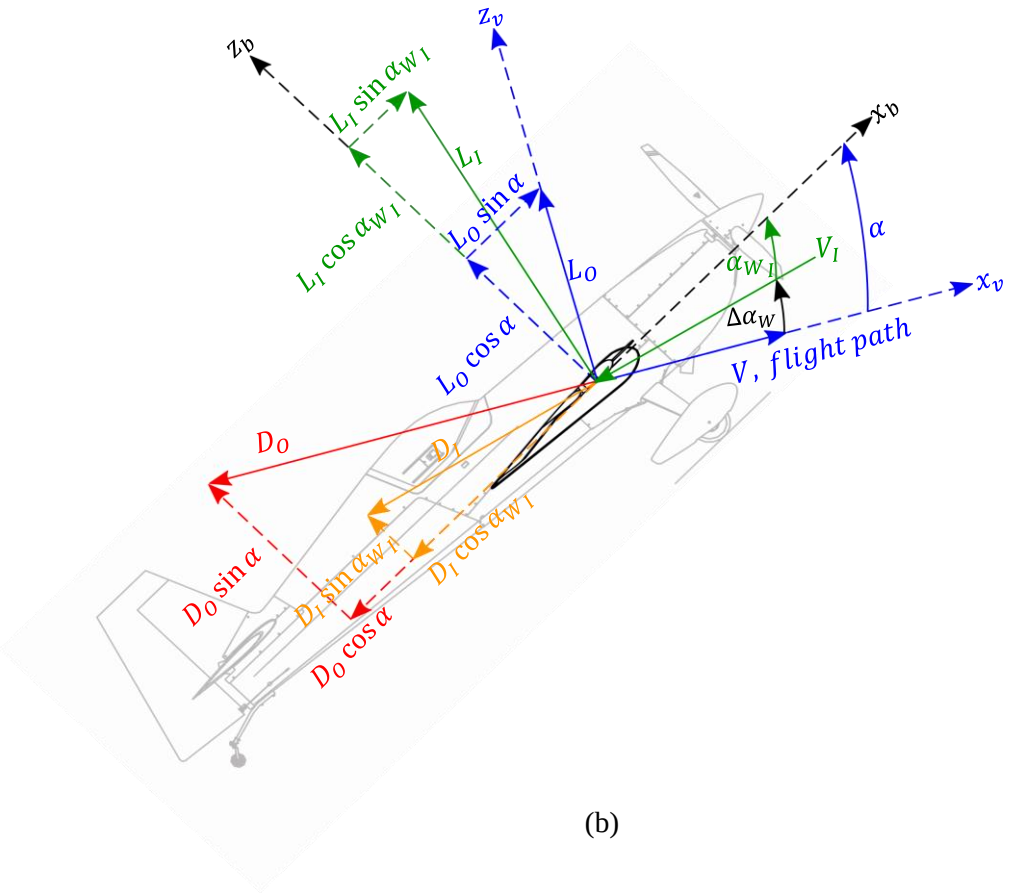

(b)

Figure 106: Wing aerodynamic forces at high angles of attack in (a) the velocity axis and (b) the body axis

4.4.3. Fuselage

The fuselage will be addressed in an identical fashion to the inner wing section in that the fuselage will be affected by the propeller slipstream. At lower angles of attack ($<\approx 20°$) the propeller slipstream velocity will be the sole velocity component, while at higher angles of attack the velocity vector will consist of the propeller slipstream as well as the free stream velocity.

The forces developed on the fuselage at high angles of attack are presented in Figure 107. The X and Z forces in the velocity axis are provided in Equation (215) and (216) respectively. Equations (217) and (218) provide the X and Z forces in the body axis, respectively.

$$X_v = -L_f \sin \Delta\alpha_f - D_f \cos \Delta\alpha_f \quad (215)$$

$$Z_v = L_f \cos \Delta\alpha_f - D_f \sin \Delta\alpha_f \quad (216)$$

$$X_b = -D_f \cos \alpha_f + L_f \cos \alpha_f \quad (217)$$

$$Z_b = L_f \sin \alpha_f + D_f \sin \alpha_f \quad (218)$$

Where:

- L_f is the fuselage lift [N]
- D_f is the fuselage drag [N]
- $\Delta\alpha_f$ is the angle between the free-stream velocity vector and the vector of the overall fuselage velocity [deg]
- α_f is the angle between the vector of the overall fuselage velocity and the body axis x_b [deg]

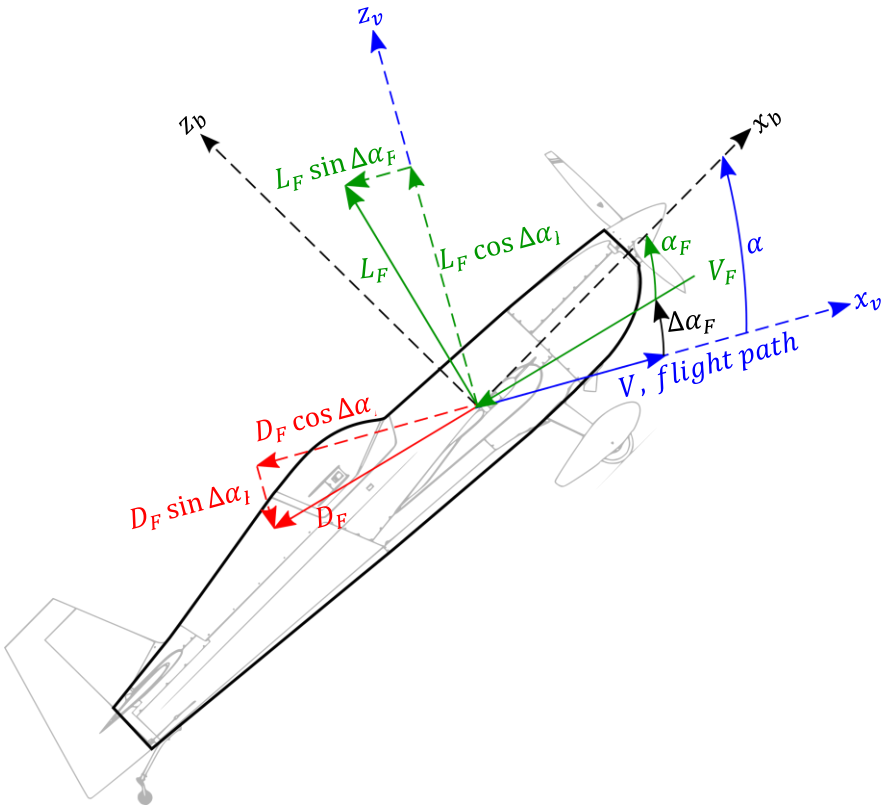

(a)

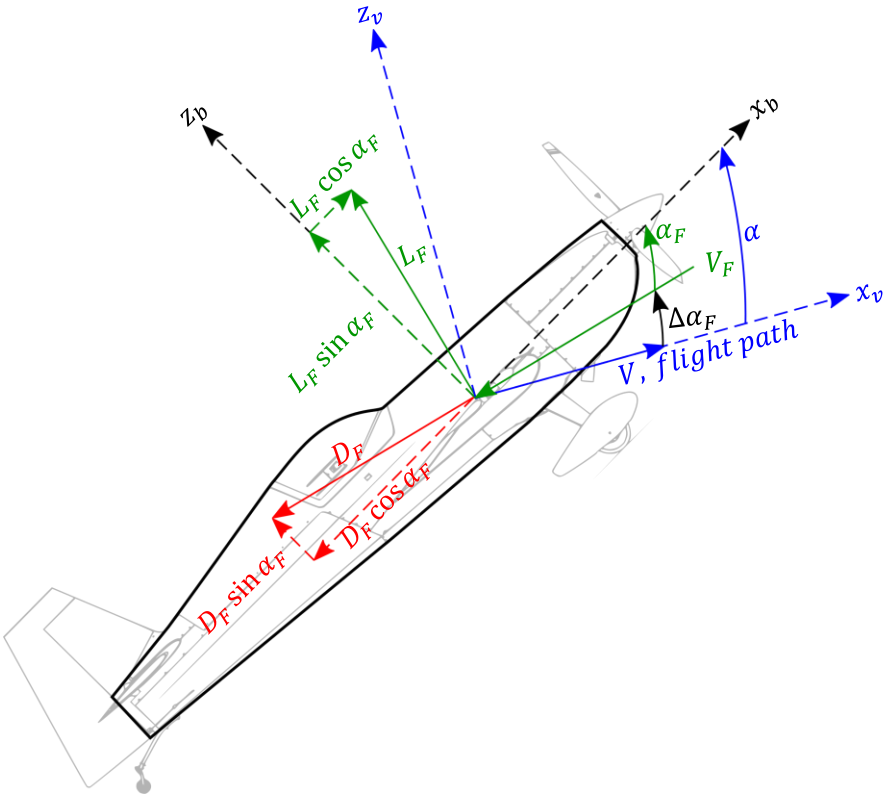

(b)

Figure 107: Fuselage aerodynamic forces at high angles of attack in (a) the velocity axis and (b) the body axis

4.4.4. Tail

The high angle of attack forces generated by the tail are presented in Figure 109. The tail surface is blown by the propeller slipstream, much like the inner wing section and the fuselage. The tail velocity vector is also influenced by a rotational component, in addition to the propeller slipstream and the free stream velocity (at higher angles of attack). The three velocity components making up the total tail velocity vector are illustrated in Figure 108.

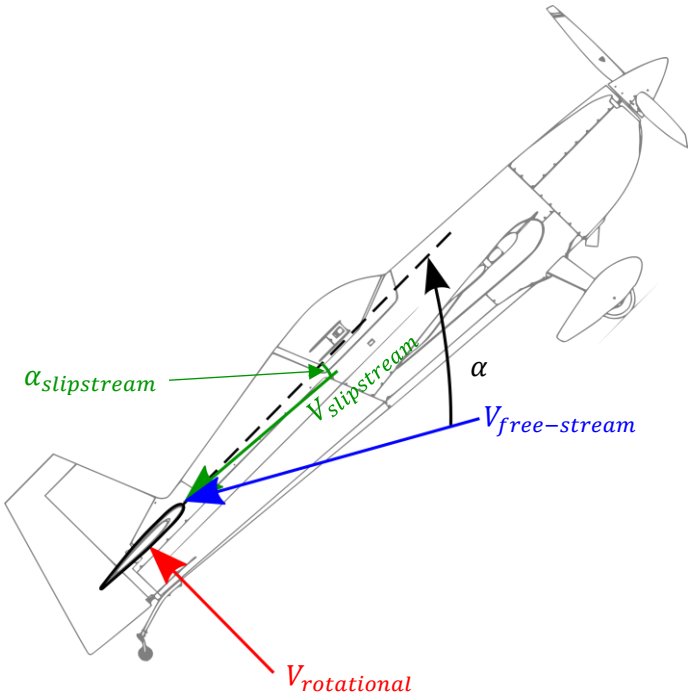

Figure 108: Tail velocity components

The forces developed on the horizontal stabiliser at high angles of attack are presented in Figure 109. The X and Z forces in the velocity axis are provided in Equation (219) and (220) respectively. Equations (221) and (222) provide the X and Z forces in the body axis respectively. It should be noted that the lift force acting on the horizontal stabiliser surface is shown to be acting in the positive Z direction of both the velocity and body axes. However, in the tumble manoeuvre the lift force acting on the horizontal stabiliser will act in the negative Z direction in both the velocity and body axes due to the deflection direction of the elevator surface. This will be accounted for by simply changing the sign in front of the lift force. This will correct both the force and resulting moment from the force.

$$X_v = D_t \cos \Delta\alpha_t - L_t \sin \Delta\alpha_t \quad (219)$$

$$Z_v = L_t \cos \Delta\alpha_t - D_t \sin \Delta\alpha_t \quad (220)$$

$$X_b = L_t \sin \alpha_t - D_t \cos \alpha_t \quad (221)$$

$$Z_b = L_t \cos \alpha_t + D_t \sin \alpha_t \quad (222)$$

Where:

- L_t is the horizontal stabiliser lift [N]
- D_t is the horizontal stabiliser drag [N]
- $\Delta\alpha_t$ is the angle between free-stream velocity vector and the vector of the overall horizontal tail velocity [deg]
- α_t is the angle between vector of the overall horizontal stabiliser velocity and the body axis x_b [deg]

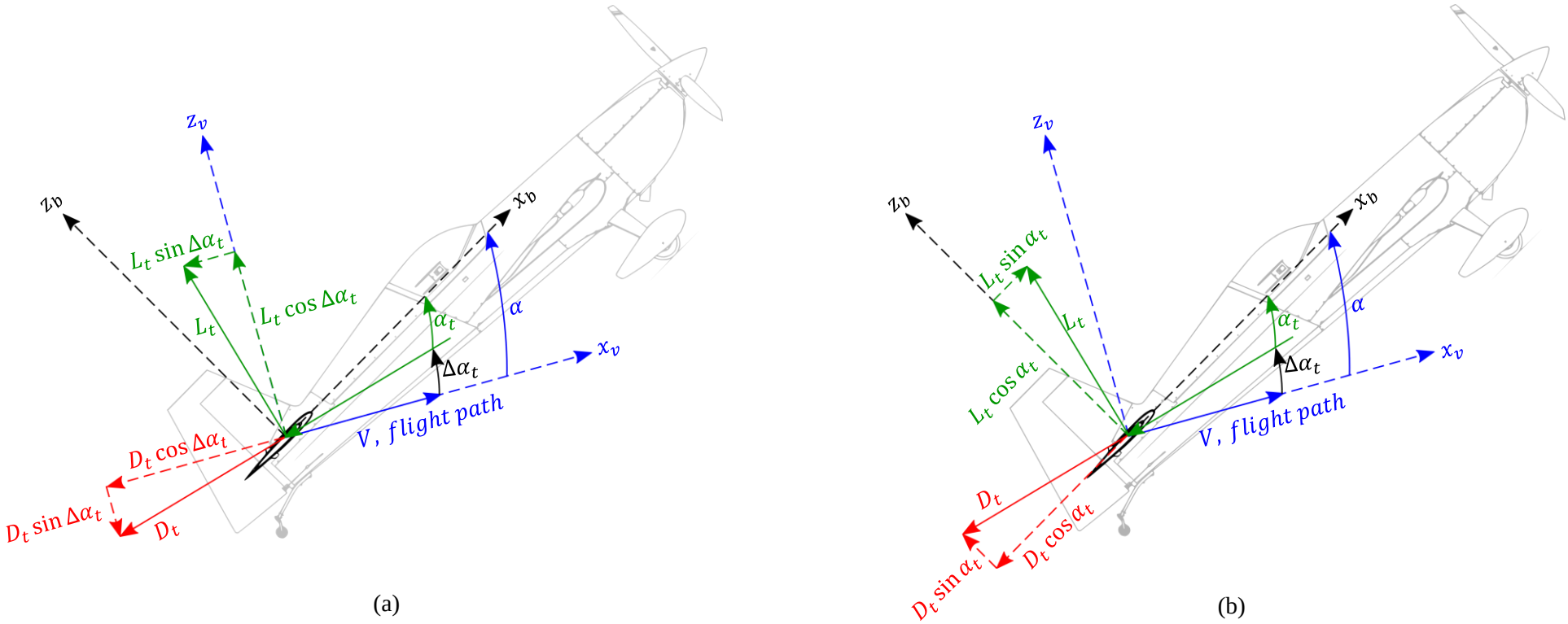

Figure 109: Tail aerodynamic forces at high angles of attack in (a) the velocity axis and (b) the body axis

4.5. Load Factor Calculation at High Angles of Attack

Aircraft forces and force components in both the velocity and body axes at high angles of attack have been illustrated in Figure 105 - Figure 109. The load factor required to determine the radius of a looping manoeuvre is defined in Equation (203), relative to the flight path vector. The sum of the forces in the Z direction is required in the velocity axis. These forces were used to determine a net acceleration in the normal or Z direction of the velocity axis. Gravitational accelerations were included in the same direction. This is illustrated by Figure 110.

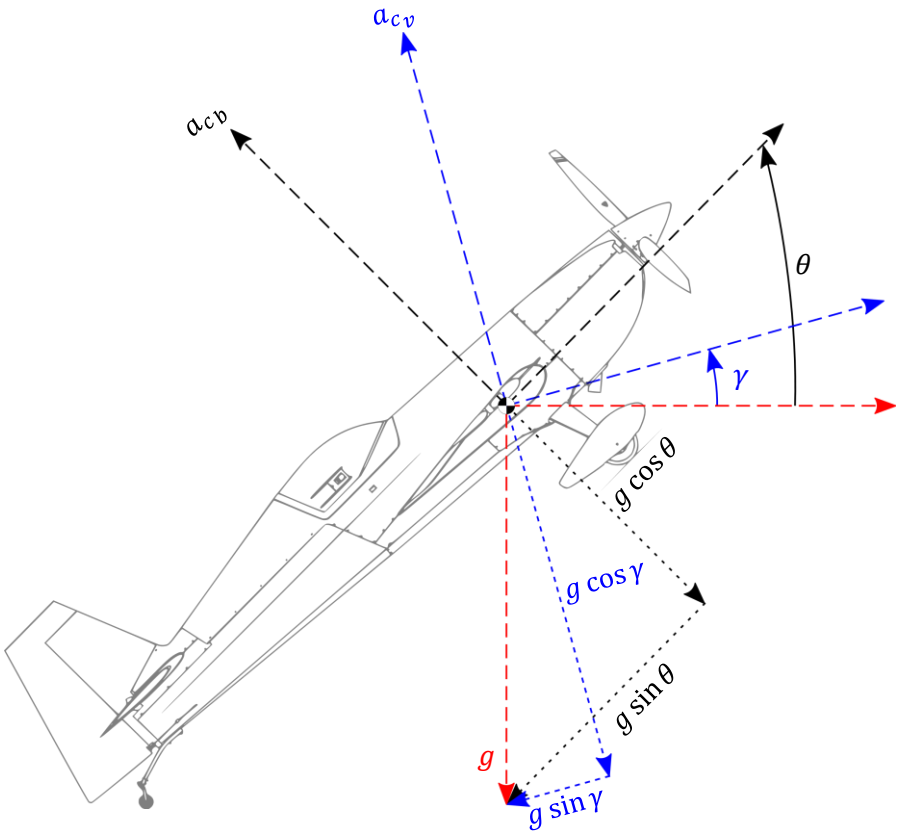

Figure 110: Aircraft centrifugal acceleration directions in the velocity and body axes with gravitational acceleration components

In a conventional loop or pull-up manoeuvre, the angle of attack is kept at or below the stall angle. The velocity and body axes are roughly aligned. In these conventional cases, the only aerodynamic force that contributes to the centrifugal acceleration is the total lift. In performing a tumble manoeuvre, the aircraft pitches to very large angles of attack ($\approx 60° - 80$ °), leading to components of the propulsive unit adding to the forces in the normal direction. Forces generated by the fuselage also become much larger than at higher angles of attack and must be considered.

Velocity Axes

The sum of forces in the Z direction of the velocity axes is given by Equation (223). Forces acting towards the centre of the loop, pulling the aircraft into the manoeuvre were taken as positive. Any forces acting outwards, pulling the aircraft out of the manoeuvre were taken as negative. The component of aircraft weight acting in the normal direction of the velocity axes was included in the force summation.

$$\begin{aligned}\Sigma F_{Z_v} = L_O + L_{W_I}\cos(\Delta\alpha_{w_I}) - D_{W_I}\sin(\Delta\alpha_{w_I}) + L_f\cos(\Delta\alpha_f) - D_f\sin(\Delta\alpha_f) \\ + L_t\cos(\Delta\alpha_t) - D_t\sin(\Delta\alpha_t) + T\sin\alpha + N_p\cos\alpha - W\cos\gamma\end{aligned} \quad (223)$$

Taking the sum of the forces developed in Equation (223) and dividing by the mass of the aircraft provides the centrifugal acceleration of the aircraft in the velocity axis. This is shown in Equation (224).

$$\begin{aligned}F_{Z_v} = ma_z \rightarrow a_z = \frac{F_{Z_v}}{m} \\ = \frac{L_O + L_{W_I}\cos(\Delta\alpha_{w_I}) - D_{W_I}\sin(\Delta\alpha_{w_I}) + L_f\cos(\Delta\alpha_f) - D_f\sin(\Delta\alpha_f) + L_t\cos(\Delta\alpha_t) - D_t\sin(\Delta\alpha_t) + T\sin\alpha + N_p\cos\alpha - mg\cos\gamma}{m}\end{aligned} \quad (224)$$

The component of gravitational acceleration in the normal direction of the velocity axis is provided by Equation (225).

$$a_{gravitational} = g\cos\gamma \quad (225)$$

The total normal acceleration is the summation of the centrifugal acceleration and the component of gravitational acceleration, as shown in Equation (226).

$$a_{v_{Total}} = a_{Centrifugal} + a_{gravitational} \quad (226)$$

Substituting Equations (224) and (225) into Equation (226) leads to the development of Equation (227)

$$n_v g = \frac{L_O + L_{W_I}\cos(\Delta\alpha_{w_I}) - D_{W_I}\sin(\Delta\alpha_{w_I}) + L_f\cos(\Delta\alpha_f) - D_f\sin(\Delta\alpha_f) + L_t\cos(\Delta\alpha_t) - D_t\sin(\Delta\alpha_t) + T\sin\alpha + N_p\cos\alpha}{m} - g\cos\gamma + g\cos\gamma \quad (227)$$

Solving Equation (227) for n_v leads to Equation (228), which is the load factor or total normal acceleration in the velocity axis.

$$n_v = \frac{L_{w_O} + L_{W_I}\cos(\Delta\alpha_{w_I}) - D_{W_I}\sin(\Delta\alpha_{w_I}) + L_f\cos(\Delta\alpha_f) - D_f\sin(\Delta\alpha_f) + L_t\cos(\Delta\alpha_t) - D_t\sin(\Delta\alpha_t) + T\sin\alpha + N_p\cos\alpha}{W} \quad (228)$$

Body Axes

An identical modelling approach was taken in developing the load factor in the body axis and is provided by Equation (229).

$$n_b = \frac{L_{w_O}\cos\alpha + L_{W_I}\cos\alpha_{w_I} + D_{W_O}\sin\alpha + D_{W_I}\sin\alpha_{w_I} + L_f\cos\alpha_f + D_f\sin\alpha_f + L_t\cos\alpha_t + D_t\sin\alpha_t + N_p}{W} \quad (229)$$

4.6. Mathematical Modelling

The mathematical modelling of the tumble was performed as a series of linear segments of equal flight path angle (γ) increments, varying from 0° flight path angle to 360° flight path angle. An illustration of this can be seen in Figure 111. It should be noted that segments illustrated in Figure 111 are exaggerated or magnified for graphic purposes. This range of angles will capture the entry and exit of the tumble as well as the tumble itself. The approximation of linear segments only holds if the segment length is quite small $(L_{increment} \ll L_{aircraft})$, which can only be achieved through small angle increments. Angle increments of 1° or less were sufficiently small enough for the approximation to hold true. A flowchart is provided in Figure 112 as an overview of the modelling procedure for the tumble manoeuvre while a more detailed explanation of the procedure is provided throughout §4.6.

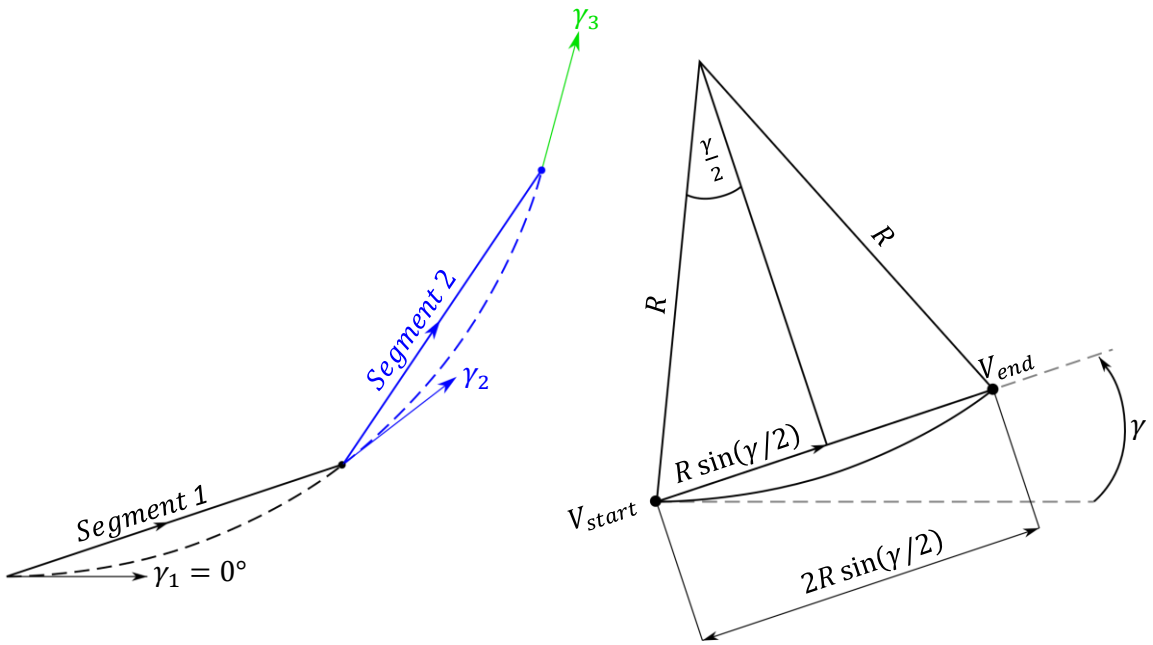

Figure 111: Tumble segments illustration

A number of parameters will be calculated for each segment, where the outputs from the previous segment are used as the inputs for the next segment (with the exception of the first segment where the initial parameters will be set). The procedure for calculating the required variable at each segment is outlined below.

Tumble Procedure

The modelling of each segment began by obtaining the starting x_E and z_E locations. The starting location (in both the X and Z directions of the Earth axes) of each segment was determined by adding the length of the previous segment to the starting location of the previous segment. This is seen in Equation (230) for the distance change in the X direction and Equation (231) for the distance change in the Z direction. For the first segment the x_e and z_e locations may be set. In both Equations (230) and (231) the "i" subscript refers to the segment number in question.

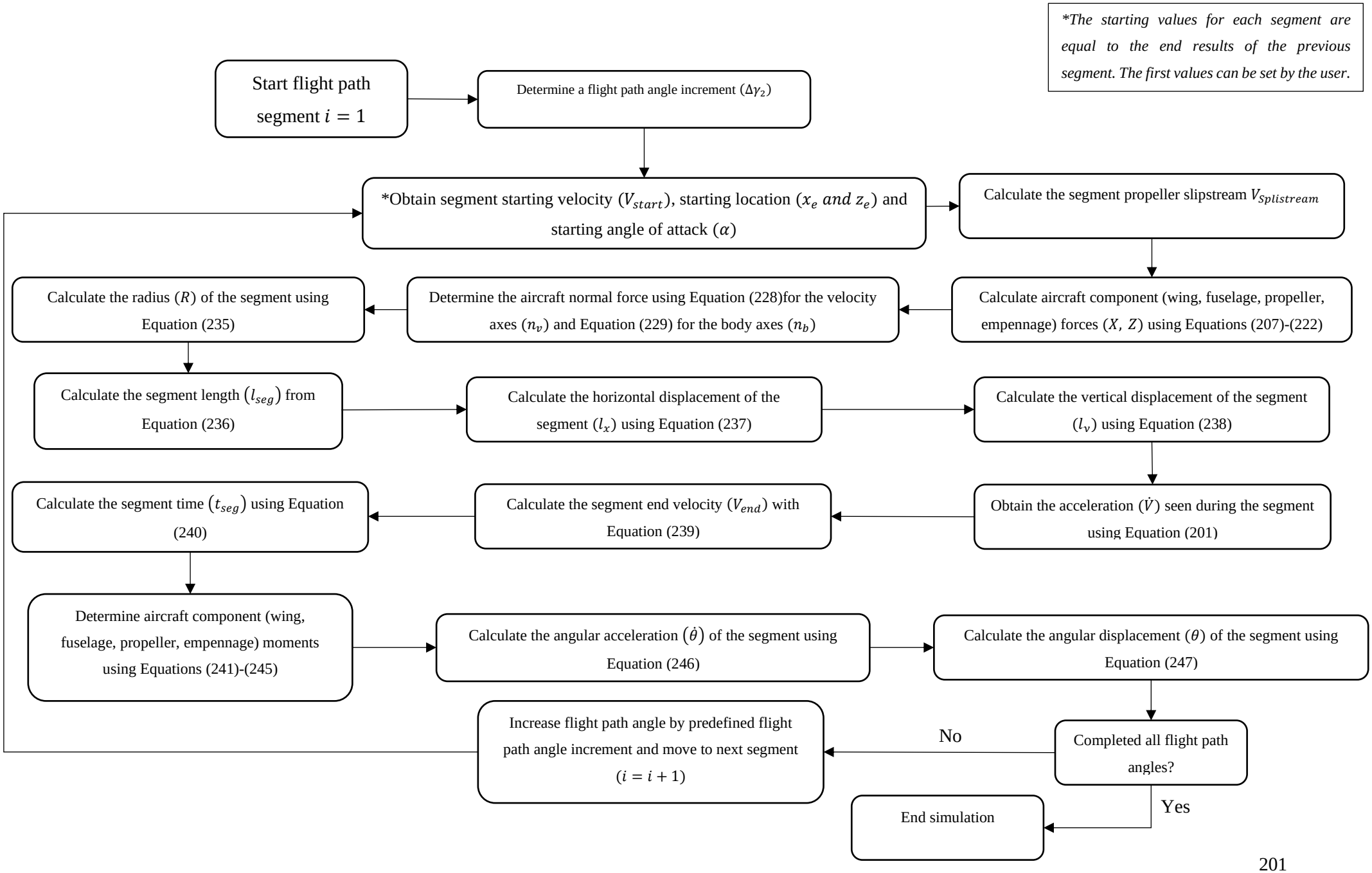

201

Figure 112: Mathematical modelling flowchart

$$x_{E_i} = x_{E_{i-1}} + l_{x_{i-1}} \tag{230}$$

$$z_{E_i} = z_{E_{i-1}} + l_{z_{i-1}} \tag{231}$$

The starting velocity and angle of attack of each segment may be taken as the end velocity and angle of attack of the previous segment, given by Equations (232) and (233) respectively

$$V_{Start_i} = V_{end_{i-1}} \tag{232}$$

$$\alpha_{Start_i} = \alpha_{end_{i-1}} \tag{233}$$

Given the starting velocity of the segment and the angle of attack at the start of the segment, the propeller slipstream velocity may then be determined as a function of the angle of attack of the aircraft and the velocity. This is seen in Equation (234).

$$V_{Slipstream_i} = f(V_{start_i} \cos(\alpha_{start_i})) \tag{234}$$

While the exact angle of the propeller slipstream velocity relative to the various aircraft surfaces was not known, an angle of between 0° and 5° was selected. The angle for each surface was dependent on the surface in question. With the angle of the propeller slipstream set and the free-stream velocity known, the resultant angle of attack of the inner and outer wing surfaces, the fuselage and the tail can be determined, as discussed in §4.4.

With the velocity magnitude and angle of each surface known, the forces acting on each respective surface as well the angles of each surface relative to the body and velocity axes can be determined. The various forces can then be used to determine the load factor acting on the aircraft in both the body and velocity axes. With the load factor and segment starting velocity known the radius of the maneouve at the current segment can be determined. This is done with the use of Equation (235), which is effectively Equation (203). There is a difference included in Equation (235). The term $0.5\left(V_{start_i} - V_{start_{i-1}}\right)$ has been included in Equation (235) as an average velocity over the segment.

$$R_i = \frac{\left[V_{start_i} - 0.5\left(V_{start_i} - V_{start_{i-1}}\right)\right]^2}{g[n_i - \cos(\gamma_i + 0.5\gamma_{seg})]} \tag{235}$$

Using the radius of the segment determined in Equation (235), the length and height of the segment can be obtained by assuming that the arced motion of the profile is approximately linear. This will be true for very small angular segment increments (the smaller the increment the more accurate this approximation becomes). Figure 111 illustrates the linear approximation over the arced path. Using the radius over the segment as well as the change in angle over the segment (which is identical for each segment since the flight path angle increments are set) the total linear distance over the segment can be calculated. The linear distance over a segment is provided by Equation (236).

$$l_{seg_i} = 2R_i \sin\left(\frac{\gamma_{seg}}{2}\right) \tag{236}$$

The angle of the straight line of the linear segment relative to the horizontal is equal to the flight path angle. Thus, knowing the length of the segment and the angle of that length relative to the horizontal, the horizontal and vertical changes in that segment can then be calculated and are provided by Equations (237) and (238) respectively.

$$l_{x_i} = l_{seg_i} \cos\left[\gamma_i + \left(\frac{\gamma_{seg}}{2}\right)\right] \tag{237}$$

$$l_{z_i} = l_{seg_i} \sin\left[\gamma_i + \left(\frac{\gamma_{seg}}{2}\right)\right] \tag{238}$$

Having previously obtained the forces acting on the aircraft (for each component) in the current segment, the acceleration (or deceleration) can be obtained using Equation (201). With the acceleration, the velocity at the end of the segment can then be calculated using Equation (239).

$$\mathrm{V}_{\mathrm{end}_i} = \sqrt{V_{start_i}^{\ 2} + 2\dot{V} l_{seg_i}} \tag{239}$$

Having the speed delta over the segment length as well as the distance of the segment, the time taken for the aircraft to traverse each segment can be calculated using Equation (240). The total time for the manoeuvre can be found by summing the time for each segment.

$$t_{seg_i} = \frac{l_{seg_i}}{0.5\left(V_{start_i} + V_{end_i}\right)} \tag{240}$$

With the relevant linear parameters determined, the angular parameters should be addressed. The angular acceleration in pitch (in the body axes) can be obtained using Equation (206). The moments created by the various aircraft components can be seen in Equations (241)-(245) for the propeller, inner wing section, outer wing section, fuselage and horizontal tail respectively.

$$M_{Propeller} = TZ_p + N_p X_p \tag{241}$$

$$M_{wing-inner} = L_{W_I}\cos(\alpha_{W_I})\,X_{W_I} + L_{W_I}\sin(\alpha_{W_I})\,Z_{W_I} - D_{W_I}\cos(\alpha_{W_I})Z_{W_I} + D_{W_I}\sin(\alpha_{W_I})X_{W_I} \tag{242}$$

$$M_{wing-outer} = L_{W_O}\cos(\alpha)X_{W_O} + L_{W_O}\sin(\alpha)\,Z_{W_O} - D_{W_O}\cos(\alpha)\,Z_W + D_{W_O}\sin(\alpha)\,X_{W_O} \tag{243}$$

$$M_{fuselage} = -L_F\cos(\alpha_F)\,X_F - D_F\sin(\alpha_F)X_F \tag{244}$$

$$M_{tail} = L_t\cos(\alpha_t)\,X_t + L_t\sin(\alpha_t)\,Z_t - D_t\cos(\alpha_t)\,Z_t + D_t\sin(\alpha_t)\,X_t \tag{245}$$

Using the angular acceleration, the angular velocity (in the body axes) can be obtained with Equation (246). For the first segment the term $\dot{\theta}_{i-1}$ will be omitted from Equation (246).

$$\dot{\theta}_i = \ddot{\theta}_i t_{seg_i} + \dot{\theta}_{i-1} \tag{246}$$

The angular displacement or pitch angle of the aircraft can be obtained using the angular acceleration and is given by Equation (247). For the first segment the term θ_{i-1} will be omitted from Equation (247).

$$\theta_i = 0.5\left(\dot{\theta}_i + \dot{\theta}_{i-1}\right) + \theta_{i-1} \tag{247}$$

Finally, with the use of the pitch angle obtained by Equation (247) and the flight path angle (segment angle), the angle of attack can be obtained using Equation (5). This will determine the change in angle of attack over each segment. The change in angle of attack can then be used to determine the aerodynamic forces in the next segment.

The procedure described in §4.6 was solved using a series of scripts in Octave (.m files). The scripts used to model the tumble manoeuvre are provided in §8 APPENDIX A – OCTAVE MODELLING SCRIPTS.

5. RESULTS AND DISCUSSION

5.1. Introduction

Results are presented and discussed for various tumble manoeuvres that include variations in entry velocity, centre of gravity locations, masses and pitch inertias. The best overall tumble manoeuvre is presented first to the reader to provide an overview of the expected shape and size of the manoeuvre. Minimum radius tumbles for each entry velocity are then provided. The forces and moments that allow each of minimum radius tumbles to be performed are discussed. The results from the complete test matrix are then discussed. The complete set of results was not discussed first as a detailed understanding was required to assess why the various cases resulted in different manoeuvre sizes and shapes. The deficiencies in the failed tumble models are discussed in relation to the successful tumble models. An alternative strategy to the manoeuvre is examined in which the risk of the manoeuvre is marginally reduced. A comparison to video footage is presented as a form of validation for the model in the absence of flight test data.

5.2. Best Overall Tumble Overview

The best tumble is one in which the radius and size of the manoeuvre is minimised. The flight path of the best overall tumble manouevre is presented in Figure 113. The optimal tumble case occurred at a centre of gravity of $x_{cg} = 2.17$ m, an aircraft mass of $m = 742.88$ kg and a pitch inertia of $I_{yy} = 975.26$ kg·m^2. The entry velocity of the manoeuvre was 30 m/s. The engine was assumed to be operating at maximum power, providing maximum propeller thrust and slipstream throughout the manoeuvre. The manoeuvre exhibits an elongated shape with the aircraft traversing a greater horizontal than vertical distance. The manoeuvre extends to a maximum horizontal distance of 46.34 m and reaches a maximum height of 14.12 m. The manoeuvre is completed with the aircraft only having travelled ≈ 7 aircraft lengths forward and ≈ 2 aircraft lengths upward. The looping portion of the manoeuvre takes place over a width of 6.16 m and a height of 5.40 m. The tumble portion of the manoeuvre is performed in a space that is smaller in width and in height than the length of the aircraft. The total time taken to complete the manoeuvre was 5.02 s, which given the small distances travelled, is indicative of a large deceleration (loss in airspeed).

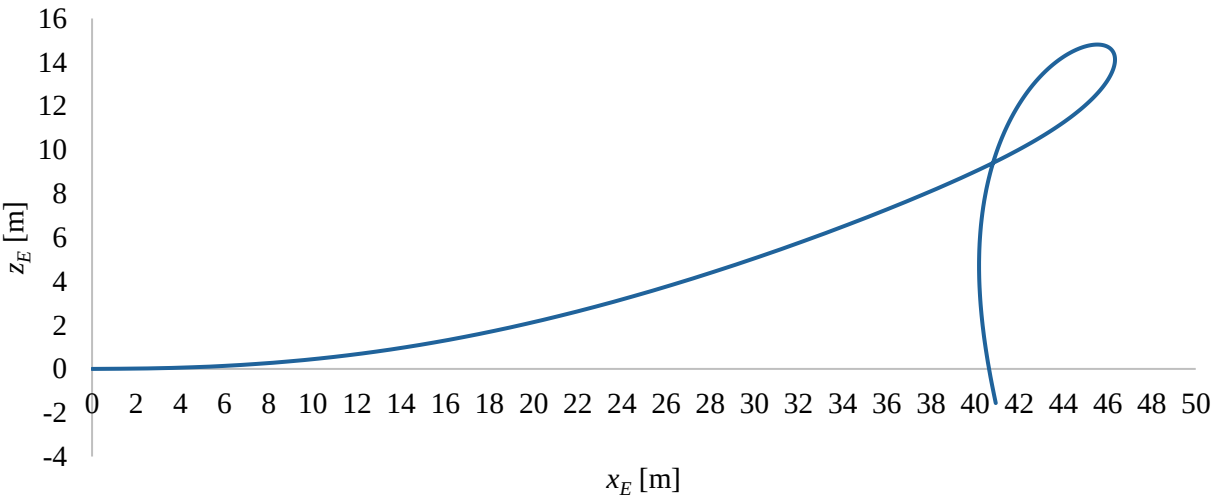

Figure 113: Smallest radius tumble manoeuvre flight path for an entry velocity of $V_{entry} = 30$ m/s

5.3. Minimum Radius Tumbles

5.3.1. Flight Path

The smallest radius tumble manoeuvres are presented in Figure 114 for entry speeds ranging from 25 m/s to 40 m/s, in increments of 5 m/s. Each of the tumble manoeuvres presented were obtained at the most rearward centre of gravity position ($x_{cg} = 2.17$ m). The mass of the aircraft for each manoeuvre was $m = 742.88$ kg, with a pitch inertia of $I_y = 975.26$ kg·m^2. The propeller thrust and slipstream were each set to 100 % throughout the entirety of the manoeuvres. The propeller normal force was set to 84 % of the values seen in §3.3.6. This was done as the initial values provided forces and moments that were in excess of what the Extra 330SC propeller was capable of.

Each of the tumble manoeuvres presented can be divided into 5 phases. The 40 m/s tumble case will be used to describe the various phases using the letters and flight path angles indicated in Figure 114. The flight path angles indicated may not be the same at the start of each phase for each tumble but should be within $\pm 10°$ of the values provided. The ***entry*** phase of the manoeuvre occurs from points $O - A$ and consists of a long (relative to other portions of the manoeuvre), flat and shallow inclination. From points $A - B$ the aircraft traverses the ***climb*** phase which sees the aircraft follow a tighter radial path with a steeper inclination. The climb phase terminates at the forwardmost point of the manoeuvre. The start of the climb phase is the entry point to the looping portion of the manoeuvre. Points $B - C$ is termed the ***backflip*** phase, in which the aircraft transitions from the forwardmost part of the manoeuvre to a completely inverted orientation. A small change in altitude is seen in this phase. The ***reversal*** phase involves a change in travel direction with the aircraft travelling back towards the direction of the entry point, while rotating to a nose-down aircraft orientation. This phase occurs from points $C - D$. Point D should occur near the cross-over point of the manoeuvre, where the aircraft passes back over the entry phase path. The reversal phase concludes the looping portion of the manoeuvre. The ***exit and recovery*** phase of the manoeuvre takes place from point D to the end of the manoeuvre and involves a downward and forward trajectory while the aircraft continues to rotate, attempting to enter a normal flight regime.

The entry phase for each tumble is near identical, until a horizontal distance of $X \approx 38$ m, after which the paths begin to deviate. Lower entry velocities deviate from the entry path sooner. The manoeuvres all follow the same long, shallow gradient paths, reaching a vertical height of $z_R \approx 8.5$ m in a horizontal distance of $x_E \approx 38$ m. Initially the aircraft travels forward a distance of $x_E \approx 7.5$ m before climbing. This is seen for all entry velocities. The start of the climb point to the end of the entry phase sees the aircraft undergo a horizontal displacement of $x_E \approx 30.5$ m and a vertical displacement of $z_E \approx 8.5$ m. This results in a climb angle of $\approx 15.5°$. In isolation, this result may seem unremarkable but is notable when considered in relation to the aircraft pitch angle. The climb phase of each of the manoeuvres occurs further away from the entry point with greater entry speed. The distance between points A and C and the distance between points B and D is also influenced by the entry velocity. Entry velocities of

20 m/s and 40 m/s show similar tumble shapes with a greater height (C_Z-A_Z = 8.07 m and 9.48 m respectively) over width (B_X-D_X = 5.77 m and 6.10 m, respectively).

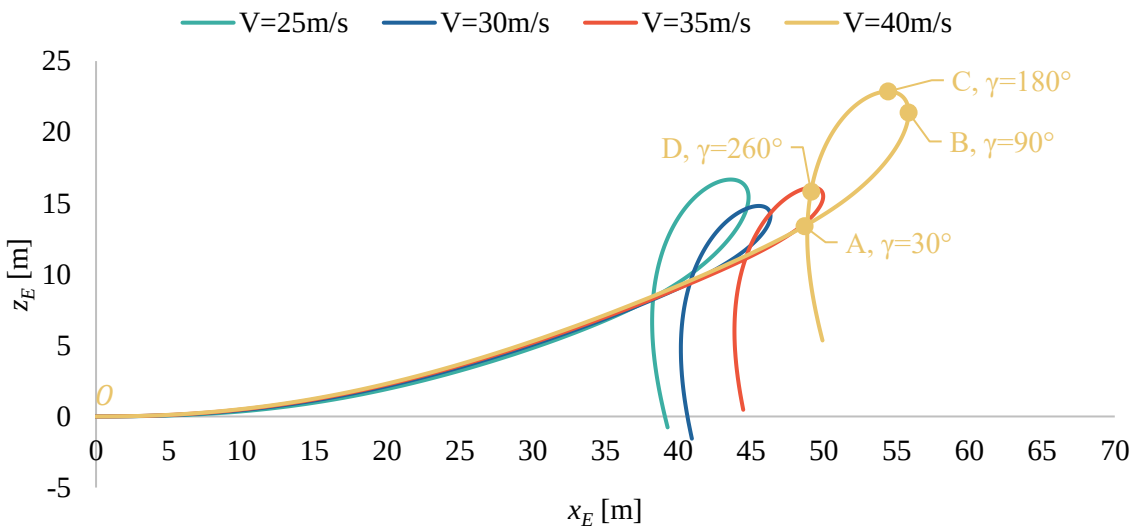

Figure 114: Smallest radius tumble manoeuvre flight paths for entry velocities of V_{entry} = 25 m/s, 30 m/s, 35 m/s and 40 m/s

Entry velocities of 30 m/s and 35 m/s show similar tumble shapes to one another with a marginally greater width (B_X-D_X = 5.29 m and 5.23 m, respectively) over height (C_Z-A_Z = 4.48 m and 4.02 m, respectively). The minimum radius tumble manoeuvre occurs at an entry velocity of 30 m/s, which is marginally below the stall speed of the aircraft (V_{stall} = 31.38 m/s). While it may appear that higher entry velocities take longer to complete (due to the longer distance covered in the entry phase for greater entry velocities), the phase times and completion times for each entry velocity are similar. This can be better understood by replotting Figure 114 with time markers at the start of each of the phases. This is shown in Figure 115. The time markers illustrate that the time taken to enter each phase of the manoeuvre is similar across all entry velocities.

The entry phase (concluding at point *A*) takes place in ≈ 2 s for each of the entry velocities presented. The distance at which each entry phase concludes is different for each entry velocity. Greater entry velocities result in entry phases that conclude at greater horizontal and vertical distances. An entry velocity of 40 m/s concludes the entry phase ≈ 10 m further horizontally and ≈ 4.8 m higher vertically than the 25 m/s entry velocity. While these distances may seem large in relation to the size of the manoeuvre, they are only slightly larger (10 m) and smaller (4.8 m) than the length of the aircraft (6.88 m). Such small distances are likely to go unnoticed by the vast majority of spectators. The time is near identical for each entry phase while the displacements are dissimilar, meaning that the velocities through the entry phase must be different for each entry case. Observing the time and distance travelled

in the entry phase of each of the tumble manoeuvres presented, it is evident that the entry phase is the longest phase of the entire manoeuvre both in terms of time and displacement.

The climb phases take place over $\approx 1\text{ s}-1.5\text{ s}$ depending on the entry velocity. The phase concludes at a total manoeuvre time of $\approx 3.1\text{ s}-3.5\text{ s}$. For each entry velocity the climb phase finishes at a flight path angle of $\gamma = 90°$. Entry velocities of 25 m/s, 30 m/s, 35 m/s and 40 m/s conclude the climb phase at vertical/horizontal distances of $44.84\text{ m}/15.41\text{ m}$, $46.34\text{ m}/14.12\text{ m}$, $49.96\text{ m}/15.49\text{ m}$ and $55.83\text{ m}/21.37\text{ m}$ respectively. The horizontal distances attained at the end of the climb phase are the forwardmost points in the manoeuvre for all entry velocities considered. The gradient of this phase is steeper for entry velocities of 25 m/s and 40 m/s, resulting in greater vertical displacements and phase times for those entry velocities. Entry velocities of 30 m/s and 35 m/s illustrate shallower climb gradients, reaching the end of the climb phase $\approx 0.4\text{ s}$ sooner than the other entry velocities. This difference in displacements in the climb phase directly influences the shape of the manoeuvre, resulting in either flatter or taller flight paths. Figure 115 demonstrates that an entry velocity of $30\text{ m/s} < V_{entry} < 35\text{ m/s}$ is ideal for the lowest displacement and time for the climb phase. While more detailed information is required to completely describe the reasoning behind this result, a high-level explanation is that the combination of velocity and load factor is ideal in the given entry velocity range. Velocities greater than and less than the ideal range result in velocity and load factor combinations where either the velocity value is too high, or the load factor value is too low. This results in a marginally greater manoeuvre radius throughout this phase.

The backflip phase occurs over a small distance ($x_E < 1.23\text{ m}$, $z_E < 1.5\text{ m}$) for all entry velocities. The phase occurs over a time of $\approx 0.4\text{ s}-0.5\text{ s}$, with entry velocities of 20 m/s and 40 m/s taking marginally longer. The end of this phase occurs at an overall manoeuvre time of $\approx 3.5\text{ s}-4\text{ s}$. The end of the backflip phase occurs at the topmost point of the manoeuvre, at a flight path angle of $\gamma = 180°$. The 'minimum radius' aspect of the tumble is highlighted in this phase by the small displacements and large changes in pitch angle. The centre point of the manoeuvre rotation is close to coinciding with the centre of mass of the aircraft. The vertical displacements at the end of this phase measured from the entry to the manoeuvre, are 16.67 m, 14.81 m, 16.11 m and 22.87 m for entry velocities of 25 m/s, 30 m/s, 35 m/s and 40 m/s respectively. The total height attained by the aircraft in the manoeuvre is $\approx 2.15 - 3\times$ the length of the aircraft. Such small gains in height illustrate that only a small portion of the aircraft kinetic energy is converted in potential energy. A great deal of the airspeed is transformed into a pitch rate which is then lost as drag. The small displacements that occur during this phase indicate that the aircraft velocities in this phase are significantly lower than those seen during the entry and climb phases. The backflip phase also sees the aircraft transition from a forward moving trajectory to a reverse trajectory where the aircraft is now pointed towards the entry point. While the duration and distance covered by this phase is small, it is critical in completing the manoeuvre safely as it forms the foundation

for the reversal and exit and recovery phases. Should this phase not be successfully completed the aircraft will be orientated near vertically with very low airspeed. This results in a dangerous and difficult recovery scenario with the aircraft falling backwards towards the ground.

The reversal phase sees the aircraft travel downwards and towards the entry point over a period of $\approx 0.8\,\text{s} - 0.9\,\text{s}$, concluding at a flight path angle of $250° < \gamma < 265°$, depending on the entry velocity. The total manoeuvre time upon completing this phase $\approx 4.3\,\text{s} - 4.8\,\text{s}$. Once again entry velocities of 20 m/s and 40 m/s occur over a marginally longer time. The gradients present in this phase follow a similar, albeit mirrored, trend to those seen in the climb phase. Entry velocities of 20 m/s and 40 m/s illustrate a steeper gradient and occur over a larger distance. Entry velocities of 20 m/s, 30 m/s, 35 m/s and 40 m/s conclude this phase at a horizontal distance of 38.21 m, 40.18 m, 43.86 m and 48.87 m respectively, from the entry point to the manoeuvre. The total width of the looping portion of the manoeuvre is thus, 6.63 m, 6.16 m, 6.1 m and 6.96 m respectively for the various entry velocities.

The exit and recovery phase should be flown in a similar manner to any normal pull-out manoeuvre, albeit at lower airspeeds than the exit of a traditional loop manoeuvre. The lower airspeeds indicate that larger attitude losses and potentially greater load factors are required to attain normal flight velocities.

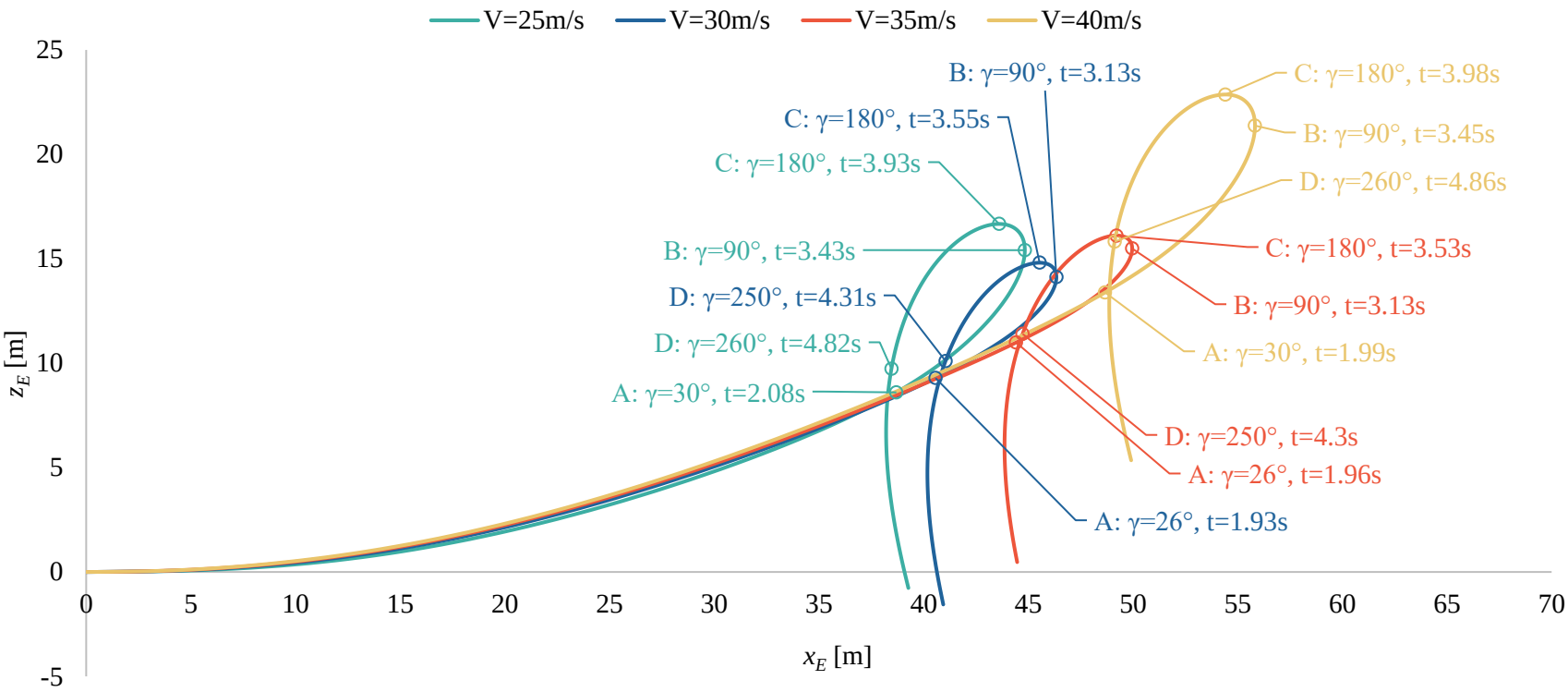

Figure 115: Minimum radius tumble manoeuvre flight paths for various entry velocities, with time stamps at flight path angles of $\gamma = 26°/30°, 90°, 180°$ and $250°/260°$

5.3.2. Radius

The shape of an entire tumble can be further understood by considering the radius throughout the manoeuvre. The distribution of the manoeuvre radius, for each of the tumbles in consideration, is plotted in Figure 116. Flight path angles for each entry velocities are highlighted at various points in the figure, separating each of the various phases. The magnitude of the radius at each point is a function of the velocity of the aircraft and the load factor at that point, as described by Equation (235). Higher velocities and lower load factors result in larger radii. To achieve a minimum radius loop or tumble, a combination of low velocities and higher loads factors are required. In conventional flight lower velocities and higher load factors are usually not achievable. Larger load factors require larger aerodynamic forces which arise as a result of higher velocities. The velocity terms present in Equation (235) are squared whereas the load factor is not. This indicates that the velocity will have a greater influence on the radius of the manoeuvre than the load factor. At lower velocities excessive load factors are not required. Load factors that occur beyond the conventional lift limit of the aircraft wings are, however, necessary.

In Figure 116 it is evident that the entry phase of the tumble manoeuvre, for all entry velocities, undergoes numerous slope and magnitude changes. Shortly after entering the manoeuvre radius values of 183 m, 144 m, 127 m and 118 m are seen for entry velocities of 25 m/s, 30 m/s, 35 m/s and 40 m/s respectively. These comparatively large values of radius indicate that the aircraft entered the manoeuvre from a near horizontal orientation. Upon entering the manoeuvre, a steep decrease in radius is seen for all entry velocities until $\gamma \approx 10°$. This decrease in radius occurs in ≈ 0.5 s-0.75 s depending on the entry velocity. This is indicative of a sharp and sudden change in aircraft heading, an upward pitch in this case. An interesting observation seen in Figure 116 is that upon entering the manoeuvre, lower entry velocities initially experience greater radii. This is a product of the load factor that the aircraft is able to exert at each entry velocity. Each of the entry velocities reach a minimum radius value of ≈ 70 m-75 m before the radius increases again. While the radius has decreased in the entry phase for each of the entry velocity cases the values seen up until $\gamma = 10°$ are not indicative of a minimum radius manoeuvre. An increase in radius is seen after $\gamma = 10°$ for each of the entry velocity cases. The increase in radius suggests that the aircraft is travelling in a near linear fashion. The aircraft follows a shallow curvilinear path. The increase in value suggests that forces are acting to prevent the aircraft from pulling into the manoeuvre and act to force it outwards. The increase in radius is sustained for ≈ 0.5 s before decreasing once again. The increase and second decrease follow a sinusoidal fashion, across all entry velocities with gradients (both for the increase and decrease) similar to those seen in the initial decrease in radius. Greater entry velocities see greater increases in radius and subsequently larger decreases. Due to the large magnitudes of the radius in the in the entry phase, compared to each of the other phases, only a minor change in flight path is seen in this phase. This is despite distinctly different radius distributions for the four entry velocity cases. The large disparities in radius magnitude across the

various entry velocities, in each phase, results in the flat, shallow flight paths illustrated in Figure 114 and Figure 115 for the entry phase.

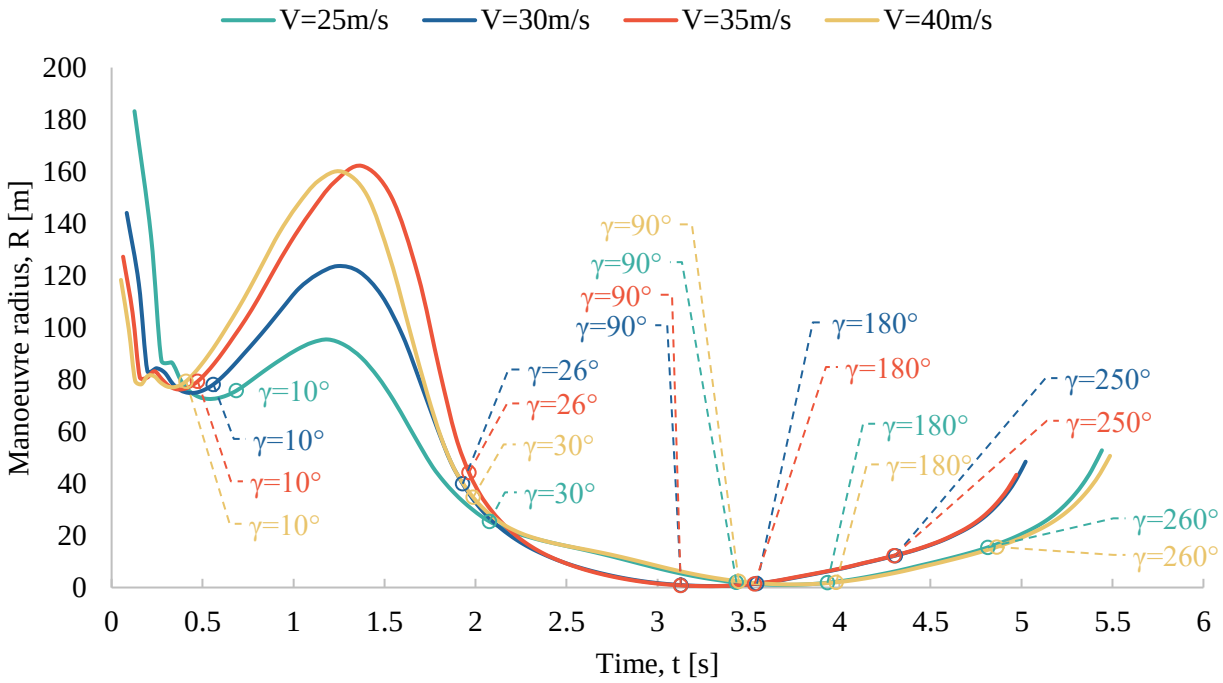

Figure 116: Tumble manoeuvre radii for various entry velocities

The climb phase begins at radius values of 25.42 m, 39.9 m, 44.23 m and 34.70 m for entry velocities of 25 m/s, 30 m/s, 35 m/s and 40 m/s respectively. The climb phase of the manoeuvres sees a continued decrease in radii albeit with shallow gradients than at the end of the entry phase. Radius values reach a minimum value of ≈ 0.8 m for each of the entry velocity cases. The incredibly small radius indicates that the aircraft is rotating about a centre point that is very near to the centre of mass of the aircraft. This highlights the 'minimum radius' nature of the manoeuvre. While all entry velocities exhibit the same trends in the climb phase, entry velocities of 20 m/s and 40 m/s demonstrate higher (near identical) radius values throughout this phase. These two entry velocities demonstrate a 4 m - 5 m higher radius through most of this phase when compared to the 30 m/s and 35 m/s entry velocities. These higher radius values result in the marginally larger widths and heights seen from points $A - D$ in Figure 115. Entry velocities of 30 m/s and 35 m/s show identical radius values throughout this phase. The two sets of identical radii illustrate the two different sets of climb profiles seen in Figure 114 and Figure 115.

The backflip phase shows near constant radius values of ≈ 0.8 m radius across all entry velocities. The low radius values in this phase indicate that the aircraft undergoes large rotations with little linear movement in either the horizontal or vertical directions. The only distinguishable difference between the various entry velocity cases in this phase is in the time over which this phase occurs. The backflip phase occurs over a marginally longer period of time for the 20 m/s and 40 m/s cases. The reversal and exit and recovery phases collectively illustrate a mirrored image of the climb phase, showing similar magnitudes, slopes and time patterns. This mirrored set of radii illustrates the circular, 'looping' nature of the manoeuvre. Some difference is observed in the radius values from the start of the climb phase to the end of the exit and recovery phase for the various entry velocities. The most notable differences occur in the entry phase. highlighting the importance of the entry phase to the overall success of the manoeuvre. The completion of the manoeuvre hinges on the ability of the aircraft to reduce the radius to near 0 m values. This can be achieved through a large reduction in velocity or by maintaining larger load factors (relative to the maximum load factor values achievable at low velocities). An ideal recovery phase would see the aircraft approach large radius values. This indicates that the aircraft has re-entered straight level flight.

5.3.3. Velocity and Load Factor in The Velocity Axes

To understand the features of the radii presented in Figure 116, the velocity and load factor distributions in the velocity axes have been plotted in Figure 117 and Figure 118 respectively. Time is plotted on both sets of axes as a function of the flight path angle as link between Figure 116, Figure 117 and Figure 118.

During the entry phase the free-stream velocity values for each entry velocity see a slight increase to ≈ 26.5 m/s, 30.9 m/s, 35.6 m/s and 40.35 m/s for entry velocities of 25 m/s, 30 m/s, 35 m/s and 40 m/s respectively. These are the highest velocity values seen by the aircraft throughout the manoeuvre. This increase occurs over a period of $\approx 0.2\,\text{s} - 0.3$ s and result in peak values for each of the entry velocities. These small and brief changes in velocity are brought about by an additional velocity component from the initial pitch rate of the aircraft. Shortly after peaking the free-stream velocity values sharply decrease. The steepness of the slope is indicative of a large retarding force. The load factor mimics the increase seen in the velocity distributions and occurs over the same duration of time as the free-stream velocity rise. Peak load factors of 1.96 g, 2.26 g, 2.63 g and 3.06 g are seen for entry velocities of 25 m/s, 30 m/s, 35 m/s and 40 m/s respectively. These peak values are well within the structure limitations of the airframe. It should be noted that the load factors are in excess of the lift limit of the aircraft at the velocities at which they occur. This suggests an influence from dynamic effects (which is seen to accelerate the velocity) and additional force components that act in the lift direction. The 40 m/s entry velocity case illustrates a higher load factor than the other entry velocity cases. The short time over which these peaks occur is unlikely to have any noticeable impact on the loads the pilot or airframe experience. This is despite a 1 g difference in load factor between the 25 m/s

and 40 m/s entry velocity cases. The peak load factor values are not sustained and sharply decrease almost immediately after reaching the peak. Despite the slight increase in velocity over the first 0.3 s of the entry phase, the radius is seen to decrease over this same time frame. The reduction in radius is a direct result of the increasing load factor over this period. This is seen for each of the entry velocity cases. The effect on the manoeuvre radius due to sharp increase in load factor is greater than the effect of the small increase in velocity. The peak velocities occur at $\gamma = 5°$ while the load factors peak at $\gamma \approx 10°$. The load factor peaks coincide with the base of the first decrease seen in the radius values presented in Figure 116. This illustrates that the radius is primarily driven by the load factor at the start of the entry phase. After their respective peak values, the velocity and load factor distributions sharply decrease. The load factor distributions illustrate a steeper gradient than the velocity distributions. The load factor reduces at a faster rate than the velocity. This difference in reduction of the two distributions accounts for the increase in radius in the entry phase. Once the velocity values reach a sufficiently low magnitude the radius begins to decrease once again. The brief increase in radius is necessary in decelerating the aircraft. A change in gradient is seen at the end of the entry phase for both the load factor and velocity distributions. Higher entry velocities carry more speed and greater load factors through the initial stages of the entry phase but appear to almost converge near the end of the phase. The most notable occurrence in the entry phase is the rapid decrease in velocity to values well below the stall velocity of the aircraft. The significance of these low velocities is that the aircraft enters a very low energy state. While the aircraft drag power is reduced due to the low velocities the thrust power is also minimised. This situation may result in a dangerous scenario should the manoeuvre not be executed properly. Energy recovery would likely need to be extracted from the mechanical stores. Should the pilot need to abandon the manoeuvre during the entry phase the aircraft has little airspeed and will likely need to trade altitude for airspeed. This places a large emphasis on correctly executing the entry phase of the manoeuvre to transition to subsequent phases.

Between the climb phase and the end of the backflip phase the load factor distribution continues to decrease with a near constant gradient that is shallower than the gradients seen in the entry phase. A minimum load factor is reached at $\gamma = 180°$ for all entry velocities. A load factor of ≈ 0.05 g is obtained by the 30 m/s and 35 m/s entry velocity cases while entry velocities of 25 m/s and 40 m/s reach a minimum load factor of ≈ 0.45 g. These minimums occur at the apex of the manoeuvre, as with a traditional loop manoeuvre. At the end of the backflip phase the load factors are low enough such that the aircraft is in a near 'weightless' scenario at the peak of the manoeuvre, particularly for the 30 m/s and 35 m/s cases. Similar load factor values are seen for all entry velocities during the climb phase. During the backflip phase lower load factors are seen for entry velocities of 30 m/s and 35 m/s.

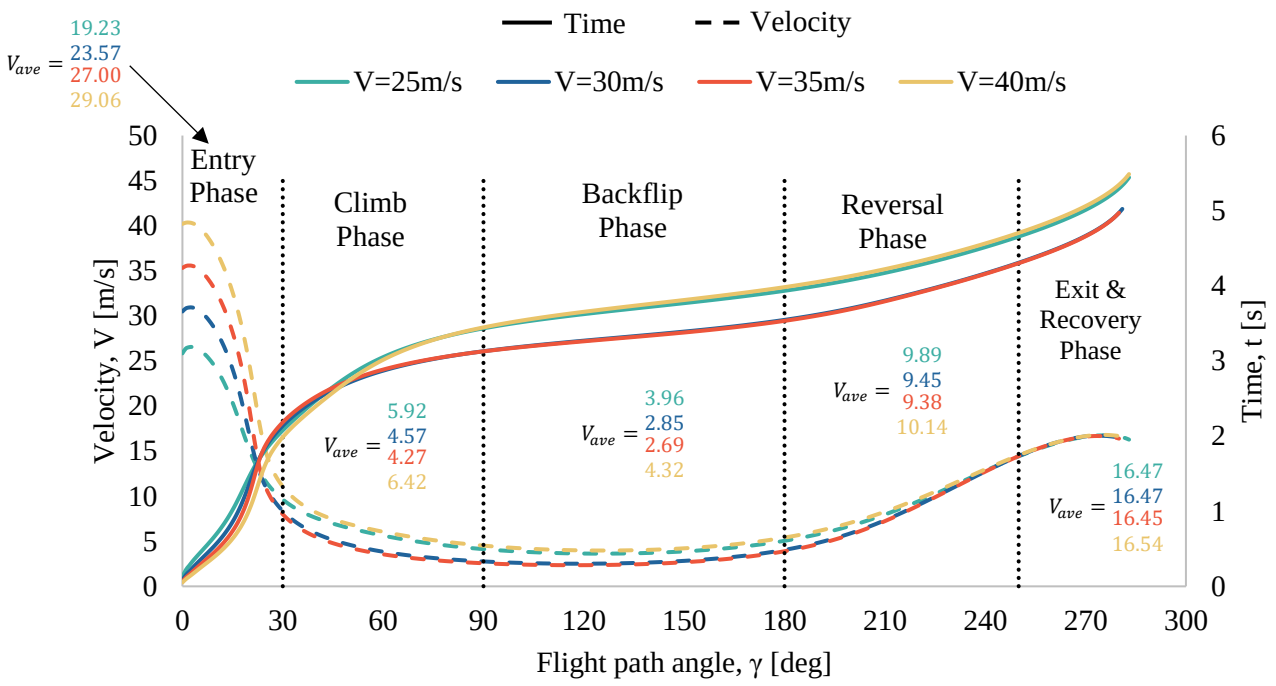

Figure 117: Minimum radius tumble manoeuvre velocity and time vs flight path angle plots for various entry velocities

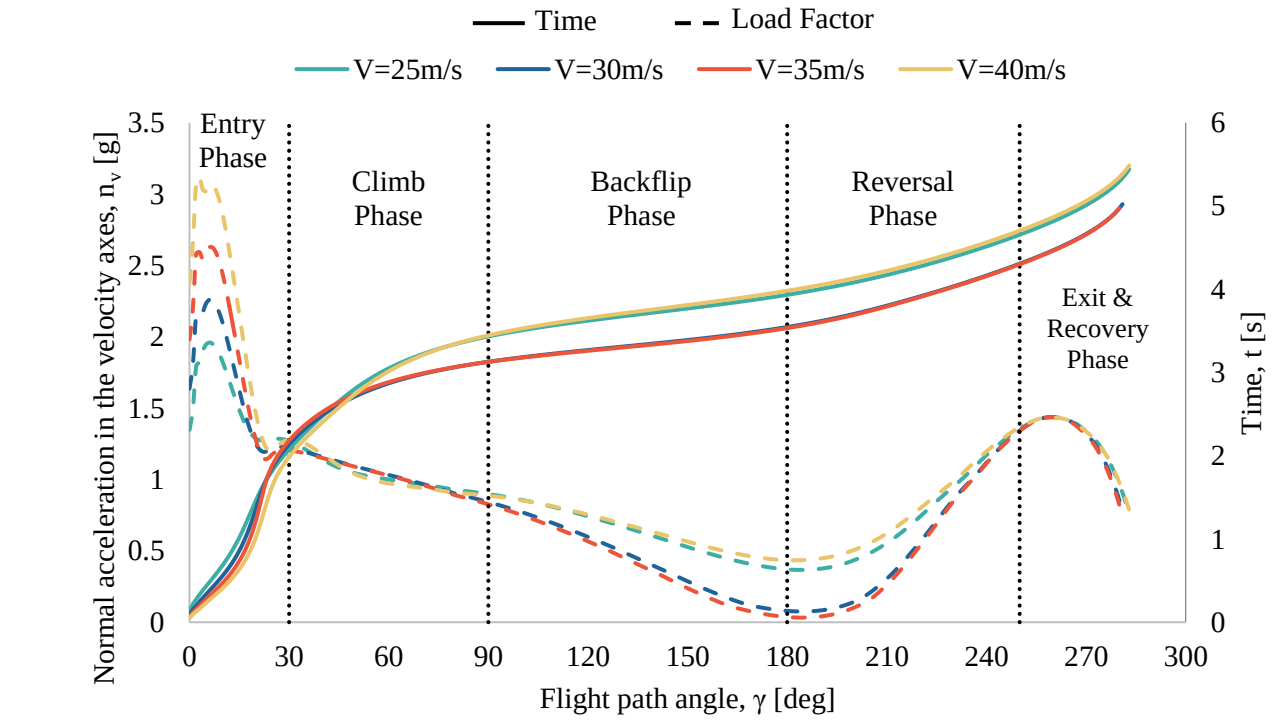

Figure 118: Load factor in the velocity axes of a tumble manoeuvre for various entry velocities

The slight differences in load factor are due to differences in aerodynamic forces that arise from marginally differing velocity distributions in the backflip phase. The velocity distribution continues to decrease with a shallow gradient at the beginning of the climb phase. Only marginal changes in velocity are observed in the climb phase. The climb phase concludes at velocity values of ≈ 2.7 m/s for entry velocities of 30 m/s and 35 m/s. A velocity of ≈ 4.15 m/s is seen at the end of the climb phase for entry velocities of 25 m/s and 40 m/s. While these velocity values are incredibly low, they are not zero. The aircraft also does not lose any altitude in this phase, as seen in Figure 115. This is significant as it illustrates that the thrust power of the aircraft is capable of supplying enough energy to the aircraft to prevent it from both losing altitude and dropping to a zero airspeed. The thrust force is able to briefly counteract the drag and mass forces present in this phase. This would be impossible with a standard aerobatic aircraft engine. The lowest velocity values throughout the manoeuvre occur at the end of the climb phase. These velocity values are carried through much of the backflip phase, seeing only a slight increase at the end of the phase. During the climb and backflip phases entry velocities of 20 m/s and 40 m/s show similar velocity distributions that are higher than the other two entry speeds, which, in turn, also show similar distributions. In the climb and backflip regions, each of the entry velocities illustrate a similar path, despite the differences in velocity and load factor. The higher velocity and load factor combination result in radii that are similar to the lower speed and lower load factor combination. The ability of the aircraft to exert higher load factors is also linked to being at a higher velocity. This suggests that the entry velocity has only a marginal effect on the climb and backflip phases when compared to the entry phase.

Beyond the backflip phase the velocity and load factor distributions increase during the reversal phase. The velocity distributions for each of the entry velocities increase gradually and reach near identical values at the start of the exit and recovery phase. The reasoning behind the convergence of velocities values can be ascribed to the aircraft in each case essentially “falling” at a similar orientation and thus gaining velocity from a similar starting velocity and at a similar rate. Each entry velocity case reaches a velocity of ≈ 15 m/s at the end of the reversal phase. While a recovery of energy has occurred, the aircraft is still below the stall velocity. This implies that additional velocity must still be gained in recovering from the manoeuvre. The load factors increase shortly after entering the reversal phase, with steep gradients. Load factors of ≈ 1.5 g are seen at the end of the reversal phase for each of the entry velocity cases. This is indicative of an increase in aerodynamic load on the airframe. This suggests that energy is being gained. This occurs as a result of the mass vector acting in a similar direction to the thrust and a small trade in altitude for airspeed. As with the velocity distributions the load factor distributions converge at the start of the exit and recovery phase, with the reasoning being similar to that of the velocity distributions.

During the exit and recovery phase a turnaround is seen in both the velocity and load factor distributions. The reversals seen in this phase are not realistic. Full up elevator was modelled during the manoeuvre

which continued to rotate the aircraft. In reality, the pilot would set the elevator to a neutral position or change the direction of elevator deflection to counter the angular accelerations through the manoeuvre. Despite the unlikely scenario, the plot illustrates the situation that could arise should the elevator malfunction or if the pilot makes corrections too late. Continued application of the elevator in the exit and recovery phase places the aircraft in a situation where there is an insufficient amount of airspeed and an inability to exert load factors. This would require a large amount of altitude to adequately correct the aircraft orientation and velocity such that a recovery is possible before impacting the ground.

From the start of the climb phase to the end of the reversal phase, each of the tumble manoeuvres presented show near identical trends in both the time, velocity and load factor distributions. Beyond $\gamma \approx 50°$ entry velocities of 20 m/s and 40 m/s exhibit near identical time and velocity traces in both shape and magnitude. Entry speeds of 30 m/s and 35 m/s illustrate similar plot shapes to the other two entry velocities, though at a different magnitude. This suggests that the entry velocity to the manoeuvre has the largest influence in the initial phases of the manoeuvre and has only a small influence on the middle and end portions of the manoeuvre. The only notable difference is the location (both vertical and horizontal distance) at which the middle and end portions of the manoeuvre occur. This should be expected considering all input variables were identical for each of the manoeuvres apart from the entry speed.

5.3.4. Component Z Forces in the Velocity Axes

The load factor presented in Figure 118 is effectively the ratio of the sum of the forces acting in the Z direction of the velocity axes to the aircraft mass. The summation of forces includes contributions from the inner wing section lift $\left(L_{W_{I_{Z_v}}}\right)$ and drag $\left(D_{W_{I_{Z_v}}}\right)$, the outer wing section lift $\left(L_{W_{O_{Z_v}}}\right)$, the fuselage lift $\left(L_{f_{Z_v}}\right)$ and drag $\left(D_{f_v}\right)$, the horizontal stabiliser lift $(L_{t_{Z_v}})$ and drag $\left(D_{t_{Z_v}}\right)$ as well as the propeller thrust (T_{Z_v}) and normal force $\left(N_{p_{Z_v}}\right)$. The drag of the outer wing section does not contribute to the Z forces in the velocity axes as the lift is perpendicular to the X axis in the velocity reference frame. The force contribution for each component in the Z direction of the velocity axes is presented in Figure 119 for each entry velocity. The Z forces for each aircraft component were determined using the velocity axes equations provided in §4.4. Each of the entry velocity cases illustrate similar distributions for all the force components, with increasing component magnitudes for increasing entry velocity. The outer wing lift, inner wing lift and drag, propeller thrust and normal force act to increase the force in the Z direction. The outer wing drag, fuselage lift and drag and horizontal stabiliser lift and drag all act to reduce the force in the Z direction.

The Z forces present in the entry phase of the manoeuvre are largely driven by the inner and outer wing lift along with the propeller thrust. The lift force generated by the inner wing section is larger than that of the outer wing section across all entry velocities. Peak values of 7965 N, 9612 N, 11574 N and

13820 N are seen for the inner wing lift for entry velocities of 25 m/s, 30 m/s, 35 m/s and 40 m/s respectively. These peak values are greater in magnitude than the weight of the aircraft. In conventional flight these values would be impossible to obtain. The effects of the propeller slipstream and the large dynamics present in the initial stages of the entry phase allow for these peak values to be briefly obtained. These peak values were attained at a flight path angle of 6°. The inner wing lift decreases immediately after the peak. The large and sudden rise and fall of the lift values indicates a large dynamic impulse that is not sustained. While these values may seem unrealistic, the time over which they occur makes the values plausible. Large values near the peak are sustained for < 0.4 s for all entry velocity cases. The shape of rise, peak and fall of the inner wing lift is identical to that of the load factors seen in Figure 118. This suggests that the load factors distributions in early stages of the entry phase are largely driven by the inner wing lift. The lift values of the outer wing section illustrate values closer to those seen for conventional manoeuvring. Peak values of $3254\text{ N}, 4686\text{ N}, 6378\text{ N}$ and 8330 N for entry velocities of 25 m/s, 30 m/s, 35 m/s and 40 m/s respectively. These peak values are obtained at the very start of the manoeuvre and are a result of the large dynamic pitch rate. The peak outer wing lift values decrease immediately. The large differences seen in the lift of the inner and outer wing sections is due to the propeller slipstream acting over the inner wing section. The slipstream accelerates the flow over the inner wing section giving rise to larger lift forces and aids in reducing the angle of attack of the inner wing section. The dynamic coefficients for the inner and outer wing were generated independently to any angular rates. This leaves an element of uncertainty in the lift values generated in the entry phase of the manoeuvre. The propeller thrust was set to remain constant throughout the entry phase of the manoeuvre. Based on Equation (208) this then implies that the varying thrust distributions, present in each entry velocity case, are a function of the aircraft angle of attack. The thrust rises from a value of ≈ 1500 N at the very start of the manoeuvre to values of $6950\text{ N}, 7336\text{ N}, 7410\text{ N}$ and 6997 N near the end of the entry phase, for entry velocities of 25 m/s, 30 m/s, 35 m/s and 40 m/s respectively. The increase in the thrust component in the Z direction suggests that the angle of attack and the pitch angle of the aircraft is continually increasing throughout the entry phase. The increasing angle of attack is further highlighted by the decrease in the lift force of the inner and outer wing sections. Despite undergoing two different velocity profiles, the inner and outer wing sections decrease with similar slopes through the entry phase. This is indicative of an increase in angle of attack and decrease in free-stream velocity throughout the phase.

The drag of the inner wing section contributes negative Z forces in the velocity axes. The contribution of the inner wing section drag is largest (in magnitude) in the entry phase and remains negative in value throughout the manoeuvre. The drag of the inner wing section contributes to the Z force in the velocity axes as the angle of attack of the inner wing velocity vector is different to that of the free-stream velocity vector.

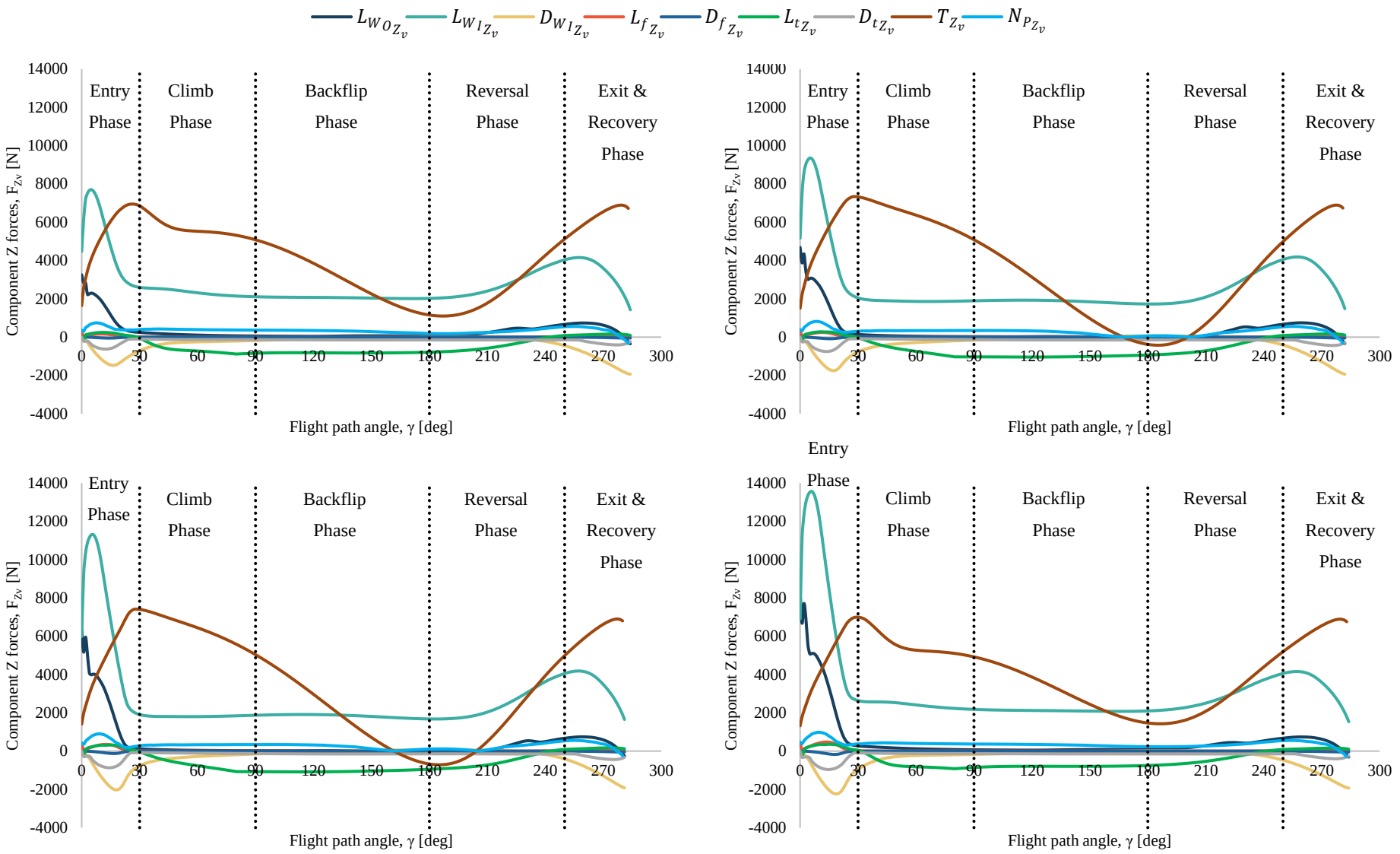

Figure 119: Component Z forces in the velocity axes for entry velocities of 25 m/s (top left), 30 m/s (top right), 35 m/s (bottom left) and 40 m/s (bottom right)

This creates a component of drag in the Z direction. The bucket shape of the inner wing drag distribution indicates that the overall aircraft undergoes a large increase in angle of attack. This must be the case as the velocity is seen to decrease in the entry phase. Peak (negative) drag values of -1471 N, 1752 N, 2025 N and 2235 N are obtained for entry velocities of 25 m/s, 30 m/s, 35 m/s and 40 m/s respectively. The differences in magnitude are due to differing free-stream velocity values acting over the horizontal stabiliser for the various entry velocity cases. These maximum magnitudes pale in comparison to the inner wing lift. The large difference in values can be understood by observing the position of the maximums. The maximum drag values occur at a flight path angle of $\approx 20°$. This is a flight path angle of $14°$ later than the peak lift values. In the very early stages of the manoeuvre ($\gamma \leq 6°$) the dynamic effects due to pitch rate increase the velocity and flow over the inner wing. The propeller slipstream acts to reduce the angle of attack of the inner wing. This results in lower coefficients of drag and higher coefficients of lift, allowing for greater lift forces. Beyond a flight path angle of 6°, the angle of attack is seen to increase, resulting in larger coefficients of drag and lower coefficients of lift. At the same time as the angle of attack increase the free-stream velocity undergoes a large decrease. This decrease in free-stream velocity is the mechanism that reduces the drag values at higher angles of attack.

The propeller normal force provides a small increase in the total force in the Z direction of the velocity axes and illustrates a near sinusoidal shape. The Z component of the normal force peaks at the same flight path angle as the inner wing section lift. Peak values of 743 N, 819 N, 900 N and 983 N are obtained for entry velocities of 25 m/s, 30 m/s, 35 m/s and 40 m/s respectively. While small in magnitude these values assist in 'pulling' the aircraft into the manoeuvre. The fuselage lift and drag forces contribute almost insignificant amounts to the overall force in the Z direction of the velocity axes. The force contributions of the fuselage are minimised by two factors. Comparatively low coefficient magnitudes at lower angles of attack and low free-stream velocities when the aircraft is at high angles of attack. The horizontal tail section contributes a small amount to the overall Z force in the velocity axes. The lift of the horizontal tail contributes a positive force throughout the entry phase, while the horizontal tail drag contributes a negative force. The distributions of the lift and drag of the horizontal stabiliser are obtained in a similar fashion to the inner wing section. The direction of the lift force of the horizontal tail in the entry phase is opposite to the desired direction. The drag force also illustrates larger magnitudes than the lift force of the horizontal tail throughout the entry phase. These two observations are suggestive of a large angle of attack over the horizontal stabiliser. These large angles of attack over the horizontal stabiliser are likely due to the rotational component of velocity over the horizontal tail. The large pitch rates at the very beginning of the manoeuvre would have given rise to large rotational velocity components over the horizontal tail. The positive lift value over the horizontal stabiliser suggests that the angle of attack over this surface is $> 20°$. This is the point at which the coefficient of lift becomes positive in Figure 100 in §3.3.5.

The climb phase of the manoeuvre illustrates linear, horizontal line values for each force component with the exception of the thrust force and horizontal tail lift force. The linear magnitudes of each of the force components are largely unremarkable apart from the inner wing lift. The inner wing lift exhibits a near constant value of $2200\ \text{N}, 2000\ \text{N}, 2000\ \text{N}$ and $2300\ \text{N}$ for entry velocities of $25\ \text{m/s}$, $30\ \text{m/s}$, $35\ \text{m/s}$ and $40\ \text{m/s}$ respectively. The lift force is largely identical in this phase for all entry velocity cases. The differences occur due to marginal differences in the free-stream velocity. These lift forces occur despite free-stream velocities of $< 10\ \text{m/s}$ for all entry velocity cases. The inner wing remains effective due to the propeller slipstream velocity. While the magnitudes are not enough to oppose the weight of the aircraft the contribution of the lift is noteworthy for such low-speed flight. The Z component of the thrust force decreases at the start of the climb phase, indicating a decrease in the angle of attack of the aircraft. This is seen for all entry velocities. The distributions of the Z component of the thrust force for entry velocities of $30\ \text{m/s}$ and $35\ \text{m/s}$ illustrate a near constant gradient through the climb phase. Entry velocities of $25\ \text{m/s}$ and $40\ \text{m/s}$ illustrate a change in slope from a steeper gradient to a shallower gradient. This difference is due to dissimilar forces acting on the aircraft caused by slightly different velocity distributions. These differences in velocity result in different moment distributions that in turn produce different angles of attack.

While it may seem contradictory that certain Z force values remain constant while the angle of attack of the aircraft decreases, this scenario is indeed valid and can be better understood by considering the velocity distributions presented in Figure 117. In the climb phase of Figure 117 the free-stream velocity values are very low. These velocities are sufficiently low enough that they dictate the value of the forces (for all component not exposed to the propeller slipstream). The free-stream velocity values remain largely constant in this phase and dictate the shape of the force distributions. Despite a changing angle of attack, the velocity values are sufficiently low and constant that the force values remain near constant. The slipstream effects also influence the forces on the horizontal tail. The force of the horizontal tail acts in the negative Z direction in the climb phase. These negative values indicate that the angle of attack of the horizontal stabiliser has reduced to a value that is $< 20°$.The increase (in the negative direction) of the Z force of the horizontal tail in the climb phase is due to a decreasing angle of attack. This decrease of horizontal tail angle is brought on by a lower angular rate, reducing the angular velocity component and subsequently the angle of attack of the horizontal stabiliser. The decrease in angular rates can be seen through the loss of angle of attack as the flight path angle increases.

The backflip and reversal phases show largely constant force values across all aircraft component apart from the propeller thrust force, inner wing lift and horizontal stabiliser lift. The propeller thrust values continue to decrease with near constant gradients through the backflip phase. This indicates a continued decrease in aircraft angle of attack. The Z component of the thrust force reaches a minimum at the end of the backflip phase, suggesting that the minimum angle of attack is reached at the end of this phase. Minimum thrust values of $1100\ \text{N}, -423\ \text{N}, -714\ \text{N}$ and $1320\ \text{N}$ are observed for entry velocities of

25 m/s, 30 m/s, 35 m/s and 40 m/s respectively. The negative values for entry velocities of 30 m/s and 35 m/s signify negative angles of attack.

An increase in thrust is seen throughout the reversal phase. The magnitude of the gradient of the thrust increase is similar to that of the decrease in the backflip phase. This produces a cosine-like distribution for each of the entry velocity cases. At the end of the reversal phase thrust force values of ≈ 5800 N are seen for each of the entry velocity cases. This suggest that large angles of attack are once again attained. This is not ideal near the exit of the manoeuvre. High angles of attack limit the rate at which energy may be gained due to a large drag power requirement. At the end of the reversal phase the Z components of inner wing section lift force, the fuselage drag force and propeller normal force begin to increase. These increases can be directly correlated to the increase in free-stream velocity in this phase. The horizontal stabiliser lift force approached a positive value towards the end of the reversal phase. This may indicate a rise in angular velocity once again. This notion confirms the increases in angle of attack described by the Z component of the propeller force.

The Z component of most of the forces are largely unremarkable in the exit and recovery phase. The thrust force continues to increase in this phase, resulting in a growing angle of attack. This increase is likely large as the inner wing section lift decreases sharply in this phase while the inner wing drag force continually increases (negatively) throughout this phase. These changes in inner wing forces are indicative of large angles of attack. The Z components of the fuselage drag and propeller normal forces follow similar trends to that of the inner wing section, further suggesting large angles of attack are seen by the aircraft.

What is evident from the plots in Figure 119 is that the Z components of the propeller thrust and inner wing lift forces contribute the largest proportions of the normal force in the velocity axes. The thrust force relies on large angles of attacks, pointing the thrust in the correct direction in the velocity axes. The inner wing lift forces are dependent on the propeller slipstream effects. While the horizontal tail and fuselage and engulfed by the same slipstream velocity as the inner wing, the forces these components generate are far smaller. The fuselage is not a lifting body and thus produces significantly smaller lift and drag values in comparison to the wing. The horizontal stabiliser produces far smaller values as a result of a smaller surface area, a different airfoil profile and larger rotational velocity influences. The distance of the horizontal stabiliser from the centre of mass creates significantly larger rotational velocity components. To complete a tumble manoeuvre high angles of attack and propeller slipstream are imperative. These two factors contribute both to the normal force, pulling the aircraft into the manoeuvre and to the deceleration of the aircraft, to reduces restoring moments.

5.3.5. Load Factor In The Body Axes

The load factor in the velocity axes provides some insight into the radius and subsequently the flight path of a tumble manoeuvre. While informative, a more familiar representation of the normal forces acting on the aircraft, would be given by the load factor in the body axes. This is an indication of the normal accelerations perpendicular to the longitudinal axis of the aircraft. Load factor in the body axes is used by aircraft manufacturers to provide pilots with an indication of the structural limitations of the aircraft. The load factor in the body axes is plotted in Figure 120 against the velocities seen throughout the entire tumble manoeuvre for an entry velocity of 30 m/s. A load factor diagram for normal flight operation of the Extra 330SC is provided in addition to the tumble load factor distribution in Figure 120.

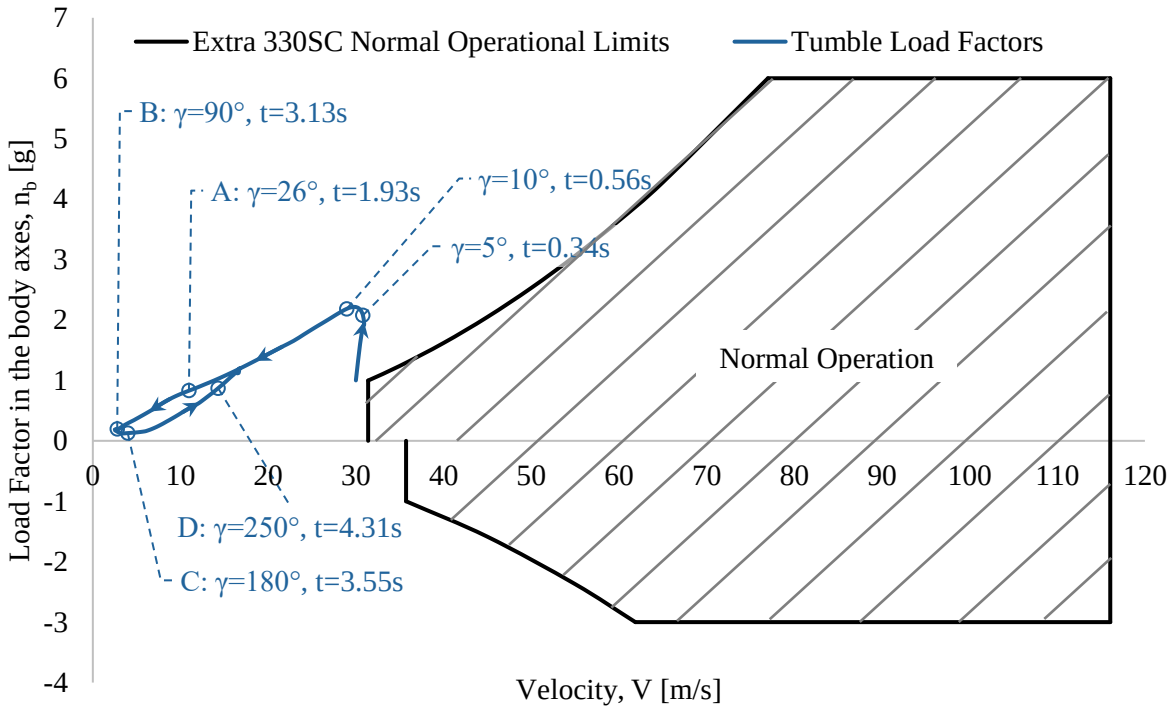

Figure 120: Extra 330SC normal operational load factor diagram with tumble manoeuvre load factors at an entry velocity of $V_{entry} = 30$ m/s

At the very start of the tumble manoeuvre the aircraft load factor is set to the maximum attainable value in normal flight operation. As soon as elevator deflection is applied the load factor increases beyond normal operational limits to a value of 2.21 g at a flight path angle of 10°. In a conventional situation the normal forces would compromise primarily of the lift force from the wing. At these loads speeds the wing would not be able to supply enough lift to match the load factors seen in Figure 120. This suggests that forces must be acting in a direction normal to the aircraft longitudinal axis that consist of more than just the wing lift. To achieve such a scenario the aircraft would need to be at very high angles of attack. This does occur during a tumble manoeuvre. The initial increase in load factor is not sustained,

only lasting for ≈ 0.5 s before decreasing. This reduction in load factor is likely due to a decrease in the velocity components (free-stream and due to pitch rate) experienced by the aircraft and a subsequent reduction in forces. While the load factors experienced by the aircraft decrease towards the end of the entry phase, the values seen are still higher than those achievable in normal operating conditions. During the climb phase the load factor continues to decrease and approaches values that are closer to the lift limitations in normal operating conditions. The backflip phase sees a marginal reduction in velocity with the load factor approaching a value of 0 m/s. Shortly after entering the reversal phase, the load factor once again increases to values greater than the limitations of normal operating conditions. By keeping the elevator applied during the entire reversal, exit and recovery phases the load factor continues to remain outside of the bounding lines of normal operation. To execute a successful exit and recovery phase the aircraft should re-enter the bounds of the load factor diagram. To achieve this, normal angles of attack and pitch are required. This implies that the rotation performed for the tumble must be stopped and possibly counteracted at some point before the exit of the manoeuvre is reached. The entire manoeuvre notably takes place outside of normal operating conditions and lift limits. It is evident that unconventional aircraft orientations are required such that various force components are directed in the positive Z direction of the body axes.

5.3.6. Linear Acceleration

The large reductions in free-stream velocity seen in §5.3.3 are a result of large decelerations. These decelerations occur due to retarding forces that act in opposition to the direction of motion of the aircraft. The linear accelerations experienced by the aircraft in the velocity axes are presented in Figure 121 for various entry velocities.

Upon entering the manoeuvre, a momentary positive linear acceleration of ≈ 0.5 g is seen across all the given entry velocities. This acceleration is typical for an aerobatic aircraft. This positive acceleration produces the momentary increase in free-stream velocity seen in §5.3.3. After the initial positive values, a sudden decrease is observed for all entry velocities. The decreases in linear accelerations show a sharp gradient, reaching a maximum negative value at a flight path angle of $\approx 15°$ for all entry velocities. Maximum negative accelerations of -1.23 g, -1.53 g, -1.85 g and -2.195 g for entry velocities of 25 m/s, 30 m/s, 35 m/s and 40 m/s respectively. While these decelerations may not seem out of the ordinary what makes them remarkable is that they were achieved at maximum thrust. Average acceleration values of -1.01 g, -1.27 g, -1.53 g and -1.74 g are seen in the entry phase for entry velocities of 25 m/s, 30 m/s, 35 m/s and 40 m/s respectively. The close proximity of the mean values to the maximum negative values suggest that large decelerations are seen through entire entry phase. Larger entry velocities undergo larger linear decelerations. The larger free-stream velocities seen in larger entry velocities produce larger drag forces. The large decelerations seen in the entry phase of Figure 121 are required to produce the necessary velocities decreases seen in Figure 117. The minimum acceleration values are not sustained and begin to increase shortly after reaching the minimum values.

While the acceleration values increase after the minimum, they remain negative throughout the entry phase. The increase in acceleration is likely due to a reduction in free-stream velocity and subsequently a reduction in forces acting in the drag direction.

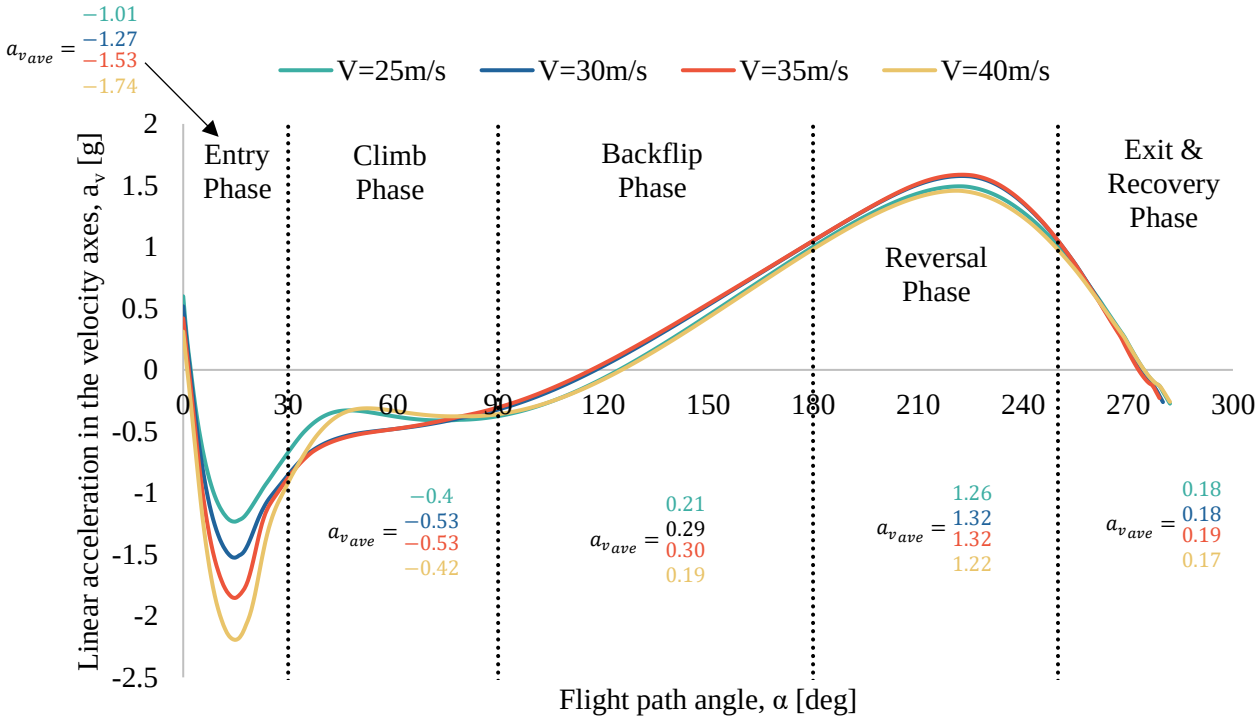

Figure 121: Linear accelerations during a tumble manoeuvre in the velocity axes, for various entry velocities

In the climb phase linear accelerations continue to remain negative but increase slightly. Average accelerations of -0.4 g, -0.53 g, 0.53 g and -0.42 g are observed for entry velocities of 25 m/s, 30 m/s, 35 m/s and 40 m/s respectively. The average decelerations have more than halved from the large (negative) accelerations seen in the entry phase. Entry velocities of 30 m/s and 35 m/s follow an identical distribution shape and share a common average value in this phase. A flat gradient increase in value is seen. Entry velocities of 25 m/s and 40 m/s illustrate near horizontal gradients, following a almost constant linear acceleration value for a large portion of this phase. While entry velocities of 20 m/s and 40 m/s share similar shapes and values in this region the flight path angle at which the change in gradient is seen differs for each entry velocity. The 25 m/s case transitions to the flatter gradient $\approx 5°$ sooner in flight path than the 40 m/s case. Once again while the values presented may seem unremarkable, they are achieved at maximum thrust. This suggests that large retarding forces are present in the climb phase. The high angles of attack would result in a large component of the mass acting in the drag direction. At the end of the backflip phase an acceleration of ≈ -0.5 g is seen for

each of the entry velocity cases. This indicates that the aircraft velocity is still decreasing at the end of this phase. The velocity values at this stage in the manoeuvre are small. This implies that the change in velocity will also be small and as such, the deceleration values may mislead the reader into believing that far greater losses in velocity are present than is actually the case. During the entry and climb phases, gravitational force helps decelerate the aircraft in the absence of aerodynamic drag forces.

The gradient and sign of the linear acceleration curves changes in the backflip phase. The gradient remains positive but is slightly steeper than during the climb phase. A portion of the phase continues to show negative accelerations while the remainder of the phase illustrates positive accelerations. The acceleration for entry velocities of 30 m/s and 35 m/s changes sign at a flight path angle of $\approx 118°$. Entry velocities of 25 m/s and 40 m/s show a change in sign at a flight path angle of $\approx 127°$. Average acceleration values of 0.21 g, 0.29 g, 0.3 g and 0.19 g are seen for entry velocities of 25 m/s, 30 m/s, 35 m/s and 40 m/s respectively. The positive average accelerations suggest that a larger portion of the phase is spent with positive accelerations. This is indicative of a larger thrust force component than aircraft mass component. The drag forces are comparatively low due to the low airspeeds in this phase. The mass component should contribute less to the X component as the phase progresses. At an aircraft pitch angle of $180°$ the mass component acts purely in the Z direction. All entry velocity cases illustrate very similar gradients in this phase. Entry velocities of 30 m/s and 35 m/s show slightly higher values through most of this phase. The velocity increases in Figure 117 are seen to lag behind the positive accelerations in this phase. The reasoning behind this slow gain in velocity is due to the magnitude of the velocity values. The velocity values are small enough that even large accelerations produce only small changes in velocity. As a fraction of the current velocity the changes may be large but as a magnitude the velocity changes are small and thus take time to cumulatively result in significant changes in velocity. The positive values attained during this phase are due to the thrust forces outweighing the drag and gravitational forces. The low velocity values and lower angular rates result in lower aerodynamic forces.

The linear accelerations in the reversal phase continue to increase with the same gradient seen at the end of the backflip phase. This trend continues until $\gamma \approx 225°$ where a maximum is reached. Maximum accelerations of 1.49 g, 1.58 g, 1.59 g and 1.46 g are seen for entry velocities of 25 m/s, 30 m/s, 35 m/s and 40 m/s respectively. The similarity is accelerations is indicative of identically orientated aircraft accelerating with little impedance from drag forces. The continued increase in acceleration at the beginning of the reversal phase is largely due to the direction in which the mass component now acts. Beyond a flight path angle of $180°$ the aircraft should be orientated at a pitch angle of $> 180°$. This results in a component of the aircraft mass acting in the same direction as the thrust. Average acceleration values of 1.26 g, 1.32 g, 1.32 g and 1.22 g are seen for entry velocities of 25 m/s, 30 m/s, 35 m/s and 40 m/s respectively. The close proximity of the mean acceleration values to the maximum acceleration values in this phase suggest high positive accelerations are achieved throughout this phase.

This indicates that drag forces are still relatively small in magnitude. The slope of each of the entry velocities is identical and largely similar in magnitude with only a small difference occurring between the entry velocities near the maximum points. Shortly after the maximum acceleration a decrease is seen with a similar slope to that seen for the increase, albeit negative in value. The point at which the accelerations begin to decrease in magnitude in the reversal phase occurs at the same point at which the velocity noticeably increases in Figure 117. The increase in velocity seen at this flight path angle results in larger drag forces acting on the aircraft. This causes a decrease in the magnitude of the acceleration values. The linear acceleration continues to decrease for the remainder of the reversal phase, reaching a value of ≈ 1 g by the end of the phase for all the entry velocity presented.

The exit and recovery phase sees the linear accelerations continue to decrease with the same negative gradient seen at the end of the reversal phase. Average acceleration values of 0.18 g, 0.18 g, 0.19 g and 0.17 g are seen for entry velocities of 25 m/s, 30 m/s, 35 m/s and 40 m/s respectively. These values are comparatively small and indicate only minor gains in average velocity through this phase. To adequately recover from a tumble manoeuvre, larger acceleration values should be seen in the exit of the manoeuvre. The values seen by each entry velocity in this phase are near identical. The same argument could be made here as for the exit and recovery phase values seen in the velocity plot. The aircraft is falling at approximately the same velocity and in a similar orientation, in this phase for each of the entry velocity cases. With similar starting velocities and orientations, the aircraft should therefore accelerate at the same rate. The negative gradient accelerations seen in this phase are due to the continued application of upward elevator deflection causing a continued rotation of the aircraft. The deceleration is caused by growing drag forces as the aircraft falls downwards. The continued application of elevator in this phase illustrates the dangerous scenario that could arise should the pilot not take corrective action at the start of the phase (or even towards the latter ends of the previous phase). The continued application of upward elevator results in a decreasing and subsequently negative acceleration. This results in a reduction in free-stream velocity when it should be increasing. With low airspeed and a drag power outweighing the thrust power the only available gain in energy will be from altitude. Losses in altitude will be the only means of gaining energy. If an insufficient height is budgeted by the pilot a ground impact is likely.

5.3.7. Component X Forces In the Velocity Axes

The contribution of the X forces in the velocity axes for the various aircraft components are plotted in Figure 122 for each entry velocity. These force components contribute to the linear acceleration of the aircraft. The force components comprise of the outer wing section drag $\left(D_{W_{O_X}}\right)$, the inner wing section lift $\left(L_{W_{I_X}}\right)$, the inner wing section drag $\left(D_{W_{I_X}}\right)$, the fuselage lift $\left(L_{f_X}\right)$, the fuselage drag $\left(D_{f_X}\right)$, the horizontal stabiliser (tail) lift $\left(L_{t_X}\right)$, the horizontal stabiliser (tail) drag $\left(D_{t_X}\right)$, the propeller thrust (T_X), the propeller normal force $\left(N_{P_X}\right)$ and the weight of the aircraft (W_X).

The entry phase of the manoeuvre sees large contributions from all force components apart from the aircraft fuselage. The force components generated by the fuselage are negligible when compared to each of the other force components. They illustrate a near zero value throughout the entire manoeuvre. The only force component with a positive value in the entry phase is the propeller thrust. Thrust force component values of $5992\ \text{N}, 5699\ \text{N}, 5395\ \text{N}$ and $5092\ \text{N}$ are seen for entry velocities of 25 m/s, 30 m/s, 35 m/s and 40 m/s respectively. Lower entry velocities illustrate higher initial thrust values. This explains the marginally higher initial linear accelerations for lower entry velocities seen in Figure 121 of §5.3.6. The X force generated by the propeller thrust decreases in magnitude through majority of the entry phase with a steep gradient. The minimum thrust values show a reduction of $61\ \%, 67\ \%, 70\ \%$ and $71\ \%$ for entry velocities of 25 m/s, 30 m/s, 35 m/s and 40 m/s respectively. This is significant as it illustrates a large reduction in the thrust power of the aircraft. The propeller force in the X direction of the velocity axes is a function of the propeller thrust and the angle of attack. The large reductions in the X component of the propeller thrust indicate large angles of attack. The propeller thrust vector illustrates a shift from a more horizontal orientation to a more vertical orientation. While the free-stream velocity would affect the propeller thrust, the variation of velocities through the manoeuvre is small enough to not vary the thrust by a large amount. This then implies that the propeller thrust component in the X direction of the velocity axes was driven largely by the aircraft angle of attack. The X force component of the propeller thrust in the velocity axes is a cosine function of the angle of attack, as illustrated in Equation (207). The large changes in angle of attack are vital in the entry phase as they reduce the magnitude of the only positive X force, aiding in decelerating the aircraft. An adverse effect of the high angles of attack created in the entry phase is that large losses in velocity and thus energy occur. A reduction in the thrust power is observed. That is coupled with an increase in the drag power. Should an issue arise, the aircraft will be orientated at high angles with little means of adding energy, resulting in a difficult recovery scenario. The X force due to the propeller normal force aids in decelerating the aircraft. It provides a negative force throughout the entry phase. The propeller normal force component in the X direction increases in magnitude with a gentle slope attaining a maximum (negative) value near the end of the entry phase. The steepness of the slope of the propeller normal force component is different to that of the force component of the propeller thrust because the normal force is more sensitive to changes in free-stream velocity than the thrust. The point at which the propeller normal force component begins increasing is identical to that of the propeller thrust component.

The weight component acting in the X direction of the velocity axes increases in magnitude throughout the entry phase, becoming more negative. A gradient similar to that of the propeller thrust component is seen in the entry phase. The weight component is seen to be ≈ 0 N at the very start of the manoeuvre for all entry velocity cases. This is due to the orientation of the aircraft. At the start of the manoeuvre the aircraft flight path angle is at a near horizontal orientation. This results in a weight vector that acts

almost completely in the Z axis in the velocity frame. The force from the aircraft weight is negative throughout the entry phase. As the flight path angle increases through the entry phase the magnitude of the weight component increases in a sinusoidal fashion. By the end of the entry phase the aircraft weight component has grown to an appreciably large value. Aircraft weight force components of -3195 N, -3644 N, -3644 N and -3195 N are seen at the end of the entry phase for entry velocities of 25 m/s, 30 m/s, 35 m/s and 40 m/s respectively. The weight component in the X axis is a function of the flight path angle only. The free-stream velocity has no influence on the weight component. Two identical sets of weight components are seen at the end of the entry phase for two sets of flight path angles. Entry velocities of 25 m/s and 40 m/s conclude the entry phase at flight path angles of 26°. Entry velocities of 30 m/s and 35 m/s conclude the entry phase at flight path angles of 30°. These differences in flight path result in the two sets of weight components. The weight component values alone are sufficient to overcome the thrust force components at the end of the entry phase. This is in spite of the increase in thrust force component seen towards the end of the entry phase. While the weight component assists in decelerating the aircraft, the large negative force places the aircraft in a precarious situation should an issue arise. The aircraft weight component cannot be directly controlled by the pilot during flight.

The X component of the aerodynamic drag of the outer wing section along with the lift and drag components of the inner wing section all provide negative force in the velocity axes during the entry phase of the manoeuvre. The drag of the outer wing follows a sinusoidal shape in the entry phase, increasing and then decreasing in magnitude. A steep slope is seen as the outer wing drag component increases in magnitude (becoming more negative). This rapid change illustrates a large increase in angle of attack. The free-stream velocity decreases decrease over the same period in which the outer wing section drag increases. This suggests that the drag increase is driven by the angle of attack change. The decrease in the free-stream velocity will act to reduce the magnitude of the drag values. Minimum outer wing drag force components of -2735 N, -3595 N, -4614 N and -5720 N are seen entry velocities of 25 m/s, 30 m/s, 35 m/s and 40 m/s respectively in the entry phase. These values are greater than the thrust force component at the flight path angles at which they occur. This illustrates the large decelerating effect the outer wing has of the flight path. The X component due to the drag of the inner wing section illustrates an identical shape to that of the outer wing drag and exhibits similar magnitudes for all entry velocity cases apart from the 40 m/s case. There is a slight offset in the flight path angle at which the minimums occur for each of the entry velocity cases. This is due to a mismatch in surface angle of attack. The outer wing section is influenced solely by the free-stream velocity while the inner wing section is influenced by the free-stream velocity and propeller slipstream velocity. The similar magnitudes occur despite the inner wing section showing smaller drag coefficients than the outer wing section. This is due to the accelerated flow over the inner caused by the propeller slipstream. The slipstream reduces the angle of attack of the inner wing section compared to the overall angle of attack

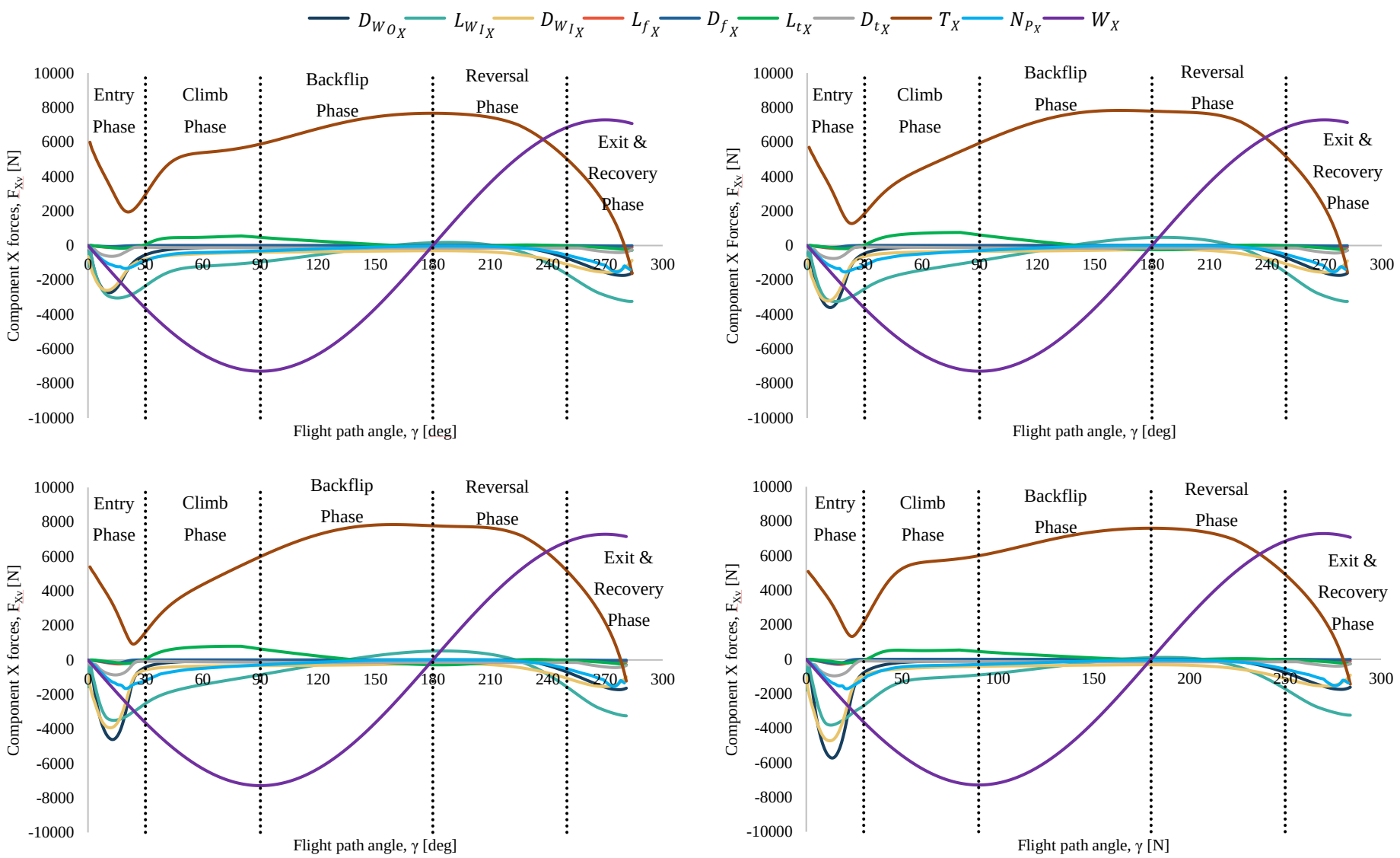

Figure 122: Component X forces in the velocity axes for entry velocities of 25 m/s (top left), 30 m/s (top right), 35 m/s (bottom left) and 40 m/s (bottom right)

of the aircraft and provides an increased velocity over the inner wing section. The lift component of the inner wing section acting in the X axis of the velocity axes provides additional negatives forces. The comparatively large lift values in the X axis indicate that larger angles of attack are experienced by the aircraft than in conventional flight. In conventional flight the wing lift would contribute little (if anything) towards the X forces. The lift component of the inner wing section increases in magnitude (becoming more negative) with a slope similar to that of the drag component of the inner wing section. Minimum drag values of -3044 N, -3245 N, -3498 N and -3817 N are seen for entry velocities of 25 m/s, 30 m/s, 35 m/s and 40 m/s respectively. Larger differences between the X component of the outer wing section lift and drag are seen for larger entry velocities. These differences are largely due to differences in the free-stream velocity for the various entry velocity cases. A change of slope is seen at a similar flight path angle to that of the inner wing drag component. The lift component does not decrease in magnitude as rapidly as the drag component. While both the lift and drag components experience the same velocity term, this would suggest that the inner wing section coefficient is larger than that of the drag. Observing Figure 78 and Figure 79 in §3.3.2, it would appear that the angle of attack of the inner wing section is $\approx 40°$. At this angle of attack the coefficient of lift is noticeably larger than the coefficient of drag but is still post-stall. The changes in slope of the inner and outer wing section components occur due to a rapid decrease in free-stream velocity, as seen in Figure 117. The horizontal tail surface contributes only a small amount of force in the X direction of the velocity axes during the entry phase. The drag component in the X direction of the horizontal tail contributes a small amount to the total force and follows a near sinusoidal shape.

The X force component of the propeller thrust continues to increase in the climb phase. This continued increase in propeller thrust illustrates a continued decrease in angle of attack and free-stream velocity. By the end of the climb phase, propeller thrust components of 5884 N, 5939 N, 5992 N and 6002 N are illustrated for entry velocities of 25 m/s, 30 m/s, 35 m/s and 40 m/s respectively. At this stage in the manoeuvre the X component of the thrust values have already recovered their starting values with some cases even exceeding their starting values. This is due to a reduction in the aircraft angle of attack but also a large reduction in free-stream velocity. It is unlikely that the starting angles of attack would be recovered at this stage of the manoeuvre. The increases in thrust must be due to smaller free-stream velocities. The distributions of the X component of the propeller thrust for entry velocities of 30 m/s and 35 m/s illustrate identical shapes, while entry velocities of 25 m/s and 40 m/s exhibit similar distributions. These two sets are different to one another. Entry velocities of 25 m/s and 40 m/s illustrate a notably sharper gradient and an appreciable change in slope. Entry velocities of 30 m/s and 35 m/s continue through the phase with a near constant gradient. These differences can be attributed to dissimilar angle of attack distributions between the two sets. The shaper gradient for entry velocities of 25 m/s and 40 m/s would indicate a greater decrease in angle of attack when compared to the 30 m/s and 35 m/s entry velocity cases. The X component of the propeller normal force decreases in magnitude

with a flat slope, approaching a zero value near the end of the climb phase. Similar distributions can be observed for the inner and outer wing section drag components in the X axis. This is particularly true near the latter stages of the climb phase for all entry velocity cases. These distributions are shaped by the low free-stream velocity values and the decreasing aircraft angle of attack. The X force due to the inner wing section lift decreases in magnitude, much like the other wing force components. The lift, however, illustrates greater magnitudes due to the propeller slipstream effects. While some force is still generated by the inner wing section lift, the magnitudes are almost insignificant when compared to the propeller thrust and aircraft weight components. The shape of the distributions of the inner wing lift X force follows a similar shape to that of the propeller thrust X force for the respective entry velocity cases.

The aircraft weight component continues to provide a negative X force in the climb phase with increasing magnitude. The slope with which the X force of the aircraft weight decreases with is similar to the slope seen at the end of the entry phase. By the end of the climb phase the minimum weight values are obtained for each of entry velocity cases. An aircraft weight component value of -7287 N is achieved for all entry velocities. This is the total weight of the aircraft. This demonstrates that the complete magnitude of the aircraft acts in opposition to the thrust when on a purely vertical flight path. A gentle change in slope is seen for the X force of the aircraft weight towards the end of the climb phase. This is an important period in the manoeuvre as it has the aircraft orientated in the least favorable orientation for recovery, assuming that the free-stream velocity is low and that the aerodynamics from the free-stream component are not driving. The X force due to the horizontal tail drag is negligible during the climb phase, however the X component of the lift force now provides a positive force. While the magnitude of this force is small compared to the driving forces in this phase, the positive value indicates that the horizontal tail has regained efficacy. This illustrates that a reduction of angular velocity has likely taken place and that the free-stream velocity component has reduced. A greater force magnitude for the horizontal tail X component of lift is seen for entry velocities of 30 m/s and 35 m/s as compared to 25 m/s and 40 m/s. This suggests that the horizontal tail is more efficient for entry velocities of 30 m/s and 35 m/s. This notion provides some validation for the smaller tumbles seen in Figure 114 of §5.3. This slight increase in efficiency accounts for the marginally lower free-stream velocities seen in Figure 117 during this phase. The greater tail efficiency will also allow these two entry velocity cases to sustain higher angles of attack through the climb phase.

The backflip phase sees the X component of the propeller thrust continue to increase in magnitude until a flight path angle of $\approx 150°$, after which a near constant value is sustained. This is true for all entry velocity cases. The change in slope to a near constant value is due to near constant free-stream velocity and low angles of attack. The sustained value does not specifically indicate a constant angle of attack but rather that the angles of attack are sufficiently low that the X force of the propeller thrust is near constant. Magnitudes of 7668 N, 7835 N, 7848 N and 7598 N are achieved for the propeller thrust

component for entry velocities of 25 m/s, 30 m/s, 35 m/s and 40 m/s respectively. These values are close to the maximum thrust illustrated in Figure 102 of §3.3.6. This suggests that very low airspeeds and angles of attack are present at this stage in the manoeuvre. The X force due to the propeller normal force continues to decrease with a gradient similar to that seen in the climb phase and reaches a minimum at a flight path angle of $\approx 150°$. Similar trends are observed for the inner and outer wing section X force drag components. The minimum values are sustained for the remainder of the phase. While the inner wing lift force continues to decrease in a similar manner to the wing drag forces, entry velocities of 30 m/s and 35 m/s illustrate a positive value of ≈ 500 N halfway through the phase. This is indicative of a negative angle of attack, as the wing lift is now acting downwards. The aircraft weight X component creates a mirror image of the X force weight distributions seen in the entry and climb phase. The weight component decreases during this phase and reaches a 0 N value at a flight path angle of $180°$ for all entry velocity cases. This indicates that the weight component acts perpendicular to the flight path at the end of the backflip phase. The end of the backflip phase is a critical position to reach in terms of the X force contribution from the aircraft weight as beyond this point the aircraft weight no longer decelerates the aircraft but aids in accelerating it. For a recovery from the manoeuvre, accelerations are an important aspect of regaining regular flight velocities. While the aircraft is still in a non-standard orientation and in a potentially dangerous situation, recovery is more easily achieved beyond this point, should any issues arise. The X force of the horizontal tail lift gradually decreases in magnitude throughout the phase, reaching a near zero value mid-way through the phase. This suggests that an increase in angular velocity takes place over the horizontal tail as the free-stream velocity remains near constant through this phase.

The reversal phase sees the X force due to the propeller thrust maintain value until a flight path angle of $\approx 220°$ before decreasing with an appreciably large negative slope. This decrease in X force due to propeller thrust is maintained through to the end of the phase. By the end of the phase the propeller thrust component reduces to a value that is 60 % that of the starting value. This holds true for all entry velocity cases. The largest reduction in the X force of the propeller thrust is indicative of an increase in angle of attack. The X force distributions of the inner and outer wing components in this phase, also illustrate a negative gradient, albeit shallower than that of the thrust force X component. These components all increase in magnitude, at the same flight path angle at which the X force of the propeller thrust decreases. The force components are near constant up until this point. These changes occur after the free-stream velocity has already increased. This suggests that the change in value for these components occurs as a result of an angle of attack change. The steeper gradient of the X force component of the inner wing suggests that the angle of attack of the inner wing section is less than that of the free-stream velocity component. The X component of the inner wing section lift shows values of -2293 N, 1568 N, -1564 N and -2394 N for entry velocities of 25 m/s, 30 m/s, 35 m/s and 40 m/s respectively at the end of the reversal phase. The contribution of the horizontal tail to the X force is near

negligible in this phase. The inner and outer wing drag values illustrate magnitudes approximately half those of the inner wing section lift for all entry velocity cases. Magnitudes similar to those seen at the end of the entry phase are illustrated at the end of the reversal phase for the wing lift and drag. The contribution of the aircraft weight to the X force increases with a moderate slope as the phase progresses. It continues to follow a sinusoidal trend. The contribution of the aircraft weight component indicates that the aircraft is now orientated such that it is on a trajectory towards the ground. This is highlighted by the positive contribution of the weight to the X force. Due to a constant application of elevator deflection, the aircraft continues to rotate through this phase. The constant rotational moment created in this phase results in large angles of attack being attained leading into the exit and recovery portion of the manoeuvre. Ideally, the pilot would want to ease and even switch the elevator deflection angle mid-way through this phase to position the aircraft in a more beneficial orientation for recovery. The increase of negative X force components and decrease of positive X force components in this phase results in larger drag powers than thrust power. This acts to decrease the energy gain of the aircraft in a phase where energy should be built up.

Due to the constant application of elevator in the reversal, exit and recovery phases the X force component due to the propeller thrust continues to decrease with a steep gradient. The X force due to the propeller thrust attains a negative value at a flight path angle of $\approx 280°$. This is an indication that the aircraft is falling towards the ground at a very steep angle of attack ($\geq 90°$). The thrust becomes negative because the aircraft trajectory is aimed towards the ground while the thrust vector is pointed forwards. This places the aircraft in a very dangerous scenario as the thrust is now decelerating the aircraft instead of accelerating it. The X forces arising from the inner and outer wing sections continue to increase in magnitude through this phase and attain larger negative values. This is an indication that both the free-stream velocity and angle of attack are increasing. This shows that the aircraft is accelerating towards the ground at a high angle of attack. The larger magnitude of the X force component of the inner wing lift illustrates that the propeller slipstream is still actively blowing air over the inner wing section and that the angle of attack of the inner wing section is less than that of the aircraft. The recovery phase is traversed in a very short period of time and can lead to a very undesirable situation if corrective action is not taken in a timely manner. This highlights the dangers of manoeuvre and the speed at which potentially dangerous situations could arise.

5.3.7.1. Specific Excess Power in the Velocity Axes

The force components that were processed to obtain the acceleration of the aircraft in the velocity axes may also be used to generate specific excess power values. Figure 123 presents the specific excess power throughout the tumble manoeuvre for various entry velocities. Two sets of distributions are presented: one which includes the effects of the aircraft mass on the specific excess power and another which excludes the aircraft mass. The two sets of data are presented together to illustrate the effect of the mass on the ability of the aircraft to recover energy.

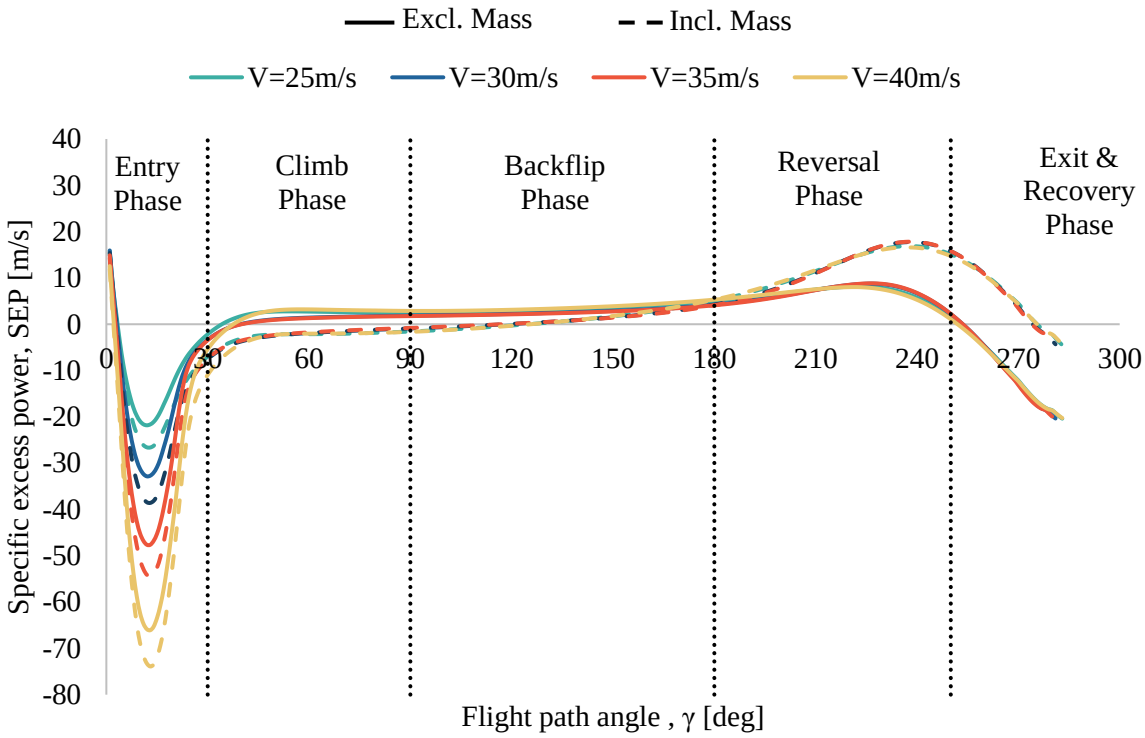

Figure 123: Specific excess power

Identical values of specific excess power are seen at the entry to the manoeuvre for cases including and excluding the effects of the aircraft mass. This is due to the orientation of the aircraft at the beginning of the manoeuvre. A pitch angle and angle of attack of $\approx 14°$ are seen at the entry but more importantly, the flight path angle is $= 0°$. This means that the mass of the aircraft makes no contribution to either the thrust power or the drag power. Specific excess power values of 15.78 m/s, 15.93 m/s, 14.89 m/s and 12.56 m/s are seen at the start of the manoeuvre for entry velocities of 25 m/s, 30 m/s, 35 m/s and 40 m/s respectively. While not excessively large, the aircraft begins the manoeuvre with a small amount of excess energy. The energy quickly dissipates as it is transformed into a rotational motion and is then subsequently lost as aerodynamic drag. This large decrease in specific excess power mimics the shape of the acceleration curve in Figure 121 of §5.3.6. The largest losses in energy are seen midway through the entry phase of the manoeuvre. This coincides with the large decelerations seen in the entry phase. These strongly negative excess powers indicate that the aircraft no longer has an ability to gain energy and that energy must be taken from the mechanical stores. This occurs in the form of a loss in airspeed as altitude is not lost. The aircraft mass reduces the specific excess power of the aircraft as flight path angle increases. This is because it acts in the drag direction, resulting in a greater drag power. Minimum values of -21.83 m/s, -32.85 m/s, -47.62 m/s and -66.10 m/s are seen for entry velocities of 25 m/s, 30 m/s, 35 m/s and 40 m/s respectively without the inclusion of the aircraft mass. These values decrease to -26.59 m/s, -38.58 m/s, -54.44 m/s and -73.90 m/s with the inclusion of the aircraft mass. This effectively means that the aircraft mass helps reduces the energy and thus airspeed at a faster rate. After

the peak magnitudes in the entry phase an increase in specific excess power is observed. This is due to the reduction in free-stream velocity. As the velocity approaches a 0 m/s value so does the specific excess power.

Shortly after the start of the climb phase the specific excess power values become positive at a flight path angle of $\approx 40°$ for cases excluding the mass of the aircraft. This means that without the mass, the aircraft would be able to start gaining energy shortly after the entry phase. The distributions that include the aircraft mass follow remain negative for the entirety of the climb phase. This means that in reality the aircraft would need to continue losing small amount of mechanical energy in the climb phase. The magnitudes of both sets of distributions are seen to be small through the duration of the climb phase. This is due to the low free-stream velocity values observed in this phase. The low velocity values result in low thrust and drag powers. The specific excess power remains near constant for a large portion of the climb phase for cases without the aircraft mass included. The specific excess power distributions with the inclusion of the aircraft mass illustrate a steady but small increase in value, approaching a 0 m/s value.

During the backflip phase the specific excess power curves without the inclusion of mass show the same constant value seen in the climb phase. A small gain in specific excess power is seen towards the end of the phase. The distributions of specific excess power that include the aircraft mass continue to increase in the backflip phase and become positive at a flight path angle of $\approx 120° - 125°$ depending on the entry velocity. This is a significant point in the manoeuvre as it indicates a position at which the aircraft can start gaining energy again. While the aircraft mass still acts in the drag direction this aircraft orientation the forces acting in the thrust direction are able to overcome those due to the aerodynamic drag and mass of the aircraft. The manoeuvre can be aborted from this point with a fairly high chance of success. The specific excess power curves with the inclusion of the aircraft mass continue to increase through the phase. At the very end of the phase the values from both sets of meet. This is due to the direction of the weight vector at this orientation. At a flight path angle of $180°$ the weight vector acts perpendicular to the free-stream velocity and thus has no influence on the specific excess power. Specific excess power values of 5.06 m/s, 4.24 m/s, 4.09 m/s and 5.30 m/s are seen at the end of the backflip phase for entry velocities of 25 m/s, 30 m/s, 35 m/s and 40 m/s respectively. While these values are not large, they indicate that the aircraft may begin gaining airspeed from this point onward.

In the reversal phase the specific excess power distributions without the inclusion of the aircraft mass continue to increase slowly up until a flight path angle of $\approx 230°$ for all entry velocity cases. The decrease in specific excess power is a result of a high angle of attack and an increase in free-stream velocity. As the aircraft continues to rotate the angle of attack and pitch angle of the aircraft increase. At steep enough angles the propeller thrust acts in a direction that does not coincide with the free-stream velocity vector. This means that the propeller thrust no longer adds thrust power to the aircraft. Increases

in free-stream velocity also increase the drag power of the aircraft. The specific excess power values become negative again for the distributions excluding the aircraft mass at a flight path angle of $\approx 250°$. The inclusion of mass changes the specific excess power distributions in the reversal phase. Beyond a flight path angle of $180°$ the aircraft mass acts in the thrust power direction and aids in gaining energy. This the means that the specific excess power continues to increase in the reversal phase. While the aircraft mass is detrimental in terms of energy in the entry phase, it becomes beneficial in the reversal phase. Peak values of 16.87 m/s, 17.69 m/s, 17.82 m/s and 16.60 m/s for entry velocities of 25 m/s, 30 m/s, 35 m/s and 40 m/s respectively. This occurs at flight path angles of $\approx 240°$. At this point pilots should begin to ease or reverse the elevator deflection and begin a recovery. A failure to do this will result in a loss of specific excess power as angles of attack and pitch angles continue to increase. This is seen as the specific excess power values decrease towards the end of the phase, both with and without the inclusion of mass.

In the exit and recovery phase the specific excess power curves continue to decrease with the same negative gradient seen at the end of the reversal phase. The specific excess power curves with the inclusion of mass become negative at a flight path angle of $\approx 275°$. This indicates an aircraft orientation at which the aircraft thrust no longer acts in the desired direction. The aircraft mass is the only component adding thrust power to the system and is not sufficient in overcoming the drag power. This is an unfavorable scenario as the aircraft is unable to add additionally energy to the system. Energy must thus be taken from the mechanical stores. The airspeed is relatively low, suggesting that altitude must be lost in order to gain energy.

5.3.8. Angle of Attack and Pitch Angle

The ability of the aircraft to exert accelerations both in the longitudinal and normal directions that exceed the limitations of normal operation are made possible by flying at high angles of attack. Angles of attack well beyond the stall limit of the aircraft are required. Angles of attack less than or equal to the stall value would not allow sufficient deceleration nor would they allow the required load factors to be applied in order to complete a tumble manoeuvre. Lower angles of attack would result in a normal loop being performed. Distributions of the angle of attack and pitch angles seen during a tumble manoeuvre for various entry velocities are plotted in Figure 124.

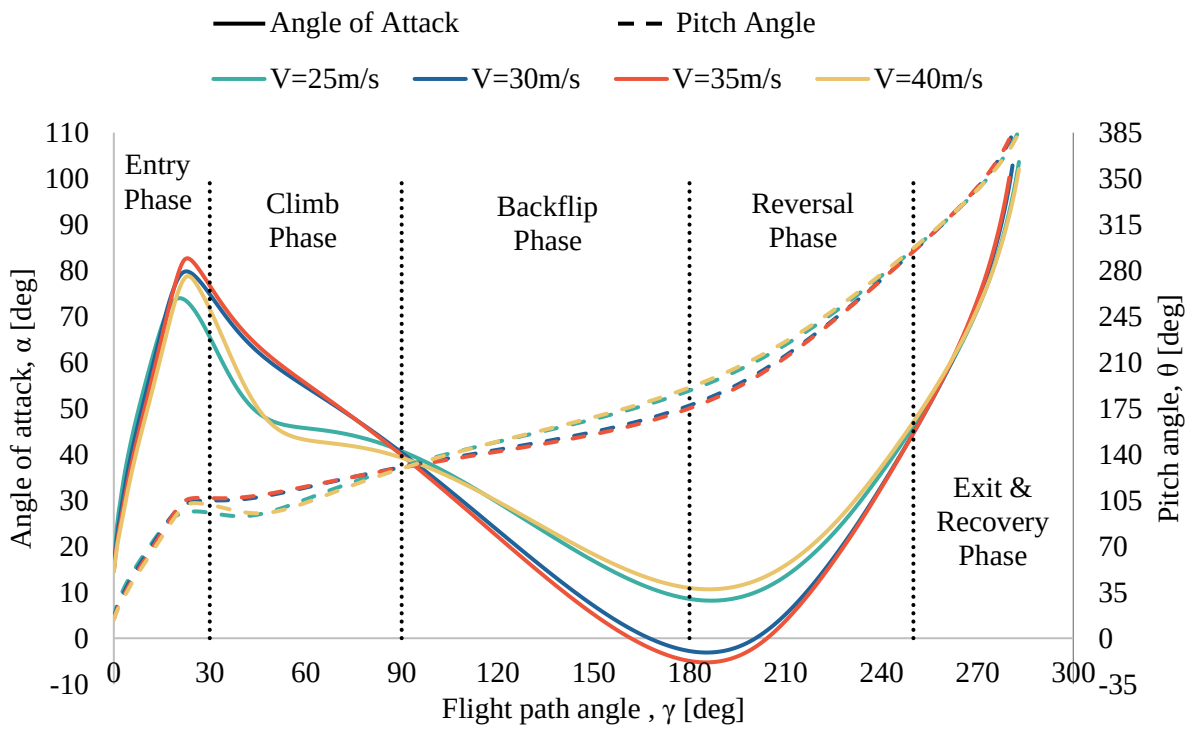

Figure 124: Angle of attack and pitch distributions for tumble manoeuvres of various entry velocities

At the very start of the entry phase the angle of attack and pitch angle share the same value (14°). Once the elevator is deflected the pitch angle increases sharply relative to the flight path angle. This rapid increase in pitch, relative to the flight path angle, causes the angle of attack to subsequently increase as well. The angle of attack values show very similar magnitudes for all entry velocities up until $\gamma \approx 20°$, after which a divergence in values is seen. The angle of attack for entry velocities of 25 m/s, 30 m/s, 35 m/s and 40 m/s peak at $21°, 23°, 23°$ and $23°$ respectively. Peak angle of attack values of $73.95°, 79.79°, 82.66°$ and $78.57°$ are seen for the respective entry velocity cases. While these peak values are significant the short time over which they arise is noteworthy. A large impulse and angular momentum is required to produce these values. After peaking the angle of attack values begin to decrease with a shallower slope magnitude than the slope magnitude with which they increased. The decrease in angle of attack value can be attributed to the change in slope that occurs for the pitch angles. The change in slope of the pitch angle distributions results in a pitch rate that is lower than the rate of change of the flight path angle. This results in a reduction in angle of attack. The pitch distributions change from a steep, positive gradient to a near flat gradient. These flat gradients are caused by an increase in counteracting aerodynamic moments as the aircraft angle of attack increases. This results in losses in angular momentum. The brief period of constant pitch angle results in a decrease in angle of attack, as while the pitch angle remains constant the flight path angle continues to increase.

The start of the climb phase shows the pitch angle slopes experience a negative gradient for entry velocities of 25 m/s and 40 m/s. This is seen up until a flight path angle of $\approx 45°$ for these two cases before a change to a positive slope is seen. Entry velocities of 30 m/s and 35 m/s see a positive, shallow gradient throughout the climb phase. The gradients seen for entry velocities of 30 m/s and 35 m/s are smaller in magnitude than the positive gradient seen for the 25 m/s and 40 m/s cases. The differences in pitch angle seen through the climb phase are a result of different free-stream velocities and aerodynamic moment distributions. These variations in pitch angle in the climb phase result in slightly differing angle of attack distributions for the various entry velocities. The near constant, flat and positive gradient for the 30 m/s and 35 m/s cases results in a decrease in the angle of attack for these cases with a near constant slope. The angle of attack for entry velocities of 25 m/s and 40 m/s decreases in value throughout the climb phase with two different gradients. Initially the angle of attack decreases with a steep gradient, before transitioning to a shallower gradient when the pitch values begin to increase again. At the end of the climb phase the angle of attack and pitch angle values all approach similar values for each of the entry velocity cases. The aircraft pitch angles approach a value of $\approx 130°$ while the angles of attack approach an angle of $\approx 40°$. Despite an evident reduction in angular momentum the pitch values still illustrate a greater magnitude than the flight path angles at the end of the phase by $\approx 40°$. This emphasises the size and speed of rotation seen in the entry phase. Entry velocities of 30 m/s and 35 m/s end the climb phase with the same negative gradient slope, while entry velocities of 25 m/s and 40 m/s have similar negative gradient slopes but are marginally offset from one another.

In the backflip phase the gradients of the pitch distributions continue with the same slope seen at the end of the climb phase, for all entry velocities. This results in constant gradient decreases in angle of attack as the pitch rate increases at a slower rate than the flight angle. Negative angles of attack are seen for entry velocities of 30 m/s and 35 m/s at flight path angles of $> 165°$. Angles of attack for entry velocities of 25 m/s and 40 m/s remain positive for the entire duration of the phase. At the end of the phase angles of attack of $8.56°, -2.79°, -4.98°$ and $10.93°$ are seen for entry velocities of 25 m/s, 30 m/s, 35 m/s and 40 m/s respectively. The pitch angles conclude the backflip phase at values of $188.56°, 175.48°, 175.05°$ and $190.93°$ respectively. The magnitudes of these values are significant in recovering from the manoeuvre. At the end of the backflip phase the aircraft is orientated near horizontally, albeit inverted and is at low angles of attack. This combination of angles presents the best possible orientation for recovery.

The reversal phase sees a change in gradient for the pitch angle distributions, for all entry velocities. The gradients remain positive and transition to a steeper slope. This causes the pitch angle to increase at a greater rate relative to the flight path angle. The result of this change in pitch rate is that the angle of attack once again increases. The increase in pitch rate is due to an increase in angular velocity. The increased angular velocity is due to a reduction in opposing moments. The gradient of the slope is

greater (and similar) for entry velocities of 30 m/s and 35 m/s as compared to those seen for entry velocities of 25 m/s and 40 m/s. This results in greater changes in pitch angle and angle of attack over this phase for entry velocities of 30 m/s and 35 m/s. The end of the phase the pitch angle and angle of attack values converge for all entry velocities. Pitch angles of $\approx 317°$ and angles of attack of $\approx 57°$ are seen for all entry velocities. The continued application of elevator in this phase results in a large angle of attack at the end of the phase. This is not ideal as higher angles of attack make for more difficult recoveries. The pitch angle has once again grown larger than the flight path angle. This illustrates a gain in angular momentum.

The exit and recovery phase sees each of the entry velocity distributions, for both pitch angle and angle of attack, increase with an almost identical gradient slope. The slopes for the pitch angles and angles of attack are different. This produces pitch angle and angle of attack values, for all entry velocity cases, with similar values throughout the phase. The gradient of the slopes is steep resulting in large pitch angle changes and subsequently large angle of attack changes. The large, positive changes that occur in this phase illustrate the dangerous angles of attack and trajectories that can be attained if corrective measures are not implemented. The rapid increase in angle of attack to values approaching $100°$ indicates a downward trajectory with large vertical velocity components and low horizontal velocity components. These factors are in contrast to the desired variables for recovery when exiting the manoeuvre. To recover, a more horizontal trajectory with larger horizontal velocity components is favored.

5.3.8.1. Pitch Angle Visualisation

To better visualise the pitch angle changes required for a minimum radius tumble manoeuvre, aircraft pitch illustrations have been overlaid on the flight path of a tumble manoeuvre in Figure 125. This was performed for an entry velocity of 30 m/s. Each of the Extra 330SC aircraft images in Figure 125 have been scaled such that the aircraft images are correctly scaled to the figure axes. The most notable occurrence takes place in the entry phase where the aircraft very clearly increases its pitch angle to large values at the start of the manoeuvre. From a flight path angle of $20°$ onward, the aircraft appears to increase only slightly in pitch angle until the end of the climb phase (at $\gamma = 90°$). This can be attributed to restoring aerodynamic moments counteracting the inertial, angular moments induced by the initial angular impulse. The initial increase in pitch angle occurs in a very short time frame with the more static (but large) pitch angles occurring over a much longer time frame. The backflip phase sees large pitch changes occur over a short period of time, suggesting the aerodynamics now no longer act to counteract the desired angular motion. The reversal phase shows the thrust directing the aircraft in a backward and downward trajectory initially but quickly changing to a downward and forward acting force. The rotations of the aircraft in the reversal phase rotate the tail of the aircraft upward and backward in a short time span. The exit and recovery phase clearly illustrate the hazardous situation

that could arise as a result of continued elevator deflection. The aircraft can be seen travelling on a downward trajectory at a steep angle of pitch.

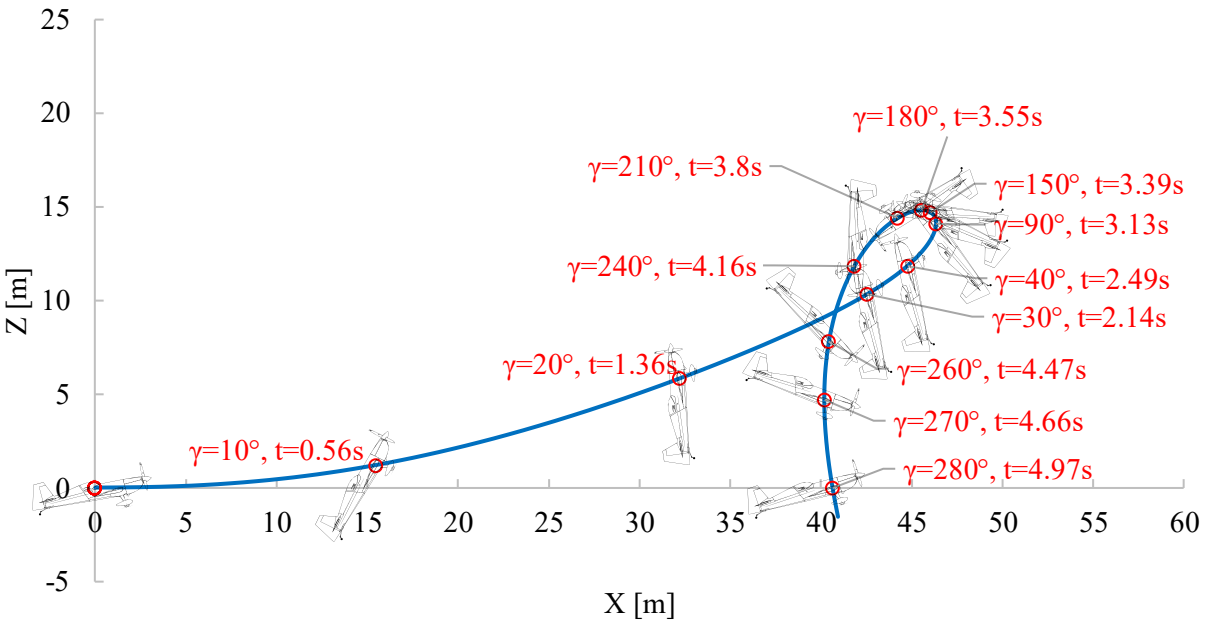

Figure 125: Flight path of a tumble manoeuvre with aircraft pitch angle illustration for a 30 m/s entry velocity

5.3.9. Aerodynamic Moments and Angular Velocity

The angular accelerations and velocities an aircraft experiences are a result of the inertial kinematics as well as the aerodynamic moments. Angular accelerations are required to create destabilising moments. The aircraft pitch angles and angles of attack required to perform an aerobatic tumble manoeuvre involve specific aerodynamic moments and angular accelerations. The aerodynamic moments produced during a tumble manoeuvre for various entry velocities are presented in Figure 126. The resulting angular velocities are provided in Figure 127.

As full elevator deflection is applied at the very beginning of the manoeuvre a large, negative moment is seen in Figure 126. This acts to create a nose-up, destabilising rotation of the aircraft. Larger entry velocities create larger initial destabilising moments. Moment values of -1984 Nm, -2173 Nm, -2367 Nm and -2542 Nm are seen for entry velocities of 25 m/s, 30 m/s, 35 m/s and 40 m/s respectively. The large negative moments give rise to a large increase in angular acceleration and subsequently angular velocity. This can be seen by the near vertical increase in angular velocity shown at the start of Figure 127. The angular accelerations rise to peak values of 109 °/s, 121.68 °/s, 133.84 °/s and 144.45 °/s for entry velocities of 25 m/s, 30 m/s, 35 m/s and 40 m/s respectively.

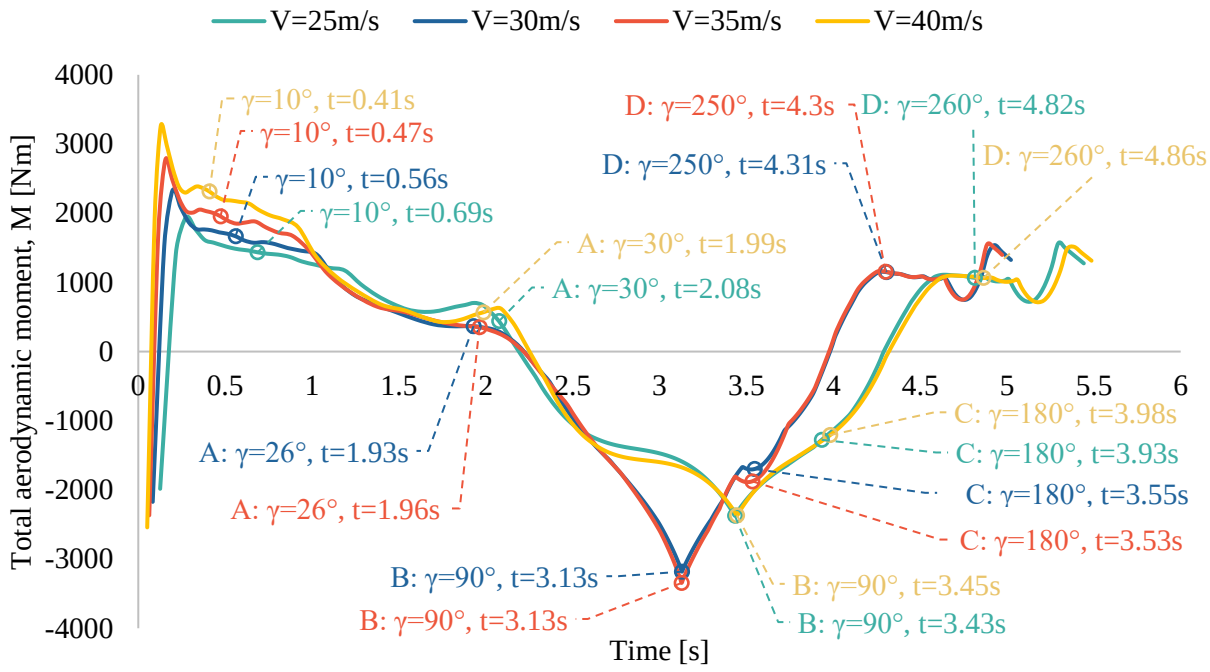

Figure 126: Total aerodynamic moment for tumble manoeuvres for various entry velocities

These values are far greater than regular rates of pitch and while they are large, they are not sustained for any considerable period of time, decreasing as soon as they are reached. As soon as the angular velocity increases the moment sees a near vertical gradient, increasing the total moment acting on the airframe from negative values to positive values. The apex of the rise results in the maximum moment values of the manoeuvre. Peak values of 1940 Nm, 2328 Nm, 2765 Nm and 2992 Nm are seen for entry velocities of 25 m/s, 30 m/s, 35 m/s and 40 m/s respectively. The magnitude of these peak moments and the short time in which they occur illustrates that the aerodynamic moments act to counter the desired direction of rotation almost immediately after the initial impulse. This change in sign for the total moment implies that the aerodynamic forces now act to stabilise the aircraft and create a nose-down moment. The sudden, large increase in moment is brought upon by the change in angular velocity and the resulting change in angle of attack. The sudden angular impulse gives rise to angular velocity components that generate larger forces. The high angles of attack, at which these forces are generated, create large positive, stabilising moments. The effect of the stabilising moments is seen in the decreasing values of the angular velocity distributions in Figure 127, immediately after the peak. While the angular velocity decreases over the duration of the entry phase, the value of each of the distributions remains positive throughout the phase. This is in spite of strongly positive, aerodynamic restoring moments. This suggests that the angular momentum (inertia) of the aircraft, generated from the initial angular impulse, is large enough to slow the rate of angular deceleration, keeping the angular velocity positive. This allows the aircraft to retain higher pitch angles and angles of attack throughout the entry phase.

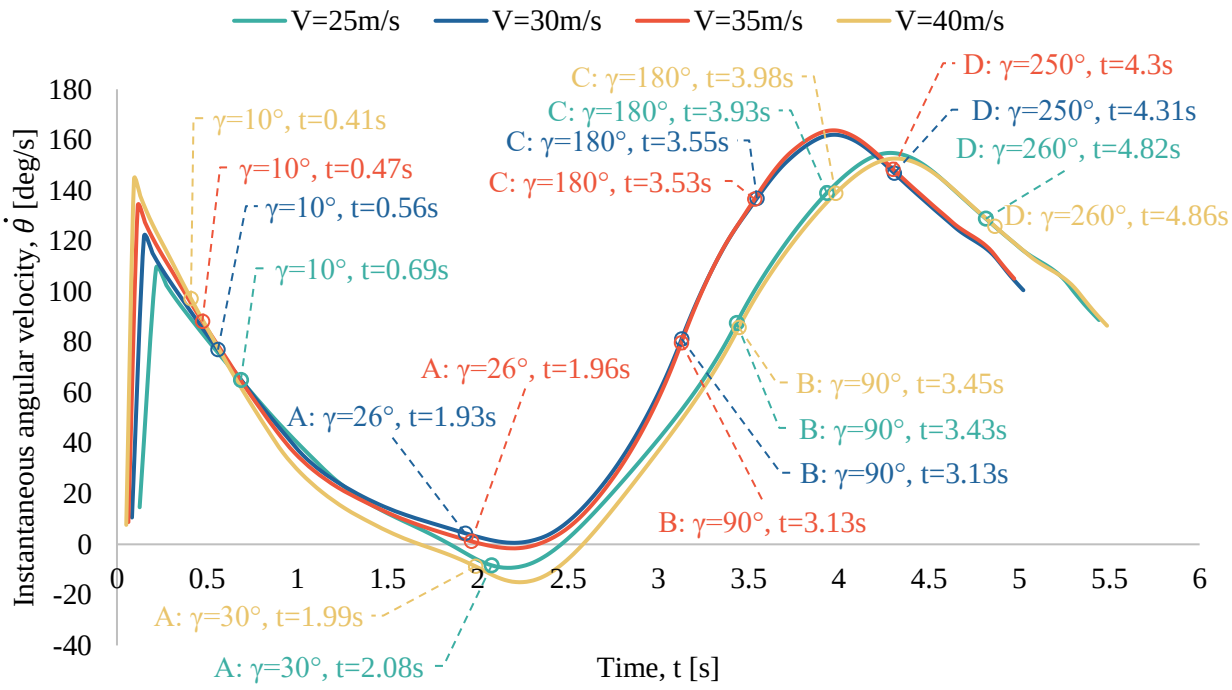

Figure 127: Angular velocity for tumble manoeuvres with various entry velocities

Retaining high pitch angles and angles of attack is vital in completing a tumble manoeuvre, making the entry phase pivotal to the success of the manoeuvre. The high angles of attack act to decelerate the aircraft velocity to a point at which the aerodynamic moments no longer counteract the desired direction of rotation. In addition to the decelerations provided by the high angles of attack, the high pitch angles position the aircraft such that it is easily (relatively speaking) able to transition into subsequent phases of the manoeuvre. The climb and backflip phases would not be possible from low pitch angles. From the peak of the total moment curves the values decrease in three distinct sections. The first section shows a small decrease of total moment with a step gradient, reaching moment values of 1611 Nm, 1866 Nm 2032 Nm, 2298 Nm for entry velocities of 25 m/s, 30 m/s, 35 m/s and 40 m/s respectively. These values illustrate the speed at which the peak moments decrease. A flat, shallow gradient is then seen before finally returning to a steeper gradient once again for the remainder of the entry phase. The entry phase concludes with aerodynamic moments of 439 Nm, 367 Nm, 352 Nm and 568 Nm for entry velocities of 25 m/s, 30 m/s, 35 m/s and 40 m/s respectively. These values are comparatively low and indicate that the restoring moments reduce significantly by the end of the entry phase. This reduction in moment allows for continued rotation. The decreases in total moment are a result of the decreasing velocity throughout the entry phase. The distributions of the angular velocity are less complicated than those of the total moment. This is due to the influence of the aircraft inertia. After the peak angular velocities, the distributions decrease with an $\approx 45°$ gradient before transitioning into a slightly shallower gradient at the same point at which the third gradient occurs in the total moment plots. The

angular velocities decrease from the peak points reaching < 60 °/s rates after ≈ 0.7 s of manoeuvre time. Towards the end of the entry phase the angular velocities approach a zero value. Entry velocities of 30 m/s and 35 m/s approach a near zero angular velocity value at the end of the entry phase while entry velocities of 25 m/s and 40 m/s see small negative angular velocity values at the end of the entry phase. The constantly decreasing angular velocity distributions in the entry phase illustrate why the aircraft appears to be unable to rotate any further in the entry phase in Figure 125, after the large initial rotation. The inertial destabilising moments and aerodynamic restoring moments also appear to be almost in balance after the initial rise in pitch angle. This illustrates why very little change in pitch angle is observed.

The climb phase shows a large change in gradient for the total moment plots. The total aerodynamic moments attain negative values for the first time since the initial impulse. The various entry velocities experience similar total aerodynamic moment values until ≈ 2.6 s. After this point the curves diverge. Entry velocities of 30 m/s and 35 m/s continue decreasing with the same gradient, while entry velocities of 25 m/s and 40 m/s shift to a far shallower gradient. The differences in gradients are created by the different angle of attack and velocities seen by both sets of entry velocity cases. The effect of the transition from positive aerodynamic moments to negative aerodynamic moments is that the angular velocity distributions increase shortly after commencing the climb phase. The gradient with which the angular velocity values increases is steep. Despite this steep increase in angular velocity an unremarkable pitch angle change is observed. This occurs as the duration over which the climb phase occurs is small and thus only small pitch angle changes can occur, even at high pitch rates. At the start of the climb phase the angular momentum is also low, meaning that some time is required to build back to a noticeable angular rate. The total aerodynamic moment distributions decrease throughout the entirety of the climb phase, reaching a minimum value at the end of the phase. Minimum values of -2373 Nm, -3182 Nm, -3345 Nm and -2370 Nm are observed for entry velocities of 25 m/s, 30 m/s, 35 m/s and 40 m/s respectively. These minimum values are achievable due to the low free-stream velocity values and the propeller slipstream velocities seen during this phase. The low free-stream velocities mean that only components exposed to the propeller slipstream create noticeable aerodynamic moments. This is particularly true for the horizontal stabiliser. The propeller slipstream allows the horizontal tail to see a high velocity airstream at lower angles of attack while the aircraft velocity is near 0 m/s. The propeller slipstream allows the horizontal tail and elevator to remain effective even without any airspeed. This implies that the thrust transfers its energy to the horizontal stabiliser. The stabiliser then uses that energy to create an angular motion. The continued decrease in aerodynamic moment can also be attributed to the effects of the propeller normal force. The normal forces produced by the propeller gyroscopic effects at high angles of attack create large normal forces. These forces create a destabilising, nose-up moment for the Extra 330SC. During the climb phase a

change is seen in which the rotation of the aircraft transitions from being inertially driven to aerodynamically driven.

The backflip phase sees an immediate reversal in the total aerodynamic moment. An increase is seen, with a gradient identical to that which the moments decreased with, for both sets of entry velocities. The change in direction of aerodynamic moment is due to the increasing angular velocity and a loss in elevator efficacy with the increase angular velocity component. The two sets of entry velocities continue to increase with a constant gradient throughout this phase. A change in gradient is seen at the end of the phase for entry velocities of 30 m/s and 35 m/s. This is linked to the negative angles of attack seen in Figure 124 for these two entry velocities towards the end of the backflip phase. The angular velocity distributions in the backflip phase are largely unaltered, increasing with similar gradients to those seen in the previous phase, for all entry velocity cases. The continued increase in angular velocity is due to the decreasing but still negative aerodynamic moment values. The backflip phase concludes with aerodynamics moment approximately half the value with which they began the phase. The angular velocities have once again rise to large values of 138 °/s for all entry velocities cases. This large angular velocity should provide enough momentum to rotate the aircraft around from its no

The aerodynamic moment values continue to increase in the reversal phase but change to a slightly steeper gradient. The total aerodynamic moments cross the x-axis and become positive in value at ≈ 4 s, for entry velocities of 30 m/s and 35 m/s. Entry velocities of 25 m/s and 40 m/s see a change in sign occur at ≈ 4.25 s. Both sets of entry velocity cases continue on the same gradient path through this phase of the manoeuvre until a transition to a flat, horizontal gradient is seen just before the end of the phase. The increase in total aerodynamic moment seen in this phase is due to an increase in free-stream velocity, seen in Figure 117 of §5.3.3. The increasing velocities give rise to increased aerodynamic forces which result in larger restoring aerodynamic moments. The angular velocity continues to increase along the same path, for both sets of entry velocity cases. A maximum value of 154 °/s is reached for entry velocities of 25 m/s and 40 m/s. A value of 162 °/s is reachd for entry velocities of 30 m/s and 35 m/s. These values are likely unrealistic as the pilot would have taken some corrective action at this point in the manoeuvre. The peak values are not sustained and the angular velocity values begin to decrease shortly after peaking. The maximum angular velocities for the two sets of entry velocity cases coincide directly with the time at which the total aerodynamic moments become positive in value. The positive moment values act to decrease the angular velocities. The gradient of the decreasing slopes is similar in magnitude to the gradient with which the values increased in this phase.

The exit and recovery phase sees the total aerodynamic moment values remain constant for ≈ 0.5 s, before dipping and increasing once again. The high values for each of the entry velocities are due to a continually and sharply increasing angle of attack, as seen in Figure 124 of §5.3.8. The angular velocity continues to decrease with the same gradient as in the previous phase, for all entry velocities. The

angular velocity values remain positive. The large increase in pitch angle and angle of attack is not solely dependent on the angular velocity of the aircraft. Due to the downward trajectory of the aircraft the angle of the velocity vectors leans toward the vertical more than the horizontal component. This further illustrates the 'falling' nature of the aircraft in this phase with continued application of the elevator. In the exit and recovery phase a high, sustained or increasing angular velocity is desired, to continue through a second tumble as quickly as possible. For a recovery after a single tumble a low or zero angular velocity is preferred. This is so the pilot can change the direction of rotation from a neutral position, in terms of angular rates. The end phases of the plots provided in Figure 126 and Figure 127 further iterate the notion that elevator deflection should be relaxed or have its direction altered prior to entering the exit and recovery phase.

5.3.10. Aerodynamic Moment Components

The total aerodynamic moment distributions plotted in Figure 127 undergo many changes in value and slope. Understanding why these changes take effect requires the moment distributions from each aircraft component. The aerodynamic moments produced by various aircraft components are plotted in Figure 128 for all entry velocities. The total aerodynamic moment (M_{tot}) has also been include in the plots. Moment components include contributions from the outer wing $\left(M_{W_o}\right)$, the inner wing $\left(M_{W_I}\right)$, the fuselage $\left(M_f\right)$, the horizontal stabiliser/tail (M_t), the propeller thrust (M_T) and the propeller normal force $\left(M_{P_N}\right)$. The flight path angles, at the end of each phase, and the times at which they occur, are indicated on each of the subplots. All aircraft moment components were determined in the body axes.

At the very beginning of the entry phase of the tumble manoeuvre, a large impulse is applied to the aircraft by the horizontal tail surface creating a large negative, destabilising moment. Horizontal stabiliser moments of -3094 Nm, -3321 Nm, -3583 Nm and -3854 Nm are seen for entry velocities of 25 m/s, 30 m/s, 35 m/s and 40 m/s respectively. While the force contributions from the horizontal stabiliser is seen to be unremarkable in §5.3.4 and §5.3.7, the moment contributions are pivotal in performing a tumble manoeuvre. This moment acts to rapidly rotate the aircraft nose-up and provide the necessary angles of attack to decelerate the aircraft. The overall starting moment is driven by the horizontal stabiliser moment. Smaller destabilising moments are also contributed by the fuselage and propeller normal force. The inner and outer wing sections along with the propeller thrust act to stabilise the aircraft and create a nose-down, restoring moment. The outer wing section contributes a larger moment than the inner wing section due to a longer moment arm. The aerodynamic centre of the outer wing section is located further rearward of the centre of mass than the inner wing section. The total initial moment contribution of the wing (inner and outer) is 681 Nm, 897 Nm, 1159 Nm and 1463 Nm for entry velocities of 25 m/s, 30 m/s, 35 m/s and 40 m/s respectively. The largest positive moment contribution is from the propeller thrust. Propeller thrust moments of 1222 Nm, 1155 Nm, 1091 Nm and 1028 Nm are seen for entry velocities of 25 m/s, 30 m/s, 35 m/s and 40 m/s respectively.

The sum total of the initial wing and propeller thrust moments still fall well short of the horizontal stabiliser moment. This illustrates the initial power of the horizontal stabiliser in driving the aerodynamic moments.

Immediately after the initial impulse, the moment of the horizontal stabiliser begins to rapidly decrease in magnitude (becoming less negative) with a steep positive gradient. This occurs for all entry velocity cases. This sudden change is induced by the angular velocity component acting on the horizontal tail surface. This large increase in angular velocity is seen in Figure 127 in §5.3.9. The large and sudden impulse creates a large perpendicular velocity component on the horizontal tail surface which increases the angle of attack of the horizontal tail. The increase in angle of attack decreases the lift and increases the drag of the horizontal tail surface, both of which reduce the destabilising moment. The moment created by the horizontal tail surface becomes positive $\approx 0.1\text{ s}-0.2\text{ s}$ after the initial impulse, depending on the entry velocity. As the moment from the horizontal stabiliser becomes positive, the overall moment follows an identical path to that of the horizontal stabiliser and sharply increases. The total moment becomes positive shortly before the horizontal stabiliser moment and has a steeper (positive) gradient. This is due to moment contributions from other components. The aerodynamic moment of the horizontal stabiliser continues to increase for a short period after becoming positive before abruptly changing gradient to a flatter, almost horizontal slope. The moment from the horizontal tail maintains a near constant value for $\approx 1\text{ s}$ before gradually decreasing for the remainder of the entry phase.

The fuselage provides a negative moment contribution throughout the entry phase. The fuselage moment increases in magnitude to a maximum magnitude at a flight path angle of $\approx 10°$ after which it begins to decrease in magnitude. This change in magnitude undergoes a sinusoidal shape through the entry phase for all entry velocities. Maximum fuselage moment magnitudes of -206 Nm, -299 Nm, -415 Nm and -548 Nm for entry velocities of 25 m/s, 30 m/s, 35 m/s and 40 m/s respectively. Although small, the fuselage moments assist in creating and maintaining a destabilising moment. The fuselage moment magnitude together with the inner wing section contributes the least to the overall moment. The inner wing moments exhibit similar magnitude and distributions to that of the fuselage in the entry phase, albeit mirrored about the X-axis. The opposite signs of the inner wing and fuselage moments are due to the aerodynamic centres of each of these components relative to the centre of mass.

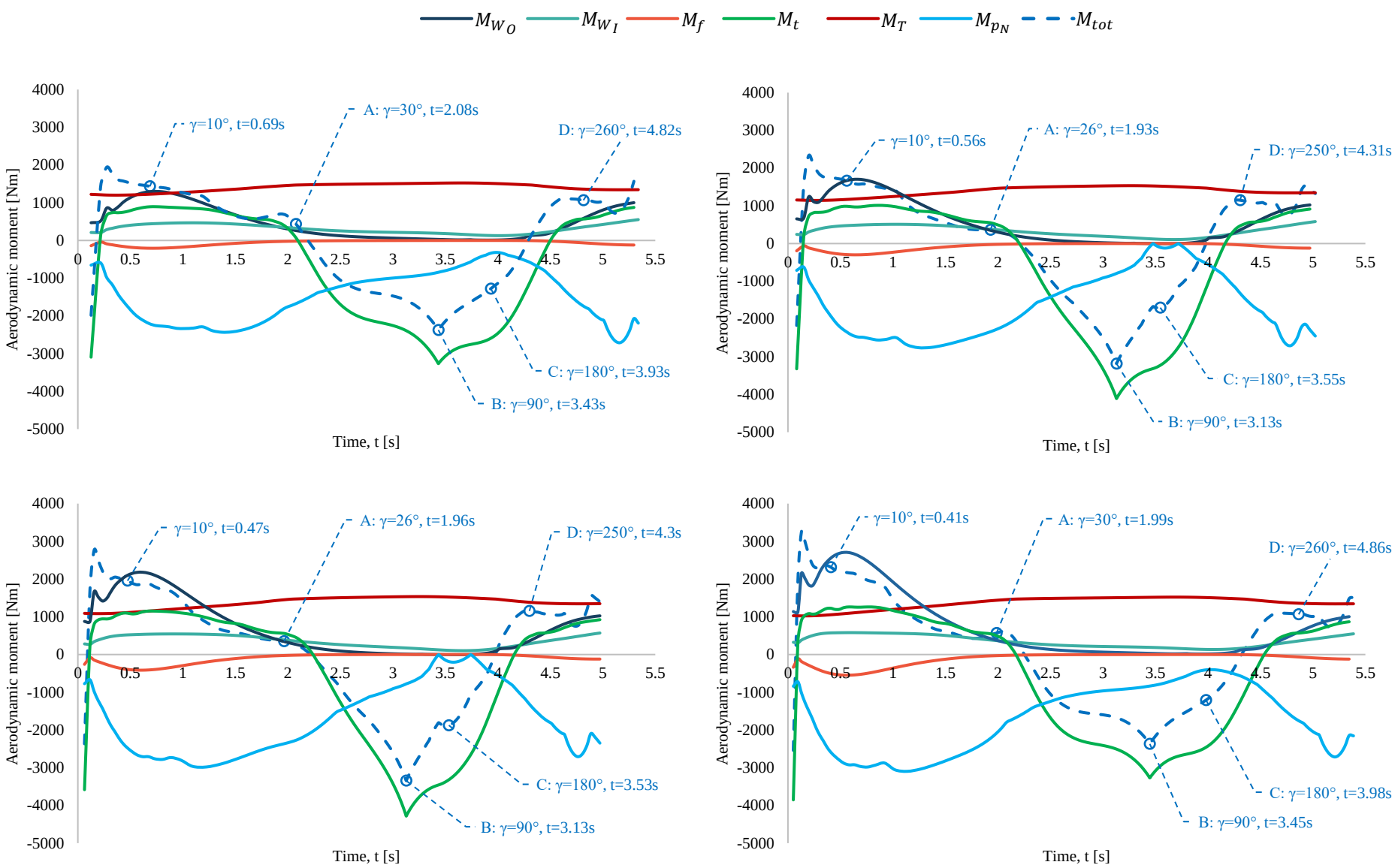

Figure 128: Aerodynamic moment components in the body axes for entry velocities of 25 m/s (top left), 30 m/s (top right), 35 m/s (bottom left) and 40 m/s (bottom right)

The aerodynamic centre of the inner wing lies aft of the centre of mass and shifts further rearward with increasing angle of attack. The aerodynamic centre of the fuselage is forward of the centre of mass, shifting rearward with increasing angle of attack. The rearward shift of the aerodynamic centre of the inner wing section creates a larger moment arm while the rearward shift of the aerodynamic centre of the fuselage produces a smaller moment arm. The 'flat' nature of the moment distribution of the inner wing section when compared to the outer wing section is due to the propeller slipstream velocity. The angle of attack of the inner wing section is kept relatively low by the propeller slipstream velocity. Even when the aircraft rises to large angles of attack. The coefficients of lift, inner wing velocities and moment arms combine across the entry phase to provide a near constant moment contribution. The inner wing moment and the fuselage moments almost cancel out in the entry phase with the inner wing moment provides a slightly greater magnitude, resulting in a small net positive moment. While the inner wing section only contributes a small amount to the total moment, it plays a far more pivotal role for the total normal force. The fuselage makes only a small contribution to both the normal forces and moments but aids in performing a tumble manoeuvre.

The propeller thrust provides a relatively large positive moment throughout the entry phase. The propeller thrust moment is independent of the angle of attack of the aircraft and is only marginally affected by the velocities seen during a tumble manoeuvre. Changes in velocity are small enough to not have a considerable influence on the propeller thrust and subsequently the propeller thrust moment. This is emphasised by changes in propeller thrust moment of only 323 Nm, 391 Nm, 452 Nm and 497 Nm for entry velocities of 25 m/s, 30 m/s, 35 m/s and 40 m/s respectively. These are the maximum differences in thrust across the entire manoeuvre. A minor increase in propeller thrust moment can be seen through the entry phase as the velocity decreases. While the propeller thrust moment remains near constant throughout the entry phase of the manoeuvre, the propeller normal force undergoes large changes in magnitude throughout the phase. The propeller normal force and moment are functions of the velocity of the aircraft as well as the angle of attack. The moment produced by the propeller normal force follows a sinusoidal trend, much like other moment components, though produces a far greater magnitude. The moment from the propeller normal force is negative throughout the entirety of the entry phase. The increase in magnitude of the propeller normal force moment can be attributed to the small increase in velocity up until a flight path angle of $\approx 10°$ as well as the increase in angle of attack. The increase angle of attack change is far more influential than the velocity changes. The normal force values do not significantly change over the velocity range seen in the entry phase. The magnitude of the moment due to the propeller normal force is vital to the success of the manoeuvre. So much so that the manoeuvre would be impossible without its contribution. The moment from the propeller normal force is the largest destabilsing moment through the entry phase (with the exception of the initial moment impulse from the horizontal stabiliser). Together with the inertia of the aircraft, the moment due to the propeller normal force act to retain a high angle of attack throughout the entry phase.

Maximum magnitudes of -2712 Nm, -2760 Nm, -2981 Nm and -3097 Nm are seen for the moment due to the propeller normal force for entry velocities of 25 m/s, 30 m/s, 35 m/s and 40 m/s respectively. The moment from the propeller normal force acts to reduce the overall moment on the airframe such that the aerodynamic moments do not completely overcome the inertia of the aircraft and force the nose of the aircraft downward. The sustained high angles of attack are paramount in obtaining the correct normal forces and linear forces to produce minimum radii through the manoeuvre and decelerate the aircraft sufficiently.

The outer wing section initially provides a small positive moment as the manoeuvre begins before sharply increasing. The outer wing provides a positive moment throughout the entry phase due to the position of the aerodynamic centre of the outer wing relative to the centre of mass. The aerodynamic centre of the outer wing is situated behind the centre of mass. Increases in angle of attack force the aerodynamic centre of the outer wing rearward, increasing the moment arm. The increase in outer wing moment can be attributed to an increase in velocity (up until a flight path angle of $\approx 10°$) and a sharp increase in angle of attack. The first peak of the moment distribution of the outer wing section illustrates the time at which the outer wing stalls. This indicates that the wing stalls shortly after entry to the manoeuvre. The moment of the outer wing section can thus be primarily attributed to the outer wing drag as the drag force outweighs the lift force at higher angles of attack. The outer wing section follows an almost sinusoidal distribution throughout the entry phase, passing through a double slope change near the very start of the manoeuvre due to the wing stalling. In reality, the rapid rotation of the outer wing section will result in a smooth curve rather than the 'serrated' shapes presented in Figure 128. The sinusoidal trend follows the shape of the coefficient of drag for the outer wing. Maximum moment values for the outer wing section are obtained in the entry phase. Maximum outer wing moment values of 1300 Nm, 1704 Nm, 2181 Nm and 2707 Nm for entry velocities of 25 m/s, 30 m/s, 35 m/s and 40 m/s respectively. These peak values illustrate the large restoring moments that typically prevent aircraft from achieving large nose-up rotations. Beyond the maximum moment of the outer wing, a gradual decrease ensues. This decrease corresponds to the decreasing free-stream velocity. The outer wing moment decreases despite an increasing angle of attack as the velocity component of the lift and drag terms of the outer wing has a larger effect than the coefficients of lift and drag. The decrease in free-stream velocity results in a reduction in lift and drag, thereby reducing the moment contribution of the outer wing.

The trends described for the moment components in the entry phase are applicable to each of the entry velocity cases. The entry phase of the tumble is arguably the most important phase in term of the moment components. The initial impulse from the horizontal tail is vital in providing the necessary inertia to maintain the required high alpha characteristics of the phase. The moment from the propeller normal force is also pivotal in reducing the overall moments acting on the aircraft, such that they do not

completely overcome the inertial influence of the aircraft. The destabilising moment in the entry phase can be seen as largely inertially driven rather than aerodynamically driven.

The climb phase sees a notable change in the moment component contributions with the exception of the moment from the propeller thrust. The moment from the propeller thrust remains relatively constant throughout the climb phase due to a near constant velocity throughout this phase. The moment from the propeller thrust is marginally larger in magnitude in the climb phase than during the entry phase due to the decrease in velocity. The magnitude of the moment from the propeller normal force decreases in a gently arced manner, reaching a similar moment value compared to the entry value. The moment due to the normal force of the propeller decreases due to a reduction in both velocity and angle of attack. The moment caused by the fuselage exhibits a near zero value throughout the climb phase. This reduction in fuselage moment is due to two factors; a reduction in angle of attack, resulting in a reduced fuselage lift and drag force, as well as a small moment arm from the aerodynamic centre of the fuselage to the aircraft centre of mass. The inner and outer wing sections also illustrated a reduction in moment throughout the climb phase. The moment from the outer wing sections decreases to a near zero value due to a reduction in both velocity and angle of attack. The moments due to the inner wing section do not reach the same minimum values as the outer wing sections due to the propeller slipstream velocity. During the climb phase the fuselage, inner wing and outer wing contribute very little by way of aerodynamic moments due to the low airspeeds and small angles of attack.

With a reduction in the free-stream velocity and angular velocity, the horizontal stabiliser is influenced largely by the propeller slipstream velocity. This results in far smaller horizontal stabiliser angle of attacks and greatly increases the effectiveness of the horizontal stabiliser in creating a destabilising moment. The moment produced by the horizontal stabiliser is positive at the beginning of the climb phase but quickly becomes negative and increases in magnitude (becoming more negative) with a steep gradient. The change in sign of the horizontal tail moment is significant in that it indicates a shift from an inertially driven manoeuvre to an aerodynamic driven one. In the climb phase the total aerodynamic moment is dictated largely by the horizontal stabiliser moment. The total moment follows a similar distribution to the horizontal tail albeit at reduced magnitudes due to the opposing moment created by the propeller thrust. Maximum magnitudes for the moment due to the horizontal stabiliser are seen at the end of the climb phase. Values of -3265 Nm, -4110 Nm, -4284 Nm and -3854 Nm are seen for entry velocities of 25 m/s, 30 m/s, 35 m/s and 40 m/s respectively. The moments created by the horizontal stabiliser in the climb phase reach a larger magnitude for entry velocities of 30 m/s and 35 m/s as compared to the 25 m/s and 40 m/s entry velocity cases. This difference is due to the lower free-stream velocities seen by the aircraft through this phase for entry velocities of 30 m/s and 35 m/s. The lower free-stream velocities result in smaller wing forces and thus reduced stabilising moments from the wing. This difference in the magnitude of the various moments results in increased angles of attack through the climb phase for the 30 m/s and 35 m/s entry velocity cases. The increased angle of

attack results in further and faster reductions in free-stream velocity while also rotating the aircraft faster through this phase. Despite the minor differences in horizontal tail moments between the various entry velocity cases this moment generated by the horizontal tail is important in allowing the aircraft to regain a sufficient angular acceleration to rotate the airframe around during the backflip and reversal phases.

The moment distributions of the inner and outer wing sections, the fuselage and the propeller thrust remain largely unchanged throughout the backflip phase. The most notable changes occur in the moment distributions of the propeller normal force and the horizontal stabiliser. The moment produced by the propeller normal force continues to decrease throughout the backflip phase due to the continually decreasing aircraft angle of attack. For entry velocities of 30 m/s and 35 m/s 0 Nm values are obtained and a bucket shape distribution occurs at the end of the phase due to a brief period of negative angles of attack. In reality, the moment distribution of the propeller normal force over this region is likely to remain constant rather than undergo rapid changes in magnitude. Despite the increasing angular velocity in this phase, the angular rates are not yet large enough to exceed the rate of change of flight path angle. This results in a continued decrease in angle of attack. While the angular pitch rates are smaller than the flight path angle rates, the magnitudes of the angular pitch velocity are still sufficiently high enough to create a noticeable angular velocity component on the horizontal stabiliser. This increases the angle of attack of the horizontal stabiliser through the backflip phase. This increase in angle of attack results in a decreasing horizontal tail moment magnitude. Reduction of $\approx 20\,\%$ are seen for all horizontal stabiliser moments by the end of the backflip phase.

The reversal phase, together with the backflip phase illustrates a near mirror image of the climb phase for all moment components apart from the moment due to the propeller normal force. In the reversal phase, the moments from the inner and outer wing sections remain constant for a brief period before increasing in magnitude with a gentle slope. This increase in moment magnitude for the wing sections is due to an increasing free-stream velocity as well as an increase in angle of attack. The increase in free-stream velocity reduces the thrust force by a small amount and subsequently the moment due to the thrust force. A gradual decrease in moment due to the propeller thrust is seen throughout the reversal phase as the velocity gradually increases. The moment created by the propeller normal force increases in magnitude becoming more negative during the reversal phase. The moment of the propeller normal force quickly increases with a relatively steep slope. This sharp increase in magnitude can be directly attributed to an increasing angle of attack. The horizontal stabiliser moment continues to decrease in magnitude with a positive slope that is slightly steeper than the slope seen in the backflip phase. The horizontal tail moment continues to lose efficacy throughout this phase and becomes positive in value shortly before the end of the phase. This change in sign signifies a shift from aerodynamically driven angular rates to inertially driven rates. After becoming positive in value, the moment distribution of the horizontal tail changes gradient. A transition to a flatter but still positive gradient is seen. This change

in gradient can be attributed to a decreasing angular velocity near the end of the phase. The main driving moment components in this phase are from the propeller thrust and horizontal tail.

The exit and recovery phase illustrates changes in each of the moment components as the free-stream velocity increases. The moment from the propeller thrust decreases gradually through this phase due to an increasing free-stream velocity. Moment values similar to those seen at the very start of the manoeuvre are seen for the propeller thrust moment. A gradual increase in fuselage moment is seen through the phase due to the increase in velocity. The moment contribution from the fuselage in this phase is still largely insignificant. The moment contributions from the inner and outer wing sections increase and create a stabilising moment. The slope of the outer wing section increases with a steeper gradient than the inner wing section due to the outer wing section having a greater moment arm. The moment due to the horizontal stabiliser section continues to increase throughout the exit phase due to the high angles of attack over the surface. The gradient with which the moment distribution of the horizontal tail increases is similar to that of the outer wing section. The largest destabilising moment in the exit and recovery phase is from the propeller normal force. The moment created by the propeller normal force increases in magnitude with a steep negative gradient due to an increasing angle of attack and increasing modified advance ratio. Magnitudes close to those seen in the entry phase are obtained. While the combination of components provides a net positive and stabilising moment, it is difficult to draw meaningful conclusions about recovery in isolation to other variables. One aspect that could be addressed is the moment from the horizontal tail. A change in direction of the elevator would provide a far greater positive, stabilising moment that would aid in recovery and reduce the inertial effects thereby reducing the angular velocity. This change in elevator direction should be applied just before or at the start of the exit and recovery phase.

While the horizontal tail becomes ineffective shortly after the entry to the manoeuvre, the impulse it imparts to the airframe is crucial to the success of the manoeuvre. Without the large initial impulse the inertial effects keeping the nose of the aircraft elevated would not be possible. The restoring aerodynamic moments would dominate and the airframe would rotate nose-down. The aircraft would be unable to complete a tumble manoeuvre. The aircraft would either enter a loop or would be unable to complete any manoeuvre, depending on the entry velocity. The moment from the propeller normal force, while irregular, is important is reducing the overall moment such that the stabilising moments do not completely overcome the inertial effects.

5.4. Test Envelope

While only the minimum radius tumbles were presented and discussed in §5.3, many cases were examined across a wide range of aircraft configurations. The various configurations that were investigated can be found in Table 29. The resulting flight paths for the various aircraft configurations at various entry velocities can be seen in Figure 129.

From the flight paths presented in Figure 129 it is evident that for each of the tested cases, all entry velocities, result in a looping manoeuvre with a teardrop shape. Only cases 1 and 2 result in a tumble manoeuvre. The radius of the manoeuvre grows larger for each subsequent case number. No direct correlation can be made between the radii of the various cases and the aircraft mass or inertia. The centre of gravity location does appear to influence the manoeuvre radius, with a further forward centre of gravity location resulting in a larger manoeuvre radius. This result should be expected as further forward centre of mass positions make for more stable aircraft. While a direct correlation cannot be made between the manoeuvre shape and the mass or inertia of the aircraft, it cannot be concluded that the manoeuvre shape is unaffected by the mass and inertia of the aircraft. The centre of mass locations are not too dissimilar. This illustrates the very specific conditions required to complete a tumble manoeuvre. While the overall manoeuvre shapes are similar, a notable difference between successful and failed tumble attempts can be observed in the exit phase. The cases that failed to perform a tumble manoeuvre result in a much flatter exit trajectory and finish the manoeuvre at a lower altitude than the successful cases. While the altitude losses are not excessively large, a height budget of ≈ 20 m - 30 m (excluding a recovery) should be given before performing the manoeuvre.

The key difference in the various cases occurs during the entry phase of the manoeuvre. If the aircraft is not able to reach a high enough angle of attack and sustain high angles of attack for long enough, the aircraft will not decelerate sufficiently. This results in a situation where the stabilising moments overcome the inertia and destabilising moments, thereby reducing the angle of attack of the aircraft. This is illustrated in Figure 130, where the angles of attack have been plotted for each case presented in the test matrix and for each entry velocity. The most significant and important difference occurs in the entry phase of the manoeuvres. It is clear that cases 1 and 2 attain far higher angle of attack values through the entry phase than any other case, with case 2 reaching the highest angles of attack of any case. Cases 4 – 8 do not reach an angle of attack higher than $40°$ for each of the entry velocities. While case 3 illustrates a higher angle of attack than cases 4-8, an angle of attack of only $57°$ is reached. The peak values are also not sustained for any appreciable period of time. Cases 4-8 illustrate $< 20°$ angles of attack by the end of the entry phase. Case 3 exhibits marginally higher angles of attack by the end of the entry phase. The differences in angle of attack occur as a result of varying aerodynamic moments. The aerodynamic moments are influenced by the centre of mass of the aircraft and by the free-stream velocity. Test cases with centre of mass locations that are further forward provide larger moment arms for the stabilising moment components, resulting in a larger overall stabilising moment. This larger

stabilising moment overcomes the inertial effects and results in lower angles of attacks through the entry phase. The angle of attack values attained in the entry phase also influence the angle of attack values through the remainder of the manoeuvre. While most cases exhibit very similar plot shapes through the manoeuvre, case 2 illustrates a very different curve. Case 2 sustains higher angles of attack values through the entry and climb phases than any other case, before sharply decreasing. Lower angles of attack are illustrated through the backflip and reversal phases, before once again experiencing higher angle of attack values through the exit and recovery phase. The remainder of the cases demonstrate an almost undulating change in angle of attack, illustrating that a constant conflict between stabilising and destabilising moments occurring throughout the manoeuvre. The aircraft is unable to reach the required angles of attack to adequately decelerate and rotate such that a tumble manoeuvre is performed. Instead, an imperfect loop is performed at dangerously low velocity values. The failed configurations illustrate the dangers in not only performing a tumble but also in attempting a tumble and having it fail.

The angles of attack experienced during the tumble manoeuvre have a significant influence on various aircraft variables. The most notable impact is on the free-stream velocity. The free-stream velocities for each of the tested cases and for each entry velocity are provided in Figure 131. What is immediately apparent in Figure 131 is that the cases that reach lower angles of attack see lower losses in velocity throughout the manoeuvre. A notable difference in gradient at the beginning of the manoeuvre can be seen between cases 1-3 and cases 4-8. Cases 1-3 exhibit a far steeper negative gradient, losing airspeed faster than cases 4-8. This can be seen for each of the entry velocity cases presented in Figure 131. Case 2 illustrates a minimum velocity of < 5 m/s. Cases 1 and 3 illustrate a minimum velocity of 8 m/s$\leq V \leq 15$ m/s. Cases 4-8 presented velocity values of 10 m/s$\leq V \leq 20$ m/s. The inequalities illustrate the range of minimums for the various entry velocity cases. While the differences in velocities are not notably large, the small differences have a large impact in the ability of an aircraft to complete a tumble. The differences that occur between cases 1-3 and 4-8 can be attributed to the angle of attack of the aircraft in each of the cases and the resulting decelerating forces. Higher angles of attack result in larger decreases in free-stream velocity, which subsequently results in lower stabilising moments. The lower velocities and stabilising moments, result in a far smaller manoeuvre radius. While the cases that result in a loop manoeuvre do not obtain the desired velocity distributions, the velocity values obtained still see the aircraft experience free-stream velocities below the stall value. This illustrates the potentially dangerous scenarios that may arise when merely attempting a tumble manoeuvre.

From the cases present it is evident that the ability of the aircraft to reach high angles of attack in the entry phase of the manoeuvre is crucial in completing a successful tumble manoeuvre. Should the required angles of attack not be attained, the aircraft will be left in a position where it is unable to decelerate and rotate sufficiently. The centre of gravity placement is vital in providing the correct combination of aerodynamic moments and angular velocities to reach the require angles of attack.

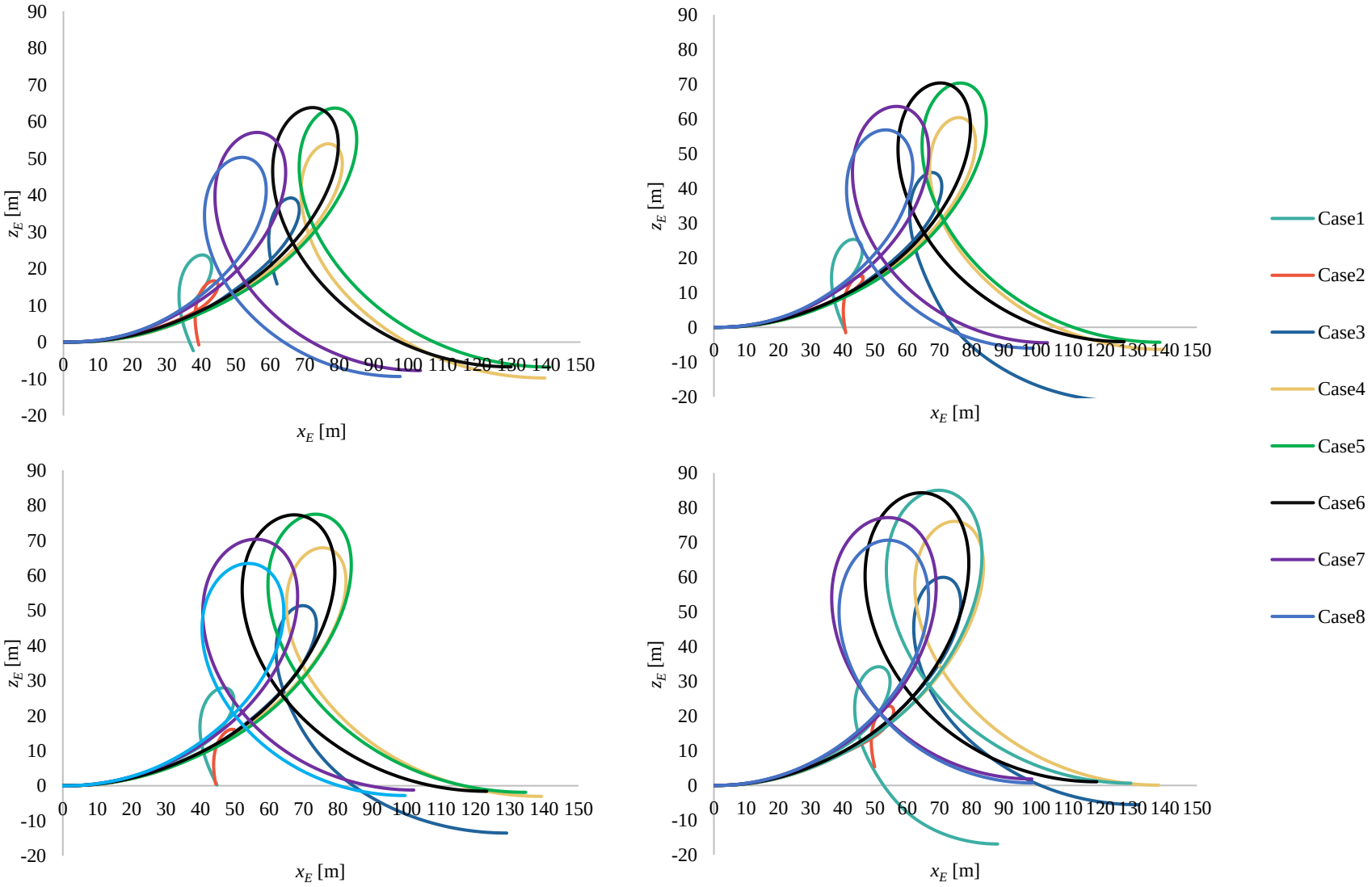

Figure 129: Resulting tumble manoeuvres from entire test matrix for entry velocities of 25 m/s (top left), 30 m/s (top right), 35 m/s (bottom left) and 40 m/s (bottom right)

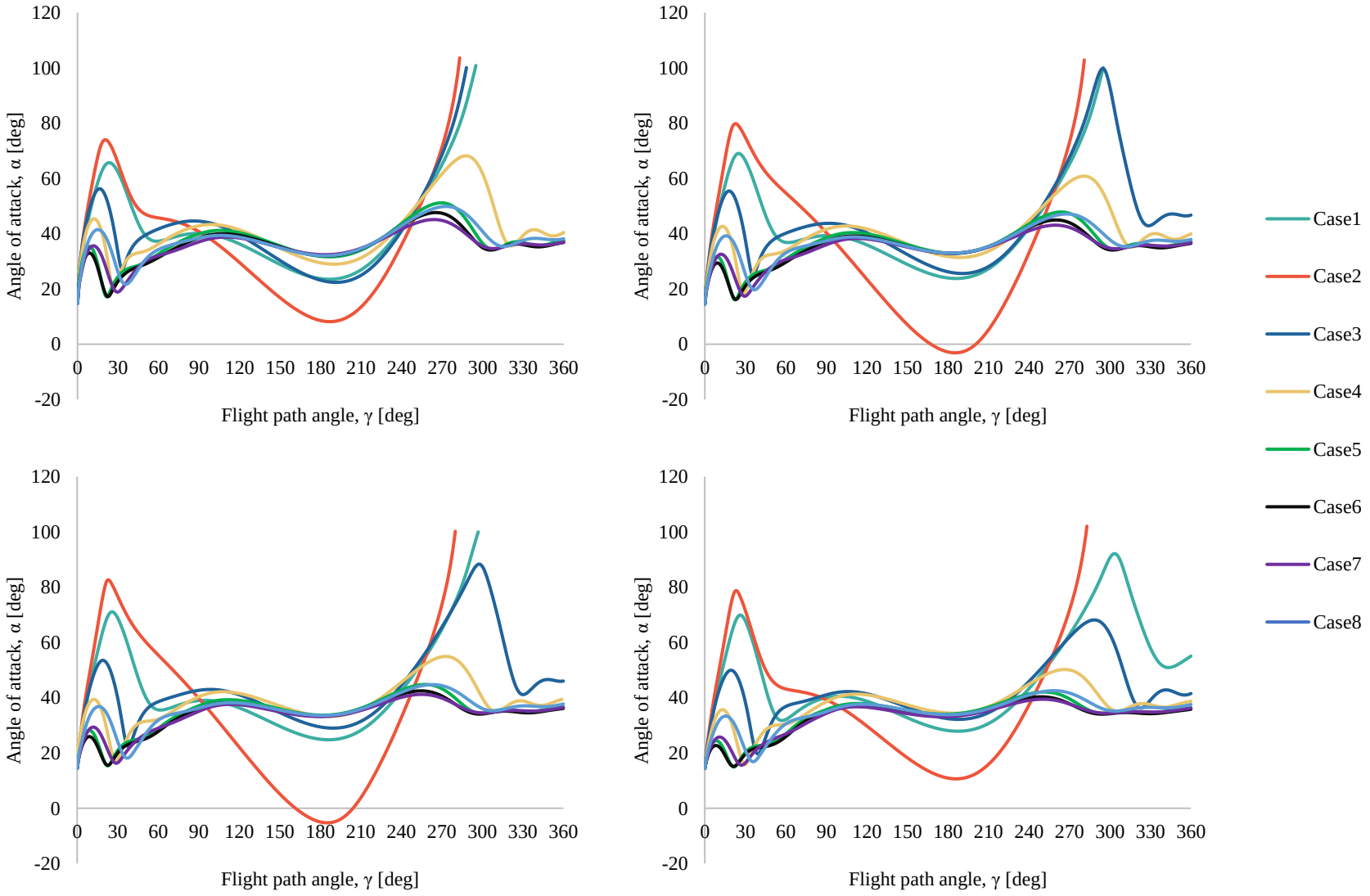

Figure 130: Aircraft angle of attack for entire test matrix for entry velocities of 25 m/s (top left), 30 m/s (top right), 35 m/s (bottom left) and 40 m/s (bottom right)

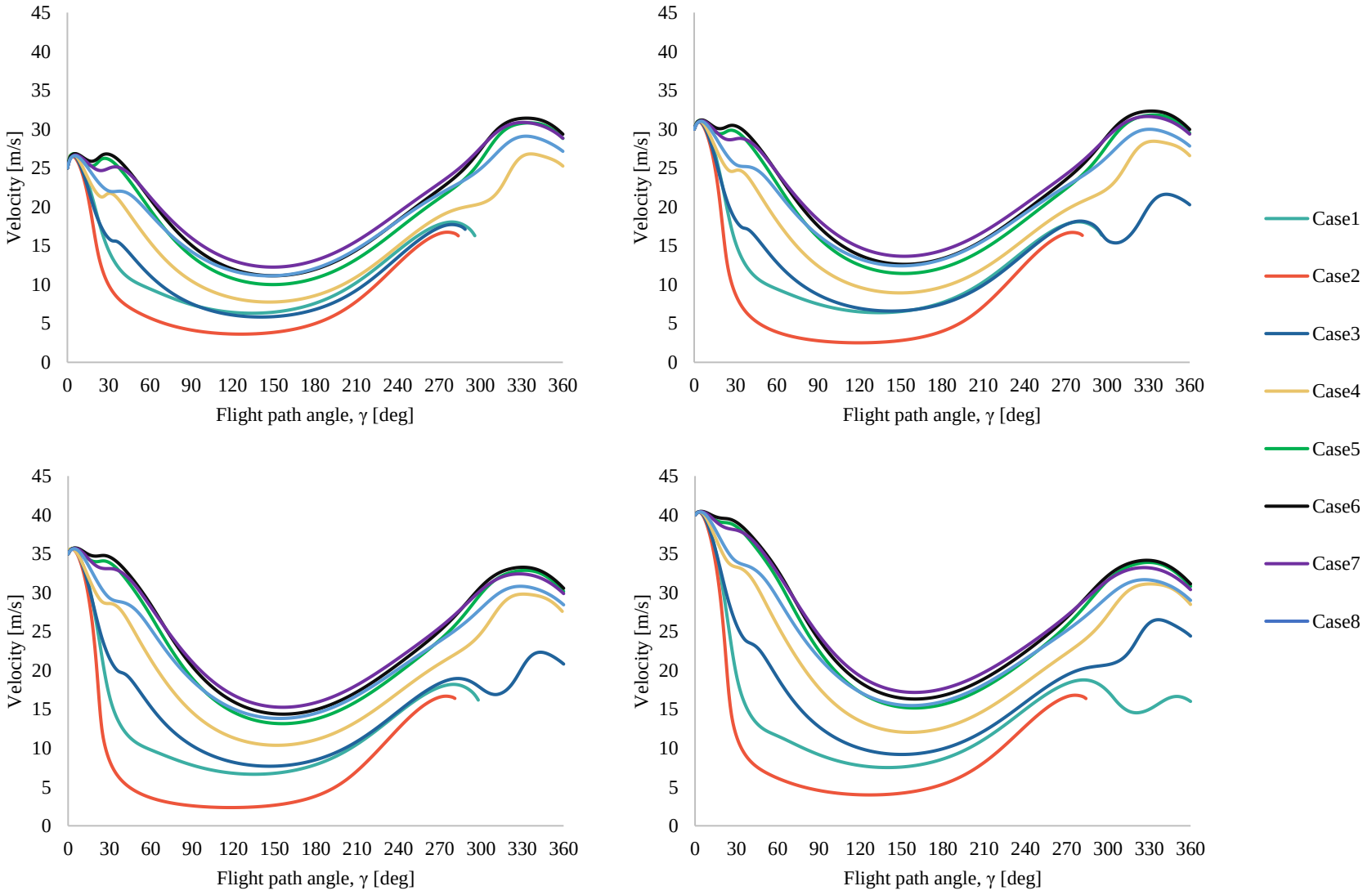

Figure 131: Free-stream velocities for entire test matrix for entry velocities of 25 m/s (top left), 30 m/s (top right), 35 m/s (bottom left) and 40 m/s (bottom right

5.5. Minimised Risk Tumbles

While a minimised radius tumble provides the most visually spectacular and impressive manoeuvre, a tumble in which the risk is minimised can be achieved without losing a significant amount of showmanship. A tumble manoeuvre in which the radius marginally increases, but an overall higher velocity and lower angle of attack is carried through the manoeuvre is possible by varying force and moment parameters. Minimised risk tumble manoeuvres are plotted in Figure 132 alongside the minimised radius tumble manoeuvres from §5.3. Both variations of the tumble have been performed by top aerobatic pilots, most notably the minimised radius tumble by Skip Stewart and the minimised risk tumble by Sean Tucker. A good example of the minimised radius tumble can be seen in Skip Stewarts performance at the 2015 Battle Creek Airshow [77] (with the tumble manoeuvre performed at 3:49). A text book performance of a minimised risk tumble manoeuvre is performed by Sean Tucker at the 2015 Oshkosh Airventure Airshow [78] (with the tumble manoeuvre performed at 6:44).

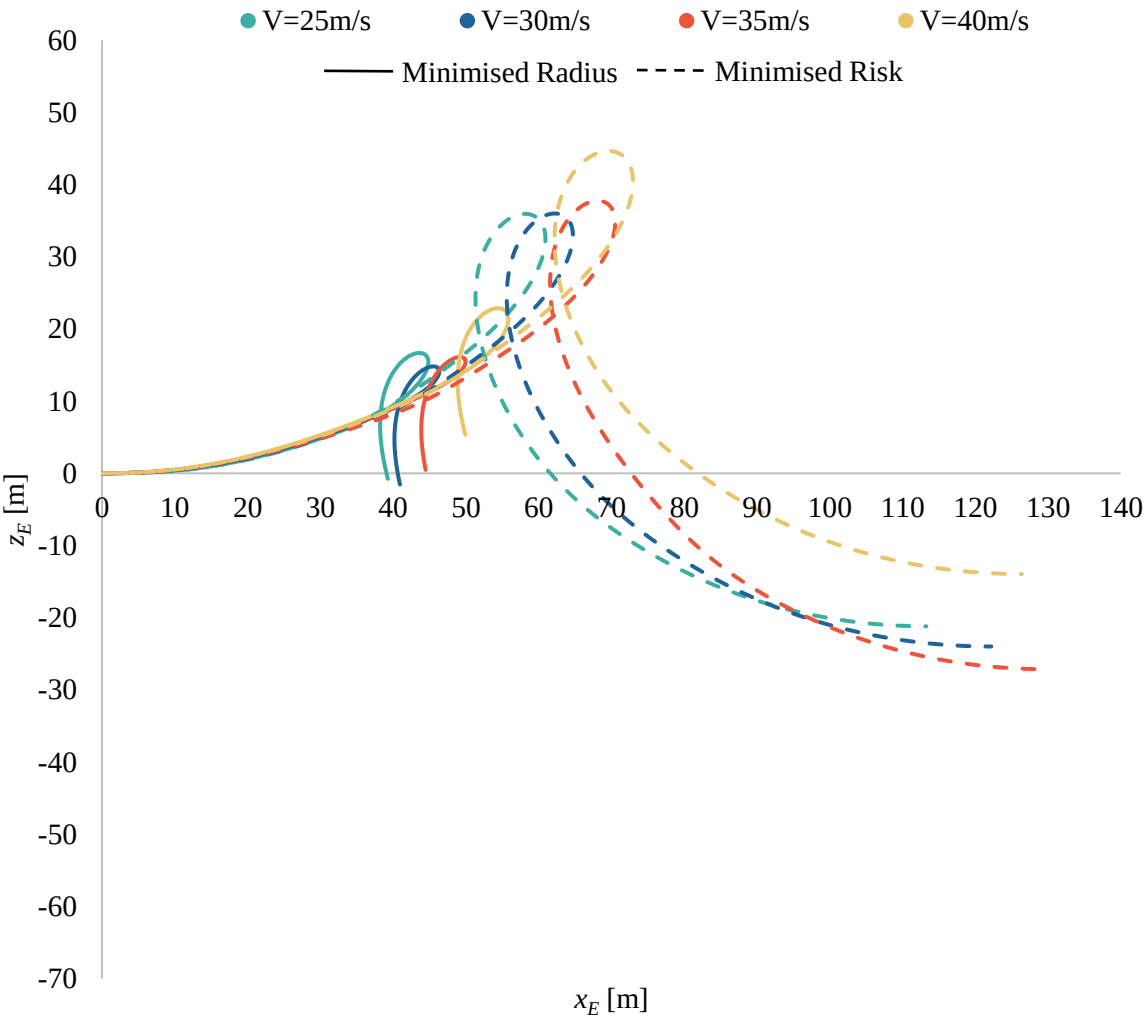

Figure 132: Minimised radius and risk tumble manoeuvre for various entry velocities

The minimised risk tumble manoeuvres presented in Figure 132 are achieved by reducing the propeller normal force from 84 % to 70 % of the values presented in §3.3.6. The normal force from the propeller can be varied by altering the blade pitch angle (β). The alteration of blade pitch angle was assumed to not alter the propeller thrust and slipstream values significantly. The propeller thrust and slipstream remained unaltered. Altering the propeller normal force value resulted in a reduction in the total normal force, the linear acceleration and the total moment acting on the aircraft. The propeller normal force was selected as the variable parameter over other input parameters as it is the parameter with the least uncertainty. Values are obtained from test data (as discussed in §3.3.6). While the uncertainty of the propeller normal force data is considered to be the least, there still lies an amount of uncertainty in the propeller normal force data as the test results were obtained for a different propeller and adapted to the Extra 330SC propeller.

The shape of the minimised risk tumble manoeuvres are similar to those of the minimised radius tumble manoeuvres but are larger both vertically and horizontally. While the overall manoeuvre is larger for the minimised risk tumbles, the radius is still much smaller than that of a loop. The minimised risk tumble manoeuvres also see a much tighter grouping of the various manoeuvres across the entry velocities presented. Entry velocities of 25 m/s, 30 m/s and 35 m/s showing very similar flight paths. This should allow for more consistent displays as the entry velocity can be varied with a similar outcome. The entry, climb, backflip and reversal phases are larger for the minimised risk tumble manoeuvres and result in a far more gradual and longer exit and recovery phase. The key difference in terms of manoeuvre safety is seen in the exit and recovery, in which the pilot has a greater period of time to recover should an issue arise. This notion is better illustrated by Figure 133 and Figure 134 in which the velocities and angles of attack are plotted, respectively. These results are plotted for the various entry velocities and for both minimised radius and risk tumbles manoeuvres.

Figure 133 illustrates the various velocity plots for different entry velocities of the minimised radius and minimised risk tumble scenarios. The entry phase for each of the different types of tumble scenarios exhibit near identical trends and magnitudes for each of the entry velocity cases presented. Beyond the entry phase the minimised risk tumble manoeuvres illustrate a higher velocity throughout the remainder of the manoeuvre as compared to the minimised radius tumble manoeuvres. The differences in velocity between the two sets of data vary between 5 m/s and 10 m/s depending on the flight path angle. The higher velocity values seen by the minimised risk tumble manoeuvres provide the pilot with slightly more margin for error should any issue arise. The higher velocities result in higher kinetic energy values. This is particularly true in the exit and recovery phase, as seen towards the end of the distributions shown in Figure 133.

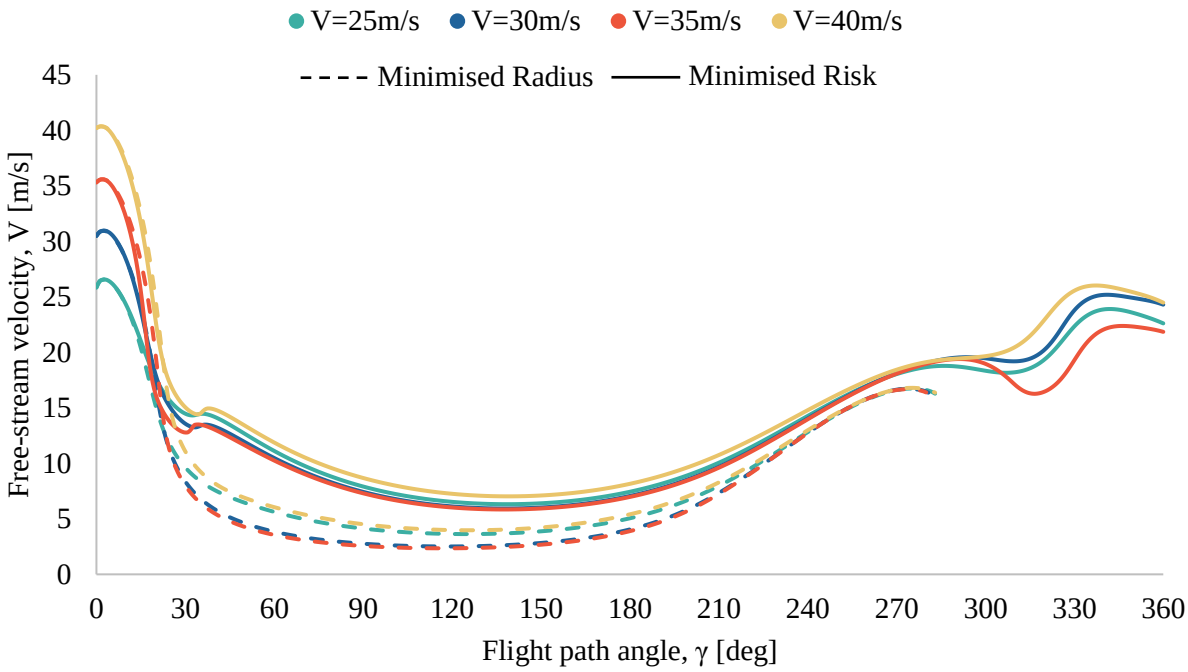

Figure 133: Free-stream velocity for minimised radius and risk tumble manoeuvre for various entry velocities

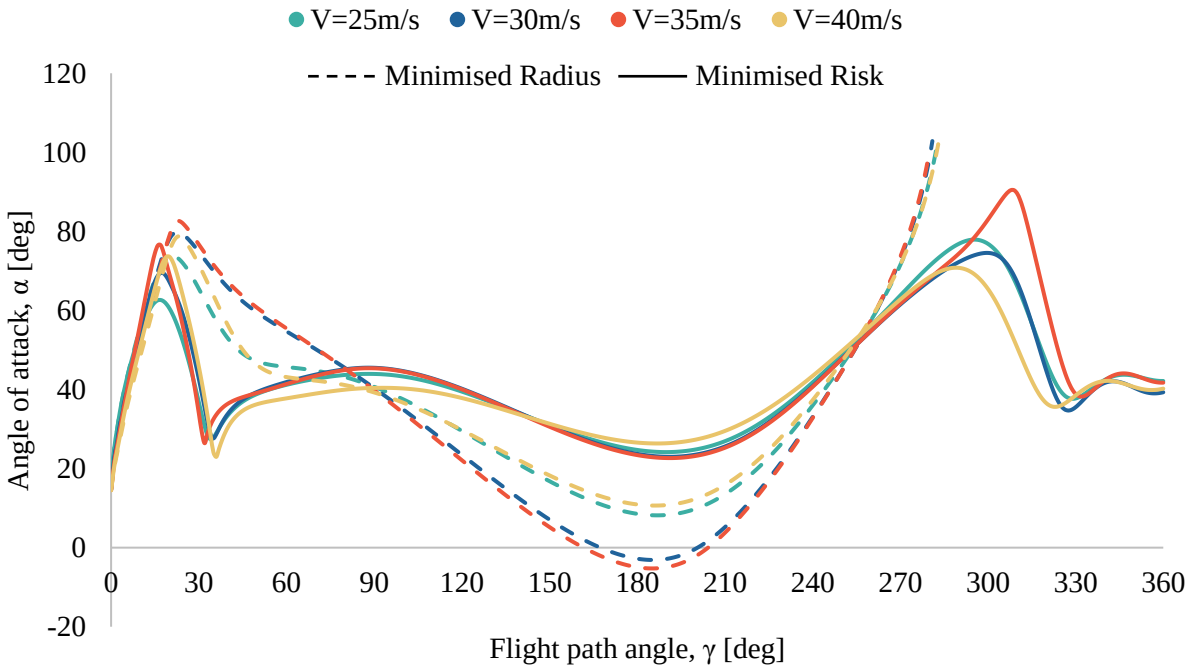

Figure 134: Angle of attack for minimised radius and risk tumble manoeuvre for various entry velocities

Figure 134 presents the aircraft angle of attack for different entry velocities of the minimised radius and minimised risk tumble scenarios. In the entry phase the angles of attack of the various entry velocity cases follow similar plots for both the minimised radius and minimised risk tumble manoeuvres. Similar peaks are obtained for both sets of data with the minimised risk tumble illustrating angles of attack that are $\approx 5°$ lower. Beyond the entry phase the two different tumble manoeuvre scenarios follow very different distributions. The minimised risk tumble manoeuvres see a large loss and decrease in angle of attack immediately after the end of the entry phase. This loss in angle of attack results in a decreased deceleration, as compared to the minimised radius tumble manoeuvres. This results in higher free-stream velocities. The steady decrease in angle of attack seen in the minimised radius tumble manoeuvres is not seen by the minimised risk tumble manoeuvres. Instead, a recovery is seen in angle of attack just after the beginning of the climb phase. The angle of attack increases and follows a sinusoidal trend between angles of attack of $20°$ and $40°$. In the latter stages of the manoeuvre both tumble manoeuvre scenarios see a sharp increase in angle of attack. The only notable difference seen lies in the steepness of the increase. The angle of attack in the latter stages of the manoeuvre of the minimised risk tumble manoeuvres cases increase with a shallower gradient than those of the minimised radius. This slower increase coupled with a change in positive to negative gradient implies that the aircraft is still flying, albeit in a low energy state and is not falling downward as with the minimised radius cases. While this difference may seem somewhat trivial, it could mean the difference between a recovery and a crash in the event of a failure.

By varying the propeller normal force, minimised risk tumble manoeuvres can be performed at the expense of the manoeuvre radius. While the minimised risk tumble manoeuvres result in a larger overall manoeuvre, radii much smaller than those of a loop manoeuvre can be achieved with greater margins for recovery. The minimised risk tumble manoeuvres are similar, in terms of flight path to cases 1 and 3 presented in §5.3. While the different configurations follow a similar path through the manoeuvre, the exit and recovery velocities differ, with the minimised risk tumble manoeuvre cases illustrating better velocities in this phase. The minimised risk tumble manoeuvres provide a better means of exiting the manoeuvre and illustrates representative losses in altitude. The height losses illustrated in Figure 132 suggest that ≈ 30 m of height are lost. This is not representative of a complete recovery and a more traditional recovery should be completed after this initial recovery phase.

5.6. Comparison With Video Footage

Comparing the results presented in §5.3 and §5.5 to any test data is not possible due to the lack of information provided in the public domain. In the absence of any test data, with which to compare results, still images obtained from video footage were patched together to form a complete tumble manoeuvre. This composition was performed for both the minimum radius and minimised risk tumble manoeuvres. The minimum radius tumble is presented in Figure 135 while the minimised risk tumble is presented in Figure 136. While these images do not provide the most accurate form of comparison, they are the only available source of information with which a comparison to the result data can be made. The still images can be used to compare aircraft orientations and manoeuvre times at various points along the path of the manoeuvre.

5.6.1. Minimal Radius Tumble

A comparison between the 30 m/s minimum radius tumble manoeuvre from §5.3 and a framework of still images of a minimum radius tumble performed by Skip Stewart [77] is presented in Figure 135. The starting velocity of the aircraft in the video footage is unknown but was assumed to be $30 \text{ m/s} \leq V_{entry} \leq 35 \text{ m/s}$. It should also be noted that the patch work of images slightly exaggerates the shape of the manoeuvre to better illustrate the aircraft at each phase of the manoeuvre. The effects of the aircraft smoke seen in the video footage also cannot be captured using a collection of still images. The manoeuvre times for the video footage were obtained by scrubbing through the video footage and recording the times at various points during the manoeuvre. The time scale used was accurate to 0.01 s.

The entry to both the video footage and the model data illustrate the aircraft orientated at a pitch angle of $\approx 14°$. A rapid nose up pitch rotation is seen in the model data and video footage, reaching a pitch angle of $\approx 60°$ in a time of ≈ 0.5 s for both cases. A small, but negligible, discrepancy is seen in the time values. The end of the entry phase (point A) illustrates a slightly longer manoeuvre time for the model data as compared to the video footage. A difference of 0.4 s is seen and is likely due to a difference in aircraft pitch angle during the phase. The model data illustrates a greater aircraft pitch angle ($\theta \approx 100°$) at the end of this phase when compared to the aircraft pitch angle seen in the video footage ($\theta \approx 80°$). The greater pitch angle seen at the end of the model data results in a faster deceleration and subsequently a larger time, through this phase. While there are some differences present between the model data and video footage, the discrepancies are small enough to suggest that the model is adequately capturing the general aircraft dynamics and time through this phase. Some difference may also be a result of a comparison of two different aerobatic aircraft. The modelled aircraft (Extra 330SC) is a single, mid-wing aircraft while the aircraft seen in the video footage is a bi-plane aircraft (Pitts Special).

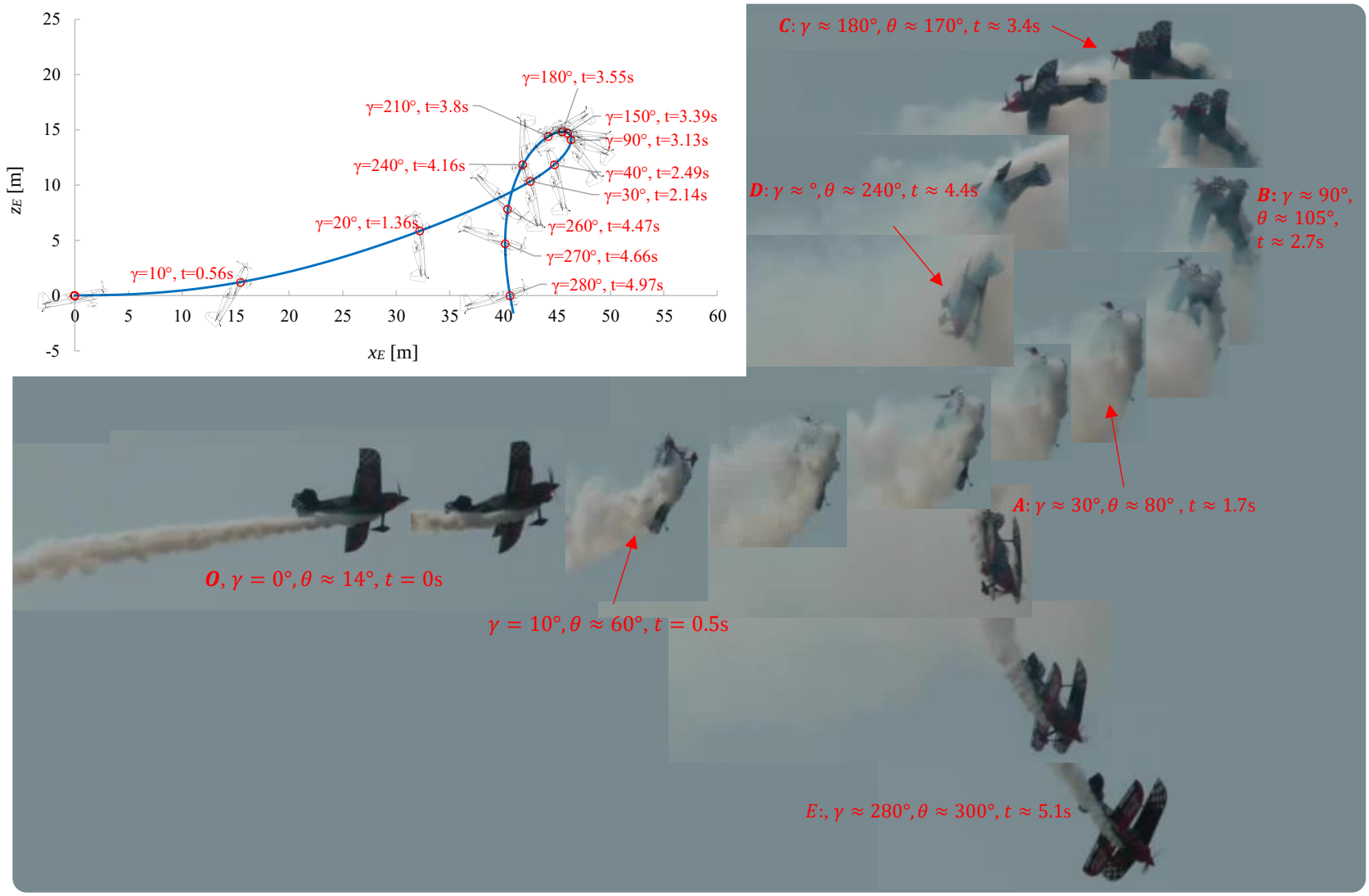

Figure 135: Patched still images for a minimum radius tumble compiled from video footage from reference [77]

The time difference seen in the entry phase is carried through the climb phase (points A-B) and a difference of ≈ 0.4 s is seen between the model data and the video footage by the end of the climb phase. This suggests that the two sets of information traverse this phase is a near identical time. The aircraft pitch angles through this phase illustrates similar angles with the model data presenting a flight path angle of $\theta \approx 110°$ at the end of the phase as compared to a flight path angle of $\theta \approx 105°$ from the video footage. Good correlation is seen between the model data and video footage in the climb phase with the aircraft in the video footage matching the steeper flight path angles seen by the test data at the end of the entry phase.

The conclusion of the backflip phase depicts the aircraft in both the model data and4 video footage at an aircraft pitch angle of $\approx 170°$. While the pitch angles show good correlation between the two sets of information, some discrepancy in the completion time was seen. The model data completes the backflip phase in ≈ 0.45 s while the video footage shows a phase time of ≈ 0.7 s. This difference in phase time could be due to a thrust and/or drag mismatch during this phase, resulting in different accelerations.

The reversal phases presented for the model data and video footage show marginally dissimilar phase times and notably different aircraft pitch angles. The begging of the reversal phase illustrates similar aircraft pitch angles that diverge as the phase continues. The differences seen between the two sets of information is due to a different approach. The model data assumes a constant application of elevator through this phase while the video footage appears to ease the application of elevator to reduce the rotation rate of the aircraft. The differences in elevator application through this phase result in different angular rates and phase times due to differences in linear acceleration. A constant application of elevator through the reversal phase and subsequently at the start of the exit and recovery phase is possible and is seen in the video footage of the minimised risk tumble manoeuvre presented in Figure 136.

A large difference in aircraft pitch angles is observed in the exit and recovery phase between the model data and the video footage. The time data shows good correlation. The difference in aircraft pitch angle between the two sources of information carry through from the different approaches discussed in the reversal phase. The relaxation of elevator performed by the pilot in the video footage is likely as a response to the trajectory of the aircraft. A near vertical trajectory is seen with very little forward momentum. As such, continued elevator deflection greatly hinders the recovery ability of the aircraft as no forward acceleration can be obtained.

While the two sets of exit and recovery phases are not completely comparable, a sufficient amount of the manoeuvre is comparable (given identical elevator inputs). A satisfactory correlation is shown through majority of the manoeuvre to conclude that the minimised tumble provided by the video footage is adequately captured by the model.

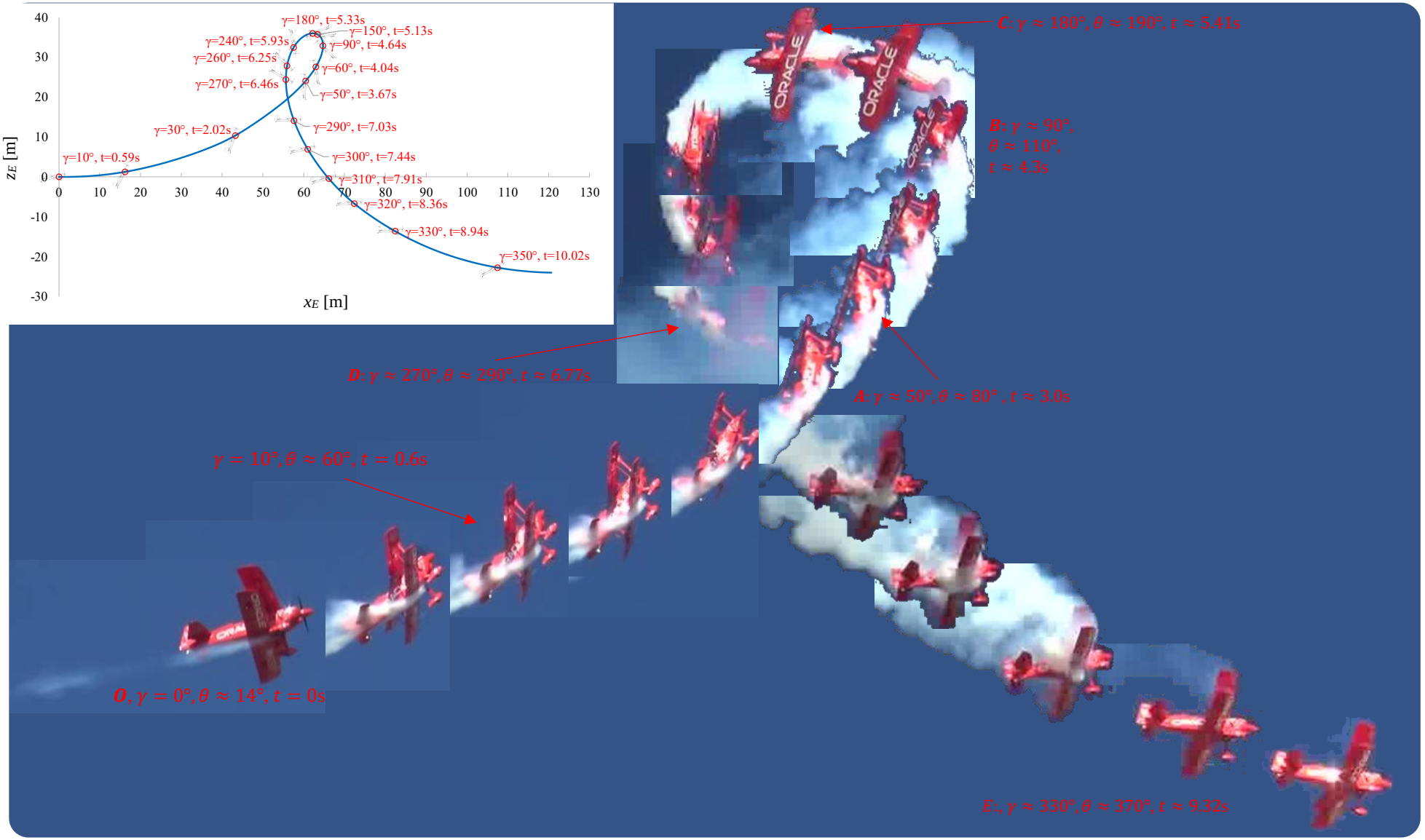

Figure 136: Patched still images for a minimised risk tumble compiled from video footage from reference [78]

5.6.2. Minimised Risk Tumble

The flight path of a 30 m/s entry velocity, minimised risk model is presented in Figure 136 alongside a patchwork of still images from a tumble manoeuvre performed by Sean D. Tucker [78]. The starting velocity of the aircraft in the video footage is unknown but was assumed to be 30 m/s$\leq V_{entry} \leq 35$ m/s. The framework of images slightly distorts the shape of the manoeuvre to better illustrate the aircraft at each phase of the manoeuvre. The effects of the aircraft smoke seen in the video footage also cannot be captured using a collection of still images, resulting in a patchwork that may appear to be somewhat different to the video footage. The manoeuvre times for the video footage were obtained by scrubbing through the video footage and noting the times at various points during the manoeuvre. The time scale that was used to record manoeuvre times was accurate to 0.01 s.

The entry into the tumble manoeuvre shows the aircraft orientated at a pitch angle of $\approx 14°$ for both the video footage and model data. The aircraft then undergoes a sharp nose up rotation, reaching an aircraft pitch angle of $\approx 60°$ in a time of ≈ 0.6 s. This is seen in both the video footage and model data. As in the minimised radius tumble case, the conclusion of the entry phase (at point A) illustrates that the model data requires a greater time to reach this position. The model data indicates that the conclusion of the entry phase occurs at a manoeuvre time of ≈ 3.67 s, while the video footage indicates that this phase concludes at a manoeuvre time of ≈ 3.1 s. This ≈ 0.5 s time difference during this phase is attributed to the differences in aircraft pitch angles. The model data demonstrates a greater aircraft pitch angle through the manoeuvre from a flight path angle of $\approx 10°$ onward. The greater aircraft pitch angles seen in the model data result in larger decelerations, lowering the free-stream velocity faster, resulting in larger flight path times. The conclusion of the phase shows the aircraft at a pitch angle of $\approx 90°$ for the model data and $\approx 80°$ for the video footage. The differences in pitch angle occur as a result of a difference in rotational moments. The model data is incorrectly predicting the total moments acting on the aircraft. This may be due to aerodynamic damping that has not been considered in the model. While there are some differences present between the model data and video footage, the disparities are small enough to suggest that the model is adequately capturing the general aircraft dynamics and time through the entry phase. Some difference may also be a result of a comparison of two different aerobatic aircraft. The modelled aircraft (Extra 330SC) is a single, mid-wing aircraft while the aircraft seen in the video footage is a bi-plane aircraft (Pitts Special).

The climb phase (points A-B) shows good correlation in aircraft pitch angle through the phase, apart from the aircraft pitch angles at the very end of the phase. Both the video footage and model data illustrate the aircraft at a near $\approx 90°$ aircraft pitch angle through most of the phase. The model data illustrates the aircraft at a pitch angle of $\approx 135°$ at the end of the phase, which is greater than the pitch angle illustrates by the video footage, $\approx 110°$. The difference in aircraft pitch angle in the climb phase is a result of the pitch angle differences in the entry phase. The model data showed greater aircraft pitch

angles, resulting in greater decelerations. These slightly larger decelerations reduce the velocity and allow for quicker aircraft rotations in the climb phase. The higher speeds carried through the video footage result in larger restoring moments and subsequently marginally slower aircraft nose-up rotations. A small difference is seen in the completion time through the climb phase. The model data completes the phase in ≈ 1 s, whereas the video footage illustrates a time of ≈ 1.3 s. The difference in time can be attributed to the differences in pitch angle and subsequently velocity. Despite the small differences in time and pitch angle, acceptable correlation is shown between the video footage and model data in this phase.

The backflip phase (points B-C) illustrates the same marginal disparities in both aircraft pitch angle and time between the video footage and the model data. The model data completes the backflip phase in a time of ≈ 0.7 s, reaching an aircraft pitch angle of $\approx 200°$ while the video footage suggests the backflip phase is completed in ≈ 1.1 s, reaching a pitch angle of $\approx 190°$. The differences seen in this phase are not due to velocity differences as at this point the velocities in both sets of information should be similar and near 0 m/s. The differences seen are likely due to differences in the earlier phases. The model data begins each phase at a higher pitch angle, carrying the extra rotation through subsequent phases. The pitch angle change in the backflip phase is identical for each of the two sets of information, changing by a pitch angle of $\approx 80°$. The consistent change in angle provides acceptable correlation between the model data and video footage in this phase.

The reversal phase (points C-D) shows the model data completing the phase in a time of ≈ 1.1 s, concluding at a flight path angle of $\approx 320°$. The video footage illustrates that the reversal phase is completed in a time of ≈ 1.3 s, reaching a flight path angle of $\approx 305°$. The time and pitch angles illustrate the closest correlation in this phase as compared to prior phases. A slightly greater acceleration is seen in the video footage in this phase compared to the model data, thus bringing the two sets of data closer together. This illustrates a small convergence of the data between the two sets of information. A better correlation is seen in this phase for the minimised risk tumble as compared to the minimal radius tumble due to the constant application of elevator deflection in the video footage. The model data in the minimal radius tumble in this phase is better represented by the video footage for the minimised risk tumble.

The exit and recovery phase shows very good correlation between the model data and video footage, with the aircraft effectively falling at a flat angle. The video footage concludes at a flight path angle of $\approx 330°$, after which the pilot takes corrective action and reduces elevator deflections. The model data retains full elevator up until a flight path angle of $360°$ and is thus not comparable beyond a flight path angle of $330°$. The conclusion of the phase for both the model data and video footage will be assumed to be at a flight path angle of $330°$. The model data completes this phase in a time of ≈ 2.5 s, concluding at an aircraft pitch angle of $\approx 5°$. The video footage completes the phase in a time of ≈ 2.5 s and reaches

an aircraft pitch angle of $\approx 5°$. Very good correlation is seen in this phase in both time and pitch angle. The type of exit seen in this phase can be applied to the minimal radius tumble manoeuvre, should the trajectory of the aircraft have a sufficient forward component.

Evaluation of the time and aircraft pitch angle through the various phases of a tumble manoeuvre for video footage and model data illustrates very good correlation between the two sets of data. Small differences do occur and can be attributed to slightly difference moment values which can arise from incorrect aerodynamic data or different aircraft or a combination of the two. In spite of the small differences, an acceptable level of correlation is seen to suggest the model data adequately captures the dynamics of a minimised risk tumble manoeuvre.

6. CONCLUSION

This chapter summarises the main findings of the dissertation. Future research directions are also proposed in the final part of this chapter.

The findings and conclusions of this dissertation can be summarised as follows:

- Tumble manoeuvres are indeed achievable by modified aerobatic aircraft.
- A tumble manoeuvre can be completed in a space that is less than ≈ 50 m (7.26 aircraft lengths) long and ≈ 20 m (2.9 aircraft lengths) high for entry velocities of 25 m/s $\leq V_{entry} \leq$ 40 m/s.
- A 30 m/s entry velocity provides the best overall tumble in terms of manoeuvre size for the Extra 330SC.
- Maximum aft centre of mass locations are required to perform a minimum radius tumble manoeuvre.
- The mass and the pitch inertia of the aircraft are not as critical as the centre of mass location. The mass should still be within the limits of a single seat aerobatic configuration.
- The entry to the tumble manoeuvre requires high angles of attack, that are sustained through the entry phase. These are required to:
    - Sufficiently decelerate the aircraft using high drag forces
    - Generate normal forces that are outside the limitations of conventional flight. Requiring forces that act in the lift direction other than just the wing.
- The portion of wing influenced by propeller slipstream and propeller thrust component acting in the normal direction are essential in providing the load factor values required for the tumble.
    - Angling the thrust in the direction of the normal force requires high angles of attack.
- The horizontal stabiliser is required to provide the initial pitch impulse to enter the manoeuvre and to supply aerodynamic moments at low free-stream velocities.
- The moment due to the propeller normal force is required to aid in maintaining high angles of attack in the entry phase of the manoeuvre. Without the influence of the moment due to the propeller normal the aerodynamic restoring moments would prevent a tumble from occurring by lower the nose of the aircraft.
- Propeller slipstream effects that act over a portion of the wing, the fuselage and the horizontal stabiliser are essential in performing an aerobatic tumble manoeuvre.
- Modified engines that are capable of outputting at least 400 HP are required to generate adequately thrust and sufficient propeller slipstream velocities.
- The risk of the tumble manoeuvre can be minimised by lowering the total normal force and aerodynamic pitching moments.

    - This can be achieved by altering the blade pitch angle of the propellers and reducing the total normal force of the propeller.
- The best flight path angle for recovery is $\approx 240°$ where the specific excess power reaches a maximum.
- Flight path angles of greater than $270°$ illustrate negative specific excess power values and result in dangerous recovery situations.
- Approximately $10\,\text{m}$ - $30\,\text{m}$ are required to exit a tumble manoeuvre. This is not the total recovery height. A regular pull up manoeuvre is still required after the tumble exit.
- The model results illustrate good correlation to both a minimised radius and a minimised risk tumble manoeuvre.

Recommendations And Future Work

Recommendations to the current work as well as future work are proposed below:

Recommendations:

- Verify horizontal stabiliser and elevator aerodynamic data at high angles of attack in and out of the effect of propeller slipstream. Ideally through test data
- Obtain aerodynamic test data for the wing of an Extra 330SC, in which a portion of the wing is subjected to the effects of propeller slipstream.
- Verify the aerodynamics of the inner and outer wing sections for dynamic cases with various rotational rates.
- Verify aerodynamic test data for an aerobatic aircraft propeller with a 400 HP engine.
- Investigate whether the work contained within the dissertation could be extended into spin recovery margins and procedures for general and commercial flying.

Future Work:

- Create a full six degree of freedom model in which all yaw and roll forces and moments and included.
- Simulate an engine failure at various flight path angles during the tumble manoeuvre.
- Expand the model to include a pull-up manoeuvre at the end of the tumble.
    - This will require aerodynamic coefficients for various elevator deflections angles.
- Expand the model to a selection of aerobatic aircraft.

7. REFERENCES

[1] Federal Aviation Administration , "Code of Federal Regulations Part 91 Subpart D Sec. 91.303," USA Federal Aviation Administration, 1991.

[2] New Zealand Civil Aviation Authority, "Civil Aviation Rules Part 1 - Definitions and Abbreviations," Civil Aviation Authority of New Zealand, 30 October 2017.

[3] I. Y. Burdun and O. M. Parfentyev, "Analysis of Aerobatic Flight Safety Using Autonomous Modeling and Simulation," SAE Technical Paper Series, Daytona Beach, Florida, 2000.

[4] W. Langewiesche, in *Stick and Rudder*, New, McGraw Hill, 1944, p. 327.

[5] Federal Aviation Administration, Airplane Flying Handbook (FAA-H-8083-3C), Oklahoma City: U.S. Department of Transportation, 2022, p. Chapter 4.

[6] A. a. Intersoft, "Extra 330SC," EXTRA Flugzeugproduktions, [Online]. Available: https://www.extraaircraft.com/330SC.php. [Accessed 18 April 2018].

[7] "Aerotek Pitts S-2A “Special”," The Skytamer Archive, [Online]. Available: https://www.skytamer.com/Aerotek_Pitts_S-2A.html. [Accessed 18 April 2018].

[8] K. Palt, "Suchoi / Sukhoi Su-29F," Flugzeug Info, [Online]. Available: http://www.flugzeuginfo.net/acdata_php/acdata_suchoi_su29_en.php. [Accessed 18 April 2018].

[9] N. a. H. Creative, "Edge Aircraft," Zivko Aeronautics Inc., [Online]. Available: https://www.zivko.com/edge/. [Accessed 18 April 2018].

[10] X. GmbH, "X4A1," XtremeAir, [Online]. Available: https://www.xtremeair.com/xa41/. [Accessed 18 April 2018].

[11] M. Aircraft, "MX2 Aircraft," MX Aircraft, [Online]. Available: http://www.mxaircraft.com/mx2/. [Accessed 18 April 2018].

[12] "WAAC Registration List 2021," FAI, 27 July 2021. [Online]. Available: https://civa-results.com/2021/WAAC_2021/WebRegList.htm. [Accessed 05 June 2022].

[13] Extra Flugzeugproduktions , "Information Manual Extra 300/SC," Extra Flugzeugproduktions, Federal Republic of Germany, 4 March 2016.

[14] D. Barker, "Airshow Incident Accident Review 2019," 2020.

[15] "ASN Wikibase Occurrence # 43997," Flight Safety Foundation, [Online]. Available: https://aviation-safety.net/wikibase/43997. [Accessed 27 May 2022].

[16] "ASN Wikibase Occurrence # 43987," Aviation Safety Network, [Online]. Available: https://aviation-safety.net/wikibase/43987. [Accessed 27 May 2022].

[17] "ASN Wikibase Occurrence # 179176," Aviation Safety Network, [Online]. Available: https://aviation-safety.net/wikibase/179176. [Accessed 27 May 2022].

[18] "ASN Wikibase Occurrence # 59627," Aviation Safety Foundation, [Online]. Available: https://aviation-safety.net/wikibase/59627. [Accessed 27 May 2022].

[19] "ASN Wikibase Occurrence # 70463," Aviation Safety Foundation, [Online]. Available: https://aviation-safety.net/wikibase/70463. [Accessed 27 May 2022].

[20] "ASN Wikibase Occurrence # 75217," Aviation Safety Foundation, [Online]. Available: https://aviation-safety.net/wikibase/75217. [Accessed 27 May 2022].

[21] "ASN Wikibase Occurrence # 156202," Aviation Safety Foundation, [Online]. Available: https://aviation-safety.net/wikibase/156202. [Accessed 27 May 2022].

[22] "ASN Wikibase Occurrence # 160552," Aviation Safety Foundation, [Online]. Available: https://aviation-safety.net/wikibase/160552. [Accessed 27 May 2022].

[23] "ASN Wikibase Occurrence # 179205," Aviation Safety Foundation, [Online]. Available: https://aviation-safety.net/wikibase/179205. [Accessed 27 May 2022].

[24] "ASN Wikibase Occurrence # 186515," Aviation Safety Foundation, [Online]. Available: https://aviation-safety.net/wikibase/186515. [Accessed 27 May 2022].

[25] "ASN Wikibase Occurrence # 200520," Aviation Safety Foundation, [Online]. Available: https://aviation-safety.net/wikibase/200520. [Accessed 27 May 2022].

[26] "ASN Wikibase Occurrence # 245806," Flight Safety Foundation, [Online]. Available: https://aviation-safety.net/wikibase/245806. [Accessed 03 June 2022].

[27] "Belgian Airshow Disaster," [Online]. Available: https://www.youtube.com/watch?v=T6vSM5rdUMg. [Accessed 3 June 2022].

[28] "Extra 300 Aerobatic Plane Crashed During An Airshow In Buenos Aires," 1001Crash, [Online]. Available: https://www.1001crash.com/aviation-video-Extra300_crash-lg-2-extra-300-aerobatic-plane-crashed-during-airshow-in-buenos-aires.html. [Accessed 3 June 2022].

[29] "Plane Crash at an Airshow in Austria," [Online]. Available: https://www.youtube.com/watch?v=X3WytXncgkQ. [Accessed 3 June 2022].

[30] D. Barker, "World Airshow Accident/Incident Overview 2015," European Airshow Council, Airshow South Africa, 2016.

[31] M. E. Eshelby, "Aircraft Performance," in *Theory and Practice*, 2000, p. Appendix A.

[32] S. S. o. M. a. A. Engineering, "Chapter 4: Dynamic Equations for Flight Vehicles," 2011. [Online]. Available: https://courses.cit.cornell.edu/mae5070/DynamicEquations.pdf. [Accessed 25 October 2017].

[33] USAF, "Chapter 4 Equations of Motion," USAF Test Pilot School, California, October 1988.

[34] B. Etkin and L. D. Reid, "Stability and Control, 3rd Edition," in *Dynamics of Flight*, John Wiley & Sons, Inc., 1996, p. 104.

[35] N. M. Rouyan, "Model Simulation Suitable for an Aircraft At High Angles of Attack," Cranfield University, Bedfordshire, 2016.

[36] H. Ashley, "On the Feasibility of Low - Speed Aircraft Maneuvers Involving Extreme," *Journal of Fluids and Structures*, pp. 319-335, 1987.

[37] R. F. Stengel, Flight Dynamics, New Jersey: Princeton University Press, 2004.

[38] C. C. Critzos, H. H. Heyson and R. W. Boswinkle Jr, "Aerodynamic Characteristics of NACA 0012 Airfoil Section at Angles of Attack from 0 to 180 degrees," National Advisory Committee for Aeronautics, Washington, January 1955.

[39] M. S. Selig, "Modelling Full-Envelope Aerodynamics of Small UAVs in Realtime," AIAA, Toronto, 2010.

[40] C. Cutler, "How Does Lowering Flaps Affect an Airplanes Angle of Attack (AOA)?," Bold Method, 23 October 2013. [Online]. Available:

https://www.boldmethod.com/blog/2013/10/how-does-lowering-flaps-affect-angle-of-attack/. [Accessed 10 September 2022].

[41] B. N. Pamadi and L. W. J. Taylor, "Semiempirical Method for Prediction of Aerodynamic Forces and Moments on a Steady Spinning Light Airplane," NASA, Virginia, 1987.

[42] L. H. Jorgensen, "Prediction of Static Aerodynamic Characteristics for Slender Bodies Alone and with Lifting Surfaces to Very High Angles of Attack, NASA TR R-474," Ames Research Center, California, Spetember 1977.

[43] L. H. Smith, "Aerodynamic Characteristics of an Axisymmetric Body Undergoing a Uniform Pitching Moment," Calhoun, Institutional Archive of the Naval Postgrad School, California, 1964.

[44] P. F. Yaggy and V. L. Rogallo, "A Wind Tunnel Investigation of Three Propellers Through An Angle of Attack Range From 0 to 85," NASA, Washington, 1960.

[45] C. H. McLemore and M. D. Cannon, "Aerodynamic Investigation fo a Four-Blade Propeller Operating Through and Angle-of-Attack Range from 0 to 180," NASA, Washington, 1954.

[46] S. F. Hoerner and H. V. Borst, "Practical Information on Aerodyanmic and Hydrodynamic Lift," in *Fluid-Dynamic Lift, Second Edition*, New York, Mrs. Liselotte A. Hoerner, 1985, pp. 4-24 to 4-25.

[47] F. Conner, C. Willey and W. Twomey, "A Flight and Wind Tunnel Investigation of the Effect of Angle of Attack Rate on Maximum Lift Coefficient," NASA, Washington D.C, 1965.

[48] J. L. Anderson, "Tests of NACA 65(216)-429 and 66(218)-420 Airfoils at High Speeds," NACA, Washington D.C, 1944.

[49] G. Bangga, T. Lutz and M. Arnold, "An Improved Second-Order Dynamic Stall Model for Wind Turbine Airfoils," eawe, 2020.

[50] R. Modarres, "Semi-Empirical Modeling of Two-Dimensional and Three-Dimensional Dynamic Stall," Washington University in St. Louis, Saint Louis, 2016.

[51] M. H. Hansen, M. Gaunaa and H. A. Madsen, "A Beddoes-Leishman Type Dynamic Stall Model In State-Space and Indicial Formulations," Riso National Laboratory, Roskilde, 2004.

[52] R. Nave, "Moment of Inerita," Hyperphysics, [Online]. Available: http://hyperphysics.phy-astr.gsu.edu/hbase/mi.html. [Accessed 12 April 2017].

[53] C. Lanham, "Inertia Calculation Procedure for Preliminary Design," Wright-Patterson Air Force Base, Ohio, 1979.

[54] W. Gracey, "NASA TN780 - Measured Moments of Inertia of 32 Airplanes," NASA, Washington, 1940.

[55] J. Roskam, Aiplane Design Part V: Component Weight Estimation, Ottawa, Kansas: Roskam Aviation and Engineering Corporation, 1985.

[56] R. Ali, "Aircraft weight estimation in interactive design process," University of Hertfordshire, Hertfordshire.

[57] S. Gudmundsson, "General Aviation Aircrat Design," Elsevier, 2104, pp. 133-180.

[58] E. Torenbeek, Synthesis of Subsonic Airplane Design, Springer, 1982.

[59] D. P. Raymer, Aircraft Design: A Conceptual Approach, AIAA, 1989.

[60] D. A. Spera, "Models of Lift and Drag Coefficients of Stalled and Unstalled Airfoils in Wind Turbines and Wind Tunnels," NASA, Cleveland, October, 2008.

[61] R. Ali, "Aircraft Weight Estimation in Interactive Design Process," University of Hertfordshire, N/A.

[62] I. H. Abbott and A. E. Von Doenhoff, Theory of Wing Sections Including a Summary of Airfoil Data, New York: Dover Publications, INC., June 1958.

[63] M. Drela and H. Y. Guppy, "XFOIL Subsonic Airfoil Development System," [Online]. Available: https://web.mit.edu/drela/Public/web/xfoil/.

[64] U. o. t. Witwatersrand, "MECN3008," in *Introduction to Aeronautics 2*, Johannesburg, University of the Witwatersrand, 2014, pp. 6-2.

[65] J. L. Tangler and C. Ostowari, "Horizontal Axis WInd Turbine Post Stall Airfoil Characteristics Synthesization," in *Horizontal-Axis Wind Turbine Technology Conference*, Cleveland, 1984.

[66] C. Lindenburg, "Stall Coefficients, Aerodynamic Airfoil Coefficient at Large Angles of Attack," in *ECN Wind Energy*, Colorado, 2000.

[67] G. K. Ananda and M. S. Selig, "Stall/Post-Stall Modeling of the Longitudinal Characteristics of a General Aviation Aircraft," in *AIAA Aviation*, Washington D.C, 2016.

[68] W. Bihrle, Jr. and B. Barnhart, "Static Aerodynamic Characteristics of a Typical Single-Engine Low-Wing General Aviation Design for an Angle-of-Attack Range of -8 to 90," NASA, 1978.

[69] University of the Witwatersrand, "Aircraft Design 3," in *MECN3005*, Johannesburg, University of the Witwatersrand, 2014, pp. IX-6.

[70] J. Roskam and C.-T. E. Lan, Airplane Aerodynamic and Performance, Kansas: DARcorporation, 1997.

[71] E. Flugzeugproduktions, "Maintenance Manual Extra 300/SC, Chapter 53," Extra Flugzeugproduktions, 2008.

[72] A. Chabord, "Extra 330 SC exhaust," Atelier Chabord , [Online]. Available: https://www.echappement-chabord.fr/en/realisations/extra-330-sc-exhaust/. [Accessed 10 July 2022].

[73] M. Jefferies, "Mark Jefferies Airdisplays," Mark Jefferies Airdisplays, [Online]. Available: https://markjefferiesairdisplays.com/mark-jefferies-extra-330sc-aerobatic-air-display-aircraft/#:~:text=Extra%20330sc&text=The%20engine%20produces%20an%20impressive,of%20420%20degrees%20per%20second.. [Accessed 10 July 2022].

[74] "Airfoil Tools," Airfoil Tools, [Online]. Available: http://airfoiltools.com/. [Accessed 16 July 2022].

[75] H. J. Allen, "Estimation of the Forces and Moments Acting on Inclined Bodies of Revolution of High Fineness Ratio, NACA RM A9I26," NACA, Washington, November 14 1949.

[76] J. Dorfling and K. Rokhsaz, "Integration fo Airfoil Stall and Compressibility Models into a Propeller Blade Element Model," Journal of Aerospavce Engineering, 2015.

[77] AirshowStuffVideos, " Skip Stewart Aerobatics - Battle Creek Airshow 2015," AirshowStuffVideos, 8 July 2015. [Online]. Available: https://www.youtube.com/watch?v=C3DQ9rcLBXE&ab_channel=AirshowStuffVideos.

[78] horsemoney, " Sean D. Tucker - Oshkosh 2015 - Saturday," 27 July 2015. [Online]. Available: https://www.youtube.com/watch?v=Dqsl--WOxxY&ab_channel=horsemoney.

8. APPENDIX A – OCTAVE MODELLING SCRIPTS

batchRunTumbles.m

```
clear all
clc
close all
close h

V = 40; %Starting Velocity 25,30,35,40
Tf = 1; %Thrust ratio
SSf = 1; %Slipstream ratio
m = [690.5307 742.8807 781.7807 781.7807 759.7807 730.2807 668.5307 668.5307];    %Aircraft masses
cgx = [2.167898 2.169884 2.150569 2.125242 2.092819 2.087261 2.102835 2.125871];  %Aircraft centre of mass locations
Iyy = [981.996021 975.25998 1040.5 990.246095 961.759426 979.41025 929.828252 961.296785];  %Aircraft pitch inertias

[thetaPlot] = loopEnergyMethods(V, m, cgx, Iyy, Tf, SSf)  %Call tumble function
```

loopEnergyMethods.m

```
%%Tumble Manoeuvre Main Script
function [thetaPlot] = loopEnergyMethods(V, m, cgx, Iyy, Tf, SSf)

    pkg load io

    for r = 1:length(m)
         clearvars -except V m cgx Iyy r Tf SSf
         close h

         %-------------------------------------------------------------------------------------------------------
         %Constants
         rho = 1.225;                   %Air density at sea level [kg/m^3]
         g = 9.81;                          %Acceleration due to graity [m/s^2]

         %-------------------------------------------------------------------------------------------------------
         %Altitude Correction to Air Density
         z = 0;  %Altitude [ft]
         sigma =  0.284392*(10332*(1-0.0000225577*z*0.3048)^5.255874*9.81/100)/(288.16-0.0065*z*0.3048); %Density
correction factor for change in altitude
         rhoalt =
rho*sigma;
                                    %Corrected density [kg/m^3];

         %-------------------------------------------------------------------------------------------------------
         %Initial Variables
         nlim = 6; %Limit load factor (number of total Gs) that can be pulled during the manoeuvre (if possible) [g]
         Vbot = V;  %Entry speed [m/s]
         W(r) = m(r)*g;  %Aicraft weight [N]
         segd =  1;  %Segment size [deg]
```

```
        segr = segd*(pi/180);  %Segment size [rad]

        %-------------------------------------------------------------------------------------------------------
        %Wing Variables
        b = 7.5;  %Wing span of aircraft [m]
        Sref = 9.81; %Wing reference area [m^2]
        SrefI = 3.32; %Inner wing reference area [m^2] (Wing area blown by propeller slipstream)
        SrefO = 6.39; %Outer wing reference area [m^2]
        AR = inf;
        wMAC = 1.366; %Wing mean aerodynamic chord
        alpha_I = 14.3; %Assumed angle of attack of wing section within propeller slipstream [deg]

        %-------------------------------------------------------------------------------------------------------
        %Aerodynamic Coefficients for Wing and Fuselage for AoAs from 0 to 180
        [alpha_start CLa_wing CLwMax CdwI CLw CDw CMw alphaw ACw] = wingCoefficientsFunc(AR,wMAC); %Wing lift and drag
coefficients for infinite AR

        alphaf = [-50  -45 -40 -35 -30 -25 -20 -15 -10 -5  0 5
10  15  20  25  30  35  40  45  50  55  60  65  70  75  80  85  90  95  100 105 110 115 120 125 130 135 140 145 150 155
160 165 170 175 180];
        CLf = [-0.14581    -0.13827    -0.12551    -0.10868    -0.089185   -0.068574   -0.048438   -0.030302   -
0.015517   -0.0051686  0   0.0051686   0.015517    0.030302    0.048438    0.068574    0.089185    0.10868 0.12551
0.13827 0.14581 0.14728 0.14224 0.13064 0.11286 0.089663    0.062169    0.031759    2.2383e-17  -0.031746   -
0.062067   -0.089331   -0.11211    -0.12926    -0.14003    -0.14409    -0.14155    -0.13295    -0.11924    -0.10169    -
0.081809   -0.061237   -0.041624   -0.024519   -0.011259   -0.0028699  0];
        CDf = [0.17376 0.13827 0.10532 0.076099    0.051491    0.031976    0.01763
0.0081194   0.0027361   0.00045219  0   0.00045219  0.0027361   0.0081194   0.01763
0.031976    0.051491    0.076099    0.10532 0.13827 0.17376 0.21034 0.24636 0.28015 0.31007 0.33463 0.35258 0.36301
0.36539 0.36286 0.352   0.33339 0.30801 0.2772  0.24254 0.20578 0.16869 0.13295 0.10005
0.071204    0.047233    0.028555    0.01515 0.0065699   0.0019852   0.00025109  0];
```

```
        ACf = [0.25553 0.24992 0.24335 0.23549 0.22577 0.21326 0.19623 0.17121 0.12985 0.1 0.1 0.1 0.12985 0.17121
0.19623 0.21326 0.22577 0.23549 0.24335 0.24992 0.25553 0.26042 0.26475 0.26863 0.27215 0.27535 0.27828 0.28099 0.28348
0.28574 0.2878  0.28967 0.29137 0.29292 0.29432 0.29559 0.29673 0.29775 0.29865 0.29944 0.30012 0.30069 0.30115 0.30151
0.30176 0.30191 0.3]*5.6;

        xm(r) = cgx(r);

        %-----------------------------------------------------------------------------------------------------------
        %Tail Variables
        delta_e = -25; %Elevator deflection (Negative implies upward elevator deflection) [deg]
        delta_tab = 0; %Tab deflection (Negative implies downward tab deflection) [deg]
        b_tab = 0; %Span of the trim tab [m]
        b_tail = 2.66; %Span of an elevator (one half of the entire horizontal tail assembly) [m]
        Sstab = 2.13; %Area of the horizontal stabilizer [m^2]
        Se = 1.04; %Area of the elevator [m^2]
        ARt = 3.32; %Aspect ratio of the horizontal tail
        et = 0.75; %Oswalds factor of the horizontal tail

        %-----------------------------------------------------------------------------------------------------------
        %Tail Angle of Attack and Slopes
        alpha_tail = 10.5; %Tail angle of attack
        a1 = 0.6*CLa_wing(1); %Horizontal stabilizer lift curve slope [/deg]
        a2 = 0.6*a1; %Elevator lift curve slope [/deg]
        a3 = 0.42*a2; %Trim tab lift curve slope [/deg]

        %-----------------------------------------------------------------------------------------------------------
        %Thrust Lookups
        refV = [0 10 15 20 25 30 35 40 45 50 60 70 80 90 100 110
120];
                                        %Thrust reference velocities
```

```
        refT= [625.779 590.625 551.250 519.750 491.400 464.625 438.750 413.438 388.500 363.825 315.000 273.375 236.250
207.375 183.094 161.080 142.734];       %Reference thrust (2700RPM) - maximum continuous operation
        refT2 = [600.946 568.125 530.250 499.950 472.680 446.925 422.036 397.688 373.700 349.965 306.788 269.454
235.772 204.525 181.800 160.108 142.031];    %Reference thrust 2 (.......RPM)
        refT3 = [552.774 536.250 500.500 471.900 446.160 421.850 401.421 380.738 357.500 336.765 294.938 260.464
230.588 204.967 182.325 161.850 138.531];    %Reference thrust 3 (.......RPM)

        %-------------------------------------------------------------------------------------------------------
        %Propeller Constants & Variables
        RPM = 2700; %Propeller RPM
        n = RPM/60; %Propeller revs/s
        D = 2; %Propeller diameter [m]
        Xnp = -1.75; %Moment arm from aircraft C.G to propeller line [m] (negative value implies the propeller disk is
ahead of the aircraft C.G)

        cNpLookUp = load('propCnData.txt'); %Propeller coefficient of normal force lookup table [-]

        %-------------------------------------------------------------------------------------------------------
        %V-N Speeds
        [Vs Va Vno Vne clMax] = extra330VN(m(r),g, Sref, nlim, Vbot, rhoalt); %Design airspeeds & VN Diagram
        disp(["Vs = " num2str(Vs) " m/s"]); %Display stall speed

        gamma = 0:segr:(2*pi); %Flight path segments
        h = waitbar(0, "Tumble Calculating"); %Calculation progress bar

        %-------------------------------------------------------------------------------------------------------
-------------------------------------------------------------------------------------------------------
        %Potential+Kinetic Energy with Excess Thrust & Drag (Tumble Manoeuvre)

        tE = 0;
        ttotE = 0;
```

```
        for j = 1:length(gamma)
            %-------------------------------------------------------------------------------------------------------
            %Starting Segment
            if j == 1
                %-------------------------------------------------------------------------------------------------------
                %Starting X, Y Locations and Velocity
                XE(j) = 0; %Starting X location
                HE(j) = 0; %Starting Z location
                HEft(j) = HE(j)*3.28084;
                sigma(j) =  0.284392*(10332*(1-0.0000225577*HEft(j)*0.3048)^5.255874*9.81/100)/(288.16-
0.0065*HEft(j)*0.3048); %Density correction factor for change in altitude
                rhoalt(j) = rho*sigma(j);
                VstartE(j) = Vbot; %Starting velocity [m/s]
                VtStart(j) = (((-0.000159491283531057*(VstartE(j)^3)) + (0.0192336064854577*(VstartE(j)^2)) -
(0.971041248674716*VstartE(j)) + 27.7193781820963)*1.3)+VstartE(j); %Propeller slipstream velocity without AoA
correction [m/s]
                VpropIn(j) = VstartE(j)*cosd(alpha_start(1)); %Flow component perpendicular to propeller disk [m/s]
                Vss(j) = ((((-0.000159491283531057*(VpropIn(j)^3)) + (0.0192336064854577*(VpropIn(j)^2)) -
(0.971041248674716*VpropIn(j)) + 27.7193781820963)*1.30)+VpropIn(j))*SSf; %Tail velocity with 30% increase to accomodate
bigger engine (400HP vs 300HP) and better propeller
                %-------------------------------------------------------------------------------------------------------
                %Wing Lift & Drag
                clwE(j) = interp1(alphaw, CLw, alpha_start(1), "pchip"); %Outer wing section coefficient of lift [-]
                cdwE(j) = interp1(alphaw, CDw, alpha_start(1), "pchip"); %Outer wing section coefficient of drag [-]
                LwI(j) = (0.5*rhoalt(j)*SrefI*(Vss(j)^2)*CLwMax(1)); %Inner wing section lift force[N] (It is assumed
that the inner wing section is operating at maximum coefficient of lift at start of manouevre)
                LwO(j) = (0.5*rhoalt(j)*SrefO*(VstartE(j)^2)*clwE(j)); %Outer wing section lift force [N]
                LwE(j) = LwI(j) + LwO(j); %Total wing lift [N]
                DwI(j) = 0.5*rhoalt(j)*SrefI*(Vss(j)^2)*CdwI(2); %Inner wing section drag force [N]
                DwO(j) = 0.5*rhoalt(j)*SrefO*(VstartE(j)^2)*cdwE(j); %Outer wing section drag force [N]
                DwE(j) = DwI (j)+ DwO(j); %Total wing drag [N]
```

```
                    AC(j) = interp1(alphaw, ACw, alpha_start(1), "pchip"); %Wing aerodynamic center [%MAC]
                    %-------------------------------------------------------------------------------------------
                    %Fuselage Lift, Drag & AC
                    VfuseX(j) = Vss(j); %Fuselage velocity in the X direction (along the fuselage) [m/s]
                    VfuseZ(j) = 0; %Fuselage velocity in the Z direction (perpendicular to the fuselage) [m/s]
                    Vfuse(j) = sqrt(VfuseX(j)^2 + VfuseZ(j)^2); %Total fuselage velocity [m/s]
                    alphaFuse(j) = atand(VfuseZ(j)/VfuseX(j)); %Angle of fuselage velocity relative to the fuselage
longitudinal axis [deg]
                    deltaFuse(j) = alpha_start(1)-alphaFuse(j); %Difference in angle between fuselage air angle and
flight path angle [deg]
                    clfE(j) = interp1(alphaf, CLf, alpha_start(1), "pchip"); %Fuselage coefficient of lift [-]
                    cdfE(j) = interp1(alphaf, CDf, alpha_start(1), "pchip"); %Fuselage coefficient of drag [-]
                    LfE(j) = 0.5*rhoalt(j)*Sref*(Vss(j)^2)*clfE(j); %Fuselage lift force [N]
                    DfE(j) = 0.5*rhoalt(j)*Sref*(Vss(j)^2)*cdfE(j); %Fuselage drag force [N]
                    xACf(j) = interp1(alphaf, ACf, alpha_start(1), "pchip"); %Fuselage aerodyanmic center [m] (Referenced
to start of fuselage/propeller???)
                    lACf(j) = xm(r) - xACf(j); %Moment arm from fuselage aerodynamic center to aircraft center of gravity
[m]
                    %-------------------------------------------------------------------------------------------
                    %Thrust
                    TE(j) = (interp1(refV, refT, VstartE(j)))*g*1.3*Tf; %Thrust (function of velocity) [N] (the thrust
value from the lookup has been multiplied by 1.3 to accomodate a more power engine, 400HP vs 310HP and better propeller)
                    %-------------------------------------------------------------------------------------------
                    %Propeller Advance Ratio, Normal Force and Moment
                    J(j) = VstartE(j)/(n*D); %Advance ratio [-]
                    modJ(j) = (VstartE(j)*cosd(alpha_start(1)))/(n*D); %Modified advance ratio [-] (Accomodates large
angles of attack)
                    modJLookup(j) = (modJ(j)*10) + 1; %Advance ratio lookup row
                    alphaLookup(j) = (alpha_start(1)/10) +1; %Angle of attack lookup column
                    cNp(j) = interp2(1:columns(cNpLookUp), 1:rows(cNpLookUp), cNpLookUp, modJLookup(j), alphaLookup(j));
%Coefficient of propeller normal force [-]
```

```
                    Np(j) = rhoalt(j)*(n^2)*(D^4)*cNp(j); %Propeller normal force [N]
                    Mnp(j) = Np(j)*Xnp; %Moment due to propeller normal force [Nm]
                    %-------------------------------------------------------------------------------------------------
                    %Load Factors
                    NvE(j) = (LwI(j)*cosd(alpha_start(1)-14.3)) + LwO(j)+ LfE(j) + (TE(j)*sind(alpha_start(1))) +
(Np(j)*sind(alpha_start(1))); %Normal force in the velocity axes
                    NbE(j) = (LwE(j)*cosd(alpha_start(1))) + (DwE(j)*sind(alpha_start(1))) +Np(j); %Normal force in the
body axes
                    nEv(j) = NvE(j)/W(r); %Load facotr in the veloicty axes (this is the load factor that determines the
radius of the manoeuvre)
                    nEb(j) = (NbE(j))/W(r); %This load factor is the total normal acceleration felt by the aircraft
                    nE(j) = nEv(j);
                    %-------------------------------------------------------------------------------------------------
                    %Radius
                    RE(j) = ((Vbot)^2)/(g*(nEv(j)-cos(0+(0.5*segr))));
                    %-------------------------------------------------------------------------------------------------
                    %Segment Lengths
                    lsegE(j) = 2*RE(j)*sin(segr/2);
                    lxE(j) = lsegE(j)*cos(gamma(j)+(0.5*segr));
                    lyE(j) = lsegE(j)*sin(gamma(j)+(0.5*segr));
                    %-------------------------------------------------------------------------------------------------
                    a(j) = (((TE(j)*cosd(alpha_start(1)))-DwE(j)-(W(r)*sin(gamma(j))))/m(r))-(DfE(j)*cosd(deltaFuse(j)));
                    deltaVE(j) = (sqrt((VstartE(j)^2)+(2*(((TE(j)*cosd(alpha_start(1)))-DwE(j)-
(W(r)*sin(gamma(j))))/m(r))*(lsegE(j)))))-VstartE(j);
                    VendE(j) = (sqrt((Vbot^2)-(2*g*(HE(j)+lyE(j)))))+(deltaVE(j));
                    VendE(j) = VstartE(j) + (deltaVE(j));
                    tsegE(j) = lsegE(j)/((VendE(j)+VstartE(j))/2);
                    tE(j) = tsegE(j);
                    Acent(j) = (VendE(j)^2)/RE(j);
                    Agrav(j) = 1*g*cos(gamma(j));
                    Atot(j) = (Acent(j)+Agrav(j))/g;
```

```
                    q(j) = (LwE(j)-W(r))/(m(r)*VendE(j));
                    Net(j) = (TE(j)-DwE(j)-(W(r)*sin(gamma(j))));
                    %-----------------------------------------------------------------------------------------------

                    Vr(j) = 0;
                    if alpha_start(1) < 30
                         VtailX(j) = (Vss(j)*cosd(14));
                         VtailZ(j) = (Vss(j)*sind(14)) + Vr(j);
                    else
                         VtailX(j) = (Vss(j)*cosd(14)) + (VstartE(j)*cosd(alpha_start(1)));
                         VtailZ(j) = (Vss(j)*sind(14)) + (VstartE(j)*sind(alpha_start(1))) + Vr(j);
                    end
                    Vtail(j) = sqrt(VtailX(j)^2 + VtailZ(j)^2);
                    alphaTail(j) = atand(VtailZ(j)/VtailX(j));
                    CLhstab(j) = 0.6*interp1(alphaw, CLw, alphaTail(j), "pchip");
                    theta_dot0 = 0;
                    theta0 = gamma(j) + (alpha_start(1)*(pi/180));
                    alphaFuse(j) = 0;
                    [Lw(j) Dw(j) CLt(j) CDt(j) Lt(j) Dt(j) Mthrust(j) MwingI(j) MwingO(j) Mfuse(j) Mtail(j) Mtot(j)
ang_acc(j) ang_vel(j) theta(j) alpha_tail_pitchEq(j) vtail(j)] = pitchRate(gamma(j), rhoalt(j), Sref, SrefI, SrefO,
VendE(j), CLwMax(1), CdwI(2), clwE(j), cdwE(j), clfE(j), cdfE(j), AC(j), lACf(j), Vss(j), alpha_start(1), CLa_wing(1),
alpha_I, TE(j), Iyy(r), tsegE(j), theta_dot0, theta0, CLhstab(j), j, Mnp(j),alphaFuse(j),  xm(r));
                    alpha(j) = (theta(j)*(180/pi)) - (gamma(j)*(180/pi));
                    theta_dot(j) = ang_acc(j);
               %-----------------------------------------------------------------------------------------------
-----------------------------------------------------------------------------------------------------------------
               else
                    %-----------------------------------------------------------------------------------------------
                    %Current X, Y Locations and Velocity
                    XE(j) = XE(j-1) + lxE(j-1); %X location at start of segment [m]
                    HE(j) = HE(j-1) + lyE(j-1); %Y location at start of segment [m]
```

```
                HEft(j) = HE(j)*3.28084;
                sigma(j) =  0.284392*(10332*(1-0.0000225577*HEft(j)*0.3048)^5.255874*9.81/100)/(288.16-
0.0065*HEft(j)*0.3048); %Density  correction factor for change in altitude
                rhoalt(j) = rho*sigma(j);
                VstartE(j) = VendE(j-1); %Segment starting speed (set equal to the previous segment end speed)
                VtStart(j) = (((-0.000159491283531057*(VstartE(j)^3)) + (0.0192336064854577*(VstartE(j)^2)) -
(0.971041248674716*VstartE(j)) + 27.7193781820963)*1.3)+VstartE(j);
                VpropIn(j) = VstartE(j)*cosd(alpha(j-1));
                Vss(j) = ((((-0.000159491283531057*(VpropIn(j)^3)) + (0.0192336064854577*(VpropIn(j)^2)) -
(0.971041248674716*VpropIn(j)) + 27.7193781820963)*1.3)+VpropIn(j))*SSf;      %Tail velocity with 30% increase to
accommodate bigger engine (400HP vs 300HP) and better propeller
                %-------------------------------------------------------------------------------------------
                %Wing Lift & Drag
                alphawILookup = [-20 -14 -10 0 10 14 20 30 40 45 50 60 70 80 90];
                clwILookup = [-0.83855 -0.640848 -0.471468 0 0.471468 0.640848 0.838548 1.042932 1.037664 0.943404
0.887832 0.7935 0.629184 0.35 0.074028];
                cdwILookup = [0.14743 0.076958 0.041356 0.006 0.041356 0.076958 0.14743 0.32421 0.52934 0.61964
0.70611 0.86075 0.98092 1.0571 1.0831]*1.3;
                alphawOLookup = [-30 -20 -14 -10 0 10 14 20 30 40 50 60 70 80 90 100 110 120 130];
                clwOLookup = [-0.73275 -1.0998 -0.9343 -0.71329 0 0.7229 0.94139 1.1004 0.73336 0.76645 0.74404
0.66476 0.52678 0.32748 0.062036 -0.22277 -0.42969 -0.56802 -0.64302]*1.1;
                cdwOLookup = [0.43395 0.143847 0.0742896 0.041437 0.0066 0.041437 0.0742896 0.143847 0.43395 0.709918
0.957506 1.16435 1.31989 1.41647 1.44925 1.41647 1.31989 1.16424 0.957451]*1.1;

                vWIX(j) = Vss(j)*cosd(14) + VstartE(j)*cosd(alpha(j-1));
                vWIZ(j) = Vss(j)*sind(14) + VstartE(j)*sind(alpha(j-1));
                vWI(j) = sqrt(vWIX(j)^2+vWIZ(j)^2);
                alphawI(j) = atand(vWIZ(j)/vWIX(j));
                clwI(j) = interp1(alphawILookup, clwILookup, alphawI(j), "pchip"); %Inner wing section coefficient of
lift
                cdwI(j) = interp1(alphawILookup, cdwILookup, alphawI(j), "pchip");
```

```
                clwE(j) = interp1(alphawOLookup, clwOLookup, alpha(j-1), "pchip");
                cdwE(j) = interp1(alphawOLookup, cdwOLookup, alpha(j-1), "pchip");
                LwI(j) =   (0.5*rhoalt(j)*SrefI*(vWI(j)^2)*clwI(j));
                LwO(j) = (0.5*rhoalt(j)*SrefO*(VstartE(j)^2)*clwE(j)); %Outer wing section lift force [N]
                LwE(j) = LwI(j) + LwO(j);
                DwI(j) = 0.5*rhoalt(j)*SrefI*(vWI(j)^2)*cdwI(j);
                DwO(j) = 0.5*rhoalt(j)*SrefO*(VstartE(j)^2)*cdwE(j); %Outer wing section drag force [N]
                DwE(j) = DwI(j)*cosd(alpha(j-1) - alphawI(j))+ DwO(j); %Total wing drag [N]
                AC(j) = interp1(alphaw, ACw, alpha(j-1), "pchip"); %Wing aerodynamic center [%MAC]
                %-------------------------------------------------------------------------------------------------
                %Fuselage Lift, Drag & AC
                if (gamma*(180/pi)) < 30
                     VfuseX(j) = Vss(j);
                else
                     VfuseX(j) = Vss(j) + (VstartE(j)*cosd(alpha(j-1)));
                end
                VfuseZ(j) = (VstartE(j)*sind(alpha(j-1)));
                Vfuse(j) = sqrt(VfuseX(j)^2 + VfuseZ(j)^2);
                alphaFuse(j) = atan(VfuseZ(j)/VfuseX(j));
                deltaFuse(j) = alpha(j-1)-(alphaFuse(j)*(180/pi));
                clfE(j) = interp1(alphaf, CLf, (alphaFuse(j)*(180/pi)), "pchip");
                cdfE(j) = interp1(alphaf, CDf, (alphaFuse(j)*(180/pi)), "pchip");
                LfE(j) = 0.5*rhoalt(j)*Sref*(VstartE(j)^2)*clfE(j);
                DfE(j) = 0.5*rhoalt(j)*Sref*(VstartE(j)^2)*cdfE(j);
                xACf(j) = interp1(alphaf, ACf, (alphaFuse(j)*(180/pi)), "pchip");
                lACf(j) = xm(r) - xACf(j);
                %-------------------------------------------------------------------------------------------------
                %Tail Lift & Drag
                alphaTRef = [-30.08  -25.08  -20.08  -15.08  -10.08  -
5.08   0.03    2.03    4.03    6.03    8.03    10.03   12.03   14.03   16.03   18.03   20.03   22.03   24.04   26.04   2
8.04   30.04   32.04   34.04   36.04   38.04   40.04   42.04   44.04   46.04   48.04   50.04   52.04   54.04   56.04   5
```

```
8.04   60.04   62.04   64.04   66.04   68.04   70.04   72.04   74.04   76.04   78.04   80.04   82.04   84.04   86.04   8
8.04   90.04   92.04];
                    clTRef = [-1.6268    -1.6914 -1.7144 -1.6824 -1.5179 -1.3968 -1.5264 -1.4603 -1.3452 -1.1924 -1.0129
-0.81788    -0.62831    -0.4349 -0.25871    -0.11085    -0.00244    0.05542 0.08    0.1
0.125   0.15    0.175   0.19    0.225   0.25226 0.29503 0.32773 0.35117 0.36631 0.37396 0.37481 0.36986 0.35954 0.34459
0.32563 0.30317 0.27773 0.24984 0.21988 0.1882  0.15518 0.12112 0.086263    0.05084 0.015025    -0.021018   -
0.057194   -0.093405   -0.12961    -0.16578    -0.20193    -0.23807];
                    cdTRef = [1.0427 0.9327  0.79918 0.64163 0.44179 0.232   0.10389 0.10307 0.10241 0.10192
0.1016  0.10144 0.10145 0.10163 0.10197 0.10247 0.10314 0.10398 0.10957 0.19403 0.27835 0.36237 0.44596 0.52899 0.61071
0.67836 0.74215 0.80208 0.85816 0.91041 0.95889
1.0036  1.0446  1.0821  1.116   1.1465  1.1738  1.1979  1.219   1.2373  1.253   1.2661  1.277   1.2858  1.2927  1.298
1.3016  1.3041  1.3053  1.3057  1.3053  1.3042  1.3026];

                    Vr(j) = theta_dot(j-1) * 3.52;
                    tailAngSmooth(j) = ((-12/80)*(gamma(j)*(180/pi))) + 12;
                    if gamma(j)*(180/pi) < 80
                         VtailX(j) = (Vss(j)*cosd(tailAngSmooth(j))) + (VstartE(j)*cosd(alpha(j-1)));
                         VtailZ(j) = (Vss(j)*sind(tailAngSmooth(j))) + (VstartE(j)*sind(alpha(j-1))) + Vr(j);
                    else
                         VtailX(j) = (Vss(j)*cosd(0)) + (VstartE(j)*cosd(alpha(j-1)));
                         VtailZ(j) = (Vss(j)*sind(0)) + (VstartE(j)*sind(alpha(j-1))) + Vr(j);
                    end

                    Vtail(j) = sqrt(VtailX(j)^2 + VtailZ(j)^2);
                    alphaTail(j) = atand(VtailZ(j)/VtailX(j));
                    deltaTail(j) = (alpha(j-1)-alphaTail(j));
                    cltE(j) = interp1(alphaTRef, clTRef, alphaTail(j), "pchip");
                    cdtE(j) = interp1(alphaTRef, cdTRef, alphaTail(j), "Pchip");

                    %-------------------------------------------------------------------------------
                    %Tail Lift and Drag Forces
```

```
                    Vt(j) = (((-0.0001594912835310 57*(VstartE(j)^3)) + (0.0192336064854577*(VstartE(j)^2)) -
(0.971041248674716*VstartE(j)) + 27.7193781820963)*1.3)+VstartE(j);
                    LtE(j) = 0.5*rhoalt(j)*Sstab*((0.95*Vss(j))^2)*cltE(j);          %Tail lift force [N]
                    DtE(j) = 0.5*rhoalt(j)*Sstab*((0.95*Vss(j))^2)*cdtE(j);         %Tail drag force [N]
                    %-------------------------------------------------------------------------------------------------------
                    %Thrust
                    TE(j) = (interp1(refV, refT, VstartE(j)))*g*1.3*Tf;
                    %-------------------------------------------------------------------------------------------------------
                    %Propeller Advance Ratio, Normal Force and Moment
                    J(j) = VstartE(j)/(n*D);
                    modJ(j) = (VstartE(j)*cosd(alpha(j-1)))/(n*D);
                    if modJ(j) < 0
                         modJ(j) = 0;
                    end
                    modJLookup(j) = (modJ(j)*10) + 1;
                    alphaLookup(j) = (abs(alpha(j-1))/10) +1;
                    cNp(j) = interp2(1:columns(cNpLookUp), 1:rows(cNpLookUp), cNpLookUp, modJLookup(j), alphaLookup(j));
                    Np(j) = rhoalt(j)*(n^2)*(D^4)*cNp(j)*0.70;   %30m/s-0.55, 30m/s-0.55, 35m/s-0.55, 40m/s-0.55/0.84
                    Mnp(j) = Np(j)*Xnp;
                    %-------------------------------------------------------------------------------------------------------
                    %Load Factor
                    if gamma*(180/pi) < 90
                         NvE(j) = (LwI(j)*cosd(alpha(j-1) - alphawI(j))) - (DwI(j)*sind(alpha(j-1) - alphawI(j))) +
LwO(j)  + (LfE(j)*cosd(deltaFuse(j))) - (DfE(j)*sind(deltaFuse(j))) + (TE(j)*sind(alpha(j-1))) + (Np(j)*cosd(alpha(j-
1))) + (LtE(j)*cosd(deltaTail(j))) - (DtE(j)*sind(deltaTail(j)));          %Normal force in the velocity axes
                    else
                         NvE(j) = (LwI(j)*cosd(alpha(j-1) - alphawI(j))) - (DwI(j)*sind(alpha(j-1) - alphawI(j))) +
LwO(j)  + (LfE(j)*cosd(deltaFuse(j))) - (DfE(j)*sind(deltaFuse(j))) + (TE(j)*sind(alpha(j-1))) + (Np(j)*cosd(alpha(j-
1))) + (LtE(j)*cosd(deltaTail(j))) - (DtE(j)*sind(deltaTail(j)));
                    end
```

```
                fzv(j) = NvE(j);
                NbE(j) = (LwI(j)*cosd(alphawI(j))) + (LwO(j)*cosd(alpha(j-1))) + (DwI(j)*sind(alphawI(j))) +
(DwO(j)*sind(alpha(j-1))) + (LtE(j)*cosd(alphaTail(j))) + (DtE(j)*sind(alphaTail(j))) + (LfE(j)*cos(alphaFuse(j))) +
(DfE(j)*sin(alphaFuse(j))) + Np(j);                                                                    %Normal
force in the body axes
                fzb(j) = NbE(j);

                nEv(j) = NvE(j)/W(r); %Load facotr in the veloicty axes (this is the load factor that determines the
radius of the manoeuvre)
                nEb(j) = (NbE(j))/W(r); %This load factor is the total normal acceleration felt by the aircraft

                %-------------------------------------------------------------------------------------------------
                %Radius
                RE(j) = (((VstartE(j)-(0.5*(VstartE(j)-VstartE(j-1))))^2)/(g*(nEv(j)-cos(gamma(j)+(0.5*segr))));
                gammaDot(j) = (g*(nEv(j)-cos(gamma(j)+(0.5*segr))))/(VstartE(j));
                %-------------------------------------------------------------------------------------------------
                %Segment Lengths
                lsegE(j) = 2*RE(j)*sin(segr/2);
                lxE(j) = lsegE(j)*cos(gamma(j)+(0.5*segr));
                lyE(j) = lsegE(j)*sin(gamma(j)+(0.5*segr));
                %-------------------------------------------------------------------------------------------------
                %Excess Speed
                DE(j) = DwO(j) + (DwI(j)*cosd(alpha(j-1) - alphawI(j))) + (LwI(j)*sind(alpha(j-1) - alphawI(j))) +
(DfE(j)*cosd(deltaFuse(j))) + (LfE(j)*sind(deltaFuse(j))) + (DtE(j)*cosd(deltaTail(j))) + (LtE(j)*sind(deltaTail(j))) +
(Np(j)*sind(alpha(j-1)));
                a(j) = (((TE(j)*cosd(alpha(j-1)))-(DE(j))-(W(r)*sin(gamma(j-1))))/m(r));
                deltaVE(j) = (sqrt((VstartE(j)^2)+(2*(((TE(j)*cosd(alpha(j-1)))-(DE(j))-(W(r)*sin(gamma(j-
1))))/m(r))*(lsegE(j))))) -VstartE(j);
                VendEkp(j) = (sqrt((Vbot^2)-(2*g*(HE(j)+lyE(j))))+(deltaVE(j));
                VendE(j) = VstartE(j) + (deltaVE(j));
```

```
                %-------------------------------------------------------------------------------------------------
                %Time
                tEnew(1) = 0;
                tsegE(j) = lsegE(j)/(0.5*(VendE(j)+VstartE(j)));
                tsegE_temp(j) = (VendE(j-1)-VendE(j))/((TE(j)*cosd(alpha(j-1)))-DwE(j)-(W(r)*sin(gamma(j))));
                tE(j) = tE(j-1)+tsegE(j);
                tEnew(j) = tEnew(j-1)+tsegE_temp(j);
                ttotE = ttotE+tsegE(j);
                deltaVE2(j) = ((TE(j)-DE(j))/(m(r)))*tsegE(j);
                VdiffE(j) = VstartE(j)-VendE(j);
                %-------------------------------------------------------------------------------------------------
                %Accelerations
                Acent(j) = (VendE(j)^2)/RE(j);
                Agrav(j) = 1*g*cos(gamma(j));
                Atot(j) = (Acent(j)+Agrav(j))/g;

               %-------------------------------------------------------------------------------------------------
                %Forces in X and Z Velocity and Body Axes
                FZv(j) = (-LwI(j)*cosd(alpha(j-1) - alphawI(j))) + (DwI(j)*sind(alpha(j-1) - alphawI(j))) - LwO(j)  -
(LfE(j)*cosd(deltaFuse(j))) + (DfE(j)*sind(deltaFuse(j))) - (TE(j)*sind(alpha(j-1))) - (Np(j)*cosd(alpha(j-1))) -
(LtE(j)*cosd(deltaTail(j))) + (DtE(j)*sind(deltaTail(j)));
                FZb(j) =  (-LwI(j)*cosd(alphawI(j))) - (LwO(j)*cosd(alpha(j-1))) - (DwI(j)*sind(alphawI(j))) -
(DwO(j)*sind(alpha(j-1))) - (LtE(j)*cosd(alphaTail(j))) - (DtE(j)*sind(alphaTail(j))) - (LfE(j)*cos(alphaFuse(j))) -
(DfE(j)*sin(alphaFuse(j))) - Np(j);

                FXv(j) =  (TE(j)*cosd(alpha(j-1))) - DwO(j) - (DwI(j)*cosd(alpha(j-1) - alphawI(j))) -
(LwI(j)*sind(alpha(j-1) - alphawI(j))) - (DfE(j)*cosd(deltaFuse(j))) - (LfE(j)*sind(deltaFuse(j))) -
(DtE(j)*cosd(deltaTail(j))) - (LtE(j)*sind(deltaTail(j))) - (Np(j)*sind(alpha(j-1)));
                FXb(j) = TE(j) + (LwI(j)*sind(alphawI(j))) + (LwO(j)*sind(alpha(j-1))) - (DwI(j)*cosd(alphawI(j))) -
(DwO(j)*cosd(alpha(j-1))) + (LtE(j)*sind(alphaTail(j))) - (DtE(j)*cosd(alphaTail(j))) + (LfE(j)*sin(alphaFuse(j))) -
(DfE(j)*cos(alphaFuse(j)));
```

```
                    FXbv(j) = (FXv(j)*cosd(alpha(j-1))) - (FZv(j)*sind(alpha(j-1)));
                    FZbv(j) = (FXv(j)*sind(alpha(j-1))) + (FZv(j)*cosd(alpha(j-1)));
                    deltaFX(j) = FXb(j) - FXbv(j);
                    deltaFZ(j) = FZb(j) - FZbv(j);

                    %-------------------------------------------------------------------------------------------------
                    % Pitching Moments
                    CLhstab(j) = 0.6*interp1(alphaw, CLw, alphaTail(j), "pchip");

                    [Lw(j) Dw(j) CLt(j) CDt(j) Lt(j) Dt(j) Mthrust(j) MwingI(j) MwingO(j) Mfuse(j) Mtail(j) Mtot(j)
ang_acc(j) ang_vel(j) theta(j) alpha_tail_pitchEq(j) vtail(j)] = pitchRate(gamma(j), rhoalt(j), Sref, SrefI, SrefO,
VendE(j), CLwMax(1), CdwI(1), clwE(j), cdwE(j), clfE(j), cdfE(j), AC(j), lACf(j), Vss(j), alpha(j-1), CLa_wing(1),
alphawI(j), TE(j), Iyy(r), tsegE(j), theta_dot(j-1), theta(j-1), CLhstab(j), j, Mnp(j), alphaFuse(j),  xm(r));
                    alpha(j) = (theta(j)*(180/pi)) - (gamma(j)*(180/pi));
                    theta_dot(j) = ang_vel(j);
                    %-------------------------------------------------------------------------------------------------
                    %Net Forces X
                    Net(j) = (TE(j)-DE(j)-(W(r)*sind(alpha(j)+(gamma(j)*(180/pi)))));
                    %-------------------------------------------------------------------------------------------------
                    %Waitbar Progression
                    waitbar(j/length(gamma), h);
               end
          end

          close (h);
          disp(["TE = " num2str(ttotE) " s"])
          disp(["Xdiff = " num2str(XE(91)-XE(271)) " m"])

          xUp = XE(1:181);
          yUp = HE(1:181);
```

```
xDown = XE(182:end);
yDown = HE(182:end);

[x0,y0,iout,jout] = intersections(xUp,yUp,xDown,yDown,1);

if isempty(y0)
     deltaZ = '#N/A';
else
     deltaZ = (max(HE)-y0);
endif

disp(["Zdiff _" num2str(r)  "= " num2str(max(HE)-y0) " m"])

thetaPlot = [];
thetaPlotCount = 1;
for i = 1:10:length(gamma)
     thetaPlot(1,thetaPlotCount) = theta(i)*(180/pi);
     thetaPlot(2, thetaPlotCount) = i-1;
     thetaPlot(3, thetaPlotCount) = alpha(i);
     thetaPlotCount = thetaPlotCount + 1;
end

disp(thetaPlot)

%-------------------------------------------------------------------------------------------------------
%Plotting & Excel Files
 if r == 1
     figure (r)
     plot(XE, HE, "r")
     hold on
     ang2 = 11;
```

```
            angText2 = 10;
            while ang2 <=361
                plot(XE(ang2), HE(ang2), 'o', 'color','r');
                deg2 = [num2str(angText2) "deg"];
                if ang2 <=180;
                    text(XE(ang2), HE(ang2), deg2, 'fontsize', 7, 'color', 'r',
'VerticalAlignment','bottom','HorizontalAlignment','right');
                else
                    text(XE(ang2), HE(ang2), deg2, 'fontsize', 7, 'color', 'r',
'VerticalAlignment','bottom','HorizontalAlignment','left');
                end
                ang2 = ang2+10;
                angText2 = angText2 +10;
            end
            hold off
        end

        MnpPlot = [];
        for i = 1:length(gamma)
            if i <= 45
                MnpPlot(i) = Mnp(i);
            else
                MnpPlot(i) = Mnp(i);
            end
        end

        colNames = {"gamma", "XE", "HE", "VstartE", "VtStart", "VpropIn", "Vss", "vWIX", "vWIZ", "vWI", "alphawI",
"clwI", "cdwI", "clwO", "cdwO", "LwI", "LwO", "LwE", "DwI", "DwO", "DwE", "ACw", "VfuseX", "VfuseZ", "Vfuse",
"alphaFuse", "deltaFuse", "clfE", "cdfE", "LfE", "DfE", "xACf", "lACf", "Vr", "VtailX", "VtailZ", "Vtail", "alphaTail",
"deltaTail", "cltE", "cdtE", "LtE", "DtE", "TE", "J", "modJ", "modJLookup", "alphaLookup", "cNp", "Np", "Mnp", "NvE", "
```

```
NbE", " nEv", " nEb", " RE", " lsegE", " lxE", " lyE", " DE", " a", " deltaVE", " VendE", "tsegE", " tE", " Mthrust", "
MwingI", " MwingO", " Mfuse", " Mtail", " Mtot", " ang_acc", " ang_vel", " theta", " alpha"};
        tumbleData = [gamma*(180/pi); XE; HE; VstartE; VtStart; VpropIn; Vss; vWIX; vWIZ; vWI; alphawI; clwI; cdwI;
clwE; cdwE; LwI; LwO; LwE; DwI; DwO; DwE; AC; VfuseX; VfuseZ; Vfuse; alphaFuse*(180/pi); deltaFuse; clfE; cdfE; LfE;
DfE; xACf; lACf; Vr; VtailX; VtailZ; Vtail; alphaTail; deltaTail; cltE; cdtE; LtE; DtE; TE; J; modJ; modJLookup;
alphaLookup; cNp; Np; Mnp; NvE; NbE; nEv; nEb; RE; lsegE; lxE; lyE; DE; a; deltaVE; VendE; tsegE; tE; Mthrust; MwingI;
MwingO; Mfuse; Mtail; Mtot; ang_acc*(180/pi); ang_vel*(180/pi); theta*(180/pi); alpha]';

        disp(r)
        fName = ['tumbleDataV' num2str(V) 'T' num2str(Tf*100) 'SS' num2str(SSf*100) '.xlsx'];
        cName = ['caseNo' num2str(r)];
        hCell = ['H' num2str(r+2)];

        xlswrite(fName, colNames,cName, 'A1:BW1')
        xlswrite(fName, tumbleData, cName, "A2")
        xlswrite(fName, deltaZ, 'tumbleZ', hCell )

    end

    endfunction
```

extra330VN.m

```
%V-N Diagram Extra 330

function [Vs Va Vno Vne CLmax] = extra330VN(m, g, Sref, nlim, Vbot, rhoalt)

    %-------------------------------------------------------------------------------------------------------------
    %Design Airspeeds [knots] (Obtained from 300SC POH)
    Vs_ka = 61;                          %Stall speed, acrobatic category [knots]
    ##Vs_kn = 64;                           %Stall speed, normal category [knots]
    Va_ka = 154;                           %Manoeuvre speed, acrobatic category [knots]
    ##Va_kn = 138;                          %Manoeuvre speed, normal category [knots]
    Vno_k = 154;                           %Maximum structural cruising speed [knots]
    Vne_k = 219;                           %Never exceed speed [knots]

    %-------------------------------------------------------------------------------------------------------------
    %Design Airspeeds [m/s] (Obtained from 300SC POH)
    Vs = round((Vs_ka*0.514444)*100)/100;       %Stall speed, acrobatic category [m/s]
    ##Vs = Vs_kn*00.514444;                 %Stall speed, normal category [m/s]
    ##Va = Va_ka*0.514444;                  %Manoeuvre speed, acrobatic category [m/s]
    ##Va = Va_kn*0.514444;                  %Manoeuvre speed, normal category [m/s]
    Vno = Vno_k*0.514444;                  %Maximum structural cruising speed [m/s]
    Vne = Vne_k*0.514444;                  %Never exceed speed [m/s]

    %-------------------------------------------------------------------------------------------------------------
    %Variables and Constants
    nMax = 6;
    nMax_neg = -0.5*nMax;
    CLmax = 1.2915;
    CLmax_neg = -1;
    Va = (Vs)*sqrt(nMax);                                  %Manoeuvre speed, calculated [m/s]
```

```
%-------------------------------------------------------------------------------------------------------------
%Design Airspeeds for Negative Load Factors
Vs_down = round((sqrt((-2*m*g)/(rhoalt*Sref*CLmax_neg)))*100)/100;
Va_down = Vs_down*sqrt(0.5*nMax);
V = 0:0.01:Vne;

%-------------------------------------------------------------------------------------------------------------
%Limits for Positive Load Factors
for i = 1:length(V)
     if V(i) <= Va
          n_up(i) = (0.5*rhoalt*Sref*CLmax*V(i)^2)/(m*g);
     else
          n_up(i) = nMax;
     end
end

%-------------------------------------------------------------------------------------------------------------
%Limits for Negative Load Factors
for i = 1:length(V)
     if V(i) < Va_down
          n_down(i) = (0.5*rhoalt*Sref*CLmax_neg*V(i)^2)/(m*g);
     else
          n_down(i) = -0.5*nMax;
     end
end

Vlim = sqrt((2*m*g*nlim)/(rhoalt*Sref*CLmax));
Vlimit = 0:0.01:Vbot;

%-------------------------------------------------------------------------------------------------------------
```

```
    %Limited VN Diagram
    for i = 1:length(Vlimit)
         if Vlimit(i) <= Vlim
              n(i) = (0.5*rhoalt*Sref*CLmax*Vlimit(i)^2)/(m*g);
         else
              n(i) = nlim;
         end
    end

    Vne_x = [V(end) V(end)];
    Vne_y = [n_up(end) n_down(end)];
    Vlim_x = [Vbot Vbot];
    Vlim_y = [n(end) 0];
    Zeroline_x = [0 Vne];
    Zeroline_y = [0 0];

    index_stallup = find(V==Vs);
    index_stalldown = find(V==Vs_down);

    linew = 1.75;

    %-------------------------------------------------------------------------------------------------------
    %Plotting
##     figure 1
####     plot(V(1:index_stallup), n_up(1:index_stallup), "k","linewidth",linew, "linestyle",":", V(1:index_stalldown),
n_down(1:index_stalldown), "k","linewidth",linew, "linestyle",":",Vlimit(1:index_stallup), n(1:index_stallup),
"r","linewidth",linew, "linestyle","--")
##     plot(V(1:index_stallup), n_up(1:index_stallup), "k","linewidth",linew, "linestyle",":", V(1:index_stalldown),
n_down(1:index_stalldown), "k","linewidth",linew, "linestyle",":")
##     hold on
```

```
##     plot(V(index_stallup:end), n_up(index_stallup:end), "k","linewidth",linew, "linestyle","-",
V(index_stalldown:end), n_down(index_stalldown:end), "k","linewidth",linew, "linestyle","-",Vne_x, Vne_y,
"k",Vlimit(index_stallup:end), n(index_stallup:end), "r","linewidth",linew, "linestyle","-",Vlim_x, Vlim_y,
"r",Zeroline_x, Zeroline_y, "k");
##     hold off
##     ylim([nMax_neg-2, nMax+2])

endfunction
```

pitchRate.m

```
function [Lf Df CLt CDt Lt Dt Mthrust MwingI MwingO Mfuse Mtail Mtot theta_dbl theta_dot theta alpha_tail Vtail] =
pitchRate(gamma, rhoalt, Sref, SrefI, SrefO, V, CLwMax, CDwI, CLwO, CDwO, CLf, CDf, ACw, Xf, Vt, alpha_wing, CLa_wing,
alpha_wingI, T, Iyy, t, theta_dotPre, thetaPre, CLhstab, j, Mnp, alphaFuse, xcg);

    ##     alphaTRef = [-1 0 1.6181 3.2362 4.8543 6.4723 8.0904 9.7085 11.327 12.945 14.563 16.181 17.799 19.417 19.427
20.427 21.427 22.427 23.427 24.427 25.427 26.427 27.427 28.427 29.427 30.427 31.427 32.427 33.427 34.427 35.427 36.427
37.427 38.427 39.427 40.427 41.427 42.427 43.427 44.427 45.427 46.427 47.427 48.427 49.427 50.427 51.427 52.427 53.427
54.427 55.427 56.427 57.427 58.427 59.427 60.427 61.427 62.427 63.427 64.427 65.427 66.427 67.427 68.427 69.427 70.427
71.427 72.427 73.427 74.427 75.427 76.427 77.427 78.427 79.427 80.427 81.427 82.427 83.427 84.427 85.427 86.427 87.427
88.427 89.427 90.427 91.427 92.427 93.427 94.427 95.427 96.427 97.427 98.427 99.427 100.43 101.43 102.43 103.43 104.43
105.43];
    ##     alphaTRef =
[0   1   2   3   4   5   6   7   8   9   10  11  12  12.01   13.01   14.01   15.01   16.01   17.01   18.01   19.01   20.
01   21.01   22.01   23.01   24.01   25.01   26.01   27.01   28.01   29.01   30.01   31.01   32.01   33.01   34.01   35.
01   36.01   37.01   38.01   39.01   40.01   41.01   42.01   43.01   44.01   45.01   46.01   47.01   48.01   49.01   50.
01   51.01   52.01   53.01   54.01   55.01   56.01   57.01   58.01   59.01   60.01   61.01   62.01   63.01   64.01   65.
01   66.01   67.01   68.01   69.01   70.01   71.01   72.01   73.01   74.01   75.01   76.01   77.01   78.01   79.01   80.
01   81.01   82.01   83.01   84.01   85.01   86.01   87.01   88.01   89.01   90.01   91.01   92.01   93.01   94.01   95.
01   96.01   97.01   98.01   99.01   100.01  101.01  102.01  103.01];
    ##     clTRef = [-0.918 -0.81823    -0.71985    -0.62425    -0.53281    -0.44694    -0.368  -0.2974 -0.23652    -
0.18675    -0.14948    -0.1261 -0.118  -0.118  -0.12674    -0.15355    -0.19981    -0.26693    -0.32584    -0.27361    -
0.22424    -0.17767    -0.13384    -0.092693   -0.054164   -0.018199   0.015261    0.046271    0.074888    0.10117
0.12517 0.14694 0.16655 0.18404 0.19946 0.21287 0.22433 0.23388 0.24158 0.24748 0.25163 0.25407 0.25486 0.25405 0.25169
0.24782 0.2425  0.23576 0.22766 0.21823 0.20754 0.19561 0.1825  0.16825 0.1529  0.1365  0.11908 0.10069
0.081362    0.061145    0.040075    0.018191    -0.0044701  -0.02787    -0.051972   -0.076739   -0.10214    -
0.12813    -0.15469    -0.18178    -0.20936    -0.2374 -0.26588    -0.29477    -0.32403    -0.35363    -0.38355    -
0.41376    -0.44423    -0.47495    -0.50587    -0.53699    -0.56828    -0.59972    -0.63128    -0.66295    -0.69471    -
0.72655    -0.75844    -0.79037    -0.82234    -0.85432    -0.88632    -0.91832    -0.95032    -0.9823 -1.0143 -1.0462 -
1.078  -1.1098 -1.1414 -1.1729 -1.2043 -1.2355 -1.2664];
```

```
    ##     cdTRef
=[0.0055  0.0055207   0.0055828   0.0056864   0.0058314   0.0060178   0.0062456   0.0065148   0.0068254   0.0071775   0.
007571    0.0080059   0.0084822   0.0084872   0.0094224   0.051662    0.093885    0.13607 0.17821 0.22027 0.26224
0.30412 0.34586 0.38747 0.42892 0.47019 0.51128 0.55215 0.5928  0.63321 0.67335 0.71322 0.7528  0.79206
0.831   0.8696  0.90784 0.94571 0.98318
1.0203  1.0569  1.0931  1.1289  1.1642  1.199   1.2333  1.2671  1.3004  1.3332  1.3654  1.397   1.4281  1.4585  1.4884
1.5176  1.5463  1.5742  1.6016  1.6282  1.6542  1.6795  1.7041  1.7281  1.7512  1.7737  1.7954  1.8164  1.8367  1.8561
1.8749  1.8928  1.9099  1.9263  1.9418  1.9566  1.9705  1.9837  1.996   2.0075  2.0181  2.0279  2.0369  2.045   2.0523
2.0587  2.0643  2.069   2.0729  2.0759  2.078   2.0793  2.0797  2.0793  2.078   2.0758  2.0728  2.0689  2.0642  2.0586
2.0522  2.0449  2.0367  2.0277  2.0179  2.0072];
        alphaTRef = [-30.08    -25.08  -20.08  -15.08  -10.08  -
5.08   0.03    2.03    4.03    6.03    8.03    10.03   12.03   14.03   16.03   18.03   20.03   22.03   24.04   26.04   2
8.04   30.04   32.04   34.04   36.04   38.04   40.04   42.04   44.04   46.04   48.04   50.04   52.04   54.04   56.04   5
8.04   60.04   62.04   64.04   66.04   68.04   70.04   72.04   74.04   76.04   78.04   80.04   82.04   84.04   86.04   8
8.04   90.04   92.04];
    ##     clTRef = [-1.6268    -1.6914 -1.7144 -1.6824 -1.5179 -1.3968 -1.5264 -1.4603 -1.3452 -1.1924 -1.0129 -
0.81788    -0.62831    -0.4349 -0.25871    -0.11085    -0.00244    0.05542 0.05142 -0.02556    -0.14049    -
0.03946    0.05039 0.12955 0.19828 0.25226 0.29503 0.32773 0.35117 0.36631 0.37396 0.37481 0.36986 0.35954 0.34459
0.32563 0.30317 0.27773 0.24984 0.21988 0.1882  0.15518 0.12112 0.086263    0.05084 0.015025    -0.021018   -
0.057194   -0.093405   -0.12961    -0.16578    -0.20193    -0.23807];
        clTRef = [-1.6268  -1.6914 -1.7144 -1.6824 -1.5179 -1.3968 -1.5264 -1.4603 -1.3452 -1.1924 -1.0129 -
0.81788    -0.62831    -0.4349 -0.25871    -0.11085    -0.00244    0.05542 0.08    0.1
0.125   0.15    0.175   0.19    0.225   0.25226 0.29503 0.32773 0.35117 0.36631 0.37396 0.37481 0.36986 0.35954 0.34459
0.32563 0.30317 0.27773 0.24984 0.21988 0.1882  0.15518 0.12112 0.086263    0.05084 0.015025    -0.021018   -
0.057194   -0.093405   -0.12961    -0.16578    -0.20193    -0.23807];
        cdTRef = [1.0427   0.9327  0.79918 0.64163 0.44179 0.232   0.10389 0.10307 0.10241 0.10192 0.1016  0.10144
0.10145 0.10163 0.10197 0.10247 0.10314 0.10398 0.10957 0.19403 0.27835 0.36237 0.44596 0.52899 0.61071 0.67836 0.74215
0.80208 0.85816 0.91041 0.95889
1.0036  1.0446  1.0821  1.116   1.1465  1.1738  1.1979  1.219   1.2373  1.253   1.2661  1.277   1.2858  1.2927  1.298
1.3016  1.3041  1.3053  1.3057  1.3053  1.3042  1.3026];
```

```
        cmTRef=[0.23565    0.23965 0.23504 0.21838 0.1782  0.1468  0.17748 0.1663  0.1428  0.10899 0.067164    0.01985
-0.027209   -0.073915   -0.11474    -0.14718    -0.16899    -0.17819    -0.17331    -0.15739    -0.1354 -0.15905    -
0.18002    -0.19848    -0.21438    -0.22375    -0.23069    -0.23551    -0.23843    -0.23969    -0.2395 -0.23802    -
0.2355 -0.23204    -0.22781    -0.22294    -0.21754    -0.21172    -0.20559    -0.19922    -0.19268    -0.18603    -
0.17934    -0.17264    -0.16597    -0.15937    -0.15286    -0.14646    -0.14018    -0.13403    -0.12803    -0.12218    -
0.11646];

        alphaWIRef = [-20 -14 -10 0 10 14 20 30 40 45 50 60 70 80 90];
        cmWIRef = [0.030821866 0.030865173 0.026313397 0 -0.044732776 -0.066037114 -0.097207425 -0.148525614 -
0.198303483 -0.21071074 -0.229463675 -0.261780399 -0.298402573 -0.326035348 -0.3520075];

        alphaWORef = [-30 -20 -14 -10 0 10 14 20 30 40 50 60 70 80 90 100 110 120 130];
        cmWORef = [0.1331 0.1474 0.1132 0.0804 0.0000 -0.0814 -0.1141 -0.1474 -0.1332 -0.1837 -0.2366 -0.2873 -0.3313 -
0.3666 -0.3953 -0.4225 -0.4418 -0.4442 -0.4248];

        %-------------------------------------------------------------------------------------------------------
        %Thrust Parameters
        Zthr = 0.195;       %Thrust veritcal distance from C.G [m]

        %-------------------------------------------------------------------------------------------------------
        %Wing Parameters
        XwI = 1.70625+0.44375 - xcg;     %Wing horizontal distance from C.G [m]
        XwO = 1.815625+(ACw*1.2146) - xcg;
        Zw = -0.02;    %Wing vertical distance from C.G [m]

        %-------------------------------------------------------------------------------------------------------
        %Tail Parameters
        Xt = 5.534375+(0.25*0.842)-xcg;           %Tail horizontal distance from C.G [m]
        Zt = 0.45;             %Tail vertical distance from C.G [m]
        delta_e = -30;      %Elevator deflection (Negative implies upward elevator deflection) [deg]
        delta_tab = 0;       %Tab deflection (Negative implies downward tab deflection) [deg]
```

```
b_tab = 0;              %Span of the trim tab [m]
b_tail = 2.66;         %Span of an elevator (one half of the entire horizontal tail assembly) [m]
Sstab = 2.13;         %Area of the horizontal stabilizer [m^2]
Se = 1.04;              %Area of the elevator [m^2]
ARt = 3;                %Aspect ratio of the horizontal tail
et = 0.75;               %Oswalds factor of the horizontal tail

%-------------------------------------------------------------------------------------------------------
%Wing Lift and Drag Forces
LwI = (0.5*rhoalt*SrefI*(Vt^2)*CLwMax);      %Inner wing section lift force[N]
LwO = (0.5*rhoalt*SrefO*(V^2)*CLwO);             %Outer wing section lift force [N]
Lw = LwI + LwO;                                          %Total wing lift [N]
DwI = 0.5*rhoalt*SrefI*(Vt^2)*CDwI;              %Inner wing section drag force [N]
DwO = 0.5*rhoalt*SrefO*(V^2)*CDwO;             %Outer wing section drag force [N]
Dw = DwI + DwO;                                          %Total wing drag [N]

CMwI = interp1(alphaWIRef , cmWIRef, alpha_wingI, "Pchip");
CMwO = interp1(alphaWORef, cmWORef, alpha_wing, "Pchip");
MwI = 0.5*rhoalt*SrefI*(Vt^2)*CMwI*1.33;
MwO = 0.5*rhoalt*SrefO*(V^2)*CMwO*1.33;

%-------------------------------------------------------------------------------------------------------
%Fuselage Lift and Drag Forces
Lf = 0.5*rhoalt*Sref*(V^2)*CLf;          %Wing  lift force [N]
Df = 0.5*rhoalt*Sref*(V^2)*CDf;         %Wing drag force [N]

%-------------------------------------------------------------------------------------------------------
%Tail Angle of Attack and Slopes
Vr = theta_dotPre * Xt;
tailAngSmooth = ((-14/90)*(gamma*(180/pi))) + 14.75; %25m/s-13.5, 30m/s-14, 35m/s-14.5, 40m/s-15.5/14.6
```

```
        if gamma*(180/pi) < 90
             VtailX = (Vt*cosd(tailAngSmooth)) + (V*cosd(alpha_wing));
             VtailZ = (Vt*sind(tailAngSmooth)) + (V*sind(alpha_wing)) + Vr;
        else
             VtailX = (Vt*cosd(0)) + (V*cosd(alpha_wing));
             VtailZ = (Vt*sind(0)) + (V*sind(alpha_wing)) + Vr;
        end

        Vtail = sqrt(VtailX^2 + VtailZ^2);
        alpha_tail = atan(VtailZ/VtailX);

        %-------------------------------------------------------------------------------------------------------
        %Tail Coefficients of Lift and Drag
        CLt = interp1(alphaTRef, clTRef, (alpha_tail*(180/pi)), "pchip");
        CDt = interp1(alphaTRef, cdTRef, (alpha_tail*(180/pi)), "Pchip");
        CMt = interp1(alphaTRef, cmTRef, (alpha_tail*(180/pi)), "Pchip");

        %-------------------------------------------------------------------------------------------------------
        %Tail Lift and Drag Forces
        Lt = 0.5*rhoalt*Sstab*((0.925*Vt)^2)*CLt;          %Tail lift force [N]
        Dt = 0.5*rhoalt*Sstab*((0.925*Vt)^2)*CDt;         %Tail drag force [N]
        Mt = 0.5*rhoalt*Sstab*0.84*((0.925*Vt)^2)*CMt;

        %-------------------------------------------------------------------------------------------------------
        %Moments
        Mthrust = T*Zthr;        %Moment due to propeller thrust [Nm]
        MwingI = (LwI*cosd(alpha_wingI)*XwI) + (LwI*sind(alpha_wingI)*Zw) - (DwI*cosd(alpha_wingI)*Zw) +
(DwI*sind(alpha_wingI)*XwI)-MwI;       %Moment due to inner wing section aerodynamic forces [Nm]
        MwingO = (LwO*cosd(alpha_wing)*XwO) + (LwO*sind(alpha_wing)*Zw) - (DwO*cosd(alpha_wing)*Zw) +
(DwO*sind(alpha_wing)*XwO)-MwO;    %Moment due to inner wing section aerodynamic forces [Nm]
```

```
        Mfuse = (-Lf*cos(alphaFuse)*Xf) -
(Df*sin(alphaFuse)*Xf);
                 %Moment due to fuselage aerodynamic forces [Nm]
        Mtail = (Lt*cosd(alpha_tail)*Xt) + (Lt*sind(alpha_tail)*Zt) - (Dt*cosd(alpha_tail)*Zt) +
(Dt*sind(alpha_tail)*Xt) - Mt;                                          %Moment due to tail aerodynamic forces [Nm]

        Mtot = Mthrust + MwingI + MwingO + Mfuse + Mtail + Mnp;         %Total moment acting on airframe [Nm]

        %-------------------------------------------------------------------------------------------------
        %Angular Kinematics
        theta_dbl = (-Mtot/Iyy);  %Angular acceleration (assumed to be constant over time interval) [rad/s^2]
        theta_dot = ((-Mtot*t)/Iyy) + theta_dotPre;   %Angular velocity [rad/s]
    ##     theta = -theta_dot*t;     %Change in angle over time interval (assuming constant angular acceleration) [rad]
        theta = (0.5*(theta_dot+theta_dotPre)*t) + thetaPre;      %Change in pitch angle over segment [rad]

    endfunction
```

wingCoefficientsFunc.m

```
%%Wing Aerodynamic Coefficients Function

function [ACL1 S1 CL1max CD1max CL CD CM alpha AC] = wingCoefficientsFunc(AR, wMAC);

    %-------------------------------------------------------------------------------------------------------
    %NACA0012 Reference Data
    NACAalpha = [0 10 14 20 30 40 45 50 60 70 80 90 100 110 120 130 140 150 160 170 180 190 200 210 220 230 240 250 260
270 280 290 300 310 315 320 330 340 343 346 346 350 360];                                    %NASA reference
angle of attack test data for coefficient of lift
    NACACL = [0 1.02 1.33 0.75 1 1.15 1.15 1.13 0.98 0.72 0.4 0.08 -0.22 -0.54 -0.8 -0.98 -1.08 -0.98 -0.7 -0.78 0 0.77
0.68 0.95 1.07 1 0.8 0.58 0.3 -0.05 -0.4 -0.7 -1 -1.15 -1.18 -1.15 -0.94 -0.6 -0.6 -0.71 -1.33 -1.1 0];     %NASA
reference coefficient of lift data
    NACAalpha2 = [0 10 15 20 30 40 50 60 70 80 90 100 110 120 130 140 150 160 170 175 180 185 190 200 210 220 230 240
250 260 270 280 290 300 310 320 330 340 345 350 360];
    NACACD = [0.006 0.006 0.2 0.3 0.6 1 1.38 1.67 1.9 2.03 2.08 2.03 1.9 1.67 1.4 1.08 0.7 0.38 0.19 0.06 0.014 0.06
0.19 0.38 0.65 1.05 1.4 1.66 1.87 2 2.08 2.05 1.95 1.7 1.4 1 0.6 0.34 0.22 0.08
0.006];                              %NASA reference angle of attack test data for coefficient of drag
    NACAalpha3 = [0 10 13 15 20 30 40 50 60 70 80 90 100 110 120 130 140 150 155 160 170 172 175 180 188 190 200 207 210
220 230 240 250 260 270 280 290 300 310 320 330 340 345 350 360];
    NACACM = [0 0 0 -0.07 -0.08 -0.18 -0.27 -0.35 -0.41 -0.46 -0.51 -0.55 -0.58 -0.599 -0.6 -0.59 -0.56 -0.46 -0.38 -
0.35 -0.39 -0.4 -0.3 0 0.4 0.35 0.34 0.4 0.44 0.55 0.59 0.6 0.6 0.59 0.57 0.54 0.48 0.42 0.34 0.26 0.18 0.09 0.08 0 0];

    %-------------------------------------------------------------------------------------------------------
    %Infinite Aspect Ratio%


    %Infinite Aspect Ratio Variables
    A0 = 0;                                                  %Zero lift angle of attack, for all aspect ratios
[deg]
```

```
    ACL1_prime = [14.3 10];                                 %Angle of attack at maximum pre-stall lift [LE TE] [deg]
    CL1max_prime = [1.33 0.77];                             %Maximum pre-stall lift coefficient, at alpha = ACL1_prime [LE
TE]
    S1_prime = [0.115 0.11];                                    %Slope of linear segment of pre-stall lift coefficient [LE
TE] [1/deg]
    CD0 = [0.006 0.014];                                     %Minimum drag coefficient, at alpha = A0, for all aspect
ratios [LE TE]
    ACD1_prime = [14 10];                                   %Angle of attack at maximum pre-stall drag [LE TE] [deg]
    CD1max_prime = [0.008 0.19];                             %Maximum pre-stall drag coefficient, at alpha = ACD1_prime

    %Infinite Aspect Ratio Calculations
    alpha_linear = 0:0.01:ACL1_prime(1);
    for i = 1:length(alpha_linear)
         CL1_prime(i) = alpha_linear(i)*S1_prime(1);
    end

    %-----------------------------------------------------------------------------------------------------------------
    %Corrections for Aspect Ratio%

    %Aspect Ratio Corrections in the Pre-Stall Regime

    %Finite Aspect Ratio Variables
    ##AR = inf;

    %Finite Aspect Ratio Calculations
    ACL1 = [ACL1_prime + (18.2*CL1max_prime*(AR^-0.9))];                    %Angle of attack at maximum pre-stall lift
corrected for aspect ratio
    S1 = [(S1_prime)./(1+(18.2*S1_prime*(AR^-0.9)))];                               %Sloper of linear segment of pre-
stall lift curve corrected for aspect ratio
    ACD1 = [ACD1_prime + (18.2*CL1max_prime*(AR^-0.9))];                    %Angle of attack at maximum pre-stall drag
corrected for aspect ratio [deg]
```

```
    CD1max = [CD1max_prime + (0.28*(CL1max_prime.^2)*(AR^-0.9))];       %Maximum pre-stall drag coefficient, at alpha =
ACD1 corrected for aspect ratio
    CL1max = [CL1max_prime*(0.67+(0.33*exp(-((4/AR)^2))))];                 %Maximum pre-stall lift coefficient, at
alpha = ACL1 corrected for aspect ratio

    for i = 1:length(alpha_linear)
         alpha1(i) = alpha_linear(i) + (18.2*CL1_prime(1,i)*(AR^-0.90));
    end
    %-------------------------------------------------------------------------------------------------------------
    %Coefficient Calcualtions%

    %-------------------------------------------------------------------------------------------------------------
    %Alpha Variation
    ##alpha2 = [alpha1 round(alpha1(end))];
    alpha2 = alpha1;
    alpha3 = alpha2(end)+0.01:0.01:180;
    ##alpha4 = alpha3(end):0.01:360;
    alpha180 = [alpha2 alpha3];
    alpha360 = 360-fliplr(alpha180(1:end-1));

    %-------------------------------------------------------------------------------------------------------------
    %Pre-Stall and Post-Stall Variables
    rNose = 0.0159;
    tc = 0.12;                          %Thickness to chord
    CL0_pos = 92;                           %Zero lift coefficient post-stall [TE first]
    polyCL = [1.63117714367481E-09 -1.4650560200664E-06 5.24789180743336E-04...
         -9.37118377327748E-02 8.3424091410401 -2.96205426040171E+02 1.63117714367481E-09];
    polyCD = [0.000126333333333334 -0.00754500000000001 0.167216666666667 -1.037];
    polyCD180 = [-0.00000680327868852427 0.00357991803278674 -0.648274590163911 40.3429098360644];

    %-------------------------------------------------------------------------------------------------------------
```

```
    %Pre-Stall and Post-Stall Calculations
    F1 = 1.19*(1-(tc^2));                   %Empirical function of t/c (pre-stall regime)
    F2 = 0.65 + (0.35*exp(-((9/AR)^2.3)));      %Empirical function of aspect ratio (pre-stall regime)
    CL2max = (F1*F2);                       %Maximum lift coefficient in the post-stall regime [LE first]
    CL2max_neg = 1.02*CL2max;               %Maximum lift coefficient in the post-stall regime [TE first]
    G1 = 2.3*exp(-((0.65*tc)^0.9));         %Empirical function of t/c (post-stall regime)
    G2 = 0.52 + (0.48*exp(-((6.5/AR)^1.1)));    %Empirical function of aspect ratio (post-stall regime)
    CD2max = G1*G2;                     %Maximum drag coefficeint in the post-stall regime

    RCL1 = [S1.*(ACL1-A0)-CL1max];          %Reduction from extension of linear segment of lift curve to CL1max
    N1 = [1+(CL1max./RCL1)];                %Exponent defining shape of lift curve at ACL1max
    M = 2;
    RCL2 = -0.032*(41-CL0_pos)-CL2max;          %Reduction fro ectension of linear segmemnt of lift curve to CL2max [LE
first]
    RCL3 = -0.032*(38-CL0_pos)-CL2max_neg;      %Reduction fro ectension of linear segmemnt of lift curve to CL2max [TE
first]
    N2 = 1+(CL2max/RCL2);                   %Exponent defining shape of lift curve at CL2max [LE first]
    N3 = 1+(CL2max_neg/RCL3);               %Exponent defining shape of lift curve at CL2max [TE first]


    CL12diff = 1;
    CL34diff = 1;
    alpha12 = ACL1(1);
    alpha34 = (180-ACL1(2));


    while CL12diff > 0.00001
         CL1 = (S1(1)*(alpha12-A0)) - (RCL1(1)*(((alpha12-A0)/(ACL1(1)-A0)).^N1(1)));
         CL2 = (-0.032*(alpha12-CL0_pos)) - (RCL2*(((CL0_pos-alpha12)/51).^N2));
         CL12diff = abs(CL1-CL2);
         alpha12 = alpha12 + (CL1-CL2);
```

```
    end

    while CL34diff > 0.00001
         if AR == inf
              CL3 =
(polyCL(1)*alpha34^6)+(polyCL(2)*alpha34^5)+(polyCL(3)*alpha34^4)+(polyCL(4)*alpha34^3)+(polyCL(5)*alpha34^2)+(polyCL(6)
*alpha34^1)+(polyCL(7));
         else
              CL3 = (S1(2)*(alpha34-180-A0)) + (RCL1(2)*(((A0-(alpha34-180))/(ACL1(2)-A0)).^N1(2)));
         end
         CL4 = (-0.032*(alpha34-CL0_pos)) + (RCL3*(((alpha34-CL0_pos)/50)^N3));
         CL34diff = abs(CL4-CL3);
         alpha34 = alpha34 - (CL4-CL3);
    end

    alpha56 = 180 + (180-alpha34);
    alpha78 = 360 - alpha12;

    alphaCD12 = 0;
    alphaCD34 = ACD1(1);
    alphaCD56 = 180-ACD1(2);
    alphaCD78 = alphaCD56;
    alphaCDf = 180;
    CD12diff = 1;
    CD34diff = 1;
    CD56diff = 1;
    CD78diff = 1;
    CDfdiff = 1;

    while CD12diff > 0.0001
         CD1 = CD0(1) + ((CD1max(1)-CD0(1))*(((alphaCD12-A0)/(ACD1(1)-A0))^M));
```

```
     CD2 = (polyCD(1)*alphaCD12^3)+(polyCD(2)*alphaCD12^2)+(polyCD(3)*alphaCD12)+(polyCD(4));
     CD12diff = abs(CD2-CD1);
     alphaCD12 = alphaCD12 + (CD1-CD2);
end

while CD34diff > 0.0001
     CD3 = (polyCD(1)*alphaCD34^3)+(polyCD(2)*alphaCD34^2)+(polyCD(3)*alphaCD34)+(polyCD(4));
     CD4 = CD1max(1)+(CD2max-CD1max(1))*sind(((alphaCD34-ACD1(1))/(90-ACD1(1)))*90);
     CD34diff = abs(CD4-CD3);
     alphaCD34 = alphaCD34 + (CD3-CD4);
end

while CD56diff > 0.0001
     CD5 = CD1max(1)+(CD2max-CD1max(1))*sind(((alphaCD56-ACD1(1))/(90-ACD1(1)))*90);
     CD6 = (polyCD180(1)*alphaCD56^3)+(polyCD180(2)*alphaCD56^2)+(polyCD180(3)*alphaCD56)+(polyCD180(4));
     CD56diff = abs(CD5-CD6);
     alphaCD56 = alphaCD56 - (CD6-CD5);
end

while CD78diff > 0.0001
     CD7 = (polyCD180(1)*alphaCD78^3)+(polyCD180(2)*alphaCD78^2)+(polyCD180(3)*alphaCD78)+(polyCD180(4));
     CD8 = CD0(2) + ((CD1max(2)-CD0(2))*(((180-alphaCD78-A0)/(ACD1(2)-A0))^M));
     CD78diff = abs(CD7-CD8);
     alphaCD78 = alphaCD78 + (CD8-CD7);

end

while CDfdiff > 0.0001
     CD1f =  CD1max(1)+(CD2max-CD1max(1))*sind(((alphaCDf-ACD1(1))/(90-ACD1(1)))*90);
     CD2f =  CD0(1) + ((CD1max(1)-CD0(1))*(((180-alphaCDf-A0)/(ACD1(1)-A0))^M));
     CDfdiff = abs(CD2f-CD1f);
```

```
        alphaCDf = alphaCDf - (CD2f - CD1f);
    end

    ##h1 = waitbar(0, "Calculating Wing Aerodynamic Data");
    for i = 1:length(alpha180)
        %-------------------------------------------------------------------------------------------------------
        %Lift Coefficient
        if alpha180(i) >= A0 && alpha180(i) <= alpha12
            CL180(i) = (S1(1)*(alpha180(i)-A0)) - (RCL1(1)*(((alpha180(i)-A0)/(ACL1(1)-A0))^N1(1)));
        elseif alpha180(i) > alpha12 && alpha180(i) <= CL0_pos
            CL180(i) = (-0.032*(alpha180(i)-CL0_pos)) - (RCL2*(((CL0_pos-alpha180(i))/51)^N2));
        elseif alpha180(i) > CL0_pos && alpha180(i) <= alpha34
            CL180(i) = (-0.032*(alpha180(i)-CL0_pos)) + (RCL3*(((alpha180(i)-CL0_pos)/50)^N3));
        elseif alpha180(i) > alpha34 && alpha180(i) <= 180
            if AR == inf
                CL180(i) =
(polyCL(1)*alpha180(i)^6)+(polyCL(2)*alpha180(i)^5)+(polyCL(3)*alpha180(i)^4)+(polyCL(4)*alpha180(i)^3)+(polyCL(5)*alpha
180(i)^2)+(polyCL(6)*alpha180(i)^1)+(polyCL(7));
            else
                CL180(i) = (S1(2)*(alpha180(i)-180-A0)) + (RCL1(2)*(((A0-(alpha180(i)-180))/(ACL1(2)-A0)).^N1(2)));
            end
        end
        %-------------------------------------------------------------------------------------------------------
        %Drag Coefficient
        if AR == inf
            if alpha180(i) >= ((2*A0)-ACD1) && alpha180(i) <= alphaCD12
                CD180(i) = CD0(1) + ((CD1max(1)-CD0(1))*(((alpha180(i)-A0)/(ACD1(1)-A0))^M));
            elseif alpha180(i) > alphaCD12 && alpha180(i) < alphaCD56
                    if alpha180(i) <= alphaCD34
                        CD180(i) =
(polyCD(1)*alpha180(i)^3)+(polyCD(2)*alpha180(i)^2)+(polyCD(3)*alpha180(i))+(polyCD(4));
```

```
                    else
                         CD180(i) = CD1max(1)+(CD2max-CD1max(1))*sind(((alpha180(i)-ACD1(1))/(90-ACD1(1)))*90);
                    end
               elseif alpha180(i) >= alphaCD56   && alpha180(i) < alphaCD78
                    CD180(i) =
(polyCD180(1)*alpha180(i)^3)+(polyCD180(2)*alpha180(i)^2)+(polyCD180(3)*alpha180(i))+(polyCD180(4));
               elseif alpha180(i) >= alphaCD78 && alpha180(i) <= 180
                    CD180(i) = CD0(2) + ((CD1max(2)-CD0(2))*(((180-alpha180(i)-A0)/(ACD1(2)-A0))^M));
               end
          else
               if alpha180(i) >= ((2*A0)-ACD1) && alpha180(i) <= ACD1(1)
                    CD180(i) = CD0(1) + ((CD1max(1)-CD0(1))*(((alpha180(i)-A0)/(ACD1(1)-A0))^M));
               elseif alpha180(i) > ACD1(1) && alpha180(i) < alphaCDf
                    CD180(i) = CD1max(1)+(CD2max-CD1max(1))*sind(((alpha180(i)-ACD1(1))/(90-ACD1(1)))*90);
               elseif alpha180(i) >=alphaCDf && alpha180(i) <=180
                    CD180(i) = CD0(1) + ((CD1max(1)-CD0(1))*(((180-alpha180(i)-A0)/(ACD1(1)-A0))^M));
               end
          end
     ##  waitbar(i/length(alpha180), h1);
     end

     for j = 1:length(alpha180)
          %-------------------------------------------------------------------------------------------------------
          %Normal Force
          CN180(j) = 2.08*((1/(0.56+0.44*sind(alpha180(j))))-(0.41*(1-exp(-17/AR))))*(sind(alpha180(j)));
          %-------------------------------------------------------------------------------------------------------
          %Quarter Chord Pitching Moment
          CM180(j) = -(0.25-0.175*(1-(alpha180(j)/90)))*CN180(j);
     end

     ##close(h1);
```

```
CL_temp = fliplr(CL180);
CD_temp = fliplr(CD180);
CN_temp = fliplr(CN180);
CM_temp = fliplr(CM180);

for k = 1:length(alpha360)
     CL360(k) = -CL_temp(k);
     CD360(k) = CD_temp(k);
     CN360(k) = -CN_temp(k);
     CM360(k) = -CM_temp(k);
end

alpha = [alpha180 alpha360];
CL = [CL180 CL360];
CD = [CD180 CD360];
CN = [CN180 CN360];
CM = [CM180 CM360];

for m = 1:length(alpha)
     alphaCheck = alpha(m);
     if ((alphaCheck) == (180))
          AC(m) = 0.75;
     else
          AC(m) = (CM(m)/((-CL(m)*cosd(alpha(m)))-(CD(m)*sind(alpha(m))))) + 0.25;
     end
end


alphaR = -flip(alpha180(: , 2:end));
alpha = [alphaR alpha180];
```

```
    CL = [-flip(CL360) CL180];
    CD = [flipud(CD360) CD180];
    CN = [-flip(CN360) CN180];
    CM = [-flip(CM360) CM180];

    ACR = flip(AC);
    for i = 1:round(length(alpha)/2)
         AC180(i) = AC(i);
    end

    for j =  round(length(alpha)/2)+1 : length(alpha)-1
         AC360(j-round(length(alpha)/2)+1) = AC(j);
    end

    AC = [AC360 AC180];
    AC(18001) = 0.29;

endfunction
```

fuselageCoefficients330Func.m

```
%%Fuselage Aerodynamic Coefficients

function[CL_Sref CD_Sref lAC_Sref alpha] = fuselageCoefficients330Func()

    %-------------------------------------------------------------------------------------------------------
    %Reference Data
    NASA_Alpha = [0 5 10 15 20 25 30 35 40 45 50 55 60 65 70 75 80 85 90];
    NASA_CL = [0 0.011 0.033 0.056 0.09 0.13 0.18 0.225 0.265 0.295 0.31 0.32 0.31 0.29 0.26 0.22 0.17 0.1 0];
    NASA_CD = [0 0 0.001 0.01 0.026 0.055 0.09 0.14 0.205 0.28 0.36 0.45 0.55 0.62 0.68 0.73 0.755 0.77 0.77];
    NASA_CM = [0 0.05 0.085 0.115 0.135 0.15 0.15 0.14 0.12 0.1 0.07 0.04 0 -0.04 -0.085 -0.13 -0.175 -0.22 -0.28];
    L330 = [0 0.280 0.560 0.839 1.119 1.399 1.679 1.958 2.238 2.518 2.798 3.077 3.357 3.637 3.917 4.196 4.476 4.756
5.036 5.315 5.595];
    A330 = [0.333 0.561 0.640 0.678 0.694 0.680 0.660 0.614 0.569 0.603 0.590 0.532 0.461 0.386 0.315 0.253 0.191 0.143
0.099 0.062 0.033];
    r330 = [0.326 0.423 0.451 0.464 0.470 0.465 0.458 0.442 0.426 0.438 0.433 0.412 0.383 0.350 0.317 0.284 0.246 0.213
0.177 0.140 0.102];
    Cn0_SB330 = [0.589685226 0.736040609 0.806965174 0.837438424 0.857142857 0.874371859 0.917450366 0.962264151
1.020166074 1.262820513 1.481741573 1.580152672 1.642140468 1.685185185 1.757322176 1.837708831 1.991404011 2.147766323
2.401746725 2.861445783 3.932038835];
    Cn0_Newt330 = [0.598112547 0.74914745 0.819237246 0.84873314 0.86761001 0.883990609 0.924444137 0.965776431
1.019760725 1.226406979 1.395248378 1.466947704 1.510978185 1.541079695 1.590713059 1.644905857 1.74555729 1.844376022
1.998033358 2.256380023 2.764953794];

    %-------------------------------------------------------------------------------------------------------
    %Variables
    Ar = 0.694;
    X = 5.6;
    mu = 0.625;
    CDn = 1.2;
```

```
    l = 5.6;
    xm = 2.15;
    Sref = 9.81;
    MAC = 1.366;

    %-------------------------------------------------------------------------------------------------------
    %Polynomials
    polySB = [0.014356786688558 -0.0949312064225191 0.174464732106765 0.105940339560774 -0.627235332087879
0.685194491588983 0.589770485560822];
    polySB2 = [0.0568294896277007 -1.2632421727596 11.5010299532438 -54.6900086474994 142.684449647985 -192.485066667386
105.44664010547];
    polyNewt = [0.0114556126559397 -0.0690901246216395 0.0864198890580485 0.248568402519923 -0.741675630259316
0.724538554036178 0.598197688076809];
    polyNewt2 = [0.0248460849593586 -0.551494082773233 4.99678565676874 -23.5129178008289 60.1682923406902 -
78.4283646740802 41.2329550877902];
    polyArea = [-0.0516157707869556 0.433746380274154 -1.43751708834283 2.41170937359216 -2.29524855160416
1.293177703023 0.33313242403353];
    polyArea2 = [0.000621170466574574 -0.00949722861199657 0.0231881676931921 0.363620910574166 -2.84727769390764
7.48978677508495 -6.13487461676752];
    polyRadius = [-0.027803243988994 0.22822075333896 -0.74119841302878 1.21718327276252 -1.10928370844649
0.574885465012449 0.325629736062586];
    polyRadius2 = [0.00012381603948808 -0.00156788914211277 -0.00414570567955748 0.1624371222469 -1.02395359328614
2.57871452715492 -1.86136214634898];
    polydArea = [-0.309694624721734 2.16873190137077 -5.7500683533713 7.23512812077647 -4.59049710320833
1.293177703023];
    polydArea2 = [0.00372702279944744 -0.0474861430599828 0.0927526707727686 1.0908627317225 -5.69455538781527
7.48978677508495];

    %-------------------------------------------------------------------------------------------------------
    %Calculations
    alpha = 0:0.01:180;
```

```
    fuse_l = 0:0.01:l;
    ##fuse_l = [0 .27975 0.56 0.839 1.119 1.399 1.679 1.958 2.238 2.518 2.798 3.077 3.357 3.637 3.917 4.196 4.476 4.756
5.036 5.315 5.595];
    l2d = l/(0.508*2);

    for i = 1:length(fuse_l)
         fuse(i) = fuse_l(i);
         if fuse(i) < 2.238
              Cn0_SB(i) = (polySB(1)*fuse_l(i)^6) + (polySB(2)*fuse_l(i)^5) + (polySB(3)*fuse_l(i)^4) +
(polySB(4)*fuse_l(i)^3) + (polySB(5)*fuse_l(i)^2) + (polySB(6)*fuse_l(i)) + polySB(7);
              Cn0_Newt(i) = (polyNewt(1)*fuse_l(i)^6) + (polyNewt(2)*fuse_l(i)^5) + (polyNewt(3)*fuse_l(i)^4) +
(polyNewt(4)*fuse_l(i)^3) + (polyNewt(5)*fuse_l(i)^2) + (polyNewt(6)*fuse_l(i)) + polyNewt(7);
              A(i) = (polyArea(1)*fuse_l(i)^6) + (polyArea(2)*fuse_l(i)^5) + (polyArea(3)*fuse_l(i)^4) +
(polyArea(4)*fuse_l(i)^3) + (polyArea(5)*fuse_l(i)^2) + (polyArea(6)*fuse_l(i)) + polyArea(7);
              dA(i) =  (polydArea(1)*fuse_l(i)^5) + (polydArea(2)*fuse_l(i)^4) + (polydArea(3)*fuse_l(i)^3) +
(polydArea(4)*fuse_l(i)^2) + (polydArea(5)*fuse_l(i)) + polydArea(6);
    ##      dA(i) = (A(i)-A(i-1))/(fuse_l(i)-fuse_l(i-1));
              r(i) = (polyRadius(1)*fuse_l(i)^6) + (polyRadius(2)*fuse_l(i)^5) + (polyRadius(3)*fuse_l(i)^4) +
(polyRadius(4)*fuse_l(i)^3) + (polyRadius(5)*fuse_l(i)^2) + (polyRadius(6)*fuse_l(i)) + polyRadius(7);
              int1(i) = Cn0_SB(i)*dA(i);
              int2(i) = Cn0_Newt(i)*r(i);
              int3(i) = Cn0_SB(i)*dA(i)*(xm-fuse_l(i));
              int4(i) =  Cn0_Newt(i)*r(i)*(xm-fuse_l(i));
         else
              Cn0_SB(i) = (polySB2(1)*fuse_l(i)^6) + (polySB2(2)*fuse_l(i)^5) + (polySB2(3)*fuse_l(i)^4) +
(polySB2(4)*fuse_l(i)^3) + (polySB2(5)*fuse_l(i)^2) + (polySB2(6)*fuse_l(i)) + polySB2(7);
              Cn0_Newt(i) = (polyNewt2(1)*fuse_l(i)^6) + (polyNewt2(2)*fuse_l(i)^5) + (polyNewt2(3)*fuse_l(i)^4) +
(polyNewt2(4)*fuse_l(i)^3) + (polyNewt2(5)*fuse_l(i)^2) + (polyNewt2(6)*fuse_l(i)) + polyNewt2(7);
              A(i) = (polyArea2(1)*fuse_l(i)^6) + (polyArea2(2)*fuse_l(i)^5) + (polyArea2(3)*fuse_l(i)^4) +
(polyArea2(4)*fuse_l(i)^3) + (polyArea2(5)*fuse_l(i)^2) + (polyArea2(6)*fuse_l(i)) + polyArea2(7);
```

```
            dA(i) =  (polydArea2(1)*fuse_l(i)^5) + (polydArea2(2)*fuse_l(i)^4) + (polydArea2(3)*fuse_l(i)^3) +
(polydArea2(4)*fuse_l(i)^2) + (polydArea2(5)*fuse_l(i)) + polydArea2(6);
    ##      dA(i) = (A(i)-A(i-1))/(fuse_l(i)-fuse_l(i-1));
            r(i) = ((polyRadius2(1)*fuse_l(i)^6) + (polyRadius2(2)*fuse_l(i)^5) + (polyRadius2(3)*fuse_l(i)^4) +
(polyRadius2(4)*fuse_l(i)^3) + (polyRadius2(5)*fuse_l(i)^2) + (polyRadius2(6)*fuse_l(i)) + polyRadius2(7));
            int1(i) = Cn0_SB(i)*dA(i);
            int2(i) = Cn0_Newt(i)*r(i);
            int3(i) = Cn0_SB(i)*dA(i)*(xm-fuse_l(i));
            int4(i) = Cn0_Newt(i)*r(i)*(xm-fuse_l(i));
        end
    end

    for j = 1:length(fuse_l)
        if j == 1
            IntSB_temp(j) = 0;
            IntNewt_temp(j) = 0;
            IntSBM_temp(j) = 0;
            IntNewtM_temp(j) = 0;
        else
            IntSB_temp(j) = ((int1(j)+int1(j-1))/2)*(fuse_l(j)-fuse_l(j-1));
            IntNewt_temp(j) = ((int2(j)+int2(j-1))/2)*(fuse_l(j)-fuse_l(j-1));
            IntSBM_temp(j) = ((int3(j)+int3(j-1))/2)*(fuse_l(j)-fuse_l(j-1));
            IntNewtM_temp(j) = ((int4(j)+int4(j-1))/2)*(fuse_l(j)-fuse_l(j-1));
        end
    end

    IntSB = -sum(IntSB_temp);
    IntNewt = sum(IntNewt_temp);
    IntSBM = sum(IntSBM_temp);
    IntNewtM = sum(IntNewtM_temp);
    TotalA = sum(A);
```

```
    ##disp(IntSB)
    ##disp(IntNewt)
    ##disp(["Total Area = " num2str(TotalA) " m^2"])

    ##h2 = waitbar(0, "Calculating Fuselage Aerodynamic Data");
    for i =1:length(alpha)
         if alpha(i)<=90
              CN(i) = (((sind(2*alpha(i))*cosd(alpha(i)/2))/Ar)*(IntSB)) +
(((2*mu*CDn*(sind(alpha(i))^2))/(Ar))*(IntNewt));
              CN_Sref(i) = ((CN(i)*Ar)/Sref);
              CN_SB(i) = (((sind(2*alpha(i))*cosd(alpha(i)/2))/Ar)*(IntSB));
              CN_Newt(i) = (((2*mu*CDn*(sind(alpha(i))^2))/(Ar))*(IntNewt));
              Cm(i) = (((sind(2*alpha(i))*cosd(alpha(i)/2))/(Ar*X))*(IntSBM)) +
(((2*mu*CDn*(sind(alpha(i))^2))/(Ar*X))*(IntNewtM));
              Cm_Sref(i) = ((Cm(i)*Ar*max(r330))/(Sref*MAC));
              xAC(i) = (xm - ((Cm(i)/CN(i))*l))/l;
              xAC_Sref(i) = (xm - ((Cm_Sref(i)/CN_Sref(i))*l))/l;
              lAC_Sref(i) = xAC_Sref(i)*l;
         else
              CN(i) = (((sind(2*(180-alpha(i)))*cosd((180-alpha(i))/2))/Ar)*(IntSB)) + (((2*mu*CDn*(sind((180-
alpha(i)))^2))/(Ar))*(IntNewt));
              CN_Sref(i) = ((CN(i)*Ar)/Sref);
              CN_SB(i) = (((sind(2*(180-alpha(i)))*cosd((180-alpha(i))/2))/Ar)*(IntSB));
              CN_Newt(i) = (((2*mu*CDn*(sind((180-alpha(i)))^2))/(Ar))*(IntNewt));
              Cm(i) = (((sind(2*(180-alpha(i)))*cosd((180-alpha(i))/2))/(Ar*X))*(IntSBM)) + (((2*mu*CDn*(sind((180-
alpha(i)))^2))/(Ar*X))*(IntNewtM));
              Cm_Sref(i) = ((Cm(i)*Ar*max(r330))/(Sref*MAC));
              xAC(i) = (xm - ((Cm(i)/CN(i))*l))/l;
              xAC_Sref(i) = (xm - ((Cm_Sref(i)/CN_Sref(i))*l))/l;
              lAC_Sref(i) = xAC_Sref(i)*l;
```

```
        end
        CL(i) = CN(i)*cosd(alpha(i));
        CD(i) = CN(i)*sind(alpha(i));
        CL_Sref(i) = (CL(i)*Ar)/Sref;
        CD_Sref(i) = (CD(i)*Ar)/Sref;
    ##  waitbar(i/length(alpha), h2);
    end
    lAC_Sref(1) = lAC_Sref(2);

    alphaR = -flip(alpha);
    CN_SrefR = flipud(CN_Sref);
    CL_SrefR = flipud(CL_Sref);
    CD_SrefR = flipud(CD_Sref);
    Cm_SrefR = flipud(Cm_Sref);
    lAC_SrefR = flipud(lAC_Sref);

    alpha  = [alphaR(:,1:end-1) alpha];
    CN_Sref = [CN_SrefR(:,1:end-1) CN_Sref];
    CL_Sref = [CL_SrefR(:,1:end-1) CL_Sref];
    CD_Sref = [CD_SrefR(:,1:end-1) CD_Sref];
    Cm_Sref = [Cm_SrefR(:,1:end-1) Cm_Sref];
    lAC_Sref = [lAC_SrefR(:,1:end-1) lAC_Sref];

endfunction
```